energies

Special Issue Reprint

Heat Transfer Analysis

Recent Challenges and Applications—2nd Edition

Edited by
Andrzej Frąckowiak, Bartosz Ciupek, Łukasz Brodzik
and Wojciech Prokopowicz

mdpi.com/journal/energies

MDPI

Heat Transfer Analysis: Recent Challenges and Applications—2nd Edition

Heat Transfer Analysis: Recent Challenges and Applications—2nd Edition

Guest Editors

Andrzej Frąckowiak
Bartosz Ciupek
Łukasz Brodzik
Wojciech Prokopowicz

MDPI

Basel • Beijing • Wuhan • Barcelona • Belgrade • Novi Sad • Cluj • Manchester

Guest Editors

Andrzej Frąckowiak
Institute of Thermal Engineering
Poznan University of Technology
Poznan
Poland

Bartosz Ciupek
Department of Fuels and Renewable Energy
Poznan University of Technology
Poznan
Poland

Łukasz Brodzik
Institute of Thermal Engineering
Poznan University of Technology
Poznan
Poland

Wojciech Prokopowicz
Ministry of National Defense
Warsaw
Poland

Editorial Office

MDPI AG
Grosspeteranlage 5
4052 Basel, Switzerland

This is a reprint of the Special Issue, published open access by the journal *Energies* (ISSN 1996-1073), freely accessible at: https://www.mdpi.com/journal/energies/special_issues/434940DQJ8.

For citation purposes, cite each article independently as indicated on the article page online and as indicated below:

Lastname, A.A.; Lastname, B.B. Article Title. *Journal Name* **Year**, *Volume Number*, Page Range.

ISBN 978-3-7258-8403-2 (Hbk)
ISBN 978-3-7258-8404-9 (PDF)
https://doi.org/10.3390/books978-3-7258-8404-9

© 2026 by the authors. Articles in this reprint are Open Access and distributed under the Creative Commons Attribution (CC BY) license. The reprint as a whole is distributed by MDPI under the terms and conditions of the Creative Commons Attribution-NonCommercial-NoDerivs (CC BY-NC-ND) license (https://creativecommons.org/licenses/by-nc-nd/4.0/).

Contents

About the Editors . . . . . **vii**

Preface . . . . . **ix**

Artur Piasecki and Magdalena Piasecka
Correlation-Based Single-Phase Heat Transfer Assessment of Binary HFE/Ethyl Acetate Mixtures in Minichannels
Reprinted from: *Energies* **2026**, *19*, 2291, https://doi.org/10.3390/en19102291 . . . . . **1**

Janusz T. Cieśliński, Jacek Barański, Kamil Stasiak, Krzysztof Tesch and Paweł Dąbrowski
Comparison of Analytical and Numerical Methods for Predicting the Shell-Side Heat Transfer Coefficient in Heat Exchanger with Segmental Baffles
Reprinted from: *Energies* **2026**, *19*, 2114, https://doi.org/10.3390/en19092114 . . . . . **19**

Sabina Kordana-Obuch and Mariusz Starzec
SHAP-Based Insights into Environmental and Economic Performance of a Shower Heat Exchanger Under Unbalanced Flow Conditions: A Feasibility Study
Reprinted from: *Energies* **2026**, *19*, 1845, https://doi.org/10.3390/en19081845 . . . . . **38**

Chengkun Li, Yujia Cai, Han Wang, Zhihang Zhang, Fang Han, Xiaoqing Zhu, et al.
Heat Transfer and Thermo-Mechanical Analysis of Plastic-Strain Evolution in Laser-Welded Thin-Walled Laminated Cooling Plates with Non-Uniform Stiffness
Reprinted from: *Energies* **2026**, *19*, 1536, https://doi.org/10.3390/en19061536 . . . . . **65**

Anatoliy Pavlenko
Evaluation of the Intensity of Heat and Mass Transfer Processes in Cavitation Environments
Reprinted from: *Energies* **2026**, *19*, 1120, https://doi.org/10.3390/en19051120 . . . . . **85**

Łukasz Brodzik, Bartosz Ciupek, Grigore Cican, Łukasz Semkło and Dominik Schroeder
Numerical Analysis of the Flow Downstream of the Exhaust Nozzle of a Miniature Turbojet Engine During Co-Combustion of Kerosene and Hydrogen
Reprinted from: *Energies* **2026**, *19*, 938, https://doi.org/10.3390/en19040938 . . . . . **107**

Bartosz Jagieła and Magdalena Jaremkiewicz
Experimental Verification of a Method for Improving the Efficiency of an Evaporative Tower Using IEC
Reprinted from: *Energies* **2026**, *19*, 554, https://doi.org/10.3390/en19020554 . . . . . **138**

Ji-Woon Ko, Tae Hwan Song, Jong-Hoon Lee, Jong Hyeon Peck and Seung Jin Oh
Analysis of Heat Transfer Characteristics in a Latent Heat Storage Module Using Circular-Finned Tubes
Reprinted from: *Energies* **2025**, *18*, 6325, https://doi.org/10.3390/en18236325 . . . . . **158**

Kirttayoth Yeranee, Yuli Cheng and Yu Rao
Conjugate Study on Thermal–Hydraulic Performance of Topology-Optimized Lattice-Filled Cooling Channel for Thermal Management of Solid-Oxide Fuel Cells
Reprinted from: *Energies* **2025**, *18*, 6001, https://doi.org/10.3390/en18226001 . . . . . **172**

Samson Sogbaike, Celestina Ezenwajiaku, Amir Badiee, Chris Bingham and Aliyu M. Aliyu
Pathways for Greenhouse Thermal Management's Contribution to Net-Zero Food Production
Reprinted from: *Energies* **2026**, *19*, 1975, https://doi.org/10.3390/en19081975 . . . . . **202**

Magda Joachimiak and Damian Joachimiak
Applications of Methods of Solving Inverse Heat Conduction Problems for Energy-Intensive Industrial Processes and Energy Conversion—Current State of the Art and Recent Challenges
Reprinted from: *Energies* **2026**, *19*, 1291, https://doi.org/10.3390/en19051291 . . . . . **256**

Janusz Badur and Piotr Józef Ziółkowski
The Port-Hamiltonian Formulation of Thermodynamics—A New Perspective
Reprinted from: *Energies* **2026**, *19*, 324, https://doi.org/10.3390/en19020324 . . . . . **275**

About the Editors

Andrzej Frąckowiak

Andrzej Frąckowiak is employed as a full professor at the Institute of Thermal Energy, Poznań University of Technology. His research focuses on heat transfer and computational fluid mechanics, with particular attention paid to the modeling of heat transfer processes through nanotube-coated surfaces and the inverse cooling of gas turbine blades using porous materials. He has conducted his research in collaboration with, and as part of research fellowships at, the University of Stuttgart, the Institute for Thermodynamics of Air and Space, the Technical University of Munich, Forschungseinheit M6, and the Free University of Berlin, Institute of Experimental Physics.

Bartosz Ciupek

Bartosz Ciupek is employed as an assistant professor at the Institute of Thermal Energy, Poznań University of Technology. His research focuses on the design and operation of heating systems and equipment, particularly boilers. He is currently conducting research on improving air quality and reducing pollutant emissions from solid fuel boilers through chemical modification of the combustion process, the use of exhaust gas cleaning systems, and alternative environmentally friendly solid fuels. He also works on improving the thermal and environmental performance of aircraft engines. He conducts his research in collaboration with, and through research fellowships with, the Cracow University of Technology, the Military University of Technology in Warsaw, the Kielce University of Technology, and the University of Kalisz. He holds a scholarship from the City of Poznań and has authored 18 patents.

Łukasz Brodzik

Łukasz Brodzik is employed as an assistant professor at the Institute of Thermal Energy, Poznań University of Technology. His research activities are focused on two fields, the first of which is space technology. In this field, he has experience solving problems with heating orbiter heat shields. His research focuses on heat transfer via thermal radiation for porous coatings in high-temperature environments, as well as their impact on structures in the event of damage. The second field is aviation. In this case, the analyses conducted concern two aspects. The first is research on miniature turbojet engines for co-combustion of aviation kerosene and hydrogen. The analyses focus on the impact of hydrogen on engine operation, primarily in terms of temperature changes in individual sections. The second aspect of our aviation sector activities is aircraft performance analysis, which involves calculating flight parameters, primarily for smaller aircraft.

Wojciech Prokopowicz

Wojciech Prokopowicz graduated from the Faculty of Electronics at the Military University of Technology in Warsaw, earning a Master of Science. He obtained his Ph.D. in technical sciences in 2016 at the Faculty of Machines and Transport at Poznań University of Technology. He specializes in non-destructive testing of composite structures and vibroacoustics of machines and devices. Currently, his research focuses on the use of space segment in military operations and the alternative applications of unmanned aerial vehicles. His work also covers energy consumption prediction and decision-making support using artificial intelligence algorithms. He has authored numerous publications on these topics. He participated in the introduction of the F-16 aircraft into the Polish Air Force. He graduated from the Air Force Safety University in the United States and served as Flight

Safety Inspector at the 33rd Air Transport Base in Powidz. As an Assistant Professor at the Faculty of Military Studies in the Department of Air Force and Air Defense at the War Studies University in Warsaw, he lectured on the use of space assets in Air Force operations. He held the position of the Head of the Department in the Aviation Technology Directorate of the Inspectorate for Armed Forces Support of the Polish Armed Forces. Currently, he serves as a Chief Specialist in the Team of the Plenipotentiary of the Minister of National Defense for Aviation at the Ministry of National Defense, where he deals with issues related to the support for aircraft operations.

Preface

This Reprint brings together selected contributions addressing contemporary issues in applied heat transfer. Its scope covers theoretical investigations, modeling, and optimization of heat transfer processes, as well as applied solutions implemented in energy devices and installations. The main purpose is to provide a comprehensive overview of innovative approaches that not only improve thermal efficiency but also support environmental protection by reducing the consumption of conventional energy sources.

The motivation for preparing this Reprint arises from the dynamic development of modern energy technologies and the growing need for sustainable practices. Heat transfer remains a central area of research with direct impact on efficiency, performance, and ecological responsibility in power engineering and related fields.

This Reprint is intended for researchers, engineers, and professionals who deal with the challenges of designing, optimizing, and implementing energy systems. It may also be of interest to graduate students and decision makers seeking insight into current research trends and technological advances in heat transfer applications.

Andrzej Frąckowiak, Bartosz Ciupek, Łukasz Brodzik, and Wojciech Prokopowicz
Guest Editors

energies

MDPI

Article

Correlation-Based Single-Phase Heat Transfer Assessment of Binary HFE/Ethyl Acetate Mixtures in Minichannels

Artur Piasecki [1] and Magdalena Piasecka [2,*]

[1] Faculty of Environmental Engineering, Geomatics and Renewable Energy, Kielce University of Technology, 25-314 Kielce, Poland; apiasecki@tu.kielce.pl
[2] Faculty of Mechatronics and Mechanical Engineering, Kielce University of Technology, 25-314 Kielce, Poland
* Correspondence: tmpmj@tu.kielce.pl; Tel.: +48-41-34-24-320

Abstract

This work presents a correlation-based framework for comparative assessment of single-phase forced convection of binary hydrofluoroether/ethyl acetate (HFE/EA) mixtures in rectangular minichannels. Density, kinematic viscosity, and thermal conductivity were measured at 293.1, 313.1, and 328.1 K for selected compositions of HFE-7100/EA, HFE-7300/EA, and HFE-73DE/EA. Because several DSC-derived mixture-specific heat values were not sufficiently reliable for direct use, the mixture-specific heat capacity was estimated from literature-supported pure-component values using an ideal-mixture, mass-fraction-weighted approximation and used only for evaluation of the Prandtl number. Heat transfer was then assessed using the Sieder–Tate correlation for laminar thermally developing flow in two representative minichannel geometries. The highest predicted values for the HFE-7100/EA and HFE-7300/EA families were obtained for the most EA-rich retained compositions, whereas in the retained HFE-73DE/EA subset, the 50/50 mixture performed best because of its higher thermal conductivity. Validation against an experimental dataset for pure HFE-7100 in the short module showed systematic overprediction, with a mean relative difference of −13.44% and a MAPE of 15.6%. The calculated values should, therefore, be used for relative comparison rather than treated as unbiased absolute predictions.

Keywords: binary mixtures; thermophysical properties; dielectric fluids; minichannel; heat transfer coefficient; Nusselt number; single-phase forced convection

1. Introduction

Heat transfer devices are used in a wide range of technologies, including refrigeration, HVAC systems, thermal management of high-power electronics, cryogenic equipment, photovoltaic systems, and industrial processes. Their operating efficiency is largely governed by the properties of the selected coolant or process fluid. In practice, the fluid must be compatible with the required temperature and pressure levels, expected flow conditions, construction materials, and safety requirements. Fluorinated liquids, including hydrofluoroethers (HFEs), perfluoropolyethers (PFPEs), and Fluorinert-type fluids (FCs), are often considered for such applications because they combine dielectric behaviour with good chemical inertness and thermal resistance. Their normal boiling points cover a broad temperature interval, approximately from 300 K to more than 500 K, which makes them suitable for the thermal control of electronic and optoelectronic devices. A drawback of these fluids is their relatively poor heat conduction and, in many cases, high price. For this reason, increasing attention is being paid to liquid blends whose properties can be adjusted

for a given thermal process. In particular, binary systems composed of fluorinated liquids and organic solvents, or two fluorinated components, offer a practical route to modify boiling point, density, viscosity, and specific heat while preserving acceptable material compatibility and ease of circulation in typical pumping systems.

The work presented in [1] proposes the use of differential scanning calorimetry (DSC) for acquiring atmospheric-pressure boiling-point and vapor–liquid equilibrium data for binary liquid mixtures. The approach is especially relevant to mixtures whose components exhibit large differences in volatility, since such systems are susceptible to pre-evaporation effects during measurement. These errors were limited by optimising the sample size and heating programme. The methodology was first assessed for several model mixtures and was then used to investigate the previously undocumented carvacrol–DMSO binary system. The experimental boiling line was correlated with the NRTL thermodynamic model, which confirmed significant non-ideal behaviour and suggested the presence of an azeotropic point.

Recent studies show a clear shift towards computational and machine-learning tools for predicting properties of HFE-based and related fluid mixtures. For example, Aminian et al. [2] combined ab initio calculations with the Peng–Robinson equation of state to evaluate ideal-gas heat capacities and critical properties of HFE-7000–7500 compounds. In another contribution, Urata et al. [3] applied artificial neural networks to estimate vapour–liquid equilibrium behaviour in HFE-containing mixtures. Similar data-oriented strategies have been extended to other refrigerant and hydrocarbon systems. Wu et al. [4] proposed a machine-learning-assisted group-contribution approach for predicting critical temperatures of binary refrigerant mixtures from molecular information, while Soria-Lopez et al. [5] reported improved viscosity predictions for binary alkane mixtures compared with traditional mixing rules, owing to the ability of ML models to capture nonlinear dependence on composition.

Reliable high-pressure property data are available for several HFE-containing binary systems. For the HFE-7200 + 2-propanol mixture, Muñoz-Rujas et al. [6] measured thermophysical properties between 293.15 and 393.15 K and at pressures from 0.1 to 140 MPa. The authors represented the density data using a Tait-type equation, calculated related derivative properties, and supplemented the analysis with speed-of-sound results at 0.1 MPa. In another study [7], analogous density and sound-speed measurements were reported for HFE-7500 + diisopropyl ether mixtures up to 100 MPa. Thermodynamic properties of hydrofluoroether systems with selected organic solvents were further investigated by Ogawa et al. [8], who observed positive excess molar volumes and excess enthalpies dependent on composition.

From an engineering viewpoint, zeotropic mixtures offer promising opportunities for improving heat transfer performance. In pulsating heat pipes, Xu et al. [9] observed that partially immiscible zeotropic fluids can form dispersed emulsion structures, leading to enhanced heat transfer. For condensation processes, Eissa et al. [10] formulated a generalised non-equilibrium heat transfer model for binary zeotropic mixtures. Their approach includes vapour-side mass diffusion and interfacial temperature effects, and its validation against 871 experimental data points showed strong predictive capability, with 92% of the results lying within a $\pm 30\%$ deviation band. This makes the model relevant for compact heat-exchanger analysis and design.

Tagliaferri et al. [11] showed that, for CFD of bubbling fluidized bidisperse mixtures, a first-order upwind discretization can introduce strong numerical diffusion that suppresses bubble holdup and mixing, whereas a second-order upwind scheme yields more realistic bubble dynamics and correctly predicts the transition to a fully mixed state; the restitution coefficient has a minor influence except near the quasi-ideal value $e \approx 0.99$, and explicit

https://doi.org/10.3390/en19102291

vs implicit time integration mainly affects the transient duration rather than the pseudo-steady behaviour.

Additional studies have addressed related features of binary liquid systems, such as intermolecular effects, equilibrium characteristics, and behaviour at phase boundaries. Verma et al. [12] used density, ultrasonic velocity, and refractive-index measurements to show pronounced donor–acceptor interactions in ether/hydrocarbon mixtures. Tsai et al. [13], in turn, evaluated the ability of molecular dynamics simulations to predict transport properties in alcohol/water systems and indicated which force-field combinations most accurately describe diffusion coefficients and density variations.

In previous work [14], the authors combined thermophysical property measurements with validated conjugate CFD to assess HFE-73DE/ethyl acetate mixtures for laminar minichannel cooling and to identify compositions offering a heat transfer/pressure-drop compromise. In that study, the thermophysical properties of the working fluids were determined experimentally at the Faculty of Civil Engineering, Mechanics and Petrochemistry, Warsaw University of Technology in Płock, Poland. Liquid density was measured with a Mettler Toledo Densito densimeter in accordance with ASTM D1250 [15], while kinematic viscosity over the investigated temperature range was determined using a Ubbelohde capillary viscometer thermostated in water baths according to EN ISO 3104 [16]. The initial boiling point was determined by atmospheric distillation following ASTM D86 [17]. Thermal measurements were performed by differential scanning calorimetry (DSC) using a Netzsch Maia 200 F3 instrument, with an empty crucible as the reference and liquid sample masses of approximately 60–70 mg [18,19].

These measurements provided the experimental property basis for the present comparative assessment. The mixtures were prepared in the laboratory from commercially available components rather than purchased as ready-made formulations. Because this study aims at a correlation-based comparison under identical hydraulic assumptions, directly measured temperature-dependent properties were treated as the primary input data wherever their consistency was confirmed. This is particularly important for dielectric multicomponent systems, for which simple mixing rules may be insufficient to represent the actual behaviour over the full temperature and composition range. The present work uses that earlier experimental property base as an input layer for a simplified correlation-based comparison, rather than repeating the full conjugate CFD framework reported previously [14]. However, because several DSC-derived mixture-specific heat values were found to be insufficiently reliable for direct use in the final calculations, the specific heat capacity of the mixtures was estimated from pure-component data using an ideal-mixture, mass-fraction-weighted mixing rule.

For each mixture series (HFE-7100/EA, HFE-7300/EA, and HFE-73DE/EA), mixtures were considered at selected mass fractions (first component/second component) and characterised at 293.1, 313.1, and 328.1 K under near-atmospheric pressure. The dataset used in the final comparative analysis includes experimentally determined density, kinematic viscosity, and thermal conductivity, while specific heat was estimated from pure-component mass fractions for calculation of the Prandtl number. This article presents a transparent, correlation-based workflow for converting the measured thermophysical properties into comparable single-phase forced-convection heat transfer characteristics for rectangular minichannels. The novelty lies in combining a dedicated property dataset for HFE/EA mixtures with a consistent minichannel assessment framework applied to two representative module geometries and in anchoring the assessment with an independent validation dataset for pure HFE-7100 obtained in the short multi-minichannel module using IR thermography and an energy-balance data reduction.

https://doi.org/10.3390/en19102291

2. Characteristics of Pure Liquids and Selected Binary Mixtures

The present study considers three binary mixture series based on hydrofluoroethers (HFEs) and an organic ester: 3M^{TM} Novec^{TM} HFE-7100/Ethyl acetate EA, 3M^{TM} Novec^{TM} HFE-7300/Ethyl acetate EA, and 3M^{TM} Novec^{TM} HFE-73DE/Ethyl acetate EA. These liquids were selected because they are electrically insulating, chemically stable, and relevant to thermal-management and compact heat-exchanger applications, while the ester co-solvent enables tunability of density, viscosity, and boiling behaviour.

Table 1 provides selected reference properties of the base fluids (reported at 298 K unless stated otherwise). For HFE-7100 [20], HFE-7300 [21], and HFE-73DE [22], the listed densities, viscosities, and boiling temperatures illustrate the range of base-fluid properties relevant to minichannel applications. Ethyl acetate [23] is included as the organic co-solvent used to modify the density, viscosity, and boiling behaviour of the analysed HFE/EA mixtures.

Table 1. Selected reference properties of the base fluids [20–23].

Physical Properties	HFE-7100	HFE-7300	HFE-73DE	EA
Density, kg/m^3	1520	1660	1280	902
Viscosity, mm^2/s	0.401	0.71	0.403	0.463
Boiling temperature, K	334.1	371.1	321.1	350.2

The HFE-7100/EA, HFE-7300/EA, and HFE-73DE/EA systems were considered at mass fractions of 10/90, 25/75, 50/50, and 75/25 and at three temperature levels. The 10/90 composition was available only for HFE-7100/EA and HFE-73DE/EA. The 75/25 HFE-73DE/EA case was excluded from the final dataset, and all remaining compositions were used as input to the correlation-based calculations reported in the following tables.

3. Experimental Rig and Minichannel Modules

3.1. General Information

The present study comprises (i) a correlation-based assessment of selected binary mixtures using experimentally measured mixture properties, performed for two minichannel modules—a long reference module (Setup #1) and a short multi-minichannel module (Setup #2), and (ii) an experimental validation dataset acquired in the short module (Setup #2) using a pure reference fluid (HFE-7100). For the flow of either mixtures or pure liquids in the single minichannel (Setup #1) or in the central minichannel of the parallel-channel group (Setup #2), laminar single-phase forced convection was assumed.

Setup #1, incorporating the long minichannel, had been investigated in the authors' previous experiments using liquid crystal thermography to obtain the outer-wall temperature distribution of the heated foil. The corresponding data were not considered in the present study [24].

The configuration with a short minichannel module (Setup #2) was used in recent experimental studies by the authors, in which infrared thermography was employed to measure the temperature of the outer surface of the heated foil [25]. These IR-based data were selected for the present analysis because they provide a more complete and reliable wall-temperature field. In the liquid-crystal thermography measurements, portions of the foil surface could not be evaluated when the local temperature fell outside the active temperature range of the liquid-crystal coating; therefore, this technique was not adopted for the validation dataset used here.

Uncertainty estimates for the principal measured variables were reported in [24,25]. Since the heat transfer coefficient is calculated from temperature-dependent quantities, its uncertainty is largely governed by the precision of the temperature measurements.

It should also be noted that the mixtures addressed in this article were not tested experimentally in the heat transfer rig. Therefore, the heat transfer coefficients and Nusselt numbers reported for the mixtures are calculated estimates obtained from the measured thermophysical properties and a selected literature correlation, applied to the geometries and operating assumptions defined in this work.

3.2. Experimental Rig with a Minichannel Module

The validation experiments were performed in single-phase forced convection. The working fluid was circulated through the test section at controlled inlet temperature and mass flow rate, while the heat input was supplied electrically at the heated wall of the minichannel module (Setup #2). Inlet and outlet temperatures and pressures were monitored continuously, while infrared (IR) thermography was used to capture the temperature distribution over the external side of the heater foil, yielding spatially resolved thermal data. The validation dataset for the reference fluid (HFE-7100) was collected using Setup #2.

A schematic of the experimental loop and the interchangeable test sections is shown in Figure 1.

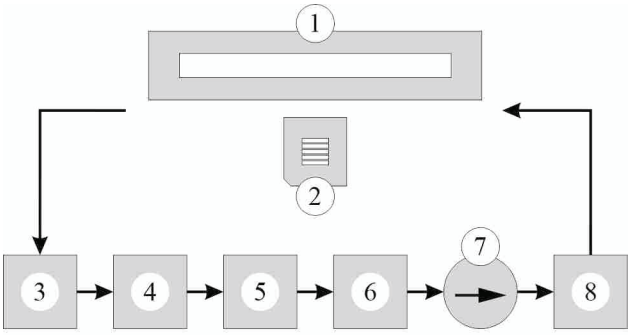


Figure 1. Schematic diagram of the experimental facility: 1—Setup #1 (long module with the minichannel); 2—Setup #2 (short module with the 5 minichannels); #3—condenser; #4—pressure-control unit; #5—deaerator; #6—filter; #7—pump; #8—mass flow meter.

In the experimental loop, the working fluid was pumped to a pressure-control vessel, which also acted as an expansion chamber. The vessel was divided into two zones: one filled with liquid and the other with compressed air, allowing the required system pressure to be maintained. After leaving this unit, the fluid flowed through a preheater, where it was brought to the prescribed inlet temperature, usually slightly below the saturation point, before entering the test section. Further details of the experimental facility are given in [24,25]. All tests were performed under steady-state conditions for several values of electrical power delivered to the heater, which produced different imposed heat-flux levels.

3.3. Reference Minichannel Modules

Both modules comprise minichannels with a depth of 1 mm. In each minichannel, the heated wall was made of Haynes-230 alloy foil, approximately 0.1 mm in thickness, the opposite wall was a glass window, and the side walls were made of PTFE. This work focuses on the short module with five parallel minichannels (Setup #2), which is schematically shown in Figure 2.

The principal geometrical dimensions of both modules are summarised in Table 2. Setup #1 employs a single minichannel with a length of 0.36 m, whereas Setup #2 uses five parallel minichannels, each 0.043 m long; in both modules, the minichannel depth is 1 mm.

https://doi.org/10.3390/en19102291

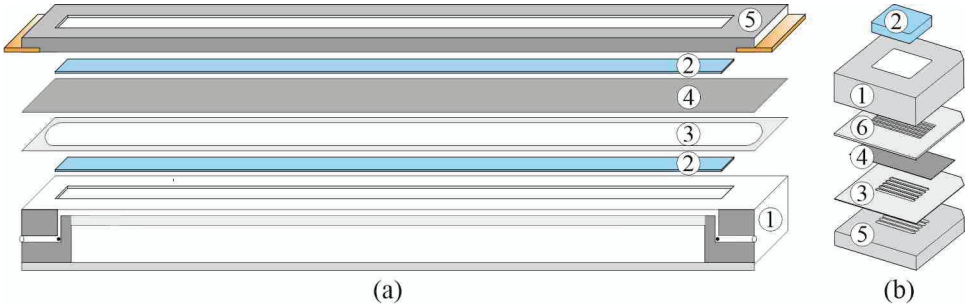


Figure 2. Schematic diagrams of (**a**) the long module with a single minichannel (Setup #1), (**b**) the short module with five parallel minichannels (Setup #2), 1—body, 2—glass plate, 3—PTFE minichannel insert, 4—heated foil, 5—cover plate, and 6—PTFE electrically insulating insert.

Table 2. Geometrical characteristics of the test modules.

	Setup #1	**Setup #2**
Number of minichannels (-)	1	5
Minichannel length L (m)	0.36	0.043
Minichannel width w (m)	0.004	0.006
Minichannel depth s (m)	0.001	0.001

4. Calculations and Correlation-Based Assessment Method

To compare selected mixtures of HFE-7100, HFE-7300, HFE-73DE, and ethyl acetate (EA) under identical hydraulic conditions and a fixed operating point, a correlation-based assessment approach was adopted for single-phase forced convection in a reference rectangular minichannel. The assessment geometry and operating point were fixed as follows: channel width w = 0.004 m, channel depth s = 0.001 m, length L = 0.36 m, hydraulic diameter D_h = 1.6 mm, and mass flux G = 200 kg/(m^2·s).

All thermophysical property measurements for the mixtures were carried out at the Faculty of Civil Engineering, Mechanics and Petrochemistry, Warsaw University of Technology in Płock (Poland). The dataset was collected at three temperature levels (293.1, 313.1, and 328.1 K). In the final comparative calculations, experimentally determined density, kinematic viscosity, and thermal conductivity were used directly. However, several DSC-derived mixture-specific heat values were found to be insufficiently reliable for direct use in the correlation-based calculations, mainly due to volatility-related measurement artefacts and the lack of a repeat verification campaign at the revision stage. Therefore, in the present manuscript, specific heat was not taken directly from the disputed mixture DSC results. Instead, c_p values for the mixtures were estimated from pure-component mass fractions and used only for evaluation of the Prandtl number within the comparative assessment framework. Details of the original property measurement procedures are given in [14].

For each mixture and temperature, the dynamic viscosity was computed from density and kinematic viscosity. The Reynolds and Prandtl numbers were then calculated according to the following relations:

$$Re = \frac{G \cdot D_h}{\mu} \tag{1}$$

$$Pr = \frac{\mu c_p}{k} \tag{2}$$

where D_h is the hydraulic diameter of the minichannel, G is mass flux, μ is the dynamic viscosity, c_p is the specific heat, and k is the thermal conductivity of the fluid.

The average Nusselt number Nu_{corr} was estimated using the classical Sieder–Tate-type correlation [26] for laminar internal flow with thermal development effects:

$$Nu_{corr} = 1.86\left(Re{\cdot}Pr{\cdot}\frac{D_h}{L}\right)^{\frac{1}{3}}\left(\frac{\mu}{\mu_w}\right)^{0.14} \quad (3)$$

where L is the heated length of the minichannel.

The viscosity ratio is the Sieder–Tate correction accounting for property variations between the bulk fluid and the wall: μ is the dynamic viscosity evaluated at the bulk (mean) fluid temperature, while μ_w is the dynamic viscosity evaluated at the wall temperature. In the present calculations, this viscosity-ratio correction was not applied, and $(\mu/\mu_w)^{0.14}$ was set to unity. This choice keeps the workflow uniform across all mixtures and temperature levels and avoids introducing an additional wall-property model not supported by direct mixture data. Its effect is modest unless the wall-to-bulk viscosity contrast is strong: for μ/μ_w = 0.8, 1.2, 1.5, and 2.0, the correction factor equals 0.969, 1.026, 1.058, and 1.102, respectively. Therefore, omission of the term should be interpreted as acceptable for first-stage comparative assessment, but not as a substitute for a detailed local-property treatment. The use of the hydraulic diameter to extend tube correlations to non-circular ducts is standard practice in preliminary internal-flow heat transfer estimates, while detailed aspect-ratio-dependent solutions for fully developed laminar duct flow can be found in dedicated duct-flow sources [27]. Accordingly, the Sieder–Tate correlation is used here as a uniform comparative metric across all cases, not as a geometry-specific predictive model for rectangular minichannels.

Finally, the heat transfer coefficient was obtained from the definition of the Nusselt number Nu ($Nu = h{\cdot}D_h/k$, where h is the heat transfer coefficient). Using the Sieder–Tate correlation to compute Nu_{corr}, the corresponding coefficient h_{corr} is

$$h_{corr} = \frac{Nu_{corr}{\cdot}k}{D_h} \quad (4)$$

where k is the thermal conductivity evaluated at the bulk (reference) fluid temperature.

The assessment is restricted to single-phase forced convection with no phase change, no conjugate heat conduction in the wall, and no pressure-drop constraint included in the ranking criterion. Properties are evaluated at discrete temperatures (293.1/313.1/328.1 K) and assumed uniform for each case. The adopted correlation targets laminar flow with thermal development along the heated length; therefore, the computed Nu and h should be interpreted as relative heat transfer metrics under the specified geometry and operating point, suitable for experimental validation.

Because the present framework is intended for comparative assessment rather than high-fidelity local prediction, the adopted property treatment was kept deliberately simple and internally consistent across all cases. Density, kinematic viscosity, and thermal conductivity were taken directly from the experimentally determined mixture dataset at each temperature level, whereas mixture-specific heat capacity was estimated from pure-component data only for evaluation of the Prandtl number. This approach preserves the measured transport-property trends while avoiding direct use of disputed DSC-derived mixture c_p values in the final calculations.

5. Results and Analysis

5.1. Heat Transfer Assessment Outputs for Investigated Mixtures

This section presents the measured thermophysical property trends and the resulting heat transfer assessment outputs for the investigated mixtures.

For each mixture series (HFE-7100/EA, HFE-7300/EA, and HFE-73DE/EA), mixtures were considered at selected mass fractions (first component/second component) and characterised at 293.1, 313.1, and 328.1 K under near-atmospheric pressure. The dataset used in the final comparative analysis includes experimentally determined density, kinematic viscosity, and thermal conductivity, while specific heat was estimated from pure-component mass fractions. These properties were used to evaluate the Reynolds and Prandtl numbers. For each mixture and temperature, dynamic viscosity was calculated from the experimentally determined density and kinematic viscosity and then used in the Reynolds- and Prandtl-number calculations.

The specific heat capacity of each mixture was estimated using an ideal-mixture, mass-fraction-weighted mixing approximation, according to the following relation [28]:

$$c_{p,mix}(T) = \sum w_i \cdot c_{p,i}(T) \quad (5)$$

where $c_{p,mix}(T)$ is the estimated isobaric specific heat capacity of the mixture at temperature T, w_i is the mass fraction of component i, and $c_{p,i}(T)$ is the isobaric specific heat capacity of pure component i at the same temperature. This approximation corresponds to neglecting the excess heat-capacity contribution of the mixture.

Pure-component c_p values were assembled as follows. For ethyl acetate, liquid c_p data from the NIST Chemistry WebBook [23] were used to assign near-ambient values at 293.1, 313.1, and 328.1 K. For HFE-7300, ambient-pressure liquid c_p data from the thermodynamic study of Kocian et al. [29] were interpolated to the three target temperatures. For HFE-7100, a literature-backed reference value of 1183 J/(kg·K) at 25 °C [30] was retained as a narrow-range approximation across the analysed temperatures. For HFE-73DE, no reliable public temperature-dependent $c_p(T)$ dataset was identified; therefore, the reference value of 1201 J/(kg·K), reported in [31], was used as a constant approximation. Because c_p enters the adopted screening only through Pr and then through the one-third power in Equation (3), the resulting sensitivity of Nu_{corr} and h_{corr} to residual c_p uncertainty is limited. These assumptions should nevertheless be treated as a limitation of the present comparative screening framework.

Table 3 summarises the physical properties of the mixtures at 293.1 K, Table 4 shows the data at 313.1 K, whereas Table 5 concerns data at 328.1 K. Within the analysed composition ranges, density, viscosity, thermal conductivity, and specific heat vary systematically with both temperature and composition, providing a consistent basis for comparative thermal-hydraulic assessment.

Table 3. Summary of experimentally determined properties (ρ, ν, k), estimated specific heat capacity c_p obtained from the mass-fraction-weighted mixing rule, and assessment outputs for all selected mixtures and compositions retained for analysis at T = 293.1 K (reference Setup #1: w = 4 mm, s = 1 mm, L = 0.36 m, D_h = 1.6 mm, G = 200 kg/(m^2·s)).

Mixture	Mass Fraction (%)	ρ (kg/m^3)	μ (mPa·s)	k (W/(m·K))	c_p (J/(kg·K))	Re (–)	Nu_{corr} (–)	h_{corr} (W/(m^2·K))
HFE-73DE/EA	10/90	931	0.4731	0.165	1848.5	676.4	4.68	482.7
HFE-73DE/EA	25/75	969	0.4877	0.189	1740.6	656.1	4.38	517.9
HFE-73DE/EA	50/50	1035	0.4839	0.207	1560.8	661.3	4.10	530.6
HFE-7100/EA	10/90	940	0.5194	0.125	1846.8	616.1	5.13	401.0
HFE-7100/EA	25/75	1017	0.5039	0.116	1736.1	635.0	5.15	373.7
HFE-7100/EA	50/50	1111	0.5341	0.105	1551.8	599.1	5.13	336.9
HFE-7100/EA	75/25	1216	0.5787	0.089	1367.4	553.0	5.20	289.2
HFE-7300/EA	25/75	1006	0.5005	0.133	1719.3	639.4	4.91	408.1
HFE-7300/EA	50/50	1154	0.578	0.101	1518.0	553.6	5.16	325.9
HFE-7300/EA	75/25	1348	0.741	0.087	1316.8	431.8	5.17	281.3

https://doi.org/10.3390/en19102291

Table 4. Summary of experimentally determined properties (ρ, ν, k), estimated specific heat capacity obtained from the mass-fraction-weighted mixing rule, and assessment outputs for all selected mixtures and compositions retained for analysis at T = 313.1 K (reference Setup #1: w = 4 mm, s = 1 mm, L = 0.36 m, D_h = 1.6 mm, G = 200 kg/(m^2·s)).

Mixture	Mass Fraction (%)	ρ (kg/m^3)	μ (mPa·s)	k (W/(m·K))	c_p (J/(kg·K))	Re (–)	Nu_{corr} (–)	h_{corr} (W/(m^2·K))
HFE-73DE/EA	10/90	902.1	0.3804	0.155	1852.7	841.2	4.78	463.3
HFE-73DE/EA	25/75	951.7	0.399	0.177	1744.1	802.0	4.48	496.1
HFE-73DE/EA	50/50	933.0	0.3613	0.194	1563.0	885.7	4.19	508.4
HFE-7100/EA	10/90	888.0	0.3719	0.123	1850.9	860.4	5.16	397.0
HFE-7100/EA	25/75	785.2	0.3239	0.111	1739.6	988.0	5.23	363.1
HFE-7100/EA	50/50	1044.0	0.4143	0.1	1554.0	772.4	5.22	326.2
HFE-7100/EA	75/25	1042.3	0.4158	0.082	1368.5	769.6	5.35	274.0
HFE-7300/EA	25/75	1067.4	0.4475	0.107	1730.2	715.1	5.29	353.7
HFE-7300/EA	50/50	1138.0	0.4603	0.095	1535.3	695.2	5.29	314.0
HFE-7300/EA	75/25	1470.8	0.6413	0.08	1340.4	499.0	5.35	267.6

Table 5. Summary of experimentally determined properties (ρ, ν, k), estimated specific heat capacity obtained from the mass-fraction-weighted mixing rule, and assessment outputs for all selected mixtures and compositions retained for analysis at T = 328.1 K. (reference Setup #1: w = 4 mm, s = 1 mm, L = 0.36 m, D_h = 1.6 mm, G = 200 kg/(m^2·s)).

Mixture	Mass Fraction (%)	ρ (kg/m^3)	μ (mPa·s)	k (W/(m·K))	c_p (J/(kg·K))	Re (–)	Nu_{corr} (–)	h_{corr} (W/(m^2·K))
HFE-73DE/EA	10/90	894.4	0.3292	0.148	1858.8	972.1	4.86	449.7
HFE-73DE/EA	25/75	951.6	0.3543	0.169	1749.2	903.2	4.56	481.5
HFE-73DE/EA	50/50	916.3	0.3478	0.185	1566.5	920.1	4.26	492.9
HFE-7100/EA	10/90	888.0	0.327	0.12	1857.0	978.6	5.21	390.9
HFE-7100/EA	25/75	766.3	0.2802	0.11	1744.7	1142.0	5.26	361.3
HFE-7100/EA	50/50	1030.0	0.3594	0.097	1557.5	890.4	5.28	319.9
HFE-7100/EA	75/25	1022.0	0.3431	0.081	1370.2	932.7	5.37	271.8
HFE-7300/EA	25/75	1084.0	0.4036	0.097	1740.9	792.9	5.48	332.0
HFE-7300/EA	50/50	1107.2	0.3906	0.093	1550.0	819.3	5.34	310.6
HFE-7300/EA	75/25	1458.6	0.5479	0.073	1359.0	584.0	5.54	252.9

5.2. Thermophysical Property Trends

Across all mixture series, density decreases with temperature and changes systematically with composition. Kinematic viscosity also decreases with temperature, which increases the Reynolds number under the fixed mass-flux conditions adopted here. However, because the viscosity-ratio correction term was set to unity, the adopted correlation yields $Re{\cdot}Pr$ independent of viscosity for fixed geometry and mass flux. As a result, $Nu_{corr} \propto (c_p/k)^{1/3}$, while $h_{corr} \propto {c_p}^{1/3}\, k^{2/3}$. Under these assumptions, thermal conductivity is the dominant property controlling the predicted h_{corr} levels, while viscosity primarily affects the hydraulic interpretation and verification of the laminar-flow range.

5.3. Correlation-Based Assessment Results for Setup #1 (Long Test Section)

The long-channel assessment (Tables 3–5), together with Figure 3, shows clear differences between mixture families within the compositions retained for analysis. Under the fixed reference operating point, EA-rich compositions generally yield higher correlation-based heat transfer coefficients.

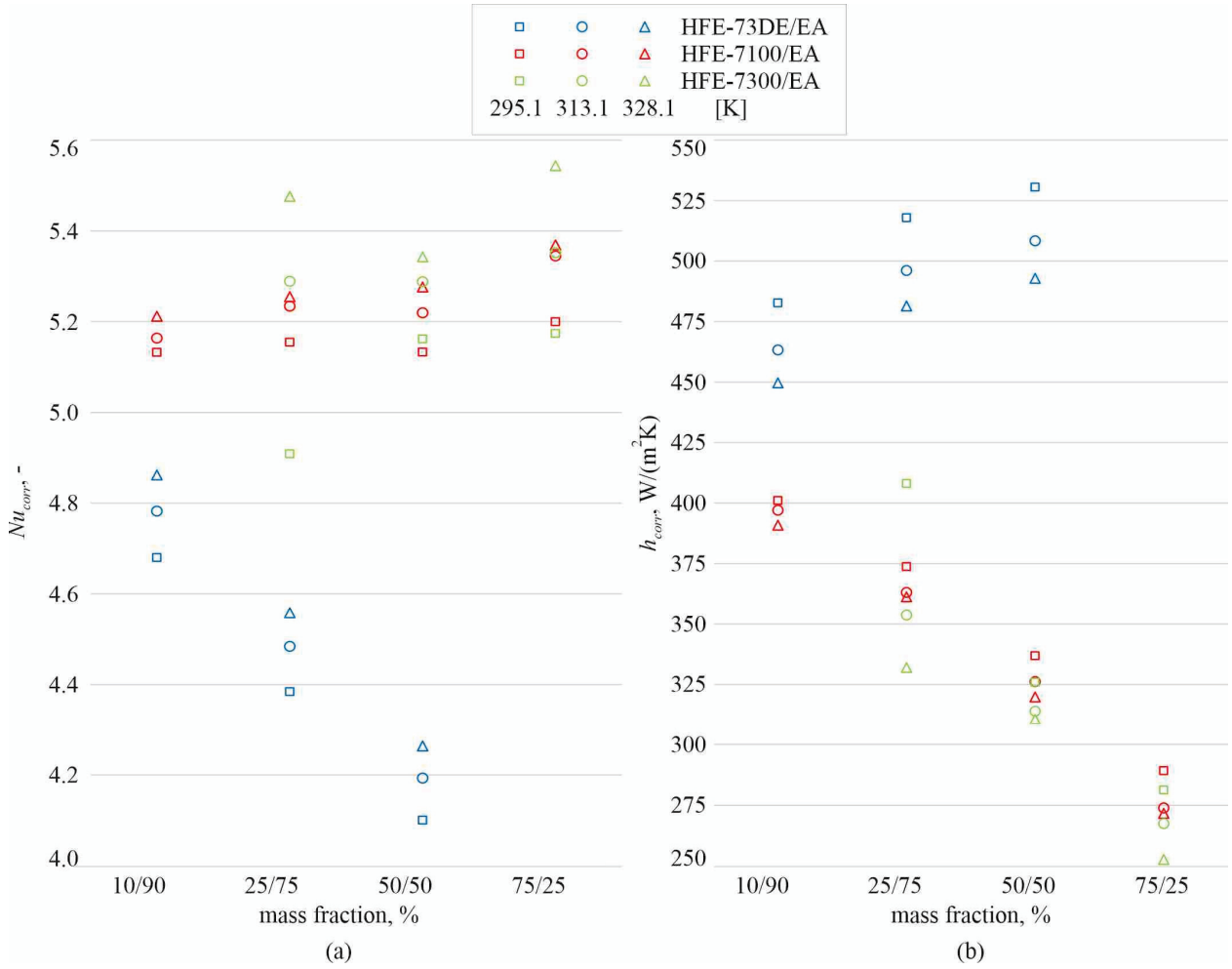


Figure 3. Correlation-based estimates under the Setup #1 reference conditions: (**a**) Nusselt number versus mass fraction; (**b**) heat transfer coefficient versus mass fraction for the binary mixtures.

Under the present assumptions, this trend reflects primarily the effect of thermal conductivity and, to a lesser extent, the contribution of c_p through the corrected Prandtl number treatment. Reynolds number is still reported for hydraulic interpretation, but it is not the dominant factor in the ranking of h_{corr} when the viscosity-ratio correction is set to unity.

For the HFE-7100/EA family, the highest h_{corr} values occur at the most EA-rich composition available (10/90) across the investigated temperature range. For HFE-7300/EA, the highest h_{corr} values occur at 25/75 throughout the analysed range. For HFE-73DE/EA, the comparison is limited to 10/90–50/50 because the 75/25 composition was excluded; within the retained set, the 50/50 mixture yields the highest h_{corr} at all three temperature levels, followed by 25/75 and 10/90. This difference relative to the HFE-7100/EA and HFE-7300/EA families follows from the stronger contribution of thermal conductivity in the adopted correlation-based ranking.

Using the reference geometry and operating point defined in Section 4, Reynolds and Prandtl numbers were computed for each mixture at 293.1, 313.1, and 328.1 K. In the corrected c_p treatment, an increase in temperature does not automatically increase h_{corr}. In most of the retained cases, h_{corr} decreases with temperature because the reduction in thermal conductivity outweighs the relatively weak one-third-power influence of c_p. Figure 3 summarises the correlation-based Nusselt number and heat transfer coefficient as functions of mass fraction under the Setup #1 reference conditions.

https://doi.org/10.3390/en19102291

5.4. Correlation-Based Assessment Results for Setup #2 (Short Test Section)

For the short-module geometry, the same correlation framework was applied using the module-specific hydraulic diameter and heated length. In contrast to the long-module assessment, the mass flux was set to the value corresponding to the selected convection-only operating point used for validation (Section 6). This ensures that the correlation-based estimates for Setup #2 are evaluated under the same hydraulic conditions as the experimental dataset, enabling a consistent comparison.

For the Setup #2 assessment (Tables 6–8 and Figure 4), the reference conditions were defined by the Setup #2 geometry (five parallel minichannels with w = 0.006, s = 0.001 m, and L = 0.043 m; Table 2). The hydraulic diameter was evaluated accordingly, and mixture properties at each temperature level were treated as constant reference values, in analogy to the long-module calculations. Based on the experimental operating conditions, a fixed mass flux of G = 372.5 kg/(m^2·s) was adopted.

Table 6. Summary of correlation-based assessment outputs for the selected mixtures and compositions retained for analysis at T = 293.1 K under the Setup #2 reference conditions.

Mixture	Mass Fraction (%)	Re (–)	Nu_{corr} (–)	h_{corr} (W/(m^2·K))
HFE-73DE/EA	10/90	1939.7	12.24	1178.4
HFE-73DE/EA	25/75	1802.4	11.47	1264.5
HFE-73DE/EA	50/50	1836.0	10.73	1295.6
HFE-7100/EA	10/90	1952.9	13.43	979.0
HFE-7100/EA	25/75	2279.3	13.48	912.4
HFE-7100/EA	50/50	1776.9	13.43	822.4
HFE-7100/EA	75/25	1861.0	13.60	706.2
HFE-7300/EA	25/75	1582.3	12.84	996.3
HFE-7300/EA	50/50	1635.0	13.50	795.6
HFE-7300/EA	75/25	1165.5	13.53	686.9

Table 7. Summary of correlation-based assessment outputs for the selected mixtures and compositions retained for analysis at T = 313.1 K under the Setup #2 reference conditions.

Mixture	Mass Fraction (%)	Re (–)	Nu_{corr} (–)	h_{corr} (W/(m^2·K))
HFE-73DE/EA	10/90	1678.5	12.51	1131.2
HFE-73DE/EA	25/75	1600.4	11.73	1211.2
HFE-73DE/EA	50/50	1767.4	10.97	1241.4
HFE-7100/EA	10/90	1717.2	13.51	969.2
HFE-7100/EA	25/75	1971.2	13.70	886.6
HFE-7100/EA	50/50	1541.5	13.65	796.5
HFE-7100/EA	75/25	1535.8	13.98	668.9
HFE-7300/EA	25/75	1426.9	13.84	863.6
HFE-7300/EA	50/50	1387.3	13.83	766.6
HFE-7300/EA	75/25	995.8	14.00	653.4

Tables 6–8 compile the correlation-based assessment outputs for the selected mixtures and compositions retained for analysis under the Setup #2 reference conditions at T = 293.1, 313.1, and 328.1 K. Figure 4 illustrates the corresponding Nusselt number and heat transfer coefficient as functions of mass fraction for the binary mixtures under the same Setup #2 reference conditions. The same property interpretation applies here as in Setup #1: the shorter heated length increases the absolute Nu_{corr} and h_{corr} levels, whereas the relative ranking remains governed primarily by the $c_p - k$ combination embedded in the adopted correlation.

Table 8. Summary of correlation-based assessment outputs for the selected mixtures and compositions retained for analysis at T = 328.1 K under the Setup #2 reference conditions.

Mixture	Mass Fraction (%)	Re (–)	Nu_{corr} (–)	h_{corr} (W/(m^2·K))
HFE-73DE/EA	10/90	1349.9	12.72	1098.1
HFE-73DE/EA	25/75	1309.4	11.92	1175.5
HFE-73DE/EA	50/50	1319.5	11.15	1203.5
HFE-7100/EA	10/90	1229.5	13.64	954.5
HFE-7100/EA	25/75	1267.1	13.75	882.1
HFE-7100/EA	50/50	1195.5	13.80	781.1
HFE-7100/EA	75/25	1103.5	14.05	663.7
HFE-7300/EA	25/75	1275.8	14.33	810.6
HFE-7300/EA	50/50	1104.9	13.98	758.2
HFE-7300/EA	75/25	861.7	14.50	617.5

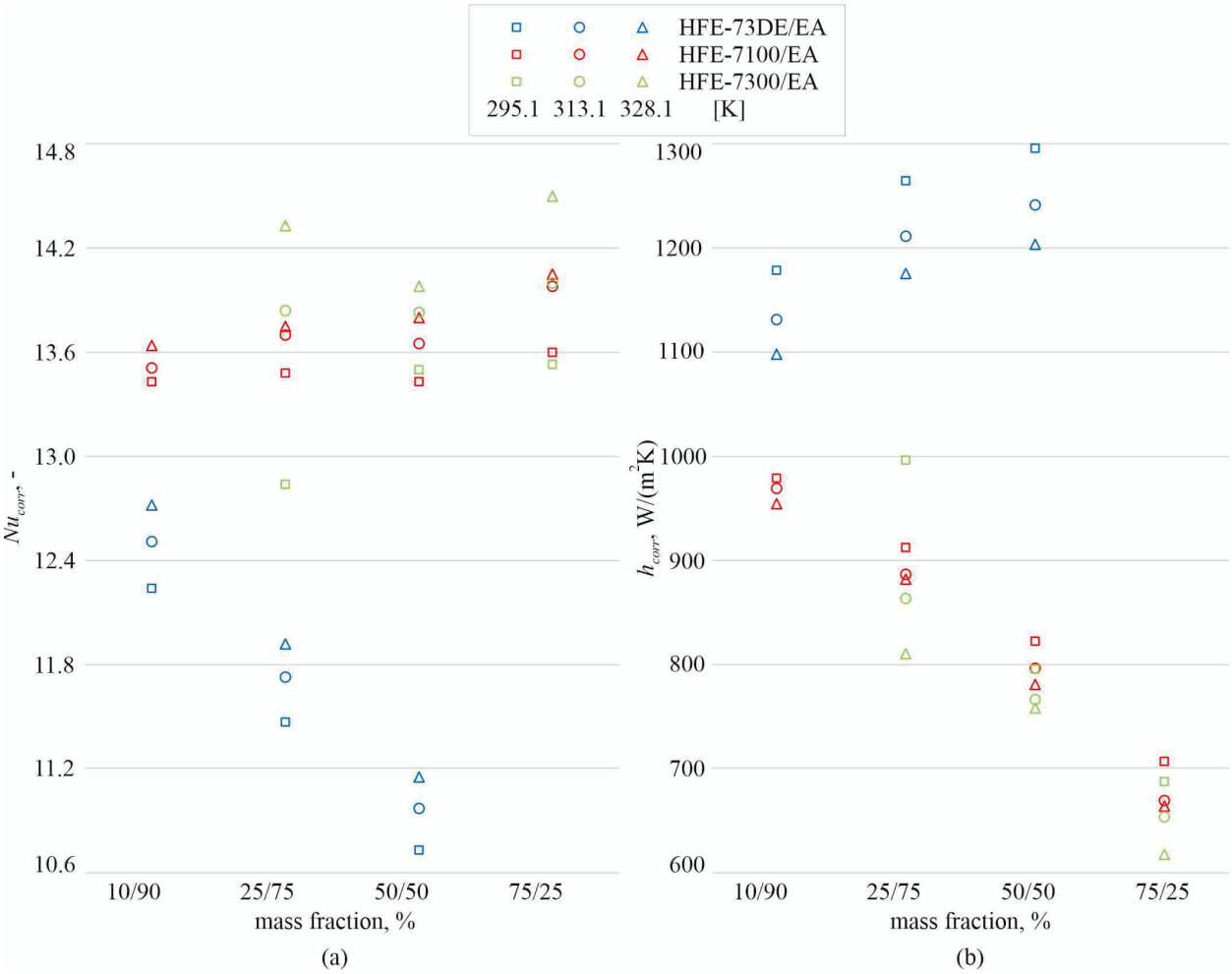


Figure 4. Correlation-based estimates under the Setup #2 reference conditions: (**a**) Nusselt number versus mass fraction; (**b**) heat transfer coefficient versus mass fraction for the binary mixtures.

The results in Tables 6–8 and Figure 4 show that the mixture ranking is not specific to the long-channel geometry. The same ranking pattern is retained in the short-module geometry, although the absolute Nu_{corr} and h_{corr} levels are higher because of the shorter heated length. Under the present corrected c_p treatment and with the viscosity-ratio term set to unity, the relative ranking is governed primarily by thermal conductivity, with a weaker contribution from c_p through its one-third-power effect. The validation presented

in Section 6 shows that the correlation systematically overpredicts h_{corr} for HFE-7100 under the tested conditions; therefore, the reported absolute values should be treated cautiously, whereas the comparative ranking remains the main intended output of the framework.

6. Validation of the Correlation-Based Estimates Against the Experimental Dataset

The correlation-based estimates were validated against an experimental dataset obtained for pure HFE-7100 in the short multi-minichannel module (Setup #2, five parallel minichannels) under single-phase forced convection. The selected convection-only operating point corresponded to a mean mass flux of G_{mean} = 372.5 (kg/(m^2·s)), inlet and outlet bulk-fluid temperatures of $T_{f,in}$ = 287.3 K and $T_{f,out}$ = 288.5 K, inlet and outlet gauge pressures of p_{in} = 25,559.9 Pa and p_{out} = 24,399.2 Pa, and an imposed heat flux of q'' = 6473.2 W/m^2 calculated from the measured electrical current and voltage. The IR-measured outer-foil temperature ranged from 294.7 K to 303.7 K; the ambient-air temperature was 294.9 K, and the atmospheric pressure was 0.96 bar.

The experimental heat transfer coefficient was evaluated from the spatial wall-temperature field measured by IR thermography. For each frame, the local coefficient was computed as

$$h_{exp}(x) = \frac{q''}{\left[T_F(x) - T_f(x) - \Delta T_{cond}\right]} \tag{6}$$

where $T_F(x)$ is the local outer-surface temperature of the heated foil measured by infrared thermography, $T_f(x)$ is the linear HFE-7100 bulk-temperature profile between the measured inlet/outlet temperatures (measured by K-type thermocouples placed in the inlet and outlet of the minichannel collector), and q'' is determined from the measured current and voltage, the heated area, and the assumed heat-loss correction.

Furthermore, ΔT_{cond} accounts for conduction through the heater foil and is calculated as follows:

$$\Delta T_{cond} = \frac{q'' \cdot \delta_F}{k_F} \tag{7}$$

where δ_F is the heater foil thickness and k_F is the foil conductivity.

A minimal quality criterion was applied (temperature difference in Equation (6) > 0.5 K and $h_{exp} > 0$), and $h_{exp,mean}$ was obtained by averaging over the retained axial positions. The correlation-based heat transfer coefficient h_{corr} was computed by first evaluating Re and Pr from Equations (1) and (2), then calculating Nu_{corr} using the laminar thermally developing correlation (3), and finally, converting Nu_{corr} to h_{corr}. For this first-stage validation, μ, c_p, and k were treated as constant reference values for HFE-7100 (near 298.1 K). For the selected 30 low-heat-flux frames (convection-only subset), the mean $h_{exp,mean}$ was 480.6 ± 11.7 W/(m^2 K), while the mean h_{corr} was 555.2 ± 0.1 W/(m^2 K). The mean relative difference was defined as

$$\Delta h_{rel} = \frac{\left(h_{exp} - h_{corr}\right)}{h_{corr}} \cdot 100\%, \tag{8}$$

and equalled −13.44% (median −14.15%; 10th–90th percentiles −15.23% to −10.72%). The RMSE was 75.5 W/(m^2 K), and the MAPE (relative to h_{exp}) was 15.6%. This level of discrepancy is not negligible and confirms that the adopted correlation systematically overpredicts the absolute heat transfer coefficient for the validated case. The most likely contributors are the following: use of a circular-tube laminar entrance correlation with hydraulic diameter for a rectangular five-minichannel module, neglect of the Sieder–Tate viscosity correction, treatment of properties as spatially uniform, and omission of conjugate wall-conduction, and other module-specific effects from the reduced comparison model. For this reason, the

https://doi.org/10.3390/en19102291

framework is retained as a comparative screening tool under fixed assumptions, not as a bias-free predictive correlation for absolute heat transfer coefficient values.

Table 9 lists the 30 low-heat-flux (convection-only) validation cases for Setup #2, including the mass flux G, imposed heat flux q'', the experimentally obtained mean heat transfer coefficient $h_{exp,mean}$, the corresponding correlation-based value h_{corr}, and the resulting relative difference Δh_{rel}.

Table 9. Validation dataset for the short module (Setup #2, HFE-7100): experimental mean heat transfer coefficient $h_{exp,mean}$, compared with the correlation-based value h_{corr} calculated using Equation (3), and the resulting relative difference Δh_{rel} calculated from Equation (8).

G (kg/(m^2·s))	q'' (W/m^2)	$h_{exp,mean}$ (W/(m^2·K))	h_{corr} (W/(m^2·K))	Δh_{rel} (%)
372.2	4291.5	470.8	555.1	−15.2
372.1	4859.2	503.8	555.1	−9.2
372.2	5773.7	520.7	555.1	−6.2
372.7	6144.2	470.8	555.4	−15.2
372.4	6163.8	473.2	555.2	−14.8
372.4	6169.3	476.4	555.2	−14.2
372.1	6176.0	468.1	555.1	−15.7
372.3	6181.7	478.1	555.2	−13.9
372.1	6181.8	478.4	555.1	−13.8
372.4	6184.6	475.9	555.2	−14.3
372.5	6186.8	473.3	555.3	−14.8
372.3	6187.8	466.8	555.2	−15.9
372.6	6198.7	475.1	555.3	−14.4
372.5	6199.8	473.5	555.3	−14.7
372.5	6208.4	476.0	555.3	−14.3
372.5	6209.7	482.0	555.3	−13.2
372.6	6210.7	480.9	555.3	−13.4
372.3	6214.7	476.8	555.2	−14.1
372.4	6217.4	470.6	555.2	−15.2
372.4	6220.7	476.3	555.2	−14.2
372.3	6223.7	489.1	555.2	−11.9
372.6	6226.7	502.6	555.3	−9.5
372.4	6227.8	479.5	555.2	−13.6
372.0	6229.8	487.1	555.0	−12.2
372.4	6230.8	475.2	555.2	−14.4
372.4	6232.8	474.1	555.2	−14.6
372.7	6232.8	480.5	555.4	−13.5
372.6	6241.8	484.5	555.3	−12.8
372.6	6242.5	482.6	555.3	−13.1
372.5	6247.8	495.0	555.3	−10.9

7. Conclusions

Thermophysical property data for three binary HFE/ethyl acetate systems (HFE-7100/EA, HFE-7300/EA, and HFE-73DE/EA) were compiled at 293.1, 313.1, and 328.1 K to support comparative single-phase forced-convection analysis in minichannel geometries. In the final assessment workflow, experimentally determined density, viscosity, and thermal conductivity were used directly, whereas mixture-specific heat capacity was estimated from pure-component mass fractions using a literature-supported ideal-mixture approximation solely for evaluation of the Prandtl number.

Under the adopted assumptions, the calculated correlation-based heat transfer coefficients span about 253–531 W/(m^2·K) for the long reference module (Setup #1) and about 618–1296 W/(m^2·K) for the short multi-minichannel module (Setup #2). For the

HFE-7100/EA and HFE-7300/EA families, the highest h_{corr} values were obtained for the most EA-rich retained compositions, whereas within the retained HFE-73DE/EA subset, the 50/50 composition gave the highest h_{corr} because of its more favourable thermal conductivity level. In the corrected c_p treatment, the ranking is governed primarily by thermal conductivity, while c_p contributes more weakly through the one-third-power dependence embedded in the adopted correlation.

Validation against the short-module dataset for pure HFE-7100 showed a mean relative difference of −13.44% and a MAPE of 15.6%, confirming that the simplified framework systematically overpredicts the absolute heat transfer coefficient under the tested conditions. The most likely reasons are the use of a tube-derived entrance correlation with hydraulic diameter for a rectangular five-minichannel module, neglect of the viscosity-ratio correction, and omission of conjugate and module-specific effects. Accordingly, the proposed framework should be interpreted as a comparative screening tool under fixed assumptions rather than as a geometry-exact predictive model for absolute heat transfer coefficient values.

The dataset and workflow support early-stage selection of binary (and potentially more complex) dielectric working fluids for compact heat exchangers and mini-/microchannel thermal management, where limited space, low fluid charge, and electrical safety are key constraints. Application areas include electronics and power electronics cooling, HVAC&R components with confined internal passages, and compact laboratory- or process-scale heat-exchanger modules requiring a balance between heat transfer performance, pressure-drop (pumping-power) penalties, and the target operating temperature range.

Limitations include the restriction to single-phase forced convection, the use of a tube-derived correlation applied via the hydraulic diameter, and the simplified treatment of thermophysical properties at each temperature level. Further work should extend validation to additional operating points and consider rectangular-duct-specific laminar formulations, temperature-dependent properties, and joint heat transfer/pressure-drop criteria for mixture down-selection.

Author Contributions: Conceptualization, A.P.; Methodology, A.P.; Software, M.P.; Validation, M.P.; Formal analysis, A.P. and M.P.; Investigation, A.P.; Resources, A.P.; Data curation, A.P. and M.P.; Writing—original draft, A.P. and M.P.; Writing—review & editing, A.P. and M.P.; Visualization, A.P.; Supervision, M.P.; Project administration, M.P.; Funding acquisition, M.P. All authors have read and agreed to the published version of the manuscript.

Funding: This research was funded by the National Science Centre, Poland, grant no. UMO-2025/57/B/ST8/00907. For the purpose of Open Access, the authors have applied a CC BY public copyright licence to the Author Accepted Manuscript (AAM) version arising from this submission.

Data Availability Statement: The original contributions presented in this study are included in the article. Further inquiries can be directed to the corresponding author.

Conflicts of Interest: The authors declare no conflicts of interest.

Nomenclature

Symbols

c_p	isobaric specific heat capacity ($J \cdot kg^{-1} \cdot K^{-1}$)
$c_{p,i}$	isobaric specific heat capacity of pure component i, ($J \cdot kg^{-1} \cdot K^{-1}$)
$c_{p,mix}$	estimated isobaric specific heat capacity of the mixture ($J \cdot kg^{-1} \cdot K^{-1}$)
D_h	hydraulic diameter, $D_h = 2w \cdot s/(w + s)$ (m)
G	mass flux ($kg \cdot m^{-2} \cdot s^{-1}$)

h_{exp}	experimental heat transfer coefficient, calculated according to Equation (6) ($W \cdot m^{-2} \cdot K^{-1}$)
h_{corr}	correlation-based heat transfer coefficient ($W \cdot m^{-2} \cdot K^{-1}$)
$h_{exp,mean}$	experimentally obtained mean heat transfer coefficient ($W \cdot m^{-2} \cdot K^{-1}$)
I	electric current supplied to the heater (A)
k	thermal conductivity ($W \cdot m^{-1} \cdot K^{-1}$)
L	minichannel length (m)
Nu_{exp}	experimental Nusselt number, $Nu_{exp} = h_{exp} \cdot D_h / k$
Nu_{corr}	correlation-based Nusselt number (–)
p	pressure (Pa)
Pr	Prandtl number, $Pr = \mu \cdot c_p / k$ (–)
Q''	heat flux at the heated wall ($W \cdot m^{-2}$)
Re	Reynolds number, $Re = G \cdot D_h / \mu$ (–)
s	minichannel depth (m)
T	temperature (K)
w	minichannel width (m)
w_i	mass fraction of component i in the mixture (-)
x	axial coordinate along the minichannel (m)
Greek letters	
ΔT_{cond}	temperature drop across the heater foil due to one-dimensional conduction $\Delta T_{cond} = q'' \cdot \delta / k_F$ (K)
Δh_{rel}	relative difference between $h_{exp,mean}$ and h_{corr} (%)
μ	dynamic viscosity (Pa·s)
μ_w	dynamic viscosity evaluated at the wall temperature (Pa·s)
ν	kinematic viscosity ($m^2 \cdot s^{-1}$)
ρ	density ($kg \cdot m^{-3}$)
δ	heater foil thickness (m)
Subscripts	
corr	value calculated from a correlation
exp	value obtained from experiment
F	foil (heater wall)
f	fluid (bulk)
i	component index
in/out	inlet/outlet
max	maximum value
mean	mean (averaged) value
min	minimum value
mix	mixture
Abbreviations	
EA	ethyl acetate
HFE	hydrofluoroether
IR	infrared thermography
LCT	liquid crystal thermography

References

1. von Westarp, W.G.; Jupke, A. Improved methodology for the measurement of vapor–liquid equilibria of binary mixtures with large boiling point differences via differential scanning calorimetry. *Thermochim. Acta* **2026**, *757*, 180222. [CrossRef]
2. Aminian, A.; Celný, D.; Mickoleit, E.; Jäger, A.; Vinš, V. Ideal Gas Heat Capacity and Critical Properties of HFE-Type Engineering Fluids: Ab Initio Predictions of Cp,ig, Modelling of Phase Behaviour and Thermodynamic Properties Using Peng–Robinson and Volume-Translated Peng–Robinson Equations of State. *Int. J. Thermophys.* **2022**, *43*, 87. [CrossRef]
3. Urata, S.; Takada, A.; Murata, J.; Hiaki, T.; Sekiya, A. Prediction of vapour–liquid equilibrium for binary systems containing HFEs by using artificial neural network. *Fluid Phase Equilibria* **2002**, *199*, 63–78. [CrossRef]
4. Wu, J.; Pan, Y.; Ren, J.; Li, Q. Exploring structure–property relationships of critical temperatures for binary refrigerant mixtures via group contribution and machine learning. *DeCarbon* **2025**, *9*, 100123. [CrossRef]

5. Soria-Lopez, A.; Simal-Gandara, J.; Mejuto, J.C. Viscosity mixing rules and machine learning-based models for predicting the viscosity of liquid binary mixtures of aliphatic alkanes. *J. Mol. Liq.* **2025**, *437*, 128401. [CrossRef]
6. Muñoz-Rujas, N.; Aguilar, F.; Garcia-Alonso, J.M.; Montero, E.A. Thermodynamics of binary mixtures 1-ethoxy-1,1,2,2,3,3,4,4,4-nonafluorobutane (HFE-7200) + 2-propanol: High-pressure density, speed of sound and derivative properties. *J. Chem. Thermodyn.* **2019**, *131*, 630–647. [CrossRef]
7. Muñoz-Rujas, N.; Bazile, J.P.; Aguilar, F.; Galliero, G.; Montero, E.; Daridon, J.-L. Speed of sound, density and derivative properties of binary mixtures HFE-7500 + diisopropyl ether under high pressure. *J. Chem. Thermodyn.* **2019**, *128*, 19–33. [CrossRef]
8. Ogawa, H.; Karashima, S.; Takigawa, T.; Murakami, S. Excess molar enthalpies and volumes of binary mixtures of two hydrofluoroethers with hexane, or benzene, or ethanol, or 1-propanol, or 2-butanone at T=298.15 K. *J. Chem. Thermodyn.* **2003**, *35*, 763–774. [CrossRef]
9. Xu, R.; Zhang, C.; Chen, H.; Wu, Q.; Wang, R. Heat transfer performance of pulsating heat pipe with zeotropic immiscible binary mixtures. *Int. J. Heat Mass Transf.* **2019**, *137*, 31–41. [CrossRef]
10. Eissa, M.S.; Kotb, A.; Liu, L.; Wang, S. The prediction of binary zeotropic mixtures in-tube flow condensation—A generalized non-equilibrium heat transfer model. *Energy Convers. Manag.* **2026**, *347*, 120562. [CrossRef]
11. Tagliaferri, C.; Mazzei, L.; Lettieri, P.; Marzocchella, A.; Olivieri, G.; Salatino, P. CFD simulation of bubbling fluidized bidisperse mixtures: Effect of integration methods and restitution coefficient. *Chem. Eng. Sci.* **2013**, *102*, 324–334. [CrossRef]
12. Verma, S.; Rani, M.; Lee, Y.; Maken, S. Thermophysical properties of binary mixtures of diethyl ether as oxygenate with cyclohexane and aromatic hydrocarbons. *J. Mol. Liq.* **2023**, *387*, 122663. [CrossRef]
13. Tsai, M.-Y.; Wu, Y.-Y.; Lin, L.-C. Transport properties of alcohol/water mixtures: Evaluation of molecular potentials. *J. Mol. Liq.* **2025**, *433*, 127870. [CrossRef]
14. Piasecki, A.; Maciejewska, B.; Piasecka, M.; Grabowski, M.; Grabowski, P. Evaluation of HFE-73DE/ethyl acetate mixtures for use in minichannel heat exchangers. *Energies* **2026**, *19*, 110. [CrossRef]
15. *ASTM D1250*; Standard Guide for Use of the Petroleum Measurement Tables. ASTM International: West Conshohocken, PA, USA, 2013.
16. *EN ISO 3104:2020*; Petroleum Products—Transparent and Opaque Liquids—Determination of Kinematic Viscosity and Calculation of Dynamic Viscosity. ISO: Geneva, Switzerland, 2020.
17. *ASTM D86*; Standard Test Method for Distillation of Petroleum Products at Atmospheric Pressure. ASTM International: West Conshohocken, PA, USA, 2012.
18. Makomaski, G.; Ciesińska, W.; Zieliński, J. Thermal properties of pitch-polymer compositions and derived activated carbons. *J. Therm. Anal. Calorim.* **2012**, *109*, 767–772. [CrossRef]
19. Pecchi, M.; Goldfarb, J.L.; Baratieri, M. Hydrothermal carbonization enthalpy using differential scanning calorimetry: Assessing the accuracy of the exhaust sample method. *Thermochim. Acta* **2022**, *718*, 179388. [CrossRef]
20. 3M™ Novec™ 7100 Engineered Fluid, Product Information, 3M. Available online: https://multimedia.3m.com/mws/mediawebserver?mwsId=SSSSSu9n_zu8l00xl8mBm8mePv70k17zHvu9lxtD7xt1evSSSSSS-(accessed on 1 August 2025).
21. 3M™ Novec™ 7300 Engineered Fluid, Product Information, 3M. Available online: https://multimedia.3m.com/mws/mediawebserver?mwsId=SSSSSu9n_zu8l00x4Y_9lx2U4v70k17zHvu9lxtD7xt1evSSSSSS- (accessed on 1 August 2025).
22. 3M™ Novec™ 73DE Engineered Fluid, Product Information, 3M. Technical Data, May 2016. Available online: https://multimedia.3m.com/mws/mediawebserver?mwsId=SSSSSu9n_zu8l00xm8_el8m9lv70k17zHvu9lxtD7xt1evSSSSSS-(accessed on 1 August 2025).
23. NIST Chemistry WebBook. *Ethyl Acetate (CAS 141-78-6)*; NIST: Gaithersburg, MD, USA, 2026. Available online: https://webbook.nist.gov/cgi/cbook.cgi?ID=C141786 (accessed on 1 October 2025).
24. Piasecka, M.; Piasecki, A.; Maciejewska, B. Liquid Crystal Thermography and Infrared Thermography Application in Heat Transfer Research on Flow Boiling in Minichannels. *Energies* **2025**, *18*, 940. [CrossRef]
25. Piasecka, M.; Maciejewska, B.; Michalski, D.; Dadas, N.; Piasecki, A. Investigations of Flow Boiling in Mini-Channels: Heat Transfer Calculations with Temperature Uncertainty Analyses. *Energies* **2024**, *17*, 791. [CrossRef]
26. Sieder, E.N.; Tate, G.E. Heat Transfer and Pressure Drop of Liquids in Tubes. *Ind. Eng. Chem.* **1936**, *28*, 1429–1435. [CrossRef]
27. Shah, R.K.; London, A.L. *Laminar Flow Forced Convection in Ducts: A Source Book for Compact Heat Exchanger Analytical Data*; Academic Press: New York, NY, USA, 1978.
28. Kleiber, M.; Joh, R. D1 Calculation Methods for Thermophysical Properties. In *VDI Heat Atlas*; Springer: Berlin/Heidelberg, Germany, 2010.
29. Kocian, Š.; Knöbel, E.; Klink, S.; Prokopová, O.; Vrbka, P.; Čenský, M.; Fulem, M.; Růžička, K.; Richter, M.; Jäger, A.; et al. Thermodynamic Properties of HFE-7300. *Int. J. Thermophys.* **2026**, *47*, 45. [CrossRef]

30. Zheng, Y.; Wei, Z.; Song, X. Measurements of Isobaric Heat Capacities for HFE-7000 and HFE-7100 at Different Temperatures and Pressures. *Fluid Phase Equilibria* **2016**, *425*, 335–341. [CrossRef]
31. Best Technology. Solvent Cleaning with 3M™ Novec™ Engineered Fluids & Solvents. n.d. Available online: https://www.besttechnologyinc.com/3m-novec-engineered-fluids-solvents/cleaning-vapor-degreasing/ (accessed on 17 April 2026).

Disclaimer/Publisher's Note: The statements, opinions and data contained in all publications are solely those of the individual author(s) and contributor(s) and not of MDPI and/or the editor(s). MDPI and/or the editor(s) disclaim responsibility for any injury to people or property resulting from any ideas, methods, instructions or products referred to in the content.

energies

MDPI

Article

Comparison of Analytical and Numerical Methods for Predicting the Shell-Side Heat Transfer Coefficient in Heat Exchanger with Segmental Baffles

Janusz T. Cieśliński *, Jacek Barański, Kamil Stasiak, Krzysztof Tesch and Paweł Dąbrowski

Institute of Energy, Gdańsk University of Technology, Narutowicza 11/12, 80-233 Gdańsk, Poland; jacek.baranski@pg.edu.pl (J.B.); kamil.stasiak@pg.edu.pl (K.S.); krzysztof.tesch@pg.edu.pl (K.T.); pawel.dabrowski@pg.edu.pl (P.D.)
* Correspondence: jcieslin@pg.edu.pl

Abstract

This study reports the calculated values results of the shell-side heat transfer coefficient for a shell-and-tube heat exchanger with an inner shell diameter of 200 mm and a length of 518 mm, containing 85 tubes arranged in a staggered layout. Shell-side cross-flow was generated by nine standard segmental baffles with a 25% baffle cut and a baffle pitch of 48 mm. In particular, the effect of 13 combinations of shell-to-baffle and baffle-to-tube gaps on the heat transfer coefficient was investigated. Moreover, the influence of sealing strips and tube bundle diameter on the heat transfer coefficient was also examined. The calculations were carried out using three different approaches, namely the Gaddis-Gnielinski method, the extended Bell-Delaware method, and Aspen EDR code. Numerical simulations for an idealized heat exchanger were also conducted using Ansys Fluent and OpenFOAM. As far as the authors are aware, this is the first study to compare two computational methods widely regarded as reference approaches for shell-and-tube heat exchangers, namely the Bell-Delaware and the Gaddis-Gnielinski approaches. The results obtained using the Aspen EDR code, a widely recognized software tool for modeling and design of heat exchangers, were evaluated against the forecast of the Bell-Delaware and Gaddis-Gnielinski approaches.

Keywords: heat transfer coefficient; segmental baffles; leakage; shell-and-tube heat exchanger

1. Introduction

In most thermal systems, heat exchangers serve as essential components. Some, such as car radiators, are produced in tens of millions of units each year. Due to dwindling resources of raw materials and energy, computational methods for heat exchangers have been continuously developed for over a hundred years.

Several parameters affect the heat transfer coefficient (HTC) inside shell. Apart from baffle spacing and baffle cut, these parameters include tube layout and tube pitch, the tube bundle diameter, the gap between the baffle and the tube, the gap between the shell and the baffle, and the number of sealing strips [1–4]. Each of these parameters influences the shell-side flow pattern and, consequently, the obtained HTC.

1.1. Analytical Approaches

A considerable number of models for analytical prediction of shell-side HTCs have been published in the literature [5]. Most modern analytical models of shell-and-tube

heat exchangers (STHEx) are founded on Tinker's approach, which assumes that the fluid stream entering the shell is divided into four main streams, namely the cross-flow, the baffle-to-tube leakage flow, the shell-to-baffle flow and the bypass flow [6,7]. The most important parameters affecting the formation of these streams are baffle spacing and baffle cut [8]. Consequently, most studies concentrate on baffling [9]. Among the analytical models, the Kern model [10], the Donohue model [11], the Žhukauskas model [12], the extended Bell-Delaware (Bell-D) approach [13], and the Gaddis-Gnielinski approach, known as the Verein Deutscher Ingenieure (VDI) method [14], are most frequently chosen as reference approaches. Roetzel and Lee [15] showed that the Žhukauskas model predicts the shell-side HTC, as determined from their empirical dispersion model, to within $\pm 5\%$. Kücük et al. [16] experimentally demonstrated that the Kern and VDI methods predict the HTC within a range -15% to $+10\%$ for a mini-channel heat exchanger. Abdelkader and Zubair [17] calculated the HTC using the Kern, Bell-D, and Wills et al. methods [18] across a range of baffle numbers, mass flow rates, tube bundle layouts, fluid thermal properties, as well as baffle cuts. They established that the Bell-D approach most accurately predicts the published experimental findings. Abbas et al. [19] experimentally established that the Donohue and Kern approaches underpredicted their experimental findings by approximately 40–48%. Recently, Di Bono et al. [20] determined the HTC using the Kern and Bell-D approaches, utilizing the technical specifications of the STHEx experimentally examined by Zhang et al. [21]. Moreover, Di Bono et al. compared the calculation results obtained using the Kern and Bell-D approaches with those generated by Alperen et al. [22] using the standard HTRI Xchanger code, for the technical specifications of the STHEx examined by Zhang et al. [21]. The study found that the Bell-D approach predicts the experimental findings reported by Zhang et al. exceptionally well, whereas the Kern method and the HTRI Xchanger code overestimate the experimental HTC by about 10% and 21% for the same mass flow rate. Moreover, it was established that, under identical baffle pitch and the count of sealing strips, the HTC estimated by the Bell-D approach may differ by approximately 50% to 180% compared with that calculated by the Kern approach. On the basis of the literature review, the Bell-D approach emerges as the most commonly cited reference model.

1.2. Numerical Approaches

Increasingly, with advances in computing power, numerical methods are being used more often, including those based on commercial software such as Ansys Fluent, as well as tools that offer greater freedom in defining the mathematical description, such as the OpenFOAM software. Mohammadi et al. [23] used Fluent 6.1 code to investigate the impact of baffle cut position on the HTC, defined in a manner similar to the VDI method. It was found that the discrepancy between the Computational Fluid Dynamics (CFD) results and the predictions of the VDI method ranged from -50% to $+50\%$ for fluids with Prandtl number $0.7 \leq \mathrm{Pr} \leq 206$. It was emphasized that the baffle-to-tube and bypass streams can explain the differences between performance of vertical and horizontal configurations of segmental baffles. Ozden and Tari [24] used Ansys Fluent 6.3 package to examine the influence of baffle cut on the shell-side HTC for a small (seven tubes) STHEx. It was observed that both methods, namely the Bell-D and Kern approaches, underestimate the HTC relative to the numerically calculated values, with maximum deviations of 52% and 35%, respectively. Mellal et al. [25] used COMSOL Multiphysics 5.1 software to examine the influence of baffle spacing and orientation, as well as the number of baffles for an unconventional 38% baffle cut on the HTC of a small—only nine tubes—STHEx. By contrast to the findings of Ozden and Tari [24], the Kern method overpredicts the CFD results with a maximum deviation of about 20.8%. Alperen et al. [22] used the HTRI

Xchanger software [13] to calculate the HTC related to the heat exchanger examined experimentally by Zhang et al. [21]. Two additional calculation methods employed were the Kern and Bell-D approaches. The empirical results reported by Zhang et al. served as the benchmark for evaluating the results. The predictions indicate that the Kern approach and HTRI Xchanger code overestimate the HTC across the entire mass flow rate range considered, from about 10% at lower mass flow rates to a maximum of approximately 35% at higher mass flow rates. Conversely, the Bell-D method yields HTC values that are, on average, approximately 11% lower, and its agreement with the experimental results improves with increasing mass flow rate. Gómez et al. [26] proposed an OpenFOAM approach to support the design of STHEx. The calculation findings were compared with empirical results from an existing heat exchanger. The difference between measured and calculated heat transfer flow rate was less than 4.5%. He et al. [27] proposed an OpenFOAM solver for 3D numerical calculations of STHEx using the concept of the porous media model. The CFD predictions were experimentally validated with a maximum deviation of $\pm$13.3%. Arumsari and Ginting [28] also used the HTRI Xchanger software to estimate the shell-side HTC. The HTC calculated using HTRI Xchanger software was approximately 83% higher than that obtained from the Gnielinski correlation [29]. Wang et al. [30] used Ansys Fluent to study the impact of leakage between the shell and the baffle, as well as between the baffle and the tubes, on the flow pattern inside the shell and the thermal performance of the STHEx. The deviation between the simulation results and the predictions from the Bell-D approach was below 7.1%. Adebayo et al. [31] employed Ansys Fluent to examine the performance of a small seven-tube STHEx equipped with segmental baffles and an unconventional 36% baffle cut. It was established that the Kern method underpredicts the HTC, with a maximum deviation of about 25% at the highest mass flow rate. This result may appear questionable, since the Kern method is generally considered applicable only to a 25% baffle cut [32]. Hoang et al. [33] used Ansys Fluent to study the performance of STHEx with new types of baffles. For the validation test of the STHEx with segmental baffles (23% baffle cut, 70 mm spacing), it was revealed that the mean deviation between the numerically predicted HTC and the value estimated by the Bell-D approach, used as the reference, did not exceed 6.7%. Ullah et al. [34] used Aspen EDR to design a reference model of the STHE using industrial data. The literature review indicates that the most frequently used approach for modeling STHEx is based on Ansys Fluent, while studies employing OpenFOAM are comparatively rare.

The above review reveals that no published study has been identified in which the two methods regarded as references approaches, namely the VDI and Bell-D methods, were directly compared. Moreover, no study has been identified in which the HTC was determined using not only the Bell-D and VDI methods, but also the Aspen EDR code, which is founded on the same underlying principles as the other two approaches. The only study in which Aspen EDR was employed as a reference benchmark is that reported in [19]. Another novel contribution is the comparison of the shell-side HTC predictions obtained numerically using two CFD codes, namely OpenFOAM and Ansys Fluent, with those produced by three reference methods for a quasi-ideal STHEx, defined as a configuration without any clearances, but with a bypass stream around the tube bundle. The calculations placed particular emphasis on the influence of the clearances on the resulting HTC.

2. Model Heat Exchanger

The geometry and dimensions of the analyzed STHEx were adopted from [35]. Figure 1 illustrates the flow arrangement and the principal dimensions of the tested STHEx, whereas Table 1 summarizes the dimensions and the operating conditions.

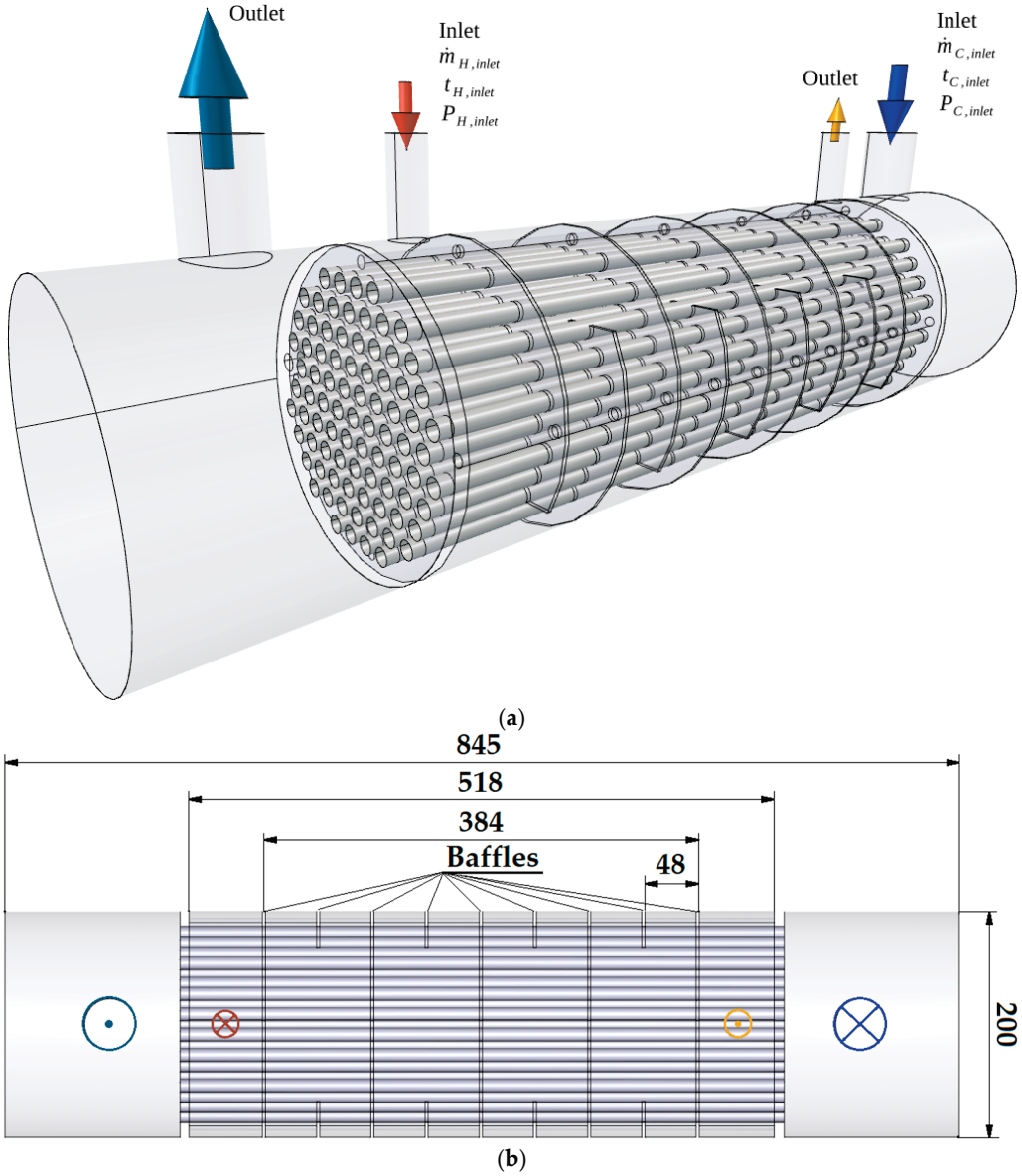


Figure 1. The model STHEx: (**a**) flow arrangement, (**b**) principal dimensions.

Table 1. Dimensions and flow parameters of the tested STHEx [35].

Item	Value/Type
Shell inner diameter	200 mm
Length of shell	518 mm
Total tube number	85
OD/ID tube diameter	12/10 mm
Tube layout	Triangular (30°)
Tube pitch	1.5
Total number of baffles	9
Baffle cut	25%
Central baffle spacing	48 mm
Inlet and outlet sections	67 mm
Hot water mass flow rate	1–6 kg/s
Cold water mass flow rate	3 kg/s
Mean hot water temperature	69 °C

Table 2 illustrates the gap combinations used in the analysis.

https://doi.org/10.3390/en19092114

Table 2. The set of the analyzed clearances [35].

Case	$\delta_d = (d_B - d_o/2)$	d_B	$\delta_D = (D_s - D_1)/2$	D_1
A	0.0	0.01200	0.0	0.2000
B1	0.00012	0.01224	0.0	0.2000
B2	0.00025	0.01250	0.0	0.2000
B3	0.00050	0.01300	0.0	0.2000
B4	0.00100	0.01400	0.0	0.2000
C1	0.0	0.00012	0.0001	0.1998
C2	0.0	0.00012	0.0007	0.1986
C3	0.0	0.00012	0.0012	0.1976
C4	0.0	0.00012	0.0025	0.1950
C5	0.0	0.00012	0.0050	0.1900
D1	0.00012	0.01224	0.0001	0.1998
D2	0.00025	0.01250	0.0007	0.1986
D3	0.00050	0.0130	0.0012	0.1976
D4	0.00100	0.014	0.0025	0.1950

3. Materials and Methods

3.1. Hand Calculation Methods

This study employed two widely accepted and commonly used manual calculation methods: the Bell-D and VDI approaches. Both methods allow for input of thermal-flow parameters, such as mass flow rate and temperature, as well as very detailed data concerning the geometry of the STHEx.

3.1.1. The Bell-Delaware Method

Essentially, the Bell-D method is based on determining the HTC for an ideal tube bundle and applying numerous correction factors that account for, among other things, the effects of clearances between the baffle and the shell, as well as between the baffle and the tube bundle. As the procedures used to determine the correction factors are highly complex, their detailed presentation is beyond the scope of this article. The computational milestones of the Bell-D method are presented in [13,36], while the calculations in this study were based on [37], which provides a step-by-step algorithm for calculating the HTC.

3.1.2. The VDI Method

In essence, the VDI method involves determining the HTC for a single tube and then using several correction factors that account for the complex geometry of the STHEx. Similarly to the Bell-D method, the procedures used to predict the HTC are highly intricate; therefore, their discussion is beyond the scope of this paper. The key computational steps of the VDI method are presented in [14,36], while calculations in this study were based on [38], which provides a step-by-step algorithm for predicting the HTC.

3.2. Numerical Methods

3.2.1. OpenFOAM Approach

The system of equations governing flow with heat transfer can be expressed as

$$\frac{\partial \rho}{\partial \tau} + \nabla \cdot (\rho \boldsymbol{u}) = 0 \quad (1)$$

https://doi.org/10.3390/en19092114

$$\frac{\partial}{\partial \tau}(\rho \boldsymbol{u}) + \nabla \cdot (\rho \boldsymbol{u}\boldsymbol{u}) = \rho \boldsymbol{g} - \nabla P + \nabla \cdot (\mu \nabla \boldsymbol{u}) + \nabla \cdot \left(\mu \mathrm{dev}_2 (\nabla \boldsymbol{u})^T\right) \quad (2)$$

$$\frac{\partial}{\partial \tau}(\rho (K + h)) + \nabla \cdot (\rho \boldsymbol{u}(K + h)) = \frac{\partial P}{\partial \tau} + \rho \boldsymbol{g} \cdot \boldsymbol{u} + \nabla \cdot (\lambda \nabla h) \quad (3)$$

In the system in Equations (1)–(3), $\boldsymbol{u}$ is the velocity vector, $\mathrm{dev}_2\ \mathbf{T} = \mathbf{T} - 2/3\ \boldsymbol{\delta} \mathrm{tr}\mathbf{T}$, and $\boldsymbol{\delta}$ is the unity tensor. The kinetic energy is of the form $\mathrm{K} = 1/2\ \|\mathbf{u}\|^2$.

The boundary conditions, such as inlets and outlets to individual domains, are shown in Figure 1. All other surfaces are defined as no-slip walls. The averaged transport Equations (1)–(3) were solved using the Reynolds-Averaged Simulation approach to turbulence, together with the *k*-ω SST turbulence model [39]. The open-source software OpenFOAM 2312 [40] was used to solve the discretized equations by means of the Finite Volume Method (FVM). The computational Cartesian mesh consisted of 9.92 million nodes—Figure 2. Mesh details near the walls are presented in Figure 3. The SIMPLE algorithm and the GAMG solver were used to solve the system Equations (1)–(3). More details about the OpenFOAM procedure are discussed in [35,36].

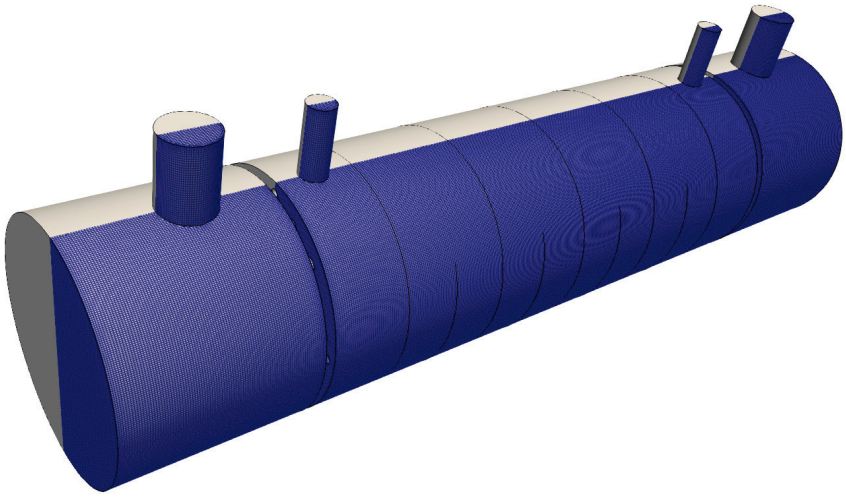


Figure 2. Computation domain for OpenFOAM.

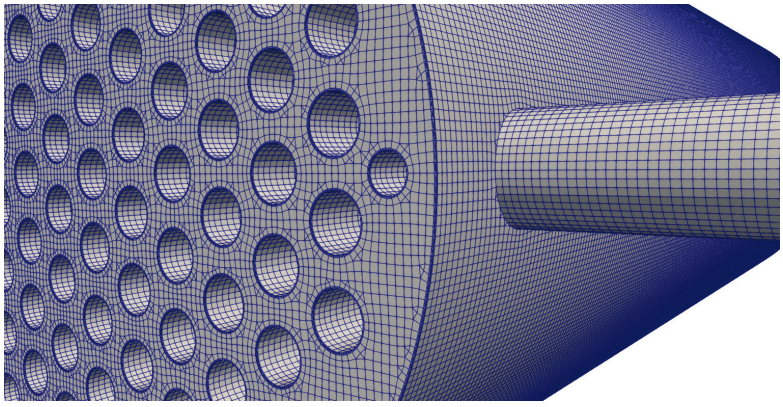


Figure 3. Mesh details near the walls for OpenFOAM.

Figure 4 presents the effect of the computational mesh on the outlet temperature of both hot, t_H, and cold, t_C, fluids. Six cases were examined, spanning from 2.2 million to almost 11 million nodes.

Figure 4 shows that the exit temperature of both hot and cold fluids vary with mesh refinement up to 9.9 million nodes. Further refinement of the mesh does not lead to appreciable changes. A mesh of 9.92 million nodes was therefore selected for subsequent

https://doi.org/10.3390/en19092114

analysis. The mesh sensitivity was investigated for $\dot{m}_H$ = 2.707 kg/s, $t_{H,in}$ = 77.82 °C, $\dot{m}_C$ = 3.173 kg/s, and $t_{C,in}$ = 9.81 °C.

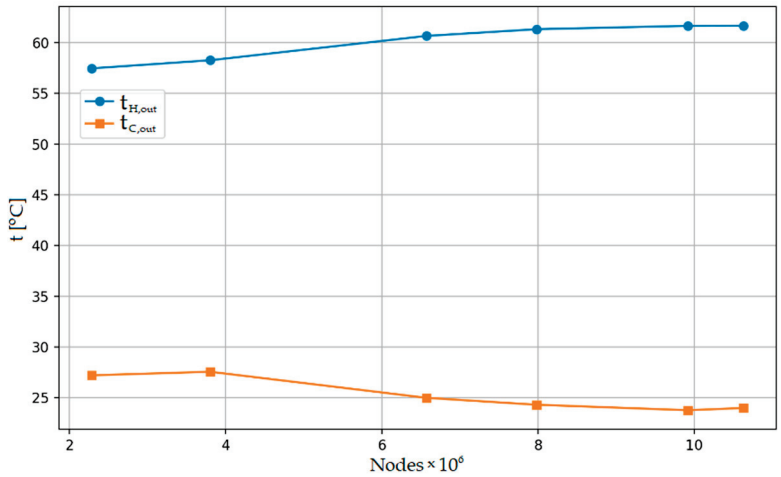


Figure 4. Mesh sensitivity for OpenFOAM.

3.2.2. Ansys Fluent Approach

Ansys Fluent 21.1 was utilized for conducting the numerical simulations [41]. For the case considered, the system of conservation equations was resolved in the following form

$$\nabla \cdot \boldsymbol{u} = 0 \tag{4}$$

$$\rho(\boldsymbol{u} \cdot \nabla \boldsymbol{u}) = -\nabla P + \nabla \cdot \boldsymbol{\tau} \tag{5}$$

$$\rho c_p(\boldsymbol{u} \cdot \nabla T) = \nabla \cdot \left(\lambda_{eff} \nabla T\right) \tag{6}$$

where $\boldsymbol{\tau}$ represents the stress tensor including the contributions of molecular and turbulent viscosity of the fluid.

Similarly to the OpenFOAM approach, the boundary conditions, including the inlets and outlets to individual domains, are shown in Figure 1. All other surfaces are defined as no-slip walls. The system of Equations (4)–(6) was solved by means the FVM together with the *k*-*ε* turbulence model. The SIMPLE algorithm was applied to solve the pressure–velocity coupling. The computational domain—shown in Figure 5—was generated using the ANSYS Gambit 2.4.6 program (Fluent Inc., Lebanon, NH, USA). Due to geometric symmetry, only half of the domain was simulated. More details about the Ansys Fluent procedure are discussed in [35,36].

Figure 6 shows the effect of mesh resolution on the exit temperature of both hot, $t_{H,out}$ and cold, $t_{C,out}$ fluids. Four cases were considered, with 1.538 million–5.422 million finite volumes.

Figure 6 indicates that increasing the number of finite volumes from 3.071 million to 5.422 million resulted in an insignificant change in the predicted exit temperatures of both fluids. The mesh sensitivity was investigated for $\dot{m}_H$ = 3.0 kg/s, $t_{H,in}$ = 75.80 °C, $\dot{m}_C$ = 3.0 kg/s, and $t_{C,in}$ = 10.0 °C. Since the computation time for the mesh with 5.422 million finite volumes did not differ substantially from that for the mesh with 3.071 million finite volumes, the mesh with the larger number of finite volumes was adopted for further calculations.

Because the *k*-*ω* SST and *k*-*ε* models are widely used in numerical heat transfer simulations, it was decided to use both in this study. In the modeling of the STHEx, the *k*-*ε* model proves effective as a tool for rapid, stable calculations of the system's overall parameters, whereas the *k*-*ω* SST model is more suitable in cases where high local accuracy is crucial—

particularly in wall-adjacent regions and in intricate flow inside the shell. Furthermore, the ability of the *k*-*ω* SST model to accurately capture near-wall behavior and flow separation phenomena, which predominate inside the shell, has been well documented. This is because the model combines the advantages of the *k*-*ω* formulation in near-wall regions and those of the *k*-*ε* formulation in the bulk flow. However, the *k*-*ε* model is a well-established and reliable approach commonly employed in industrial simulations involving fully developed turbulence, and its computational efficiency and extensive validation studies in the field of heat exchangers make it a suitable reference model for comparative purposes.



Figure 5. Computational domain and unstructured tetrahedral mesh developed in Ansys Gambit pre-processor.

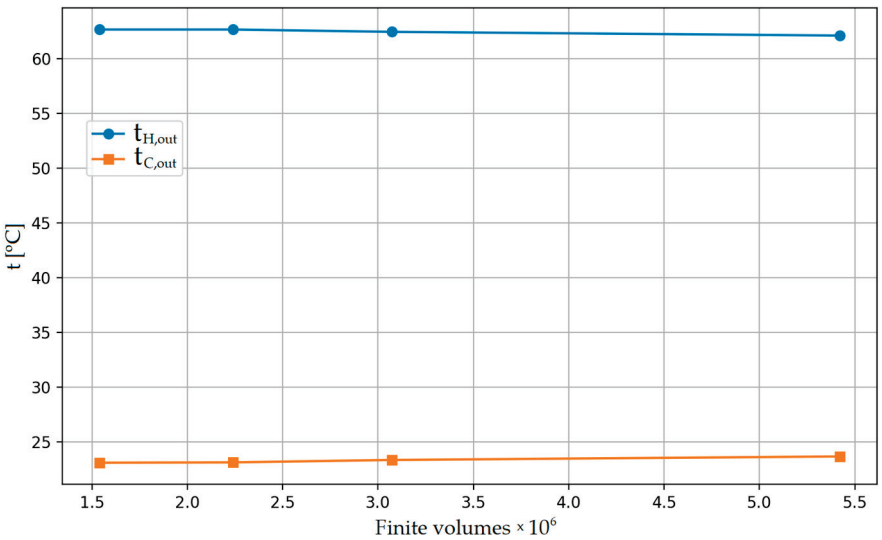


Figure 6. Mesh sensitivity for Ansys Fluent.

3.3. Industrial Software

The academic license under which the calculations were performed does not permit disclosure of the specific correlations used in Aspen Exchanger Design and Rating (Aspen EDR) V15.0 [42]. The shell-side thermohydraulic analysis is performed based on the concept of flow paths in the STHEx originally proposed by Tinker [5,6] and subsequently refined

by Palen and Taborek [43]. Aspen EDR is intended primarily for heat exchanger design. However, as demonstrated by the calculations carried out in this study, it also proves to be a highly effective tool for thermohydraulic analysis.

3.4. Water Properties

The properties of hot and cold water were determined using correlations developed on the basis of the database reported in [44]:

- Dynamic viscosity.

$$\mu = 2.2551418931 - 3.3948447154 \times 10^{-2}T + 2.0532435429 \times 10^{-4}T^2 - 6.2294811154 \times 10^{-7}T^3 + 9.4740755112 \times 10^{-10}T^4 - 5.7750953816 \times 10^{-13}T^5 \quad (7)$$

- Thermal conductivity.

$$\lambda = 2.7689426052 \times 10 - 4.1570211623 \times 10^{-1}T + 2.4968651122 \times 10^{-3}T^2 - 7.3889761073 \times 10^{-6}T^3 + 1.0839020278 \times 10^{-8}T^4 - 6.3292341999 \times 10^{-12}T^5 \quad (8)$$

- Density.

$$\rho = -5.8593636805 \times 10^3 + 9.8968557714 \times 10T - 5.7474749375 \times 10^{-1}T^2 + 1.6856053180 \times 10^{-3}T^3 - 2.4989340377 \times 10^{-6}T^4 + 1.4908022754 \times 10^{-9}T^5 \quad (9)$$

- Specific heat.

$$c_p = 1.8561445426 \times 10^5 - 2.7374285462 \times 10^3T + 1.6544683581 \times 10T^2 - 5.0060497615 \times 10^{-2}T^3 + 7.5807970466 \times 10^{-5}T^4 - 4.5941525532 \times 10^{-8}\mathrm{T}^5 \quad (10)$$

- Prandtl number.

$$Pr = 1130.643576 - 10.068594\mathrm{T} + 0.030127T^2 - 3 \times 10^{-3}T^3 \quad (11)$$

The applicable range of Equations (7)–(11) is 10 °C to 80 °C. Within the considered temperature range, the coefficient of determination (R^2) equals 1.00000 for dynamic viscosity, thermal conductivity, and density, whereas for specific heat is 0.99987.

4. Results

4.1. An Idealized Heat Exchanger

An idealized STHEx is characterized by the absence of leakage between the baffle and the tubes, as well as between the baffle and the shell. However, a bypass stream occurs between the tube bundle and the shell. This fluid stream flows around the outer tubes of the bundle and is therefore not fully utilized for heat transfer. Figure 7 illustrates a comparison of the HTC predicted by all five methods for case A (Table 2).

Figure 7 exhibits that the VDI method predicts the highest HTC, whereas Ansys Fluent yields the lowest value. The discrepancy between the VDI method predictions and the Ansys Fluent results increases as mass flow rate rises, reaching 45% at the highest mass flow rate. The solid black line represents the arithmetic average of the five methods considered, hereafter referred to as the mean. With the exception of the VDI method, the HTCs predicted by the Bell-D method, CFD-OpenFOAM, Ansys Fluent, and Aspen EDR deviate from the mean by no more than ±20%, which indicates close agreement among these methods. The maximum deviation between the values predicted by the VDI method and the mean value was about 34%.

Figure 8 illustrates the HTC predicted by the *k*-ε and *k*-ω SST turbulence models for the idealized STHEx corresponding to case A in Table 2.

https://doi.org/10.3390/en19092114

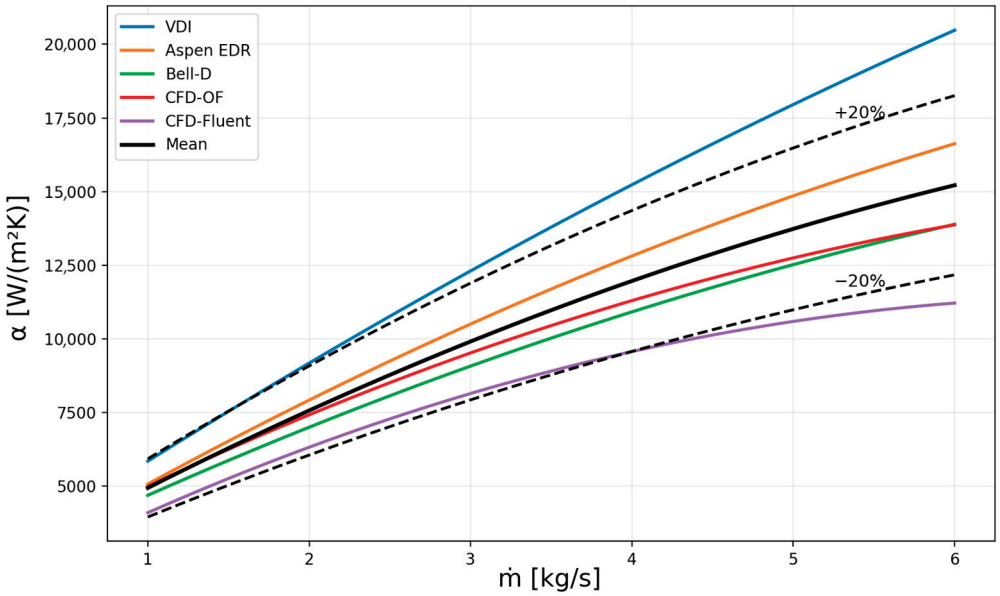


Figure 7. Shell-side HTC from considered five methods.

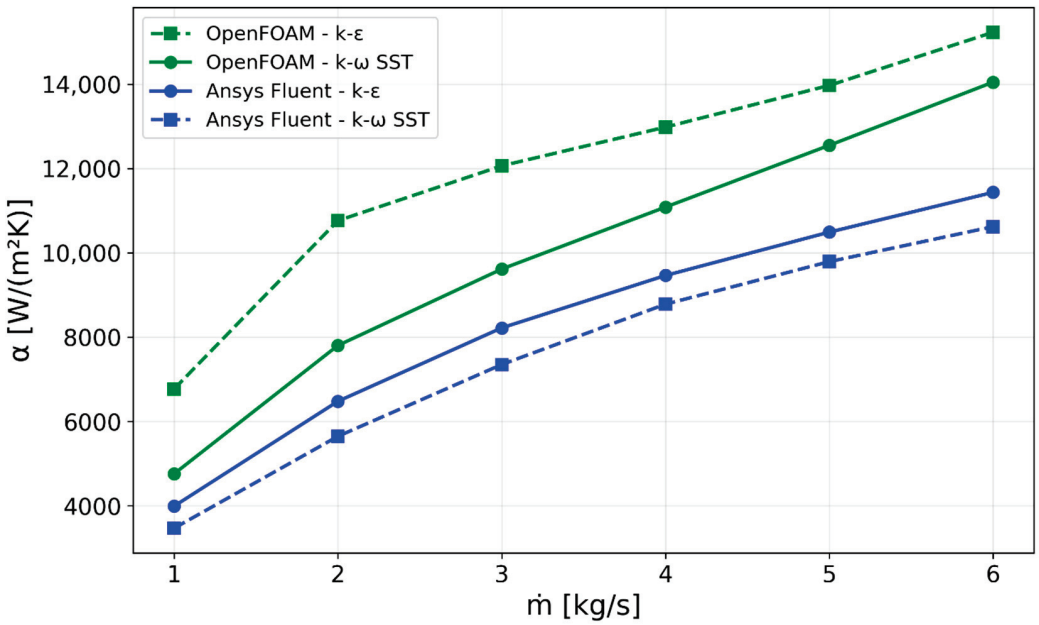


Figure 8. Comparison of the HTC for different turbulence models.

Figure 8 exhibits that the *k*-ε formulation implemented in OpenFOAM predicts the highest HTC, while the *k*-ω SST formulation incorporated in Ansys Fluent yields the lowest. In both CFD approaches, the *k*-ε turbulence model predicts a higher HTC than the *k*-ω SST. In the case of OpenFOAM, the discrepancy between the HTC predictions of the *k*-ε and the *k*-ω SST models decreases markedly as the mass flow rate increases, amounting to 28% for the lower mass flow rate and 15% for higher mass flow rate. In Ansys Fluent, the discrepancy between the results using the two turbulence models also decreases as the mass flow rate increases, declining from approximately 13% to 7%. The discrepancy between the OpenFOAM predictions and the Ansys Fluent results for the *k*-ω SST turbulence model decreases slightly as the mass flow rate increases, dropping from approximately 28% to 21%. Similarly, the discrepancy between the OpenFOAM predictions and the Ansys Fluent results for the *k*-ε model decreases as the mass flow rate increases, falling from approximately 39% to 27%.

Generally, it can be stated that, in Ansys Fluent, the use of either the *k*-ε or *k*-ω SST turbulence model does not significantly affect the predicted HTC, whereas for OpenFOAM, the differences in the resulting HTCs are much greater. Importantly, in the case considered, the results obtained with the *k*-ω SST formulation in OpenFOAM and the *k*-ε formulation in Ansys Fluent were more consistent than those obtained using the same turbulence model across different computational codes. Therefore, different turbulence models were adopted for the subsequent analysis in the two codes: the *k*-ω SST in OpenFOAM and the *k*-ε in Ansys Fluent. It should also be borne in mind that the *k*-ω SST model provides better handling of near-wall flows, adverse pressure gradients, and flow separation. However, the enhanced predictive capabilities of the *k*-ω SST model are achieved at the expense of increased computational time. This is because the model is more sensitive to the quality of the computational mesh and requires a correspondingly denser mesh near the wall.

Figure 9 exhibits a cross-sectional view of the idealized STHEx, whereas Figure 10 illustrates the HTC for the cases without and with sealing strips.

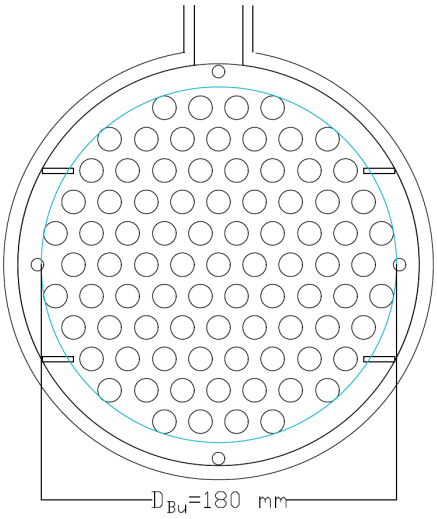


Figure 9. The idealized STHEx with two pairs of sealing strips.

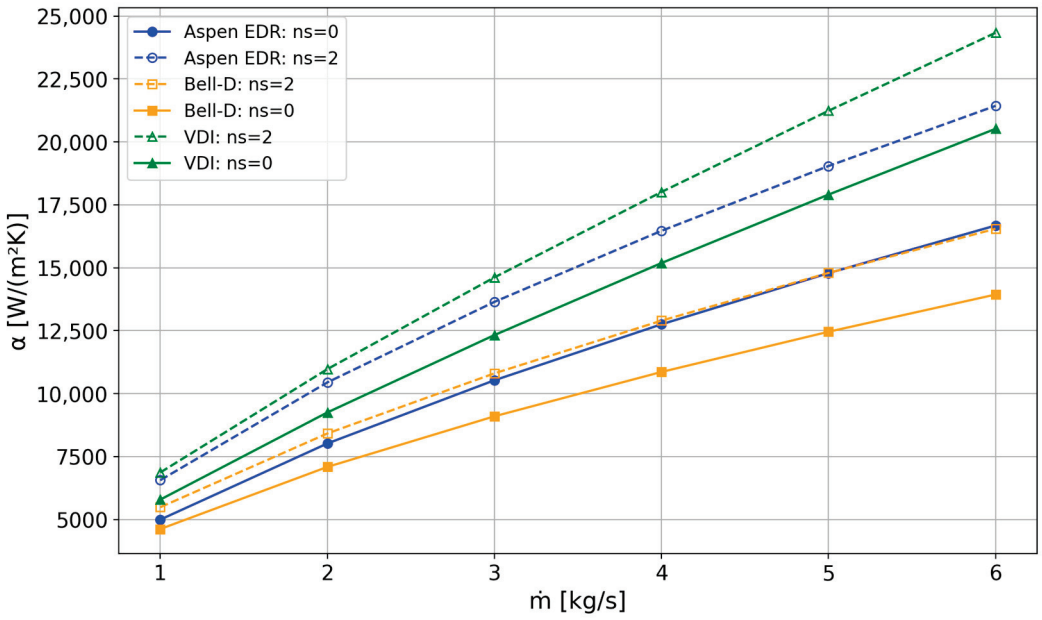


Figure 10. Influence of sealing strips on the HTC.

Figure 10 exhibits that all three considered methods predict a rise in HTC for the STHEx equipped with sealing strips, as expected, since the sealing strips redirect the bypass stream into cross-flow. While the VDI and Bell-D methods predict virtually the same increase in HTC—18.6% and 18.7%, respectively—regardless of mass flow rate, Aspen EDR yields a rise in HTC of about 30%, which is slightly higher at lower mass flow rates.

Figure 11 illustrates the temperature distribution obtained from numerical simulations carried out in Ansys Fluent for $\dot{m}_H$ = 3 kg/s and $\dot{m}_C$ =3 kg/s, respectively, with inlet temperatures of $t_{H,in}$ = 75.8 °C and $t_{C,in}$ = 10 °C, respectively.

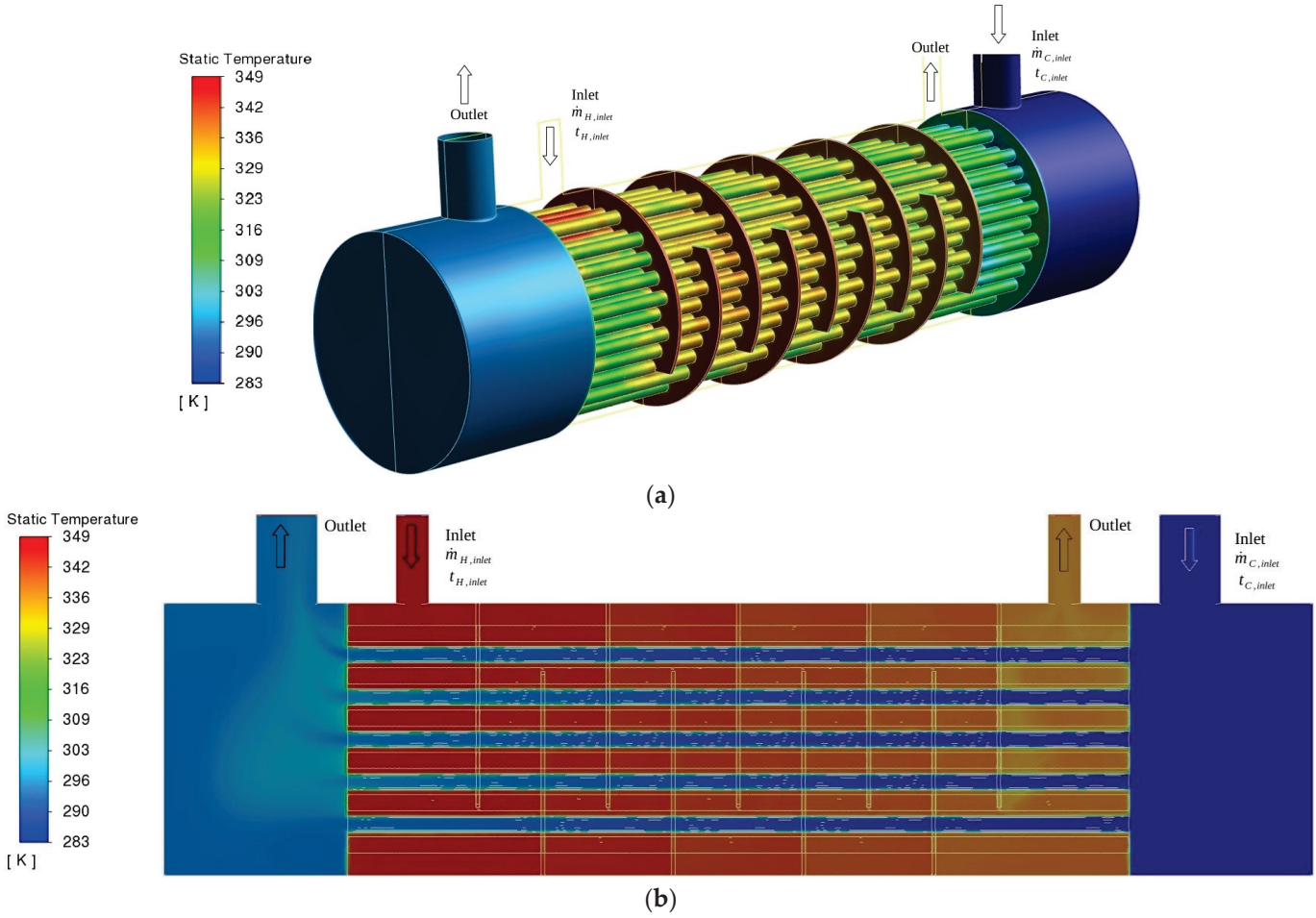


Figure 11. Temperature distribution: (**a**) axonometric view; (**b**) longitudinal cross section.

In Figure 11a, the temperature distribution of the baffles is particularly noteworthy. The first three baffles on the hot water inlet side have nearly identical high temperatures, whereas from the fourth baffle onward a clear drop in the baffle temperature can be observed. In Figure 11b, it is characteristic that the hot water temperature drops very sharply already in the first section of the STHEx, which is expected since the hot water comes into contact there with tube surfaces at the lowest temperature, resulting from cold water inlet temperature.

Figure 12 shows the flow map inside the shell of the idealized STHEx for $\dot{m}_H$ = 3.0 kg/s.

Figure 12 exhibits that the hot water flow is relatively uniform throughout most of the exchanger, with the exception of the region near the outlet port. The velocity distribution at the outlet port is more uniform than at the inlet port, where a clearly higher velocity is observed along the port axis. Since the case considered involves an idealized STHEx, Figure 12 shows no leakage flows associated with the gaps between the baffle and the tubes or between the baffle and the shell.

https://doi.org/10.3390/en19092114

Figure 13 shows the velocity distribution in the idealized STHEx.

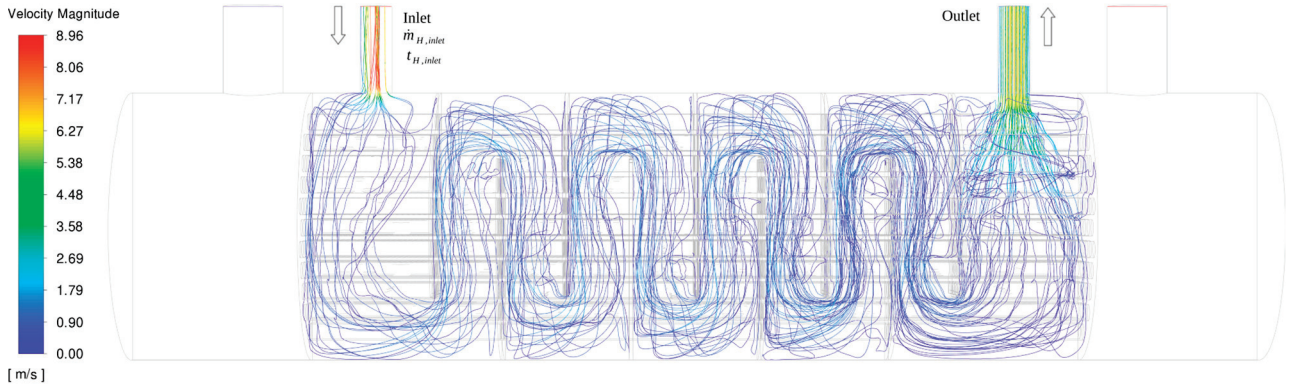


Figure 12. Streamlines of hot water in the idealized STHEx.

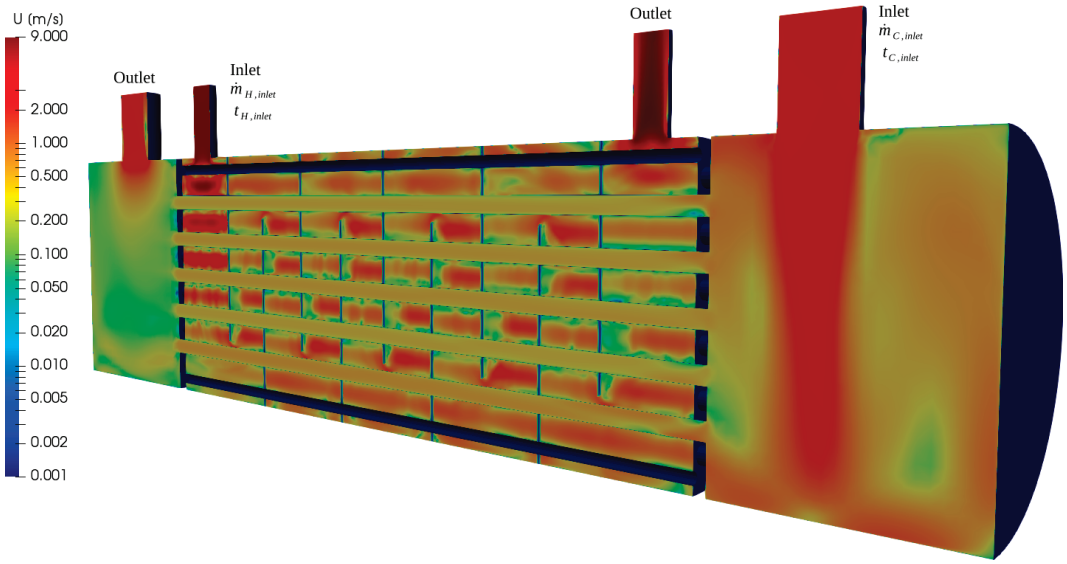


Figure 13. Velocity distribution in the idealized STHEx.

Figure 13 shows the velocity distributions in the form of vector magnitude in a longitudinal view of the entire unit. The distribution is presented on a logarithmic scale, which permits better visualization of the full range of velocities compared to a linear scale. Figure 13 shows that there are no stagnation zones on either side of the exchanger, which would be represented by dark blue color. In both computational domains, the peak velocities are located in the entrance and exit ports. Localized velocity drops are also visible where the water flows around the baffles. Figure 13 shows that, although the baffles cause the flow to decelerate, these regions are not true stagnation zones, as the velocity remains approximately 0.2 m/s. This local reduction in velocity is accompanied by a slight change in temperature, as shown in Figure 11b. These velocity variations are only visible on a logarithmic scale; otherwise, the distribution would appear uniform.

4.2. Heat Exchanger with Leakage

Figure 14 compares the shell-side HTC from the VDI, Bell-D, and Aspen EDR approaches for cases B1 to B4 (Table 2), i.e., for the instances without leakage between the baffle and the shell and with leakage between the baffle and the tubes.

https://doi.org/10.3390/en19092114

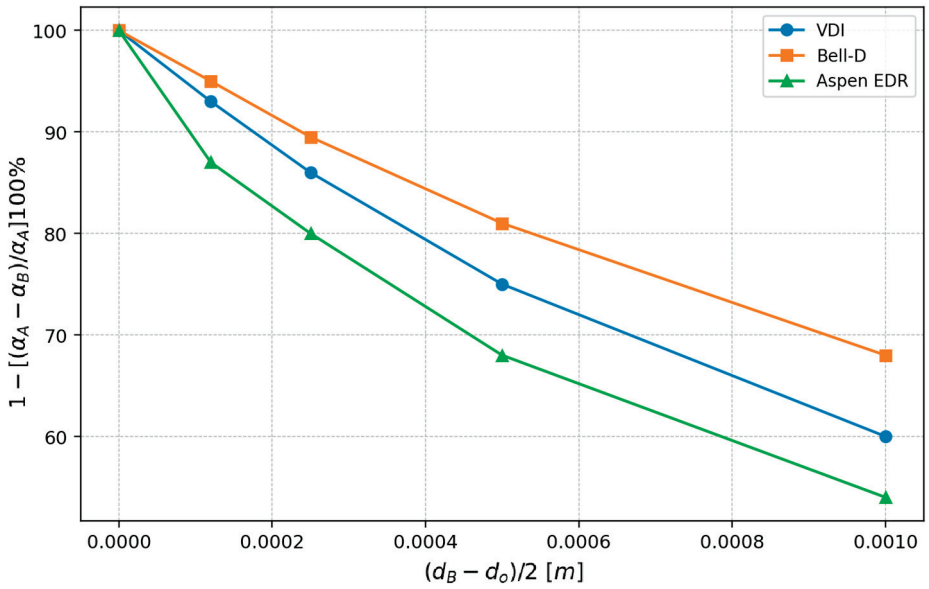


Figure 14. Effect of baffle-to-tube leakage on the HTC.

As illustrated in Figure 14, the results show that the HTC decreases as the baffle-to-tube gap increases. This is expected, since baffle-to-tube leakage reduces cross-flow. It should be noted that the decrease in the HTC becomes more pronounced as the clearances increase. At the maximum gap ($\delta_d = 1$ mm), the Bell-D, VDI, and Aspen EDR approaches predict an HTC reduction of about 32%, 40%, and 46%, respectively.

Figure 15 exhibits the variation in the HTC obtained using the VDI, Bell-D, and Aspen EDR approaches with the shell-to-baffle gap for the cases C1–C5 relative to the reference case A (Table 2).

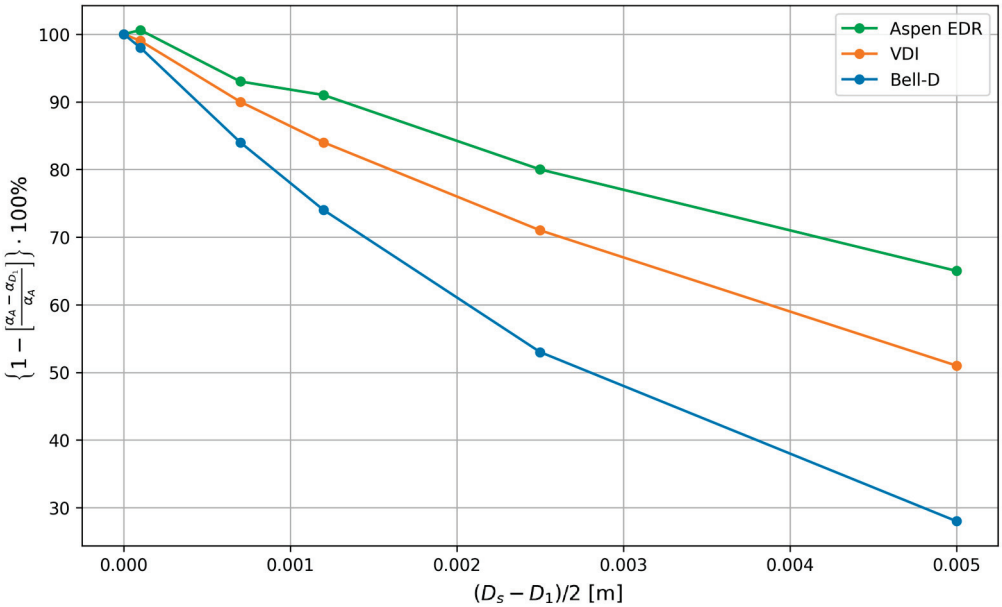


Figure 15. Influence of shell-to-baffle leakage on the HTC.

As can be seen from Figure 15, the HTC decreases as the shell-to-baffle gap increases, irrespective of the calculation method applied. This behavior is expected, since a larger shell-to-baffle gap promotes a greater bypass stream, which does not contribute effectively to heat transfer from the tube bundle. The individual methods exhibit different sensitivities to increasing clearances. The most conservative results are obtained with the Bell-D method,

https://doi.org/10.3390/en19092114

which indicates a 72% decrease in HTC for the largest shell-to-baffle gap ($\delta_D = 5$ mm). Aspen EDR is the least sensitive to increasing shell-to-baffle clearances and predicts an HTC decrease of approximately 35% for the largest clearance. The VDI method predicts an HTC reduction of about 50% for the largest clearance.

Figure 16 shows the HTC calculated according to the VDI, Bell-D, and Aspen EDR approaches for cases A, D1, and D4 listed in Table 2, which correspond to conditions involving leakage between the baffle and the tubes, as well as between the baffle and the shell.

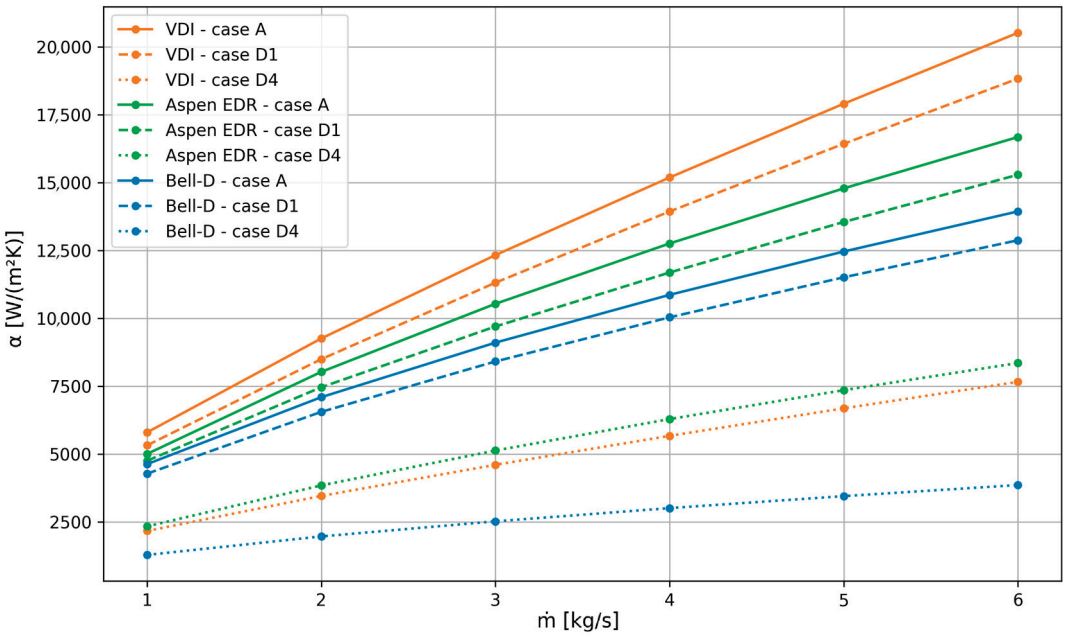


Figure 16. Influence of two leakage types on the HTC.

As can be seen from Figure 16, all three considered methods show a rise in HTC with higher mass flow rate, irrespective of the gap size, from case A with no leakage (solid lines) to case D4 with the maximum values of both types of leakage (dotted lines). Importantly, for case D1 (i.e., for the combination of the smallest gaps, represented by the dashed lines), the considered methods exhibit the same HTC tanking as in case A: the VDI approach yields the highest values, Aspen EDR intermediate, while the Bell-D approach presents the lowest. For case D4, the HTC ranking differs: Aspen EDR predicts the highest HTC values, the VDI method yields intermediate values, while the Bell-D approach gives the lowest.

Figure 17 shows the influence of both types of leakage on the HTC, as calculated using the VDI, Bell-D, and Aspen EDR approaches for cases D1 and D4 relative to the reference case A for each method (Table 2).

Figure 17 shows clearly that a reduction in the HTC is predicted by all methods of about 8% for case D1 relative to case A within each respective method. For case D4, however, the situation differs: Aspen EDR, the VDI and Bell-D approaches predict HTC reductions of 55%, 60%, and 65%, respectively, relative to case A.

https://doi.org/10.3390/en19092114

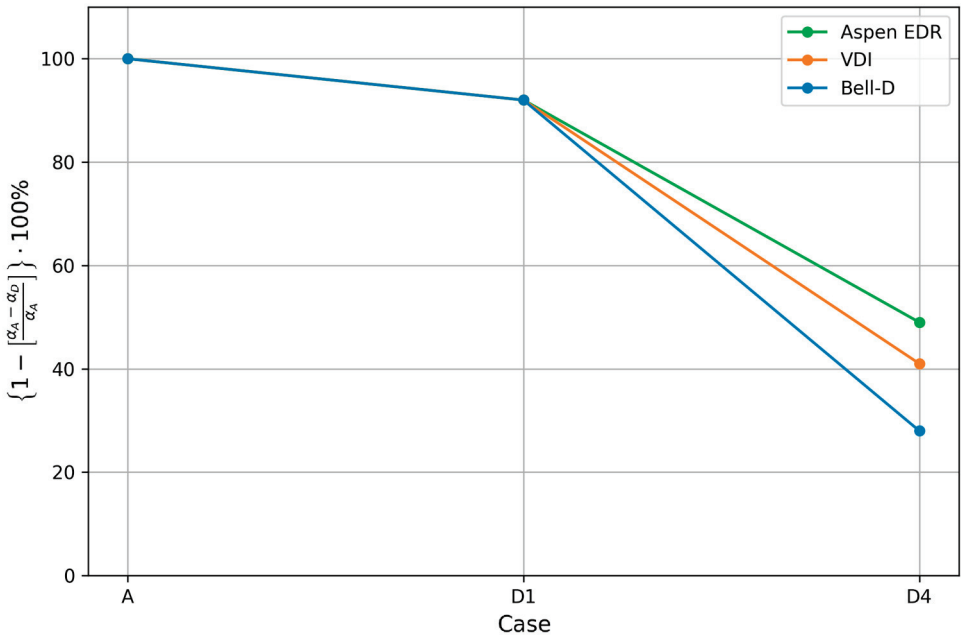


Figure 17. Relative impact of both clearance types on shell-side HTC.

5. Conclusions

- Two analytical approaches, namely the VDI method and the extended Bell-D method, two software tools, namely OpenFOAM and Ansys Fluent, as well as Aspen EDR were applied to estimate the shell-side HTC in the STHEx with segmental baffles, considering a wide range of gaps between the baffle and the shell and between the baffle and the tubes as well as varying fluid mass flow rates. This comparative analysis, using analytical methods as the reference benchmark, represents a preliminary stage of a comprehensive study that includes an extensive experimental component for validation.
- For the idealized STHEx, with the exception of the VDI method, the remaining four methods predict the HTC within ±20% of the mean, defined as the arithmetic average of the results obtained using the five methods considered. The VDI approach overestimates the HTC by approximately 34%.
- The predictions showed that using two pairs of sealing strips in the idealized STHEx increased the HTC by more than 18% in the VDI and Bell-D approaches, and approximately 30% in Aspen EDR.
- The calculations showed a strong negative effect of leakage between the baffle and the tubes on the HTC. Specifically, when no shell-to-baffle gap occurs, Aspen EDR predicts a 46% reduction in HTC relative to the idealized STHEx.
- Shell-to-baffle clearances have a similarly negative impact on the HTC. For the largest clearance-to-shell radius ratio of 5%, and with no leakage between the baffle and the tubes, the Bell-D method predicts an HTC reduction of up to 72% relative to the idealized STHEx.
- In real STHEx units, both types of leakage occur due to assembly reasons. For the configuration of maximum clearances considered in the calculations, the HTC decreased by at least 50%. The most conservative prediction was obtained with the Bell-Delaware method, which indicated an HTC reduction of about 65% compared with the quasi-ideal STHEx.
- Both CFD approaches used—OpenFOAM and Ansys Fluent—were found to be highly sensitive to the method used to average the fluid temperature from the computed temperature field (Figure 11), which is a necessary step in determining the HTC.

https://doi.org/10.3390/en19092114

Future work will include systematic experimental investigations of STHEx units with different baffle configurations.

Author Contributions: Conceptualization, J.T.C.; methodology, J.T.C.; software, J.B., P.D., K.S. and K.T.; validation, J.T.C., J.B., P.D., K.S. and K.T.; formal analysis, J.T.C.; investigation, J.T.C., J.B., P.D., K.S. and K.T.; data curation, J.T.C., J.B., P.D., K.S. and K.T.; writing—original draft preparation, J.T.C.; writing—review and editing, J.T.C., P.D., J.B. and K.T. All authors have read and agreed to the published version of the manuscript.

Funding: This research received no external funding.

Data Availability Statement: The original contributions presented in this study are included in the article. Further inquiries can be directed to the corresponding author.

Conflicts of Interest: The authors declare no conflicts of interest.

Nomenclature

d_o	Tube diameter	[m]
d_B	Baffle tube hole diameter	[m]
D_1	Baffle diameter	[m]
D_{Bu}	Tube bundle diameter	[m]
D_s	Shell diameter	[m]
g	Acceleration due to gravity	[m/s^2]
h	Specific enthalpy	[J/kg]
$\dot{m}$	Mass flow rate	[kg/s]
P	Pressure	[Pa]
T	Temperature	[K]
u	Velocity	[m/s]
Greek letters		
α	Heat transfer coefficient	[W/(m^{2}K)]
δ	Clearance	[m]
λ	Thermal conductivity	[W/(mK)]
ρ	Density	[kg/m^3]
μ	Dynamic viscosity	[Pas]
Subscripts		
A	Case A	
C	Cold	
eff	Effective	
H	Hot	
in	Inlet	
out	Outlet	
s	Shell	

Abbreviations

Bell-D	Bell-Delaware
CFD	Computational Fluid Dynamics
FVM	Finite Volume Method
HTC	Heat Transfer Coefficient
ID	Inside Diameter
OD	Outside Diameter
OF	OpenFOAM
STHEx	Shell-and-Tube Heat Exchanger
VDI	Verein Deutscher Ingenieure

References

1. Gupta, J.P. *Heat Exchanger and Pressure Vessel Technology*; Hemisphere Publishing Corporation: Washington, DC, USA, 1986.
2. Shah, R.K.; Sekulić, D.P. *Fundamentals of Heat Exchanger Design*; Wiley & Sons, Inc.: Hoboken, NJ, USA, 2003.
3. Thulukkanam, K. *Heat Exchanger Design Handbook*, 2nd ed.; CRC Press: Boca Raton, FL, USA, 2013.
4. Kakaç, S.; Liu, H.; Pramuanjaroenkij, A. *Heat Exchangers: Selection, Rating, and Thermal Design*, 4th ed.; CRC Press: Boca Raton, FL, USA; London, UK; New York, NY, USA, 2020.
5. Taborek, J. Survey of Shell-Side Flow Correlations. In *Heat Exchanger Design Handbook*; Begell House, Inc.: Danbury, CT, USA, 2025.
6. Tinker, T. *Shell Side Characteristics of Shell and Tube Heat Exchanger, Parts I–III, General Discussion of Heat Transfer*; Institution of Mechanical Engineers: London, UK; ASME: New York, NY, USA, 1951; pp. 84–110.
7. Tinker, T. Shell-Side Characteristics of Shell and Tube Heat Exchanger. *J. Heat Transf.* **1958**, *80*, 36–52.
8. Mukherjee, R. Effectively design shell-and-tube heat exchangers. *Chem. Eng. Prog.* **1998**, *94*, 21–37.
9. Marzouk, S.A.; Abou Al-Sood, M.M.; El-Said, E.M.S.; Younes, M.M.; El-Fakharany, M.K. A comprehensive review of methods of heat transfer enhancement in shell and tube heat exchangers. *J. Therm. Anal. Calorim.* **2023**, *148*, 7539–7578. [CrossRef]
10. Kern, D.Q. *Kern's Process Heat Transfer*, 2nd ed.; Wiley & Sons, Inc.: Hoboken, NJ, USA, 2019.
11. Donohue, D.A. Heat Transfer and Pressure Drop in Heat Exchangers. *Ind. Eng. Chem.* **1949**, *41*, 2499–2511. [CrossRef]
12. Žukauskas, A. Heat transfer from tubes in crossflow. *Adv. Heat Transf.* **1972**, *8*, 93–160.
13. Serth, R.W.; Lestina, T.G. *Process Heat Transfer*; Elsevier: Amsterdam, The Netherlands, 2014.
14. Gaddis, E.S.; Gnielinski, V. G8 Shell-Side Heat Transfer in Baffled Shell-and-Tube Heat Exchangers. In *VDI Heat Atlas*; Springer: Berlin/Heidelberg, Germany, 2010; pp. 731–741.
15. Roetzel, W.; Lee, D. Experimental investigation of leakage in shell-and-tube heat exchangers with segmental baffles. *Int. J. Heat Mass Transf.* **1993**, *36*, 3765–3771.
16. Kücük, H.; Ünverdi, M.; Yılmaz, M.S. Experimental investigation of shell side heat transfer and pressure drop in a mini-channel shell and tube heat exchanger. *Int. J. Heat Mass Transf.* **2019**, *143*, 118493. [CrossRef]
17. Abdelkader, B.A.; Zubair, S.M. The Effect of a Number of Baffles on the Performance of Shell-and-Tube Heat Exchangers. *Heat Transf. Eng.* **2019**, *40*, 39–52. [CrossRef]
18. Wills, M.J.N.; Johnston, D.; Harwell, A.E.R.E. A new and accurate hand calculation method for shell-side pressure drop and flow distribution. In *Proceedings of the 22nd National Heat Transfer Conference, HTD*; ASME: New York, NY, USA, 1984; Volume 36.
19. Abbas, A.; Ismail, T.; Ayub, Z.; Ayub, A.; Cheema, T.A.; Li, W.; Ye, J. Shell Side Single-Phase Experimental Heat Transfer Analysis of a Vertically Oriented Single Segmental Baffle Bundle with Dimpled Tubes. *J. Therm. Sci. Eng. Appl.* **2020**, *12*, 011017. [CrossRef]
20. Di Bono, G.; Corcione, M.; Quintino, A. Systematic comparative analysis of Kern and Bell-Delaware methods for the design of shell-and-tube heat exchangers. *Appl. Therm. Eng.* **2025**, *278*, 127327. [CrossRef]
21. Zhang, J.F.; Li, B.; Huang, W.J.; Lei, Y.G.; He, Y.L.; Tao, W.Q. Experimental performance comparison of shell-side heat transfer for shell-and-tube heat exchangers with middle-overlapped helical baffles and segmental baffles. *Chem. Eng. Sci.* **2009**, *64*, 1643–1653. [CrossRef]
22. Alperen, M.A.; Kayabaşi, E.; Hüseyin Kurt, H. Detailed comparison of the methods used in the heat transfer coefficient and pressure loss calculation of shell side of shell and tube heat exchangers with the experimental results. *Energy Sources Part A Recovery Util. Environ. Eff.* **2023**, *45*, 5661–5680. [CrossRef]
23. Mohammadi, K.; Heidemann, W.; Müller-Steinhagen, H. Numerical Investigation of the Effect of Baffle Orientation on Heat Transfer and Pressure Drop in a Shell and Tube Heat Exchanger with Leakage Flows. *Heat Transf. Eng.* **2009**, *30*, 1123–1135. [CrossRef]
24. Ozden, E.; Tari, I. Shell side CFD analysis of a small shell-and-tube heat exchanger. *Energy Convers. Manag.* **2010**, *51*, 1004–1014. [CrossRef]
25. Mellal, M.; Benzeguir, R.; Sahel, D.; Ameur, H. Hydro-thermal shell-side performance evaluation of a shell and tube heat exchanger under different baffle arrangement and orientation. *Int. J. Therm. Sci.* **2017**, *121*, 138–149. [CrossRef]
26. Gómez, A.; Montañés, C.; Cámara, M.; Cubero, A.; Fueyo, N.; Muñoz, J.M. An OpenFOAM-based model for heat-exchanger design in the Cloud. *Appl. Therm. Eng.* **2018**, *139*, 239–255. [CrossRef]
27. He, S.; Wang, M.; Tian, W.; Qiu, S.; Su, S.G. Development of an OpenFOAM solver for numerical simulations of shell-and-tube heat exchangers based on porous media model. *Appl. Therm. Eng.* **2022**, *210*, 118389. [CrossRef]
28. Arumsari, A.G.; Ginting, P.J. Analysis of Heat Transfer Coefficient of Shell and Tube on Heat Exchanger Using Heat Transfer Research Inch (HTRI) Software. *Formosa J. Sustain. Res.* **2023**, *2*, 1175–1184. [CrossRef]
29. Gnielinski, V. New Equations for Heat and Mass Transfer in Turbulent Pipe and Channel Flow. *Int. Chem. Eng.* **1976**, *16*, 359–368.
30. Wang, Y.; Liu, K.; Chen, W.; Chen, J.; Wang, K.; Zhou, G. Analysis of stream flow and its impact on thermal performance in shell-side of heat exchangers based on flow dead zone. *Appl. Therm. Eng.* **2024**, *249*, 123414. [CrossRef]
31. Adebayo, J.K.; Dare, A.A.; Petinrin, M.O. Performance characteristics of shell and tube heat exchanger using sectoral baffle. *J. Eng. Appl. Sci.* **2025**, *72*, 13. [CrossRef]

32. Prithiviraj, M.; Andrews, M.J. Comparison of a Three-Dimensional Numerical Model with Existing Methods for Prediction of Flow in Shell-and-Tube Heat Exchangers. *Heat Transf. Eng.* **1999**, *20*, 15–19.
33. Hoang, H.M.K.; Cao, H.-L.; Pham, P.M.Q.; Hajjar, A.; Nguyen, V.L. A novel shell-and-tube heat exchanger design with alternative inclined baffles. *Case Stud. Therm. Eng.* **2025**, *65*, 105542. [CrossRef]
34. Ullah, Z.; Ahmad, I.; Samad, A.; Saghir, H.; Ahmad, F.; Kano, M.; Caliskan, H.; Caliskan, N.; Hong, H. Artificial intelligence assisted prediction of optimum operating conditions of shell and tube heat exchangers: A grey-box approach. *CAAI Trans. Intell. Technol.* **2025**, *10*, 349–358. [CrossRef]
35. Cieśliński, J.T.; Stasiak, K.; Tesch, K.; Barański, J.; Dąbrowski, P. A Comparative Analysis of Calculation Methods for Flow Resistance in Shell-and-Tube Heat Exchanger with Segmental Baffles. *Energies* **2026**, *19*, 1852. [CrossRef]
36. Cieśliński, J.T.; Barański, J.; Dąbrowski, P.; Fabrykiewicz, M.; Stasiak, K.; Tesch, K. Heat Transfer and Pressure Drop in a Shell-and-Tube Heat Exchanger with Segmental Baffles. *Energies* **2026**, *19*, 1760. [CrossRef]
37. Thome, J. *Wolverine Heat Transfer Engineering Data Book III*; Wolverine Tube, Inc.: Shawnee, OK, USA, 2010.
38. Gnielinski, V.; Gaddis, E.S. Berechnung des mittleren Wärmeübergangskoeffizienten im Aussenraum von Rohrbündelwärmeaustauschern mit Segment-Umlenkblechen. *Verfahr.-Tech.* **1978**, *12*, 211–217.
39. Menter, F. Two-equations eddy-viscosity turbulence models for engineering applications. *AIAA-J.* **1994**, *32*, 1598–1605. [CrossRef] [PubMed]
40. OpenFOAM. Available online: https://www.openfoam.com (accessed on 11 June 2024).
41. *ANSYS Fluent*, version 21.1. Fluent 21.1 user's guide. ANSYS Inc.: Canonsburg, PA, USA, 2018.
42. AspenTech. *Aspen Exchanger Design and Rating, V15.0*; AspenTech Inc.: Bedford, MA, USA, 2023.
43. Palen, J.W.; Taborek, J. Solution of Shellside Flow Pressure Drop and Heat Transfer by Stream Analysis Method. *Chem. Eng. Prog. Symp. Ser.* **1969**, *65*, 53–63.
44. Lemmon, E.W.; Huber, M.L.; McLinden, M.O. *NIST Standard Reference Database 23, Reference Fluid Thermodynamic and Transport Properties (REFPROP), Version 9.0*; National Institute of Standards and Technology: Gaithersburg, MD, USA, 2010.

Disclaimer/Publisher's Note: The statements, opinions and data contained in all publications are solely those of the individual author(s) and contributor(s) and not of MDPI and/or the editor(s). MDPI and/or the editor(s) disclaim responsibility for any injury to people or property resulting from any ideas, methods, instructions or products referred to in the content.

energies

MDPI

Article

SHAP-Based Insights into Environmental and Economic Performance of a Shower Heat Exchanger Under Unbalanced Flow Conditions: A Feasibility Study

Sabina Kordana-Obuch * and Mariusz Starzec

Department of Infrastructure and Water Management, Rzeszow University of Technology, al. Powstańców Warszawy 6, 35-029 Rzeszow, Poland; mstarzec1990@prz.edu.pl
* Correspondence: sk@prz.edu.pl

Abstract

Heat recovery from greywater is one solution for improving the energy efficiency of buildings and reducing greenhouse gas emissions. Particular attention is paid to systems utilizing heat from shower water, which, due to its high temperature and regularity, represents a promising energy source. However, the interplay of parameters determining the financial and environmental effectiveness of such a solution has not yet been fully explored. Therefore, the aim of this paper was to identify key variables influencing the feasibility of using a shower heat exchanger operating under unbalanced flow conditions and to assess the consistency between financial and environmental effects. The analyzed net present values ranged from −€1381 to €52,168. Greenhouse gas emission reduction values ranged between 61 $kgCO_2e$ and 37,207 $kgCO_2e$. The analysis was conducted using predictive modeling and the SHAP (SHapley Additive exPlanations) method, which allows for the interpretation of the impact of individual variables on the forecasted net present value and potential greenhouse gas emission reduction. A global analysis was carried out to determine the relative importance of variables, as well as a local analysis for selected cases. The results showed that operational variables related to shower use, particularly shower length and mixed water flow rate, significantly influenced the prediction results of both models. In the case of emission reduction, greenhouse gas emission intensity and its change over time also had a significant impact, whilst the financial effects were determined by the energy price from the perspective of the subsequent years of the system's operation.

Keywords: European Union; greenhouse gas emission reduction; heat recovery; net present value; residential building; SHAP; vertical heat exchanger; XGBoost

1. Introduction

Buildings, including residential buildings, are responsible for a significant portion of final energy consumption and greenhouse gas emissions. It is worth noting that one of the most energy-intensive processes in the construction sector is the preparation of domestic hot water (DHW) [1], the heating of which generates additional high costs. Unlike space heating, where energy demand systematically decreases with improving energy standards in buildings [2], the share of energy allocated to DHW is becoming an increasingly dominant component of buildings' energy balances. In highly energy-efficient buildings, it can even significantly exceed the demand for other purposes. For example, research by Hall et al. [3] has shown that water-related energy use can in some cases

reach as much as 7 kWh/person/day, accounting for up to 50% of energy consumption in households. As a result, technologies based on renewable energy sources [4] and enabling energy consumption reduction and recovery at the end-user level [5–7] are becoming increasingly desirable. Furthermore, growing energy consumption in cities increases the need to implement systems that balance energy efficiency with thermal comfort [8]. This, in turn, implies an increased demand for detailed analyses enabling a reliable assessment of the energy, environmental, and economic effects of the proposed solutions.

One solution for reducing energy consumption for DHW is a shower heat exchanger (SHE) [9]. During normal operation of the installation, the thermal energy contained in greywater is permanently lost, and its energy potential remains unused. By using SHEs, the thermal energy contained in shower water is transferred to the water, which is then used during the same shower [10]. This is one of the few examples of measures that do not require changing user habits and do not affect the comfort of using the shower system. Previous studies on assessing the effectiveness of SHEs, determining their financial efficiency, or reducing CO_2 emission [11–13] have focused mainly on the use of aggregated, simplified indicators and lacked a deeper analysis of the impact of individual operating and system parameters on the analysis results. At the same time, most studies only covered balanced flow conditions [14]. This means that even with advanced computational tools [15], the scope of analytical conclusions and their practical applicability is clearly limited. In installation practice, systems operating under unbalanced flow conditions are present [16]. In such a situation, the water flow rate through the SHE is significantly lower than the drain water flow rate, which is a consequence of supplying preheated water to only one of the devices (the shower mixing valve (SMV) or the DHW heater), while the other is supplied with cold water. Despite the limited possibilities of thermal energy recovery compared to the balanced flow variant, such solutions are used to reduce the complexity of the hydraulic system or to adapt the installation to existing DHW preparation systems in which parallel supply of both devices is impossible or technically unjustified.

Despite the growing number of publications on SHEs, their operation under unbalanced flow conditions remains relatively poorly understood, and their impact on key environmental and financial indicators is often marginalized, simplified, and sometimes even overlooked. Relying on balanced flow conditions, which are often impossible to apply in installation practice, leads to systematic overestimation of the achieved energy and economic effects. Furthermore, commonly used analysis methods rarely enable clear identification of the parameters determining the environmental and financial benefits achieved, limiting their usefulness both in the design phase of shower heat recovery systems and in implementing measures supporting the realization of this type of technology.

In response to these limitations, this paper adopts an approach aimed at systematic and quantitative decomposition of the impact of input variables on environmental and financial effects in conditions close to real-world conditions, with the main goal being to analyze the impact of variables determining SHE operation under unbalanced flow conditions on the projected greenhouse gas emission reduction (R_{GHG}) and the financial efficiency of the investment expressed as net present value (NPV). The novelty of the study lies in the parallel, coherent approach to both dimensions based on a partially common set of input variables and in the identification of potential discrepancies between financial and environmental optimality, which is poorly recognized in the existing literature. The analysis was conducted for a system configuration that assumed supplying preheated water exclusively to the shower mixing valve. This choice was dictated by its widespread use in installation practice and limited interference with the existing DHW heating system. The vertical heat exchanger was chosen as the research object due to its dominant position among solutions used in installation practice and its more favorable heat transfer

https://doi.org/10.3390/en19081845

parameters compared to horizontal SHEs [17]. Furthermore, analyses of this shower heat recovery system configuration available in the literature focus primarily on horizontal heat exchangers [18], while vertical units, despite their widespread use in practice, remain relatively underexplored.

Interpretable machine-learning methods, along with SHAP analysis, were used in the analysis, which enabled transparent identification and quantification of the impact of individual input variables on the analysis results. The use of separate models for both dependent variables (R_{GHG}, NPV) allowed for the identification of key parameters determining their variability, which made it possible to assess the consistency between environmental and financial effects and to identify potential differences in the mechanisms shaping these effects. This approach represents a significant extension of the current state of knowledge, providing tools to support both design optimization and the development of policies supporting the implementation of heat recovery technologies in real-world conditions.

The research described here is a continuation of analyses conducted to assess the energy efficiency of vertical shower heat exchangers under various flow conditions, the results of which were described in [19]. The scope of this paper includes:

- Evaluation of the financial efficiency of using a vertical shower heat exchanger in a configuration where preheated water is supplied exclusively to the SMV.
- Estimation of the potential greenhouse gas emission reduction under similar operating conditions of the SHE.
- Development of eXtreme Gradient Boosting (XGBoost) models to predict NPV and R_{GHG}.
- Evaluation of the impact of individual input variables on the expected NPV and projected greenhouse gas emission reduction.

2. Materials and Methods

2.1. Environmental and Financial Analysis

2.1.1. Evaluation of the Performance of a Shower Heat Exchanger Under Unbalanced Flow Conditions

The analysis included an evaluation of the performance of a vertical "pipe-in-pipe" SHE, 1.68 m long and 50 mm internal diameter. A detailed description of the unit, along with a description of the measuring devices, can be found in [19]. Vertical shower heat exchangers are commercially available units used in residential buildings. Due to the need to meet specific installation requirements, primarily the need to install them in a vertical section of the sewage system, their application is easier in newly designed buildings, where adequate installation space can be provided for this type of unit. Failure to incorporate a vertical SHE into the building design may require a more complex retrofit of the existing facility, particularly in systems supplying preheated water to a DHW heater. In some cases, installing a vertical heat exchanger may even prove impossible.

Based on the input dataset, marked in green in Figure 1, a series of experimental studies were conducted to determine the preheated water temperature (T_{pw}) (Figure 2). The studies were conducted for a system configuration that supplied preheated water exclusively to the shower mixing valve (Figure 3). In practice, this type of configuration is often used in facilities where interfering with the existing domestic hot water system is difficult or would require significant capital expenditure. It should be noted that the heat recovery system configuration under consideration involves minimal interference with the existing internal water and sewage system and is less complex hydraulically than systems supplying a DHW heater. This makes the solution easier to implement in retrofit projects for existing buildings. In existing DHW systems, the possibility of interfering with the hydraulic system is usually limited, as a result of which preheated water can

https://doi.org/10.3390/en19081845

only be supplied to selected points of the internal system. Due to the location of the SHE below the shower, this is most often an SMV. This arrangement of preheated water pipes results in unbalanced flow conditions in the heat exchanger. It should also be noted that a configuration ensuring balanced flow requires more complex modifications to the water and sewage system, which involves the purchase of additional pipes, fittings, and often interventions in the building structure. This, in turn, significantly increases investment outlays. Therefore, solutions characterized by unbalanced flow conditions represent a practical compromise between energy efficiency and the feasibility of a drain water heat recovery system. This justifies their analysis as a scenario representative of a wide range of real-world applications. Under such conditions, the heated water flow rate is significantly lower than the drain water flow rate, which results from the fact that only a portion of the water used for showering flows through the heat exchanger. As a result, the achieved temperature effectiveness of the unit is higher than when the SHE operates under balanced flow conditions. However, the heat transfer rate is reduced in such conditions [19], which, in turn, affects the achieved financial and environmental effects.

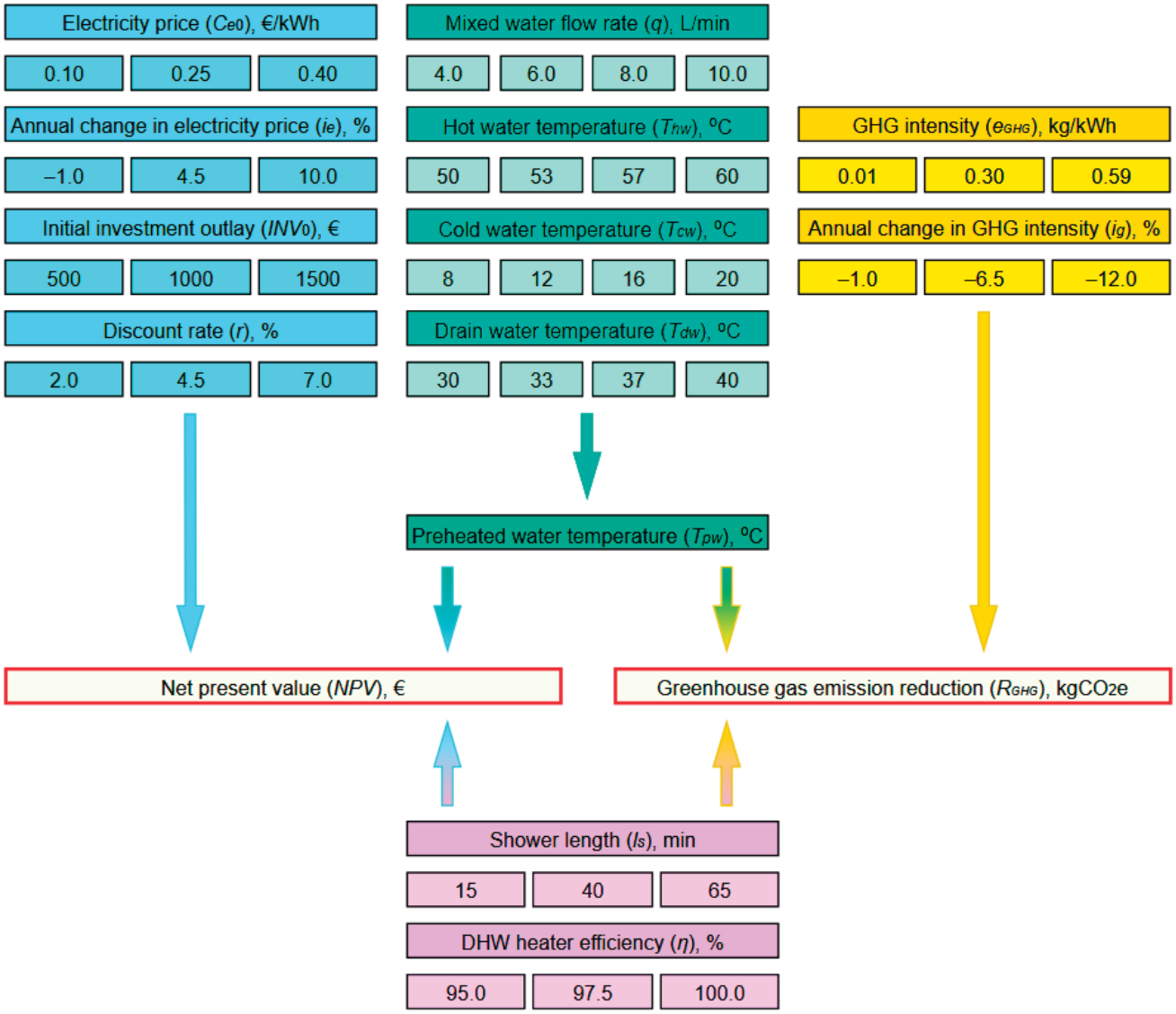


Figure 1. Input parameters with their assumed values and their corresponding output parameters (GHG—greenhouse gas; DHW—domestic hot water).

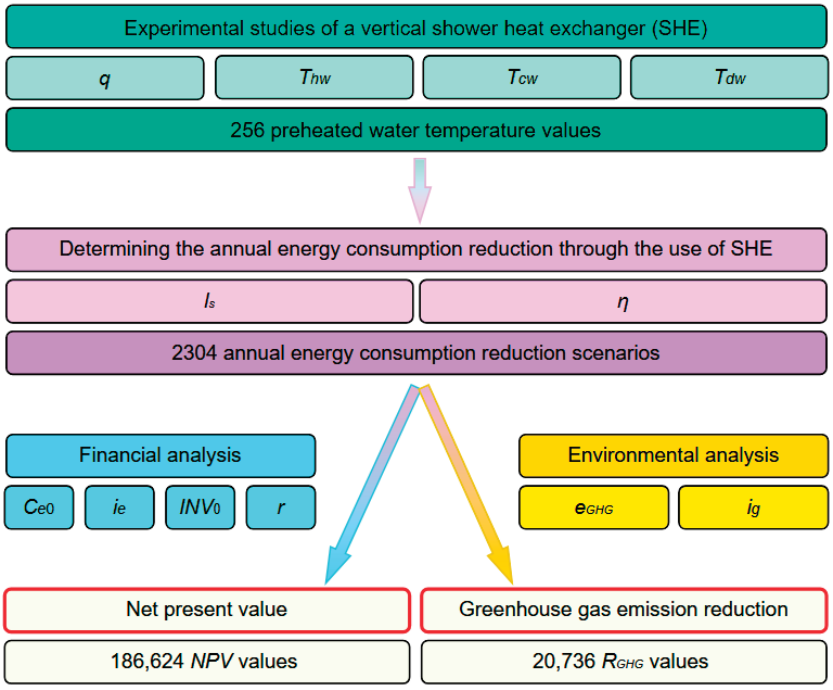
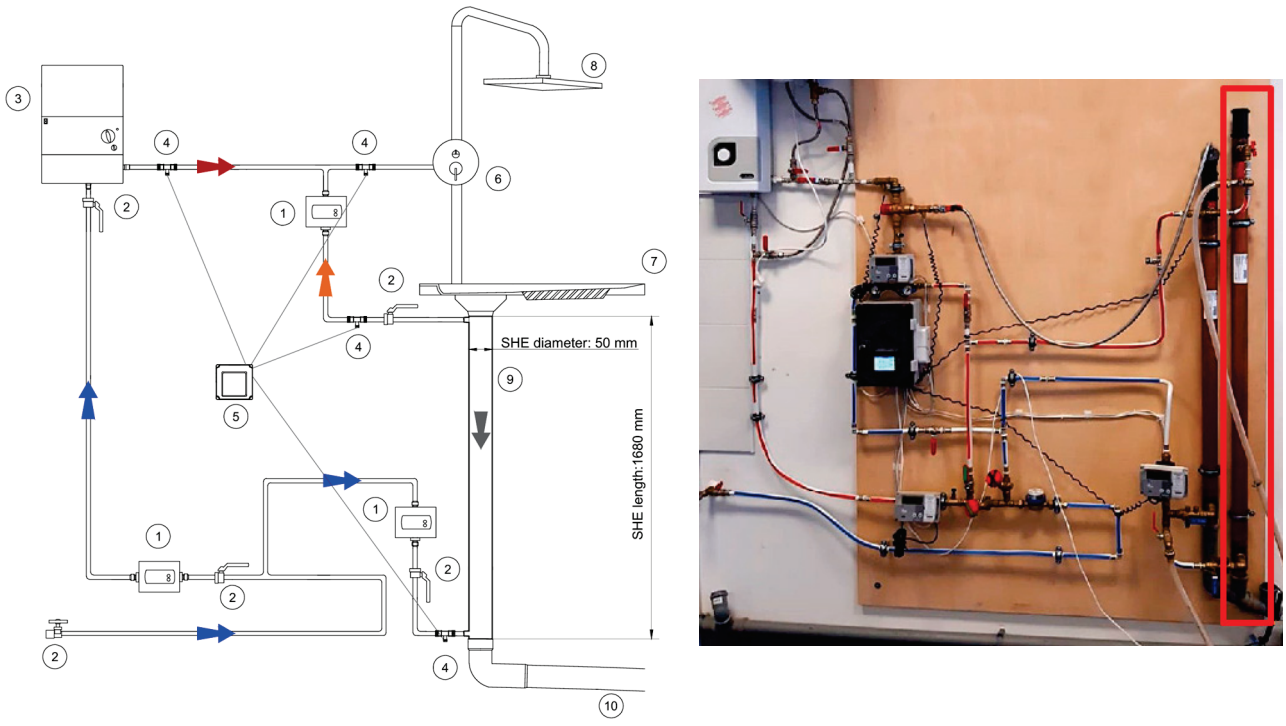


Figure 2. Research stages. Colors and designations are consistent with Figure 1.



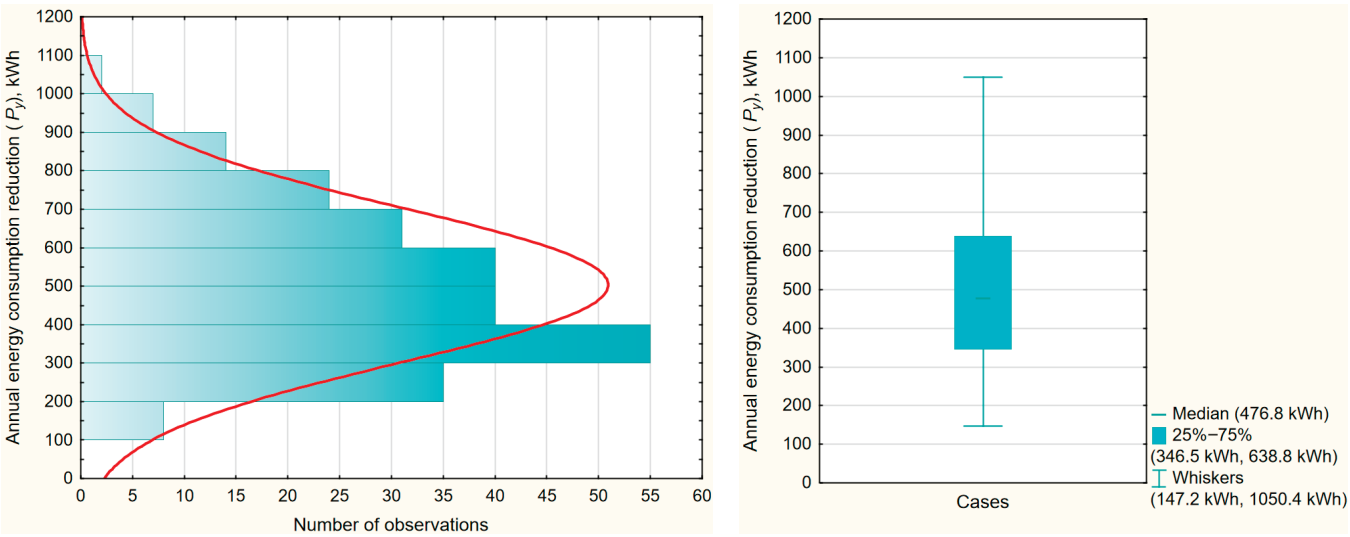
(**a**) (**b**)

Figure 3. Shower drain water heat recovery system: (**a**) System configuration diagram; (**b**) Research stand with a heat exchanger installed; the red box indicates the investigated unit (1—flowmeter; 2—cut-off valve; 3—domestic water heater; 4—temperature sensors; 5—data recorder; 6—shower mixing valve; 7—shower tray; 8—shower head; 9—shower heat exchanger; 10—drain pipe; SHE—shower heat exchanger).

For the assumed range of input variables, the water flow rate through the vertical SHE constituted several tens of percent of the drain water flow rate. Its value resulted from the assumed media temperatures in the individual sections of the system and the

mixed water flow rate (q). The tests were conducted over a 12-month period to reflect the annual variability of cold water temperature. The remaining parameters were adjusted accordingly to represent different combinations of input variables. Therefore, while the mixed water flow rate from the shower head was treated as an independent variable, the ratio of water flow rate to drain water flow rate in the SHE was not analyzed as a separate independent parameter. The unbalanced flow conditions resulted from the adopted thermal and hydraulic assumptions.

A total of 256 preheated water temperature values (T_{pw}) were obtained from experiments conducted across different combinations of input parameters. This, along with the cold water (T_{cw}) and hot water (T_{hw}) temperatures, as well as the mixed water flow rate (q), formed the basis for further calculations, which were performed over a fifteen-year time horizon. Annual energy savings (P_y), resulting from heat recovery from shower water, were calculated as the difference between the energy consumption in a building without a heat exchanger and one with the SHE installed. For the purposes of the analysis, it was assumed that water was heated using an electric DHW heater, as this is the most advantageous option, as noted by Ali et al. [20]. The domestic hot water flow rate to the shower mixing valve was determined based on the heat balance equation. For both the DHW heater efficiency (η) and the total daily shower length (l_s), three representative values of these parameters were assumed (marked in pink in Figure 1), which allowed for the consideration of various building operating scenarios. This approach enabled the mapping of diverse household shower usage conditions and the resulting annual energy consumption for DHW heating. As a result, the analysis included 2304 scenarios for reducing energy consumption for shower water heating. For example, Figure 4 shows the distribution of 256 annual energy consumption reduction values obtained assuming the most unfavorable scenario in terms of shower length, i.e., for l_s = 15 min. The results correspond to a DHW heater efficiency of 95%.



(**a**) (**b**)

Figure 4. Distribution of annual energy savings resulting from the installation of the SHE (l_s = 15 min, η = 95%): (**a**) histogram; (**b**) box-plot.

2.1.2. Net Present Value

The financial efficiency of the project involving the installation of the SHE in an existing residential building was determined based on net present value (*NPV*). This indicator can

be determined as the difference between the discounted cash flows generated by the project and the investment outlay incurred, as described by Equation (1).

$$NPV = \sum_{t=1}^{n} \frac{P_y \cdot C_{e0} \cdot (1 + i_e)^t}{(1 + r)^t} - INV_0, \quad (1)$$

where NPV is the net present value, €; P_y is the annual energy saving resulting from the installation of the SHE, kWh; C_{e0} is the initial electricity price, € per kWh; i_e is the annual change in electricity price; r is the discount rate; t is the year of operation of the SHE; n is the service life of the SHE; INV_0 is the initial investment outlay, €.

In the case under consideration, positive cash flows represented savings resulting from reduced energy consumption for DHW heating. This indicator is a commonly used metric in investment profitability assessments, as it accounts for the time value of money and enables a clear determination of whether an investment will be financially beneficial. Therefore, NPV is widely used in analyses of the implementation of pro-ecological technologies in residential buildings [21], including those aimed at improving energy efficiency [22].

In addition to the system's technical parameters, such as flow rate and media temperatures, system operating time, and DHW heater efficiency, the analysis also considered additional variables that significantly impact the financial benefits achieved. The assumed values for these variables are highlighted in blue in Figure 1. In each case, three values of the initial electricity price (C_{e0}), the annual change in electricity price (i_e), the initial investment outlay (INV_0), and the discount rate (r) were considered. As a result, the financial analysis was based on 186,624 cases characterized by varying energy demand for DHW heating and diverse economic assumptions.

The initial electricity price (C_{e0}) was assumed based on Eurostat data for European Union (EU) countries [23]. These data covered households with annual energy consumption between 2500 and 5000 kWh. According to these data [23], the highest electricity price in the first half of 2025 was recorded in Germany (C_e = €0.3835 per kWh), and the lowest in Hungary (C_e = €0.1040 per kWh). Based on data from recent years [24], the dynamics of annual changes in electricity prices in individual countries were additionally analyzed, and annual percentage changes in electricity prices (i_e) were assumed. Changes in the shorter term were not analyzed to avoid seasonal effects. Short-term, sharp price fluctuations occurring in some countries in individual years were also omitted. Such jumps are incidental and, therefore, do not provide a reliable basis for multi-year forecasting. Initial investment outlays (INV_0), including the purchase of the SHE and its installation, were estimated considering a wide range of required installation work. Notably, the heat recovery system configuration under consideration is characterized by lower hydraulic complexity than configurations involving preheated water supply to a DHW heater, thereby potentially leading to lower investment outlays than more complex systems. The adopted range of INV_0 values allowed for cost variability resulting from differences in installation conditions, location, and market prices of equipment and labor. The adopted discount rate (r) values reflect the variation in this parameter across EU countries [25]. The analysis adopted an approach based on discount rates interpreted as real rates. Values close to the lowest r levels observed in some EU countries, reflecting the overall downward trend, were considered, as well as higher discount rates corresponding to more conservative investor assumptions. This approach allowed for the incorporation of economic uncertainty into the analysis and increased the universality of the obtained results, regardless of the adopted scenario of changes in energy prices.

https://doi.org/10.3390/en19081845

2.1.3. Greenhouse Gas Emission Reduction

The reduction in greenhouse gas emission was estimated based on the projected reduction in energy consumption resulting from the use of SHE (P_y) and GHG emission intensity of electricity generation (e_{GHG}), according to Equation (2).

$$R_{GHG} = \sum_{t=1}^{n} P_y \cdot e_{GHG} \cdot \left(1 + i_g\right)^t, \quad (2)$$

where R_{GHG} is the greenhouse gas emission reduction, $kgCO_2e$; e_{GHG} is the GHG emission intensity of electricity generation, $kgCO_2e/kWh$, and i_g is the annual change in the value of e_{GHG} (the study included only negative values).

For both e_{GHG} and i_g, three values of the input variables were considered, resulting in the analysis of greenhouse gas emission reduction based on 20,736 model cases. As with the initial electricity prices (C_{e0}), the initial e_{GHG} value was assumed based on current data for individual EU countries [26]. According to the European Environment Agency [26], in 2024, the lowest e_{GHG} value was in Sweden (e_{GHG} = 0.007 $kgCO_2e/kWh$), while the highest was in Estonia (e_{GHG} = 0.585 $kgCO_2e/kWh$). Additionally, the dynamics of changes in this parameter in recent years were analyzed [26], and based on this, annual changes in greenhouse gas emission intensity of electricity generation (i_g) were assumed. Although increases in e_{GHG} values have been observed in some EU countries in recent years, a long-term downward trend was assumed for this variable. For this reason, all assumed i_g values were negative (Figure 1). This is due to the ongoing decarbonization of the energy sector, the increasing share of renewable sources in electricity production, and tightening climate policy. Short-term increases in emissions are usually temporary and result from extraordinary circumstances. Assuming a long-term decreasing trend enabled a more realistic assessment of the future environmental impact of vertical SHEs.

2.2. Prediction Models and Their Interpretation

2.2.1. eXtreme Gradient Boosting

A variety of machine-learning models are used in contemporary research [27,28]. This also applies to environmental and economic analyses. Popular models include eXtreme Gradient Boosting (XGBoost), which is successfully used both to predict CO_2 emissions [29] and in financial risk analyses [30]. It is also used to predict the thermal-hydraulic characteristics of heat exchangers [31], including SHEs [32]. Previous studies by the authors [19] involving the use of various predictive models to assess SHE performance also showed that the use of XGBoost models allows for obtaining more favorable model fitting metric values than other machine-learning models. This analysis was conducted using XGBoost version 2.1.2.

XGBoost is an ensemble learning algorithm based on gradient boosting of decision trees, in which successive trees are constructed sequentially to minimize a predefined loss function. Each subsequent tree is trained to reduce the residual errors of the previous model, allowing the algorithm to capture complex, nonlinear relationships between variables. In addition to the loss function, XGBoost incorporates a regularization term that penalizes model complexity, improving generalization and reducing the risk of overfitting. As a result, the final prediction is obtained as a sum of contributions from all individual trees. The XGBoost method allows for modeling complex, nonlinear relationships and interactions between variables, making it an appropriate tool for analyzing economic and environmental processes. Its additional advantage is high predictive accuracy and robustness to varying input data scales, which is crucial when considering both hydraulic and technical parameters, as well as economic and environmental ones [33]. Two predictive models were developed as part of the study, enabling the parallel assessment of financial

and environmental effects. The first, based on ten input variables, predicted the net present value of a project involving the installation of an SHE operating under unbalanced flow conditions. This enabled the identification of key factors influencing its financial viability. The second model was used to forecast the cumulative reduction in greenhouse gas emissions over a 15-year time horizon, allowing for the assessment of long-term environmental effects resulting from the SHE installation. In this case, the model was based on eight input variables.

The SHAP (SHapley Additive exPlanations) method was used to interpret the models and determine the impact of individual independent variables on their predictions [34]. This method enabled a quantitative assessment of the significance of individual variables and the identification of the direction and strength of their impact on model results. This led to a better understanding of the mechanisms shaping both the project's financial efficiency and its environmental impact.

2.2.2. SHAP Analysis

The SHAP (SHapley Additive exPlanations) method is based on Shapley values derived from cooperative game theory. For a given observation, the model prediction can be expressed as:

$$f(x) = \varphi_0 + \sum_i \varphi_i, \quad (3)$$

where φ_0 is the base value, and φ_i represents the contribution of the i-th feature.

This formulation enables an additive decomposition of the prediction into the effects of individual input variables and ensures a comparable interpretation of variable effects regardless of their scale [35]. SHAP analysis assigns each variable a contribution to the prediction result for individual observations and globally for the entire model [35]. In the local analysis, the distribution of SHAP values for individual predictions is examined to identify the direction and strength of the influence of individual features. This paper presents the results of such an analysis for three observations representative of each model. In each case, a positive SHAP value indicates an increase in the model's prediction value, while a negative value results in a decrease. The global analysis, on the other hand, is based on the mean absolute SHAP values for each variable, which allows for determining its overall importance. The results of these analyses for both models are presented in the paper as plots.

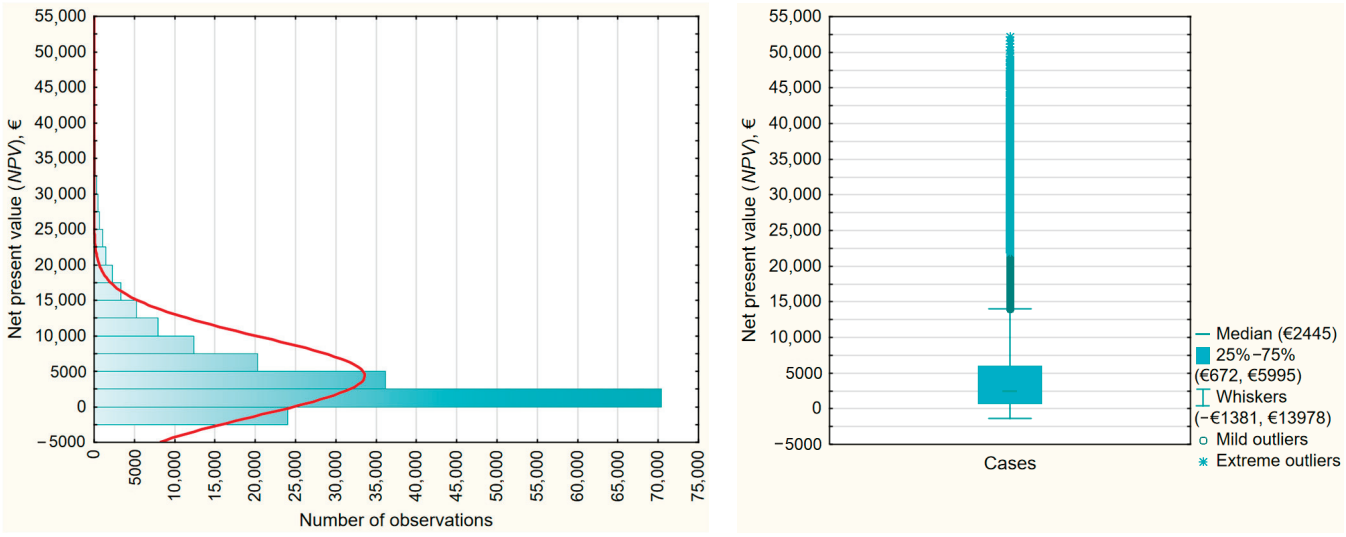
3. Results

3.1. Financial Analysis

3.1.1. Results of the Net Present Value Calculation

Analysis of 186,624 combinations of input variables showed that for the studied range, their *NPVs* remained between –€1381 and €52,168 (Figure 5). Negative values were obtained for approximately 24,000 cases, which constituted less than 13% of all combinations considered. The mean *NPV* reached €4317, and the median value was €2445, which indicates a right-sided asymmetry of the results distribution. The skewness value in this case is 2.30. Most of the results are relatively low compared to the maximum value (almost 75% of the results fall within the €0–€10,000 range). However, there is a group of combinations of input variables for which the *NPV* reached very high values, on the order of tens of thousands of euros. When analyzing the distribution of *NPVs*, it can also be seen that 25% of the obtained results exceed €5995. The same proportion of results is below €672, implying an interquartile range of nearly €5500. This indicates significant variability in results and high economic uncertainty of the project, resulting from the high sensitivity of *NPV* to the adopted model assumptions. The relatively low value of the lower quartile suggests that in a significant portion of the scenarios, the project generates only a small

surplus of positive cash flows. A high upper quartile, on the other hand, indicates the possibility of achieving very favorable results under favorable conditions. This confirms that the project's profitability is asymmetric, with high-risk scenarios dominating, while fewer but very favorable observations are present.



(**a**) (**b**)

Figure 5. Net present value distribution: (**a**) histogram; (**b**) box-plot.

The above observations are also confirmed by the obtained kurtosis value of 7.4. Its high value indicates a clearly leptokurtic nature of the distribution, i.e., a strong concentration of observations around central values combined with a large number of outliers. High kurtosis combined with right-sided skewness indicates a low-probability, high-payoff profile, where most scenarios generate moderate results, but there is a certain probability of very large, positive deviations from the median, which should be considered in decision analysis.

As mentioned earlier, the observed high variability, right-sided asymmetry, and leptokurtic nature of the *NPV* distribution indicate that the project's profitability is largely determined by the presence of specific combinations of input variables. This distribution structure suggests nonlinear and potentially heterogeneous model sensitivity to changes in input variables, which complicates the identification of key risk factors. Nonlinearity and extreme values justify explainability methods like SHAP. For this purpose, the XGBoost model was developed. This model formed the basis for the SHAP analysis performed in the next stage of the research, enabling the identification of variables that most significantly determine the *NPV* and are responsible for the observed extreme scenarios.

3.1.2. Results of the SHAP Analysis

The XGBoost model was developed to simulate the relationship between input variables and *NPV*. The input data was divided into three datasets (training, validation, and test) in a 70/15/15 ratio, with each sample appearing in only one set, which excluded the risk of data leakage. The model was assessed using standard model fitting metrics, i.e., coefficient of determination (R^2), root mean square error (*RMSE*), and mean absolute error (*MAE*) [36]. The values of the metrics for the selected model are summarized in Table 1.

Table 1. Model fitting metrics for *NPV* prediction. *RMSE* and *MAE* are reported in euros.

	R^2	*RMSE*	*MAE*
Training dataset	0.999	19.99	13.24
Validation dataset	0.999	37.53	23.00
Test dataset	0.999	38.12	23.24

The results indicate a very good model fit to the data for the *NPV* prediction task, which in the analyzed case ranged from −€1381 to €52,168 (Figure 6). The coefficient of determination (R^2) reached almost identical, very high values (0.999) for all datasets, indicating good model generalization. Such high values of the coefficient of determination may suggest the risk of model overfitting or data leakage. In the present study, however, this is primarily a consequence of the nature of the input data. Net present values were determined based on deterministic relationships resulting from the adopted equations. The XGBoost model, therefore, reproduces existing mathematical relationships, leading to very high prediction accuracy. Achieving R^2 results close to 1 may also be due to the wide range of output variable values compared to the relatively small prediction errors.

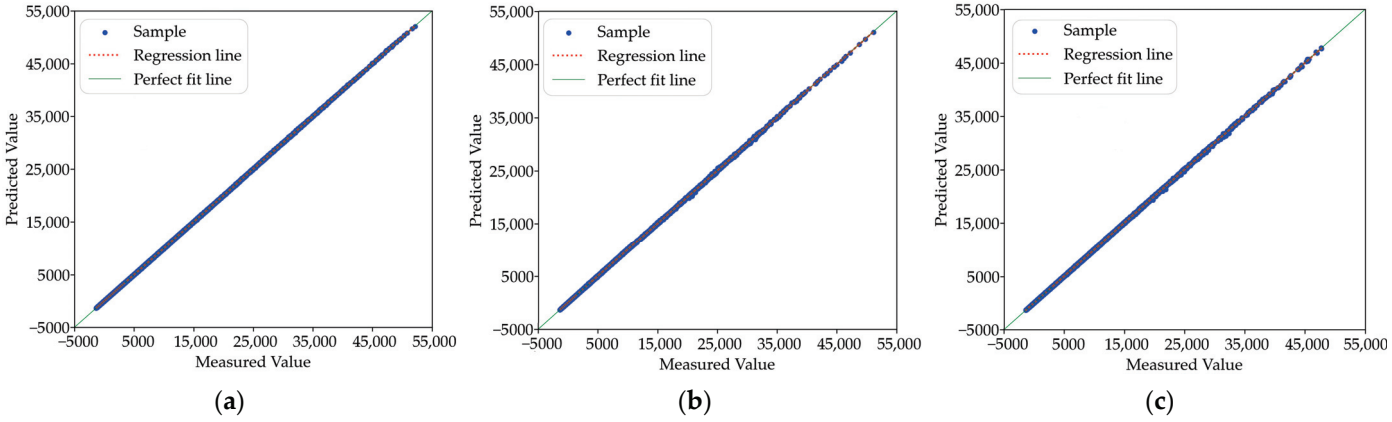


Figure 6. Comparison of predicted and observed *NPVs*: (**a**) training dataset; (**b**) validation dataset; (**c**) test dataset.

The high quality of the model, while maintaining realistic error estimation, was also confirmed by the values of the mean absolute and root mean square errors, which remained relatively low compared to the range of the predicted net present value. This demonstrates that the model is characterized by high predictive accuracy across the entire range of *NPVs* considered, as slight increases in *RMSE* and *MAE* on the validation and test datasets relative to the training dataset are expected. These results indicate that the model generalizes effectively, and the high R^2 is not the result of data leakage or overfitting.

To identify the key variables determining the financial profitability of the investment expressed as *NPV*, an analysis of the model's explainability was conducted using SHAP analysis. The prediction value can be interpreted as the sum of the baseline value and the contributions of all independent variables, expressed by their SHAP values. The model's base value, as shown in Figure 7, was €4322, meaning that individual input variables shifted the *NPV* forecast relative to this reference level. The direction of this shift was determined by the values of individual parameters.

The global analysis showed that the shower length (l_s) had the greatest impact on the *NPV*, with the mean absolute SHAP value exceeding €2200. This result confirms that the duration of installation use directly impacts the amount of energy saved and, consequently, the amount of positive cash flows generated by the project. The second most significant variable was the initial energy price (C_{e0}). However, it should be noted that the mean

https://doi.org/10.3390/en19081845

|SHAP value| for this variable is only €87 lower than for l_s, suggesting that both variables are crucial to the analysis results. Considering that the percentage change in electricity prices (i_e) is ranked next in importance, it can be assumed that long-term market conditions, reflected in the forecasted dynamics of energy prices, may significantly determine the economic impact of the investment. The mixed water flow rate (q) has only a slightly lower impact on the net present value, with its mean absolute SHAP value, as with i_e, being approximately €1500. The hierarchy of features indicates that the financial efficiency of the project is determined mainly by operational variables related to shower use intensity and by economic conditions.

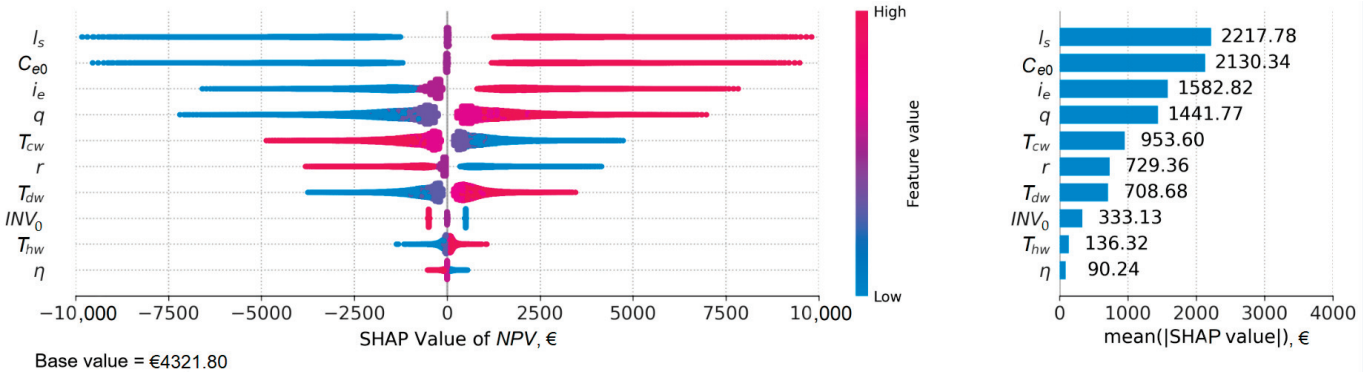


Figure 7. SHAP analysis of projected net present value (designations as in Figure 1).

Further bar plot analysis showed that the significance of the remaining input variables is significantly lower, and the mean |SHAP value| does not exceed €1000 in any case. For cold water temperature (T_{cw}), discount rate (r), and drain water temperature (T_{dw}), the mean absolute SHAP value was above €700. On the other hand, for the remaining variables, i.e., initial investment outlays (INV_0), domestic hot water temperature (T_{hw}), and DHW heater efficiency (η), it did not exceed €350. The hierarchy of significance, therefore, proves that in the case of a vertical SHE operating under unbalanced flow conditions, operational and market factors dominate over technical parameters, such as the efficiency of the primary heat source in the installation.

Beeswarm plot analysis allowed us to interpret the direction of the influence of individual variables relative to the base value (€4322). For shower length, initial electricity price, and its rate of increase, the *NPV* increased with increasing values of these variables, as evidenced by the location of the red points in Figure 7 to the right of the baseline value. A similar influence was observed for mixed water flow rate, drain water temperature, and DHW temperature. Increasing their values resulted in an increase in the projected investment profitability, resulting from greater energy recovery potential and higher financial savings.

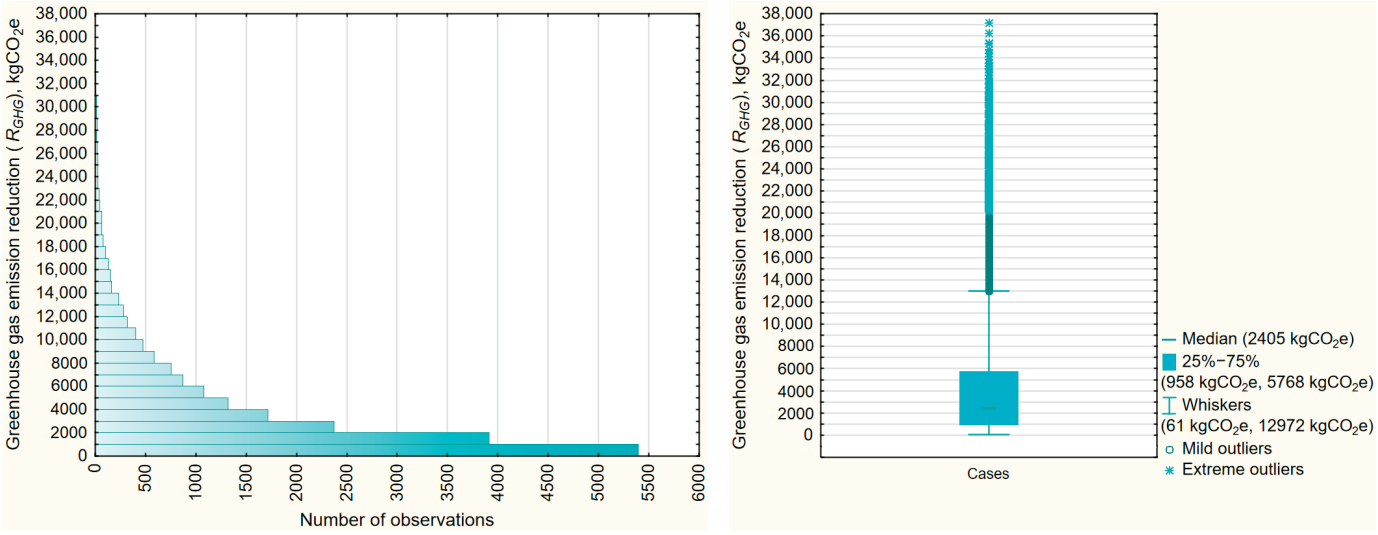
For cold water temperature, discount rate, and DHW heater efficiency, lower values (blue points) are associated with higher *NPV*, indicating that increasing these variables negatively affects the outcome. Higher cold water temperature reduces the energy demand for heating, resulting in reduced potential savings. A higher r value reduces future cash flows, which worsens the *NPV*. In turn, the higher efficiency of the DHW heater reduces the difference in energy consumption between the reference variant and the variant with the vertical SHE, limiting the benefits of using a heat exchanger (Q-Blue B.V., Emmen, The Netherlands).

https://doi.org/10.3390/en19081845

3.2. Environmental Analysis

3.2.1. Results of the Greenhouse Gas Emission Reduction Calculation

An analysis of 20,736 scenarios for the operation of a shower system in a building showed that installing a vertical shower heat exchanger operating under unbalanced flow conditions could reduce 15-year greenhouse gas emissions by up to 37,207 kgCO2e (Figure 8). However, it should be noted that the emission reduction potential varies depending on the national energy mix and the adopted decarbonization scenario for the coming years. The average R_{GHG} value obtained for European Union countries was 4185 $kgCO_2e$, while the median result was 2405 $kgCO_2e$. On the other hand, the minimum R_{GHG} value, obtained assuming the lowest input GHG emission intensity (e_{GHG}) and the highest assumed reduction in this variable in subsequent years (i_g), was only 61 $kgCO_2e$. The mean-to-median ratio itself suggests a strongly asymmetric distribution of results, as confirmed by a positive skewness of 2.1 and an increased kurtosis of 5.9. This suggests that in most of the scenarios considered, projected emission reduction is moderate, while in a limited number of cases, primarily related to high-emission countries, very high outliers appear, significantly inflating the mean. Therefore, also in this case, nonlinearity and extreme values justify the use of model interpretability methods. Importantly, however, despite the clear asymmetry of the R_{GHG} distribution, the *NPV* distribution is characterized by even greater skewness and kurtosis, which is most likely a consequence of the significant increase in energy prices over time.



(**a**) (**b**)

Figure 8. Distribution of projected greenhouse gas emission reduction: (**a**) histogram; (**b**) box-plot.

Further statistical analysis confirms significant uncertainty regarding the actual scale of the environmental effect. The interquartile range exceeds 4800 $kgCO_2e$. One-quarter of the results are lower than 958 $kgCO_2e$, and 75% of the obtained R_{GHG} values do not reach 5768 $kgCO_2e$, a value representing less than 18% of the potential maximum greenhouse gas emission reduction. The results, therefore, have a significant impact on the assessment of the environmental efficiency of the shower heat recovery technology. Relying solely on average R_{GHG} values may lead to an overestimation of the expected environmental benefits in countries with low-emission energy systems.

3.2.2. Results of the SHAP Analysis

To extend the analysis of greenhouse gas emission reduction by using a vertical SHE operating under unbalanced flow conditions, a predictive model based on the XGBoost

https://doi.org/10.3390/en19081845

algorithm was developed and then used to conduct an explainability analysis using SHAP. The main goal of the model, similar to the financial analysis, was to identify the relative importance of individual input variables and the direction of their influence on the R_{GHG} value. This approach allowed the identification of which parameters are most decisive for the environmental performance of SHEs in different countries and energy transition scenarios. As a result, the model provides a tool supporting both the interpretation of the obtained greenhouse gas emission reduction results and the formulation of recommendations for climate and energy policy.

As with the net present value, the input data was split 70/15/15 to prevent data leakage. The model fitting metrics, summarized in Table 2, indicate the model's high ability to reproduce the analyzed relationships. This is also confirmed by Figure 9. The coefficient of determination of 0.999 indicates the model's high explanatory power of data variability and the absence of significant overfitting, as high predictive accuracy characterizes all datasets, including those not used in the training process. It should be noted, however, that also in the case of R_{GHG} predictions, the XGBoost model reproduced the existing mathematical relationships. The model's high quality is also confirmed by the *RMSE* and *MAE* values, which are relatively low compared to the range of analyzed R_{GHG} values, which reach tens of thousands of $kgCO_2e$. Therefore, it can be concluded that using the model as a reliable basis for performing SHAP analysis is fully justified.

Table 2. Model fitting metrics for R_{GHG} prediction. *RMSE* and *MAE* are reported in kilograms of CO_2 equivalent ($kgCO_2e$).

	R^2	*RMSE*	*MAE*
Training dataset	0.999	17.69	11.65
Validation dataset	0.999	33.89	20.74
Test dataset	0.999	33.26	21.26

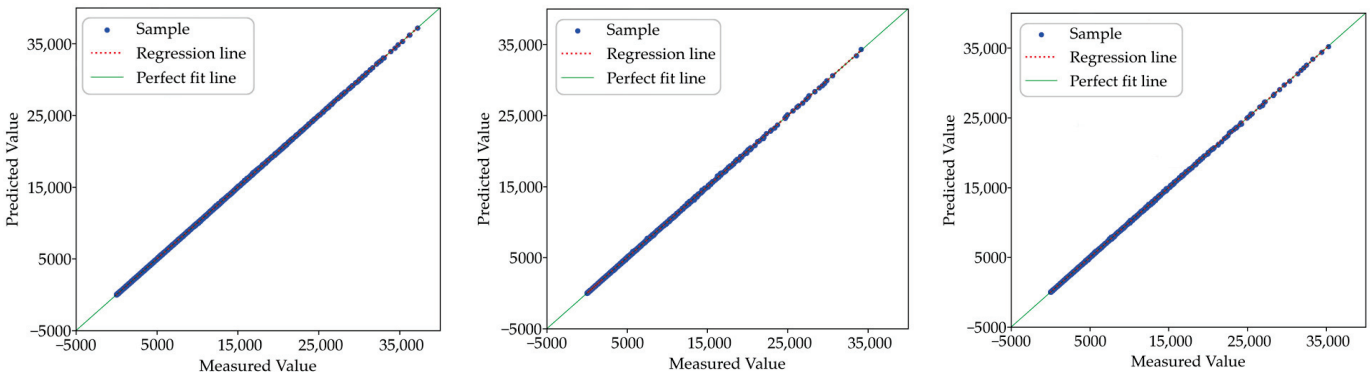


Figure 9. Comparison of predicted and observed R_{GHG} values: (**a**) training dataset; (**b**) validation dataset; (**c**) test dataset.

The global SHAP analysis (Figure 10) clearly demonstrated that the key factor determining greenhouse gas emission reduction through the use of the vertical SHE is e_{GHG}, with an average absolute SHAP value of nearly 2500 $kgCO_2e$. This variable, therefore, contributes the most to explaining the variability of the developed XGBoost model, confirming previous conclusions about the significant importance of the national energy mix for the environmental performance of SHEs. Reducing the energy source's carbon intensity is equivalent to limiting the potential for avoided emissions per unit of recovered thermal energy, resulting in significant variation in effects between countries with different energy

generation structures. This is evidenced by the beeswarm plot analysis, which allows for a detailed interpretation of the direction and scale of the impact of individual input variables on deviations from the base value (3804 $kgCO_2e$). In the case of greenhouse gas emission intensity, this range is the widest. Absolute SHAP values for individual observations reach almost 10,000 $kgCO_2e$, for both negative and positive values of this parameter. This wide range confirms that the variable can significantly increase or decrease the projected emission reduction (R_{GHG}) relative to the base value, depending on local conditions. The presence of high SHAP points (marked in red to the right of the base value) indicates that the high emission intensity of the energy system significantly increases the reduction effect of a vertical SHE operating under unbalanced flow conditions.

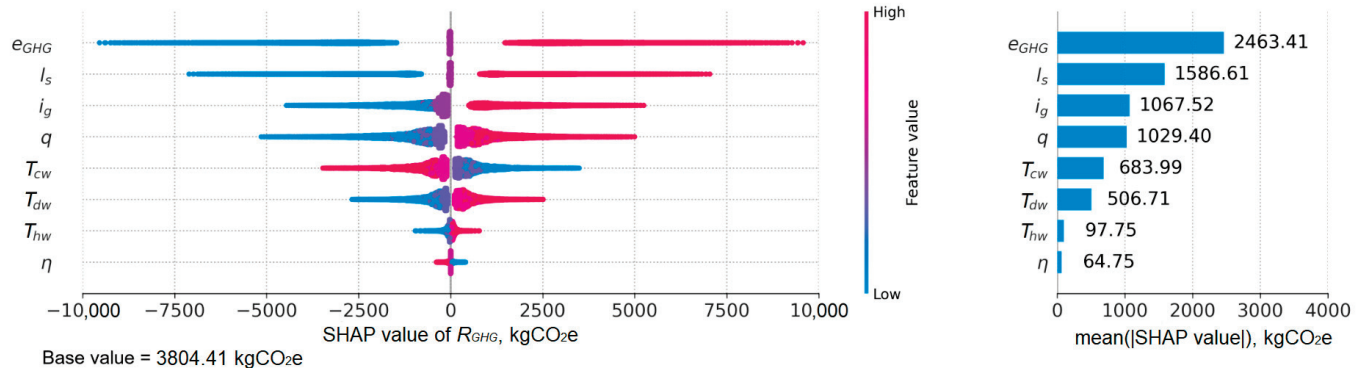


Figure 10. SHAP analysis of projected greenhouse gas emission reduction (designations as in Figure 1).

The second most significant factor was shower length (l_s), which directly impacts the amount of water used and, consequently, the amount of recoverable energy. In this case, however, the mean |SHAP value| is approximately 35% lower. This result indicates that user habits may be nearly as important as technological factors, highlighting the importance of consumption patterns in environmental efficiency analyses of projects that reduce energy consumption for water heating. Next in line were the annual change in GHG emission intensity (i_g), essentially a reduction in this indicator, and the mixed water flow rate (q). In both cases, the mean |SHAP value| exceeded 1000 $kgCO_2e$. This indicates that both energy transition dynamics and the hydraulic parameters of the building installation significantly influence long-term emission reduction potential. It should also be noted that all three factors demonstrate a similar direction of influence on the R_{GHG} prediction result as greenhouse gas emission intensity, although the range of SHAP values for individual observations is significantly smaller. An increase in water consumption per shower, resulting from extending the shower length or increasing the mixed water flow rate from the shower head, translates into an increase in the amount of recoverable thermal energy and, consequently, a higher emission reduction. The same applies to the variable i_g. The slow rate of decarbonization of the energy sector (lower emission reduction in subsequent years) may significantly enhance the environmental performance of a vertical SHE-equipped installation, especially since some observations indicate SHAP values exceeding 5000 $kgCO_2e$.

Significantly lower results were obtained for media temperatures in individual sections of the system. For cold water and drain water, they were in the range of several hundred kilograms, while the impact of DHW temperature was negligible, as the mean |SHAP value| did not reach 100 $kgCO_2e$. The significantly lower significance of temperature variables suggests that, within the considered range of their variability, they do not constitute a major limitation to the efficiency of the heat recovery system. The variable with the least impact on the projected greenhouse gas emission reduction was the efficiency of

the DHW heater, which is likely due to the high efficiency of electric DHW heaters and the narrow range of analyzed values of this parameter.

3.3. Evaluation of Extreme Cases and Medians

To broaden the interpretation of the results, an analysis of local SHAP values was conducted for three characteristic observations, corresponding to the maximum, minimum, and median values of the distribution. This analysis was performed for both models. This approach enabled an assessment of the impact of combinations of input variables on the *NPV* and R_{GHG} calculation results.

For observations corresponding to the maximum *NPV* and R_{GHG} forecasts (Figure 11), all input variables contributed to increasing the forecast compared to the baseline value. This suggests that the greatest benefits from installing a vertical SHE on the shower's greywater outlet are achieved under conditions of cumulative favorable factors, including operational factors (a large amount of water consumption), economic factors (high energy prices and their rapid growth), and environmental factors (high GHG emission intensity throughout the heat exchanger's lifetime). For the maximum *NPV* forecast, only a slight change in the hierarchy of importance of individual input variables was observed. The importance of investment outlays decreased relative to the average, resulting in this variable being moved to the last position. This means that under conditions of high positive financial flows resulting from significant energy savings for heating DHW, the INV_0 value loses its relative importance compared to the scale of generated financial savings. This phenomenon is further compounded by the fact that when preheated water is supplied exclusively to the SMV, the scope of installation work is small, significantly reducing the initial investment costs. In the case of R_{GHG}, on the other hand, the importance structure of input variables remained consistent with the global analysis.

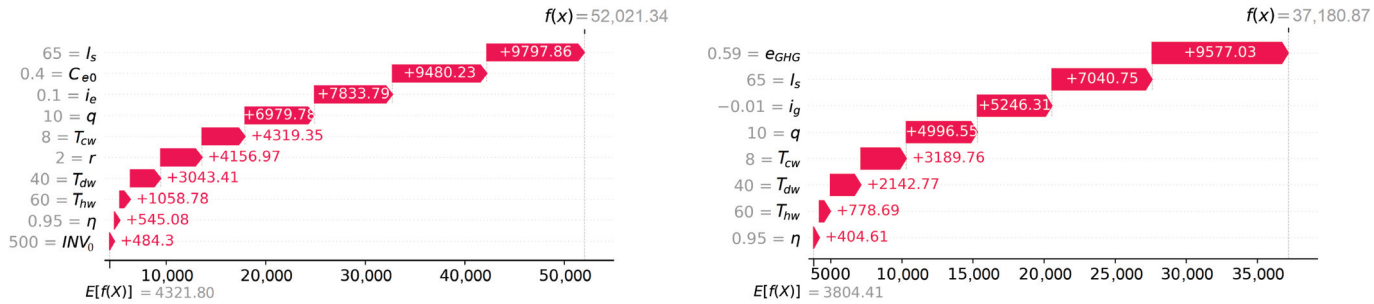


Figure 11. SHAP analysis results for maximum cases: (**a**) *NPV*; (**b**) R_{GHG} (designations as in Figure 1).

For observations corresponding to the minimum *NPV* and R_{GHG} values (Figure 12), all variables contributed to lower forecasted results. Therefore, unlike the maximum forecasts, the lowest results are a consequence of the coexistence of unfavorable conditions related to low shower system use intensity, low energy prices throughout the unit's life cycle, and parameters limiting heat recovery potential. With respect to the minimum *NPV* forecast, a slight change in the structure of variable significance was noted, consisting of an increased influence of mixed water flow rate (q) relative to the annual increase in electricity prices (i_e). A similar change occurred in the second model, where water flow rate proved more significant than changes in greenhouse gas emission intensity (i_g). This suggests that under conditions of extremely low financial savings, current operating parameters may be more important than long-term factors such as price dynamics or decarbonization.

https://doi.org/10.3390/en19081845

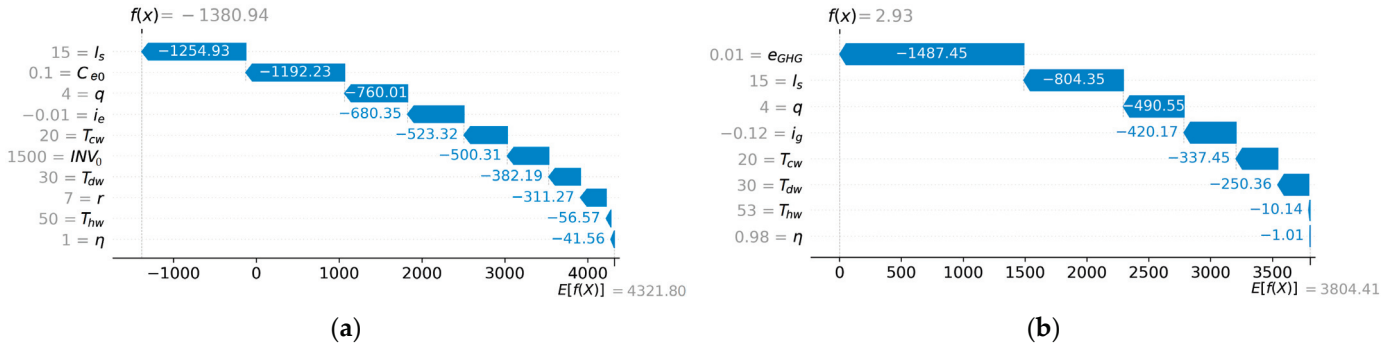


Figure 12. SHAP analysis results for minimal cases: (**a**) *NPV*; (**b**) R_{GHG} (designations as in Figure 1).

The most complex relationships were observed for observations corresponding to the median forecasts (Figure 13). In the case of the median *NPV*, the initial electricity price had the greatest impact, with a low value resulting in a lower forecast compared to the baseline. A similar trend was observed for high cold water temperature. High initial investment outlays, a moderate increase in electricity prices, high DHW heater efficiency, and low DHW temperature also contributed to the lower *NPV* forecast. On the other hand, a significant shower length increased *NPV* compared to the baseline by almost €2500. High drain water temperature, a low discount rate, and a relatively high mixed water flow rate also contributed to the increase in *NPV* forecast. This pattern indicates that, under average conditions, the effects of individual variables partially offset each other. Some of them enhance the project's financial efficiency, while others reduce it.

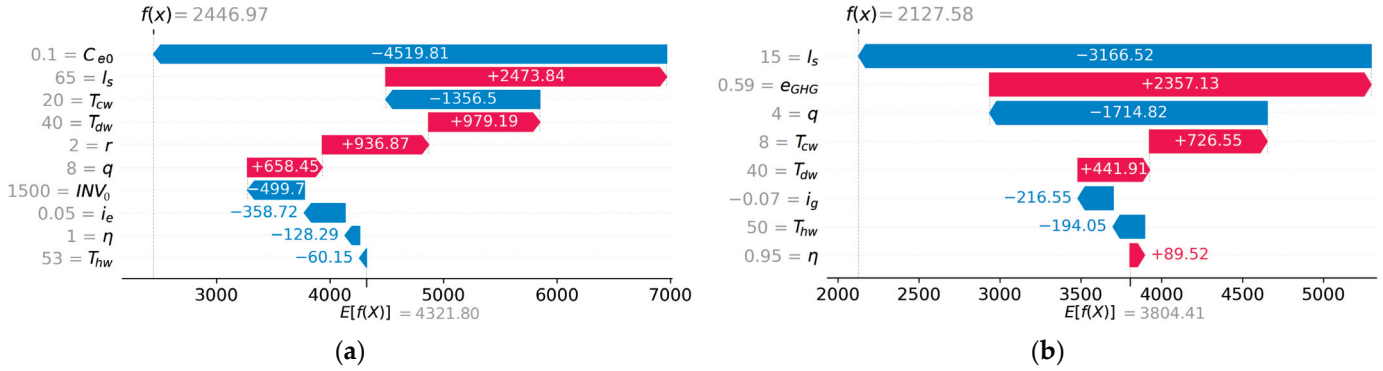


Figure 13. SHAP analysis results for median cases: (**a**) *NPV*; (**b**) R_{GHG} (designations as in Figure 1).

An equally complex hierarchy of significance was observed for the median R_{GHG}. In the considered scenario, however, the minimum shower length and low water flow rate resulted in a reduction in the environmental impact compared to the baseline value by almost 3167 $kgCO_2e$ and 1715 $kgCO_2e$, respectively. The projected level of greenhouse gas emission reduction was significantly increased by a high GHG emission intensity of electricity generation. Low cold water temperature and high drain water temperature also contributed to the improvement in the environmental impact, while the efficiency of the DHW heater had only a minimal positive effect. On the other hand, the significant annual reduction in e_{GHG} and low domestic hot water temperature reduced the projected R_{GHG} value by approximately 200 $kgCO_2e$. The different directions of influence in the above observations confirm that the individual scenarios are the result of overlapping variables with opposing impacts. Unlike the extreme cases, where a unidirectional cumulative effect dominates, other cases reflect the true complexity of interactions between individual input variables. These results highlight the importance of local analysis in interpreting predictive models. Only such an approach allows us to understand how observations with

https://doi.org/10.3390/en19081845

similar environmental or economic outcomes can result from different configurations of input variables.

3.4. Assessment of Consistency Between Financial and Environmental Effects

The assessment of consistency between financial and environmental effects was based on a comparison of the SHAP analysis results for two independent predictive models: the *NPV* model and the R_{GHG} model. Due to the different number of input variables included in both models, the comparison did not apply to full observations, but only to the part of the feature space common to both analyses. This included six input variables related to the operating and technical conditions of the shower installation (l_s, q, T_{cw}, T_{dw}, T_{hw}, η). For each combination of values of these six common input variables in the *NPV* model, there were 81 scenarios resulting from the combination of four additional economic variables, each of which assumed three values. Similarly, in the R_{GHG} model, for the same combination of common variables, there were nine scenarios resulting from the combination of two additional environmental variables, also analyzed for three different values. Therefore, representative cases were determined not for a single identical observation in both models, but within sets of observations with the same values of the common variables. For each of the analyzed common variables, SHAP values corresponding to three representative points of the prediction distribution were compared: the minimum value, the median value, and the maximum value. Detailed results for shower length (l_s), which turned out to be the most significant common variable in both models, are presented in Figure 14. Results for the remaining common variables are provided in Appendix A.

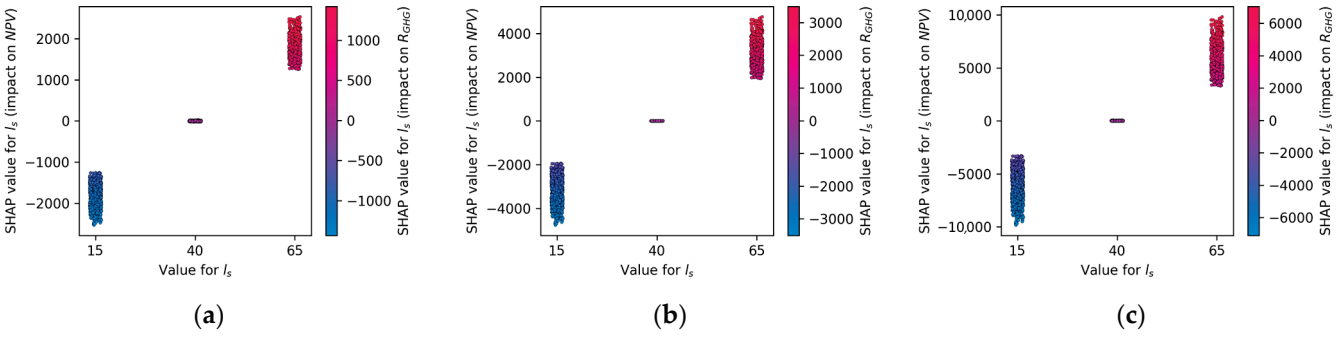


Figure 14. SHAP-based comparison of the impact of shower length (l_s) on *NPV* and R_{GHG}: (**a**) minimum; (**b**) median; (**c**) maximum.

The results indicated high consistency between the financial and environmental effects. In the minimum, median, and maximum cases considered, common input variables exhibited the same direction of influence on the prediction values of both models. This means that factors increasing the predicted *NPV* simultaneously increased the predicted greenhouse gas emission reduction, while factors reducing the financial effect had a similar effect on the environmental effect.

Furthermore, the relative importance of common variables was found to be consistent. In the global analysis, shower length (l_s) had the highest significance in both models, with subsequent common variables maintaining a similar position in terms of influence. This confirms that both financial and environmental benefits are largely determined by the same operational mechanisms, primarily related to the intensity of shower system use.

It should be emphasized, however, that in real-world conditions, the profitability of the project will also be determined by other input variables. In this context, the results obtained for the median scenarios (Figure 13) are particularly important, as they can be considered the most representative of actual operating conditions. The SHAP analysis showed that the relationships between input variables and *NPV* and R_{GHG} are more complex and less clear-

cut than in extreme cases. For key common variables, the general trend is maintained. For example, a longer shower increases the result, while a lower l_s value results in a reduction in the expected results. However, these variables do not fully determine the final values, as parameters specific to both models also play a significant role. Consequently, the observed variability in results under median conditions results from the overlapping influence of common variables and model-specific variables, whose impacts are not mutually offset. This leads to a situation in which the general trends remain unchanged, but their final effect is modified depending on the configuration of external parameters.

This indicates the necessity of apparent trade-offs between financial and environmental efficiency. However, it should be noted that not all input variables are controllable from the perspective of the user or system designer. Variables such as electricity prices and their variability over time, or greenhouse gas emission intensity, are external factors independent of the installation's operation. In the case of operational variables such as l_s or q, which the user can actually influence, a high degree of consistency is observed in the impact on *NPV* and R_{GHG}. Therefore, the observed discrepancies between both effects result largely from the system's location, not from direct user decisions. The lack of full consistency between *NPV* and emission reduction is, therefore, not due to conflicting operational objectives, but rather to the overlapping influence of controllable and uncontrollable parameters. The final effect is a result of user decisions and external conditions.

4. Discussion

The results of the analysis confirmed that the use of XGBoost models combined with SHAP analysis is an effective tool for identifying key variables determining the financial and environmental performance of a shower heat recovery system operating under unbalanced flow conditions. By quantifying the impact of individual input variables on *NPV* and R_{GHG}, this approach can provide a basis for transparent system optimization [8]. It allows not only for identifying the most important variables but also for understanding their impact in various shower system operation scenarios.

The global SHAP analysis showed that for both dependent variables considered, variables related to the intensity of shower use, i.e., shower length (l_s) and mixed water flow rate (q), significantly impact the forecast result. These parameters directly influence the amount of tap water used and, therefore, the amount of recoverable thermal energy. Local analysis of individual shower system scenarios confirmed that increasing water consumption in the shower system not only increases the potential for GHG emission reduction but also translates into increased expected financial savings. This convergence suggests that, in many cases, improving the environmental performance is correlated with economic attractiveness.

However, it is important to remember the variables that were not included in both models. In the case of GHG emission reduction, the greenhouse gas emission intensity of electricity generation (e_{GHG}) and the rate of its decline over the subsequent years of vertical SHE use play a significant role. These variables determine the "environmental value" of each unit of saved energy. On the other hand, the level and dynamics of energy price changes, and to a lesser extent, the discount rate, are crucial for financial profitability. This means that the environmental effects of drain water heat recovery strongly depend on the structure of the energy system, while the financial effects depend on market conditions. The observed differences in the mechanisms shaping the net present value and potential GHG emission reduction demonstrate that maximizing environmental benefits will not, in many cases, equate to maximizing financial benefits, particularly in the case of electricity production in low-emission systems and at relatively low energy prices.

https://doi.org/10.3390/en19081845

Interpreting the SHAP analysis results in a practical context, it can be concluded that the application of a vertical SHE is most economically and environmentally beneficial under conditions of intensive shower use. The consistency analysis results indicate that, despite differences in the model structures, common operational and technical variables exhibit consistent effects on both predicted variables. In particular, parameters related to the intensity of shower system use, such as shower length (l_s) and mixed water flow rate (q), simultaneously increase both the *NPV* and the potential reduction in greenhouse gas emission. This means that within the common part of the feature space, the financial and environmental effects are determined by converging physical mechanisms related to the amount of recovered energy. Electricity prices and their rate of increase over time also play a significant role in the investment profitability. Under conditions of high energy prices, the financial savings achieved will be the greatest, resulting in an increase in the *NPV*. The environmental effect, however, will be most visible in countries with the highest emission intensity of energy used for water heating, where the potential for GHG emission reduction will be the greatest. On the other hand, in countries that, thanks to conscious energy policies, have eliminated fossil fuels and replaced them with renewable sources and nuclear energy, the environmental impact of using vertical SHEs will be limited. Furthermore, reducing the amount of water used limits the amount of recoverable thermal energy, which impacts both the environmental and financial benefits. This means that the greatest benefits from these systems can be achieved in buildings with high and regular water consumption per shower, and in conditions of relatively high electricity prices and high emissions from their generation.

However, when considering the results of the analysis, it is important to remember the limitations of the adopted research methodology. The dataset used was synthetic in nature. In real-world operating conditions, greater data variability and the presence of random factors can lead to reduced accuracy of predictive models. Therefore, the results should be interpreted as an assessment of potential relationships between variables rather than as direct forecasts for actual installations.

Another significant limitation was that the analysis was based on an electric DHW heater, which significantly determined the results. For natural gas-powered devices, different results can be expected for both the financial and environmental performance of the tested solution. On the one hand, a lower natural gas price may lead to lower projected financial savings, and thus a reduction in *NPV*. Eurostat statistics [37] indicate that in the first half of 2025, the price of natural gas for households in the EU ranged from €0.0307 per kWh (Hungary) to €0.2128 per kWh (Sweden). The maximum price of natural gas was, therefore, almost half that of electricity. On the other hand, greenhouse gas emissions from natural gas combustion are typically lower than those from electricity generation in systems based on a high-emission energy mix. This may result in limited emission reduction potential. It should be noted, however, that in systems with very low emissions, using electricity to heat DHW may be more environmentally beneficial than burning natural gas. Data from the European Commission [38] indicate that the GHG emission factor for natural gas is approximately 0.20 kgCO2e/kWh. In countries with lower e_{GHG} values, the use of SHE could contribute to greater reductions in greenhouse gas emissions when used in conjunction with a gas DHW heater.

It should also be emphasized that the results of SHAP analysis are dependent on the assumed ranges of input variables. Feature importance reflects the influence of a variable within the analyzed dataset, not its universal significance. This means that changing the ranges of input variable values can lead to a change in their relative importance in the model. This is particularly true for variables with a wide range of values, such as shower length. Their high position in the importance hierarchy does not always result from their

actual importance. It may also be a consequence of a greater influence on the variability of the results. Therefore, the obtained variable rankings should be interpreted in the context of the assumed ranges of input variables. With different shower usage scenarios or with changed environmental or financial parameters, the hierarchy of importance of individual variables may change.

It is also important to note that the analysis focused on one specific type of shower heat exchanger and a specific system configuration, which limits the possibility of directly generalizing the obtained results to all solutions used in practice. For other SHE geometries, the absolute values of the achieved environmental and financial effects may be slightly different. However, the identified relationships, particularly those concerning the direction of the influence of individual input variables, are more universal and can be applied to other types of SHEs heating water supplied to the shower mixing valve.

The identified relationships should be considered in the context of the growing demand for energy in various sectors, as societal development and the functioning of a modern economy are largely dependent on access to energy, which should be both reliable, safe, and economically affordable [39]. It should be noted that one of the most energy-intensive areas of municipal infrastructure is the water and sewage sector. This is due, among other things, to growing requirements for water quality, climate change, and the occurrence of extreme events [40]. The need to ensure high system reliability is also important. In this context, water losses are a significant problem [41], which necessitates the collection, treatment, and transportation of additional volumes of water, increasing total energy consumption. In such conditions, the utilization of thermal energy carried by wastewater becomes particularly important, especially since, as Arsenyeva et al. [42] noted, even a few percent of the heat demand can be met through heat recovery from wastewater. The possibilities of heat recovery from wastewater are not limited to single-family homes. This technology demonstrates potential applications in many other facilities, such as multi-family buildings, hotels, and industrial facilities, where the amount of available waste energy can be significantly higher. The literature provides recommendations for the application of wastewater heat recovery systems in facilities with high hot water consumption. These may include hotels, for example, where decisions regarding the location of the heat recovery system should, in addition to energy demand and heat recovery potential, also consider the region's tourism potential [43]. Heat recovery from sanitary appliances other than showers is also justified. For example, Zanganeh et al. [44] emphasized the importance of heat recovery in commercial dishwashers. It is, therefore, clear that the range of possible applications of heat recovery technology from wastewater, primarily greywater, is much broader than that described in this paper.

This wide variety of heat recovery system configurations and operating conditions demonstrates that the use of predictive models combined with SHAP analysis can be a valuable tool in future research, enabling the identification of key parameters determining both the energy efficiency, environmental performance, and economic efficiency of various wastewater heat recovery systems. These studies should consider not only small local installations but also systems based on heat pumps [45]. Particular emphasis should be placed on hybrid systems combining various renewable and waste energy sources, such as wastewater and air heat pumps, as well as solar collectors [46]. Considering heat storage systems [47] would also be beneficial, as such a solution could further increase the flexibility of wastewater heat recovery systems and enable better adjustment to fluctuating demand. Integrating wastewater heat recovery systems with other technologies can increase both the energy and environmental efficiency as well as financial viability. For this reason, it is also worth examining available forms of support. As noted by Ogarek et al. [48], taking

https://doi.org/10.3390/en19081845

Poland as an example, the fastest-growing renewable energy sector in this region is the one receiving the highest subsidies.

Future research should also consider the development of heat recovery technology from wastewater, including greywater. Technologies used in other energy sectors could provide inspiration for new SHE solutions. For example, Ahmad and Alsalmah [49] proposed a two-pipe solar-assisted heat exchanger. The development of such technologies defines the direction in which modern energy production is heading. These are hybrid solutions, combining various energy-harvesting mechanisms. The research described in this paper suggests that even for more complex systems for heat recovery from drain water, an approach based on SHAP analysis could be a useful tool supporting their design and optimization.

Integrating the heat recovery system under consideration with broader building energy management strategies may also be an interesting direction for further research, as Li et al. [50] noted that demand-side flexibility depends on the interaction between a number of parameters that determine the building's energy profile. Although the demonstrated vertical SHE application affects only the energy demand for DHW heating, its significance can be considered in the broader context of building energy performance.

The results can also be considered in the broader context of achieving sustainable development objectives and global climate goals. Previous research indicates that modernizing and adapting existing systems to new environmental requirements is a crucial element of the transition to more sustainable energy systems [51]. Undoubtedly, SHEs also meet this requirement, contributing to rational resource management, increasing the energy efficiency of buildings, and reducing greenhouse gas emissions. Such solutions are also consistent with the concept of a circular economy, which strives to maximize the use of energy already present in the system [52]. The development and optimization of wastewater heat recovery technologies can also support the implementation of selected sustainable development goals (SDGs). Therefore, it is hoped that the integration of sustainable energy saving techniques with modern analytical methods and predictive modeling will be an important element of the transformation towards a more environmentally friendly and resilient energy future, which is particularly important given the growing exposure to the effects of climate change [53].

5. Conclusions

The analysis demonstrated that heating the water supplied to the shower mixing valve using a vertical heat exchanger enables efficient heat recovery from drain water. For the considered range of input parameter variability, *NPVs* ranged from −€1381 to €52,168. Meanwhile, the greenhouse gas emission reduction over the 15-year operation period ranged from 61 $kgCO_2e$ to 37,207 $kgCO_2e$. Using predictive modeling in conjunction with SHAP analysis, it was possible to identify key parameters influencing the financial and environmental impacts of this solution, as well as assess the consistency between these effects. It was also possible to determine the relative importance of individual input variables influencing the project's net present value and potential greenhouse gas emission reduction. The global SHAP analysis was supplemented with local analysis for selected cases, allowing for a better understanding of how individual input variables influence the predictions of both models. Key findings from these analyses include:

1. Greenhouse gas emission intensity of electricity generation and shower length are among the most important variables shaping the potential GHG emission reduction.
2. Annual change in GHG emission intensity and mixed water flow rate also have a significant impact on environmental effects.

https://doi.org/10.3390/en19081845

3. In the case of financial effects, in addition to water consumption per shower, the price of electricity and its dynamics over the entire operational life of the heat recovery installation are also crucial.
4. The direction of the impact of individual operating parameters on the projected greenhouse gas emission reduction and net present value is consistent. However, differences in the relative importance of individual variables can be noted, as confirmed by local analysis, indicating certain changes in the impact hierarchy depending on the scenario analyzed.

It should be noted, however, that the results are subject to certain limitations resulting from the model assumptions and the scope of the analyzed data. The analysis was conducted for specific technical and operational conditions of the drain water heat recovery system. Other methods of connecting the shower heat exchanger, as well as other SHE models, were not considered. Furthermore, the predictive models considered a limited number of parameters, meaning that in real-world conditions, other factors, such as the variability of water consumption profiles in the building, may also influence the system's efficiency. Another limitation may be that the local analysis was based on selected characteristic cases, which, while providing a better understanding of the model's operation, do not reflect the full variability of all possible operating scenarios.

It is also important to note the technical limitations and potential implementation risks of vertical SHEs, particularly in existing buildings. These limitations may result from local conditions, variability in operating parameters, and the need for integration with existing building systems. In each case, they may impact the actual financial and environmental performance of the solution.

Future research would benefit from conducting analyses combining predictive modeling with interpretation tools. It is also worthwhile to expand the scope of analyses to include other configurations of drain water heat recovery systems, as well as solutions used in other areas of water and sewage infrastructure. Future research could also include a larger number of scenarios, allowing for a more comprehensive assessment of the impact of variability in individual parameters on the system's financial efficiency and its potential to reduce greenhouse gas emissions.

Author Contributions: Conceptualization, S.K.-O. and M.S.; methodology, S.K.-O. and M.S.; software, S.K.-O. and M.S.; validation, S.K.-O. and M.S.; formal analysis, S.K.-O. and M.S.; investigation, S.K.-O. and M.S.; resources, S.K.-O. and M.S.; data curation, S.K.-O. and M.S.; writing—original draft preparation, S.K.-O. and M.S.; writing—review and editing, S.K.-O. and M.S.; visualization, S.K.-O. and M.S. All authors have read and agreed to the published version of the manuscript.

Funding: This research was financed by the Minister of Science and Higher Education of the Republic of Poland within the "Regional Excellence Initiative" program for the years 2024–2027 (RID/SP/0032/2024/01).

Data Availability Statement: Data are contained within this paper.

Conflicts of Interest: The authors declare no conflicts of interest. The funders had no role in the design of the study; in the collection, analyses, or interpretation of data; in the writing of the manuscript; or in the decision to publish the results.

Abbreviations

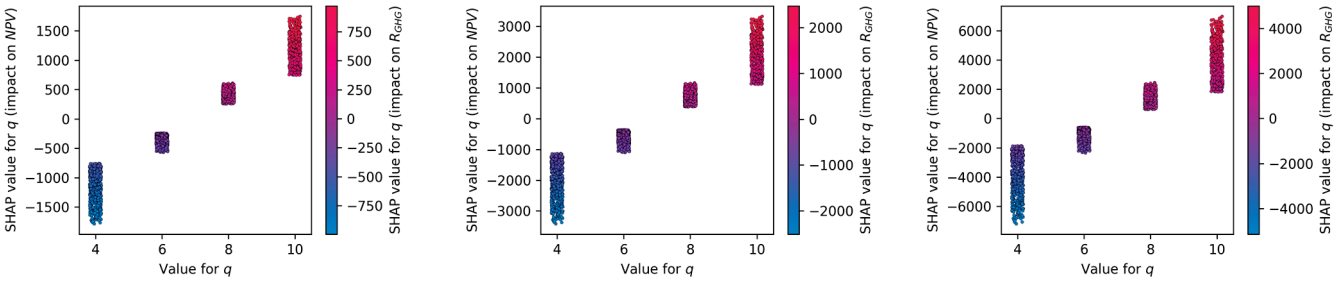
The following abbreviations are used in this manuscript:

CO_2	carbon dioxide
DHW	domestic hot water
EU	European Union

GHG	greenhouse gas
MAE	mean absolute error
NPV	net present value
RMSE	root mean square error
SDG	Sustainable Development Goal
SHAP	SHapley Additive Explanations
SHE	shower heat exchanger
SMV	shower mixing valve

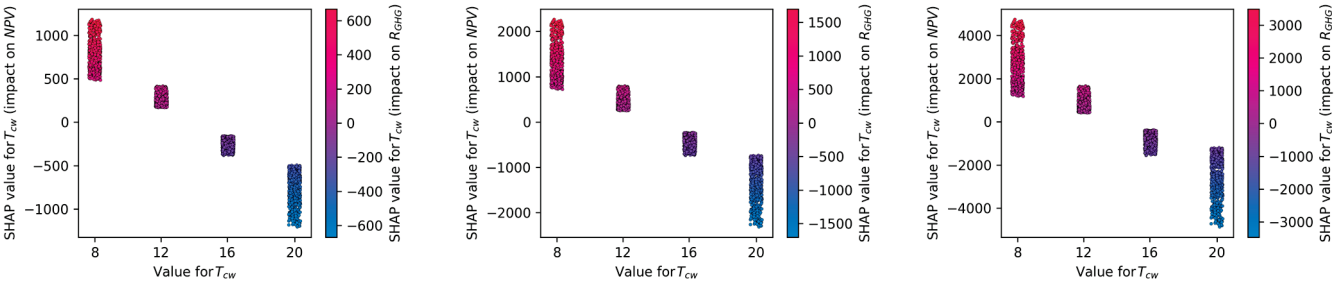
Appendix A

Figures A1–A5 present SHAP-based comparisons of the impact of selected variables on *NPV* and R_{GHG}.



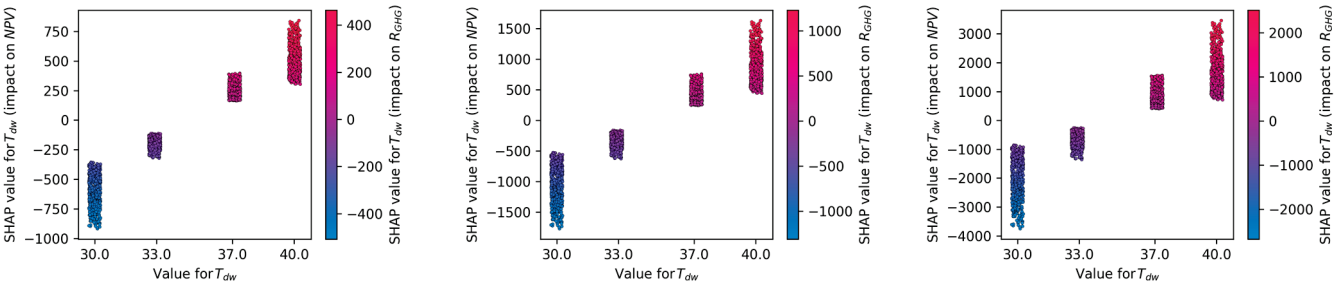
(**a**) (**b**) (**c**)

Figure A1. SHAP-based comparison of the impact of mixed water flow rate (q) on *NPV* and R_{GHG}: (**a**) minimum; (**b**) median; (**c**) maximum.



(**a**) (**b**) (**c**)

Figure A2. SHAP-based comparison of the impact of cold water temperature (T_{cw}) on *NPV* and R_{GHG}: (**a**) minimum; (**b**) median; (**c**) maximum.



(**a**) (**b**) (**c**)

Figure A3. SHAP-based comparison of the impact of drain water temperature (T_{dw}) on *NPV* and R_{GHG}: (**a**) minimum; (**b**) median; (**c**) maximum.

https://doi.org/10.3390/en19081845

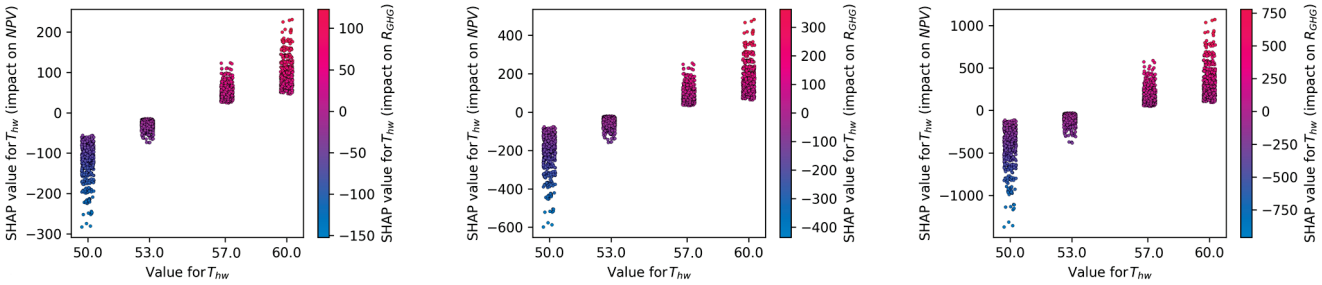


Figure A4. SHAP-based comparison of the impact of DHW temperature (T_{hw}) on *NPV* and R_{GHG}: (**a**) minimum; (**b**) median; (**c**) maximum.

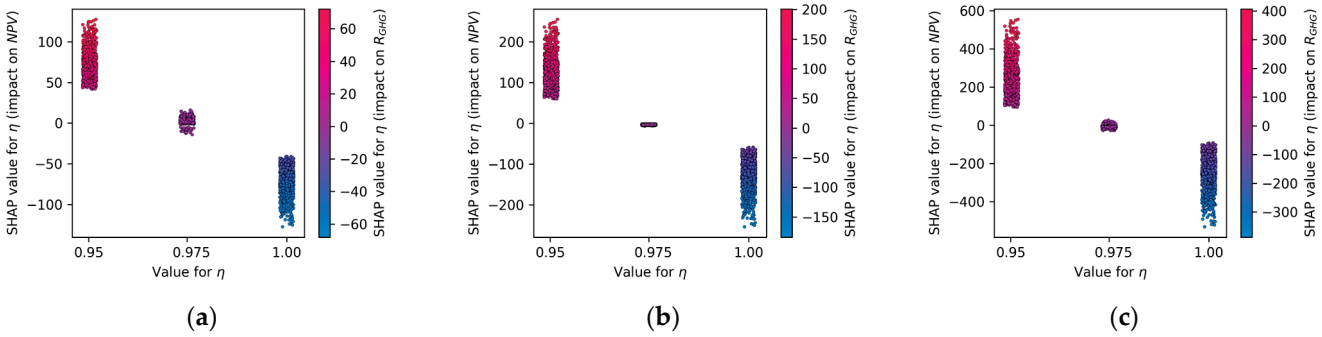


Figure A5. SHAP-based comparison of the impact of DHW heater efficiency (η) on *NPV* and R_{GHG}: (**a**) minimum; (**b**) median; (**c**) maximum.

References

1. Hall, R.J.; Kenway, S.; Memon, F.A.; O'Brien, K.R. Trade-offs between total and peak energy consumption due to plumbing layouts in Australian and UK domestic hot water systems. *J. Clean. Prod.* **2025**, *518*, 145941. [CrossRef]
2. Voznyak, O.; Dudkiewicz, E.; Laska, M.; Antypov, I.; Spodyniuk, N.; Sukholova, I.; Savchenko, O. A New Approach to the Economic Evaluation of Thermomodernization: Annual Assessment Based on the Example of Production Space. *Energies* **2024**, *17*, 2105. [CrossRef]
3. Hall, R.J.; Kenway, S.; O'Brien, K.R.; Memon, F.A. Quantification of residential water-related energy needs cohesion, validation and global representation to unlock efficiency gains. *Renew. Sustain. Energy Rev.* **2025**, *207*, 114906. [CrossRef]
4. Bednarz, K.; Stec, A.; Słyś, D. Research Trends in Renewable Energy Sources in Academic Infrastructure: A Bibliometric Analysis. *Energies* **2025**, *18*, 5812. [CrossRef]
5. Enayatollahi, R.; Appleby, A. Development of a wastewater heat recovery unit for residential buildings in New Zealand. *IOP Conf. Ser. Earth Environ. Sci.* **2025**, *1500*, 012059. [CrossRef]
6. Kaewluan, S.; Unsomsri, N.; Wiriyasart, S. Thermal Performance and Energy Consumption of Air Conditioning Systems with Heat Exchangers for Water Heater Efficiency Improvement. *ES Energy Environ.* **2025**, *29*, 1749. [CrossRef]
7. Tauseef, M.; Sharqawy, M.F. Thermal and Hydraulic Performance Analysis of a Waste Heat Recovery Device for Domestic Furnace Exhaust Gases. *Green Energy Environ. Technol.* **2026**, *5*, 1–20. [CrossRef]
8. Li, Y.; Zhang, H.; Shen, X.; Qu, K. Interpretable machine learning for predicting and optimizing residential building performance in cold regions. *Energy Build.* **2025**, *347*, 116321. [CrossRef]
9. Piotrowska, B.; Słyś, D. Variant analysis of financial and energy efficiency of the heat recovery system and domestic hot water preparation for a single-family building: The case of Poland. *J. Build. Eng.* **2023**, *65*, 105769. [CrossRef]
10. Silva, E.; Ferreira, V.; Cunha, J.; Monteiro, E. CFD Analysis on the Performance of Twisted Tapes in Horizontal Heat Exchangers for Shower Water Heat Recovery. *J. Heat Mass Transf. Res.* **2025**, *12*, 137–150. [CrossRef]
11. Forero, J.D.; Vigoya, M.F.; Casseres, D.M. Analysis of a Waste Heat Recovery System from Hot Drainage Water Using a Heat Recovery Concentric Tube Heat Exchanger Through CFD Simulation. *Int. Rev. Mech. Eng.* **2025**, *19*, 318–326. [CrossRef]
12. Kowalik, R.; Sidło, W. Drain water heat recovery for domestic hot water in polish residential buildings: Energy, economic and environmental assessment. *Desalin. Water Treat.* **2025**, *324*, 101475. [CrossRef]
13. Piotrowska, B.; Słyś, D. Analysis of the Life Cycle Cost of a Heat Recovery System from Greywater Using a Vertical "Tube-in-Tube" Heat Exchanger: Case Study of Poland. *Resources* **2023**, *12*, 100. [CrossRef]

14. Stec, A.; Piotrowska, B.; Słyś, D. Greywater as an undervalued tool for energy efficiency enhancement and decarbonizing the construction sector: A case study of a dormitory in Poland. *Energy Build.* **2025**, *330*, 115337. [CrossRef]
15. Stec, A.; Pochwat, K. Assessment of the efficiency of shower wastewater heat exchangers using machine learning-based methods. *J. Build. Eng.* **2025**, *103*, 112062. [CrossRef]
16. Purghel, D.M.; Teodosiu, C.I. Numerical Study on Shower Water Heat Recovery. *IOP Conf. Ser. Earth Environ. Sci.* **2025**, *1546*, 012025. [CrossRef]
17. Krishnan, E.N.; Muneeshwaran, M.; Rendall, J.; Brechtl, J.; Nawaz, K. Experimental investigation on heat transfer performance of drain water heat recovery heat exchangers. *Energy Build.* **2025**, *346*, 116213. [CrossRef]
18. Zhang, X.; Rhee, K.N.; Jung, G.J.; Kim, C. Exploring energy efficiency and savings potential of a horizontal domestic drain water heat recovery system in high-rise apartment buildings. *Energy Build.* **2024**, *325*, 115038. [CrossRef]
19. Kordana-Obuch, S.; Piotrowska, B.; Starzec, M. Management of waste heat in residential buildings: Predictive modelling and sensitivity analysis of variables characterising shower heat exchanger conditions. *Energy* **2025**, *318*, 134743. [CrossRef]
20. Ali, S.; Faraj, J.; Khaled, M. Heat recovery from hot water drainage: CFD simulation, energy efficiency and exergoeconomic analysis of concentric tube heat exchangers. *J. Build. Eng.* **2024**, *98*, 111034. [CrossRef]
21. Dudkiewicz, E.; Ludwińska, A. Family Dwelling House Localization in Poland as a Factor Influencing the Economic Effect of Rainwater Harvesting System with Underground Tank. *Sustainability* **2023**, *15*, 10687. [CrossRef]
22. Karimi, M.; Heidarigoujani, H.; Jahangiri, M.; Anaraki, M.T.; Janaki, D.M. Heating the Future: Solar Hot Water Collectors for Energy-Efficient Homes in Sweden. *Energy Eng.* **2026**, *123*, 6. [CrossRef]
23. Electricity Price Statistics. Available online: https://ec.europa.eu/eurostat/statistics-explained/index.php?title=Electricity_price_statistics (accessed on 17 December 2025).
24. Electricity Prices for Household Consumers—Bi-Annual Data. Available online: https://ec.europa.eu/eurostat/databrowser/view/nrg_pc_204/default/table?lang=en (accessed on 17 December 2025).
25. Commission Notice on Current State Aid Recovery Interest Rates and Reference/Discount Rates Applicable as from 1 January 2026 (Published in Accordance with Article 10 of Commission Regulation (EC) No 794/2004). Available online: https://eur-lex.europa.eu/eli/C/2025/6782/oj/eng (accessed on 7 January 2026).
26. Greenhouse Gas Emission Intensity of Electricity Generation in Europe. Available online: https://www.eea.europa.eu/en/analysis/indicators/greenhouse-gas-emission-intensity-of-1 (accessed on 17 December 2025).
27. Antosz, K.; Kozłowski, E.; Sęp, J.; Prucnal, S. Application of Machine Learning to the Prediction of Surface Roughness in the Milling Process on the Basis of Sensor Signals. *Materials* **2025**, *18*, 148. [CrossRef]
28. Mądziel, M. Investigating Real-world Emissions from Liquefied Petroleum Gas-fueled Vehicles: A Modeling Approach that Utilizes Portable Emissions Measurement Systems. *Open Transp. J.* **2025**, *19*, e26671212367963. [CrossRef]
29. Xu, Z.; Zhou, X.; Wang, Y. The implementation of machine learning models for predicting CO_2 emission in carbon capture and storage systems. *Sustain. Comput. Inform. Syst.* **2026**, *49*, 101264. [CrossRef]
30. Zhang, T.; Zhu, W.; Wu, Y.; Wu, Z.; Zhang, C.; Hu, X. An explainable financial risk early warning model based on the DS-XGBoost model. *Financ. Res. Lett.* **2023**, *56*, 104045. [CrossRef]
31. Liu, J.; Uglanov, D.A.; Kedam, N.; Zheng, G.; Shimanov, A.A.; Shimanova, A.B.; Lian, Z. Machine learning prediction of thermal–hydraulic (j–f) characteristics in compact heat exchangers with six fin configurations. *Appl. Therm. Eng.* **2025**, *280*, 128491. [CrossRef]
32. Piotrowska, B.; Kordana-Obuch, S.; Starzec, M. Using domestic drain water as affordable and clean energy: Predictive modeling and sensitivity analysis of a horizontal heat exchanger. *Energy* **2025**, *341*, 139326. [CrossRef]
33. Piotrowska, B. Modeling, optimization and sensitivity analysis of integrated photovoltaic, wind turbine, battery storage and drain water heat recovery systems. *Energy* **2026**, *346*, 140191. [CrossRef]
34. Cui, X.; Lee, M.; Koo, C.; Hong, T. Energy consumption prediction and household feature analysis for different residential building types using machine learning and SHAP: Toward energy-efficient buildings. *Energy Build.* **2024**, *309*, 113997. [CrossRef]
35. Ponce-Bobadilla, A.V.; Schmitt, V.; Maier, C.S.; Mensing, S.; Stodtmann, S. Practical guide to SHAP analysis: Explaining supervised machine learning model predictions in drug development. *Clin. Transl. Sci.* **2024**, *17*, e70056. [CrossRef]
36. Yılan, Y.; Beykent, A. Day-Ahead Electricity Price Forecasting Using the XGBoost Algorithm: An Application to the Turkish Electricity Market. *Comput. Mater. Contin.* **2025**, *86*, 1–16. [CrossRef]
37. Natural Gas Price Statistics. Available online: https://ec.europa.eu/eurostat/statistics-explained/index.php?title=Natural_gas_price_statistics (accessed on 30 March 2026).
38. GHG Emission Factors for Local Energy Use. Available online: https://data.jrc.ec.europa.eu/dataset/72fac2b2-aa63-4dc1-ade3-4e56b37e4b7c (accessed on 30 March 2026).
39. Słyś, D.; Stec, A.; Bednarz, K.; Ogarek, P.; Zeleňáková, M. Managing and Optimizing Hybrid Distributed Energy Systems: A Bibliometric Mapping of Current Knowledge and Strategies. *Energies* **2025**, *18*, 2497. [CrossRef]

40. Fisher, P.M.J.; Smith, D. The water industry and the decarbonisation of cities: A comprehensive review in the context of Cop26. *PLoS Water* **2022**, *1*, e0000023. [CrossRef]
41. Rożnowski, M.; Żywiec, J.; Szpak, D.; Tchórzewska-Cieślak, B. The Problem of Water Losses in the Visegrad Group (V4) Countries: Challenges and Opportunities. *Water* **2026**, *18*, 640. [CrossRef]
42. Arsenyeva, O.; Biletskyi, I.; Plankovskyy, S.; Kapustenko, P.; Tsegelnyk, Y.; Teliura, N. Heat Recovery Systems From Sewage: The Current State and Development Prospects. In *Sustainable Development and the Evolution of Civil Engineering*, 1st ed.; Neves Lousada, S.A., Ed.; IGI Global Scientific Publishing: Hershey, PA, USA, 2025; pp. 69–106. [CrossRef]
43. Hosseini Dehshiri, S.S.; Hosseini Dehshiri, S.J.; Mostafaeipour, A. Waste heat recovery systems integrated in hotels: An uncertain and reliable planning. *Appl. Therm. Eng.* **2025**, *281*, 128653. [CrossRef]
44. Zanganeh, J.; Seyfaee, A.; Gates, G.; Moghtaderi, B. Thermal Management and Energy Recovery in Commercial Dishwashers: A Theoretical and Experimental Study. *Energies* **2025**, *18*, 2338. [CrossRef]
45. Song, J.; Zhang, Y.; Ma, Z.; Zhang, H. Research progress and application prospect of wastewater heat pump technology in recent decade: A review. *Clean Energy* **2025**, *9*, 123–147. [CrossRef]
46. Ma, C.; Yang, Y.; Jiang, Y.; Liu, K. Control Optimization of Multi-Energy System in Residential Heating and Domestic Hot Water Application. In *Proceedings of the 12th International Conference on Cold Climate HVAC & Energy, CCHVAC 2025; Environmental Science and Engineering*; Ni, L., Wang, P., Li, J., Liu, Y., Eds.; Springer: Singapore, 2025; Volume 1, pp. 351–360. [CrossRef]
47. Amanowicz, Ł.; Turski, M. PCM-Filled Capsules (RT44HC) for Heat Storage—Laboratory Scale Pilot Study. *Energies* **2025**, *18*, 345. [CrossRef]
48. Ogarek, P.; Stec, A.; Słyś, D. Technical and economic analysis of an autonomous hybrid photovoltaic-hydrogen energy system for academic buildings with the focus on energy Independence—A case study for Poland. *Appl. Energy* **2025**, *392*, 125985. [CrossRef]
49. Ahmad, S.; Alsalmah, H.A. Numerical and artificial intelligent analysis of double pipe heat exchanger exposed to solar irradiation for sustainable energy solutions. *Results Eng.* **2025**, *27*, 105994. [CrossRef]
50. Li, W.; Sui, W.; Cheng, L.; Ji, Y.; Guo, Y.; Zhu, J. Quantifying seasonal demand-side flexibility in residential air conditioning under diverse control strategies. *Energy Build.* **2026**, *352*, 116764. [CrossRef]
51. Ciupek, B.; Frąckowiak, A. Review of Thermal Calculation Methods for Boilers—Perspectives on Thermal Optimization for Improving Ecological Parameters. *Energies* **2024**, *17*, 6380. [CrossRef]
52. Serrano-Arévalo, T.I.; Ramírez-Márquez, C.; Ponce-Ortega, J.M. Comprehensive management of energy carriers: A circular economy perspective. *Curr. Opin. Chem. Eng.* **2026**, *51*, 101224. [CrossRef]
53. Borowski, P.F.; Bandala, E.R.; Lubańska, A.; Stein, E. The Effects and Challenges of Climate Change on the Food-Energy-Water Nexus—Poland as a Case Study. In *Optimization in the Agri-Food Supply Chain: Recent Studies*; Koubaa, M., Ammar, M.H., Dhouib, D., Mnejja, S., Eds.; Wiley: Hoboken, NJ, USA, 2024; pp. 17–40. [CrossRef]

Disclaimer/Publisher's Note: The statements, opinions and data contained in all publications are solely those of the individual author(s) and contributor(s) and not of MDPI and/or the editor(s). MDPI and/or the editor(s) disclaim responsibility for any injury to people or property resulting from any ideas, methods, instructions or products referred to in the content.

energies

MDPI

Article

Heat Transfer and Thermo-Mechanical Analysis of Plastic-Strain Evolution in Laser-Welded Thin-Walled Laminated Cooling Plates with Non-Uniform Stiffness

Chengkun Li, Yujia Cai, Han Wang, Zhihang Zhang, Fang Han, Xiaoqing Zhu, Chengcheng Wang and Zhibo Dong *

National Key Laboratory of Precision Welding & Joining of Materials and Structures, Harbin Institute of Technology, Harbin 150001, China
* Correspondence: dongzhb@hit.edu.cn

Abstract

Thin-walled laminated cooling plates integrate internal channels and pin-fin cores, producing reduced and spatially non-uniform stiffness that changes welding restraint and distortion. This study investigates stiffness-controlled plastic-strain evolution in laser butt welding of GH3230 laminated plates, with geometrically identical solid plates as reference. A coupled heat-transfer and thermo-mechanical finite element model was developed in MSC Marc using a composite Gaussian surface–volumetric moving heat source and temperature-dependent properties. The thermal solution was validated against near-weld thermal cycles and fusion geometry; mechanical predictions were evaluated by CMM distortion and residual-stress measurements. Both structures show comparable residual-stress magnitudes and spatial trends, indicating that residual stress is governed mainly by the local weld thermal gradient. In contrast, the laminated plate exhibits larger angular/bending distortion. Simulations show that, although the plastic-strain pattern is similar, the laminated plate develops higher peak plastic strain confined to a narrower band near the weld, with the transverse plastic strain dominating. Plastic strain–temperature paths reveal continued transverse plastic-strain accumulation during cooling with limited recovery, consistent with restraint redistribution induced by stiffness non-uniformity. An equivalent restraint–stiffness spring model explains this "narrower-but-stronger" plastic zone and links stiffness to yielding and residual plastic-strain magnitude, supporting distortion prediction and stiffness-informed control of welded laminated cooling plates.

Keywords: heat transfer; thermo-mechanical coupling; laminated cooling plate; laser butt welding; plastic strain evolution

1. Introduction

Laminated cooling plates are key thermal-management components in advanced energy systems, where lightweight design must be achieved without compromising heat-spreading and cooling performance. Their internal flow channels and supporting pillars result in significantly reduced and spatially non-uniform stiffness, which can substantially modify the restraint conditions during fabrication. Fusion welding is widely used to manufacture such components because of its high efficiency and material utilization. However, the localized moving heat input generates a strongly non-uniform thermal cycle, together with rapid transient heat conduction through the thin walls and continuous surface heat loss, making residual stresses and welding-induced distortion largely unavoidable. This

issue is particularly critical in thin-walled structures for energy equipment, where the low bending stiffness makes them highly susceptible to angular and bending deformation, thereby compromising dimensional accuracy, assembly tolerance, and ultimately service reliability. Consequently, developing predictive and mechanistic approaches for welding distortion in thin-walled laminated cooling plates remains an important topic at the intersection of heat-transfer analysis and thermo-mechanical response. Horajski et al. [1] proposed an integrated structural–process strategy for reducing distortion in thin-walled welded structures and emphasized the continuing practical importance of deformation control in engineering applications. Qiu et al. [2] further showed that welding-induced distortion can amplify stresses and affect fatigue assessment, indicating that distortion is not merely a geometric imperfection, but also a factor that propagates into strength evaluation and safety margins. Experimental and numerical studies [3–5] have also shown that geometric scale, such as plate dimensions, and boundary constraints strongly influence both welding deformation and residual stress. These findings suggest that predictive models should be established on a mechanistic basis rather than relying solely on empirical corrections.

Factors influencing welding deformation mainly include the dimensions of the base metal, plate thickness, clamping conditions, and welding parameters [6]. For properly assembled thin-walled structures, welding deformation is mainly governed by the highly non-uniform temperature field generated during welding and by the intrinsically low stiffness of thin plates, which makes them less resistant to deformation [7]. From a mechanics perspective, welding deformation originates from non-recoverable inelastic strains accumulated under strongly non-uniform thermal cycles. In most fusion-welding processes, plastic strain is the dominant component, which forms the basis of the inherent strain concept [8,9]. Within this framework, the complex thermo-mechanical process is represented by an equivalent inelastic strain field, and the resulting global deformation is obtained by applying this field to the structure [10]. Following this concept, Lee et al. [11] developed a layered shell-element inherent strain method for thin-plate structures, improving computational efficiency for large-scale problems, and further proposed a time-saving workflow for predicting inherent deformation in large welded structures [12], thereby demonstrating its engineering applicability. To improve prediction accuracy, Wang et al. [13] introduced a stepwise loading strategy for inherent strains and validated its effectiveness in stiffened plate structures, showing that the loading scheme can significantly influence the final distortion field. Despite these advances in computational efficiency and predictive capability, a central issue remains insufficiently understood: why plastic strain evolves in a particular manner and how its spatial distribution is governed, especially under conditions of non-uniform stiffness and non-uniform restraint. In practice, the inherent strain field is still often treated as a black-box input, which limits the interpretability of distortion mechanisms and the transferability of distortion-control strategies.

The onset and evolution of plasticity during welding are governed by the combined effects of transient temperature gradients, temperature-dependent material properties, and structural constraints/stiffness [14]. A highly reliable understanding of plastic strain formation therefore typically requires thermo-mechanical coupled analysis [15]. Park et al. [16] numerically investigated the role of transverse restraint in welding distortion and residual stress, demonstrating that boundary conditions can fundamentally alter the final distortion mode and stress level. Chen et al. [17] analyzed residual stress distributions in U-rib stiffened plates, highlighting how stiffeners redistribute local restraint and, consequently, the stress/strain fields. Xu et al. [18] conducted experimental and numerical studies on residual stress and distortion in welded "I"-section curved beams, showing that section non-uniformity and curvature modify the deformation response. Collectively, these studies

https://doi.org/10.3390/en19061536

indicate a strong coupling between structural stiffness/constraint and welding response. However, most of the existing literature still evaluates outcomes mainly through final-state distortion or residual stress, while systematic and transferable explanations are scarce for how stiffness influences the restraint path and thereby governs the temporal evolution and spatial distribution of plastic strain.

This limitation becomes more pronounced for thin-walled laminated structures. Compared with conventional plates, internal channels and supporting pillars introduce pronounced spatially non-uniform stiffness, which may change how thermal strain is constrained and how the plastic zone develops. In contrast, the current research on laminated configurations has largely focused on thermal management and cooling performance [19,20], and an explicit framework is still lacking for interpreting plastic strain formation mechanisms, dominant components, and the conditions under which the spatial distribution transitions in welded joints with non-uniform stiffness.

To address these gaps, this work establishes an experimentally validated thermo-mechanical finite element model that explicitly accounts for the non-uniform stiffness characteristics of GH3230 laminated plates and systematically analyzes the initiation and evolution of plastic strain during the welding thermal cycle. By comparison with a conventional plate joint, the influence of non-uniform stiffness on plastic-strain evolution is identified and summarized. On this basis, an equivalent restraint–stiffness spring model is further proposed to parameterize how stiffness reduction and changes in the restraint path affect plastic-strain distributions, thereby providing actionable structural and process-oriented guidance for distortion control of thin-walled laminated welded components.

2. Experiments and Measurements

2.1. Welding Experiments

A TRUMPF TruDisk 6001 laser (From TRUMPF Photonics Components GmbH, Ulm, Germany) was used to perform a butt weld on two laminated plates with dimensions of 200 mm × 358 mm. The welding parameters are listed in Table 1. For comparison, a butt-welding experiment on a conventional (solid) plate with the same dimensions was carried out using the identical process parameters.

Table 1. The parameters of laser welding process.

Power (W)	Welding Speed (mm/s)	Heat Input (J/mm)	Spot Diameter (mm)	Shielding Gas
2700	30	90	0.3	Argon

Note: Specimens were tack-welded at both ends before welding. The defocus distance was 0 mm, and the focal plane was located on the top surface of the workpiece. The beam was perpendicular to the workpiece surface.

During welding, K-type thermocouples were employed to record thermal cycles at locations 3, 4, and 5 mm away from the weld center, as shown in Figure 1. The measured temperature histories were used to validate the thermo-mechanical coupled finite element model. The validation results are presented in Section 4.1.

https://doi.org/10.3390/en19061536

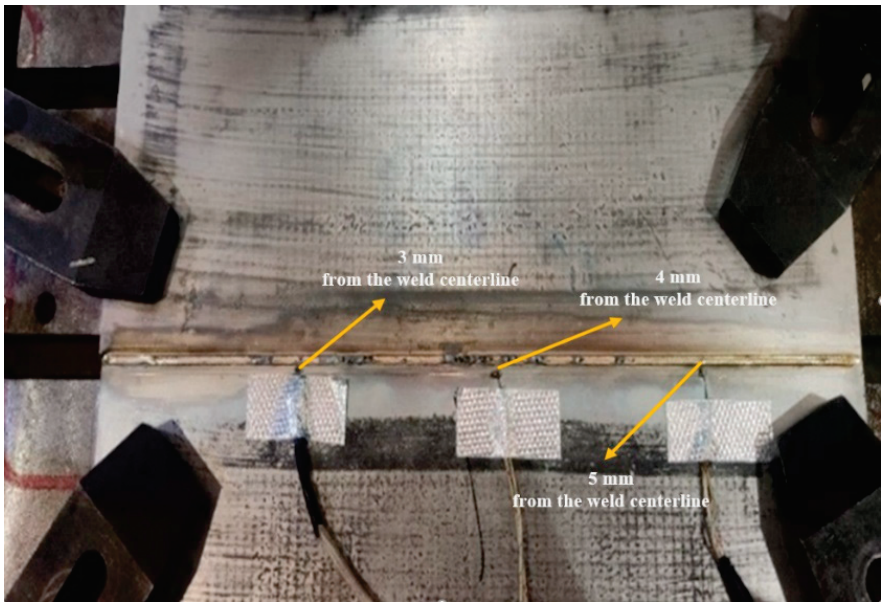


Figure 1. Schematic of thermocouple arrangement for thermal cycle measurement during welding.

2.2. Measurement of Welding Residual Stress and Distortion

Welding-induced distortion was measured using a coordinate measuring machine (CMM, Hexagon GLOBAL SILVER CLASSIC SR 09.20.08) (From Hexagon Metrology (Qingdao) Co., Ltd., Qingdao, China) with a measurement accuracy of 3 μm, as shown in Figure 2. Welding residual stresses were measured using X-ray diffraction (XRD, $\sin^2\psi$ method) and the hole-drilling method, as shown in Figure 3. Due to the size limitation of the XRD measurement stage, the central region of the welded plate was cut to a size of 90 mm × 90 mm by wire electrical discharge machining prior to XRD measurement. The associated stress relaxation induced by cutting was additionally considered in the finite element simulations. Specifically, the elements in the removed region were progressively deactivated to reproduce the material removal process and the associated stress redistribution. The corresponding simulation results after cutting are presented in Section 4.2, where the residual stress state used for comparison with the XRD measurements is discussed.

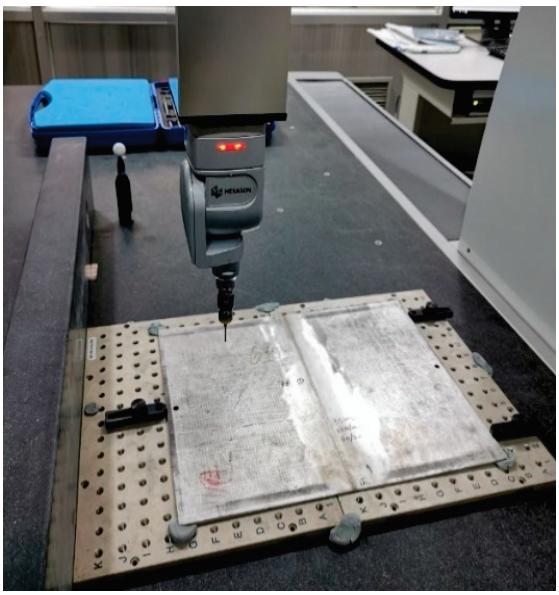


Figure 2. Measurement of welding-induced distortion using a coordinate measuring machine.



(**a**) (**b**)

Figure 3. Experimental setup for welding residual stress measurement: (**a**) hole-drilling method; (**b**) X-ray diffraction (XRD).

Before residual-stress measurements, the specimens were electropolished to remove the surface layer affected by machining and welding spatter. The material removal depth was 50 μm. The measured residual stresses and distortions are reported in Section 4.2, where they are compared with the corresponding finite element results.

3. Theory and Modeling

3.1. Governing Equations

Welding is a typical transient thermo-mechanical coupling process involving heat transfer, thermal expansion, elastic–plastic deformation, and constraint-induced stress redistribution. In the present work, the governing equations consist of the transient heat conduction equation and the mechanical equilibrium equations, which are solved in a coupled manner to capture the initiation and evolution of plastic strain during the welding thermal cycle.

The governing equation for transient heat conduction is given in Equation (1):

$$c\rho\frac{\partial T}{\partial t} = \frac{\partial}{\partial x}\left(k_x\frac{\partial T}{\partial x}\right) + \frac{\partial}{\partial y}\left(k_y\frac{\partial T}{\partial y}\right) + \frac{\partial}{\partial z}\left(k_z\frac{\partial T}{\partial z}\right) + Q(x,y,z,t) \quad (1)$$

where Q is the internal heat source generated during welding; T is the temperature; k_x, k_y, and k_z are the thermal conductivities in three directions (for an isotropic material, $k_x = k_y = k_z = k(T)$); $c(T)$ is the specific heat capacity; $\rho(T)$ is the density; t is time. It should be noted that $c(T)$, $\rho(T)$, and $k(T)$ are temperature-dependent.

In addition to heat conduction inside the welded component, heat dissipation to the surroundings occurs during welding and subsequent cooling. The heat loss consists of convection q_c and radiation q_r, which follow Newton's cooling law and the Stefan–Boltzmann law, respectively, as expressed in Equations (2) and (3):

$$q_c = -h_f(T_S - T_0) \quad (2)$$

$$q_r = -\varepsilon\sigma(T_S^4 - T_0^4) \quad (3)$$

where T_s is the surface temperature, T_0 is the ambient temperature, h_f is the convection coefficient, whose value depends on the local thermal boundary condition. $E = 0.8$ is the emissivity, and $\sigma = 5.67 \times 10^{-8}$ W/(m^2·K^4) is the Stefan–Boltzmann constant.

https://doi.org/10.3390/en19061536

Considering that the material remains at elevated temperatures only for a short duration during laser welding, creep effects were neglected [21]. The total strain increment is expressed in Equation (4) [22]

$$\Delta\varepsilon^{total} = \Delta\varepsilon^{e} + \Delta\varepsilon^{p} + \Delta\varepsilon^{th} \tag{4}$$

where $\Delta\varepsilon^{total}$ is the total strain increment, $\Delta\varepsilon^{e}$ is the elastic strain increment, $\Delta\varepsilon^{p}$ is the plastic strain increment, and $\Delta\varepsilon^{th}$ is the thermal strain increment. The thermal strain increment $\Delta\varepsilon^{th}$ is expressed in Equation (5):

$$\Delta\varepsilon^{th} = \alpha(T) \cdot \Delta T \tag{5}$$

where $\alpha(T)$ is the temperature-dependent coefficient of thermal expansion and ΔT is the temperature change.

To account for possible geometric nonlinearity in the thin-plate structure, the large-strain formulation was adopted in this work [23].

3.2. Welding Heat Source

As illustrated in Figure 4, a composite heat source model was adopted in the present laser welding simulation [24]. This model combines a Gaussian surface heat flux with a Gaussian volumetric heat source to describe energy deposition at the surface and within the penetration zone, respectively.

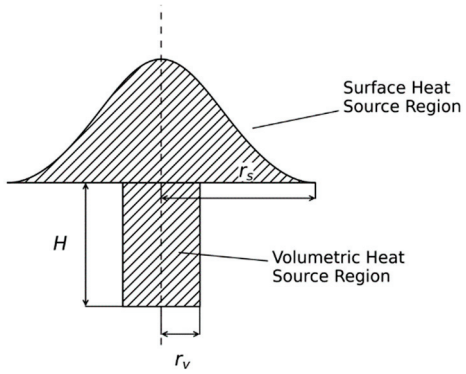


Figure 4. Schematic illustration of the composite heat source model for laser welding.

The surface heat flux distribution is expressed as

$$q_s(x,y) = \frac{\alpha Q_s}{\pi r_s^2} \exp\left[-\frac{\alpha(x^2+y^2)}{r_s^2}\right] \tag{6}$$

where α is the heat concentration coefficient, Q_s is the power of the surface heat source, and, r_s is the effective radius of the surface heat source.

The volumetric heat source distribution is expressed in Equation (7):

$$q_v(x,y,z) = \frac{6Q_V(H-\beta z)}{\pi r_v^2 H^2(2-\beta)} \exp\left[\frac{-3(x^2+y^2)}{r_v^2}\right] \tag{7}$$

where β is the decay coefficient, Q_v is the power of the volumetric heat source, r_v is the effective radius of the volumetric heat source, and H is the effective penetration depth.

The total welding power satisfies $\eta P = Q_s + Q_v$, where P is the laser power and η is the absorption efficiency.

https://doi.org/10.3390/en19061536

3.3. Material Properties

The chemical composition of GH3230 is listed in Table 2. Material nonlinearity was considered in the finite element model. The temperature-dependent thermophysical and mechanical properties of GH3230 were adopted from the relevant literature [25], as shown in Figure 5. The elastic behavior of the material was assumed to follow isotropic Hooke's law, while the plastic behavior after yielding was described by the von Mises yield criterion with isotropic strain hardening. The technical requirements for GH3230 comply with GB/T 14992-2025 [26] and this alloy is internationally equivalent to HAYNES® 230 alloy (From Junmu Steel Group, Shanghai, China).

Table 2. The chemical composition of GH3230.

Composition	Ni	Cr	Co	Mo	Al	Ti
Percentage	48%	25%	5%	2%	2.5%	1.5%

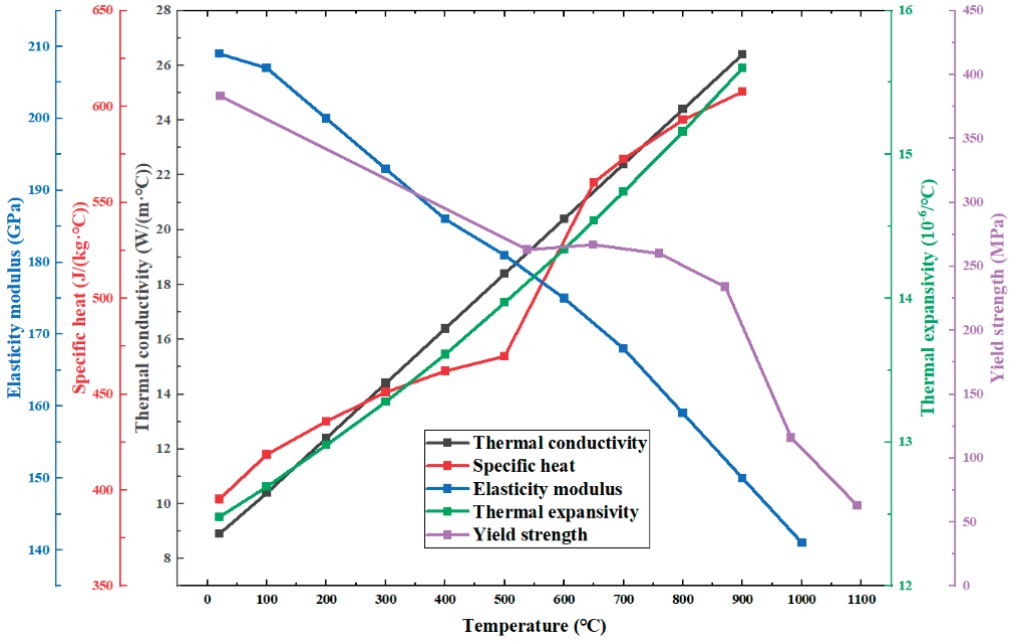


Figure 5. Temperature-dependent thermophysical and mechanical properties of GH3230.

3.4. Finite Element Mesh and Boundary Conditions

The three-dimensional finite element models of the laminated plate and the conventional solid plate are shown in Figure 6. The laminated plate model explicitly represents the outer skin, inner skin, pin-fin core, and base material, whereas the solid plate model adopts a homogeneous geometry with the same external dimensions. To reduce computational cost, a graded transition meshing scheme was employed. The mesh was refined in the vicinity of the weld seam with an element size of 0.5 mm, while a larger element size was used in regions far from the weld. All simulations were performed in MSC Marc. The models were discretized using hexahedral elements throughout. A coupled thermo-mechanical element type (Element 7) was adopted to enable fully coupled heat transfer and mechanical analysis. The extraction paths used in the subsequent result analysis (Lines 1–3) are also indicated in Figure 6. The total numbers of elements and nodes for each model are labeled in the same figure.

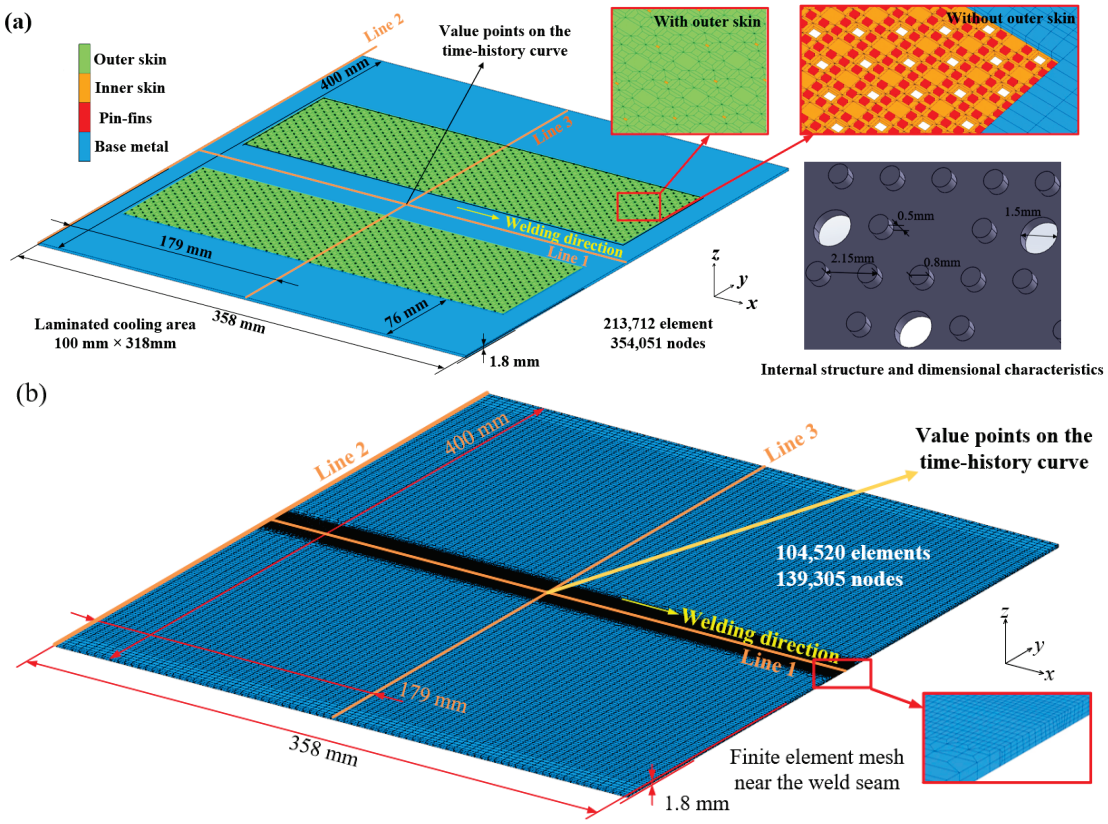


Figure 6. Finite element models and mesh configurations of the welded plates. The predefined weld path (Line 1) and reference lines for result extraction (Lines 2 and 3) are also indicated. (**a**) Finite element model of the laminated plate with internal pin-fin structure; (**b**) finite element model of the conventional solid plate.

The clamping conditions in the welding experiments, with the clamp locations shown in Figure 1, were reproduced in the FE model by constraining the corresponding nodes [27]. Since the clamps were positioned far from the weld seam, their influence on heat transfer was neglected. This assumption was later supported by the agreement between the simulated and measured thermal cycles.

To improve the accuracy of the thermal analysis, the additional heat exchange induced by the shielding gas during welding was taken into account. Specifically, an enhanced convection coefficient was applied in the weld-adjacent region exposed to the flowing shielding gas, whereas the regions without forced gas flow were assigned a natural convection coefficient [28]. Thermal radiation was incorporated by means of a temperature-dependent equivalent heat transfer coefficient [29]. The effect of solid-state phase transformation was neglected in the present model [30]. Geometric nonlinearity was included in the finite element analysis to improve computational accuracy [30].

4. Results and Discussion

4.1. Validation of Thermal Analysis

Figure 7 compares the simulated transient temperature field with the macrograph of the experimental weld cross-section. The fusion-zone geometry provides an integral validation of the underlying heat-transfer description, because it reflects the balance between the imposed moving heat input and the subsequent heat dissipation/spreading through the plate thickness and along the surface. The results confirm that the adopted heat-source model can reproduce the experimentally observed fusion zone of the laser weld. Full penetration was achieved in the experiment, and the fusion width on the top surface was

https://doi.org/10.3390/en19061536

approximately 2.2 mm; the simulation predicts an essentially identical weld-pool profile under the same heat-source parameters and heat-transfer boundary conditions. Therefore, the calibrated thermal model offers a consistent and reliable basis for subsequent thermo-mechanical analysis, and for isolating the effect of structural stiffness non-uniformity under a fixed thermal (heat-transfer) baseline.

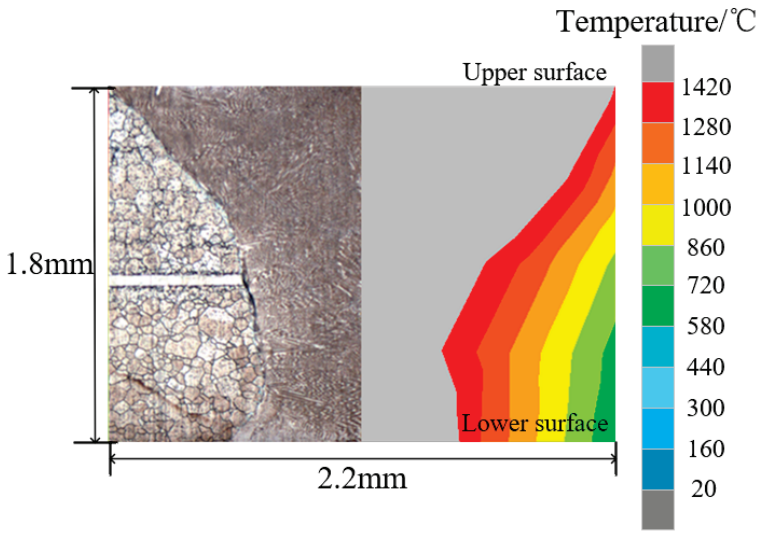


Figure 7. Comparison of simulated temperature distribution and weld cross-section.

To ensure reliable thermal predictions, the simulated thermal cycles near the weld were compared with the experimentally measured results. The comparison is shown in Figure 8. Both the experimental measurements and the finite element results were taken at the material surface.

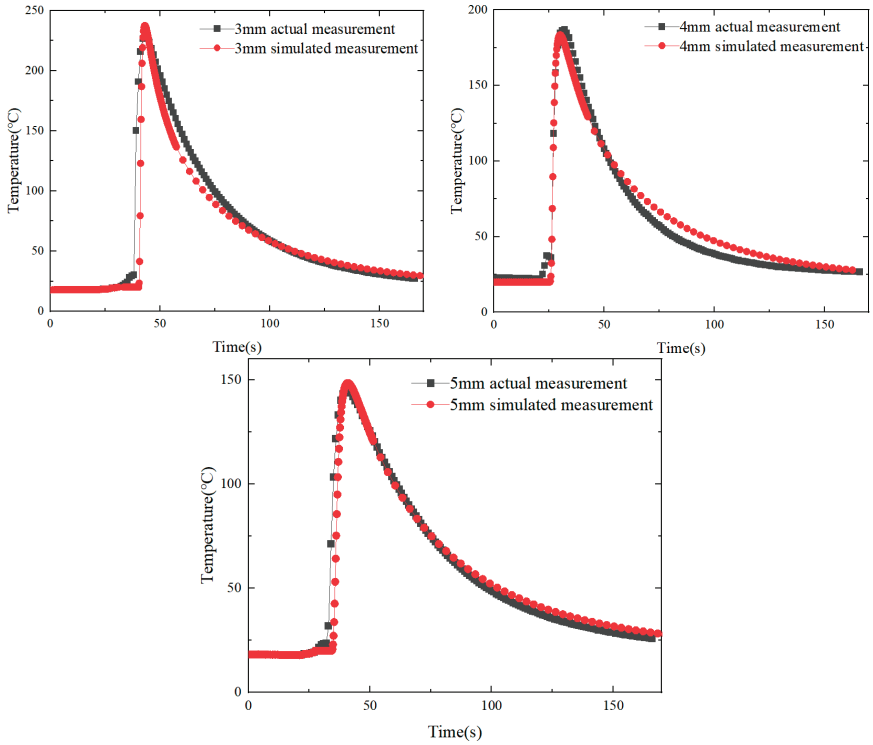


Figure 8. Comparison of simulated and measured thermal cycles at different distances from the weld centerline.

https://doi.org/10.3390/en19061536

The thermal histories measured at 3, 4, and 5 mm from the weld centerline exhibit a clear spatial attenuation of the peak temperature with increasing distance, reflecting the combined effects of localized heat input and subsequent heat spreading through conduction and surface heat loss.

Figure 9 further compares the transient temperature fields of the solid and laminated plates during the steady welding stage. In both cases, the isotherms exhibit a characteristic elongated teardrop-shaped pattern, which is associated with the highly concentrated energy input of the laser heat source and its high travel speed. The high-temperature zone is confined to the vicinity of the weld, and the isotherms are stretched along the welding direction. Owing to rapid heat spreading/conduction in thin plates and surface heat losses, the transverse temperature gradient remains very steep. Under identical heat-source parameters and heat-transfer boundary conditions, the overall heat-affected region and the melting-boundary isotherm are comparable for the two configurations, indicating that the subsequent differences in plastic-strain localization and distortion are mainly attributed to stiffness-dependent restraint redistribution.

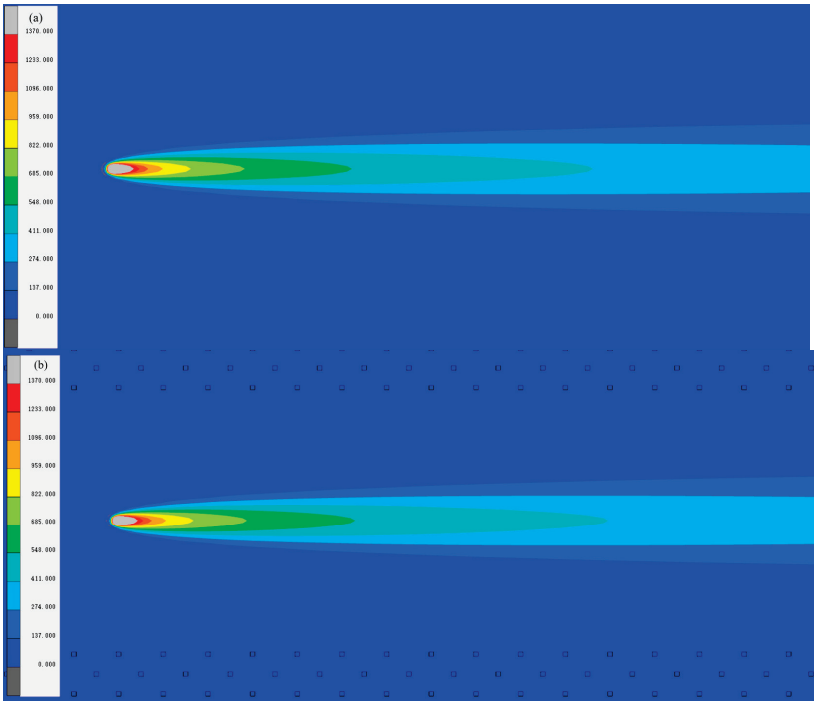


Figure 9. Transient temperature contours during the steady welding stage under identical heat input and heat-transfer boundary conditions: (**a**) solid plate; (**b**) laminated plate.

The numerical results reproduce the full heating–peak–cooling sequence with good agreement, capturing both the rapid temperature rise during heat-source passage and the post-heating decay governed by heat dissipation. This agreement indicates that the adopted moving heat-source representation, together with the applied thermal boundary conditions, can reliably describe the transient heat-transfer process in laser welding. The validated thermal model is therefore taken as a consistent heat-transfer baseline for the subsequent thermo-mechanical coupled analysis and welding-distortion prediction.

4.2. Welding Residual Stress and Distortion

The simulated stress-relief effect induced by cutting is shown in Figure 10. Both the longitudinal and transverse residual stresses are released to different extents after cutting, while boundary effects remain evident. As a result, the peak longitudinal residual

https://doi.org/10.3390/en19061536

stress decreases after cutting, whereas the maximum transverse residual stress shows a moderate increase.

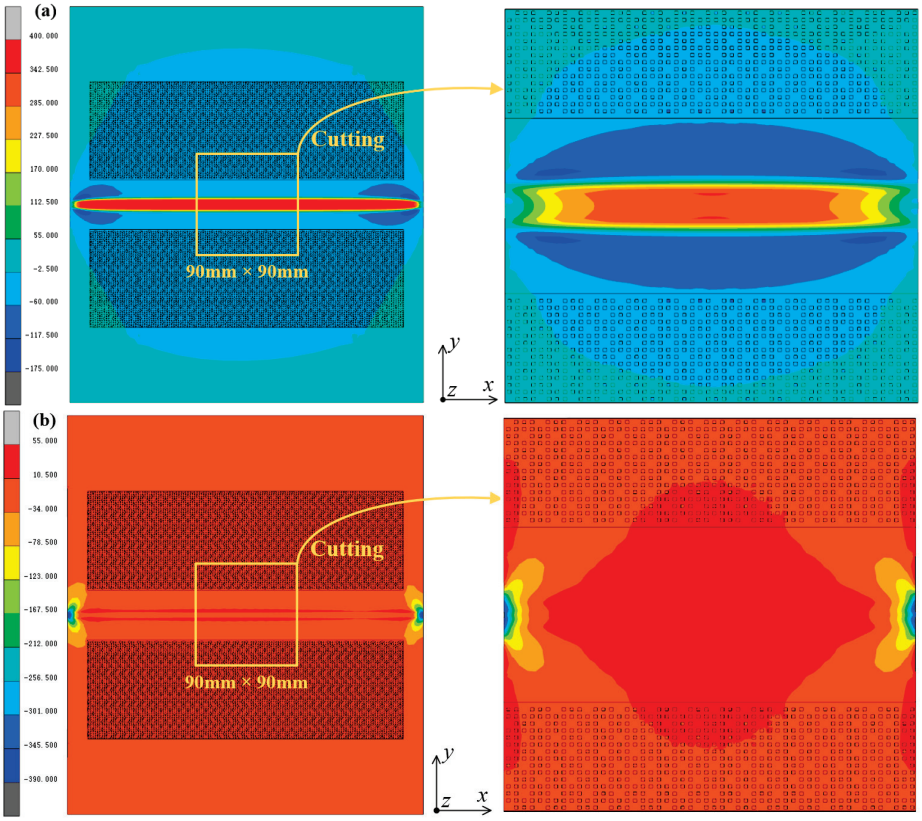


Figure 10. Simulated stress redistribution caused by cutting: (**a**) longitudinal residual stress; (**b**) transverse residual stress.

The simulated and measured welding residual stresses of the solid plate and laminated plate are presented in Figures 11 and 12. Owing to the spatial symmetry of the residual stress distribution, only half of the measurement results for each plate are shown.

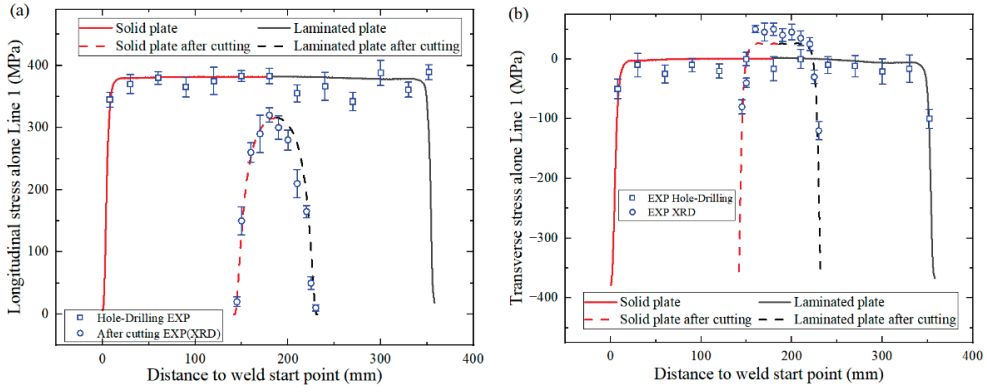


Figure 11. Simulated and measured residual stress distributions along Line 1: (**a**) longitudinal residual stress; (**b**) transverse residual stress.

Figure 11a shows the longitudinal residual stress extracted along Line 1. A stress-relaxation zone is observed near both ends of the weld seam, located approximately 12 mm from the plate edges, which is associated with edge effects. The longitudinal stress decreases to nearly zero at the ends, while it remains relatively stable in the central region at about 380 Mpa. Figure 11b presents the transverse residual stress along Line 1. A pronounced

https://doi.org/10.3390/en19061536

compressive region appears within roughly 20 mm from both seam ends; outside this zone, the transverse stress is tensile but remains below 5 Mpa. Overall, the transverse residual-stress field is nearly self-equilibrated, and the integral of transverse stress along the coordinate direction approaches zero.

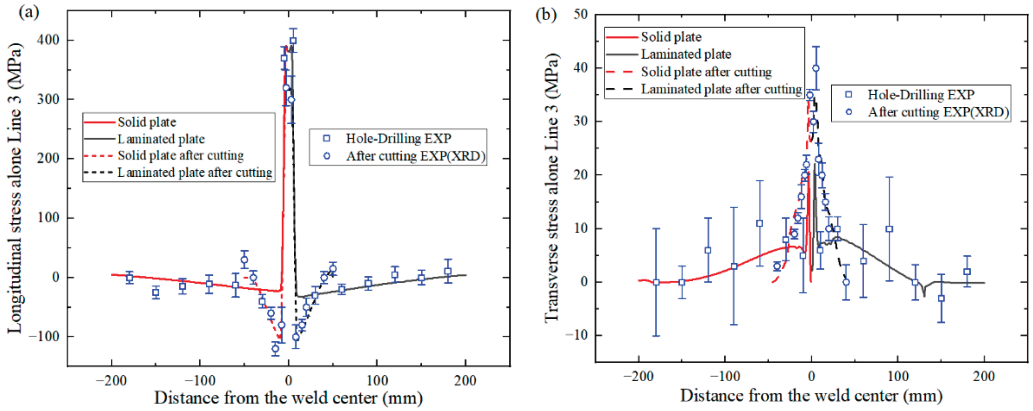


Figure 12. Simulated and measured residual stress distributions along Line 3: (**a**) longitudinal residual stress; (**b**) transverse residual stress.

No significant difference is observed between the solid and laminated plates in terms of the residual-stress distributions along Line 1. This indicates that, along the weld direction, residual-stress formation is governed primarily by the localized, highly non-uniform thermal cycle (i.e., the near-field temperature gradients and cooling conditions) imposed by the moving heat source and subsequent heat dissipation, rather than by global stiffness variations introduced by the laminated architecture. In other words, under identical heat-source parameters and heat-transfer boundary conditions, the thermal driving field dominates the residual-stress level along the seam, while stiffness non-uniformity plays a secondary role for this specific stress component and extraction path.

Figure 12a presents the longitudinal residual-stress distribution along Line 3. The tensile longitudinal residual stress is mainly concentrated within the weld seam and within approximately 15 mm on both sides, while compressive stresses develop in the remaining regions to satisfy force equilibrium. The integral of longitudinal residual stress along the transverse direction is approximately zero, indicating a self-equilibrated stress state. Owing to the highly localized laser heat input and the resulting steep thermal gradients, the thermally affected zone is narrow and the residual-stress field is correspondingly concentrated. The maximum longitudinal residual stress reaches approximately 385 Mpa for both the solid and laminated plates, and the overall distribution patterns are similar. Although the laminated plate shows slightly higher compressive levels in certain regions, the difference between the two plates is limited.

Figure 12b shows the transverse residual-stress distribution along Line 3. Both the XRD and hole-drilling measurements exhibit relatively large scatter, mainly because the transverse residual stress is much smaller than the longitudinal component, whereas the experimental uncertainty of both methods in the present study remains on the order of 10 Mpa. In addition, the presence of columnar grains in the weld region makes accurate XRD measurement more difficult. Nevertheless, the overall experimental trends are consistent with the simulation results, and the absolute deviations are generally within 10 Mpa, indicating acceptable agreement between experiment and simulation. The transverse component is much smaller than the longitudinal one, and a noticeable stress drop occurs at the weld center. This behavior can be attributed to the relatively weaker transverse restraint and to partial stress relaxation associated with welding-induced angular/bending

distortion, which modifies the constraint state during cooling. The solid and laminated plates exhibit consistent distribution trends, with only minor numerical differences.

Although the solid and laminated plates exhibit highly similar residual-stress distributions, their welding-induced distortions differ markedly, as shown in Figure 13. Figure 13 compares the post-weld out-of-plane (Z-direction) displacement profiles extracted along two representative lines (Line 1 and Line 2). The finite-element predictions agree well with the experimental measurements (EXP), supporting the credibility of the coupled analysis.

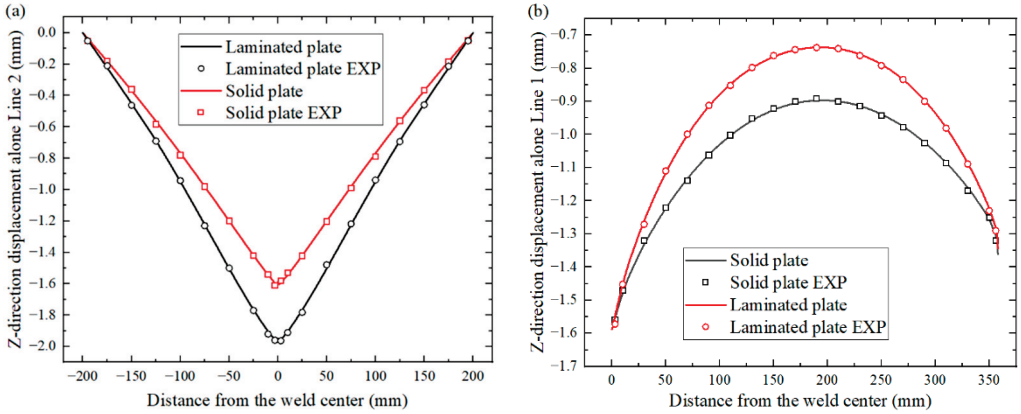


Figure 13. Comparison of simulated and measured out-of-plane (Z-direction) displacements: (**a**) displacement distribution along Line 2; (**b**) displacement distribution along Line 1.

Figure 13a shows the Z-direction displacement along Line 2. The deformation profile is approximately symmetric about the weld center and presents a characteristic "V" shape [31]. The maximum displacement occurs near the weld center and decays rapidly with increasing distance, approaching zero in the far field. This deformation mode is typical for thin-plate welding and can be interpreted as the macroscopic manifestation of the localized thermal cycle: steep temperature gradients and heat-flow-driven non-uniform expansion/contraction generate an imbalance between compressive and tensile plastic strains across the weld region, which accumulates as angular distortion during cooling. Under identical heat input and overall dimensions, the laminated plate exhibits significantly larger angular distortion than the solid plate; the maximum displacement at the weld center increases from approximately 1.6 mm to about 2.0 mm.

Figure 13b presents the Z-direction displacement along Line 1, reflecting the overall bending deformation of the plate. Line 1 corresponds to the weld zone, where plastic strain is concentrated. Owing to the difference in weld-pool width between the top and bottom surfaces, the longitudinal contraction during cooling becomes non-uniform through the thickness, leading to the maximum bending deformation in this region. Under the same boundary conditions, the laminated plate shows more pronounced deflection than the solid plate. These results indicate that welding distortion is not determined by residual stress alone. Even when the thermally induced residual-stress patterns are similar, differences in structural stiffness and the associated restraint redistribution during the heating and cooling process can still result in distinct deformation responses. Therefore, the stiffness non-uniformity introduced by the laminated configuration plays a dominant role in the observed distortion difference.

4.3. Plastic Strain Distribution

According to inherent strain theory, welding distortion is primarily governed by the spatial distribution of non-recoverable inelastic strain, with plastic strain being the dominant contributor in fusion welding. Because plastic strain is generated under a highly

localized thermal cycle, the final deformation pattern can be viewed as an integrated response to the heat-transfer-driven temperature gradients and the associated restraint conditions. Figure 14 presents the post-weld out-of-plane (Z-direction) displacement contours of the laminated and solid plates, with a magnification factor of 20 applied for clarity.

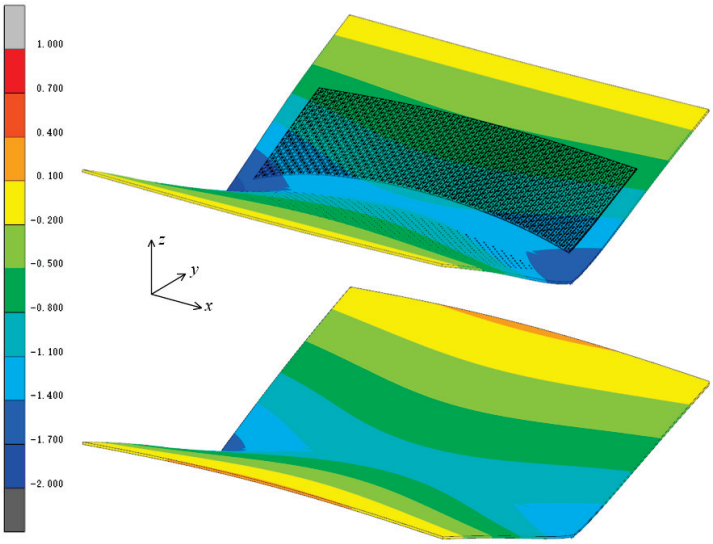


Figure 14. Contour plots of welding-induced out-of-plane deformation (20× magnification).

The global deformation modes of the laminated and solid plates are highly similar, and both exhibit the characteristic angular-distortion pattern typical of thin-plate laser welding. The representative displacement profiles extracted along selected lines (Figure 13) further confirm the similarity in deformation shape between the two plates. This consistency suggests that the overall spatial pattern of the plastic-strain field is also broadly comparable, while differences are expected mainly in magnitude and local concentration due to the stiffness non-uniformity introduced by the laminated configuration.

To further clarify the specific differences in plastic strain under identical heat transfer conditions, the distributions of plastic strain were extracted, as shown in Figures 15 and 16.

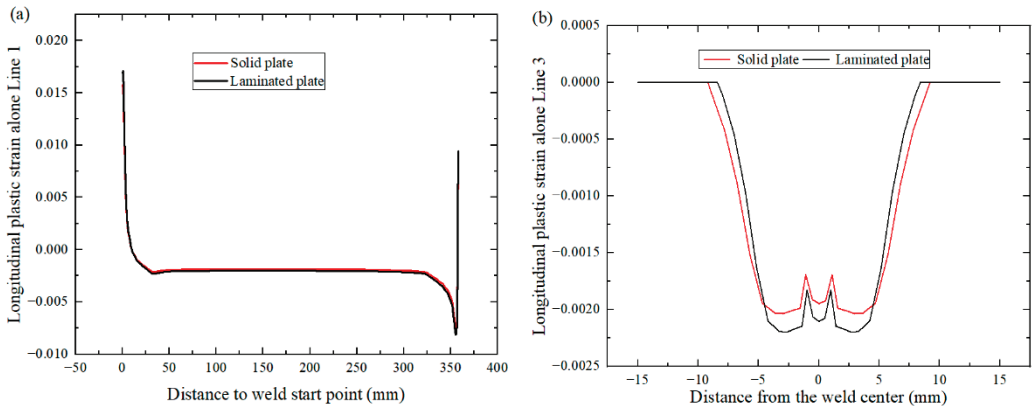


Figure 15. Longitudinal plastic strain distributions of the solid and laminated plates: (**a**) along Line 1; (**b**) along Line 3.

Figure 15a presents the post-weld longitudinal plastic strain extracted along Line 1. The laminated and solid plates exhibit similar overall trends. A pronounced positive peak appears near the weld start, followed by a rapid drop into a relatively stable plateau region; another abrupt variation occurs close to the weld termination. These end effects

are consistent with the transient thermal boundary at the weld start/stop, where the local thermal cycle (and thus thermal expansion–contraction mismatch) differs from that in the steady-travel segment. Within the plateau region, the laminated plate shows slightly larger absolute longitudinal plastic strain than the solid plate.

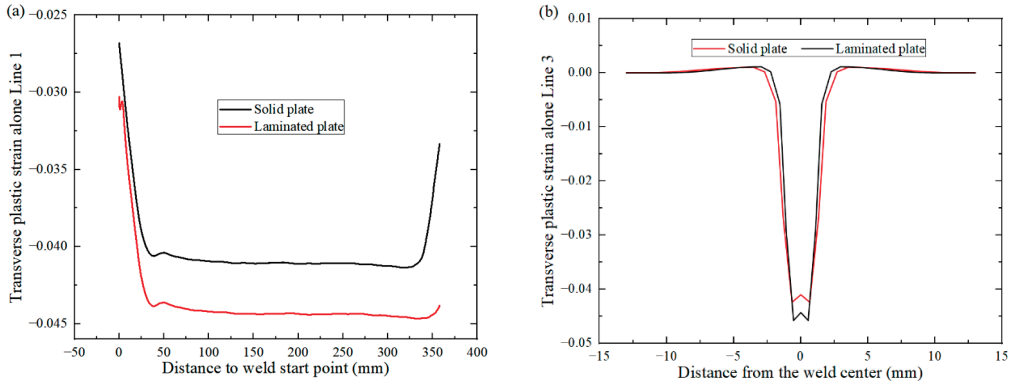


Figure 16. Transverse plastic strain distributions of the solid and laminated plates: (**a**) along Line 1; (**b**) along Line 3.

Figure 15b shows the local longitudinal plastic-strain distribution along Line 3 with the weld center as the origin. The plastic strain is strongly localized around the weld center and decays rapidly with distance, approaching zero beyond approximately 10 mm from the centerline. The narrow affected region reflects the highly concentrated laser heat input and the resulting steep temperature gradients. Although the curve shapes for the two plates are similar, differences appear in the depth of the concave region and in the local details near the weld center. The laminated plate exhibits larger absolute plastic-strain values, while the affected zone is relatively narrower, indicating a more localized longitudinal plastic response under the non-uniform stiffness condition.

Figure 16a presents the transverse plastic-strain distribution along Line 1. Both the laminated and solid plates show rapid variations near the weld start and termination, followed by a relatively stable plateau over the long central segment. This start/stop behavior is consistent with the non-steady thermal boundary at the beginning and end of welding, where the transient heat input and heat dissipation conditions differ from those in the steady-travel region. In the plateau region, the laminated plate exhibits larger absolute transverse plastic-strain values than the solid plate.

Figure 16b shows the local transverse plastic-strain distribution along Line 3 with the weld center as the origin. A sharp negative valley appears near the weld center, and the strain rapidly recovers toward zero away from the weld, becoming negligible beyond approximately 12 mm from the centerline. The strong localization reflects the highly concentrated laser heat input and the resulting steep temperature gradients. Although the overall curve shapes of the two plates are similar, differences are evident in the valley depth and local curvature near the weld center. The laminated plate develops a larger peak magnitude of transverse plastic strain, while the affected zone is relatively narrower.

Overall, the transverse plastic strain is significantly larger than the longitudinal component, consistent with the different restraint levels in the transverse and longitudinal directions during welding. By comparing Figures 15 and 16, it is evident that the laminated and solid plates share broadly similar spatial patterns of plastic strain, whereas clear differences exist in magnitude and effective distribution width. The laminated plate generally exhibits larger plastic-strain magnitudes within a narrower affected region. Under an identical thermal loading baseline (same heat-source parameters and heat-transfer boundary conditions), these differences can be attributed to the stiffness-dependent restraint

https://doi.org/10.3390/en19061536

redistribution, which modifies how the heat-transfer-driven thermal strains are constrained and hence alters the evolution and spatial distribution of plastic strain.

4.4. Plastic Strain Evolution During Thermo-Mechanical Coupling

To further clarify the roles of heat transfer and structural stiffness in governing plastic strain evolution, the temperature-dependent evolution paths of plastic strain during a representative thermal cycle were extracted, as shown in Figure 17.

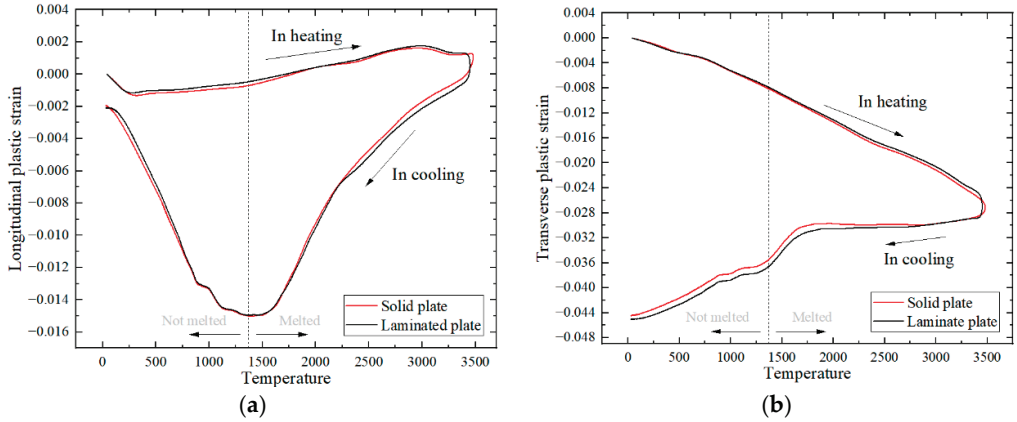


Figure 17. Evolution of plastic strain with temperature during a representative thermal cycle: (**a**) longitudinal plastic strain; (**b**) transverse plastic strain.

Figure 17 presents the plastic strain–temperature evolution for the solid and laminated plates during a representative thermal cycle. The arrows indicate the heating and cooling stages. The vertical dashed line denotes the melting boundary temperature (1370 °C), separating the non-melted and melted regimes.

Figure 17a shows the evolution of longitudinal plastic strain. During heating, the longitudinal plastic strain is slightly negative at low temperatures and increases gradually with temperature, becoming positive at elevated temperatures. During cooling, the minimum longitudinal plastic strain appears near the melting boundary temperature; as temperature decreases further, the strain partially recovers and approaches a small negative value at room temperature. The laminated and solid plates exhibit similar trajectories, while the laminated plate maintains slightly higher strain levels throughout the cycle.

Figure 17b illustrates the transverse plastic-strain evolution. During heating, the transverse plastic strain increases monotonically with temperature. During cooling, it continues to increase and reaches its maximum magnitude after complete cooling. The transverse component is markedly larger than the longitudinal one, and no sign reversal or apparent recovery is observed.

These directional differences arise from the distinct constraint paths under a highly localized welding thermal cycle. Along the longitudinal direction, each material point undergoes a sequential heating–cooling history as the moving heat source passes, and the shrinkage of previously heated regions imposes tensile effects on the subsequently heated material, enabling partial redistribution and recovery of longitudinal plastic strain during cooling. In contrast, the transverse direction is predominantly constrained by the adjacent unmelted material on both sides of the weld, and the lateral restraint under steep temperature gradients promotes the accumulation of compressive plastic strain. In addition, welding-induced angular distortion modifies the transverse constraint state during cooling, further intensifying transverse plastic-strain accumulation and leading to larger transverse magnitudes.

https://doi.org/10.3390/en19061536

4.5. Influence of Structural Stiffness on the Thermo-Mechanical Process

To provide a more quantitative interpretation of the plastic strain evolution described above, a stiffness–bar–spring model was developed, as illustrated in Figure 18. The model is intended to describe the evolution of longitudinal plastic strain during heating by representing the restraint effect of the surrounding base material with an equivalent spring.

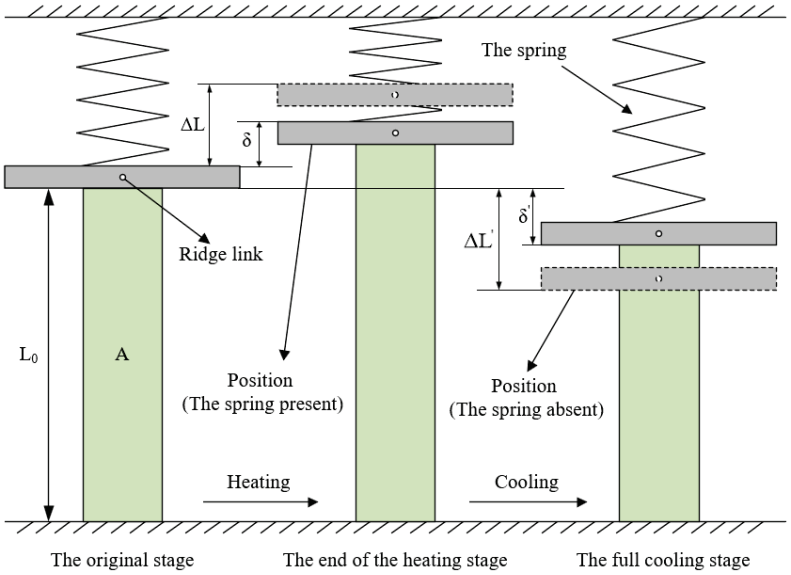


Figure 18. Schematic illustration of the proposed stiffness–bar–spring model.

In the proposed stiffness–bar–spring model, the two ends of the bar are assumed to be rigidly connected through an end link, which enforces displacement compatibility. The material is assumed to be temperature-independent for analytical simplicity, and an elastic–perfectly plastic constitutive law is adopted, such that the stress remains constant once the yield strength is reached. Owing to the sufficiently large longitudinal restraint, the bar ends are further assumed to remain horizontal during deformation. The coefficients of thermal expansion, yield strength, and elastic modulus are denoted by α, σ_s, and E, respectively. The stiffness of the equivalent spring is denoted by K.

As illustrated in Figure 18, during the heating stage, if no spring restraint is present, the free thermal elongation of the bar is

$$\Delta L = L_0 \alpha \Delta T \tag{8}$$

where L_0 is the initial length of the bar, α is the coefficient of thermal expansion, and ΔT is the temperature increment.

When the spring restraint is introduced, force equilibrium must be satisfied between the bar and the spring. The spring force equals the internal axial force in the bar, leading to:

$$\delta K = \frac{(\Delta L - \delta)EA}{L_0 + \Delta L} \approx \frac{(\Delta L - \delta)EA}{L_0} \tag{9}$$

where K is the stiffness of the equivalent spring, E is the elastic modulus, A is the cross-sectional area of the bar, and δ is the restrained displacement induced by the spring.

Solving for δ, the restrained displacement is obtained as

$$\delta = \frac{EAL_0 \alpha \Delta T}{KL_0 + EA} \tag{10}$$

https://doi.org/10.3390/en19061536

The compressive strain in the bar under restrained thermal expansion is:

$$\varepsilon = \frac{\Delta L - \delta}{L_0} \tag{11}$$

When the temperature increase is sufficiently large such that yielding occurs in the bar, the compressive strain reaches the yield strain. Therefore,

$$\varepsilon = \frac{\Delta L - \delta}{L_0} = \frac{\alpha \Delta T K L_0}{K L_0 + EA} = \varepsilon_s \tag{12}$$

from which the temperature rise required to initiate yielding is obtained as

$$\Delta T_Y = \frac{\varepsilon_s (K L_0 + EA)}{\alpha K L_0} \tag{13}$$

Equation (13) indicates that as the stiffness K increases, the required temperature increment for yielding decreases. In other words, stronger restraint promotes earlier yielding. This explains why the solid plate, which exhibits higher effective stiffness, develops a wider plastic zone, consistent with the differences observed in Figures 15 and 16.

Compared with the solid plate, the laminated plate contains numerous non-uniformly distributed internal channels, which reduce its overall structural stiffness and consequently lower its resistance to deformation. In the model shown in Figure 18, this stiffness reduction is reflected by a decrease in the equivalent external restraint parameter K. During the analysis, both the laminated plate and the solid plate were subjected to the same thermal input and surface heat-flux distribution. According to Equation (13), a smaller K leads to a higher critical temperature for yielding during the thermal expansion stage. In other words, weaker restraint delays yielding and tends to confine plastic deformation to a narrower region, whereas stronger restraint promotes yielding over a wider zone. This explains why the plastic strain in the laminated plate is more concentrated near the weld seam, as shown in Figures 15b and 16a.

After complete cooling, the stress in the weld region is assumed to approach the yield level. From force equilibrium:

$$\delta' K = \varepsilon_Y EA \tag{14}$$

The corresponding elastic recovery of the bar is

$$\varepsilon_Y L_0 \tag{15}$$

The residual compressive plastic strain is therefore expressed as:

$$\varepsilon' = \frac{\varepsilon_Y EA}{K} - \varepsilon_Y L_0 \tag{16}$$

Equation (16) shows that the peak residual compressive plastic strain decreases with increasing stiffness K. Since the solid plate has a larger effective stiffness than the laminated plate, its final compressive plastic strain remains lower. This theoretical prediction is consistent with the evolution results shown in Figure 17. Overall, the proposed model successfully captures the relationship between welding-induced plastic strain and external stiffness, and qualitatively clarifies how the external stiffness parameter K influences the magnitude of plastic strain. It therefore provides a useful mechanistic interpretation and reference for understanding the evolution of plastic strain during the thermo-mechanical process.

https://doi.org/10.3390/en19061536

5. Conclusions

1. A coupled thermo-mechanical FE model with a composite Gaussian surface–volumetric moving heat source was developed and validated using near-weld thermal cycles and fusion geometry.
2. Under identical laser welding parameters, laminated and solid plates exhibit similar residual-stress distributions, suggesting residual stress is governed primarily by the local weld thermal gradient.
3. In contrast to residual stress, the laminated plate shows larger angular/bending distortion, highlighting the effect of spatially non-uniform stiffness on restraint redistribution and deformation.
4. Plastic-strain distributions are similar in pattern but differ in magnitude and localization: the laminated plate develops higher peak plastic strain within a narrower zone, dominated by transverse plastic strain.
5. An equivalent restraint–stiffness spring model links stiffness to yielding and plastic-zone characteristics, providing a mechanistic basis for distortion prediction and stiffness-informed control of welded laminated cooling plates.

Author Contributions: Conceptualization, C.L.; Methodology, Z.D.; Software, Y.C., H.W., Z.Z., F.H., X.Z. and C.W.; Validation, C.L., Y.C., H.W., Z.Z., F.H., X.Z. and C.W.; Data curation, C.L.; Writing—original draft, C.L.; Writing—review & editing, Z.D.; Supervision, Z.D.; Funding acquisition, Z.D. All authors have read and agreed to the published version of the manuscript.

Funding: This work is supported by Heilongjiang Chunyan Innovation Team Program (CYCX24008).

Data Availability Statement: The original contributions presented in this study are included in the article. Further inquiries can be directed to the corresponding author.

Conflicts of Interest: The authors declare that they have no known competing financial interests or personal relationships that could have appeared to influence the work reported in this paper.

References

1. Horajski, D.; Cieślik, J.; Cieślik, M. Advanced Structural and Technological Method of Reducing Distortion in Thin-Walled Welded Structures. *Materials* **2021**, *14*, 504. [CrossRef] [PubMed]
2. Qiu, Y.; Yan, R.; Wang, N.; Shen, W.; Xu, S.; Li, M.; Qin, K. Stress Amplification Effect and Fatigue Strength Evaluation of Marine Thin Plate Welded Structure Considering Welding Deformation: Theoretical and Experimental Analysis. *Thin-Walled Struct.* **2023**, *188*, 110871. [CrossRef]
3. Ruíz, H.; Sanchez, A. Influence of the Plate Dimensions of a Fillet Weld Joint on Angular Deformation and Residual Stresses. *Pol. Marit. Res.* **2025**, *32*, 124–131. [CrossRef]
4. He, Y.; Yang, Z.; Yang, D.; Duan, R.; Xu, J.; Wang, W.; Shi, M.; Xu, G.; Chen, S. Numerical Simulation of Local Cooling on Residual Stress and Deformation of Welded Joints of Unequal Thickness Plates. *J. Mater. Res. Technol.* **2025**, *36*, 8410–8420. [CrossRef]
5. Liu, Y.; Ma, N.; Lu, F.; Fang, H. Measurement and Analysis of Welding Deformation in Arc Welded Lap Joints of Thin Steel Sheets with Different Material Properties. *J. Manuf. Process.* **2020**, *61*, 507–517. [CrossRef]
6. Mao, Z.; Zhou, C.; Wang, C.; Li, Y.; Huang, Z.; Deng, D. Investigation on Residual Stress and Welding Deformation in a Ultra-High-Strength Quenched Steel Thin-Plate Butt Joint. *China Weld.* **2026**, *35*, 100032. [CrossRef]
7. Wang, J.; Ma, N.; Deng, D. Progress in Welding Distortion Prediction and Control Technology for Advanced Manufacturing. *J. Manuf. Process.* **2025**, *152*, 1012–1036. [CrossRef]
8. Liang, X.; Chen, Y.; Cheng, L.; Yang, Q.; To, A. A Modified Inherent Strain Method for Fast Prediction of Residual Deformation in Additive Manufacturing of Metal Parts. In Proceedings of the 2017 Solid Freeform Fabrication Symposium, Austin, TX, USA, 7–9 August 2017.
9. Chino, T.; Kunugi, A.; Kawashima, T.; Watanabe, G.; Can, C.; Ma, N. Fast Prediction for Resistance Spot Welding Deformation Using Inherent Strain Method and Nugget Model. *Materials* **2021**, *14*, 7180. [CrossRef] [PubMed]

10. Ma, N.; Nakacho, K.; Ohta, T.; Ogawa, N.; Maekawa, A.; Huang, H.; Murakawa, H. Inherent Strain Method for Residual Stress Measurement and Welding Distortion Prediction. In *Proceedings of the ASME 2016 35th International Conference on Ocean, Offshore and Arctic Engineering*; American Society of Mechanical Engineers: New York, NY, USA, 2016; Volume 50008, p. V009T13A001. [CrossRef]
11. Lee, C.H.; Perrera, D.; Chung, H. Welding Deformation Analysis by Inherent Strain Method Based on Layered Shell Element. *J. Mar. Sci. Eng.* **2021**, *9*, 632. [CrossRef]
12. Yu, L.; Deng, D.; Xie, L.; Murakawa, H. Prediction of deformation for large welded structure based on inherent strain. In Proceedings of the International Institute of Welding (IIW), Osaka, Japan, 11–16 July 2004.
13. Wang, L.; Miao, Y.; Hu, G.; Zhao, Y.; Deng, Q. Numerical Simulations and Experimental Verification of T-Structure Welding Deformation Using the Step-by-Step Loading Inherent Strain Method. *Metals* **2023**, *13*, 1312. [CrossRef]
14. Muránsky, O.; Hamelin, C.J.; Patel, V.I.; Luzin, V.; Braham, C. The Influence of Constitutive Plasticity Models on Accumulated Plastic Strains in Finite Element Weld Analyses. *Int. J. Solids Struct.* **2015**, *66–67*, 518–530. [CrossRef]
15. Han, Y. Multiphysics Study of Thermal Profiles and Residual Stress in Welding. *Materials* **2024**, *17*, 886. [CrossRef] [PubMed]
16. Park, J.; An, G.; Ma, N.; Kim, S. Effect of Transverse Restraint on Welding Residual Stress in V-Groove Butt Welding. *Metals* **2022**, *12*, 654. [CrossRef]
17. Chen, L.; Wang, T.; Pan, J.; Ma, N.; Wang, R. Welding Residual Stress Distribution of U-Rib Stiffened Plates of Steel Box Girders and Its Influence on Structural Natural Frequencies. *Front. Mater.* **2022**, *9*, 876111. [CrossRef]
18. Xu, F.; Zhao, Y.; Chen, J. Experimental and Numerical Investigation on Residual Stress and Deformation of Welded I-Section Curved Steel Beams. *Thin-Walled Struct.* **2024**, *199*, 111821. [CrossRef]
19. Chen, Z.; Chen, X.; Yang, X.; Yu, B.; Wang, B.; Zhu, J.; Chen, Y.; Cai, W. Numerical Study on Cooling Characteristics of Turbine Blade Based on Laminated Cooling Configuration with Clapboards. *Energy* **2024**, *299*, 131372. [CrossRef]
20. Li, H.; Xie, F.; Zhuang, Y.; Wang, Y.; Yan, Y.; Xu, G.; Cui, J. Numerical Investigation of Cooling Performance of 3D-Printable Cooling Structure for Aero-Engine Combustor. *Appl. Therm. Eng.* **2024**, *238*, 122196. [CrossRef]
21. Liu, C.; Luo, Z.; He, Y.; Huang, S.; Tuo, J.; Ding, H. Numerical simulation of welding residual stresses in 6082-T6 thin aluminum alloy. *Measurement* **2024**, *234*, 114800. [CrossRef]
22. Służalec, A. *Theory of Thermomechanical Processes in Welding*; Springer: Dordrecht, The Netherlands, 2005. [CrossRef]
23. Wu, C.; Kim, J.-W. Numerical prediction of deformation in thin-plate welded joints using equivalent thermal strain method. *Thin-Walled Struct.* **2020**, *157*, 107033. [CrossRef]
24. Wang, S.; Shi, G.; Zhao, L.; Dai, Y.; Hou, T.; He, Y.; Chen, P.; Qin, F. Modelling and Optimization of Continual Laser Joining Processes for Silicon Aluminum Alloy in Microwave Devices. *Crystals* **2023**, *13*, 631. [CrossRef]
25. Li, C.K.; Dong, Z.B.; Wang, H.; Han, F.; Teng, J.F.; Lü, Y.L. Research on Service Life Prediction of Closely Spaced Array Hole Column Laminated Cooling Structure. *Trans. China Weld. Inst.* **2022**, *43*, 101–106. [CrossRef]
26. *GB/T 14992-2025*; Superalloys and Intermetallic Compounds—Designation and Chemical Composition. China Iron & Steel Association: Beijing China, 2025.
27. Alghamdi, A.; Saleh, M. Finite Element Simulation of the Effect of Phase and Thermal Boundary Conditions on Temperature Distribution and Residual Stress. *Crystals* **2022**, *12*, 1422. [CrossRef]
28. Bannour, S.; Abderrazak, K.; Mhiri, H.; Palec, G.L. Effects of Temperature-Dependent Material Properties and Shielding Gas on Molten Pool Formation During Continuous Laser Welding of AZ91 Magnesium Alloy. *Opt. Laser Technol.* **2012**, *44*, 2459–2468. [CrossRef]
29. Chiumenti, M.; Cervera, M.; Salmi, A.; Agelet de Saracibar, C.; Dialami, D.; Matsui, K. Finite Element Modeling of Multi-Pass Welding and Shaped Metal Deposition Processes. *Comput. Methods Appl. Mech. Eng.* **2010**, *199*, 2343–2359. [CrossRef]
30. Liu, Y.; Yu, Y.; Wang, P.; Fang, H.; Ma, N. Analysis and Mitigation of the Bending Deformation in Girth-Welded Slender Pipes with Numerical Modelling and Experimental Measurement. *J. Manuf. Process.* **2022**, *78*, 278–287. [CrossRef]
31. Zubairuddin, M.; Vasudevan, M.; Das, P.K.; Alam, M.M.; Kumar, K.S.; Prabhakar, S. FEM Based Thermal and Mechanical Analysis of Comparative Study of TIG and A-TIG Welding on P91 Steel. *Sci. Rep.* **2025**, *15*, 10271. [CrossRef] [PubMed]

Disclaimer/Publisher's Note: The statements, opinions and data contained in all publications are solely those of the individual author(s) and contributor(s) and not of MDPI and/or the editor(s). MDPI and/or the editor(s) disclaim responsibility for any injury to people or property resulting from any ideas, methods, instructions or products referred to in the content.

energies

MDPI

Article

Evaluation of the Intensity of Heat and Mass Transfer Processes in Cavitation Environments

Anatoliy Pavlenko

Department of Building Physics and Renewable Energy, Kielce University of Technology, Aleja Tysiąclecia Państwa Polskiego, 7, 25-314 Kielce, Poland; apavlenko@tu.kielce.pl

Abstract

This study investigates the impact of cavitation phenomena on heat and mass transfer in working fluids. To quantify the intensity of transport processes within cavitation bubble clusters, a numerical analysis of bubble dynamics was carried out with explicit consideration of fluid compressibility. The results demonstrate that physicochemical transformations induced by cavitation are governed not only by shock waves and pressure pulses generated during bubble collapse, but also by extreme thermal effects arising within collapsing cavitation clouds. Under conditions of maximum bubble compression, the vapor inside the bubbles and the surrounding liquid may undergo a transition to a supercritical state. The developed model elucidates the structure of microflows in the interbubble region and provides a quantitative evaluation of local velocity, pressure, and heat flux fields. The systematic assessment of cavitation-enhanced heat and mass transfer offers valuable insights for the advancement of conventional heat and mass transfer technologies and the design of innovative devices in mechanical and chemical engineering.

Keywords: cavitation bubble; impact pressure; bubble dynamics; bubble model; mass transfer; phase transitions

1. Introduction

Cavitation phenomena have long attracted considerable scientific interest owing to the unique effects associated with the collapse of bubble clusters, including the generation of extreme temperature fields and intense pressure fluctuations in the surrounding fluid. During bubble oscillations, heat and mass exchange occur across the bubble–liquid interface, while heat transfer in the bulk liquid may be substantially enhanced, for example, through an increase in the critical heat flux and overall heat transfer intensity [1]. A variety of cavitation-based mechanisms for heat transfer enhancement in liquids have been proposed and investigated [2,3].

Despite these advances, the influence of cavitation on heat and mass transfer remains highly complex, involving multiple interacting mechanisms that are difficult to generalize across different flow regimes and applications. Consequently, a detailed analysis of cavitation cluster dynamics and the conditions governing the onset and development of cavitation effects is essential for a fundamental understanding of cavitation-enhanced transport processes.

In the early stages of cavitation research, efforts were focused primarily on its destructive effects. Subsequently, however, researchers began to explore and exploit its unique properties. Hydrodynamic cavitation is associated with the formation and collapse of cavitation bubbles caused by pressure pulsations, leading to the creation of localized regions

of extremely high temperature and pressure. These effects can be successfully utilized in various applications, such as water purification, biomass conversion and pretreatment, and substance extraction [4].

Both acoustic and hydrodynamic cavitation enhance anaerobic digestion and fermentation processes, thereby increasing biogas production [5]. In addition to large-scale industrial applications, cavitation is also employed in smaller-scale technical processes, including homogenization, emulsification, and extraction [6,7]. Ultrasonic treatment is widely used in mineral flotation due to its ease of operation, absence of secondary pollutant formation, and high level of safety [8].

The technical applications of cavitation effects are diverse, and hydrodynamic cavitation is considered a promising technology for process intensification owing to its high energy efficiency and ability to induce chemical reactions [9]. Cavitation occurs through several stages; during bubble compression, extremely high temperatures and pressures are generated within the liquid, resulting in localized heating of the surrounding medium.

In oil and gas production technologies, gas hydrates may form under conditions of high pressure and low temperature. If the temperature remains above a critical value due to cavitation effects, gas hydrate formation can be inhibited [10,11]. As cavitation technologies continue to gain widespread application, the development of cavitation generators is also progressing rapidly [12,13]. Therefore, detailed investigation and a deeper understanding of the physical processes of cavitation—particularly those occurring within cavitation clusters—are essential for further advancement in this field of research.

In this work, we consider the patterns of bubble behaviour within a cluster, taking into account the mutual influence of the effects accompanying the cavitation development process. Regardless of whether a dynamic effect at a local point in the fluid is a consequence of the collective influence of a large number of bubbles or is solely caused by the action of a single bubble (for example, the formation of a cumulative microjet or the emission of a spherical shock wave by a collapsing bubble), all bubbles participate directly or indirectly in its creation. The difference between the behaviour of a single bubble within a bubble cloud and the behaviour of an isolated bubble in an infinite volume of liquid is primarily due to the influence of its nearest neighbours on the bubble's evolution. As they develop, these neighbours create their own pressure field in the vicinity of the bubble, which differs from the external pressure currently acting on the system. Therefore, the behaviour of an individual bubble within a cluster under variation of the external pressure is more complex than that represented in the single-bubble dynamics model.

Compared to the large volume of work dedicated to the study of single bubble dynamics, publications related to the study of the collective behaviour of bubbles and the evolution of an individual bubble within a dynamically developing ensemble are less prevalent. These studies can be broadly divided into three main groups.

The first group focuses on phenomena related to the dynamic effects of bubbles, for example, [14,15]. The authors show that hydrostatic pressure is the dominant factor in controlling cavitation activity, but due to the inertia of the cavitation cluster, dynamic effects are difficult to predict for clustered bubbles. A cavitation system possesses a specific bubble density, which can be manipulated by changing the hydrostatic pressure to enhance dynamic effects. This could serve as a promising approach for developing technologies, such as material synthesis or processing [16,17].

The core idea of the second group of studies focuses on the fact that bubbles can accumulate into clusters and thereby intensify the cavitation effect. However, many authors point to the ambiguity of such effects [18,19]. The behaviour of bubbles in clusters differs significantly from the dynamics of single bubbles. Their dynamics are mutually influenced

https://doi.org/10.3390/en19051120

by neighboring bubbles, leading to attraction or repulsion. These effects can be explained by the presence of the secondary Bjerknes force.

Some authors [20,21] indicate that the radial oscillations of a cavitation bubble are suppressed by larger neighbors when they are in close proximity, and the magnitude and direction of the secondary Bjerknes force change, leading to a transition between mutual attraction and repulsion of the bubbles. Authors in [22] assert that the suppression of bubble pulsations increases with increasing bubble density. If the bubble density exceeds a critical value, a repulsive region emerges, preventing their coalescence. For example, at a pressure of 3 MPa and a bubble density up to 1×10^{13} m^{-3}, distinct zones of attraction appear, and as the hydrostatic pressure increases, the attraction zone gradually expands towards a higher density region. In fact, increasing hydrostatic pressure can increase the stable bubble density of the cluster, which will intensify the cavitation effect. It can be argued that while there are numerous publications devoted to experimental studies of single bubbles [23,24], there are significantly fewer studies on the mutual influence of double bubbles [25,26], and very few experimental reports focus on clusters, which constitute the third approach to research. Furthermore, the question of what causes the dynamic effect—whether it is the cumulative effect of the cluster or the influence of individual bubbles surrounding the cluster—remains unexplained. Modelling of dynamic effects [27–29] is more widely applied. Among the approaches presented in publications for describing cavitation processes, several well-established types of models can be distinguished.

1. Multiscale models [30–33].

This approach can describe a compressible multiscale cavitation region where the dynamics of large vapour cavities and microbubbles are modeled, taking into account the average compressibility. The cavitation cluster is treated as a liquid–vapor mixture continuum in the Eulerian sense. These models are developed by coupling an Eulerian medium and functional dependencies, expressed in terms of velocities and radii, which are tracked in the Lagrangian sense using various approaches. For a stable transition between the Eulerian and Lagrangian frameworks, the transition criterion can be defined based on a parameter that accounts for the non-uniformity of the domain discretization. In hybrid models, the onset of cavitation is first estimated in low-pressure regions, which limits predictions using Eulerian mass transfer models.

2. Models relating fluid characteristics to thermodynamic parameters [34–37].

This method, based on equations of state that link fluid characteristics to thermodynamic parameters, is limited only to very specific problems unrelated to either bubble growth dynamics or the dynamic effects of cavitation. In general, these models represent a simplified representation of real processes and are usually solved for an averaged substance whose properties reflect the weighted average of the volume fraction of the two media. Another approach involves modelling cavitation using real gas polynomial equations of state to accurately predict the properties of water in any state. Modelling complex dynamic effects relies on numerical methods which, although accurate, require significant computational resources and databases, and are not applicable for rapid prediction in practical scenarios.

3. Phase boundary modelling [38,39].

4. Modelling using transport equations [40–43].

Such models accurately predict the dynamics of the bubble cloud in the initial stage by considering bubble interaction. However, in the final stage, the inertia effect, represented as a second-order derivative, plays a more significant role and shows a higher collapse speed.

5. Predicting bubble dynamics using the Rayleigh–Plesset equation [44–46].

The Rayleigh–Plesset equation accurately describes bubble oscillations in incompressible liquids but neglects energy losses due to acoustic frequencies, as it was based on

incompressible fluids. Therefore, this equation becomes inapplicable in cases where energy loss cannot be neglected. Nevertheless, this approach to describing cavitation processes is fundamental in the development of cavitation modelling, including the description of bubble cluster dynamics.

Still, the idea of modelling the impulse of a bubble cluster has not received significant attention in the literature, despite the fact that the mathematical interpretation of cavitation phenomena may be highly attractive for a large number of problematic cases. A critical question remains unanswered by existing models: how do neighbouring bubbles affect the dynamic effects within a cluster?

The principles of the theoretical approach to solving this problem are outlined in various works, e.g., in [47–49]. One simplified approach to modelling cavitation clusters involves describing the dynamics of an aggregate of bubbles using the cell model approximation, which allows the evolution of a monodisperse ensemble to be linked to the behaviour of a single bubble. Despite the small number of publications, the available information on the results of experimental and theoretical studies indicates the complexity and extraordinary nature of the processes being studied. These models are based on the fundamental assumption that at all stages of cloud evolution, the bubble sizes are much smaller than the distance between the nearest neighbors.

The results of theoretical calculations of pressure fields and flow velocities, even for two interacting bubbles, show poor agreement with experiments [50,51]. According to researchers, this is explained by the fact that the bubble dynamics equations are derived with the assumption of potential flow in its vicinity, although the real velocity field is neither symmetrical nor potential. Accounting for all the features of bubble cluster dynamics will likely remain an unresolved problem, but the development of simplified methods for assessing the behaviour of a cavitation cloud is a promising task.

2. Bubble Dynamics Within a Cluster Using the Cell Model Approximation

Without detailing the complex spatial configurations of velocity and pressure fields within the inter-bubble regions of a dynamically evolving cluster, the general nature of the fluid flow can be conceptualized as follows. As the bubbles expand or contract within an elementary volume of the two-phase system, an unsteady liquid flow is induced in the space between the bubbles. Relative to any given point within this volume, the liquid flow exhibits inherent asymmetry, consequently leading to a non-symmetrical pressure field. This scenario is further complicated by the continuous temporal changes in the distribution of bubble sizes and their mutual distances throughout the volume. The microflows observed in the inter-bubble space are fundamentally vortical, which causes additional localized pulsations in the fluid's velocity and pressure. When the amplitude and frequency of these pulsations are sufficiently large, a specific collective effect emerges, whereby the bubble cloud intensifies hydromechanical and heat and mass transfer processes.

The intricate pressure distribution surrounding each bubble complicates the analytical description of its dynamics. Under these conditions, the fundamental assumption of spherical symmetry for the velocity and pressure fields in the bubble's vicinity becomes inaccurate, necessitating the inclusion of higher-order effects. In contrast to a single, isolated bubble, where developing reliable and consistent models presents no significant challenges, describing the behaviour of an individual bubble within a cloud, and the cluster as a whole, is fraught with difficulties of a fundamental nature.

In the review section of this article, attention is drawn to the dependence of bubble behaviour on their concentration. The use of cell models reflects this dependency by adopting two distinct approaches: one for dilute systems [52,53] and another for concentrated clusters [54,55].

https://doi.org/10.3390/en19051120

These foundational principles of the cell model enable the utilization of established single-bubble dynamics equations as a first approximation for calculating the averaged ensemble parameters. Subsequent calculation steps then involve sequentially incorporating higher-order effects. Crucially, when a bubble is surrounded by other growing bubbles, the pressure fields generated by its nearest neighbours mutually overlap. Consequently, the character of the pressure distribution in the vicinity of each bubble, $p_b = f(r)$, deviates significantly from the distribution described by the widely recognized single-bubble equations [56,57].

$$p_b(\Delta, \tau) = p_f + \left[p_b - p_f + \frac{1}{2} \cdot \rho_b \cdot u_R^2 \cdot \left(1 - \frac{R^3}{r^3} \right) - \frac{2\sigma}{R} - \frac{4\mu \cdot u_R}{R} \right] \cdot \frac{R}{r} \tag{1}$$

where Δ is the distance between the bubbles.

The dynamic evolution of each bubble is therefore not governed by the external pressure p_f, acting on the cluster as a whole, but rather by an average pressure within the inter-bubble space, denoted as p_b, which is characteristically greater than the external pressure $p_b > p_f$. In the approximation utilized by the cell model, the external boundary condition for the pressure of an individual bubble should be applied not at infinity, but at a distance corresponding to the average spacing between adjacent bubbles—specifically, at the radius of the spherical cell within which the bubble is centrally located (Figure 1).

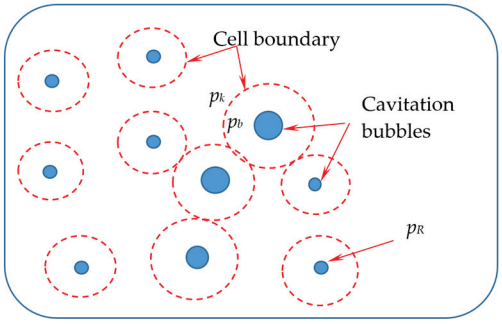


Figure 1. Computational scheme.

Analysing the available literature, the fundamental principles of the cell model, as applied to the dynamics of vapour bubbles within a cluster, can be summarized. If the volumetric vapour content (void fraction) of the two-phase bubble medium, $\gamma(\tau)$, and the mean bubble radius, R(τ), are known, then the volume allocated per bubble is given by $4/3\pi R^3\gamma(\tau)$. This volume can be conceptually treated as an elementary spherical cell containing a single bubble at its center. The outer radius of this cell, Ψ, is defined as $\Psi = R/\gamma^{0.3}$, and the thickness of the liquid layer within the cell is $\Psi = R + R(1 - \gamma^{0.3})/\gamma^{0.3}$. It is postulated that the liquid motion within the boundaries of the cell, induced by the expansion or compression of the central bubble, is strictly radial. Crucially, there is no mass exchange across the external boundary of the cell with the rest of the cluster. Consequently, the mass of the substance contained within the cell is conserved (remains constant). Within the framework of the cell model, it is further postulated that the following conditions are satisfied at the outer boundary:

$$\left.\frac{dm}{dr}\right|_{r=\psi} = 0; \quad \left.\frac{dT}{dr}\right|_{r=\psi} = 0. \tag{2}$$

This condition facilitates the incorporation of temperature variations within the cell's liquid due to heat and mass transfer with the central bubble. The temperature at the external surface of the cell only begins to change once the thickness of the thermal layer surrounding the bubble, $\theta(\tau)$, exceeds the radius of the cell [49].

https://doi.org/10.3390/en19051120

The behaviour of each bubble is treated as that of an isolated single bubble confined within the volume of a closed cell. As the cell expands or contracts, it undergoes a force interaction with the surrounding portion of the two-phase system, which dictates the pressure exerted on the cell's external surface. This pressure, $p(\Psi) = p_k$, is then employed as the external boundary condition during the derivation of the equation governing the fluid motion within the cell. The resulting pressure distribution in the liquid within the confines of the cell, according to the Lagrange–Cauchy integral [58], is given by the expression:

$$p(\theta) = p_k - \rho_f \cdot \left(\frac{\partial \varphi}{\partial \tau} - \frac{\partial \varphi}{\partial \tau}\bigg|_{r=\psi} + \frac{u^2}{2} - \frac{u^2}{2}\bigg|_{r=\psi} \right). \tag{3}$$

By applying the boundary condition for the pressure at the bubble interface, $p(R) = p_R$, and subsequently defining the parameter values on the right-hand side of Equation (3) using the following formulas:

$$u(r) = \frac{u_R R^2}{r^2}; \quad \varphi(r) = -\frac{u_R R^2}{r}; \quad \frac{\partial \varphi}{\partial \tau} = -\frac{1}{r}\left(\frac{du_R}{d\tau} \cdot R^2 + 2R \cdot u_R \cdot \frac{dR}{d\tau} \right). \tag{4}$$

Consequently, by applying the condition for pressure at $r = R$ (the bubble interface) and at r = Ψ (the cell boundary), we derive the equation for the radial motion of the fluid within the cell:

$$\frac{du_R}{d\tau} = \frac{p_R - p_k - 0.5\rho_b u_R^2 \left(3 - 4\gamma^{0.3} + \gamma^{1.3}\right)}{\rho_f R(1 - \gamma^{0.3})}. \tag{5}$$

This resulting equation differs significantly from the standard equation of motion developed for a single bubble in an infinite liquid volume [49], due to the inclusion of the cell boundary effects.

$$\frac{du_R}{d\tau} = \frac{p_R - p_f - 1.5\rho_b \cdot u_R^2}{\rho_b \cdot R} \tag{6}$$

This difference stems from two main factors: the presence of correction terms on the right-hand side of Equation (5) that account for the non-negligible volume occupied by the bubbles, and the replacement of the external pressure p_f with the currently unknown pressure at the cell boundary, p_k. As the vapor volume fraction $\gamma \to 0$, the cell radius Ψ tends towards infinity $\Psi \to \infty$, and the pressure at the cell's outer boundary p_k converges to the external pressure $p_k \to p_f$. Consequently, Equation (5) simplifies to Equation (6) under dilute conditions. It is worth noting that for the initial growth stages of small bubbles or the final collapse phase, γ is small, rendering the correction terms in Equation (5) of secondary importance. However, the cell model approximation becomes inherently flawed for comparatively high values of the two-phase system's vapour content ($\gamma > 0.5$).

The principal distinction between Equations (5) and (6) lies in their boundary conditions: the behaviour of the isolated bubble in Equation (6) is determined by the known externally applied pressure p_f. Conversely, the behaviour of a bubble surrounded by others is dependent on the pressure $p_k(\tau)$ at the external cell boundary, a value that is not known a priori and is, in turn, determined by the intensity of expansion or compression across the entire bubble cluster. Finally, the precise magnitude of the pressure in the liquid phase p_R, as well as the quantitative influence of capillary and viscous forces on this pressure, remain open questions within this modelling framework.

3. Modified Model

We consider an alternative approach to modelling bubble behaviour within a cluster, one that is based on averaging the pressure solely within the liquid's inter-bubble space. We assume that within a liquid volume, initially at temperature T_{f0}, there are uniformly

https://doi.org/10.3390/en19051120

distributed vapor bubbles of identical size, with an initial radius R_0. These bubbles are considered to be in thermodynamic equilibrium with the liquid. The initial vapour pressure inside each bubble is equal to the saturated vapor pressure at the liquid temperature, $p_{sat}(T_{f0})$. This assumption is used solely as the initial condition for the calculation. It is assumed that the liquid contains only vapor nuclei of uniform size, and their number can be estimated using established methods for various temperatures and pressures. Subsequent calculation steps account for changes in bubble size depending on their thermodynamic state and the influence of neighboring bubbles. The initial pressure in the liquid is uniform throughout the entire volume and is determined by the condition: $p_{f0} = p_{sat}(T_{f0}) - 2\sigma/R$. The number of bubbles per unit mass of the system, k_b, is assumed to be known and remains constant throughout the system's subsequent evolution, thereby excluding the effects of bubble coalescence and breakup. At time $\tau = 0$, the external pressure acting on the system, initially $p_f = p_{f0}$, begins to change according to a known law, initiating the growth or compression of all bubbles. For a monodisperse system, the volumetric vapour content (void fraction) is related to the size and concentration of the bubbles and is determined by the expression:

$$\gamma = \frac{4\pi R^3 \mathrm{k}_b \rho_b}{3 + 4\pi R^3 k_b \rho_b}. \tag{7}$$

Within the vicinity of each bubble, specifically within the boundaries of the elementary cell of radius $\psi(\tau) = R(\tau)/\gamma^{0.3}$, a spherical pressure distribution, $p_f(r,\tau)$, is established. This pressure field can be determined using Equation (8):

$$\frac{\partial \varphi}{\partial \tau} + \frac{u^2}{2} + \frac{p}{\rho_b} = f(\tau), \tag{8}$$

under the condition $p_f(R, \tau) = p_R(\tau)$.

When determining the function $f(\tau)$ on the right-hand side of Equation (8) using the boundary condition $p(\psi) = p_k$, the pressure distribution obtained takes the form of Equation (3). Conversely, if we utilize the boundary condition $p(R) = p_R$ to determine $f(\tau)$, the pressure distribution inside the cell adopts the following form:

$$p_f(r) = p_R - \rho_f \cdot \left(\frac{\partial \varphi}{\partial \tau} - \frac{\partial \varphi}{\partial \tau}\bigg|_{r=\psi} + \frac{u^2}{2} - \frac{u^2}{2}\bigg|_{r=\psi} \right). \tag{9}$$

By utilizing the relationships defined in Equation (4) for the calculation of the quantities on the right-hand side of Equation (9), we then reduce this equation to the final form (Equation (10)):

$$p_f(r,\tau) = p_R - \rho_b \left(R\frac{du_R}{d\tau} + 2u_R^2 \right) \frac{1 - R^4}{r^4} + 0.5\rho_b u_R^2 \frac{1 - R^4}{r^4}. \tag{10}$$

By setting the radial coordinate equal to the cell radius, $r = \Psi$. Equation (10) can be re-expressed as follows:

$$p_f(r,\tau) = p_R - \rho_b \left(R\frac{du_R}{d\tau} + 2u_R^2 \right) \cdot \left(1 - \gamma^{0.3} \right) + 0.5\rho_b u_R^2 \cdot \left(1 - \gamma^{1.3} \right). \tag{11}$$

Considering the right-hand side of Equation (5), we can derive the equation for calculating the pressure in the vicinity of the bubble:

$$p_b(r,\tau) = p_R - \rho_b \left(\frac{p_R - p_k + 0.5\rho_b u_R^2 \left(1 - \gamma^{1.3}\right)}{1 - \gamma^{0.3}} \right) \cdot \left(1 - \frac{R}{r} \right) + 0.5\rho_b u_R^2 \left(1 - \frac{R^4}{r^4} \right). \tag{12}$$

https://doi.org/10.3390/en19051120

The expression for the averaged pressure inside the cell is as follows:

$$p_m(\tau) = p_k + \frac{\rho^{0.3}\left[p_R - p_k + 0.5\rho_b u_R^2\left(1-\gamma^1\right)\right]}{1-\gamma^{0.3}} \cdot \left[\frac{1.5\left(1-\gamma^{0.6}\right)}{1-\gamma^{0.6}} - 1\right] - 0.5\rho_b u_R^2 \cdot \left(\frac{3\gamma \cdot \left(1-\gamma^{0.3}\right)}{1-\gamma^{0.3}} - \gamma^{1.3}\right). \quad (13)$$

The following algorithm is employed to determine the pressure at the external cell boundary p_k, the pressure at the bubble boundary p_R, the mean pressure in the liquid p_m, as well as the bubble radius R and the velocity of its surface u_R at each stage of the two-phase system's evolution.

Algorithm for dynamic parameter calculation. At the initial time $\tau = 0$, the external pressure acting on the system instantaneously changes from its initial equilibrium value $p_f = p_{f0}$ to some constant prescribed value $p_f < p_{f0}$. At this precise moment, the pressure within the inter-bubble space, including the external cell boundary, is equal to this external pressure. By substituting this value of the pressure into Equation (5) as the parameter p_k, we determine the magnitude of the liquid acceleration at the bubble interface within the cell $du_R/d\tau$. Subsequently, we calculate the new values for the system's governing parameters, including R, u_R, γ, and p_R. Substituting these newly calculated quantities into the right-hand side of Equation (13) allows us to compute the value of the liquid pressure averaged over the cell volume, p_m. The pressure value p_m found in this manner is then utilized in the next calculation step as the cell boundary pressure p_k. This value of p_k is then inserted back into Equation (5) to subsequently determine the new values for $du_R/d\tau$, u_R and R. Other governing system equations are solved simultaneously with Equation (5) to compute the new values of the remaining parameters. This procedure is repeated iteratively at each time step of the numerical solution for the bubble dynamics equations. If the external pressure p_f acting on the system does not change instantaneously but over a finite time interval $\Delta\tau$ according to some known function, for example:

$$p_f = p_{f0} - \left(p_{f0} - p_b\right) sin(0.5\pi\tau/\Delta\tau) \quad (14)$$

the change in external pressure, dp_f, within the time interval $0 < \tau < \Delta\tau$ is determined by the expression:

$$dp_f = -0.5\left(p_{f0} - p_b\right) \cdot cos(0.5\pi\tau/\Delta\tau) \cdot \pi d\tau/\Delta\tau \quad (15)$$

At each calculation step, the pressure p_f is computed according to the specified scheme, and the obtained value is then adjusted by the increment dp_f, substituting the time step interval as $d\tau$. After the change in external pressure is completed $\tau > d\tau$, p_f remains constant $p_f = const$ and $dp_f = 0$. This iterative procedure allows for the calculation of the time-dependent pressure at the cell boundary, p_k, and the mean pressure within the inter-bubble space of the ensemble, p_m, for any variation in the external pressure.

When the vapor content of the bubble system changes, the liquid temperature must vary due to the release or absorption of heat associated with phase transitions occurring at the expanded interfacial surface. The mean temperature of the liquid phase in the bubble ensemble, T_m, can be identified with the mean temperature of the liquid within the elementary cell. In the vicinity of each bubble, within the confines of the non-stationary thermal layer, a temperature distribution $T_f(r,\tau)$ exists.

The mean liquid temperature within the cell, T_m, at any given time is determined by integrating the functional expression $T_f(r,\tau)$ over the volume of the liquid in the cell and subsequently dividing by that volume. As previously noted, the cell model inherently assumes that each elementary cell is thermally isolated. Therefore, the amount of heat transferred through the bubble surface due to phase transition and heat exchange, $4\pi R^2(JQ + q)$ [16],

https://doi.org/10.3390/en19051120

uniquely determines the change in the heat content of the liquid in the cell and, consequently, its mean temperature. Thus, the energy balance can be formulated as:

$$\frac{d}{d\tau}\left[\frac{4}{3}\pi\rho_b c\left(\psi^3 - R^3\right)\cdot T_m\right] = 4\pi R^2(JQ + q). \tag{16}$$

By substituting the expression for the void fraction γ from Equation (7) into Equation (16) and performing the necessary mathematical transformations, we arrive at a simplified equation for determining the mean temperature of the liquid in the inter-bubble space of the ensemble:

$$\frac{dT_m}{d\tau} = \frac{k_b(JQ + q)}{c}. \tag{17}$$

A new initial parameter introduced into this model is the concentration of bubbles per unit mass, k_b. The system of equations, transformed in this manner and incorporating the proposed iterative scheme for determining the pressure within the inter-bubble space, can be effectively utilized to predict the dynamic behaviour of a cluster of monodisperse bubbles when subjected to variations in external pressure.

4. Liquid Flow in the Inter-Bubble Space of a Cluster

Cell models offer a capability to estimate the average pressure and void fraction within the inter-bubble space of the system at any given moment. This, in principle, allows for the investigation of steady and unsteady two-phase bubble flows in pipes and channels, as well as tracking the evolution of an individual bubble within such a system. However, these models are fundamentally incapable of detailing the hydrodynamic and heat and mass transfer phenomena that occur at the micro-level within the inter-bubble space. The model achieves pressure or void fraction averaging over a volume that significantly exceeds the volume of a single bubble. Consequently, the cluster is effectively treated as a homogeneous medium, with bubbles represented merely as singularities.

To accurately describe the behaviour of bubbles at the micro-level and to model the velocity and pressure fields in the inter-bubble space, several determining factors influencing the hydrodynamic environment in the liquid phase during intense bubble surface motion must be considered.

1. The bubbles within the cluster vary in geometrical size, shape, velocity, and the acceleration of their radial surface motion. This disparity necessitates an individualized description of each bubble's evolution.

2. The force interaction between dynamically developing bubbles results in their chaotic translational movement. This, in turn, causes continuous changes in the velocity and direction of the microflows over time, leading to pulsations of local liquid pressure.

3. The dynamic interaction between neighbouring bubbles causes their continuous deformation. This further induces oscillations on the surface and significantly complicates the hydrodynamic environment in the vicinity of each bubble.

In essence, the physical model that accounts for these complex factors is sufficiently straightforward and apparent. For instance, the non-uniformity of the bubbles within the ensemble can be addressed by specifying their initial size and spatial distribution. In estimating the force interaction between bubbles, the expression for the Bjerknes force, which arises between two oscillating bubbles [59–61], can be used as a first approximation. The nature of the surface deformation is managed by the condition of pressure equality at the interfacial surface, allowing the calculation of the bubble's radius of curvature in any direction [62]. However, the major modeling difficulty lies in the excessive duration of numerical computations, even for a single time step. Consequently, a detailed analysis

https://doi.org/10.3390/en19051120

of the behaviour of even two interacting bubbles proves to be a highly complex and labor-intensive task [63].

To analyze the nature of microflows, pressure fields, and velocity fields in the liquid phase of a dynamically evolving bubble system, we consider a model as a first approximation based on the following key assumptions:

(1) the influence of viscosity is manifested only at the interfacial surface;

(2) bubbles retain a spherical shape during their evolution, this is justifiable for relatively small bubbles, where capillary pressure counteracts the external forces from other bubbles, provided that $\gamma < 0.55$.

(3) the force interaction between neighbouring bubbles, caused by the radial motion of their surfaces, is accounted for, which results in the mutual translational movement of bubbles within the ensemble;

(4) the liquid flow in the inter-bubble space is potential.

We treat the expanding or compressing bubbles as discretely distributed dynamic and thermal sources (or sinks) within the liquid. Based on assumption (4) (potential flow), we utilize the superposition principle in accordance with potential theory: the resultant flow is the sum of flows from each source, and the magnitude of the scalar potential of the velocity field at an arbitrary point in the liquid is the sum of the potentials generated at that point by all sources.

Consider a cluster of vapour bubbles comprising k_b elements. We place the origin of the Cartesian coordinate system at some point in the center of the bubble system. If the center coordinates (x, y, z), radii R_k, and surface expansion velocity u_R, of each of the k_b bubbles are known at a specific instant in time, the total field potential at an arbitrary point in the liquid with chosen coordinates, according to the superposition rule of potentials, is determined by the formula:

$$\varphi(x,\, y,\, z) = \sum_{i=1}^{\mathrm{k}} -\frac{u_{Ri} R_i^2}{\overline{\omega}_i}, \tag{18}$$

where $\overline{\omega}_i = \sqrt{\Delta x^2 - \Delta y^2 - \Delta z^2}$.

The components of the resultant velocity vector at the point (x, y, z) are determined by the following expressions:

$$u_x = \sum_{i=1}^{k} \frac{u_{Ri} R_i^2 \Delta x}{\overline{\omega}_i^3}; \quad u_y = \sum_{i=1}^{k} \frac{u_{Ri} R_i^2 \Delta y}{\overline{\omega}_i^3};\; u_z = \sum_{i=1}^{k} \frac{u_{Ri} R_i^2 \Delta z}{\overline{\omega}_i^3}, \tag{19}$$

The spatial direction of the velocity vector is subsequently determined using the standard formulas of analytical geometry, based on the known values of its projections:

$$\frac{\partial \varphi}{\partial \tau} = \sum_{i=1}^{k} -\left(\frac{du_{Ri}}{d\tau} \cdot \frac{R_i^2}{\overline{\omega}_i} + \frac{2 R_i u_{Ri}^2}{\overline{\omega}_i} \right), \tag{20}$$

where $du_{Ri}/d\tau$ is the acceleration of the radial surface motion of the individual bubble, as determined by Equation (6).

By substituting the value of the partial derivative of the potential with respect to time, $\partial\varphi/\partial\tau$, from Equation (20) and the velocity vector from Equation (19) into the Lagrange–Cauchy integral (Equation (8)), the magnitude of the pressure at a local point (x, y, z) of the microflow can be determined. The function $f(\tau)$ on the right-hand side of Equation (8) is determined by imposing the condition that at a sufficiently large distance from the bubble cloud, the pressure in the liquid is constant and equal to p_f, and both the

https://doi.org/10.3390/en19051120

flow velocity and the potential are zero. Under these far-field conditions, the local pressure within the inter-bubble space inside the cloud is determined by the following equation:

$$p_b(x,y,z) = p_f - \rho_b \left(\frac{\partial \varphi}{\partial \tau} + \frac{\vec{u}^2}{2} \right) \quad (21)$$

by substituting the values of $\vec{u}$ and $\partial\varphi/\partial\tau$ from Equations (19) and (20), respectively, into its right-hand side.

Since the point (x, y, z) is arbitrarily chosen, this scheme allows for the estimation of the velocity and pressure magnitudes at any point within the inter-bubble space. Consequently, the instantaneous distribution of velocities and pressures throughout the two-phase system under consideration can be determined. It is essential to ensure that the point where $\vec{u}$ and p_b are determined does not fall within the region currently occupied by the bubble's gas phase. Determining the pressure field in the liquid between the bubbles makes it possible to average the pressure over the volume of each individual cell (which are not necessarily identical). This averaged pressure is then used in the next time step to solve the single-bubble dynamics equation for each of the k_b bubbles, thereby determining the new values for R, u_R, $du_R/d\tau$, and the new spatial coordinates x, y, z. Subsequently, the entire aforementioned procedure for calculating the velocity and pressure fields is performed again.

In this model, the correct calculation of the dynamics of each individual bubble within the finite-volume ensemble is of fundamental importance. As previously indicated, Equation (5) must be used as the equation of motion to determine the value of the radial acceleration $du_R/d\tau$ on the right-hand side of Equation (20).

The main question centers on the appropriate values for the parameters p_k and γ to be substituted into these equations. During the derivation of Equation (5), it was established that the void fraction γ in this equation characterizes the cell radius $\Psi = R/\gamma^{0.3}$ surrounding the specific bubble, while p_k represents the liquid pressure averaged over the volume of that cell. These bubbles located on the periphery of the cloud are in constant contact with an unlimited volume of the liquid phase, where the pressure p_f = const. For these peripheral bubbles, the cell radius Ψ is assumed to be half the distance from their centers to the center of their nearest neighbours, which determines the corresponding value of γ. The pressure calculated via Equation (13) is substituted as p_k into Equation (5). These peripheral bubbles essentially behave as isolated bubbles in an infinite liquid volume throughout the process. However, the pressure that these bubbles create in the outer layer of the cluster, calculated using Equation (13), is hypothesized to be transmitted as the cell boundary pressure p_k for all bubbles situated in the next adjacent spherical layer—the layer bordering the outer cloud layer. This pressure p_k, created by the bubbles in the second layer, is then passed on as the boundary condition for the bubbles in the third spherical layer, and so on. Consequently, the averaged pressure within a spherically shaped bubble cloud will vary from the periphery to the center, and the pressure gradient along the cloud's radius depends on the intensity of expansion or compression of the bubbles within each spherical layer. This macro-level procedure for determining pressures within a finite ensemble allows for the calculation of the current parameters of each bubble as a function of its distance from the cloud center and its initial size. Subsequently, at each computational time step, the known values of the radial acceleration $du_R/d\tau$ and velocity u_R for every bubble enable the estimation of the velocity, pressure magnitudes, and direction of the microflow at any point in the inter-bubble space, utilizing the field Equations (18)–(21). In summary, the presented equations for both unlimited and finite numbers of vapour bubbles, combined with the single-bubble dynamics equations, provide a framework for predicting the behaviour

https://doi.org/10.3390/en19051120

of bubbles within a cluster and the cluster's overall behaviour under varying external pressure, as well as for determining the velocity and pressure fields in the inter-bubble space and their temporal evolution under any operational parameters.

5. Discussion

Based on the modified model, an analysis of the behaviour of vapor bubbles in water was performed under different operating modes and various external pressure change conditions. Below, some of the prediction results are presented as examples to illustrate the model's capabilities

5.1. Dynamics of Bubble Growth and Collapse in a Cluster

Within the framework of the modified model, the evolution of a monodisperse vapour bubble cloud was considered for known initial values of the liquid temperature T_{f0} and initial pressure и p_{f0}. At the initial instant, all bubbles with radius R_0 and concentration k_b are in equilibrium with the liquid. At the initial time $\tau = 0$, the external pressure acting on the system begins to change. In analyzing various experimental methodologies related to the rapid change of pressure in a liquid volume [64–66], we established that, regardless of the method used to change the pressure in the system, the nature of the actual curve $p_f = f(\tau)$ is well approximated by a cosinusoidal dependence, taking the form:

$$p_f(\tau) = P + \frac{p_{f0} - P}{2} \cdot \left[1 + cos\left(\frac{\pi\tau}{\Delta\tau}\right)\right] \qquad \text{at } 0 < \tau < \Delta\tau;$$

$$p_f(\tau) = P \qquad \text{at } \tau \geq \Delta\tau, \tag{22}$$

where P represents the constant pressure established in the liquid far from the bubble as a result of the change in external pressure, and $\Delta\tau$ is the duration of this change. After the specified time interval $\Delta\tau$, the external pressure assumes a new constant value P.

Figure 2 illustrates how the mean pressure in the liquid within the inter-bubble space of the cluster, $p_m = p_k$, changes following an instantaneous drop in external pressure from an initial equilibrium value of 60 kPa to 15 kPa. The pressure in the liquid rapidly increases, asymptotically approaching the saturated vapour pressure $p_{sat}(T_f)$, which corresponds to approximately 30 kPa under the conditions presented in the figure. The figure also includes a graph showing the pressure pulsations within a cavitation cloud, based on the data presented in the study [67–70].

The presented data suggests that the pressure within the cluster undergoes an averaging process, but the dynamic effects originating from the bubbles at the cloud boundaries can be substantially greater than those observed inside the cluster. These internal effects within the cavitation cloud become more prominent as the bubble concentration increases. Figure 3 illustrates the change in the liquid pressure inside a monodisperse cloud of collapsing bubbles following an instantaneous increase in the external pressure from the equilibrium value of 70 kPa to 150 kPa. Due to the intense initial compression of the bubble ensemble and the associated stretching of the liquid, the pressure in the inter-bubble space initially drops sharply to nearly 70 kPa. However, the rapid compression leads to a significant increase in the vapour pressure inside the bubble, which in turn causes the pressure to rise in the liquid layers adjacent to the surface. This elevated pressure then propagates throughout the entire cell volume. Similarly to the previous case of bubble growth, the pressure inside the cell is controlled by the vapour pressure in the bubble, and this control is more noticeable as the cell size decreases, meaning the higher the bubble concentration. Consequently, as shown in the figure, at high concentrations, the mean pressure in the liquid substantially exceeds the external pressure until the bubbles completely collapse.

https://doi.org/10.3390/en19051120

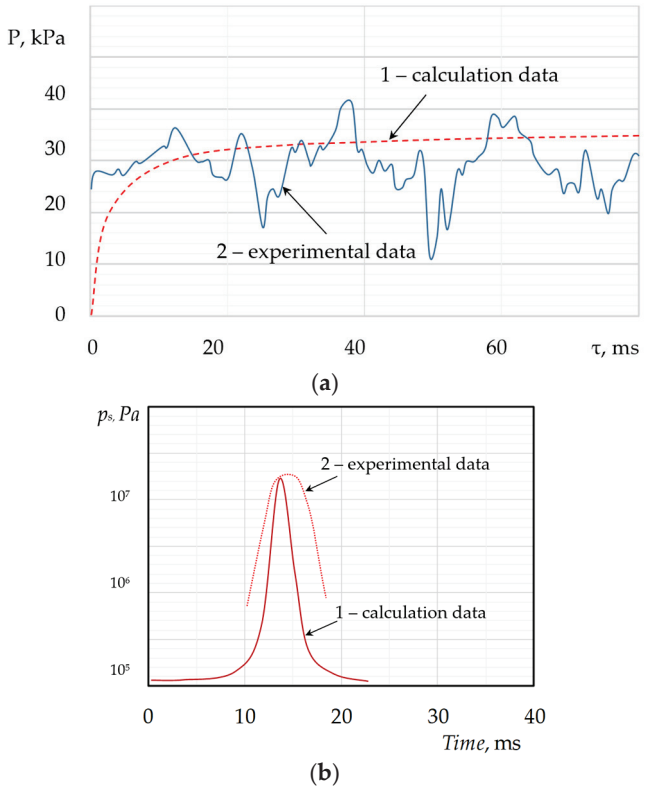


Figure 2. Comparison of bubble cluster and single bubble dynamics: (**a**) change in averaged pressure within the cluster during vapor bubble growth in water following a sudden reduction in external pressure. The calculation is based on the modified model using the following conditions: T_{f0} = 380 K; p_{f0} = 60 kPa; p_f = 15 kPa; R_0 = 20 μm; k_b—10^4 kg^{-1}; (**b**) change in the pressure of a single bubble during its maximum compression stage in the process of collapse, under the same conditions. Curve 1 represents the model calculation, and curve 2 represents the data reported in: (**a**)—[67]; (**b**)—[68].

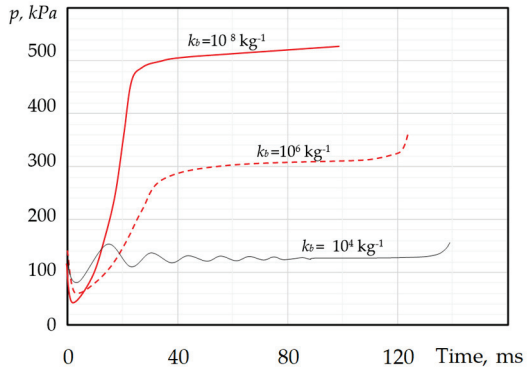


Figure 3. Change in averaged pressure $p_m = p_k$ in the liquid phase during the cavitation collapse of vapor bubbles in water following an increase in external pressure. The calculations were performed using the following initial conditions T_{f0} = 380 K; p_{f0} = 70 kPa; p_f = 130 kPa; R_0 = 100 μm; and for various values of the bubble concentration k_b.

The elevated pressure established within the cell acts to suppress the bubble's expansion following maximum compression and its subsequent oscillation, which would be characteristic of the collapse of a single, isolated bubble. However, at comparatively low concentrations (curve 1 in Figure 3), the behaviour of the bubbles closely approaches that of a single bubble. During the collapse process, the pressure inside the cell exhibits only weak oscillation, tending toward the external pressure value, p_f = 130 kPa. The collapse of bubbles at low concentrations is accompanied by oscillation of their size, as evident from Figure 3 (curve 1), whereas at high concentrations, the bubble radius decreases mono-

https://doi.org/10.3390/en19051120

tonically until complete collapse. Interestingly, despite the qualitative difference in the compression process, the lifetime of the bubbles in the cluster does not depend on the concentration and is practically identical to the duration of the single bubble collapse under the same conditions. Furthermore, for identical values of k_b, the initial bubble size R_0 has only a minor influence on their behaviour. A study of the growth process at various R_0 values, ranging from 5 μm to 100 μm, demonstrated that shortly after the onset of bubble expansion (the time depending on concentration), the magnitude of the current pressure in the inter-bubble space and the rate of vaporization are practically independent of R_0.

The magnitude of the pressure drop or the degree of liquid superheating exerts a similarly minor influence on the dynamics of bubble growth for identical values of T_{f0} and k_b. For example, when the pressure in a monodisperse ensemble is reduced from an equilibrium value of 60 kPa to 20 kPa, the corresponding time dependencies for the averaged pressure p_m = f(τ) essentially coincide. This congruence also applies to the dependencies of $R(\tau)$, $u_R(\tau)$ and $\gamma(\tau)$. However, during the short initial growth phase, before the quasi-equilibrium pressure is established in the liquid phase, the intensity of bubble expansion is higher when the pressure differential is larger. The duration of the external pressure change, $\Delta\tau$, also has only a weak effect on the characteristics of the dependencies $p_m(\tau)$, $R(\tau)$. In the inertial stage, the rate of vapor phase growth is higher when the rate of pressure reduction $dp_f/d\tau$ is higher. At the same time, intensive bubble growth facilitates a more rapid approach to the quasi-equilibrium value p_m. Regardless of the duration of the pressure drop, the same averaged pressure p_m is established inside the cluster after a very short period. This pressure is what governs the subsequent evolution of the bubbles, meaning that after only approximately 80 μs following the onset of the bubble ensemble expansion, the recorded parameter values for R, u_R or γ no longer allow one to discern the cluster's development history or determine whether the change in external pressure has ceased or is still ongoing.

5.2. Velocity and Pressure Fields in the Inter-Bubble Space

The modified model allows for the individualization of each bubble, taking into account its current size, location within the cluster, kinematic and thermodynamic characteristics, and other properties. Information obtained through the cell model approximation is also incorporated into the description of the bubble cloud behaviour. Figure 4 is presented as an illustration, showing the instantaneous distribution of liquid microflow velocities inside the cluster at a specific moment in time. The microflows, which exhibit a complex nature, are caused by the expansion of the bubbles during the cavitation process. The arrows in the figure indicate the direction of the velocity at local points but not its magnitude. Clusters containing between 10 and 1500 bubbles were considered in the analysis. At any given time, the local values of the velocity vector $\vec{u}$ (magnitude and direction), the velocity field potential φ, and the pressure magnitude p are determined at various points in the liquid. To visualize the results, the projections of the velocity vector onto a specified plane passing through the volume occupied by the bubble cloud were calculated. It is characteristic that the velocity field exhibits a truly cellular structure. Directly at the surface of the bubbles, the flow is close to radial. However, as the distance from the surface increases, the microflow pattern becomes more complex, and at the boundaries of bubble interaction, the velocity vectors change direction sharply. This figure demonstrates that bubble growth occurs more intensely at the edges of the cloud, which is attributed to the non-uniform distribution of the averaged pressure p_k throughout the cloud volume: in the central part, $p_k >> p_f$, whereas at the periphery, $p_k \rightarrow p_f$.

https://doi.org/10.3390/en19051120

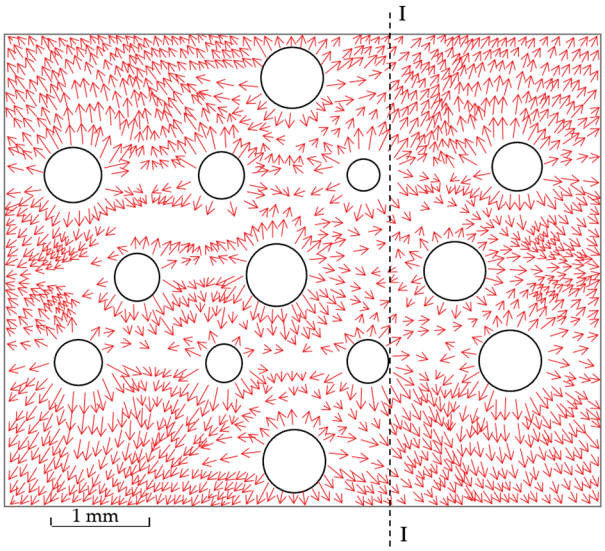


Figure 4. Directions of liquid velocity vectors inside a cavitation cloud composed of 30 bubbles growing as a result of a pressure drop in the system. The figure displays the velocity projections onto the XY plane, which intersects the center of the cluster.

Figure 5 illustrates how the magnitudes of the local pressure p and local velocity φ change along the direction I-I (as defined in Figure 4). Significant velocity fluctuations are observed within the cluster along any direction, whereas outside the cluster, even near its boundaries, the velocity magnitude changes monotonically, maintaining a practically constant direction. Despite such abrupt velocity changes in the inter-bubble space, the pressure pulsations are, as evident from Figure 5, relatively weak. Nevertheless, the magnitude of the pressure gradient reaches up to 20 kPa/mm at local points, and the velocity gradients exceed 20 m/s per 1 mm. The figure clearly indicates that the pressure within the cloud volume is higher than at the periphery. This increased internal pressure leads to a situation where the bubble size and, consequently, the void fraction are higher in the peripheral zone of the cloud than in its interior.

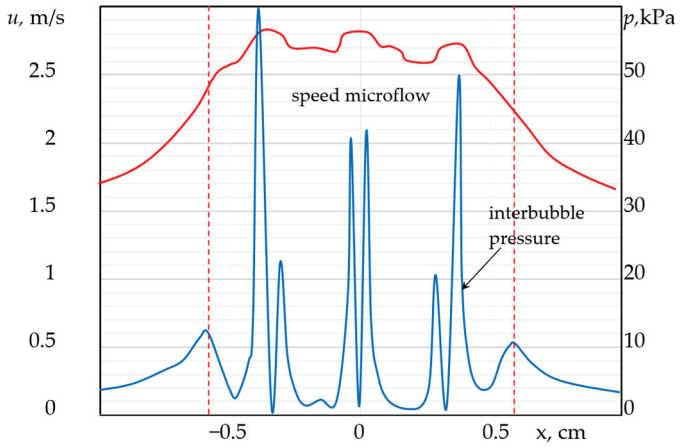


Figure 5. Variations in local flow velocity and local pressure magnitude in the liquid within the inter-bubble space along the direction I-I (Figure 4). The calculation was performed using the same conditions specified for Figure 4.

The dashed lines in Figure 5 demarcate the region occupied by the cluster. The data obtained indicates that within the inter-bubble space of the cloud, even during the monotonic expansion of the bubbles, there are sharp jumps in pressures and velocities characteristic of turbulent flow. This nature of flow contributes to the intensification and

https://doi.org/10.3390/en19051120

stimulation of heat and mass transfer and hydromechanical processes within the liquid phase of the bubble system. When cavitation conditions are realized in a liquid, a multitude of vapour-gas bubbles grow and then simultaneously collapse, forming a cavitation cluster. The effectiveness of the cavitation impact is determined by the collective influence of all bubbles within the cluster. Cluster sizes typically range from 0.1 to 5 cm. The concentration of nuclei in the cluster depends on the liquid's temperature, gas content, and the presence of impurities. The superposition of shock waves from each individual bubble forms a single destructive shock wave. However, this conventional concept does not account for the destruction of micro-objects inside the cluster itself. Furthermore, when modelling the behaviour of a cavitation cluster and developing analytical methods for cavitation reactors, temperature is often not even included as one of the model parameters [59,60]. The following section provides an assessment of the main characteristics of heat and mass transfer across the bubble surface.

5.3. Heat and Mass Transfer Across the Interfacial Surface During Bubble Collapse

As demonstrated earlier, the dynamic effects of individual bubbles at the cluster boundary during the collapse stage significantly exceed the average effects of the cluster itself. The most intense heat and mass transfer across the interfacial surface, and the most vigorous mass transfer processes (evaporation and condensation), occur during the stage of maximum bubble compression, as illustrated in Figures 6 and 7. Although the amplitude values of the heat flux impulse $JQ + q$ are extremely high during the maximum compression stage, the quantity of thermal energy transferred through the bubble wall during this time is very small. Due to the extremely short duration of this impulse, this part of the energy constitutes only a negligible fraction of the total thermal energy accumulated in the bubble after the transformation of kinetic energy into potential energy.

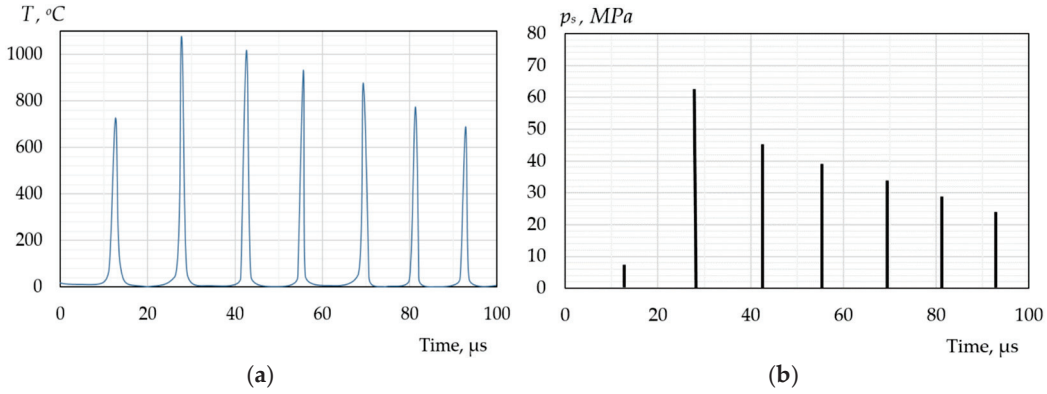


Figure 6. Change in vapor temperature (**a**) and vapor pressure (**b**) during the collapse of a vapor bubble in a subcooled liquid. A modified model was used for the calculation under the following conditions: T_{l0} = 20 °C; T_{s0} = 130 °C; p_{l0} = 100 kPa; R_0 = 100 μm.

The intensity of mass transfer, J, also increases to an extreme degree during the stage of maximum compression, but this fractional change in acquired or lost vapours mass is negligibly small in the overall mass balance. For the remainder of the bubble's development time, the inherently low rates of heat and mass transfer can still exert a relatively large influence on the bubble's dynamics. Figure 8a,b illustrates how the vapours mass in the bubble, m_s, and the quantity of heat accumulated in the bubble, q, change during the oscillation process. Despite the strong fluctuations in the bubble size, both quantities, m_s and q, decrease practically monotonically, with the largest reduction in vapours mass and thermal energy occurring during the first period of oscillations. The absolute quantities of energy and mass transferred across the bubble surface per unit time are not very large. However, considering the minute dimensions of the bubble at the moment of maximum

https://doi.org/10.3390/en19051120

compression, the specific fluxes across a unit surface area are substantial. As shown in Figures 8 and 9, the magnitude of the specific mass flux of vapours condensing into the liquid or evaporating into the bubble is estimated to be on the scale of 100 kg/m^{2}s, and the specific energy flux is on the scale of 100 MW/m^2.

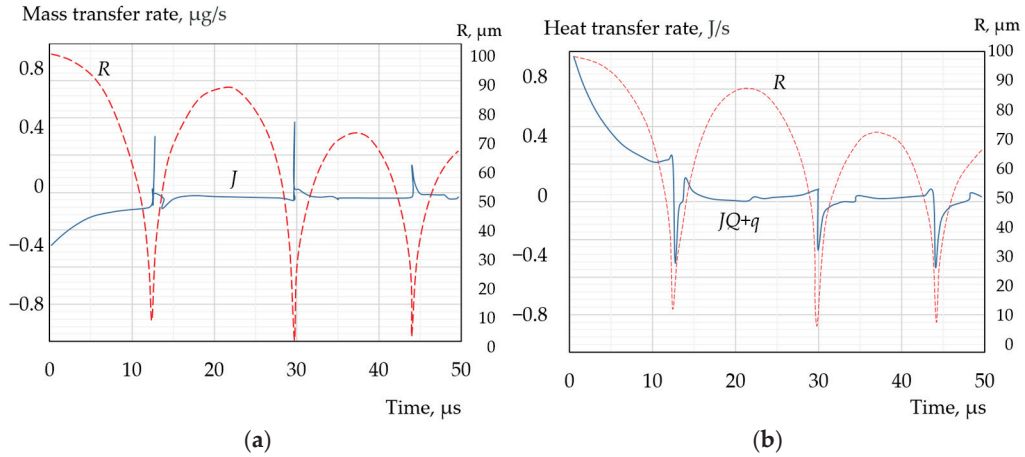


Figure 7. Variation in the intensity of heat flux (**a**) and mass flux (**b**) across the surface of a vapor bubble during its collapse in subcooled liquid. The calculation conditions are: T_{f0} = 20 °C; p_{f0} = 100 kPa; R_0 = 100 μm).

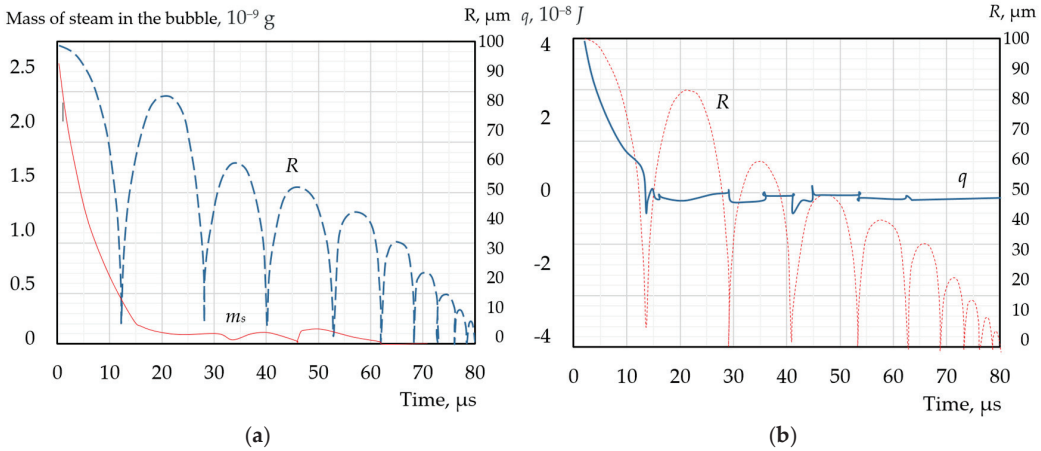


Figure 8. Vapor mass (**a**) and quantity of heat (**b**) in a vapor bubble during its collapse in subcooled liquid. The dashed curve indicates the simultaneous change in the bubble radius.

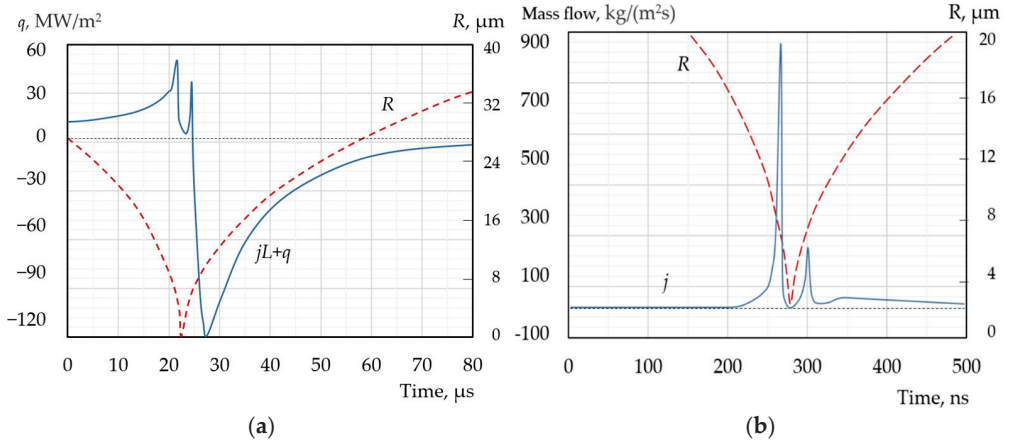


Figure 9. Intensity of Heat Flux $JQ + q$ (**a**) and Mass Flux J (**b**) across the interfacial surface during the maximum compression stage of a bubble's collapse in subcooled liquid. The dashed curve indicates the simultaneous change in the bubble radius.

https://doi.org/10.3390/en19051120

6. Conclusions

Based on the conducted analysis, a mathematical model for bubble cluster dynamics has been developed, which describes the evolution of a collection of vapour bubbles when thermodynamic equilibrium is disrupted in the vapour-liquid system. Computational experiments were performed to investigate the patterns of bubble evolution resulting from a sharp decrease or increase in external pressure. When the external pressure is released in a vapour-liquid bubble medium, the pressure in the liquid phase rapidly increases, asymptotically approaching the saturated vapour pressure corresponding to the liquid temperature. The rate of approach to saturation pressure is proportional to the bubble concentration. he degree of superheat, the rate of pressure release, and the initial size of the bubble nuclei only influence the initial stage of cavitation development.

The computational experiments provided quantitative information regarding the local values of pressure and velocity at any point in the liquid phase of the developing bubble ensemble. It was established that even during the monotonic expansion of bubbles in the thermal regime, the magnitudes of the velocity and pressure gradients reach extremely high values.

The dynamic action of cavitation is attributed to the following factors:

– during bubble growth and compression, complex non-stationary microflows are formed inside the cluster due to the superposition of radial flows towards each bubble; these flows feature extremely high values of shear rates and shear stresses, the effect of which is present throughout the entire lifetime of the cluster;
– calculations indicate that in the inter-bubble space, shear rates at local points on the boundaries of flow interaction can reach 10^6 s^{-1}, which corresponds to a shear stress of approximately 1 kPa when water is the dispersed phase;
– during collapse, each bubble in the cluster acts as the center of a spherical shock wave with a pressure amplitude that can reach 100 MPa.

The non-stationary fields of velocities and pressures in the liquid inside the cluster are extremely complex. During bubble compression, the volume-averaged pressure inside the cluster rapidly increases and can exceed 10 MPa in the final stage. The simultaneous collapse of bubbles causes the pressure within the cluster volume to drop sharply, and a high-amplitude resultant impulse is radiated into the surrounding medium.

A significant finding is that even during the stage of monotonic cluster expansion, when the bubble growth rate does not exceed 2 m/s, the shear rates in local liquid zones are quite high—on the order of 5×10^4 s^{-1}. Thus, while a high level of thermal impact is only realized during the nanosecond-scale stage of maximum cluster compression, the effective influence of shear stresses is evident throughout the entire existence of the cluster.

The question of the total dynamic effect of the cluster remains a subject for discussion. If one assumes that dynamic effects are determined only by the collapse of the outer peripheral bubbles, theoretical models are likely to predict overestimated dynamic parameter values. This is because real processes exhibit effects of mutual compensation of counter-propagating impulses directed from different bubbles, a finding confirmed by certain experimental studies.

The developed modified mathematical model is designed for the analysis of pressure and temperature fields, as well as microflows, in the inter-bubble space of the ensemble during boiling and cavitation processes.

The model is applicable to both hydrodynamic and acoustic cavitation conditions and can be used for low and high bubble concentrations. In the former case—for example, at a bubble concentration of up to 1×10^{13} m^{-3} and a pressure of 3 MPa—the bubbles can be treated as isolated local volumes that do not significantly influence one another. The initial

https://doi.org/10.3390/en19051120

input for the mathematical model specifies the bubble size distribution and concentration, while the calculation algorithm itself remains unchanged.

Funding: This research received no external funding.

Data Availability Statement: The original contributions presented in this study are included in the article. Further inquiries can be directed to the corresponding author.

Conflicts of Interest: The authors declare no conflicts of interest.

Nomenclature

p_b	pressure in the vicinity of the bubble, Pa
R	bubble radius, m
Δ	distance between bubbles, m
r	radial coordinate, m
p_f	external pressure, Pa
ρ_b	gas density inside the bubble, kg/m^3
u_R	velocity of the bubble boundary motion, m/s
μ	dynamic viscosity, Pa s
σ	interfacial surface tension, N/m
$\gamma(\tau)$	volumetric vapour content (void fraction),
Ψ	cell radius, m
θ	thickness of the thermal layer, m
p_k	pressure at the cell boundary, Pa
p_R	pressure at the bubble boundary, Pa
T	temperature, K
k_b	number of bubbles,
p_m	average pressure, Pa
Q	latent heat of vaporization, J/kg
q	specific heat flux, W/m^2
c	specific heat capacity, J/(kg K)
$\overrightarrow{u}$	modulus of the velocity vector.

References

1. Zhang, D.; Guan, J.; He, Z.; Shen, C.; Cao, H. Experimental investigation on heat transfer and flow patterns of pulsating heat pipe assisted by ultrasonic cavitation. *Int. J. Heat Mass Transf.* **2022**, *183*, 122187. [CrossRef]
2. Li, C.; Luo, Z.; Shao, Y.; Qian, Y.; Du, S.; Yang, Q.; Chen, Z.; Chen, H.; Zha, Y.; Fang, X. A review on ultrasound-enhanced heat transfer. *Ultrason. Sonochemistry* **2025**, *121*, 107570. [CrossRef] [PubMed]
3. Alenezi, A.; Ali, H.M.; Phelan, P.E. Experimental investigation of the effect of ultrasonic waves on heat transfer enhancement and pressure drop for propylene glycol/water mixtures in a rectangular minichannel heat sink. *Appl. Therm. Eng.* **2025**, *267*, 125717. [CrossRef]
4. Song, Y.; Guan, S.; Wang, Y.; Zhang, C.; Liu, J.; Zhang, L. The application of hydrodynamic cavitation technology and the synergistic effect of hybrid advanced oxidation processes: A review. *Water Sci. Technol.* **2025**, *92*, 301–325. [CrossRef]
5. Askarniya, Z.; Sun, X.; Wang, Z.; Boczkaj, G. Cavitation-based technologies for pretreatment and processing of food wastes: Major applications and mechanisms—A review. *Chem. Eng. J.* **2023**, *454*, 140388. [CrossRef]
6. Pavlenko, A.M. Change of emulsion structure during heating and boiling. *Int. J. Energy A Clean Environ.* **2019**, *20*, 291–302. [CrossRef]
7. Galloni, M.G.; Fabbrizio, V.; Giannantonio, R.; Falletta, E.; Bianchi, C.L. Applications and applicability of the cavitation technology. *Curr. Opin. Chem. Eng.* **2025**, *48*, 101129. [CrossRef]
8. Zhang, H.; Du, M.; Hu, H.; Zhang, H.; Song, N. A Review of Ultrasonic Treatment in Mineral Flotation: Mechanism and Recent Development. *Molecules* **2024**, *29*, 1984. [CrossRef] [PubMed]
9. Wang, M.; Qiu, J.; Chen, W. Towards the development of cavitation technology for gas hydrate prevention. *R. Soc. Open Sci.* **2021**, *8*, 202054. [CrossRef] [PubMed]

10. Huang, H.; Zhang, Y.; Wu, X.; Hui, C.; Tan, Y.; Li, G. Study on the Decomposition of Natural Gas Hydrate Induced by Cavitation Damage. In Proceedings of the 57th U.S. Rock Mechanics/Geomechanics Symposium, Atlanta, GA, USA, 25–28 June 2023. [CrossRef]
11. Pavlenko, A.M. Thermodynamic Features of the Intensive Formation of Hydrocarbon Hydrates. *Energies* **2020**, *13*, 3396. [CrossRef]
12. Li, J.; Li, D.; Li, T. Progress in the Understanding and Modeling of Cavitation and Related Applications. *Fluid Dyn. Mater. Process.* **2025**, *21*, 445–470. [CrossRef]
13. Koshlak, H.; Pavlenko, A. A New Mathematical Model for the Features of Bubble Collapse in Steam Cavitation Processes. *Appl. Sci.* **2025**, *15*, 9948. [CrossRef]
14. Fattahi, K.; Boffito, D.C.; Robert, E. Quantifying the chemical activity of cavitation bubbles in a cluster. *Sci. Rep.* **2024**, *14*, 7978. [CrossRef] [PubMed]
15. Li, P.; Wang, J.; Liao, Z.; Ueda, Y.; Yoshikawa, K.; Zhang, G. Microbubbles for effective cleaning of metal surfaces without chemical agents. *Langmuir* **2022**, *38*, 769–776. [CrossRef]
16. Tao, F.; Zhao, G.-Y.; Chen, W.-Z.; Tao, D. 1/2 order subharmonic waves of two cavitation bubbles. *Ultrason. Sonochemistry* **2024**, *110*, 107022. [CrossRef]
17. Kenzhaliyev, B.; Surkova, T.; Berkinbayeva, A.; Baltabekova, Z.; Smailov, K.; Abikak, Y.; Saulebekkyzy, S.; Tolegenova, N.; Omirbek, T.; Dosymbaeva, Z. Innovative Methods for Intensifying the Processing of Zinc Clinker: Synergy of Microwave Treatment and Ultrasonic Leaching. *Metals* **2025**, *15*, 246. [CrossRef]
18. Shen, X.; Wu, P.; Lin, W. A new model for bubble cluster dynamics in a viscoelastic media. *Ultrason. Sonochemistry* **2024**, *107*, 106890. [CrossRef] [PubMed]
19. Pavlenko, A.; Szwaba, R. Behaviour of vapour bubbles in an acoustic field. *Appl. Therm. Eng.* **2025**, *280*, 128495. [CrossRef]
20. Zou, Q.; Zhong, X.; Zhang, B.; Gao, A.; Wang, X.; Li, Z.; Qin, D. Bubble pulsation characteristics in multi-bubble systems affected by bubble size polydispersity and spatial structure. *Ultrasonics* **2023**, *134*, 107089. [CrossRef] [PubMed]
21. Liu, J.; Wang, X.; Liang, J.; Qiao, Y. Refined secondary Bjerknes force equation for double bubbles with pulsation, translation, and deformation. *Ultrason. Sonochemistry* **2024**, *102*, 106756. [CrossRef]
22. Liu, R.; Hu, J.; Wu, Y.; Chen, S.; Wang, C.; Mo, R.; Guo, J.; Lin, S. Manipulation mechanisms of bubble aggregation and evolution in inertial cavitation fields. *Ultrason. Sonochemistry* **2025**, *119*, 107384. [CrossRef]
23. Wang, X.; Hu, S.; Wang, Y.; Guo, Z.; Zhang, Y. Collapse dynamics of a single cavitation bubble in proximity to a wall with two protrusions. *Phys. Fluids* **2025**, *37*, 063334. [CrossRef]
24. Pavlenko, A.; Koshlak, H. Study of the Dynamics of a Single Bubble. *Energies* **2024**, *17*, 4236. [CrossRef]
25. Zhao, Y.; Jiang, S.; Wang, X.; Guo, W.; Zhao, G.; Zhao, F.; Xu, W. Study on the collapse process of double cavitation bubble based on coarse-grained force field. *J. Mol. Liq.* **2025**, *429*, 127517. [CrossRef]
26. Xu, W.; Zhou, Z.; Zhao, Y.; Zhao, G.; Guo, W.; Zhao, F.; Wang, X. Multifactorial Analysis of the Collapse Process of Double Bubbles Based on the Coarse-Grained Force Field in Free Domain. *Langmuir* **2025**, *41*, 3706–3715. [CrossRef]
27. Folden, T.S.; Aschmonei, F.J. A classification and review of cavitation models with an emphasis on physical aspects of cavitation. *Phys. Fluids* **2023**, *35*, 081301. [CrossRef]
28. Stavropoulos-Vasilakis, E.; Kyriazis, N.; Jadidbonab, H.; Koukouvinis, P.; Gavaises, M. Chapter 1—Review of Numerical Methodologies for Modeling Cavitation. In *Cavitation and Bubble Dynamics*; Koukouvinis, P., Gavaises, M., Cavitation, Dynamics, D., Eds.; Academic Press: Cambridge, MA, USA, 2021; pp. 1–35. [CrossRef]
29. Fuster, D.A. Review of Models for Bubble Clusters in Cavitating Flows. *Flow. Turbul. Combust.* **2019**, *102*, 497–536. [CrossRef]
30. Madabhushi, A.; Mahesh, K. A compressible multi-scale model to simulate cavitating flows. *J. Fluid Mech.* **2023**, *961*, A6. [CrossRef]
31. Ghahramani, E.; Ström, H.; Bensow, R.E. Numerical simulation and analysis of multi-scale cavitating flows. *J. Fluid Mech.* **2021**, *922*, A22. [CrossRef]
32. Li, J.; Carrica, P.M. A population balance cavitation model. *Int. J. Multiph. Flow.* **2021**, *138*, 103617. [CrossRef]
33. Zhang, A.-M.; Li, S.-M.; Cui, P.; Li, S.; Liu, Y.-L. Interactions between a central bubble and a surrounding bubble cluster. *Theor. Appl. Mech. Lett.* **2023**, *13*, 100438. [CrossRef]
34. Hanimann, L.; Mangani, L.; Casartelli, E.; Darwish, M.; Kclaramunt, K. Cavitation modelling using real gas state equation: A conceptual study. In *Proceedings of the 30th IAHR Symposium on Hydraulic Machinery and Systems, Lausanne, Switzerland, 21–26 March 2021*; IOP Conference Series: Earth and Environmental Science; IOP Publishing: Philadelphia, PA, USA, 2021; Volume 774, p. 012080. [CrossRef]
35. Huang, M.; Yao, C.; Wang, P.; Cheng, L.; Ying, W. Physics-informed data-driven cavitation model for a specific Mie–Grüneisen equation of state. *J. Comput. Phys.* **2025**, *524*, 113703. [CrossRef]
36. Hong, F.-W.; Zhai, S.-C.; Zheng, C.-S.; Liu, D.-C. Cavitation model of non-equilibrium between phase transition and hydrodynamics. *J. Hydrodyn.* **2025**, *37*, 489–496. [CrossRef]

37. Li, W.; Yu, Z.; Kadam, S. An improved cavitation model with thermodynamic effect and multiple cavitation regimes. *Int. J. Heat Mass Transf.* **2023**, *205*, 123854. [CrossRef]
38. Jin, W. Phase change mechanism of periodic cavitation evolution in turbulent cavitation boundary layer. *Ocean Eng.* **2023**, *289*, 116230. [CrossRef]
39. Wang, Z.; Li, L.; Li, X.; Zhu, Z.; Yang, S.; Yang, G. Investigation on multiscale features of cavitating flow in convergent-divergent test section using Eulerian–Lagrangian method. *Int. J. Mech. Sci.* **2023**, *238*, 107853. [CrossRef]
40. Budich, B.; Schmidt, S.J.; Adams, N.A. Numerical simulation and analysis of condensation shocks in cavitating flow. *J. Fluid Mech.* **2018**, *838*, 759–813. [CrossRef]
41. Asnaghi, A.; Svennberg, U.; Bensow, R.E. Numerical and experimental analysis of cavitation inception behaviour for high-skewed low-noise propellers. *Appl. Ocean Res.* **2018**, *79*, 197–214. [CrossRef]
42. Shi, Y.; Luo, K.; Chen, X.; Li, D.; Jia, L. A new cavitation model considering inter-bubble action. *Int. J. Nav. Archit. Ocean Eng.* **2021**, *13*, 566–574. [CrossRef]
43. Wang, K.; Li, Z.; Zhang, R.; Ma, R.; Huang, L.; Wang, Z.; Jiang, X. Computational fluid dynamics-based ship energy-saving technologies: A comprehensive review. *Renew. Sustain. Energy Rev.* **2025**, *207*, 114896. [CrossRef]
44. Pavlenko, A. Energy conversion in heat and mass transfer processes in boiling emulsions. *Therm. Sci. Eng. Prog.* **2020**, *15*, 100439. [CrossRef]
45. Zhang, A.-M.; Li, S.-M.; Cui, P.; Li, S.; Liu, Y.-L. A unified theory for bubble dynamics. *Phys. Fluids* **2023**, *35*, 033323. [CrossRef]
46. Abu-Nab, A.K.; Hakami, A.M.; Abu-Bakr, A.F. Charged Cavitation Multibubbles Dynamics Model: Growth Process. *Mathematics* **2024**, *12*, 569. [CrossRef]
47. Cao, P.; Hao, C.; Li, B.; Jiang, H.; Liu, Y. Effect of ruptured cavitated bubble cluster on the extent of the cell deformation by ultrasound. *Ultrason. Sonochemistry* **2021**, *80*, 105843. [CrossRef]
48. Pavlenko, A. Self-preservation Effect of Gas Hydrates. *Rocznik Ochrona Środowiska* **2021**, *23*, 346–355. [CrossRef]
49. Pavlenko, A. Numerical Modeling of the Behavior of Bubble Clusters in Cavitation Processes. *Energies* **2024**, *17*, 1741. [CrossRef]
50. Zhang, L.; Chen, W.; Shen, Y.; Wu, Y.; Zhao, G. The nonlinear characteristics of the pulsations, translations and the secondary Bjerknes force. *Chaos Solitons Fractals* **2021**, *152*, 111322. [CrossRef]
51. Wu, Y.; Lei, Z.; Liu, R.; Wang, C. The oscillations of non-spherical bubbles in liquid. *Ultrason. Sonochemistry* **2025**, *114*, 107262. [CrossRef]
52. Fuster, D.; Colonius, T. Modelling bubble clusters in compressible liquids. *J. Fluid Mech.* **2011**, *688*, 352–389. [CrossRef]
53. Nguyen, V.T.; Phan, T.H.; Park, S.H.; Trong-Nguyen, D.; Quang-Thai, N.; Warn-Gyu, P. Numerical study of shock waves and supersonic jets triggered by cavitation bubble collapse in different pressurized ambiences. *J. Mech. Sci. Technol.* **2024**, *38*, 4167–4173. [CrossRef]
54. Singhal, A.K.; Athavale, M.M.; Li, H.; Jiang, Y. Mathematical Basis and Validation of the Full Cavitation Model. *ASME J. Fluids Eng.* **2002**, *124*, 617–624. [CrossRef]
55. Lester, T.; Kyungjun, C.; Hyunji, K.; Chongam, K. Generalized physics-based cavitation model encompassing multiple cavitation regimes. *Int. J. Heat Mass Transf.* **2025**, *244*, 126898. [CrossRef]
56. Pavlenko, A.M.; Koshlak, H. Application of Thermal and Cavitation Effects for Heat and Mass Transfer Process Intensification in Multicomponent Liquid Media. *Energies* **2021**, *14*, 7996. [CrossRef]
57. Pavlenko, A. Dispersed phase breakup in boiling of emulsion. *Heat Transf. Res.* **2018**, *49*, 633–641. [CrossRef]
58. Pavlenko, A.M.; Koshlak, H. Intensification of Gas Hydrate Formation Processes by Renewal of Interfacial Area between Phases. *Energies* **2021**, *14*, 5912. [CrossRef]
59. Pavlenko, A. Analysis of Methods for Intensifying Heat and Mass Transfer in Liquid Media. *Energies* **2025**, *18*, 1419. [CrossRef]
60. Zhang, X.; Li, F.; Wang, C.; Mo, R.; Hu, J.; Guo, J.; Lin, S. Effects of translational motion on the Bjerknes forces of bubbles activated by strong acoustic waves. *Ultrasonics* **2022**, *126*, 106809. [CrossRef]
61. Radchenko, M.; Radchenko, A.; Trushliakov, E.; Pavlenko, A.; Radchenko, R. Advanced Method of Variable Refrigerant Flow (VRF) Systems Designing to Forecast On-Site Operation—Part 1: General Approaches and Criteria. *Energies* **2023**, *16*, 1381. [CrossRef]
62. Margulis, I.M.; Polovinkin, V.N.; Yashin, A.I. Modern Approaches to the Description of the Dynamics of Cavitation Bubbles and Cavitation Clouds. *Tech. Phys. Lett.* **2024**, *50*, 276–281. [CrossRef]
63. Radchenko, M.; Radchenko, A.; Trushliakov, E.; Koshlak, H.; Radchenko, R. Advanced Method of Variable Refrigerant Flow (VRF) Systems Designing to Forecast Onsite Operation—Part 2: Phenomenological Simulation to Recoup Refrigeration Energy. *Energies* **2023**, *16*, 1922. [CrossRef]
64. Deng, J.; Huang, T.; Zhu, L.; Pan, L.; Sun, W.; Zhang, L.; Ma, Z. Study on bubble growth interphase heat transfer of rapid decompression. *Prog. Nucl. Energy* **2025**, *180*, 105578. [CrossRef]
65. Jukanti, V.G.; Srinivasan, V. Modeling the chaotic dynamics of bubble growth under hydrodynamic interactions in pool boiling. *Int. J. Heat Mass Transf.* **2024**, *234*, 126114. [CrossRef]

66. Yan, S.; Chen, Y.; Lyu, K.; Qin, H.; Zhang, A.-M.; Li, S. Numerical and experimental benchmark study of nonspherical cavitation bubble dynamics near a rigid wall. *Appl. Ocean Res.* **2025**, *154*, 104423. [CrossRef]
67. Sun, T.; Zhang, X.; Zhang, J.; Wang, C. Experimental Study on the Unsteady Natural Cloud Cavities: Influence of Cavitation Number on Cavity Evolution and Pressure Pulsations. *J. Mar. Sci. Eng.* **2021**, *9*, 487. [CrossRef]
68. Mnich, D.; Reuter, F.; Denner, F.; Ohl, C.-D. Single cavitation bubble dynamics in a stagnation flow. *J. Fluid Mech.* **2024**, *979*, A18. [CrossRef]
69. Kansal, D.; Gururani, P.; Joshi, N.C.; Gaurav, P.; Avnish, C. A Comprehensive Review on Utilization of Cavitation Technology for Industrial Waste Water Treatment: A Step Toward Sustainability. *Water Air Soil Pollut.* **2025**, *236*, 438. [CrossRef]
70. Yogesh, P.; Shirish, H.S.; Perugu, S.; Xun, S.; Sivakumar, M. Hybrid hydrodynamic cavitation (HC) technique for the treatment and disinfection of lake water. *Ultrason. Sonochemistry* **2023**, *97*, 106454. [CrossRef] [PubMed]

Disclaimer/Publisher's Note: The statements, opinions and data contained in all publications are solely those of the individual author(s) and contributor(s) and not of MDPI and/or the editor(s). MDPI and/or the editor(s) disclaim responsibility for any injury to people or property resulting from any ideas, methods, instructions or products referred to in the content.

energies

MDPI

Article

Numerical Analysis of the Flow Downstream of the Exhaust Nozzle of a Miniature Turbojet Engine During Co-Combustion of Kerosene and Hydrogen

Łukasz Brodzik [1,*], Bartosz Ciupek [1,*], Grigore Cican [2,3], Łukasz Semkło [1] and Dominik Schroeder [4]

[1] Faculty of Environmental Engineering and Energy, Institute of Thermal Energy, Poznan University of Technology, 5 M. Sklodowska-Curie Square, 60-965 Poznan, Poland; lukasz.semklo@put.poznan.pl
[2] Faculty of Aerospace Engineering, National University of Science and Technology Politehnica Bucharest, 1–7 Polizu Street, District 1, 011061 Bucharest, Romania; grigore.cican@upb.ro
[3] National Research and Development Institute for Gas Turbines COMOTI, 220D Iuliu Maniu Boulevard, 061126 Bucharest, Romania
[4] Faculty of Environmental Engineering and Energy, Poznan University of Technology, 5 M. Sklodowska-Curie Square, 60-965 Poznan, Poland; dominik.schroeder@student.put.poznan.pl
* Correspondence: lukasz.brodzik@put.poznan.pl (Ł.B.); bartosz.ciupek@put.poznan.pl (B.C.)

Abstract

Research related to the use of hydrogen is crucial because it can be a significant factor in reducing exhaust emissions into the environment. This work represents the second stage of research related to the analysis of exhaust gases from a miniature GTM 400 MOD turbojet engine. Based on the parameters obtained in the experiment, a numerical study of the flow downstream of the exhaust nozzle was performed in ANSYS software (version R1, 2025). The main goal of the calculations was to obtain the temperature distribution and compare the values at checkpoints where actual measurements were taken. The study was conducted in two stages. In the first stage, the engine operated conventionally, burning kerosene. In the second stage, co-combustion of kerosene and hydrogen occurred in the engine. The numerical analysis enabled the visualization of the flow phenomenon for these stages within the considered rotational speeds. The analysis examined flow in domains where the gap was included and excluded. This gap was created by the different diameters of the container opening and the engine nozzle outlet. The study showed that ignoring the gap allows for temperatures closer to the experimental values. Results deemed satisfactory were less likely to be found in vortex areas, but more likely in areas closer to the container walls and the engine exhaust stream itself. The results of the conducted tests showed that the Root Mean Square Error RMSE was within the range of 9.5–22.8% relative to the average temperature values obtained from experimental measurements. The highest turbulence intensity occurred for hydrogen co-combustion at a higher rotational speed, reaching 284% for Variant 2 and 300% for Variant 1. The largest standard deviation for both fuel types at a distance of 0.083 m from the container wall was 68.5 K for variant 2 and 76 K for variant 1. At a distance of 0.166 m from the container wall, the deviation was 76 K for variant 2 and 83.8 K for variant 1.

Keywords: co-combustion; hydrogen; numerical analysis; turbojet engine; CFD; combustion diagnostics; RANS

1. Introduction

Engine research is currently one of the most important fields of study in the development of aviation technology. This involves continuous engine improvement, as well as its optimization in terms of fuel composition changes and the possible future use of alternative fuels, such as hydrogen. Such research can result in newly observed phenomena, which may lead to new design solutions. The existence of these phenomena can be proven primarily experimentally, but also using modern mathematical tools that solve the scientific problem through approximation, depending on the model used.

The integration of pressure gain combustion into aeroengine systems has gained increasing attention as a promising pathway to significantly enhance thermal efficiency. In this context, the study by Varatharajulu and Stathopoulos [1] presents a thermodynamic and exergy-based comparison of turbojet and turbofan engines equipped with a Rotating Detonation Combustor (RDC). Although their findings confirm potential performance benefits, the analysis relies on simplified cycle modeling and does not consider the complex flow interactions downstream of the nozzle, leaving unresolved questions regarding exhaust dynamics and structural loading.

In pursuit of alternatives to complex vectoring systems for Short Take-Off and Landing STOL applications, Zhang et al. [2] demonstrated the potential of a bypass dual throat nozzle with a bending transition duct. While their results highlight thrust vectoring feasibility, the absence of structural and unsteady flow assessments limits understanding of how such concepts would affect nozzle outlet turbulence and long-term operability. Similarly, Meng et al. [3] investigated serpentine-configured multi-stream supersonic nozzles, identifying stealth advantages at the expense of thrust. However, the lack of experimental validation or optimization studies leaves a gap in understanding how such flow distortions translate to thermomechanical impacts on nozzle walls.

Ensuring stable combustion under unconventional conditions was addressed by He et al. [4], who examined water injection in Turbine-Based Combined Cycle TBCC engines. Their combined experimental and numerical study shows improved stability, but the research remains restricted to specific regimes and does not explore how altered exhaust properties propagate through downstream nozzle sections. In parallel, Aygun et al. [5] compare metaheuristic optimization strategies for small turbojet cycles, revealing trade-offs in thrust and fuel consumption. However, these optimizations assume idealized operation, neglecting secondary effects such as structural loads or turbulent mixing in exhaust jets.

Efforts to integrate hydrogen into aviation fuels have also exposed critical challenges. Niszczota and Gieras [6] demonstrated that hydrogen inlet injection can reduce CO_2 emissions but increases NO_x formation, while long-term nozzle durability remains unaddressed. Ayaz et al. [7] provide comparative insights into kerosene, diesel, and JP-4, identifying environmental trade-offs but without assessing how fuel chemistry alters exhaust flow and structural constraints. At the combustor level, Kang et al. [8] proposed a combined injection scheme that improves detonation efficiency but also increases pulsating exhaust pressures, which could amplify nozzle thermal and mechanical stresses, yet this aspect is not explicitly analyzed.

The off-design behavior of micro gas turbines has been studied by Wu et al. [9], who achieved improved accuracy with corrected maps. While effective for performance prediction, their method does not provide detailed flow-field resolution at the nozzle exit. Zhang et al. [10] further contributed with a multi-modal combustor design, but their system-level simulations lack downstream validation, limiting their applicability for nozzle thermomechanical studies. Xu et al. [11] introduced a rotor-motion-coupled CFD framework, reducing prediction errors under crosswind conditions, but its high computational cost constrains systematic nozzle load assessments under fuel variation.

https://doi.org/10.3390/en19040938

On the broader energy landscape, Boretti [12] emphasizes hydrogen's potential in aviation while acknowledging persistent barriers, particularly in combustion stability and NO_x mitigation. Yet, as highlighted, much of the literature remains conceptual, with limited integration of fuel chemistry effects on exhaust nozzle flow, temperature fields, and material stresses.

Addressing these gaps more directly, Brodzik et al. [13] conducted a detailed thermomechanical analysis of the GTM 400 MOD turbojet nozzle operating on kerosene and kerosene–hydrogen co-combustion, supported by coupled CFD/FEM modeling. Their results confirmed that hydrogen addition did not significantly increase nozzle wall temperature or deformation, with peak temperatures below 1100 K and stresses remaining within the material yield limit. These values are consistent with the present findings for comparable engine speeds, indicating that the temperature rise induced by hydrogen enrichment is moderate and does not exceed thermal safety margins. However, Brodzik et al. [13] focused primarily on structural aspects, without analyzing the spatial evolution of the exhaust flow field beyond the nozzle exit.

Bogoi et al. [14] offered complementary insight into flow and acoustic behavior in micro turbojet exhausts using chevron and ejector nozzles. Their Schlieren imaging revealed strong local gradients and vortex formation near the nozzle exit, corresponding to flow structures similar to those observed in the present numerical results. Nevertheless, their work addressed noise attenuation rather than thermal or pressure field coupling, leaving the thermofluid interaction effects unexplored.

Related experimental investigations by Catana and Badea [15] demonstrated that variations in exhaust nozzle geometry significantly affect the operating line and thrust characteristics of gas turbine engines, indirectly confirming the strong sensitivity of downstream flow structures to geometric modifications. However, their analysis focused on global performance parameters and did not resolve local temperature or turbulence distributions in the exhaust region.

Similarly, Villarreal-Valderrama et al. [16] investigated thrust augmentation through a variable exhaust nozzle using active disturbance rejection control, showing that controlled nozzle geometry variations can strongly influence engine thrust and stability. While their results highlighted the dynamic coupling between nozzle configuration and engine performance, detailed thermofluid field analysis downstream of the nozzle was beyond the scope of their study.

In contrast, the present work explicitly quantifies temperature, pressure, and turbulence fields in a confined exhaust environment, thereby complementing these studies by providing spatially resolved thermofluid insight into the effects of exhaust geometry and operating conditions.

Ciupek et al. [17] previously conducted an experimental investigation of the GTM400 MOD turbojet engine operating under kerosene–hydrogen co-combustion, focusing on the measurement of exhaust gas temperature, emission composition (CO_2, CO, NO_x), and thrust variation at two rotational speeds (31,630 rpm and 47,110 rpm). Their results demonstrated a temperature increase proportional to the hydrogen share in the fuel mixture, reaching up to 760 K, and confirmed corresponding reductions in CO_2 and CO emissions alongside an increase in NO_x due to thermal effects. The present study therefore represents the second stage of this research, extending the earlier experimental findings through numerical modeling of the flow downstream of the exhaust nozzle, where pressure distribution, turbulence intensity, and aerodynamic structures were analyzed for the same engine configurations and operating parameters established in [17].

Overall, compared to these studies, the present numerical analysis advances understanding by correlating temperature and pressure field development behind the nozzle

with fuel composition effects, bridging the gap between thermomechanical modeling [13], acoustic investigations [14], and emission-oriented experiments [17].

Taken together, these works underline both the potential and the limitations of current research on alternative fuels and nozzle configurations. Despite recent advances in thermodynamic modeling, cycle optimization, and partial hydrogen integration in aviation propulsion, a significant research gap remains in the field of high-fidelity characterization of flow structures and thermomechanical interactions downstream of miniature turbojet nozzles operating under kerosene–hydrogen co-combustion. Filling this gap is essential for understanding how alternative fuels modify the exhaust-jet behavior of temperature, and turbulence generation factors that directly influence emission control, structural loads, and the durability of next-generation propulsion systems.

A review of the literature indicates that very limited experimental or numerical information exists on the detailed representation of exhaust-jet development behind turbojet nozzles, particularly for engines operating at small scales. Where such studies exist, they typically address conventional kerosene combustion, while comprehensive analyses for kerosene–hydrogen mixtures are absent. This lack of data complicates validation of numerical models and hinders the development of generalized predictive tools for hydrogen-enriched fuels.

In this context, the primary objective of the present study is to clearly characterize the exhaust-flow behavior downstream of a miniature turbojet nozzle operating under kerosene and kerosene–hydrogen co-combustion. The scientific significance of this work lies in its integration of dedicated experimental measurements with validated numerical modeling, enabling a detailed analysis of temperature distribution, total pressure field evolution, and turbulence intensity in regions where no such data have previously been available. By providing this combined framework, the study contributes to establishing a foundation for future development of generalized models describing exhaust-jet structure under alternative-fuel operation.

This work constitutes the second part of a broader research effort devoted to the characterization of the exhaust-gas plume of a miniature turbojet engine and its diagnostic interpretation. While previous studies in the field of turbojet engine combustion diagnostics have primarily focused on radiative heat transfer modeling in combustion environments [18,19] or on advanced non-contact diagnostic techniques applied to engine components and dynamic responses [20]. The present study provides a novel contribution by delivering a quantitative, experimentally validated numerical description of the flow and temperature field downstream of the exhaust nozzle.

The originality of this work lies in bridging the gap between combustion-oriented diagnostics and downstream exhaust analysis by demonstrating that key thermofluid characteristics of the exhaust plume can be accurately reproduced without explicit combustion modeling, using experimentally derived boundary conditions. In this way, the study complements existing combustion diagnostics approaches by extending their applicability to confined exhaust regions, offering new insights that support the validation and refinement of future theoretical and computational models of miniature turbojet engines.

2. Materials and Methods

The numerical analysis was performed using ANSYS Fluent software (version R1, 2025). It was intended to illustrate the exhaust flow in a specially designed container attached to a turbojet engine (Figure 1a). The test stand was equipped with connection points for the temperature measurements (1), an exhaust gas outlet from the engine (2), a GTM400 turbojet engine stand (3), the GTM400 turbojet engine (4), a fuel connection (5), a kerosene tank (6), a hydrogen tank (7) and a fuel mixing and dosing system (8). The

https://doi.org/10.3390/en19040938

probing temperatures stand (Figure 1b) was equipped with thermoelectric temperature sensors type K (1–2), measuring the temperature transversely to the direction of exhaust gas flow (3).

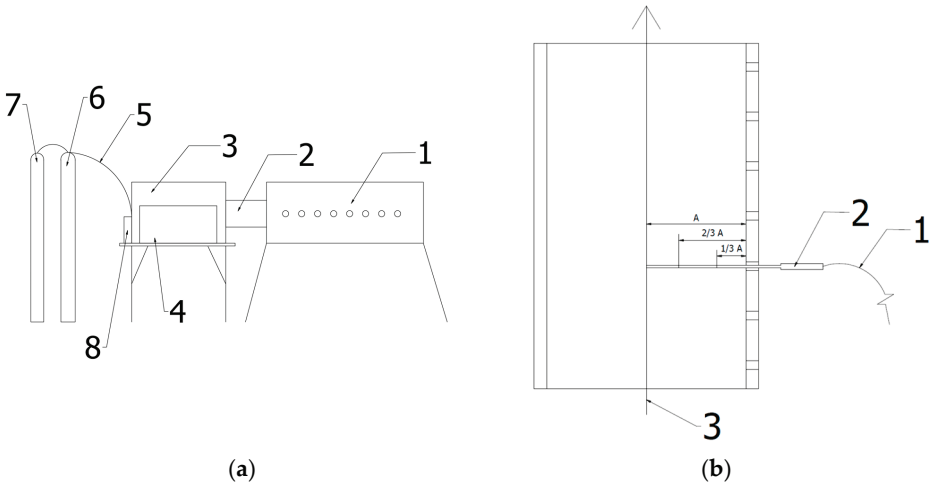


Figure 1. The test stand: (**a**) engine stand with container; (**b**) scheme of probing temperatures in the exhaust gas (A = ±250 mm) [17].

In reality, during the test, the engine was placed in a container whose diameter on the engine side was 0.13 m. In the case of the engine, the nozzle end diameter was 0.12 m. Due to this difference, there was a gap where air could freely flow between the container interior and the test stand environment. Therefore, two calculation variants were adopted in the analysis:

- Variant 1—the existence of a gap related to the difference in the mentioned diameters was taken into account, Figure 2.
- Variant 2—a simplification was applied, consisting of eliminating the gap, then the diameter of the nozzle end cross-section was equal to the diameter of the container.

The container's dimensions for length, width, and height (excluding the stand) were 1 m, 0.496 m, and 0.5 m, respectively. Its outlet was unobstructed. The dimensions of the air-filled space behind the container were 3 m, 1.5 m, and 1.5 m.

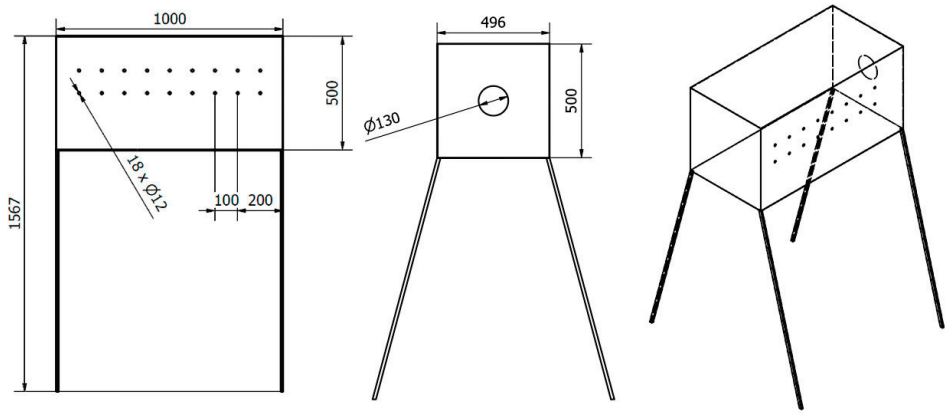


Figure 2. Location of checkpoints in the container [17].

2.1. GTM400 MOD Turbojet Engine

The calculations concern the GTM400 MOD turbojet engine manufactured by JetPol (Poznań, Poland). This is a miniature single-flow engine, modernized to enable combustion of a kerosene–hydrogen mixture in the combustion chamber. The engine specifications are shown in Table 1. Hydrogen supply was provided by a hydrogen system with hydrogen

https://doi.org/10.3390/en19040938

cylinders manufactured by Linde Gaz Polska (Poznań, Poland). The engine uses Jet A-1 kerosene and 99.955% pure hydrogen. The numerical analysis was based on experimental measurements, in which the flow conditions were determined as follows: For the co-combustion of kerosene and hydrogen, the kerosene flow was reduced to 85% each time. At this time, kerosene mass flow rate was 228 mL/min for the lower speed and 306 mL/min for the higher speed. Simultaneously, the hydrogen flow was started, which was 149 L/min for the lower speed and 393 L/min for the higher speed. Hydrogen was injected into the return duct near the inlet to the vaporizers. The engine control panel was responsible for kerosene control. A 2000 SLPM flow regulator from Alicat Scientific (Tucson, AZ, USA) was installed at the gas system outlet. The pressure regulators were designed to reduce the system pressure to 8 bar. The flow regulator was calibrated for this pressure and maintained the highest accuracy there. For pressure and temperature, the accuracy was 0.5% and 0.75 °C, respectively. The measured flux range for this device is 2000 SLPM (standard liters per minute). In this way, after feeding the kerosene and hydrogen mixture, the same rotational speed was achieved as when burning kerosene alone. More detailed data related to the gas system and the engine are described in the literature [17,21]. Initial conclusions regarding engine operation with kerosene–hydrogen co-combustion were also formulated there.

Table 1. The engine specifications.

Parameter	Value
Thrust [N]	15–300
Rotational speed [rpm]	30,000–81,000
Maximum air mass flow [kg/s]	0.59
Maximum fuel consumption [kg/min]	1.03

2.2. Experimental Studies Behind the Nozzle

The numerical simulation was performed based on experimental data presented in Table 2. The measured volumetric flow rate at the nozzle takes into account both the mass of the supplied air and the mass of the fuel burned in the combustion chamber. Tests were performed for two engine speeds: 31,630 rpm and 47,110 rpm. At the lower speed, the kerosene-fueled engine produced 14.7% less thrust than when fueled with kerosene and hydrogen. At the higher speed, the difference was similar, 8.4% less thrust. During engine operation, temperature was measured behind the nozzle using thermoelectric sensors. To measure the flue gas temperature, 18 K-type (NiCr–Ni) thermocouples were used, with a measurement range of 73 K to 1274 K. Based on the calibration of the entire measurement system, the temperature measurement uncertainty in the range of 373 K to 773 K did not exceed $\pm$1.2 K. Temperature measurements were taken in three zones (distances) from the engine nozzle. In each zone, the measurement was taken along the engine's axis of symmetry and closer to the container housing wall. A more precise arrangement of the measurement points, hereinafter referred to as checkpoints, is presented in Figure 2. More detailed information about the experiment is provided in the literature [17].

To confirm the reliability of temperature measurements, all thermocouples were calibrated before the experimental campaign using a certified dry-block temperature calibrator with an accuracy of $\pm$0.5 K and cross-checked against a platinum resistance reference thermometer. Calibration was carried out at three temperature points: 373 K, 573 K, and 773 K, covering the full range expected during testing. Each measurement series was repeated three times under the same conditions to assess repeatability, with variations between repetitions remaining within $\pm$1.2 K. Calibration and verification were performed both

prior to and after the engine tests to ensure sensor stability and to minimize the influence of possible signal drift.

Table 2. Experimental data.

Fuel Type	Kerosene	Kerosene and Hydrogen	Kerosene	Kerosene and Hydrogen
Rotation speed [rpm]	31,630	31,630	47,110	47,110
Mass flow rate [kg/s]	0.151	0.158	0.275	0.333
Temperature in the outlet cross-section of the engine nozzle [K]	650	750	660	760

2.3. Input Data for Numerical Analysis

The engine operated for an extended period at the same speed, fueled with kerosene and hydrogen at constant, set values. Simultaneously, temperature measurements were taken at various checkpoints at the same time. Therefore, the steady flow condition was used for the calculations. Flow modeling requires solving the basic equations of fluid mechanics. The first is the continuity equation:

$$\frac{\partial \rho}{\partial t} + \frac{\partial}{\partial x_i}(\rho \mathrm{v}_i) = 0 \tag{1}$$

where ρ is the fluid density, kg/m^3, t is time, s, and v_i $(i = 1,\ 2,\ 3)$ are velocity vectors in the Cartesian coordinate system, m/s.

The second is the momentum equation:

$$\rho\left(\frac{\partial \mathrm{v}_i}{\partial t} + \mathrm{v}_j \frac{\partial}{\partial x_j}\mathrm{v}_i\right) = \frac{\partial}{\partial x_j}\sigma_{ij} + \rho \mathrm{F}_i \tag{2}$$

where σ_{ij} $(i = 1,\ 2,\ 3),\ \ j = (1,\ 2,\ 3)$ is the stress tensor F_i is the external force, N.

The third is the energy equation:

$$\frac{\partial}{\partial t}(\rho c_p T) + \frac{\partial}{\partial x_i}(\rho c_p T \mathrm{v}_i) = \frac{\partial}{\partial x_i}\left(K \frac{\partial T}{\partial x_i}\right) \tag{3}$$

where c_p is the specific heat, J/(kgK), T is the temperature, K, a K s the thermal conductivity coefficient, W/mK.

Additionally, the real combustion process requires solving the diffusion equation that takes into account the combustion reaction. This formula, in simplified form, is as follows:

$$\frac{\partial c}{\partial t} + \frac{\partial c \mathrm{v}_i}{\partial x_i} = \frac{\partial}{\partial x_i}\left(D \frac{\partial c}{\partial x_i}\right) + R \tag{4}$$

where D is the diffusion coefficient, m^2/s, c is the concentration of the reacting substance, kg/m^3, R is the term describing the combustion reaction, kg/(m^{3}s).

For calculations of real flows, i.e., those that take viscosity into account, RANS (Reynolds Averaged Navier–Stokes) models are used, among others. In such an analysis, the time-averaged Navier–Stokes equations are solved. This simplification shortens the computational time. These models simulate the behavior of disturbed, vortex flow in various ways, often depending on their complexity. The SST k–ω model was used for flow analysis. Using a blending function, it combines the k–ω model near the wall and the k-ε model further from the wall, where free flow occurs. The standard k–ω model and the transformed k-ε model are multiplied by the mixing function and added [13,22]. In this case, the turbulent viscosity accounts for the transport of turbulent shear stress. Combining

https://doi.org/10.3390/en19040938

both models reduces sensitivity to turbulence in the free inlet flow and allows for more versatile calculation options [23,24]. Appropriate calculations in both layers (models) are possible due to the presence of a damped term of the cross-diffusion derivative in the ω equation. The k–ω Shear Stress Transport (SST) model contains two equations [25,26]:

(a) the specific turbulent kinetic energy for k [m^2s^{-2}]

$$\frac{\partial}{\partial t}(\rho k) + \frac{\partial}{\partial x_i}(U_i \rho k) = \frac{\partial}{\partial x_j}\left(\mu_k \frac{\partial}{\partial x_j} k\right) + \overline{P}_k - \beta * \rho \omega k \tag{5}$$

(b) the specific turbulent dissipation rate (also specific turbulent frequency) for ω [s^{-1}]

$$\frac{\partial}{\partial t}(\rho \omega) + \frac{\partial}{\partial x_i}(U_i \rho \omega) = \frac{\partial}{\partial x_j}\left(\mu_\omega \frac{\partial}{\partial x_j} \omega\right) +$$

$$+ P_\omega - \beta \rho \omega^2 + 2\rho(1 - F_1)\frac{1}{\omega}\frac{1}{\sigma_{\omega,2}}\frac{\partial}{\partial x_j} k \frac{\partial}{\partial x_j}\omega \tag{6}$$

where the effective viscosity μ_ω [$kgm^{-1}s^{-1}$]

$$\mu_k = \mu_t \frac{1}{\sigma_k} \tag{7}$$

and the effective viscosity μ_ω [$kgm^{-1}s^{-1}$]

$$\mu_\omega = \mu_t \frac{1}{\sigma_\omega} \tag{8}$$

μ_t is modified eddy (or turbulent) viscosity [$kgm^{-1}s^{-1}$] and σ_k and σ_ω are diffusion constants of the model. P_ω is the rate of production of ω [$kgm^{-3}s^{-2}$] and is given by the equation

$$P_\omega = \gamma \left[2\rho S_{ij} S_{ij} - \frac{2}{3}\rho\omega \left(\frac{\partial}{\partial x_j} U_j \right) \delta_{ij} \right] \tag{9}$$

where δ_{ij} is the Kronecker delta function and γ is a model constant. S_{ij} is the mean rate of deformation component [s^{-1}]

$$S_{ij} = \frac{\tau_{ij}}{2\mu_t} + \frac{1}{3}\frac{\rho k \delta_{ij}}{\mu_t} \tag{10}$$

The first blending function F_1 is given by the equation

$$F_1 = \tanh\left\{ \left[min\left(\max\left(\frac{L_t}{y}; \frac{500 v_t}{y^2 \omega} \right); \frac{4\omega \sigma_{\omega,2} k}{X y^2} \right) \right]^4 \right\} \tag{11}$$

X is the cross-diffusion term [$kgm^{-1}s^{-2}$]

$$X = \max\left(2\rho \frac{1}{\omega}\frac{1}{\sigma_{\omega,2}}\frac{\partial}{\partial x_i} k \frac{\partial}{\partial x_i}\omega; 10^{-10} \right) \tag{12}$$

L_t is turbulent length scale [m]

$$L_t = \frac{\sqrt{k}}{0.09\omega} \tag{13}$$

The function F_1 is equal to 0 outside the boundary layer and equal to 1 inside the boundary layer. Its values depend, among other things, on k i ω.

https://doi.org/10.3390/en19040938

v_t is the kinematic eddy viscosity [m^2s^{-1}]

$$v_t = \frac{\mu_t}{\rho} = \frac{a_1 k}{max(a_1\omega,\ SF_2)} \tag{14}$$

where a_1 is constant, S is the strain norm, and F_2 is the second mixing function

$$F_2 = \tanh\left\{\left[\max\left(\frac{\sqrt{k}}{0.09\omega y};\frac{500v_t}{y^2\omega}\right)\right]^2\right\} \tag{15}$$

In places with large shear gradients, the overestimation of the v_t value limits the expression in the denominator $max(a_1\omega,\ SF_2)$.

$\overline{P}_k$ is the effective rate of production [$kgm^{-1}s^{-3}$]

$$\overline{P}_k = \min(P_k; 10\beta^*\rho k\omega) \tag{16}$$

and prevents the formation of turbulence in stagnation areas, where

$$P_k = 2\mu_t S_{ij}S_{ij} - \frac{2}{3}\rho k\left(\frac{\partial}{\partial x_j}U_i\right)\delta_{ij} \tag{17}$$

According to the above, the specific turbulent kinetic energy k and the specific turbulent dissipation rate ω are coupled to each other via the modified eddy viscosity μ_t, the production P_k and P_ω, the dissipation and the cross-diffusion term. The k-ϵ model constants used in the calculations were $C_{2\epsilon} = 1.9$, TKE $Pr = 1$, TDR $Pr = 1.2$, Energy $Pr = 0.85$, Wall $Pr = 0.85$, where Pr is the Prandtl number.

The energy model was used in the calculations, and thermal radiation was included in the flow. The conservation of the radiative energy along a ray path of direction $\hat{s}$ can be written as

$$\hat{\mathrm{s}}\nabla I(\mathrm{r},\hat{\mathrm{s}}) = -\kappa I(\mathrm{r},\hat{\mathrm{s}}) + \kappa_a n_I^2\frac{\sigma T^4}{\pi} + \frac{\kappa_s}{4\pi}\int_{4\pi} I(\mathrm{r},\hat{\mathrm{s}}')P(\hat{\mathrm{s}}'\cdot\hat{\mathrm{s}})d\omega' \tag{18}$$

where $I(\mathrm{r},\hat{\mathrm{s}})$—radiative intensity at a point with coordinates r ($\mathrm{r}\in\Omega_2$), and direction determined by the unit vector $\hat{\mathrm{s}}$, κ—extinction coefficient, κ_a—coefficient of absorption, κ_s—coefficient of scattering, $P(\hat{\mathrm{s}}'\cdot\hat{\mathrm{s}})$—scattering phase function, n_I—refractive index, $d\omega'$—solid angle.

The radiation equation was solved by approximation, using discrete ordinates. A pressure-based solver was used, and the air density was given a constant. During the analysis, the domain was described by boundary conditions. At the inlet, the experimentally obtained mass flow and temperature were assumed, which, in simplified terms, was equal to the value measured at the closest distance from the nozzle, within the container. Atmospheric pressure of 101,325 Pa and temperature of 300 K were assumed for the slot inlet. The same values were determined at the container outlet. The container walls were assumed to be made of steel, the density of which was 8030 kg/m^3. Air density was 1.225 kg/m^3. Other material properties of the container and air are presented in Table 3. The assumed material properties are assumed and adopted as for 316 steel. The adiabatic condition was used for the outer walls of the container. The numerical analysis undertaken did not take into account the fuel combustion process in a turbojet engine. Therefore, the flow stream studied was a mixture of air, kerosene, and hydrogen. Therefore, the paper does not present any information regarding the composition of the exhaust gases. The analysis was therefore a simplification aimed at reproducing the temperature field downstream of the engine nozzle as faithfully as possible.

https://doi.org/10.3390/en19040938

Table 3. The container material and air properties.

Properties of Steel			
Temperature [K]	**Thermal Conductivity Coefficient [W/(m·K)]**	**Specific Heat at Constant Pressure [J/(kg·K)]**	**Thermal Emissivity Coefficient [-]**
300	16.0	477	0.20
400	17.0	515	0.25
500	18.0	536	0.30
600	18.5	557	0.35
700	19.0	570	0.40
800	19.5	582	0.45
900	20.0	597	0.50
1000	20.5	611	0.55
1100	21.0	626	0.60
Properties of Air			
Temperature [K]	**Thermal Conductivity Coefficient [W/(m·K)]**	**Specific Heat at Constant Pressure [J/(kg·K)]**	
300	0.0263	1005	
400	0.0338	1009	
500	0.0411	1026	
600	0.0469	1047	
700	0.0521	1068	
800	0.0569	1093	
900	0.0613	1114	
1000	0.0654	1135	
1100	0.0691	1156	

An unstructured mesh filled with polyhedral elements was used in the calculations. The number of mesh elements for variant 1 was 815,117, while for variant 2 it was 804,054. These grids were adopted after the validation stage described in the next section. An example mesh is presented in Figure 3. An example parameter for assessing mesh quality, i.e., orthogonal quality, for variant 1 was 0.693, while for variant 2 it was 0.615. These were the minimum values for both parameters. The average y+ value along the container walls was 4.62. The number of layers installed was 5 and the growth rate was 1.15.

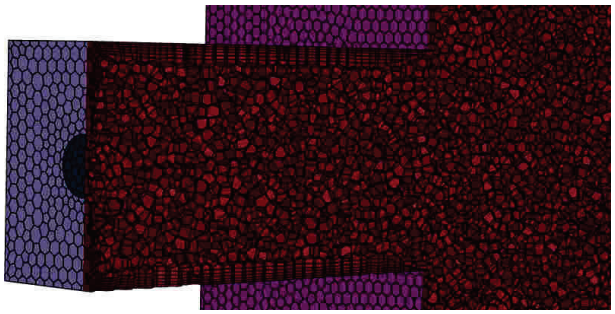


Figure 3. The domain Mesh—Variant 4, close-up of the container area.

3. Domain Validation

Before conducting the main analysis, a model validation was performed based on five sample meshes. The tests included simulations for a test engine operating at 47,110 rpm with a kerosene–hydrogen co-combustion. The domain was constructed according to the assumptions of Variant 2. In this case, its dimensions were as follows:

(a) D-1: container dimensions, i.e., 1 m, 0.496 m, and 0.500 m, variant 2;

https://doi.org/10.3390/en19040938

(b) D-2: container dimensions and the space behind its outlet: 3 m, 1.5 m, 1.5 m, variant 2;
(c) D-3: container dimensions and the space behind its outlet: 4 m, 1.5 m, 1.5 m, variant 2;
(d) D-4: container dimensions and the space behind its outlet: 6 m, 1.5 m, 1.5 m, basic mesh, variant 2;
(e) D-5: container dimensions and the space behind its outlet: 6 m, 1.5 m, 1.5 m, dense mesh, variant 2;
(f) D-6: container dimensions and the space behind its outlet: 6 m, 1.5 m, 1.5 m, basic mesh, variant 1;
(g) D-7: container dimensions, the space behind its outlet: 6 m, 1.5 m, 1.5 m, and the space around the slot 0.5 m long with external limits 1.5 m wide and 1.5 m high, variant 1.

In each case, the dimensions are given in the following order: length, width, and height. Each subsequent case considered involved a more complex computational domain. For variant 2, the domain dimensions were increasingly increased, and in case D-5, additional mesh refinement was performed. The selected parameters for each mesh are presented in Table 4. The minimum orthogonality was not less than 0.51 and the maximum skewness did not exceed 0.489. These values were considered acceptable taking into account the degree of simplification of the domain and boundary conditions. These are also parameters generally considered acceptable or good. An additional analysis involved comparing two models, namely the Realizable k-ε and the SST k–ω. In this case, a domain with 1,031,894 finite volumes was used. The minimum orthogonality was 0.57 and the minimum skewness was 0. The domain consisted of a portion of the container and the space behind the container, each measuring 3 m, 1.5 m, and 1.5 m. The Realizable k-ε model differs from the k-ε model in two respects. First, it provides an alternative formulation for turbulent viscosity. Second, it has a modified transport equation for epsilon dissipation. For these reasons, this model can better simulate regions of highly sheared flow.

Table 4. Selected parameters for mesh evaluation.

	D-1	D-2	D-3	D-4	D-5	D-6	D-7
Orthogonality (min/mean/max)	0.573/ 0.958/1	0.600/ 0.959/1	0.582/ 0.959/1	0.615/ 0.960/1	0.614/ 0.960/0.9999	0.693/ 0.992/1	0.510/ 0.960/1
Skewness (min/mean/max)	1.1×10^{-13}/ 0.041/0.42	1.4×10^{-6} 0.040/0.39	6.4×10^{-6}/ 0.041/0.42	2.7×10^{-6}/ 0.039/0.385	2.7×10^{-6}/ 0.039/0.385	5×10^{-6}/ 0.008/0.307	4.3×10^{-14}/ 0.039/0.489
Number of finite mesh volumes	531,264	640,504	733,907	804,054	1,961,564	815,117	1,098,361
Turbulence intensity	398	274	215	284	284	300	260

The validation of the computational domain was performed based on the determination of the mean absolute error according to the equation

$$MAE = \frac{1}{N}\sum_{i=1}^{N}\left|T_{i'} - \hat{T}_i\right| \quad (19)$$

where N is the number of numbers in the set, $T_{i'}$ is the temperature measured during the experiment at the checkpoint [K], and $\hat{T}_i$ is the temperature calculated during simulation at the checkpoint [K].

The values of mean absolute errors for individual domains were presented in Figure 4.

https://doi.org/10.3390/en19040938

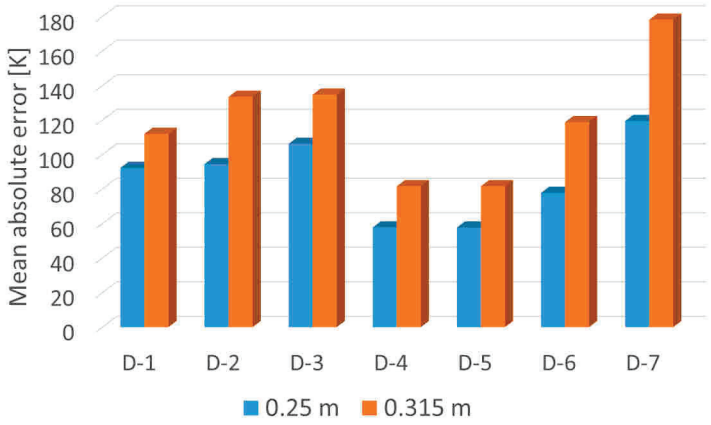


Figure 4. The mean absolute errors for domains, for the two considered measurement heights, a rotational speed of 47,110 rpm and kerosene–hydrogen co-combustion.

The largest errors with respect to experimental values occurred for domain D-1, and the smallest for domain D-4. Of these defined cases, only two were selected for further, more detailed, and fundamental research analysis. For variant 2, increasing the domain size led to increasingly smaller mean absolute errors. In variant 1, the presence of additional space outside the gap (D-7) increased the mean absolute error. It is worth noting that in domain D-3 the turbulence intensity had the lowest value, equal to 215. However, for domain D-4 much larger mean absolute errors occurred. For the domain variant including the gap, an inlet-air pressure inlet with ambient pressure (101,325 Pa) was used. Turbulence was left at the default settings: Turbulent Intensity = 5% and Turbulent Viscousity Ratio = 10. Analysis of the simulations taking into account the gap showed that the separated external area around the gap causes air to be directed into the container during engine operation, Figure 5. The presence of a gap without the external area, but using the inlet condition, does not account for this phenomenon. However, vertical flows are observed from the inside of the gap. Flows with different directions are observed in the corner of the container. In the simulation, both in domain 7 and domain 6, there are no back flows near the gap. A different image of the velocity distribution is presented by the simulation for domain 4. The visible flow directions near the gap are oriented towards the main stream and the container outlet. Ultimately, domains D-4 and D-6 were selected for further calculations. For domains 6 and 7, the first case was selected as variant 1 despite obtaining a higher turbulence intensity value. The reason for this choice was the temperature results, which contained significantly larger errors compared to domain 6.

In the comparison of the SST k–ω and Realizable k-ε models, the same regions were analyzed for Variant 2, i.e., control points at distances of 0.25 m and 0.315 m from the container wall. Calculations were also performed for a speed of 47,110 rpm in the kerosene–hydrogen co-combustion mode. Mean absolute errors were calculated for both regions. In the first case, for the Realizable k-ε model, this error was 93.8 K, which was 20.9 K greater than for the SST k–ω model. In the second case, for the Realizable k-ε model, the error was 122.6 K, which was 38.3 K greater than for the SST k–ω model. The reason for this may be that the Realizable k-ε model predicts temperature distributions in near-wall regions worse. The turbulence intensity for the SST k–ω model was equal to 289, while for the Realizable k-ε it was 280. The analysis results showed that the SST k–ω model better predicted the temperature field and was therefore used in the further part of the study.

https://doi.org/10.3390/en19040938

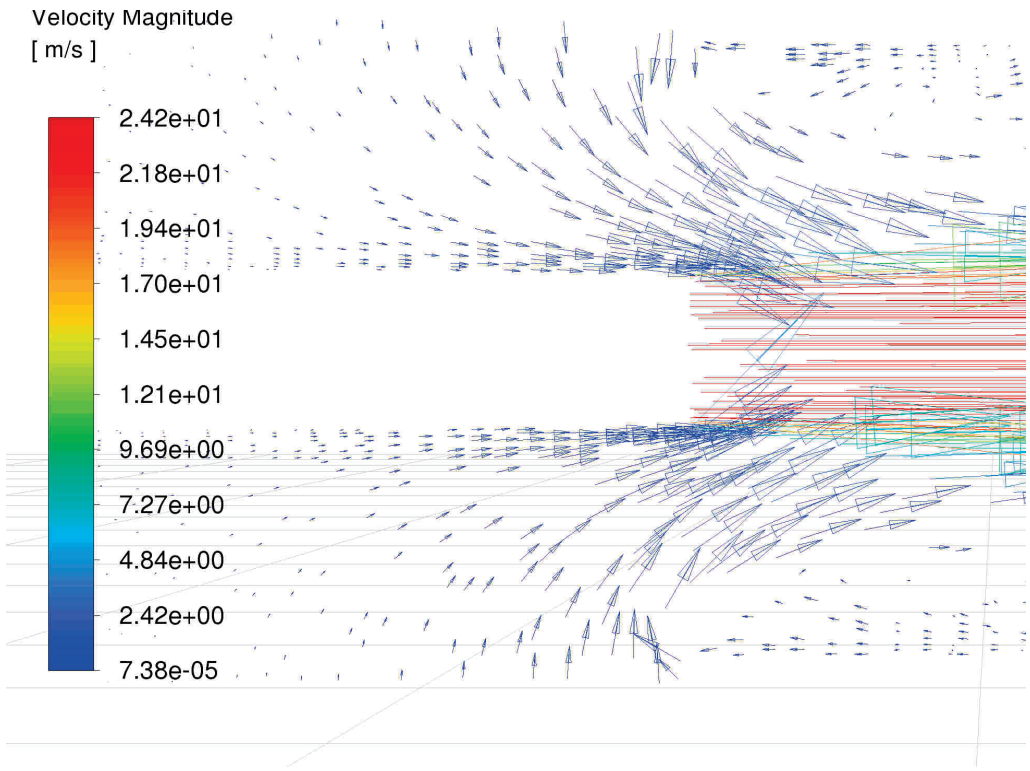


Figure 5. Velocity distribution—domain 7 (variant 1).

4. Results

The analysis of the results included a comparison of experimental measurements and the results of numerical calculations. Considering the two domain variants under consideration, parameters such as total pressure, temperature, and turbulence intensity were analyzed. In each case, speeds of 31,630 rpm and 47,110 rpm were considered, both in the kerosene combustion mode and in the kerosene and hydrogen co-combustion mode. The presented figures of the distributions of selected parameters inside the container primarily concern variant 2, for which the calculation results differed significantly less from the experimental results. This was described in Section 4.4.

4.1. Discussion Related to the Total Pressure Distribution

Combustion of a kerosene and hydrogen mixture generates a smaller area of total pressure with higher values. However, the maximum value is observed for kerosene–hydrogen co-combustion, at 31,630 rpm, at 101,388 Pa. This is an increase of 6 Pa compared to engine operation, where only kerosene is burned. The results for 47,110 rpm present a similar pattern. In this case, however, the gradient values obtained were significantly larger. For kerosene combustion, the maximum total pressure value is 101,515 Pa, while for kerosene–hydrogen co-combustion it is 101,604 Pa. For this rotational speed, the distribution area of this parameter is more similar, although the pressure gradients are stronger. The changes described above concern the domain for variant 2. The total pressure distribution was presented in Figures 6–9.

The results obtained for variant 1 differ significantly from those for variant 2. Including a gap in the domain resulted in increased pressure gradients, primarily in its immediate vicinity. At a speed of 31,630 rpm for kerosene combustion, the total pressure was 101,396 Pa, while for kerosene–hydrogen co-combustion it was 101,404 Pa. At a speed of 47,110 rpm, the total pressure was 101,560 Pa and 101,681 Pa, respectively. Pressure gradients result directly from the increased dynamic pressure. For variant 1, an increase in this parameter

https://doi.org/10.3390/en19040938

was observed for speeds of 31,630 rpm and 47,110 rpm during kerosene combustion by 25.4% and 13.7%, respectively, compared to variant 2. Similarly, for both rotational speeds during kerosene–hydrogen co-combustion, there was an increase of 24.6% and 13.9%.



Figure 6. The total pressure distribution behind the nozzle for a speed of 31,630 rpm during kerosene combustion.



Figure 7. The total pressure distribution behind the nozzle for a speed of 31,630 rpm during kerosene and hydrogen combustion.



Figure 8. The total pressure distribution behind the nozzle for a speed of 47,110 rpm during kerosene combustion.



Figure 9. The total pressure distribution behind the nozzle for a speed of 47,110 rpm during kerosene and hydrogen combustion.

4.2. Discussion Related to Temperature Distribution

The shape and pattern of temperature gradient for both analysis variants are similar. The temperature field for variant 2 is presented in Figures 10–13. However, the simulation showed that including the gap in the calculations leads to a significant temperature drop at the checkpoints. The maximum temperature for both variants, however, was the same. For the lower speed and kerosene combustion, it was 650 K, and for kerosene and hydrogen combustion, it was 750 K. For the higher speed and kerosene combustion, the temperature was 660 K, and for kerosene and hydrogen combustion, it was 760 K.

The analysis showed that in both variants, there are checkpoints where the temperature differs only slightly or not at all from the experimentally measured values. There are also points where the temperature gradients were very large. Examining the area halfway up the container at a speed of 31,630 rpm, larger temperature gradients appear much more frequently during kerosene–hydrogen co-combustion for both variants considered. A complete temperature comparison for this case was presented in Table 5.

Table 5. The temperature comparison at altitude checkpoints (0.25 m container height) for a rotational speed of 31,630 rpm.

Distance from Side Wall [m]	Distance from the Nozzle [m]	Temperature Obtained from the Kerosene Experiment [K]	Temperature Obtained from the Simulation for Kerosene [K]—Variant 2	Temperature Obtained from the Simulation for Kerosene [K]—Variant 1	Temperature Obtained from the Experiment for Kerosene and Hydrogen [K]	Temperature Obtained from the Simulation for Kerosene and Hydrogen [K]—Variant 2	Temperature Obtained from the Simulation for Kerosene and Hydrogen [K]—Variant 1
0	0.1	387	385	370	461	418	424
	0.2	-	386	375	440	420	428
	0.3	378	387	371	375	422	429
	0.4	393	387	374	467	422	426
	0.5	-	417	400	445	453	438
	0.6	384	422	403	432	461	428

Table 5. *Cont.*

Distance from Side Wall [m]	Distance from the Nozzle [m]	Temperature Obtained from the Kerosene Experiment [K]	Temperature Obtained from the Simulation for Kerosene [K]—Variant 2	Temperature Obtained from the Simulation for Kerosene [K]—Variant 1	Temperature Obtained from the Experiment for Kerosene and Hydrogen [K]	Temperature Obtained from the Simulation for Kerosene and Hydrogen [K]—Variant 2	Temperature Obtained from the Simulation for Kerosene and Hydrogen [K]—Variant 1
0.083	0.1	519	392	363	521	423	398
	0.2	-	392	370	508	422	402
	0.3	457	397	377	466	430	407
	0.4	498	412	390	549	447	419
	0.5	-	430	404	529	469	430
	0.6	423	441	418	474	484	447
0.166	0.1	681	517	460	572	582	519
	0.2	-	496	432	569	558	476
	0.3	681	478	444	564	534	492
	0.4	540	495	463	548	556	518
	0.5	-	527	504	557	597	516
	0.6	534	497	496	560	557	569
0.249	0.1	636	649	649	747	749	749
	0.2	-	645	646	747	744	745
	0.3	647	641	632	749	738	728
	0.4	579	634	616	629	730	709
	0.5	-	625	602	633	718	693
	0.6	566	618	591	636	710	678

The results are similar for a speed of 47,110 rpm. For this case, the full temperature summary was provided in Table 6. For both the lower and higher speeds, the solution approximated using variant 2 proved to be closer to the actual measured results.

Table 6. The temperature comparison at altitude checkpoints (0.25 m container height) for a rotational speed of 47,110 rpm.

Distance from Side Wall [m]	Distance from the Nozzle [m]	Temperature Obtained from the Kerosene Experiment [K]	Temperature Obtained from the Simulation for Kerosene [K]—Variant 2	Temperature Obtained from the Simulation for Kerosene [K]—Variant 1	Temperature Obtained from the Experiment for Kerosene and Hydrogen [K]	Temperature Obtained from the Simulation for Kerosene and Hydrogen [K]—Variant 2	Temperature Obtained from the Simulation for Kerosene and Hydrogen [K]—Variant 1
0	0.1	442	376	351	484	403	373
	0.2	-	379	361	433	404	394
	0.3	393	383	365	396	409	391
	0.4	420	388	362	486	414	392
	0.5	-	418	364	460	450	417
	0.6	398	421	394	439	454	417

https://doi.org/10.3390/en19040938

Table 6. *Cont.*

Distance from Side Wall [m]	Distance from the Nozzle [m]	Temperature Obtained from the Kerosene Experiment [K]	Temperature Obtained from the Simulation for Kerosene [K]—Variant 2	Temperature Obtained from the Simulation for Kerosene [K]—Variant 1	Temperature Obtained from the Experiment for Kerosene and Hydrogen [K]	Temperature Obtained from the Simulation for Kerosene and Hydrogen [K]—Variant 2	Temperature Obtained from the Simulation for Kerosene and Hydrogen [K]—Variant 1
0.083	0.1	675	386	351	561	410	372
	0.2	-	389	357	550	413	386
	0.3	538	400	365	489	427	386
	0.4	542	418	374	536	449	412
	0.5	-	459	379	529	464	426
	0.6	520	438	407	489	475	442
0.166	0.1	661	517	460	668	578	511
	0.2	-	492	432	616	545	469
	0.3	692	470	443	608	517	491
	0.4	551	490	467	640	543	507
	0.5	-	525	461	578	588	511
	0.6	565	494	507	576	548	561
0.249	0.1	665	659	659	761	759	759
	0.2	-	655	656	761	754	755
	0.3	650	651	642	770	748	738
	0.4	567	643	626	649	739	717
	0.5	-	635	612	655	729	699
	0.6	576	628	601	650	720	686

Comparing the results at the control points in the upper plane (0.315 m), both for lower and higher speeds, they are similar to those at the midpoint of the container. All temperatures were presented in Tables 7 and 8.

Table 7. The temperature comparison at altitude checkpoints (0.315 m container height) for a rotational speed of 31,630 rpm.

Distance from Side Wall [m]	Distance from the Nozzle [m]	Temperature Obtained from the Kerosene Experiment [K]	Temperature Obtained from the Simulation for Kerosene [K]—Variant 2	Temperature Obtained from the Simulation for Kerosene [K]—Variant 1	Temperature Obtained from the Experiment for Kerosene and Hydrogen [K]	Temperature Obtained from the Simulation for Kerosene and Hydrogen [K]—Variant 2	Temperature Obtained from the Simulation for Kerosene and Hydrogen [K]—Variant 1
0	0.1	366	384	376	438	416	419
	0.2	-	393	348	425	428	429
	0.3	360	396	374	381	432	434
	0.4	362	401	379	435	435	434
	0.5	-	415	397	422	452	423
	0.6	357	416	399	426	453	419

Table 7. *Cont.*

Distance from Side Wall [m]	Distance from the Nozzle [m]	Temperature Obtained from the Kerosene Experiment [K]	Temperature Obtained from the Simulation for Kerosene [K]—Variant 2	Temperature Obtained from the Simulation for Kerosene [K]—Variant 1	Temperature Obtained from the Experiment for Kerosene and Hydrogen [K]	Temperature Obtained from the Simulation for Kerosene and Hydrogen [K]—Variant 2	Temperature Obtained from the Simulation for Kerosene and Hydrogen [K]—Variant 1
0.083	0.1	512	395	375	482	424	392
	0.2	-	405	381	473	438	402
	0.3	419	409	382	441	445	414
	0.4	456	416	390	479	452	419
	0.5	-	428	405	470	467	430
	0.6	398	435	410	439	476	433
0.166	0.1	584	407	375	560	439	400
	0.2	-	444	387	544	487	413
	0.3	587	439	425	533	480	458
	0.4	496	472	429	542	524	469
	0.5	-	466	436	534	516	482
	0.6	474	476	454	528	529	504
0.249	0.1	582	555	516	640	630	559
	0.2	-	527	519	637	594	593
	0.3	583	576	488	638	657	595
	0.4	535	524	496	516	590	557
	0.5	-	546	525	507	618	564
	0.6	536	544	504	505	615	600

The largest differences between the calculated and measured values at the same points occur at a distance of 0.083 m and 0.166 m. This applies to both considered analysis variants.

Table 8. The temperature comparison at altitude checkpoints (0.315 m container height) for a rotational speed of 47,110 rpm.

Distance from Side Wall [m]	Distance from the Nozzle [m]	Temperature Obtained from the Kerosene Experiment [K]	Temperature Obtained from the Simulation for Kerosene [K]—Variant 2	Temperature Obtained from the Simulation for Kerosene [K]—Variant 1	Temperature Obtained from the Experiment for Kerosene and Hydrogen [K]	Temperature Obtained from the Simulation for Kerosene and Hydrogen [K]—Variant 2	Temperature Obtained from the Simulation for Kerosene and Hydrogen [K]—Variant 1
0	0.1	409	374	368	469	396	386
	0.2	-	396	371	444	425	406
	0.3	370	396	369	416	424	401
	0.4	392	406	364	461	437	399
	0.5	-	414	385	437	445	408
	0.6	365	414	388	416	445	409

Table 8. *Cont.*

Distance from Side Wall [m]	Distance from the Nozzle [m]	Temperature Obtained from the Kerosene Experiment [K]	Temperature Obtained from the Simulation for Kerosene [K]—Variant 2	Temperature Obtained from the Simulation for Kerosene [K]—Variant 1	Temperature Obtained from the Experiment for Kerosene and Hydrogen [K]	Temperature Obtained from the Simulation for Kerosene and Hydrogen [K]—Variant 2	Temperature Obtained from the Simulation for Kerosene and Hydrogen [K]—Variant 1
0.083	0.1	585	395	365	551	420	388
	0.2	-	403	373	537	431	401
	0.3	543	409	377	472	438	400
	0.4	504	416	377	511	447	417
	0.5	-	426	392	504	459	423
	0.6	467	431	398	463	466	428
0.166	0.1	586	402	364	687	430	385
	0.2	-	441	379	608	480	409
	0.3	596	436	409	597	473	457
	0.4	537	471	418	623	518	465
	0.5	-	464	428	548	509	473
	0.6	517	475	449	543	523	497
0.249	0.1	583	559	487	682	632	548
	0.2	-	533	518	686	597	582
	0.3	582	584	527	693	663	584
	0.4	529	527	495	608	590	539
	0.5	-	554	500	630	624	548
	0.6	528	551	531	624	620	590

Measurements were not taken at all analyzed locations during the experiment. Therefore, in such cases, the symbol "-" was used in Tables 5–8.

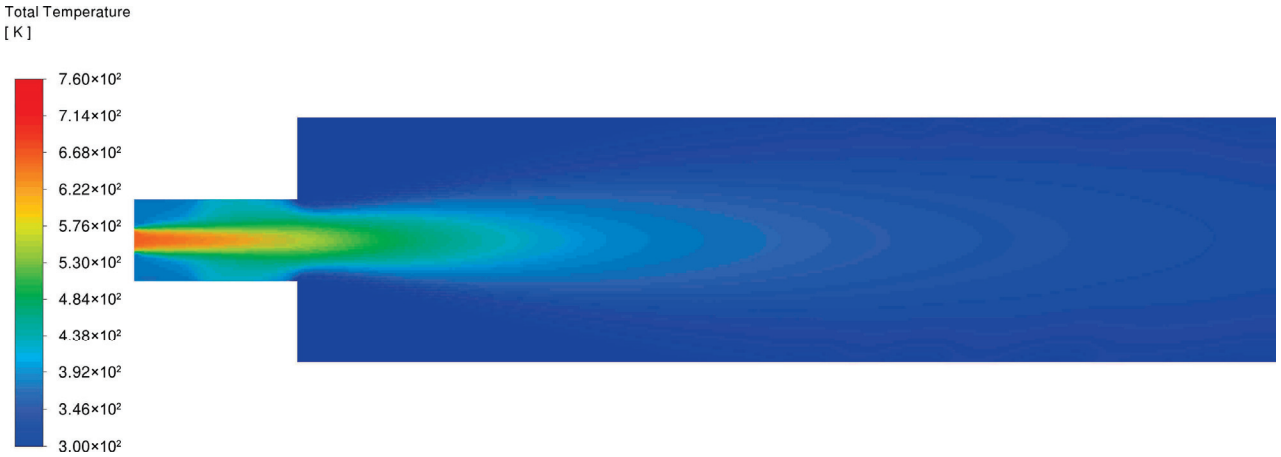


Figure 10. The temperature distribution behind the nozzle for a speed of 31,630 rpm during kerosene combustion.

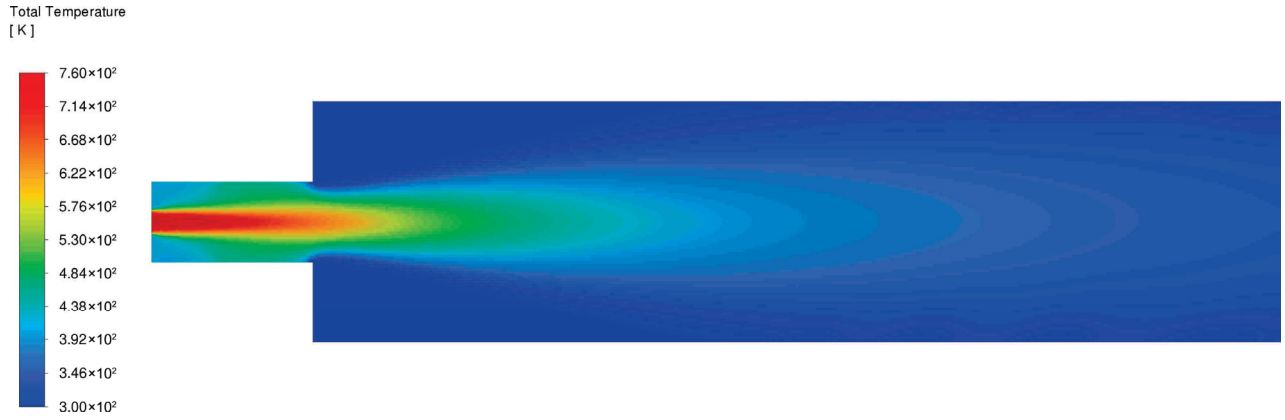


Figure 11. The temperature distribution behind the nozzle for a speed of 31,630 rpm during kerosene and hydrogen combustion.

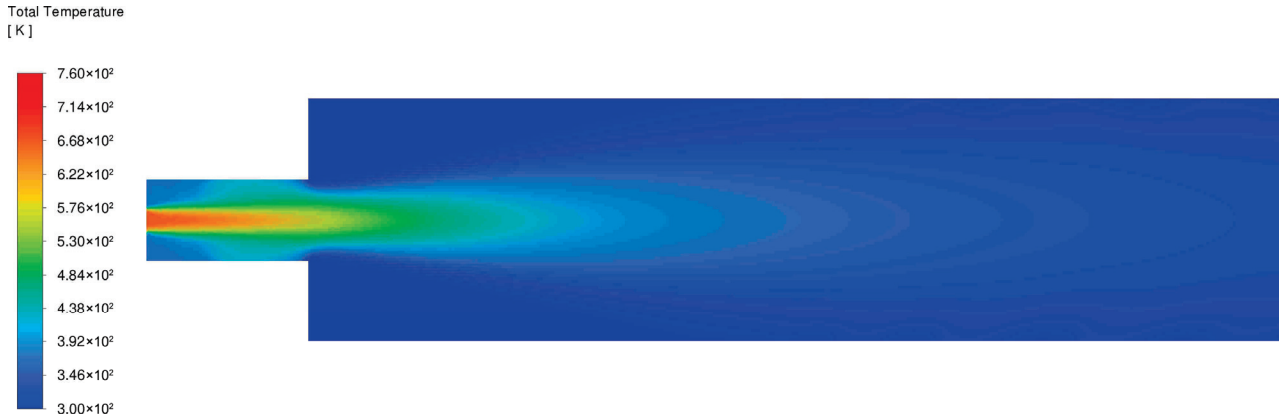


Figure 12. The temperature distribution behind the nozzle for a speed of 47,110 rpm during kerosene combustion.

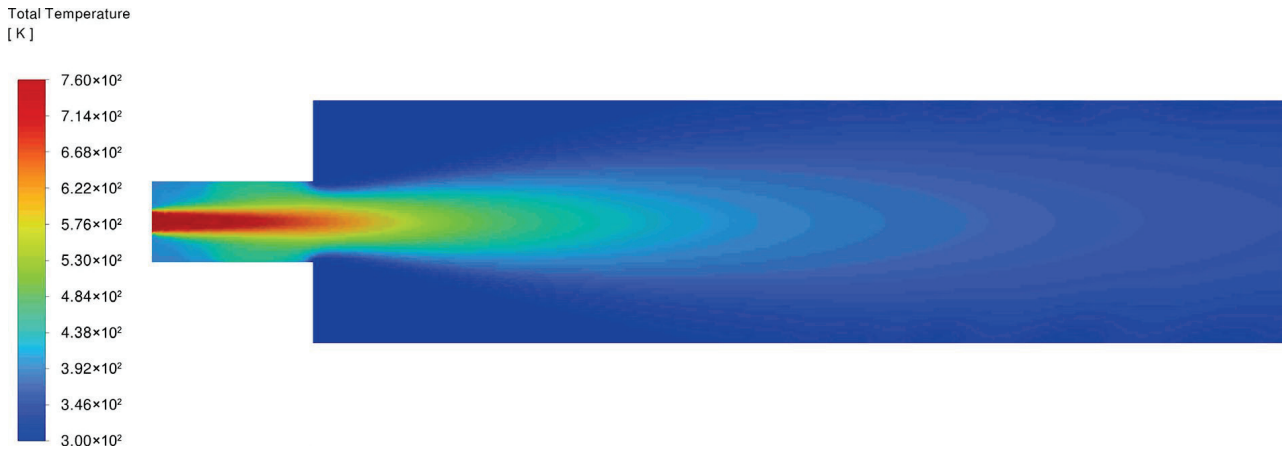


Figure 13. The temperature distribution behind the nozzle for a speed of 47,110 rpm during kerosene and hydrogen combustion.

4.3. Discussion Related to Turbulence Intensity

The next parameter examined in the analysis was turbulence intensity. The distribution field of this parameter for both speeds was presented in Figures 14–17. A turbulence intensity below 1% indicates that the flow exhibits very weak characteristics of disturbed flow. The analysis showed that such a flow occurs near the walls, primarily in the front

https://doi.org/10.3390/en19040938

part of the container, i.e., on the engine nozzle side. This parameter increases slightly in the analysis that includes the gap, i.e., for variant 1.

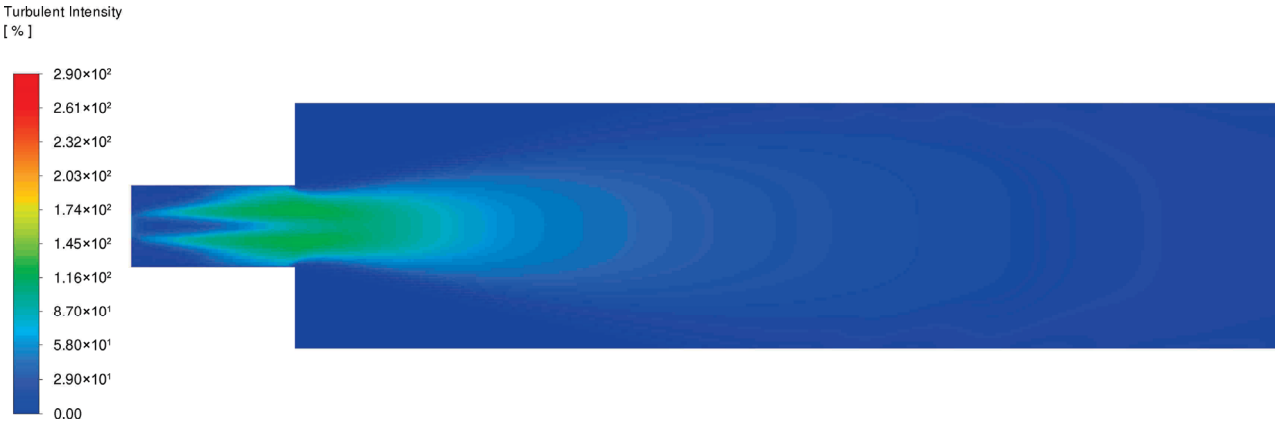


Figure 14. The turbulence intensity distribution behind the nozzle for a speed of 31,630 rpm during kerosene combustion.

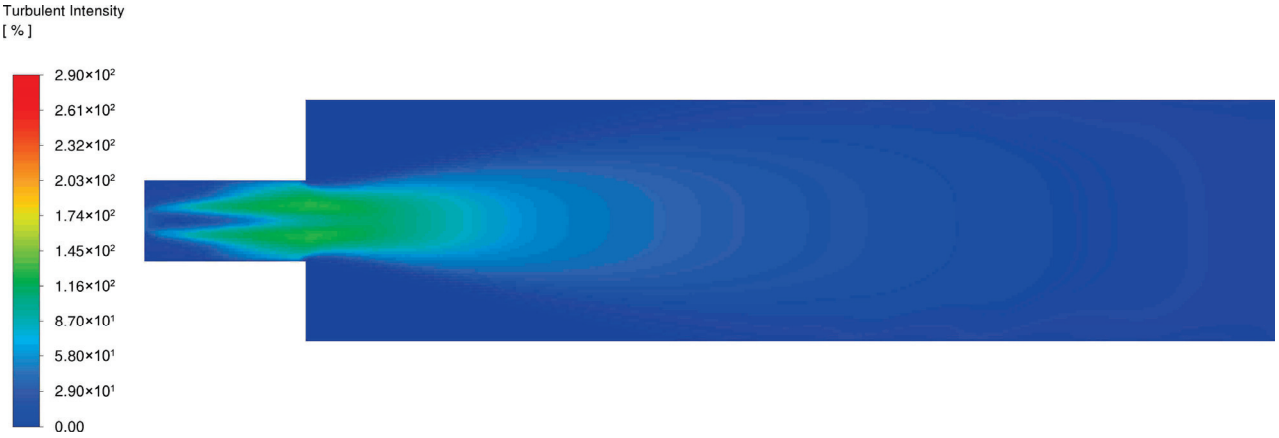


Figure 15. The turbulence intensity distribution behind the nozzle for a speed of 31,630 rpm during kerosene and hydrogen combustion.

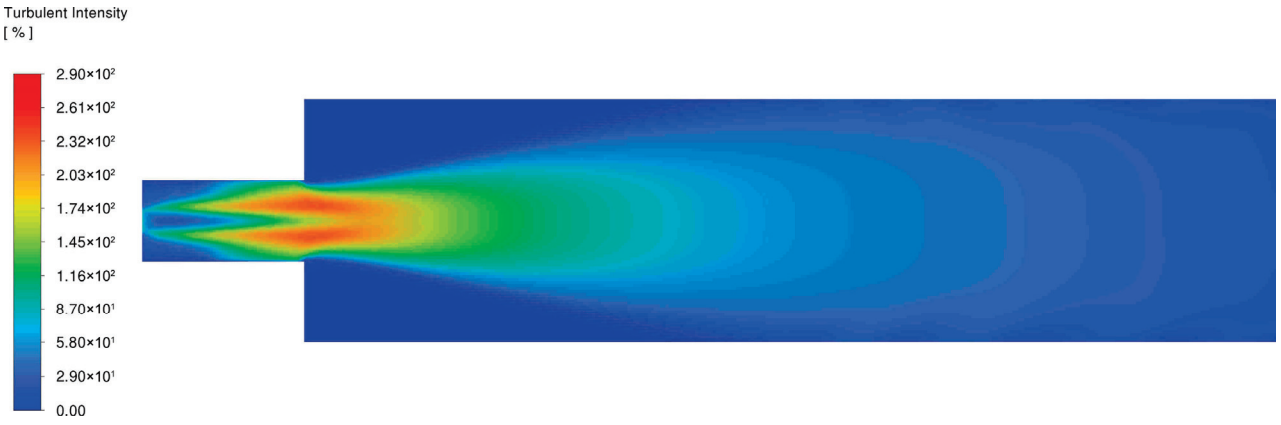


Figure 16. The turbulence intensity distribution behind the nozzle for a speed of 47,110 rpm during kerosene combustion.

The maximum turbulence intensity in analysis variant 1 at a speed of 31,630 rpm during kerosene combustion was 136% and for kerosene–hydrogen co-combustion 140%. For higher rotational speeds, this parameter was 244% for kerosene combustion and 300%

https://doi.org/10.3390/en19040938

for kerosene–hydrogen co-combustion. For analysis variant 2 at a lower speed, the turbulence intensity was 130% for kerosene combustion and 136% for kerosene–hydrogen co-combustion. For higher speeds, this parameter was 235% and 284%, respectively. Therefore, the use of the domain in variant 2 resulted in a decrease in this parameter for the lower and higher speeds in the case of using kerosene by 6% and 9%. Similarly, for the kerosene–hydrogen co-combustion, a decrease of 4% and 16% occurred, respectively.

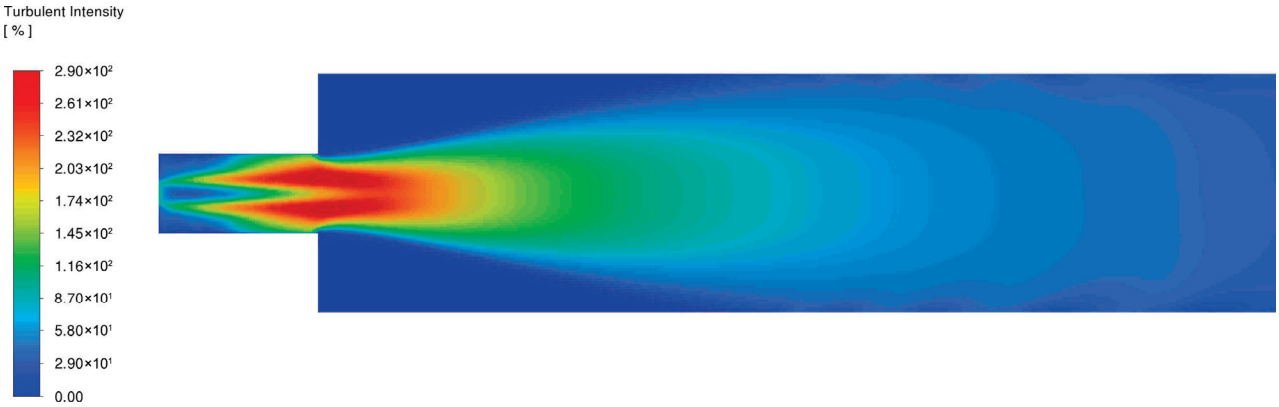


Figure 17. The turbulence intensity distribution behind the nozzle for a speed of 47,110 rpm during kerosene and hydrogen combustion.

4.4. Discussion Related to the Comparison of Experimental Measurements and Numerical Calculation Results

The temperature differences obtained at the checkpoints using numerical simulations were analyzed using several parameters. The first of these, also used during domain validation, was the mean absolute error. At a height of 0.25 m for variant 2, for kerosene, in the case of a speed of 31,630 rpm, the mean absolute error of all obtained results was 57.6 K, and for a speed of 47,110 rpm, 100.9 K. For the kerosene–hydrogen co-combustion, for a lower speed this parameter was 40.1 K, and for a higher speed 57.8 K. For variant 1, for kerosene, in the case of a speed of 31,630 rpm, the mean absolute error of all obtained results was 67.1 K, and for a speed of 47,110 rpm, 124.8 K. For the kerosene–hydrogen co-combustion, for a lower speed this parameter was 50.2 K, and for a higher speed 77.8 K.

In the case of kerosene at a measurement height of 0.315 m for variant 2, at a speed of 31,630 rpm, the mean absolute error of all obtained results was 47.5 K, and for a speed of 47,110 rpm – 67.2 K. For the kerosene–hydrogen co-combustion, for a lower speed, this parameter was 38.8 K, and for a higher speed, 58.9 K. For variant 1, for kerosene, in the case of a speed of 31,630 rpm, the mean absolute error of all obtained results was 64.1 K, and for a speed of 47,110 rpm, 91.2 K. For the kerosene–hydrogen co-combustion, for a lower speed, this parameter was 52.3 K, and for a higher speed, 94.5 K. A more accurate distribution of this parameter in the context of the considered distances from the wall is presented in Figures 18 and 19.

The distribution of the mean absolute error confirmed that its highest values occur in two intermediate areas, i.e., around 0.083 m and 0.166 m. For further evaluation of these two areas, the standard deviation was used, according to the following formula

$$\sigma = \sqrt{\frac{1}{N}\sum_{i=1}^{N}(\Delta T_{i'} - \mu)^2} \quad (20)$$

where N is the number of numbers in the set, $\Delta T_{i'}$ is the difference between the measured and calculated temperature for both rotational speeds [K], μ is the arithmetic mean of all values [K].

https://doi.org/10.3390/en19040938

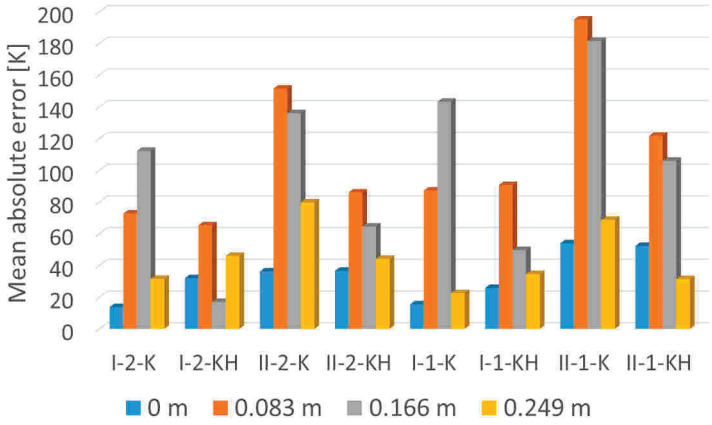


Figure 18. The mean absolute error at the checkpoints at a height of 0.25 m: I—the rotational speed of 31,630 rpm, II—the rotational speed of 47,110 rpm, 2—variant 2, 1—variant 1, K—kerosene, KH—the kerosene–hydrogen.

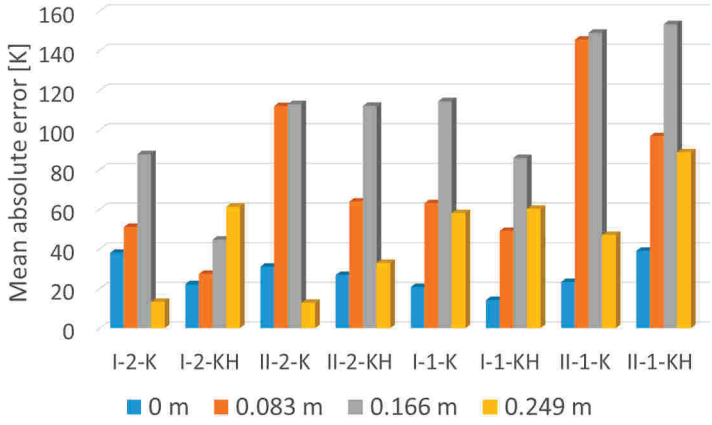


Figure 19. The mean absolute error at the checkpoints at a height of 0.315 m: I—the rotational speed of 31,630 rpm, II—the rotational speed of 47,110 rpm, 2—variant 2, 1—variant 1, K—kerosene, KH—the kerosene–hydrogen.

The analysis assumed that the standard deviation, as a certain component of uncertainty, can indirectly indicate the states of uncertainty at individual checkpoints. Therefore, at a height of 0.25 m in variant 2—for kerosene—the area with higher measurement uncertainty was located at a distance of approximately 0.166 m from the tank wall. For the kerosene–hydrogen co-combustion, this area had lower measurement uncertainty. For variant 1, in both cases, the greater measurement uncertainty was around a distance of 0.166 m from the container wall. At a height of 0.315 m, for both variants and both fuel types, the greater uncertainty was always around a distance of 0.166 m from the container wall. The standard deviation values were presented in Table 9. To improve clarity and provide a direct graphical interpretation of the deviations, the standard deviation values listed in Table 9 are additionally presented in Figure 19 in a bar-chart form. The figure enables a direct comparison of uncertainty levels between fuel types, measurement heights, and distances from the container wall. As shown in Figure 20, for both measurement heights (0.25 m and 0.315 m), the standard deviation is consistently higher at a distance of 0.166 m compared to 0.083 m, regardless of the variant considered. This trend confirms that the region located farther from the exhaust axis and closer to the container wall is characterized by stronger temperature fluctuations, which can be attributed to enhanced mixing, recirculation zones, and increased turbulence intensity. Furthermore, the graphical representation highlights that kerosene–hydrogen co-combustion generally exhibits lower

https://doi.org/10.3390/en19040938

standard deviation values at 0.083 m, indicating a more stable temperature field near the exhaust core, while at 0.166 m the differences between fuels become less pronounced, especially at the height of 0.315 m. This observation is consistent with the discussion above and confirms that uncertainty increases with distance from the jet core and with vertical elevation, where flow confinement effects dominate.

Table 9. The standard deviation for the cases considered.

Measurement Height Level [m]	**0.25**				**0.315**			
Type of variant	1		2		1		2	
Fuel type	kerosene	kerosene–hydrogen	kerosene	kerosene–hydrogen	kerosene	kerosene–hydrogen	kerosene	kerosene–hydrogen
σ [K] (for 0.083 m)	76.0	44.2	68.5	41.9	65.8	43.0	57.0	38.1
σ [K] (for 0.166 m)	83.8	49.1	76.0	49.1	69.9	75.6	69.7	69.7

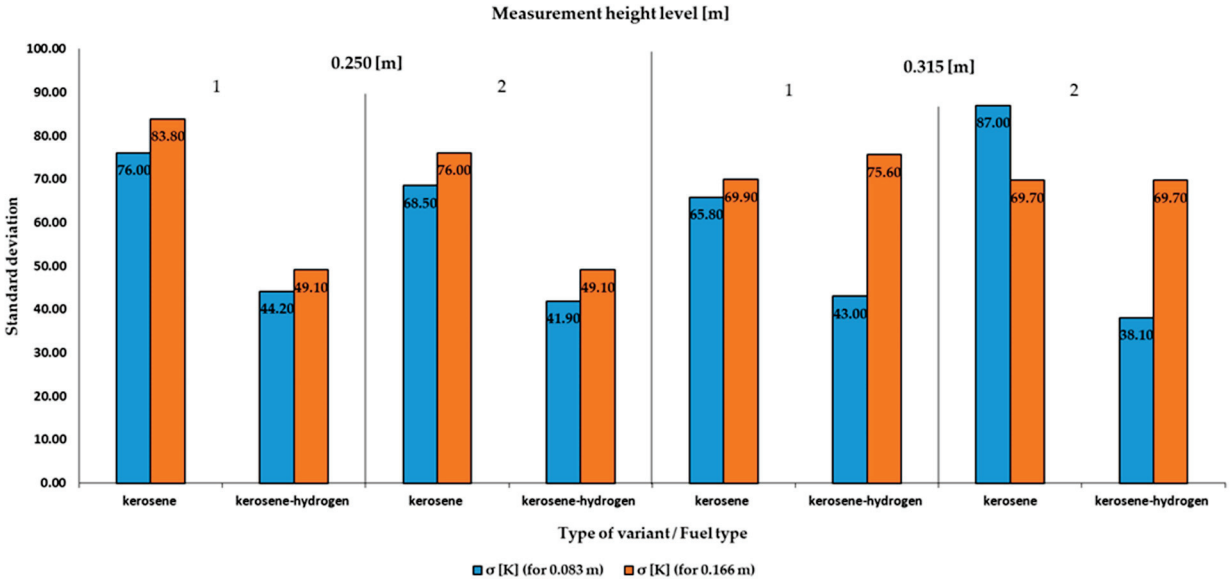


Figure 20. Standard deviation of temperature measurements for kerosene and kerosene–hydrogen co-combustion at measurement heights of 0.25 m and 0.315 m, shown for two distances from the container wall (0.083 m and 0.166 m) and for both analyzed variants.

The errors related to the difference between the experimental results and the simulation results for variant 2 were presented in the form of RMSE in Table 10. It was calculated according to the formula

$$RMSE = \sqrt{\frac{1}{N}\sum_{i=1}^{N}\left(T_{i'} - \hat{T}_i\right)^2} \tag{21}$$

and in percentage

$$nRMSE = \frac{RMSE}{\mu}\cdot 100\% \tag{22}$$

The RMSE values obtained in this work (9.5–22.8%) are within the ranges commonly reported for RANS-based temperature predictions in high-gradient jet exhaust environments. For miniature gas turbines, typical discrepancies between numerical and experimental temperature fields range an RMSE of 15% to 30%, as documented in recent small-scale turbine, afterburner and exhaust mixing studies. This confirms that the error levels observed here are consistent with limitations inherent to RANS modeling in strongly sheared, thermally stratified flows.

https://doi.org/10.3390/en19040938

Table 10. The RMSE in percent with respect to the mean experimental temperature values.

Measurement Height Level [m]	**0.25**				**0.315**			
Rotational speed [rpm]	31,630		47,110		31,630		47,110	
Fuel type	kerosene	kerosene–hydrogen	kerosene	kerosene–hydrogen	kerosene	kerosene–hydrogen	kerosene	kerosene–hydrogen
nRMSE [%]	15.7	9.5	22.8	12.4	14.7	10.4	18.1	15.1

It should be noted that the very high turbulence intensity values obtained in the analysis (up to 300%) do not indicate physically unrealistic behavior but arise from the definition of turbulence intensity used in ANSYS Fluent. The parameter is computed as the ratio of the root-mean-square fluctuation of the velocity to the local mean velocity. In regions where the mean velocity drops sharply, such as in the shear layers surrounding the exhaust jet or inside recirculation zones, velocity fluctuations remain high while the mean velocity approaches low values. This combination can produce turbulence intensities well above 100%. Similar effects have been reported in confined exhaust jets, under expanded plumes and micro gas turbine mixing layers. The peaks observed in this study therefore correspond to strongly sheared, highly vortical regions at the jet boundary rather than to the core flow.

Figures 21 and 22 present vector distributions of gas velocity in the container for both speed variants and fuel types used. The obtained results reveal differences in the form of local velocity development as well as the formation of vortex regions.

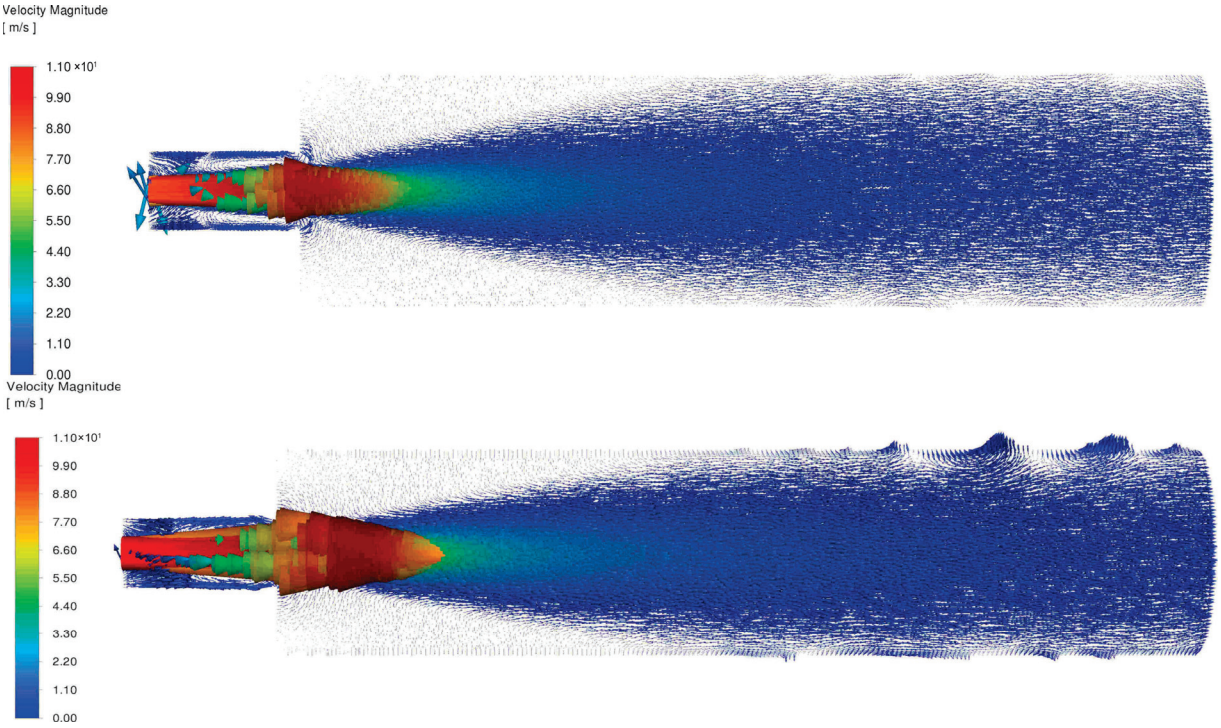


Figure 21. The velocity distribution downstream of the nozzle for a speed of 31,630 rpm during kerosene combustion: variant 2 at the (**top**); variant 1 at the (**bottom**).

The same differences are observed for both lower and higher engine speeds. Local gas velocities outside the main exhaust stream are correspondingly higher for a speed of 47,110 rpm. Due to the limited space of the container on the engine side, a more intense gas flow is observed towards the exhaust stream, where the pressure is reduced. In this case, this is the only source of motion, apart from the particle motion in the exhaust cross-section.

https://doi.org/10.3390/en19040938

This leads to an increase in turbulent kinetic energy in the shear layers of the gas flow. In the presence of a gap, this flow is more pronounced. For variant 1, the maximum turbulent kinetic energy was 8.96 m^2/s^2, and for variant 2 it was 8.28 m^2/s^2.

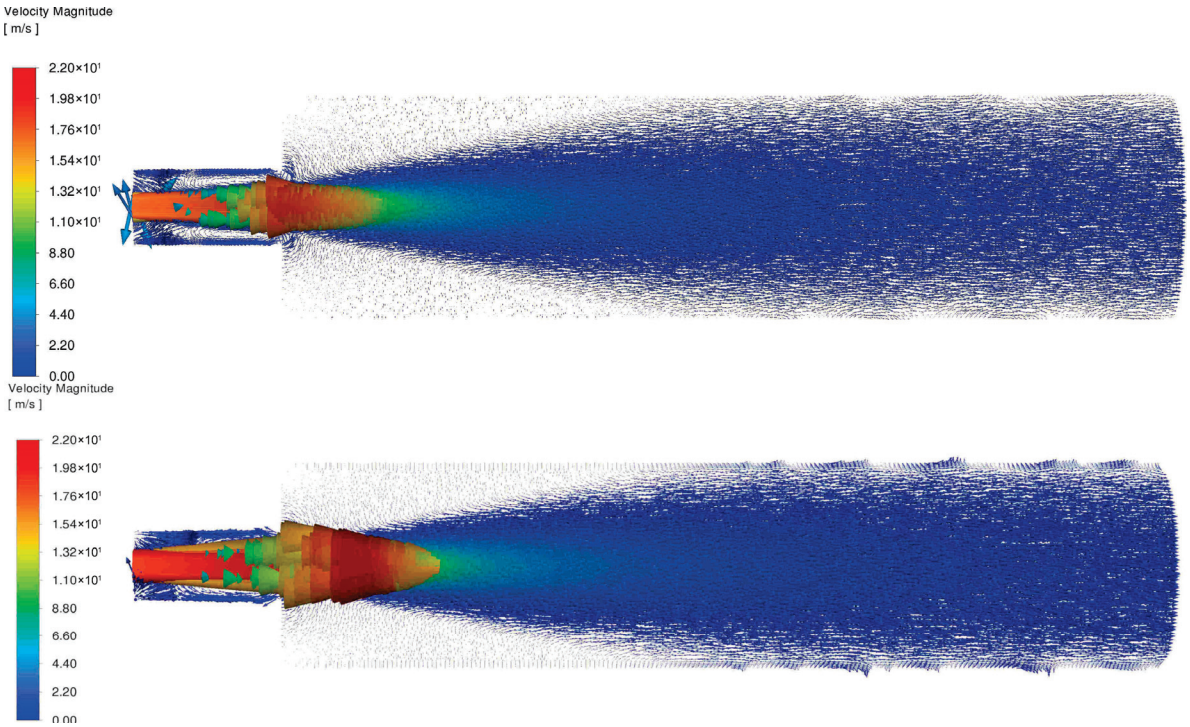


Figure 22. The velocity distribution downstream of the nozzle for a speed of 47,110 rpm during kerosene and hydrogen combustion: variant 2 at the (**top**); variant 1 at the (**bottom**).

4.5. Model Universality and Comparison with Literature

To assess the universality of the proposed CFD model and confirm its predictive reliability, a comparative analysis was conducted with published numerical and experimental investigations on miniature and small-scale turbojet engines operating under various fuel conditions. The goal was to determine whether the thermal and flow-field distributions obtained in this study are consistent with the general physical trends observed in similar engine configurations.

The obtained RMSE range (9.5–22.8%) aligns with the deviations typically reported for Reynolds-Averaged Navier–Stokes (RANS)-based simulations of small turbojet exhausts. Comparable levels of accuracy were documented by Badami et al. (2014) in their combined experimental–numerical study on small turbojets fueled by Jet-A and biofuel blends, where temperature prediction errors ranged between 10% and 25% depending on operating regime [27].

Similarly, Gao et al. (2014) investigated the flow and liner wall temperature field of a reverse-flow combustor for a miniature turbojet engine, validating CFD results against experimental data with an average temperature deviation of 12–20% [28]. Their findings confirmed that SST k–ω and standard k–ε models provide physically consistent turbulence structures downstream of the combustor, an observation mirrored by the present results.

In turn, Suchocki et al. (2014) analyzed the GTM-140 engine using a coupled non-premixed combustion and k–ε turbulence model, reporting exhaust temperatures between 870 and 950 K, which is consistent with the 890–1000 K outlet temperature range used as boundary conditions in the current simulation [29].

Furthermore, He et al. (2021) optimized a microturbojet combustor numerically and experimentally, demonstrating that turbulence intensity distributions within 200–300%

correspond to flow instabilities localized in the shear layers—closely matching the present observations [30].

Finally, Brodzik et al. (2025) conducted a comprehensive thermomechanical analysis of the same GTM 400 MOD miniature turbojet engine using a coupled CFD–FEM framework, demonstrating that nozzle wall temperatures and stress distributions remained within experimentally verified material limits under both kerosene combustion and kerosene–hydrogen co-combustion conditions [13]. Their results confirmed the predictive robustness of steady-state RANS simulations implemented in ANSYS for evaluating thermal loads and structural response in hydrogen-assisted propulsion systems.

These findings are consistent with broader numerical investigations of alternative fuel combustion in turbojet engines. For instance, Alabas [31] showed that CFD-based modeling of hydrogen- and ammonia-enriched jet fuels yields realistic temperature levels and emission trends when appropriate boundary conditions and turbulence–radiation coupling are applied, further supporting the reliability of RANS-based approaches for hydrogen-containing fuel mixtures.

Moreover, the exhaust temperature ranges and operating conditions adopted in the present study align well with the characteristic parameters reported by Gieras [32] for miniature turbojet engines, who documented typical combustion chamber outlet temperatures and turbine loading levels for small-scale propulsion systems.

Taken together, these studies provide indirect yet consistent validation of the present numerical framework, confirming that the applied modeling assumptions lead to physically realistic predictions of thermal and mechanical behavior in miniature turbojet engines operating with both conventional and hydrogen-enriched fuels.

Taken together, these comparisons indicate that the present numerical model reproduces both the magnitude and spatial character of exhaust temperature fields and turbulence structures reported by other authors (Table 11). Hence, the model can be considered universal within the domain of small-scale turbojet exhaust simulations involving hydrocarbon and hydrogen-based fuels.

Table 11. Comparison of study results and literature.

No.	Source	Engine Type/Fuel	Methods	Key Results	Comparison with Present Study
1.	Badami et al., 2014, *Energy Conv. & Management* [27]	80 N Microturbojet/Jet-A, GTL, JME	Experimental + CFD (k–ε)	CFD–exp. deviation: 10–25%, exhaust T: 700–900 K	Present model within same deviation band; similar T field at nozzle outlet
2.	Gao et al., 2014, *IHTC15 Conf.* [28]	Reverse-flow combustor/ Kerosene	Experimental + CFD (SST k–ω)	T deviation ± 20%, high turbulence near liner wall	Similar turbulence and near-wall gradients validated by SST k–ω model
3.	Suchocki et al., 2014, *Journal of KONES Powertrain and Transport* [29]	GTM-140/ Kerosene	CFD (k–ε) + DPM	Exhaust T: 870–950 K, verified combustor model	Agrees with boundary T (890–1000 K) and pressure gradients in this study
4.	He et al., 2021, Int. J. *Aerospace Eng.* [30]	Microturbojet/ Jet-A	CFD (SST k–ω) + Experiment	Turbulence intensity 200–300% in shear zones, stable combustion	Confirms realistic turbulence peak (284–300%) from current simulations
5.	Brodzik et al., 2025, *Energies* [13]	GTM400 MOD/Kerosene–H_2	CFD + FEM (ANSYS) + Experimental	Max wall T: 1090 K, stress < 261 MPa, ΔT < 12% vs. exp.	Confirms consistent exhaust T range (650–760 K) and mechanical stability under H_2 co-combustion

https://doi.org/10.3390/en19040938

5. Conclusions

This study investigated the exhaust flow downstream of a GTM 400 MOD miniature turbojet engine operating under kerosene and kerosene–hydrogen co-combustion conditions. The primary objective was to assess the influence of geometric confinement and fuel composition on the thermal and flow characteristics of the exhaust jet and to verify whether a simplified numerical approach can reliably reproduce experimentally observed temperature fields.

The applied methodology combined experimental temperature measurements with steady-state CFD simulations performed using the SST k–ω turbulence model. Two numerical domain configurations were analyzed: one including the physical gap between the exhaust nozzle and the container (Variant 1) and one neglecting this gap (Variant 2). Model validation was conducted using temperature measurements collected at multiple distances from the exhaust axis and container wall, enabling quantitative assessment through normalized RMSE values.

The results demonstrated that the largest temperature deviations occurred in regions characterized by intensified turbulence and mixing, particularly at intermediate distances from the container wall. The highest turbulence intensities were observed for kerosene–hydrogen co-combustion at higher rotational speeds, reaching approximately 300% in Variant 1 and 284% in Variant 2. The analysis further showed that the simplified configuration without the gap (Variant 2) provided better agreement with experimental data, yielding RMSE values in the range of 9.5–22.8%, which is consistent with accuracy levels reported for RANS-based simulations of confined exhaust flows.

The scientific contribution of this work lies in demonstrating that the temperature field downstream of a miniature turbojet exhaust nozzle can be accurately reproduced without explicitly modeling the combustion process, provided that experimentally derived boundary conditions are applied. Additionally, the study quantifies the effect of geometric confinement on flow and temperature distributions and confirms, through comparison with independent experimental and numerical studies, the robustness and universality of the adopted numerical framework for small-scale turbojet exhaust analysis.

From an application perspective, the developed and validated model can be used for the thermomechanical assessment of miniature turbojet nozzles, optimization of confined exhaust and test chamber geometries, and preliminary evaluation of hydrogen-assisted combustion concepts. The approach is particularly suited for low- and medium-speed operating regimes, where reliable prediction of downstream temperature fields is required without excessive computational cost.

Author Contributions: Conceptualization, Ł.B. and B.C.; Methodology, Ł.B., B.C. and G.C.; Software, Ł.B. and B.C.; Validation, Ł.B., B.C., Ł.S., D.S. and G.C.; Formal analysis, Ł.B. and G.C.; Investigation, Ł.B.; Resources, Ł.B.; Data curation, Ł.B.; Writing—original draft preparation, Ł.B., B.C. and Ł.S.; Writing, review and editing, Ł.B., B.C., Ł.S. and G.C.; Visualization, Ł.B. and D.S.; Supervision, Ł.B. and G.C.; Project administration, Ł.B. and B.C.; Funding acquisition, Ł.B. and B.C. All authors have read and agreed to the published version of the manuscript.

Funding: This research was funded by the Polish Ministry of Science and Higher Education and the Poznan University of Technology's financial resources for statutory activity. Grant numbers 0712/SBAD/5297 and 0712/SBAD/5298.

Data Availability Statement: The original contributions presented in this study are included in the article. Further inquiries can be directed to the corresponding authors.

Conflicts of Interest: The authors declare no conflicts of interest.

Nomenclature

D	diffusion coefficient
I	radiative intensity
L_t	turbulent length scale
F_1	first mixing function
F_2	second mixing function
F_i	external force
K	thermal conductivity coefficient
N	number of numbers in the set
P	scattering phase function
P_k	rate of production of turbulent kinetic energy
$\overline{P}_k$	effective rate of production of turbulent kinetic energy
Pr	Prandtl number
P_ω	rate of production of specific turbulent dissipation rate
R	term describing the combustion reaction
S_{ij}	mean rate of deformation component
T	temperature
$T_{i'}$	temperature measured during the experiment at the checkpoint
$\hat{T}_i$	temperature calculated during simulation at the checkpoint
U_i	mean flow velocity
X	cross-diffusion term
a_1	constant
c	concentration of the reacting substance
c_p	specific heat
k	specific turbulent kinetic energy
n_I	refractive index
r	coordinate
ŝ	unit vector
t	time
v	velocity
x	direction
y	direction
CFD	Computational Fluid Dynamics
FEM	Finite Element Method
MAE	Mean Absolute Errors
RDC	Rotating Detonation Combustor
RMSE	Root Mean Square Error
TBCC	Turbine-Based Combined Cycle
TKE	Turbulent Kinetic Energy
TDR	Turbulent Diffusivity Ratio
β	constant
$\beta*$	constant
γ	constant
σ	standard deviation
σ_{ij}	stress tensor
δ_{ij}	Kronecker delta function
κ	extinction coefficient
κ_a	coefficient of absorption
κ_s	coefficient of scattering
μ	arithmetic mean
μ_k	effective viscosity of specific turbulent kinetic energy
μ_t	modified eddy viscosity
μ_ω	effective viscosity of specific turbulent dissipation rate

https://doi.org/10.3390/en19040938

ρ	density
σ_k	diffusion constant
σ_ω	diffusion constant
$d\omega'$	solid angle
ω	specific turbulent dissipation rate

References

1. Varatharajulu Purgunan, G.R.; Stathopoulos, P. Performance and Exergy Analysis of TurboJet and TurboFan Configurations with Rotating Detonation Combustor. *Int. J. Thermofluids* **2024**, *23*, 100739. [CrossRef]
2. Zhang, Y.; Xu, J.; Pan, R.; Li, Y.; Ma, Z.; Huang, S. Numerical Investigation of Short Takeoff and Landing Exhaust System Using Bypass Dual Throat Nozzle. *Aerosp. Sci. Technol.* **2023**, *138*, 108316. [CrossRef]
3. Meng, Y.; Shi, J.; Zhou, L.; Wang, Z. Numerical Investigation on Flow Characteristics of Multi-Stream Supersonic Nozzle with Serpentine Configuration. *Aerosp. Sci. Technol.* **2024**, *144*, 108799. [CrossRef]
4. He, P.; Yue, C.; Fan, Y. The Stable Combustion and Blowout Characteristics Investigation of the Water Injection Pre-Cooling on the Afterburners. *Fuel* **2025**, *397*, 135422. [CrossRef]
5. Aygun, H.; Kirmizi, M.; Kilic, U.; Turan, O. Multi-Objective Optimization of a Small Turbojet Engine Energetic Performance. *Energy* **2023**, *271*, 126983. [CrossRef]
6. Niszczota, P.; Gieras, M. Inlet Injection as an Alternative, Simplified Method of Hydrogen Application in a Miniature Gas Turbine. *Appl. Therm. Eng.* **2024**, *257*, 124175. [CrossRef]
7. Ayaz, S.K.; Caliskan, H.; Altuntas, O. Environmental and Second Law Analysis of a Turbojet Engine Operating with Different Fuels. *Energy* **2023**, *285*, 129402. [CrossRef]
8. Kang, J.; Song, F.; Chen, X.; Wu, Y.; Zhang, D.; Wang, J.; Yang, Z.; Pan, W.; Wang, Z. Performance Enhancement of Rotating Detonation Afterburner through Combined Injection Scheme. *Acta Astronaut.* **2025**, *235*, 639–652. [CrossRef]
9. Wu, X.; Hu, X.; Xiang, X.; Lin, S.; You, J.; Tian, F. An Analysis Approach for Micro Gas Turbine Engine's Performance by Experiment and Numerical Simulation. *Case Stud. Therm. Eng.* **2023**, *49*, 103305. [CrossRef]
10. Zhang, K.; Yu, X.; Zhang, D.; Guo, J.; Qin, F. Evaluation of Multi-Mode Shared Combustor with Different Flame Holder Designs for an Innovative Turbo-Ramjet Combined Cycle Engine. *Energy* **2025**, *323*, 135875. [CrossRef]
11. Xu, Y.; Deng, W.; Liu, X.; Xu, H.; Li, Z. Full Engine 3D Simulation Scheme Considering Rotor Motion for Turbojet Engine under Crosswind Conditions. *Appl. Therm. Eng.* **2025**, *269*, 125951. [CrossRef]
12. Boretti, A. Towards Hydrogen Gas Turbine Engines Aviation: A Review of Production, Infrastructure, Storage, Aircraft Design and Combustion Technologies. *Int. J. Hydrogen Energy* **2024**, *88*, 279–288. [CrossRef]
13. Brodzik, Ł.; Ciupek, B.; Frąckowiak, A.; Schroeder, D. Thermomechanical Analysis of the GTM 400 MOD Turbojet Engine Nozzle During Kerosene and Hydrogen Co-Combustion. *Energies* **2025**, *18*, 4382. [CrossRef]
14. Bogoi, A.; Cican, G.; Gall, M.; Totu, A.; Crunțeanu, D.E.; Levențiu, C. Comparative Study of Noise Control in Micro Turbojet Engines with Chevron and Ejector Nozzles Through Statistical, Acoustic and Imaging Insight. *Appl. Sci.* **2025**, *15*, 394. [CrossRef]
15. Catana, R.M.; Badea, G.P. Experimental Analysis on the Operating Line of Two Gas Turbine Engines by Testing with Different Exhaust Nozzle Geometries. *Energies* **2023**, *16*, 5627. [CrossRef]
16. Villarreal-Valderrama, F.; Zambrano-Robledo, P.; Hernandez-Alcantara, D.; Amezquita-Brooks, L. Turbojet Thrust Augmentation through a Variable Exhaust Nozzle with Active Disturbance Rejection Control. *Aerospace* **2021**, *8*, 293. [CrossRef]
17. Ciupek, B.; Brodzik, Ł.; Frąckowiak, A. Research on Carbon Footprint Reduction During Hydrogen Co-Combustion in a Turbojet Engine. *Energies* **2024**, *17*, 5397. [CrossRef]
18. Mazumder, S.; Roy, S.P. Modeling Thermal Radiation in Combustion Environments: Progress and Challenges. *Energies* **2023**, *16*, 4250. [CrossRef]
19. Beer, J.M. *Methods for Calculating Radiative Heat Transfer from Flames in Combustors and Furnaces, Chapter 2 in Heat Transfer in Flames*; Afgan, N.H., Beer, J.M., Eds.; Scripta Book Company: Washington, WA, USA, 1974.
20. Prokopowicz, W.; Ciupek, B.; Maciąg, A.; Gajewski, T.; Sielicki, P.W. Advanced Spectral Diagnostics of Jet Engine Vibrations Using Non-Contact Laser Vibrometry and Fourier Methods. *Energies* **2025**, *18*, 4837. [CrossRef]
21. Brodzik, Ł. Gas temperature distribution in the combustion chamber of a GTM400 MOD turbojet engine powered by JET A-1 Fuel and Hydrogen. *Energies* **2024**, *17*, 745. [CrossRef]
22. Karim, M.M.; Rahman, M.M.; Alim, M.A. Performance of SST k–ω turbulence model for computation of viscous drag of axisymmetric underwater bodies. *Int. J. Eng.* **2011**, *24*, 2.
23. Liu, J.; Guo, W.; Yin, M.; Xi, W.; Sunden, B. Flow and heat transfer characteristic of regenerative cooling channels using supercritical CO_2 with circular tetrahedral lattice structures. *Case Stud. Therm. Eng.* **2025**, *71*, 106204. [CrossRef]

24. Liu, J.; Guo, W.; Zhao, G.; Ma, J.; Xi, W.; Sunden, B. Study on Heat Transfer Characteristics of Supercritical CO2/n-decane Composite Double Triangular Regenerative Cooling for Scramjets. *Aerosp. Sci. Technol.* **2026**, *172*, 111725. [CrossRef]
25. Goldberg, U.C.; Batten, P. A wall-distance-free version of the SST turbulence model. *Eng. Appl. Comput. Fluid Mech.* **2015**, *9*, 1. [CrossRef]
26. Rocha, P.C.; Rocha, H.B.; Carneiro, F.M.; da Silva, M.V.; Bueno, A.V. k–ω (shear stress transport) turbulence model calibration: A case study on a small scale horizontal axis wind turbine. *Energy* **2013**, *65*, 412–418. [CrossRef]
27. Badami, M.; Nuccio, P.; Pastrone, D.G.; Signoretto, A. Performance of a Small-Scale Turbojet Engine Fed with Traditional and Alternative Fuels. *Energy Convers. Manag.* **2014**, *82*, 219–228. [CrossRef]
28. Gao, X.; Duan, F.; Lim, S.C.; Yip, M.S. Experimental and Numerical Study of Flow Structure and Liner Wall Temperature in Reverse Flow Combustor. In Proceedings of the 15th International Heat Transfer Conference (IHTC-15), Kyoto, Japan, 10–15 August 2014. [CrossRef]
29. Suchocki, T.; Lampart, P.; Klonowicz, P. Numerical Investigation of a GTM-140 Turbojet Engine. *J. KONES Powertrain Transp.* **2014**, *21*, 331–338. [CrossRef]
30. He, W.; Guo, Z.; Xu, S.; Jin, Y. Numerical and Experimental Investigations on Performance Optimization of a Microturbojet Engine Combustor. *Int. J. Aerosp. Eng.* **2021**, *2021*, 6616537. [CrossRef]
31. Alabas, H.A. CFD study of jet fuel with ammonia—Hydrogen mixtures in a jet engine: Emissions and combustion characteristics analysis. *Int. J. Hydrogen Energy* **2025**, *142*, 140–150. [CrossRef]
32. Gieras, M. *Miniaturowe silniki turboodrzutowe*; Wydawnictwo Politechniki Warszawskiej: Warszawa, Poland, 2016.

Disclaimer/Publisher's Note: The statements, opinions and data contained in all publications are solely those of the individual author(s) and contributor(s) and not of MDPI and/or the editor(s). MDPI and/or the editor(s) disclaim responsibility for any injury to people or property resulting from any ideas, methods, instructions or products referred to in the content.

energies

MDPI

Article

Experimental Verification of a Method for Improving the Efficiency of an Evaporative Tower Using IEC

Bartosz Jagieła [1] and Magdalena Jaremkiewicz [2,*]

[1] Doctoral School, Cracow University of Technology, 31-155 Cracow, Poland; bartosz.jagiela@doktorant.pk.edu.pl
[2] Faculty of Environmental and Energy Engineering, Cracow University of Technology, 31-155 Cracow, Poland
* Correspondence: magdalena.jaremkiewicz@pk.edu.pl

Abstract

This paper analyses the impact of inlet air precooling on the efficiency and electricity consumption of an open-type evaporative cooling tower. An Indirect Evaporative Cooler (IEC) was used to reduce the inlet air temperature, and its influence on system efficiency was experimentally evaluated. Although IEC units and the Maisotsenko cycle are increasingly discussed in the literature, no research to date has considered their effect on evaporative tower efficiency under actual operating conditions. For this purpose, a test stand was constructed comprising an open cooling tower and an IEC unit. The system operated automatically for 2952 h, corresponding to a full cooling season in Poland. Two sets of data collected during cooling tower operation were analysed: without precooling (Stage I) and with precooling using IEC (Stage II). Measurements were recorded every 10 s. Additionally, tests were conducted at elevated thermal loads and peak ambient temperatures. The comparative analysis concluded that air precooling using IEC reduced the cooling tower's electricity consumption by approximately 15% and increased the SCOP of the cooling tower by 30%. This demonstrates the significant potential of the proposed solution.

Keywords: evaporative cooling tower; indirect evaporative cooling; inlet air precooling; Maisotsenko cycle; energy efficiency; HVAC system

1. Introduction

Meeting electricity demand in the 21st century is becoming a challenge due to climate change and a growing population. Especially since, due to the average ambient temperature, each subsequent year is usually warmer than the previous one. The Heating, Ventilation, and Air Conditioning (HVAC) market is constantly evolving to provide customers with a comfortable environment through cooling, heating, and ventilation. In certain developed nations, including Japan, the USA, and Korea, more than 90% of households have individual air conditioning units. The electricity consumption of these devices accounts for approximately 10% of total global electricity consumption [1]. Consumers frequently overlook the most energy-efficient air conditioning units, instead basing their decisions solely on cost. Investing in more efficient HVAC systems could cut future energy demand by 45% by 2050 [1].

Most modern HVAC systems are Vapour-Compression Refrigeration Systems (VCRSs), in which the refrigerant undergoes a phase change and are characterised by significant electricity consumption. They also harm the environment through the refrigerants they use. Leading HVAC manufacturers are now exploring more efficient, environmentally friendly

solutions in response to climate change. Among the known refrigerants, environmentally friendly ones, i.e., those with low ozone depletion potential (ODP) and low global warming potential (GWP), include ammonia, NH_3, known as R717 (ODP = 0 and GWP = 0); carbon dioxide, CO_2, or R744 (ODP = 1, GWP = 0); and propane, C_3H_8, or R290 (ODP = 3, GWP = 0) [2]. All of them represent the future of modern HVAC systems on an industrial scale. Unfortunately, for devices with lower cooling capacities (below 20 kW), the use of these refrigerants is limited due to their flammability, toxicity, and high operating pressure [3–5]. A refrigerant that does not have these disadvantages and is neutral and clean is water, H_2O, designated as R718 (ODP < 1, GWP = 0). Water can be used as a primary or secondary refrigerant. Due to its high heat of evaporation (approximately 2200 kJ/kg at 0 °C), it is one of the most effective refrigerants. Water is used as a refrigerant in evaporative devices, such as evaporative air conditioners and cooling towers. Cooling air using evaporative technology enables temperatures below the ambient temperature to be achieved, and since it utilises natural processes, energy consumption can be reduced. The environmental and economic issues discussed above are driving evaporative systems to become increasingly popular.

1.1. Evaporative Cooling Systems

Evaporative systems are categorised into two types: Direct Evaporative Coolers (DECs) and Indirect Evaporative Coolers (IECs). In DEC units, the cooled air comes into direct contact with water in the wet channel. During cooling, the water evaporates directly into the stream of cooled air, lowering its temperature. IEC uses a heat exchanger to cool the air, in which heat is transferred from the cooled air in the dry channel to the air flowing through the wet channel. This prevents moisture from being added to the cooled air. The lowest temperature to which air can be cooled in evaporative devices is the wet-bulb temperature, which depends on the dry-bulb temperature and relative humidity of the air. The cooled air obtained in IEC may have similar parameters to those obtained in VCRS, but unlike them, evaporation systems are innovative and can be considered a cheaper cooling technique. A variation of the IEC system is the Maisotsenko cycle (M-cycle), which allows lower temperatures than the classic ICE. Figure 1 illustrates the heat-exchange process in the IEC and diagrams the thermodynamic processes within the unit.

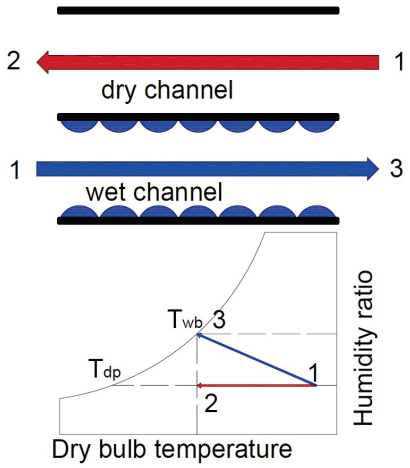


Figure 1. Principle of operation of IEC.

The effectiveness of evaporative cooling can be determined based on the wet-bulb efficiency:

$$\varepsilon_{wb} = \frac{T_{in} - T_{out}}{T_{in} - T_{wb}} \quad (1)$$

https://doi.org/10.3390/en19020554

where T_{in} is the inlet temperature, T_{out} is the outlet temperature, and T_{wb} is the wet-bulb temperature.

In the first concept of the M-cycle, the product is the main stream of cooled air, which is obtained through heat exchange with the so-called auxiliary stream of air flowing through the wet channel. The inlet air is divided into two parts, one of which, i.e., the main stream, flows through the dry channel and is used, for example, to cool rooms. The second part, i.e., the auxiliary air stream, is first pre-cooled during heat exchange with the air flowing through the wet channel, and then flows through the wet channel, further lowering its temperature. Cooling systems using the M-cycle employ cross-flow heat and mass exchangers (HMXs). As in IEC systems, the cooled air (product) is not moisturised. Theoretically, the lowest temperature achieved in the M-cycle is the dew point temperature. The efficiency of the M-cycle can be determined based on the dew point efficiency:

$$\varepsilon_{dp} = \frac{T_{in} - T_{out}}{T_{in} - T_{dp}} \quad (2)$$

where T_{dp} is the dew point temperature.

The M-cycle concept is continually being developed by its creator and other researchers and scientists, as evidenced by the increasing number of publications on topics such as improving cycle efficiency, the technologies used, and potential applications.

The M cycle is primarily used in cooling systems, but it can also be applied in water desalination and distillation processes [6,7] as well as in power plants, including NOx reduction [8,9]. The presented applications of the M-cycle have been analysed in terms of optimisation for various locations around the world, characterised by both low and high air humidity, e.g., cities in the Arabian Gulf [10], Riyadh in Saudi Arabia [11], Beijing in China [12], Bushehr in Iran [13], northern Italy [14], and Martos in Spain [15]. The research was conducted both numerically [10–14] and experimentally [14,15].

Research conducted on M cycles includes HMXs. In [16], a mathematical model of heat and mass transfer was developed for two selected HMX designs using a modified epsilon-NTU method. The authors of [17] also developed an HMX model in Python 3.10, based on a spatially discretised differential equation solver and a psychrometric chart. In both cases, the models were validated using experimental data. Research on heat exchangers also concerns technology. For example, in [18], a nanoporous membrane covering the surface of a wet channel was tested to improve heat and mass transfer. The study experimentally confirmed the beneficial effect of the coating on the heat exchanger's efficiency. Another solution studied, as described in [19], involved the use of aluminium fins in the heat exchanger's dry ducts to increase heat transfer efficiency. This increased the cooling capacity by 18%.

Evaporative cooling systems can operate in various configurations, including those with desiccant wheels, ejectors, or as hybrid systems that incorporate freon devices. The operating conditions and limitations of individual solutions are summarised in [20]. A desiccant air conditioning system uses a moisture-absorbing wheel to dehumidify air drawn from the surroundings. Then, in a typical system, the air is pre-cooled in a rotary heat exchanger, then humidified in a spray chamber, and cooled simultaneously. The air returning from the cooled space flows through the subsequent parts of the system in the opposite direction, but is heated before the desiccant wheel, allowing the desiccant wheel to be regenerated. In [21], indirect cooling using the M cycle was proposed. A numerical analysis of this system was performed, demonstrating its higher temperature efficiency. Research on such systems also concerns moisture-absorbing materials used in the desiccant wheel, as in [22]. Hybrid systems combine IEC and VCRS. Research on such a system, where IEC uses an M-cycle, is presented in [23]. The report shows

https://doi.org/10.3390/en19020554

that the tested system consumes 80% less energy than a conventional air conditioning system. In turn, a numerical simulation of two hybrid systems was conducted in [24], where preliminary cooling was achieved using a conventional IEC and an IEC with an M cycle. In this case, it was also demonstrated that systems of this type enable reduced electricity consumption in locations with a humid climate. In [25], tests were carried out on three air conditioning systems: a refrigeration unit, a refrigeration unit coupled with evaporative cooling, and a refrigeration unit coupled with regenerative evaporative cooling. An analysis of annual electricity consumption showed savings of 17% and 22% for the second and third solutions, respectively, compared to the first. In [26], an analysis of the operation of a two-stage evaporative cooling system consisting of IEC followed by DEC in public buildings in Tehran was presented. It was shown that such a system could replace VCRS while simultaneously reducing electricity consumption; however, it would consume 55% more water than a stand-alone DEC.

1.2. Cooling Towers

In cooling towers, waste heat is dissipated into the environment through a stream of coolant (usually water), which undergoes partial evaporation, causing the cooling air to reach a temperature close to that of a wet-bulb thermometer. Cooling towers can be divided into two types: natural draft and forced draft (utilising a fan). Another classification, based on the circulation of the cooled medium, is into open and closed evaporative towers. Cooling towers are commonly used across various industries, including chemical and petrochemical plants, refineries, and both conventional and nuclear power stations. The heat transfer principle in the cooling tower and the thermodynamic process occurring within the unit are illustrated in Figure 2.

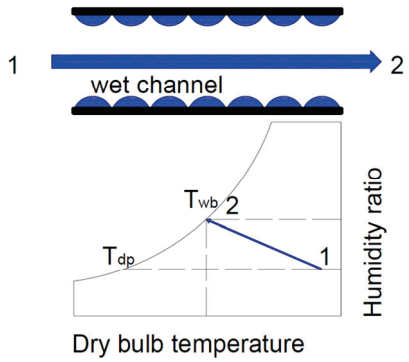


Figure 2. Principle of operation of DEC.

Research on cooling towers primarily focuses on increasing wet-bulb efficiency. In [27], the cooling tower capacity was improved by pre-cooling and dehumidifying the inlet air by using a reverse Brayton cycle. The proposed system was thermodynamically modelled and optimised for the operating conditions using a genetic algorithm to obtain the highest power plant output. The M-cycle can be used in cooling towers. A comparison between a traditional cooling tower and an M-cycle cooling tower was conducted in [28]. The comparison was carried out using a one-dimensional heat and mass transfer model based on the NTU method. It was found that using an M-cycle in a cooling tower allows the water temperature to be lowered below the wet-bulb temperature. This result cannot be achieved with a traditional approach. In [29], on the other hand, optimal dry duct lengths were sought for a cooling tower with an M-cycle, where the fill is arranged in parallel counterflow. The calculations were performed using the NTU method and based on experimental data. Determining the optimal duct length increased the efficiency of the wet thermometer.

https://doi.org/10.3390/en19020554

The IEC and the evaporation tower are considered the most efficient (low electricity consumption) and environmentally friendly (no F-gases and low water consumption). The first device cools the air to the dew point, and the second allows subcooling the process water to the wet-bulb temperature. This paper proposes a solution in which the air is pre-cooled in the IEC and then routed to the cooling tower. A key premise of the research was to demonstrate that using IEC to precool the inlet air improves the cooling tower's efficiency. To test the proposed solution, an experimental stand was constructed to compare a cooling system consisting of a cooling tower and a cooling tower with pre-cooling of the air in the IEC. The comparison focused on electricity consumption and the Seasonal Coefficient of Performance (SCOP). Based on the literature review, no studies to date have analysed the efficiency of this solution. Examples of research on cooling towers carried out so far have focused on the use of a reverse Brayton cycle to cool and dehumidify the inlet air and, above all, the use of the M-cycle in them. These studies have mainly based on simulation results, whereas this paper is based on a two-year experimental study. In addition, studies on new cooling tower solutions focused on improving wet-bulb temperature efficiency and not the SCOP, as in this paper. An increase in SCOP means lower electricity consumption in relation to the cooling energy produced by the cooling tower. The use of an IEC in combination with a cooling tower would be an advantageous solution not only because of lower operating costs, but also because of the environmental benefits of lower electricity consumption and the use of water as a refrigerant (elimination of fluorinated gases). Increasing the efficiency of cooling towers by adding an IEC could lead to greater interest in and use of evaporative units for process cooling or room air conditioning in hotels, hospitals, and office buildings. With the proposed solution, the user will achieve reduced energy consumption or more stable cooling system operation despite higher ambient temperatures.

2. Description of the Experimental Stand and Research Methodology

The study was carried out in two stages. In Stage I, the system operated in the reference (baseline) configuration, i.e., in which water heated by a heat pump was next cooled in a cooling tower using ambient air intake. In Stage II, the inlet air to the cooling tower was precooled by means of an indirect air-conditioning unit. The experimental site was located in the village of Zwrócona in the Ząbkowice district, situated in the Sudetic Foreland region of Poland. One of the most important factors influencing the selection of an appropriate cooling device is the local climate, as it directly affects the achievable final temperature of the liquid or air after cooling. Cooling equipment is designed to provide maximum cooling capacity under the least favourable ambient conditions. These conditions correspond to the highest dry-bulb and wet-bulb temperatures, both of which depend on air humidity. Using the software from the cooling tower manufacturer MITA Cooling Technologies from Siziano, Italy, based on the Meteonorm climate database [30], a suitable unit can be selected, and its operating costs analysed. This ensures the chosen unit operates optimally and is not oversized.

An analysis of climate data for Ząbkowice Śląskie was conducted to determine the most suitable cooling and heating solutions. The maximum and minimum ambient temperatures T_{amb} are 32.5 °C (occurring on 9 July at 15:00) and −17.4 °C (recorded on 12 January at 23:00), respectively. The average dry-bulb temperature is 8.6 °C. The maximum wet-bulb temperature T_{wb} is 22.7 °C on 21 July at 9:00, corresponding to an ambient temperature of T_{amb} = 26.8 °C and coupled with a relative humidity of RH = 71.3%, while the minimum wet-bulb temperature T_{wb} is −17.48 °C on 12 January at 23:00, corresponding to T_{amb} = −17.4 °C and RH = 99.3%. The average wet-bulb temperature is 6.5 °C. The maximum ambient humidity RH is 100%, occurring for approximately 276 h per year; the minimum RH was recorded on 29 May at 13:00 and amounted to 29.5%, with T_{amb} = 23.3

https://doi.org/10.3390/en19020554

°C and T_{wb} = 13.1 °C, and the average ambient humidity is 79.1%. Sorting the wet-bulb temperatures from highest to lowest, it can be seen that the sixteen consecutive highest wet-bulb temperatures correspond to dry-bulb temperatures below 30 °C. The highest wet-bulb temperature recorded for Ząbkowice Śląskie is 22.7 °C. The MITA cooling tower selection software recommends a design wet-bulb temperature of 21 °C for this location. This means that the cooling tower will not achieve the required capacity at wet-bulb temperatures above this value. In the case of Ząbkowice Śląskie, such wet-bulb temperatures only occur for about 35 h a year.

2.1. Stage I

Stage I involved the installation of the cooling device, i.e., an open-circuit cooling tower, and the heating device, represented by an air-source heat pump. The two units were hydraulically separated by a plate heat exchanger. The cooling tower circuit is the secondary circuit, while the heat pump circuit is the primary circuit. The secondary circuit was equipped with a circulation pump and the necessary fittings. The entire system was additionally equipped with an automation unit and measurement sensors. The schematic of the laboratory stand used for the Stage I tests is shown in Figure 3.

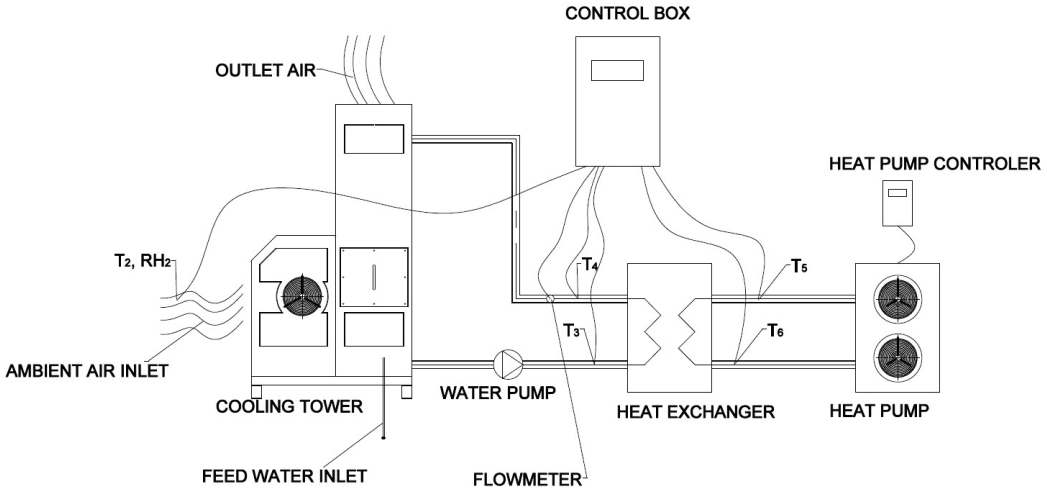


Figure 3. Schematic of the Stage I test stand.

The cooling tower was delivered as a complete solution. The delivery scope included the centrifugal fan, fill pack, spray nozzles, and a float valve for replenishing the circuit with treated water. The tower was not equipped with its own control system, which should include a water temperature sensor at the tower outlet, and the fan speed was modulated based on the setpoint. The fan can be modulated within a frequency range of 25 Hz to 60 Hz. The control system consists of a frequency inverter that adjusts the tower fan's rotational speed based on the temperature sensor's setpoint, which measures the temperature T_3 of the cooled water (i.e., the temperature of the water entering the heat exchanger). Due to water evaporation and associated losses, makeup water must meet specific quality parameters, and circulating water must be refreshed to ensure its properties, such as pH, conductivity, and hardness, do not exceed permissible limits. Because the water volume in the system is small, the refreshing process is performed manually after preliminary water-quality measurements. These measurements were performed at least once every two weeks and no more frequently than once per week.

The parameter that defines the size of a cooling tower is the hydraulic load, expressed as the ratio of the water flow rate (m^3/h) to the fill surface area (m^2). The appropriate flow rate and pressure of water in the cooling tower ensure proper distribution of water throughout the filling pack. Correct water dispersion within the filling pack is essential

https://doi.org/10.3390/en19020554

for achieving efficient operation and maintaining the required outlet water temperature. The filling pack is a wet heat exchanger in which heat transfer occurs within counterflow air–water channels. Water is introduced at the top of the exchanger and subsequently flows downward through the channels as droplets under gravity. Ambient air is supplied from the bottom of the exchanger. Evaporation occurs when the water comes into contact with the air stream. The selected cooling tower model is equipped with a single centrifugal fan providing a nominal airflow rate of 2.770 m^3/h. The unit also includes a float valve for replenishing evaporated water, a water-distribution system with spray nozzles, and a fill pack. The cooling capacity of the evaporative tower is 17 kW at a temperature difference of ΔT = 5 K. The fan power is 0.4 kW. The air inlet is located at the bottom of the unit, where the fan forces air upwards through the entire height of the tower. The manufacturer, MITA Cooling Technologies, indicates that the total pressure drop across the cooling tower is 270 ± 20 Pa at the maximum airflow rate through the device. This value corresponds to the maximum available fan static pressure in the CW3 cooler.

The use of a heat pump was essential because, for the cooling system to operate continuously throughout the study period (from the beginning of May to the end of August), it was necessary to maintain a sufficiently high and constant water temperature at the cooling tower inlet. A monoblock heat pump is an optimal solution, offering high efficiency and a compact design. In the selected air-source heat pump, 1 kilowatt of electrical power can deliver up to 6 kilowatts of thermal output, enabling efficient operation with low electrical energy consumption. The heat pump is equipped with its own control system, which modulates the operation of the refrigeration compressor and the condenser fans. The monoblock air-source heat pump was selected based on the cooling tower's capacity. The unit's circulation pump should ensure a heating-fluid (water) flow rate of approximately 3 m^3/h, and the heat pump's heating capacity should be approximately 17 kW at a temperature difference ($\Delta T = T_{in} - T_{out}$) of 5 K. A Kaysun heat pump, model KHP-MO 12 DTN, was selected. The refrigerant used in the unit is R410A, an HFC-based blend consisting of R32 and R125 in equal (50/50) mass fractions. R410A is non-flammable, has an ozone depletion potential (ODP) of 0, and a global warming potential (GWP) of 2088. This refrigerant is considered environmentally unfriendly, and as of 1 January 2027, the sale of monoblock heat pumps operating with R410A will be prohibited within the European Union.

It is recommended to hydraulically separate the open cooling tower circuit from the closed heat-pump circuit. This is necessary because the water in the cooling tower circuit is exposed to contaminants present in the air and in the tower's surroundings. The heat exchanger was selected based on the water temperatures and flow rates on both the secondary and primary sides of the research station. A plate heat exchanger manufactured by ONDA from Mussolente, Italy, model S 12-26, was chosen. The ONDA plate heat exchanger with installed sensors is shown in Figure 4. The primary function of the circulation pump is to maintain a constant flow rate and pressure of the cooled water passing through the cooling tower and the plate heat exchanger. The Yonos MAXO-Z 25/0.5–7 PN 10 pump manufactured by WILO in Warsaw, Poland, was selected for this purpose.

https://doi.org/10.3390/en19020554

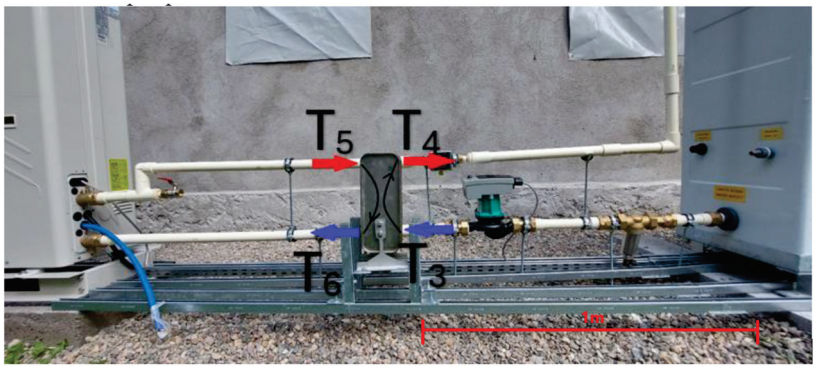


Figure 4. View of the plate heat exchanger hydraulically separating the heat pump circuit (left) from the cooling tower circuit (right).

At the core of the control system is a frequency inverter, which regulates the speed of the cooling tower fan motor group based on measurements obtained from the cooling tower outlet water temperature sensor T_3. The primary function of the system is to maintain the outlet temperature of the circulating water leaving the cooling tower at a predefined setpoint. The setpoint can be adjusted manually using a potentiometer that is synchronised with the PLC controller. Cooling towers are selected based on design conditions, which are always defined for the least favourable operating scenario. The maximum thermal load occurs under the most demanding ambient conditions, when the tower fan operates at its maximum rotational speed (60 Hz). For the remainder of the operating time throughout the year, the fan speed is modulated between 20 and 60 Hz. Measurement data from all sensors are recorded at 10 s intervals. The control and data-logging system is equipped with the following: a MIM 1205HG4C3T0 electromagnetic flow meter manufactured by KOBOLD in Settimo Milanese, Italy; PT100 temperature sensors manufactured by Limatherm Sensor in Limanowa, Poland, with a measurement range of −50 to 200 °C; an integrated TH2E thermo-hygrometer manufactured by Papouch in Prague, Czech Republic, enabling relative humidity measurements from 0% to 100%, temperature measurements from −40 to +123.8 °C, and dew-point calculation; and an ME300 frequency inverter adapted for a 0.37 kW fan, as well as an AS218 PLC equipped with a PID controller that is capable of direct data logging to a USB drive, both manufactured by Delta in Taoyuan City, Taiwan. The proper operation of the heat pump is managed by a wall-mounted controller on which the desired outlet water temperature must be set. The circulation pump of the heating circuit, installed inside the unit's housing, offers three-stage flow regulation. The controller activates the water pump when the measured temperature drops by 2 K relative to the setpoint. It also allows monitoring of the unit's electrical energy consumption, which is essential for comparing energy use between Stage I and Stage II of the experimental study.

On the laboratory bench, measurements are taken of the water temperature at the inlet (T_4) and outlet (T_3) of the cooling tower, at the inlet (T_6) and outlet (T_5) of the heat pump, as well as the air temperature (T_2) at the inlet to the cooling tower. In addition, the relative humidity (RH_2) of the air at the cooling tower inlet and the water flow rate through the tower ($\dot{V}_{cool}$) and heat pump ($\dot{V}_{hp}$) are measured, as well as the frequency and current (I) of the fan motor. The resolutions, measurement accuracies, and descriptions of the sensors used are shown in Table 1.

https://doi.org/10.3390/en19020554

Table 1. Measuring instruments and their accuracy.

Measured Parameter	Symbol	Location/Description	Resolution	Accuracy
Cooled water temperature	T_3, °C	Cooling tower outlet	0.1 °C	1.5%
Heated water temperature	T_4, °C	Cooling tower inlet	0.1 °C	1.5%
Heated water temperature	T_5, °C	Heat pump outlet	0.1 °C	1.5%
Cooled water temperature	T_6, °C	Heat pump inlet	0.1 °C	1.5%
Ambient air temperature	T_2, °C	Cooling tower air inlet	0.1 °C	1.5%
Relative humidity	RH, %	Cooling tower air inlet	1 °C	1.5%
Water flow rate	$\dot{V}_{cool}$, m^3/h	Cooling tower water loop	0.1 m^3/h	0.1%

2.2. Stage II

The research station for Stage II of the study was expanded to include a precooling system for the cooling tower inlet air. The optimal solution is the indirect evaporative cooling system Coolerado^{TM}, manufactured by Seeley International form Lonsdale, Australia, which provides a complete configuration and enables the supply-air temperature to be reduced below the wet-bulb temperature. Since this system is initially designed to cool indoor spaces by delivering conditioned air, it is equipped with fans, a water distribution system, and an integrated control unit. The complete schematic of the Stage II setup is shown in Figure 5.

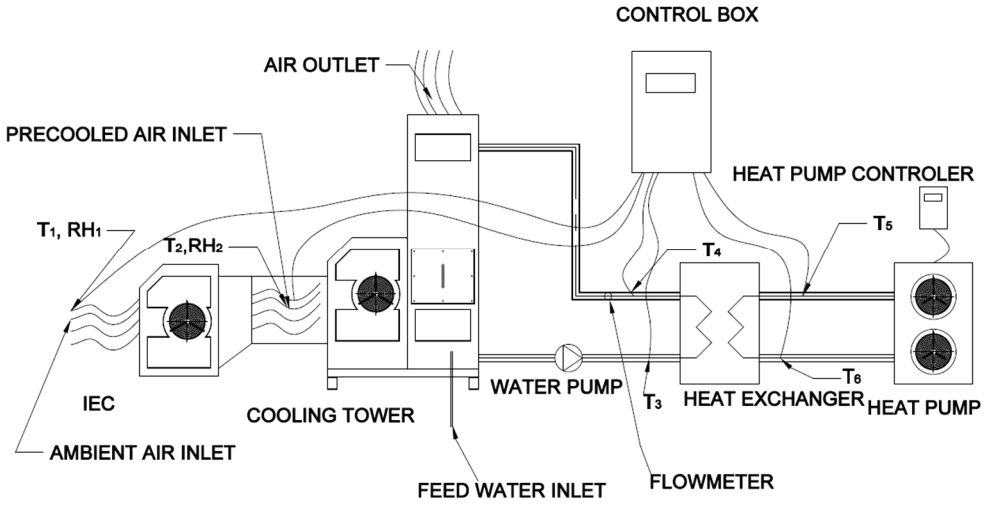


Figure 5. Scheme of Stage II of the research station.

An IEC CW3 model by Seeley International, Lonsdale, Australia, was used. This unit is a complete solution with an indirect regenerative heat exchanger. The maximum available fan static pressure is 270 Pa, which should be sufficient to overcome the highest expected pressure drops in the ventilation ducts and within the cooling tower itself. The unit has a cooling capacity of 17 kW and an electrical input of 1.75 kW. The nominal airflow rate of the fan is 5360 m^3/h, and the water consumption is 13 L/min. The IEC connection to the cooling tower is shown in Figure 6.

https://doi.org/10.3390/en19020554

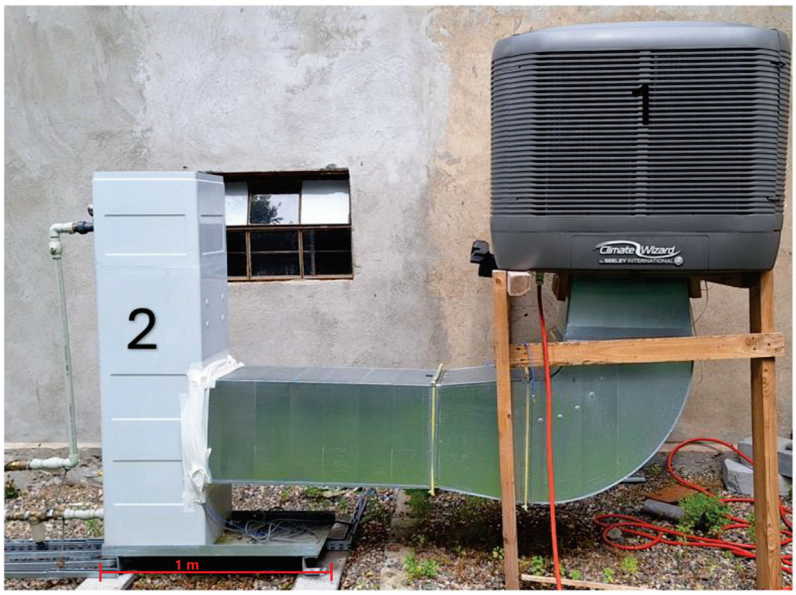


Figure 6. Connection of evaporative cooler (1) to a cooling tower (2).

The CW3 IEC is equipped with its own controller, connected to the unit via a communication cable. The cooler operates in automatic cooling mode with a minimum allowable supply air temperature set point of +16 °C.

Measurements in Stage II were extended from those in Stage I to include measurement of temperature (T_1) and relative humidity (RH_1) at the inlet to the evaporative cooler.

2.3. Methodology

To demonstrate the impact of precooling the inlet air on energy consumption and the evaporative tower's cooling capacity, experimental tests were conducted. These tests involved comparing the operation of a cooling installation equipped solely with a cooling tower to that of an installation in which the tower was supplemented with the IEC, providing precooling of the air entering the tower. The study was divided into two stages. The measured values and calculation results obtained in Stages I and II were compiled into tables and graphs.

The Stage I measurements were carried out from 1 May 2023 to 31 August 2023. In turn, the Stage II measurements were conducted from 1 May 2024 to 31 August 2024. During Stage I research, the system operated for a total of 2952 h, and during Stage II, it operated for 2951 h, with a constant heat load supplied by the heat pump. Measurements were recorded every 10 s throughout the system's operating period in Stages I and II.

Measurements taken during the operation of the experimental research station in both Stage I and Stage II did not include the data necessary to perform complete analyses. The additional quantities calculated for both research stages were as follows: the cooling capacity of the cooling tower, the thermal capacity of the heat pump, the electrical power of the fan motor in the tower, the ambient air wet-bulb temperature, and the cooling tower's Coefficient of Performance (COP).

In addition to the primary performance evaluation, supplementary analyses were conducted, including an economic assessment of the proposed system. The economic review accounted for the electricity consumption of the IEC auxiliary fans and the cooling tower fan. These analyses confirmed that the financial performance is strongly influenced by the auxiliary fans' configuration and their electricity demand; however, they did not have a significant impact on the thermodynamic performance trends or the main conclusions of

https://doi.org/10.3390/en19020554

this study. Therefore, the results of these analyses are not presented in detail, while their execution is explicitly noted here for methodological completeness and transparency.

To calculate the cooling capacity of the cooling tower $\dot{Q}_{cool}$, an energy balance equation on the cooling water side was used:

$$\dot{Q}_{cool} = \dot{m}_{w,cool} C_{w,cool} (T_4 - T_3), \tag{3}$$

where $\dot{m}_{w,cool}$ is the mass flow rate of cooling water, $C_{w,cool}$ is the specific heat capacity of water, T_4 is the inlet water temperature, and T_3 is the outlet water temperature.

The mass flow rate of the cooled water in the tower is determined on the basis of the measured volumetric flow rate $\dot{V}_{cool}$:

$$\dot{m}_{w,cool} = \rho_{w,\,cool} \dot{V}_{cool} \tag{4}$$

where $\rho_{w,\,cool}$ is the density of the cooled water in the cooling tower.

The thermal capacity of the heat pump $\dot{Q}_{hp}$ was also calculated on the basis of an energy balance, defined in this case on the heated-water side of the device:

$$\dot{Q}_{hp} = \dot{m}_{w,hp} C_{w,hp} (T_5 - T_6) \tag{5}$$

where $\dot{m}_{w,hp}$ is the mass flow rate of water in the heat pump loop, $C_{w,hp}$ is the specific heat capacity of water, T_5 is the inlet water temperature, and T_6 is the outlet water temperature.

Similarly to the cooling tower, in the case of the heat pump, the water mass flow rate was determined on the basis of the known volumetric water flow rate $\dot{V}_{hp}$:

$$\dot{m}_{w,hp} = \rho_{w,\,hp} \dot{V}_{hp} \tag{6}$$

where $\rho_{w,\,hp}$ is the density of the water heated in the heat pump.

In the case of the heat pump, the volumetric flow rate of the heated water $\dot{V}_{hp}$ is constant and equal to 2.6 m^3/h.

The density in Equations (4) and (6) and the specific heat in Equations (3) and (5) are determined from polynomial functions for the mean water temperature flowing through the cooling tower or heat pump. The water density as a function of temperature is given by the following:

$$\rho = 1003.871389 - 0.49355774\,T + 0.006389001\,T^2 - 8.7267 \times 10^{-5}\,T^3 + 3.4308 \times 10^{-7}\,T^4 - 4.6788 \times 10^{-10}\,T^5 \tag{7}$$

where T is the fluid temperature (in °C). The standard deviation of the water density is $\sigma = \pm 4.0586$ kg/m^3, and the coefficient of determination is (r^2 = 0.999).

The relationship for the specific heat capacity of water as a function of temperature is given by

$$\begin{aligned} C_w = {} & 4220.853492 + 3.969000719\,T - 0.35459395\,T^2 + 0.009487507\,T^3 - 0.00011820\,T^4 \\ & + 7.87319 \times 10^{-7}\,T^5 - 2.8613 \times 10^{-9}\,T^6 + 5.33092 \times 10^{-12}\,T^7 - 3.9578 \times 10^{-15}\,T^8 \end{aligned} \tag{8}$$

where T is the fluid temperature (in °C). The standard deviation of the specific heat capacity of water is $\sigma = \pm 39.99$ J/(kgK), and the coefficient of determination is r^2 = 0.999.

Equations (7) and (8) are valid for the temperature range from 0 to 370 °C.

To determine the active electrical power of the three-phase fan motor of the cooling tower, the following equation was used:

$$P_{fan} = \sqrt{3} U I cos(\varphi) \tag{9}$$

https://doi.org/10.3390/en19020554

where U is the voltage, I is the electric current, and $cos(\varphi)$ is the power factor.

The ambient air wet-bulb temperature was calculated using the formula proposed by Stull [31]:

$$T_{wb} = T_{amb}\, arctan\left(0.151977(RH + 8.313659)^{\frac{1}{2}}\right) + arctan(T_{amb} + RH) - arctan(RH - 1.676331) + 0.00391838\, RH^{\frac{3}{2}}\, arctan(0.023101\, RH) - 4.686035 \quad (10)$$

where T_{amb} is the ambient temperature (in °C), and RH is the relative humidity of the air (in %).

According to [32], Stull's formula provides the highest accuracy for the calculated wet-bulb temperature within the range from −1 °C to 0.65 °C, for ambient temperatures between −20 °C and 50 °C, and relative humidity from 5% to 99%.

The measurements performed also made it possible to determine the theoretical SCOP of the cooling tower, expressed by the following equation:

$$\mathrm{SCOP_{CT}} = \frac{\dot{Q}_{cool}}{P_{fan}} \quad (11)$$

where $\dot{Q}_{cool}$ is the heat flux dissipated by the cooling tower, and P_{fan} is the power consumed by the fan.

Based on the cooling tower capacity $\dot{Q}_{cool}$ calculated for each measuring point (the time step was 10 s), the amounts of heat transferred to the air during each successive 10 s were calculated. Their sum for the entire operating period of the system represents the amount of cooling energy produced by the cooling tower Q_{cool}. Similarly, the electricity consumption of the cooling tower fans W_{fan} was determined on the basis of their power P_{fan} and the amount of heat generated by the heat pump Q_{hp} on the basis of its capacity $\dot{Q}_{hp}$. These calculations were performed separately for Stage I and Stage II.

For the performed calculations of indirect measurements, their uncertainties were determined. In accordance with the law of error propagation, the precision limits, assuming a 95% confidence level, are calculated using the following equation [33]:

$$U = \sqrt{P^2 + B^2}, \quad (12)$$

where P is the precision limit of measurement, and B is the bias limit of measurement, which was omitted in these studies.

The method of determining measurement uncertainty is illustrated by the example of a cooling tower's capacity. The formula for the precision limits for cooling tower capacity is as follows:

$$\begin{aligned} P^2_{\dot{Q}_{cool}} &= \left(\frac{\partial \dot{Q}_{cool}}{\partial \dot{V}_{cool}}\right)^2 P^2_{\dot{V}_{cool}} + \left(\frac{\partial \dot{Q}_{cool}}{\partial \rho_{w,cool}}\right)^2 P^2_{\rho_{w,cool}} + \left(\frac{\partial \dot{Q}_{cool}}{\partial C_{w,cool}}\right)^2 P^2_{C_{w,cool}} + \left(\frac{\partial \dot{Q}_{cool}}{\partial T_4}\right)^2 P^2_{T_4} + \left(\frac{\partial \dot{Q}_{cool}}{\partial T_3}\right)^2 P^2_{T_3} \\ &= (\rho_{w,cool} \cdot C_{w,cool}(T_4 - T_3))^2 P^2_{\dot{V}_{cool}} + \left(\dot{V}_{cool} \cdot C_{w,cool}(T_4 - T_3)\right)^2 P^2_{\rho_{w,cool}} \\ &+ \left(\dot{V}_{cool} \cdot \rho_{w,cool}(T_4 - T_3)\right)^2 P^2_{C_{w,cool}} + \left(\dot{V}_{w,ch} \cdot \rho_{w,cool} \cdot C_{w,cool}\right)^2 P^2_{T_4} \\ &+ \left(-\dot{V}_{cool} \cdot \rho_{w,cool} \cdot C_{w,ch}\right)^2 P^2_{T_3} \\ &= \left(\frac{\dot{Q}_{cool}}{\dot{V}_{cool}}\right)^2 P^2_{\dot{V}_{cool}} + \left(\frac{\dot{Q}_{cool}}{\rho_{w,cool}}\right)^2 P^2_{\rho_{w,cool}} + \left(\frac{\dot{Q}_{cool}}{C_{w,ch}}\right)^2 P^2_{C_{w,cool}} + \left(\frac{\dot{Q}_{cool}}{T_4 - T_3}\right)^2 P^2_{T_4} + \left(\frac{-\dot{Q}_{cool}}{T_4 - T_3}\right)^2 P^2_{T_3} \end{aligned} \quad (13)$$

where $P_{\dot{V}_{cool}}$, P_{T_3}, and P_4 are the measurement uncertainties (type B) determined from the class of measurement sensors, while $P_{\rho_{w,cool}}$ and $P_{C_{w,cool}}$ are the standard deviations of the approximated densities and specific heat, respectively (type A).

https://doi.org/10.3390/en19020554

Hence, the measurement uncertainty of the cooling tower capacity is expressed by the following formula:

$$U_{\dot{Q}_{cool}} = \sqrt{\left(\frac{\dot{Q}_{cool}}{\dot{V}_{cool}}\right)^2 P^2_{\dot{V}_{cool}} + \left(\frac{\dot{Q}_{cool}}{\rho_{w,cool}}\right)^2 P^2_{\rho_{w,cool}} + \left(\frac{\dot{Q}_{cool}}{C_{w,ch}}\right)^2 P^2_{C_{w,cool}} + \left(\frac{\dot{Q}_{cool}}{T_4-T_3}\right)^2 P^2_{T_4} + \left(\frac{-\dot{Q}_{cool}}{T_4-T_3}\right)^2 P^2_{T_3}}$$
$$= \sqrt{\dot{Q}^2_{cool}\left[\left(\frac{P_{\dot{V}_{cool}}}{\dot{V}_{cool}}\right)^2 + \left(\frac{P_{\rho_{w,cool}}}{\rho_{w,cool}}\right)^2 + \left(\frac{P_{C_{w,cool}}}{C_{w,cool}}\right)^2 + \left(\frac{P_{T_4}}{T_4-T_3}\right)^2 + \left(\frac{-P_{T_3}}{T_4-T_3}\right)^2\right]} \quad (14)$$

In summary, the study used both qualitative and quantitative research methods. An overview of the applied research methods is presented in Table 2.

Table 2. Summary of research methods.

Research Methods	Description
Document examination method	A literature review was conducted, and existing research on evaporative cooling devices was analysed.
Experimental method	Measurements on the experimental stand were carried out and recorded. An analysis of the measured values was carried out.
Mathematical modelling	Based on the measurements, calculations were performed for quantities that could not be directly measured, such as $SCOP_{CT}$. An analysis of the results obtained was carried out.

3. Results

This chapter presents the measurement results for Stages I and II. The dataset was supplemented with calculations of the evaporative tower's cooling capacity $\dot{Q}_{cool}$ (from Equation (3)), the heat pump's heating capacity $\dot{Q}_{hp}$ (from Equation (5)), the ambient air wet-bulb temperature T_{wb} (from Equation (10)), and the SCOP of the cooling tower (from Equation (11)). In this chapter, ambient temperature T_{amb} is equal to temperature T_2 in Stage I and temperature T_1 in Stage II. The measurement data also include the dew-point temperature, calculated by the controller based on the dry-bulb temperature and relative humidity. Table 3 summarises the average values of selected measured and computed parameters for Stages I and II. They were calculated as arithmetic means over the entire operational period of the system in Stages I and II.

Table 3. Average values of the parameters measured and calculated in Stages I and II.

Parameter	Stage I	Stage II
T_3, °C	30.1 ± 1.5%	30.6 ± 1.5%
T_4, °C	25.1 ± 1.5%	24.8 ± 1.5%
T_5, °C	36.0 ± 1.5%	35.3 ± 1.5%
T_6, °C	30.0 ± 1.5%	29.7 ± 1.5%
$\dot{Q}_{cool}$, kW	17.3 ± 1.9%	19.9 ± 1.9%
$\dot{Q}_{hp}$, kW	18.2 ± 2.0%	19.3 ± 1.7%
T_{amb}, °C	19.0 ± 1.5%	19.9 ± 1.5%
T_{wb}, °C	15.9 ± 1.5%	17.1 ± 1.6%
Frequency, Hz	31.7 ± 5.0%	29.0 ± 5.0%
I, mA	380.4 ± 5.0%	327.6 ± 5.0%
$\dot{V}_{cool}$, m^3/h	2.9 ± 0.1%	2.9 ± 0.1%

To compare all stages, the total amount of cooling energy produced by the cooling tower Q_{cool}, the total thermal energy delivered by the heat pump Q_{hp}, and the electrical energy consumed by the cooling tower fan motor W_{fan} were calculated for the respective

measurement periods. From these results, the SCOP of the cooling tower was determined for each stage. All corresponding data are presented in Table 4.

Table 4. A summary of the cooling energy produced Q_{cool} and the electrical energy consumed W_{fan} by the cooling tower, the thermal energy delivered by the heat pump Q_{hp}, and the SCOP of the cooling tower.

	Stage I	**Stage II**
Quantity of cooling energy generated by the cooling tower Q_{cool}, kWh	51,050 ± 3.5%	58,550 ± 3.7%
Electricity consumption of the cooling tower W_{fan}, kWh	1115 ± 3.4%	980 ± 3.1%
Quantity of heat energy generated by the heat pump Q_{hp}, kWh	53,460 ± 3.8%	56,659 ± 3.9%
$SCOP_{CT}$, kWh/kWh	45.8 ± 2.2%	59.7 ± 2.4%

3.1. Test Under Increased Thermal Load—16 August 2024

On 16 August 2024, a test of the cooling system was conducted during the period of the highest ambient temperatures. The purpose of this test was to evaluate how maximum precooling of the inlet air, combined with an increased thermal load, would affect the performance of the evaporative tower. During the test period (10:45–14:45), the ambient temperature ranged from 25 °C to 32 °C, and the relative humidity ranged from 45% to 75%.

The test consisted of turning off the automatic operation of both the CW3 cooler and the MCT 25 cooling tower. Both devices were operated at maximum fan speed and with lowered setpoints for the precooled air temperature (T_2) and the water temperature (T_3). The cooling tower inverter frequency was set to 60 Hz, while the cooler's controller was switched to manual mode with the minimum allowable temperature setpoint of 18 °C and maximum supply air flow. Additionally, the outlet water temperature T_5 from the heat pump was increased to 45 °C. Table 5 presents hourly average values of selected measured and calculated parameters obtained during the test. In Table 3, the symbols T_{amb} and RH_{amb} represent the temperature T_1 and relative humidity RH_1 of the air measured at the inlet to the IEC, while $T_{precool}$ and $RH_{precool}$ represent T_2 and RH_2 measured at the cooling tower air inlet.

Table 5. Average values of the parameters measured and calculated in Stage II.

Parameter	**1st Hour 10:45/11:45**	**2nd Hour 11:45/12:45**	**3rd Hour 12:45/13:45**	**4th Hour 13:45/14:45**
T_{amb}, °C	25.1 ± 1.5%	31.1 ± 1.5%	30.9 ± 1.5%	31.1 ± 1.5%
RH_{amb}, %	71.6 ± 5.0%	52.4 ± 5.0%	51.1 ± 5.0%	48.3 ± 5.0%
$T_{precool}$, °C	20.7 ± 1.5%	21.2 ± 1.5%	21.3 ± 1.5%	21.6 ± 1.5%
$RH_{precool}$,%	90.1 ± 5.0%	90.6 ± 5.0%	89.7 ± 5.0%	86.9 ± 5.0%
T_3, °C	25.5 ± 1.5%	25.3 ± 1.5%	25.3 ± 1.5%	25.3 ± 1.5%
T_4, °C	34.9 ± 1.5%	35.1 ± 1.5%	35.1 ± 1.5%	34.8 ± 1.5%
T_5, °C	44.8 ± 1.5%	45.4 ± 1.5%	45.1 ± 1.5%	45.1 ± 1.5%
T_6, °C	34.7 ± 1.5%	35.3 ± 1.5%	35.1 ± 1.5%	34.9 ± 1.5%
$\dot{Q}_{cool}$, kW	32.8 ± 3.5%	34.2 ± 3.5%	35.1 ± 3.5%	33.4 ± 3.5%
$\dot{Q}_{hp}$, kW	30.7 ± 3.1%	33.5 ± 3.1%	32.3 ± 3.1%	31.9 ± 3.1%

3.2. Comparison of Measurements for Selected Days of Stage I and Stage II

From the available measurement data, two representative days were selected: one from Stage I (17 August 2023) and another from Stage II (11 August 2024). The selection criterion was a similar daily profile of ambient dry-bulb temperature and wet-bulb temperature.

https://doi.org/10.3390/en19020554

Table 6 presents the measured and calculated average values, while Table 7 summarises the amounts of cooling energy Q_{cool} produced by the cooling tower, thermal energy Q_{hp} produced by the heat pump, the electrical energy consumed by the fans of the cooling tower W_{fan}, and the resulting $SCOP_{CT}$ values. Figure 7 illustrates the daily distribution of the measured dry-bulb temperatures and the calculated wet-bulb temperatures.

Table 6. Average values of the parameters measured and calculated in Stages I and II.

Parameter	Stage I	Stage II
T_3, °C	25.0 ± 1.5%	25.0 ± 1.5%
T_4, °C	30.2 ± 1.5%	30.1 ± 1.5%
T_5, °C	30.0 ± 1.5%	29.9 ± 1.5%
T_6, °C	35.0 ± 1.5%	35.1 ± 1.5%
$\dot{Q}_{cool}$, kW	17.4 ± 1.5%	19.6 ± 1.9%
$\dot{Q}_{hp}$, kW	18.2 ± 1.7%	19.9 ± 2.1%
T_{amb}, °C	20.1 ± 1.5%	20.5 ± 1.5%
T_{wb}, °C	16.6 ± 1.6%	16.9 ± 1.6%
Frequency, Hz	32.5 ± 5.0%	29.3 ± 5.0%
I, mA	390.7 ± 5.0%	378.1 ± 5.0%
$\dot{V}_{cool}$, m^3/h	2.9 ± 0.1%	2.9 ± 0.1%

Table 7. A summary of the cooling energy produced Q_{cool} and the electrical energy consumed W_{fan} by the cooling tower, the thermal energy delivered by the heat pump Q_{hp}, and the $SCOP_{CT}$ of the cooling tower.

	Stage I	Stage II
Quantity of cooling energy generated by the cooling tower Q_{cool}, kWh	417.6 ± 3.4%	470.4 ± 3.7%
Electricity consumption of the cooling tower W_{fan}, kWh	9.4 ± 3.4%	9.1 ± 3.1%
Quantity of heat energy generated by the heat pumpQ_{hp}, kWh	436.8 ± 3.2%	477.6 ± 3.3%
$SCOP_{CT}$, kWh/kWh	44.4 ± 2.2%	51.7 ± 2.3%

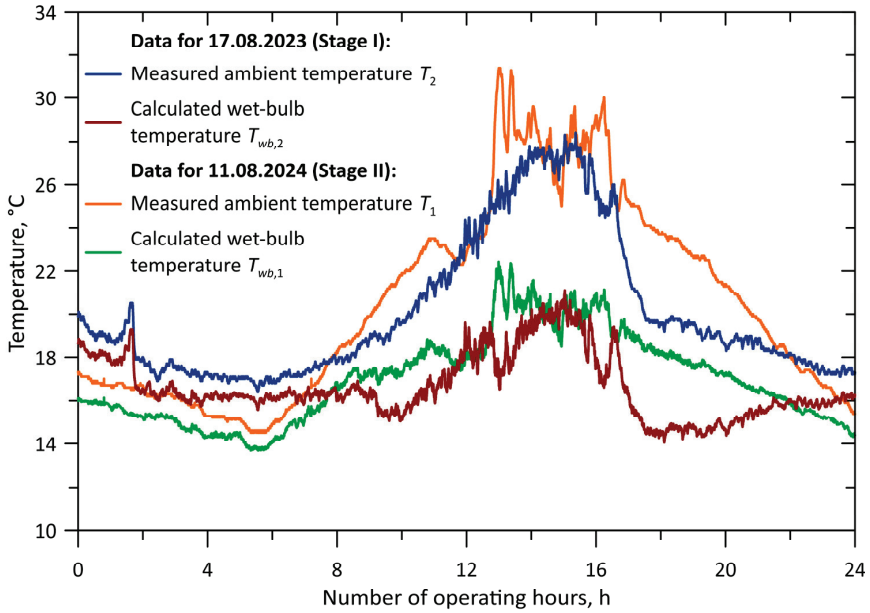


Figure 7. Ambient (dry-bulb) and wet-bulb temperatures for 17 August 2023 (Stage I) and for 11 August 2024 (Stage II).

https://doi.org/10.3390/en19020554

4. Analysis of Results and Discussion

This paper presents the results of experimental investigations (Stages I and II) conducted over two cooling seasons (from early May to the end of August) in 2023 and 2024. The statistical climate data included in the MITA software assume a wider range of dry-bulb temperatures. The minimum and maximum values are 1.5 °C and 32 °C, respectively. However, measurements from Stages I and II showed that during the analysed period, the ambient temperature did not fall below 9 °C. Figure 8 illustrates the temperature distribution for Stage I, while Figure 9 presents the corresponding distribution for Stage II. The maximum dry-bulb temperature recorded in Stage I was 32.9 °C, and in Stage II it reached 35.6 °C. The average dry-bulb temperature in Stage II was 0.9 °C higher than in Stage I.

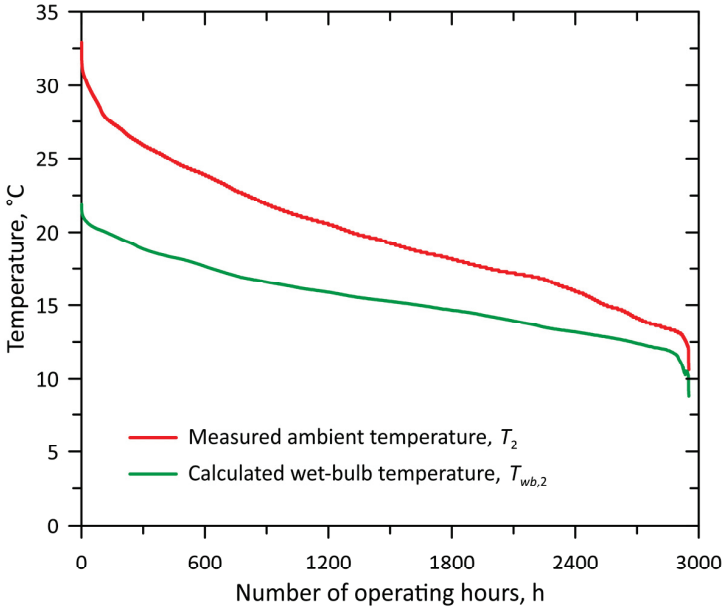


Figure 8. Hourly profiles of the ambient temperature (T_2) and the wet-bulb temperature ($T_{wb,2}$) at the inlet of the cooling tower for Stage I.

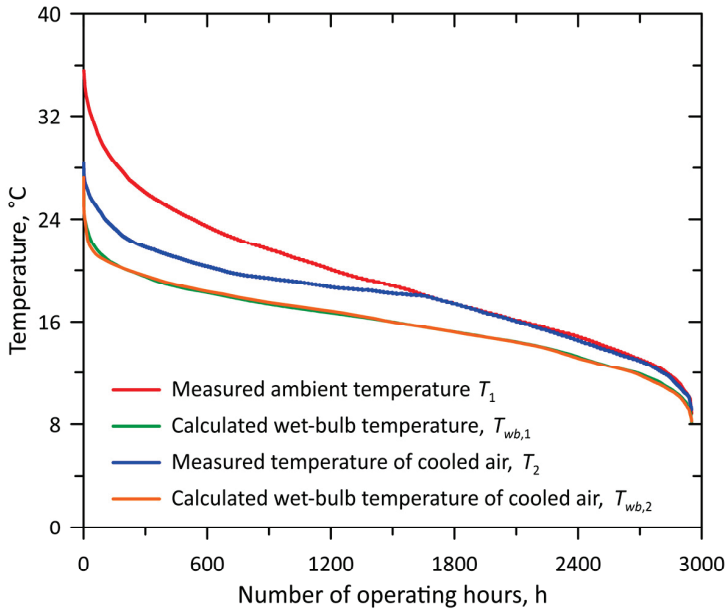


Figure 9. Hourly profile of ambient temperature T_1 and wet-bulb temperature $T_{wb,1}$ at the inlet to the IEC and air temperature T_2 and wet-bulb temperature $T_{wb,2}$ after pre-cooling at the inlet to the cooling tower for Stage II.

https://doi.org/10.3390/en19020554

The wet-bulb temperatures also differed between the two stages. Once again, the statistical data values are lower than the actual measurements. The lowest calculated wet-bulb temperature was 9.1 °C for Stage I and 8.3 °C for Stage II. The average wet-bulb temperature in 2024 was 1.2 °C higher than in 2023.

Higher ambient dry-bulb and wet-bulb temperatures reduce the available driving potential for heat and mass transfer, thereby reducing cooling tower capacity. In Stage II, the higher maximum and average dry-bulb temperatures increased the average wet-bulb temperature, further increasing the outlet water temperature from the cooling water. As a result, operation under such conditions generally leads to reduced cooling capacity, higher outlet temperatures, and increased electricity demand. Consequently, the improved capacity observed in Stage II, despite less favourable ambient conditions, highlights the beneficial impact of the air at the cooling tower inlet on the cooling tower's operation.

In Figure 9, a decreasing difference between the ambient air temperature and the cooled air temperature can be observed. This effect is associated with the control process of the CW3 cooler. The fan speed in the CW3 unit automatically adjusts to the set temperature, which in this case was 18 °C. The cooler's water consumption, which supplies the wet channels, is constant and not subject to regulation. Consequently, the closer the ambient temperature is to the set point, the lower the fan speed.

The calculated $SCOP_{CT}$ for Stage I is consistent with MITA's software's theoretical assumptions. Although the statistical dataset assumes a broader range of minimum and maximum dry-bulb and wet-bulb temperatures, these values are representative of the actual climatic conditions that may occur at the studied location. The cooling tower using precooled air from the CW3 unit achieved a $SCOP_{CT}$ approximately 30% higher than in Stage I. This improvement demonstrates that the proposed solution enables higher cooling capacity while reducing electricity consumption compared with the stand-alone cooling tower. Moreover, the cooling tower operating in combination with the IEC exhibited significantly higher efficiency, despite experiencing higher peak dry-bulb and wet-bulb temperatures than those recorded during the Stage I measurements.

The test conducted on 16 August 2024 demonstrated that the cooling tower with a precooled inlet air temperature could achieve substantially higher cooling capacity. This effect was observed under high ambient temperatures and increased thermal load from the heat pump. Under these conditions, the cooling tower maintained the outlet water temperature (T_3) below 25.5 °C, while the maximum difference between the ambient air temperature and the cooled air temperature reached 9.9 K. The cooling capacity of the evaporative tower increased from its nominal value of 17 kW to approximately 35 kW, and the heat pump's thermal output likewise increased to a maximum of about 35 kW. This enhancement was a direct result of the increased water-side temperature difference ΔT.

The comparison confirms that precooling the inlet air to the cooling tower using an IEC reduces electricity consumption and increases the thermal efficiency of the open-circuit cooling tower. The selected day of Stage II (11 August 2024) was warmer than the corresponding day of Stage I (17 August 2023), with an average dry-bulb temperature higher by 0.5 °C and an average wet-bulb temperature higher by 0.3 °C. Despite these less favourable ambient conditions, the average electricity consumption by the tower fan motor in Stage II was approximately 4% lower than in Stage I. The increased water temperature difference observed in the cooling tower of the Stage II system is a direct result of inlet air precooling, which improves heat and mass transfer by reducing the inlet air's effective wet-bulb temperature. Consequently, the higher thermal load on the heat pump is enabled by the improved air-side conditions and is not an independent effect.

https://doi.org/10.3390/en19020554

5. Conclusions

This study demonstrated that precooling of the inlet air to the cooling tower using an IEC significantly improves system capacity under both nominal and extreme operating conditions. Compared to the reference system without precooling, the proposed configuration increased cooling capacity by 14.7% and reduced the cooling tower's electricity consumption by 135 kWh, while enabling lower outlet water temperatures.

The main scientific achievement of this work is the experimental confirmation that IEC-based inlet air precooling leads to a substantial improvement in the Seasonal Coefficient of Performance of the cooling tower ($SCOP_{CT}$), which increased by approximately 30% compared to operation without precooling.

The key assumption of the research was that using IEC to precool the inlet air improves the cooling tower's efficiency, and this thesis was proven.

Unlike previous studies, which predominantly focused on improving wet-bulb efficiency, the present work introduces SCOP as a comprehensive, seasonally representative performance indicator for cooling towers. Based on an extensive literature review, no experimental studies were identified that evaluate the impact of IEC-based inlet air precooling on the SCOP of an open-circuit cooling tower, which highlights the novelty of the present research.

An increase in SCOP directly indicates lower electricity consumption relative to the useful cooling energy generated, providing a more application-oriented assessment of cooling tower performance.

Additional tests conducted at high ambient temperatures and elevated thermal loads confirmed that the integrated cooling tower and IEC system ensures reliable operation even under extreme conditions, which is particularly important for industrial facilities lacking backup cooling capacity or undergoing periodic expansions.

Although including auxiliary IEC fans increases total electricity consumption, the improved operational reliability may outweigh the associated increase in operating costs in many practical applications.

The results further indicate that additional energy savings may be achieved through alternative system configurations, particularly those that integrate only an indirect heat exchanger rather than a complete IEC with auxiliary fans.

Possible alternative configurations include the following:

- Standalone HMX or MicroCore (CW3) modules installed at the cooling tower air inlet;
- A single fan driving the ambient air stream, which is then precooled and finally exhausted from the cooling tower, overcoming total pressure losses in the system.

The proposed solution applies not only to open-circuit cooling towers but also to closed-circuit systems, where even greater efficiency improvements and extended dry-operation (free-cooling) periods can be expected. Furthermore, inlet air precooling can compensate for reduced cooling capacity associated with the transition to environmentally friendly, low-GWP refrigerants, enabling system modernisation without performance degradation.

The study confirms that precooling the inlet air using the IEC significantly enhances the capacity of open-circuit evaporative cooling towers, particularly in climates characterised by a large dry-bulb to wet-bulb temperature difference. The experimental results demonstrate that precooling the inlet air reduces cooling tower electricity consumption by approximately 15%, accompanied by a noticeable increase in cooling capacity and a lower outlet water temperature.

The benefits of precooling the inlet air to the cooling tower are most pronounced in hot, dry, or semi-arid climates, where the high evaporative potential enables effective reduction in air temperature before it enters the cooling tower. In temperate climates,

https://doi.org/10.3390/en19020554

significant electrical energy savings can still be achieved during peak summer conditions. In contrast, in hot, humid climates, the effect is more limited and is primarily suitable for precooling air-inlet applications. Overall, the study's results indicate that IEC-based inlet air precooling is an effective strategy for reducing electricity consumption and improving operational reliability of open evaporative cooling towers, particularly under high ambient temperatures.

Author Contributions: Conceptualization, B.J.; methodology, B.J.; validation, B.J.; formal analysis, B.J.; investigation, B.J.; resources, B.J. and M.J.; writing—original draft preparation, B.J.; writing—review and editing, M.J.; visualisation, B.J. and M.J.; supervision, M.J. All authors have read and agreed to the published version of the manuscript.

Funding: This research was funded by the Implementation Doctorate programme, contract No. DWD/4/25/2020.

Data Availability Statement: The data presented in this study are available on request from the corresponding author due to the know-how of producers of cooling devices.

Conflicts of Interest: The authors declare no conflicts of interest.

Abbreviations

The following abbreviations are used in this manuscript:

COP	Coefficient of Performance
DEC	Direct Evaporative Cooler
GWP	Global Warming Potential
HMX	Heat and Mass Exchanger
HVAC	Heating, Ventilation, and Air Conditioning
IEC	Indirect Evaporative Cooler
M-cycle	Maisotsenko Cycle
ODP	Ozone Depletion Potential
RH	Relative Humidity
SCOP	Seasonal Coefficient of Performance
VCRS	Vapour-Compression Refrigeration System

References

1. International Energy Agency. The Future of Cooling. Opportunities for Energy-Efficient Air Conditioning, OECD/IEA, 2018. Available online: https://www.iea.org (accessed on 3 December 2025).
2. BITZER Kuehlmaschinenbau GmbH. Refrigerant Report 20; A-501-20 EN. Available online: https://www.bitzer.de (accessed on 3 December 2025).
3. Yang, Z.; Feng, B.; Ma, H.; Zhang, L.; Duan, C.; Liu, B.; Zhang, Y.; Chen, S.; Yang, Z. Analysis of lower GWP and flammable alternative refrigerants. *Int. J. Refrig.* **2021**, *126*, 12–22. [CrossRef]
4. Artusoa, P.; Marinetti, S.; Minetto, S.; Del Col, D.; Rossetti, A. Modelling the performance of a new cooling unit for refrigerated transport using carbon dioxide as the refrigerant. *Int. J. Refrig.* **2020**, *115*, 158–171. [CrossRef]
5. Longo, G.; Mancin, S.; Righetti, G.; Zilio, C. Hydrocarbon refrigerants HC290 (Propane) and HC1270 (Propylene) low GWP long-term substitutes for HFC404A: A comparative analysis in vaporisation inside a small-diameter horizontal smooth tube. *Appl. Therm. Eng.* **2017**, *124*, 707–715. [CrossRef]
6. Dizaji, H.S.; Mrabet, B.M. Development and experimental sensitivity analysis of a Maisotsenko-cycle water desalination system under diverse climate conditions. *Appl. Therm. Eng.* **2025**, *281*, 128730. [CrossRef]
7. Pandelidis, D.; Cichoń, A.; Pacak, A.; Drąg, P.; Drąg, M.; Worek, W.; Cetin, S. Water desalination through the dewpoint evaporative system. *Energy Convers. Manag.* **2021**, *229*, 113757. [CrossRef]
8. Saghafifar, M.; Gadalla, M. Innovative inlet air cooling technology for gas turbine power plants using integrated solid desiccant and Maisotsenko cooler. *Energy* **2015**, *87*, 663–677. [CrossRef]
9. Saghafifar, M.; Gadalla, M. Analysis of Maisotsenko open gas turbine power cycle with a detailed air saturator model. *Appl. Energy* **2015**, *149*, 338–353. [CrossRef]

10. Baakeem, S.; Orfi, J.; Mohamad, A.; Bawazeer, S. The possibility of using a novel dew point air cooling system (M-Cycle) for A/C application in Arab Gulf Countries. *Build. Environ.* **2019**, *148*, 185–197. [CrossRef]
11. Sohani, A.; Sayyaadi, H.; Mohammadhosseini, N. Comparative study of the conventional types of heat and mass exchangers to achieve the best design of dew point evaporative coolers at diverse climatic conditions. *Energy Convers. Manag.* **2018**, *158*, 327–345. [CrossRef]
12. Badiei, A.; Akhlaghi, Y.G.; Zhao, X.; Li, J.; Yi, F.; Wang, Z. Can whole building energy models outperform numerical models, when forecasting performance of indirect evaporative cooling systems? *Energy Convers. Manag.* **2020**, *213*, 112886. [CrossRef]
13. Delfani, S.; Karami, M. Transient simulation of solar desiccant/M-Cycle cooling systems in three different climatic conditions. *J. Build. Eng.* **2020**, *29*, 101–152. [CrossRef]
14. Zanchini, E.; Naldi, C. Energy saving obtainable by applying a commercially available M-cycle evaporative cooling system to the air conditioning of an office building in North Italy. *Energy* **2019**, *179*, 975–988. [CrossRef]
15. Comino, F.; González, J.C.; Navas-Martos, F.J.; De Adana, M.R. Experimental energy performance assessment of a solar desiccant cooling system in Southern Europe climates. *Appl. Therm. Eng.* **2020**, *165*, 114579. [CrossRef]
16. Pandelidis, D.; Anisimov, S.; Worek, W.M. Performance study of the Maisotsenko Cycle heat exchangers in different air-conditioning applications. *Int. J. Heat Mass Transf.* **2015**, *81*, 207–221. [CrossRef]
17. Pokorný, J.; Madejski, P.; Fišer, J. Sustainable air conditioning with a focus on evaporative cooling and the Maisotsenko cycle. *Arch. Thermodyn.* **2025**, *46*, 111–121. [CrossRef]
18. Lv, J.; Zhou, B.; Zhu, M.; Xi, W.; Hu, E. Experimental Study on the Performance of a Dew-Point Evaporative Cooling System with a Nanoporous Membrane. *Energies* **2022**, *15*, 2592. [CrossRef]
19. Ali, M.; Ahmad, W.; Sheikh, N.A.; Ali, H.; Kousar, R.; Rashid, T. Performance enhancement of a cross flow dew point indirect evaporative cooler with circular finned channel geometry. *J. Build. Eng.* **2021**, *35*, 101980. [CrossRef]
20. Cuce, P.M.; Riffat, S. A state of the art review of evaporative cooling systems for building applications. *Renew. Sustain. Energy Rev.* **2016**, *54*, 1240–1249. [CrossRef]
21. Pandelidis, D.; Anisimov, S.; Worek, W.; Drag, P. Numerical analysis of a desiccant system with cross-flow Maisotsenko cycle heat and mass exchanger. *Energy Build.* **2016**, *123*, 136–150. [CrossRef]
22. Chen, C.; Hsu, C.; Chen, C.; Chen, S. Silica gel polymer composite desiccants for air conditioning systems. *Energy Build.* **2015**, *101*, 122–132. [CrossRef]
23. Kozubal, E.; Slayzak, S. *Coolerado 5 Ton RTU Performance: Western Cooling Challenge Results*; NREL: Golden, CO, USA, 2010.
24. Cui, X.; Chua, K.J.; Islam, M.R.; Ng, K.C. Performance evaluation of an indirect pre-cooling evaporative heat exchanger operating in hot and humid climate. *Energy Convers. Manag.* **2015**, *102*, 140–150. [CrossRef]
25. Khandelwal, A.; Talukdar, P.; Jain, S. Energy savings in a building using regenerative evaporative cooling. *Energy Build.* **2011**, *43*, 581–591. [CrossRef]
26. Heidarinejad, G.; Bozorgmehr, M.; Delfani, S.; Esmaeelian, J. Experimental investigation of two-stage indirect/direct evaporative cooling system in various climatic conditions. *Build. Environ.* **2009**, *44*, 2073–2079. [CrossRef]
27. Karmakar, A.; Salomon, B.C.; Acharya, S.; Kozlov, A.; Chudnovsky, Y. Utilizing Reversed Brayton Cycle for Enhanced Cooling Tower Technology. *Heat Transf. Eng.* **2025**, *46*, 928–942. [CrossRef]
28. Pandelidis, D.; Drag, M.; Drag, P.; Worek, W.; Cetin, S. Comparative analysis between traditional and M-Cycle based cooling tower. *Int. J. Heat Mass Transf.* **2020**, *159*, 120–124. [CrossRef]
29. Fan, X.; Lu, X.; Wang, J.; Li, Z.; Wang, Q.; Dong, Z.; Zhang, R. Performance Evaluation of a Maisotsenko Cycle Cooling Tower with Uneven Length of Dry and Wet Channels in Hot and Humid Conditions. *Energies* **2021**, *14*, 8249. [CrossRef]
30. MITA Cooling Technologies S.r.l.,Via del Benessere, 13, Siziano 27010, Pavia, IT. Available online: https://www.mitacoolingtechnologies.com/ (accessed on 3 December 2025).
31. Stull, R. Wet-bulb temperature from relative humidity and air temperature. *J. Appl. Meteorol. Climatol.* **2011**, *50*, 2267–2269. [CrossRef]
32. Lee, C.; Wang, Y. A novel method to derive formulas for computing the wet-bulb temperature from relative humidity and air temperature. *Measurement* **2018**, *128*, 271–275. [CrossRef]
33. Taler, D. *Calculation and Experimental Research on Heat Exchangers*; Wydawnictwo PK: Cracow, Poland, 2016. (In Polish)

Disclaimer/Publisher's Note: The statements, opinions and data contained in all publications are solely those of the individual author(s) and contributor(s) and not of MDPI and/or the editor(s). MDPI and/or the editor(s) disclaim responsibility for any injury to people or property resulting from any ideas, methods, instructions or products referred to in the content.

energies

MDPI

Article

Analysis of Heat Transfer Characteristics in a Latent Heat Storage Module Using Circular-Finned Tubes

Ji-Woon Ko [1], Tae Hwan Song [1], Jong-Hoon Lee [1,2], Jong Hyeon Peck [1] and Seung Jin Oh [1,2,*]

[1] Celan Energy Transition Group, Korea Institute of Industrial Technology, 102 Jejudaehak-ro, Jeju-si 63242, Jeju Special Self-Governing Province, Republic of Korea; jiwoonko@kitech.re.kr (J.-W.K.); xoghks4551@kitech.re.kr (T.H.S.); rrl@kitech.re.kr (J.-H.L.); pjh6240@kitech.re.kr (J.H.P.)

[2] Department of Convergence Manufacturing System Engineering, University of Science and Technology (UST), 217 Gajeong-ro, Yuseong-gu, Daejeon 34113, Republic of Korea

* Correspondence: ohs8680@kitech.re.kr

Abstract: Latent heat thermal energy storage (LHTES) using inorganic salt hydrates is a promising technology for buffering renewable energy fluctuations; however, phase-dependent heat transfer remains insufficiently understood for design optimization. In this study, a shell-and-tube storage module with a circular-finned tube was constructed and filled with 13.17 kg of barium hydroxide octahydrate (BHO). Discharge tests were conducted with heat transfer fluid (HTF) inlet temperatures ranging from 20 °C to 50 °C and flow rates of 10–25 L/min, while charging was performed at 90 °C. The overall heat transfer coefficient (U_o) was derived using the logarithmic mean temperature difference method, the inside coefficient (h_i) was calculated by the Petukhov correlation, and the outside coefficient (h_o) was obtained via thermal-resistance network. Results show that the average discharge energy was approximately 1.027 kWh (except 0.859 kWh at 50 °C inlet), with a mean utilization efficiency of 79.25%. The U_o was consistently highest in the liquid phase, followed by the latent and solid phases, with ranges of 0.257–0.863, 0.025–0.072, and 0.015–0.044 kW/m^2·°C, respectively. Sensitivity analysis revealed that the HTF flow rate strongly influenced U_o across all phases, whereas inlet temperature played only a minor role. The outside coefficient h_o was 0.033–0.162 kW/m^2·°C in the latent regime and 0.018–0.064 kW/m^2·°C in the solid regime, with a notable peak around Reynolds number 1.3×10^4 in the latent phase. These findings provide detailed phase-resolved U_o and h_o data for inorganic salt hydrate storage and highlight design insights such as the diminishing returns of flow rate increase beyond a threshold, offering valuable guidelines for sizing and operation of LHTES in Power-to-Heat applications.

Keywords: latent heat thermal energy storage (LHTES); phase change material (PCM); finned-tube heat exchanger; barium hydroxide octahydrate; overall heat transfer coefficient; Power-to-Heat (P2H)

1. Introduction

The global transition toward carbon-neutral energy systems, driven by the urgent need to address climate change and enhance energy security, has led to a rapid expansion of renewable energy sources such as solar and wind power. The International Energy Agency (IEA) projects that by 2030, the world's installed renewable energy capacity will increase by over 90% compared to 2023 levels. In response to this trend, nations are implementing ambitious long-term energy strategies. For instance, South Korea's "11th Basic Plan for Long-term Electricity Supply and Demand (2024–2038)" aims to increase renewable energy

capacity from 31.4 GW in 2023 to 125.9 GW by 2038, constituting approximately 47% of the total power generation infrastructure [1].

This fundamental shift in the energy landscape introduces significant technical challenges. The inherent intermittency of renewable energy sources, which fluctuate with weather conditions and time of day, creates a temporal mismatch between energy generation and demand. To ensure grid stability and reliably utilize this variable output, energy storage systems are indispensable [2,3]. Among the various enabling technologies, Power-to-Heat (P2H) has emerged as an effective strategy for sector coupling. P2H converts surplus renewable electricity into thermal energy, which can be stored to alleviate grid congestion and improve the overall efficiency of renewable energy utilization. The viability of P2H is critically dependent on an associated Thermal Energy Storage (TES) technology. TES systems are broadly categorized as sensible, latent, or thermochemical storage. Latent Heat Thermal Energy Storage (LHTES) is particularly attractive due to its high energy storage density and its ability to store and release heat at a nearly constant temperature during the phase transition of a Phase Change Material (PCM).

LHTES systems operate on a simple principle: during the charging process, a high-temperature Heat Transfer Fluid (HTF) melts the solid PCM, storing latent heat [4]. During discharging, the liquid PCM releases this stored heat to a low-temperature HTF, causing it to solidify. However, a major impediment to the widespread application of PCMs is their typically low thermal conductivity, which limits the rates of heat charging and discharging. To overcome this limitation, various thermal enhancement techniques have been investigated, including the dispersion of highly conductive nanoparticles and the use of porous media. Among these, the integration of fins into the heat exchanger is one of the most practical and effective methods due to its simple structure, low cost, high durability, and proven reliability [5,6]. Agyenim et al. demonstrated through extensive experiments that various fin structures can significantly improve heat transfer rates compared to unfinned tubes [7]. Moreover, Esapour et al. numerically confirmed that fin structures accelerate the movement of the phase-change interface and markedly improve the system's response time [8]. In addition to these methods, microencapsulation strategies, the incorporation of nanofillers, and the use of metal foams represent other promising approaches for enhancing the effective thermal conductivity of PCM. Rolka et al. suggested adding 1 wt% graphene nanoparticles to PCM, which increased its thermal conductivity by approximately threefold in the solid stability reduction of about 6–9% [9]. Chen et al. reported that a PCM integrating SA and MF reduced the melting time by 61.42% compared with pure PCM [10]. Anfas Mukram et al. evaluated the performance of microencapsulated PCM embedded in specially fabricated cement bricks. Their results indicated that, relative to conventional bricks, the modified bricks effectively reduced heat ingress and lowered indoor temperatures by 1.2 °C [11].

Despite these advancements, inorganic salt hydrates, which offer attractive properties such as high latent heat capacity, superior thermal conductivity, and lower cost, have faced delayed practical implementation due to inherent material challenges, including supercooling, phase segregation, and corrosiveness [12,13]. To address these limitations, numerous studies have focused on developing effective strategies for mitigating supercooling, stabilizing phase behavior, and preventing corrosion. Zhang et al. found that 4 wt% NaCl reduced the supercooling degree to 1.1 °C, while adding 0.8 wt% nano-Cu particles further lowered it to approximately 0.5 °C [14]. Cui et al. demonstrated that the incorporation of 3 wt% carboxymethyl cellulose (CMC) into nano-CU/SAT composite phase change materials effectively suppressed phase separation and preserved the latent heat of fusion even after 50 repeated heating-cooling cycles [15]. Moreno et al. investigated the corrosion behavior of eleven salt hydrates on four metallic substrates (copper,

aluminum, carbon steel, stainless steel) classifying the PCMs according to their applicability in cooling or heating systems [16]. Barium Hydroxide Octahydrate (BHO), the PCM utilized in the present study, has likewise attracted research interest aimed at resolving issues such as supercooling, phase segregation, and corrosion. Nevertheless, investigations that implement BHO in actual thermal storage modules and rigorously evaluate their performance are still limited. Advancing the practical deployment of BHO in thermal energy storage applications therefore requires precise experimental determination of its thermo-physical characteristics, accompanied by structured methodologies for system design and performance optimization.

In particular, most finned-tube LHTES studies to date have examined paraffin-based PCMs combined with straight or longitudinal fin geometries, whereas the present work focused on a single circular-finned tube module filled with the inorganic salt hydrate BHO operating in a high-temperature range relevant to P2H applications. Furthermore, previous studies on BHO and similar salt hydrates have mainly reported material-level thermophysical properties and bulk charging/discharging behavior, rather than detailed module-scale heat transfer characteristics. In contrast, the present study experimentally determines phase-resolved overall and outside heat transfer coefficients (U_o and h_o) for the solid, latent, and liquid regimes in a practical finned-tube LHTES module, thereby addressing this specific deficiency in the existing literature.

This study investigated the heat transfer characteristics of an LHTES module specifically designed for an inorganic PCM. A shell-and-tube module featuring circular fins was designed and fabricated to maximize the heat transfer area between the HTF and the PCM. BHO, an inorganic salt hydrate with a phase change temperature suitable for medium-temperature applications, was selected as the storage medium. A dedicated experimental apparatus was constructed to perform a quantitative analysis of the module's charging and discharging characteristics under a range of operating conditions. The primary objectives are to determine the phase-dependent heat transfer performance by calculating the overall and outside heat transfer coefficients and to identify the key operational parameters influencing the module's efficiency, thereby providing essential data for the design and optimization of LHTES systems for P2H and other industrial applications.

2. Materials and Methods

2.1. LHTES Module and Phase Change Material

The LHTES module for this study was designed as a shell-and-tube heat exchanger with a target thermal energy storage capacity of approximately 1 kWh, based on established heat transfer correlations and prior research [17]. The module consists of a single heat transfer tube with external circular fins, all enclosed within an outer shell. A detailed schematic and a photograph of the manufactured module are shown in Figure 1, and its specifications are summarized in Table 1.

The central heat transfer tube, made of SUS304 stainless steel, had an outer diameter of 48.6 mm, an inner diameter of 44.0 mm, and a total length of 1450 mm. To enhance heat transfer, 165 circular fins made of SUS316 stainless steel were installed on the tube's outer surface using an interference fit. Each fin had a height of 20.0 mm, and the fins were spaced with a pitch of 8.46 mm. This finned-tube assembly is housed within a shell with an outer diameter of 101.6 mm. The effective internal volume within the shell available for the PCM is 0.0076 m^3, which was filled with 13.17 kg of the selected PCM.

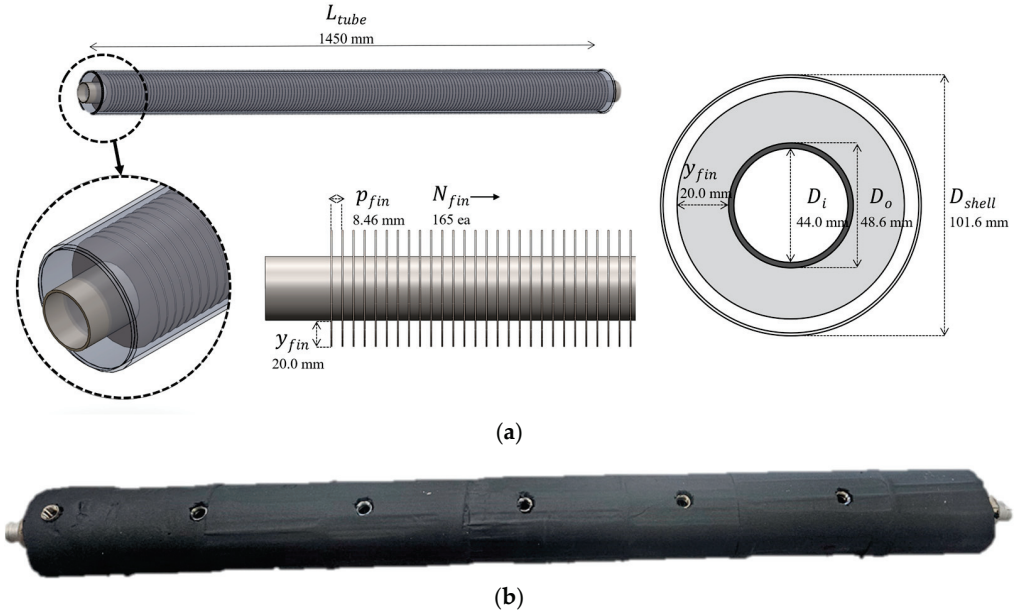


Figure 1. Latent heat thermal storage module with PCM mass of 13.17 kg: (**a**) Design drawing including a cross-sectional view and dimensions, and (**b**) photograph of the manufactured module.

Table 1. Specifications of latent heat thermal storage module.

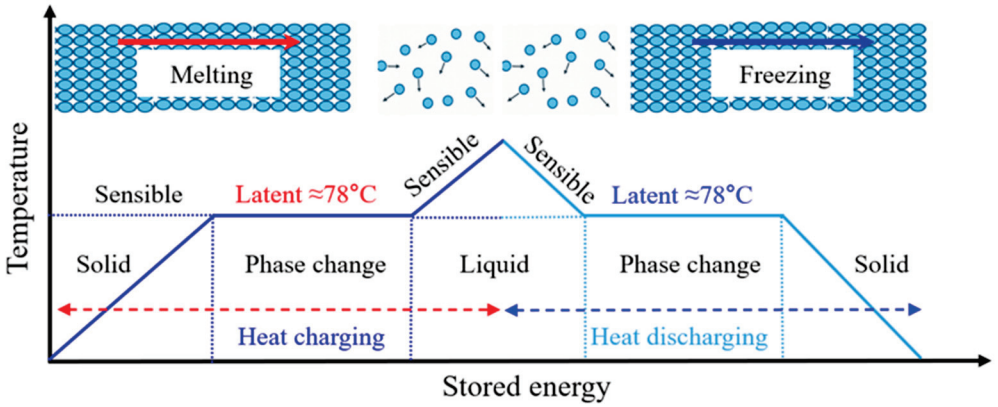
Item		Specification	
Tube side	Tube material	SUS304	[-]
	Fin material	SUS316	[-]
	Outer diameter, D_o	48.6	[mm]
	Inner diameter, D_i	44.0	[mm]
	Tube thickness, δ_{tube}	2.3	[mm]
	Tube length, L_{tube}	1450	[mm]
	Number of tubes, N_{tube}	1	[ea]
	Fin height, y_{fin}	20.0	[mm]
	Fin pitch, p_{fin}	8.46	[mm]
	Number of fins, N_{fin}	165	[-]
	Heat transfer area, A_o	0.2214	[m^2]
Shell side	Shell diameter, D_{shell}	101.6	[mm]
	External volume, V_{ext}	0.0118	[m^3]
	Effective internal volume, V_{in}	0.0076	[m^3]

The PCM selected in this study was barium hydroxide BHO, an inorganic salt hydrate. The thermophysical properties of BHO and the phase-change regimes illustrated in the above schematic are summarized in Table 2, indicating that BHO is suitable for high-temperature thermal energy storage applications. The temperature–stored-energy (enthalpy) behavior of the PCM during heat charging and discharging can be described as follows: starting from the solid state, sensible heating increases the stored energy approximately in proportion to temperature. When the phase-change temperature is reached, a nearly isothermal latent region forms around 78 °C. In this regime, melting (during charging) or freezing (during discharging) proceeds while a large amount of energy is absorbed or released at almost constant temperature. Once the phase change is completed, the PCM enters the liquid sensible region, where the stored energy again increases (or decreases) almost linearly with temperature. With a phase-change temperature of about 78 °C and a high latent heat of fusion in the range of 233–332 kJ/kg, BHO provides a substantially higher energy storage density than many organic PCMs [18]. BHO was se-

lected for this study due to its high density, making it suitable for high-density thermal storage applications. Furthermore, its specific heat capacities in both solid and liquid states contribute to its overall effective sensible heat storage.

Table 2. Thermophysical Properties of Barium Hydroxide Octahydrate (BHO) * [18,19].

Property	Value	
Phase change temperature	≈78	[°C]
Latent heat capacity	233~332	[kJ/kg]
Solid specific heat capacity	1.14~2.11 (for 25~78.5 °C)	[kJ/kg·°C]
Liquid specific heat capacity	2.56~2.61 (for 78.5~150 °C)	[kJ/kg·°C]
Density	2.18	[kg/L]



* Note: BHO properties are taken from Refs. [18,19] and were not measured in this study.

2.2. Experimental Apparatus and Procedure

To quantitatively evaluate the thermal performance of the LHTES module, a dedicated experimental apparatus was constructed, as shown schematically in Figure 2. The setup was designed to precisely control and monitor the charging and discharging processes. The HTF (water) temperature was regulated using high- and low-temperature constant-temperature baths connected via a plate heat exchanger. An inverter pump and a volumetric flow meter (accuracy: ±0.03%) were used to control and measure the HTF flow rate circulating through the module.

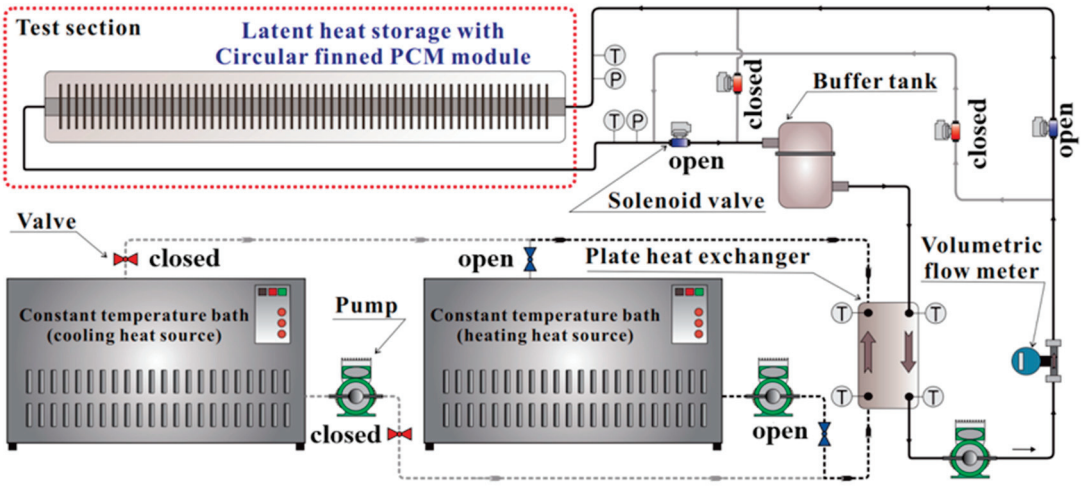


Figure 2. Schematic diagram of experimental setup.

To capture the thermal behavior and phase change dynamics of the PCM, T-type thermocouples (±0.1 °C) were strategically placed within the module. The HTF inlet and outlet temperatures were measured to determine the heat transfer rate. Inside the shell, thermocouples were installed at five equidistant points along the module's length. At each point, sensors were positioned at the tip of a fin and in the space between fins to monitor the temperature distribution and track the solid–liquid interface during phase change. All sensor signals were collected and recorded in real-time by a data acquisition system for subsequent analysis.

The experiments were conducted under various operating conditions, as detailed in Table 3, to simulate a range of real-world scenarios. For all tests, the charging process was performed with a fixed HTF inlet temperature of 90 °C and continued until the average PCM temperature reached 85 °C. The discharging process was investigated by varying both the HTF inlet temperature (20, 30, 40, 50 °C) and the HTF flow rate (10, 15, 20, 25 L/min). The discharging tests were terminated when the average PCM temperature dropped to 45 °C, except for the case with a 50 °C HTF inlet, where the termination temperature was set to 55 °C.

Table 3. Experimental Conditions for Charging and Discharging Tests.

HTF Inlet Temperature, $T_{HTF,i}$		**HTF Flow Rate, $\dot{m}_{HTF}$**
Charging	**Discharging**	
[°C]	**[°C]**	**[L/min]**
90	20	10
	30	15
	40	20
	50	25

2.3. Procedure Data Reduction and Analysis

The experimental data were processed using a set of established thermodynamic and heat transfer equations to quantify the module's performance. The instantaneous heat transfer rates for charging ($\dot{Q}_c$) and discharging ($\dot{Q}_d$) were calculated from the HTF's mass flow rate ($\dot{m}_{HTF}$), specific heat ($c_{p,HTF}$), and the temperature difference between the inlet ($T_{HTF,i}$) and outlet ($T_{HTF,o}$), as shown in Equation (1). To address measurement accuracy and uncertainty, the HTF and PCM temperatures were measured using thermocouples calibrated against a reference sensor prior to the experiments, yielding an accuracy of approximately ±0.1 °C for each sensor. Since the data reduction in this study is based on the HTF-side heat transfer rate, the uncertainty of the HTF temperature difference was evaluated using the concept of uncertainty propagation. For a representative operating condition with an HTF inlet temperature of 20 °C, the resulting relative uncertainty of the HTF-side heat quantity was found to be on the order of 10.52% on average. In the late part of discharging, during the solid phase, the HTF inlet–outlet temperature difference becomes very small, so including this region in the evaluation would further increase the relative uncertainty. However, in the liquid and latent regimes, the relative uncertainty remains on the order of a few percent, which we considered sufficient for discussing the phase-dependent heat transfer characteristics.

$$\dot{Q}_c = \dot{m}_{HTF} c_{p,HTF} (T_{HTF,i} - T_{HTF,o}) \text{ or } \dot{Q}_d = \dot{m}_{HTF} c_{p,HTF} (T_{HTF,i} - T_{HTF,o}) \quad (1)$$

The total accumulated heat stored ($Q_{c,acc}$) or released ($Q_{d,acc}$) over a process was determined by integrating the instantaneous heat transfer rate from the start time (t_s) to the final time (t_f), as given by Equation (2).

$$Q_{c,acc} = \int_{t_s}^{t_f} \dot{Q}_c dt \text{ or } Q_{d,acc} = \int_{t_s}^{t_f} \dot{Q}_d dt \tag{2}$$

The thermal utilization efficiency (ε_{eff}), representing the ratio of total energy discharged to total energy charged, was calculated using Equation (3).

$$\varepsilon_{eff} = \frac{Q_{d,acc}}{Q_{c,acc}} \times 100(\%) \tag{3}$$

For practical comparison, the total accumulated energy was converted to an hourly energy rate in kilowatt-hours (kWh) using Equation (4).

$$Q_{hr} = \frac{1}{3600} \int_{t_s}^{t_f} \dot{Q} dt \tag{4}$$

The overall heat transfer coefficient based on the outer surface area (U_o) was calculated using the Log Mean Temperature Difference (LMTD) method, as shown in Equations (5) and (6), where A_o is the total outer heat transfer area and T_{PCM} is the average PCM temperature.

$$U_o = \frac{\dot{Q}_d}{A_o \Delta T_{lm}} \tag{5}$$

$$\Delta T_{lm} = \frac{(T_{PCM} - T_{HTF,o}) - (T_{PCM} - T_{HTF,i})}{\ln\left(\frac{T_{PCM} - T_{HTF,o}}{T_{PCM} - T_{HTF,i}}\right)} \tag{6}$$

The outside heat transfer coefficient (h_o) was determined from the total thermal resistance ($1/U_o$) by subtracting the resistances due to internal convection and tube wall conduction, as expressed in Equation (7), and should therefore be interpreted as an effective, lumped outside coefficient that includes the effects of fin efficiency and fin–tube contact resistance. Here, A_i and A_o (0.2214 m^2) are the inner and outer surface areas, h_i is the inside heat transfer coefficient, and k_{tube} is the thermal conductivity of the tube material.

$$h_o = \left[\frac{1}{U_o} - \frac{A_o}{A_i h_i} - \frac{A_o \ln\left(\frac{D_o}{D_i}\right)}{2\pi k_{tube} L}\right]^{-1} \tag{7}$$

The inside heat transfer coefficient (h_i) was calculated using the Nusselt number (Nu_{HTF}), as shown in Equation (8).

$$h_i = \frac{Nu_{HTF} k_{HTF}}{D_i} \tag{8}$$

For the turbulent flow regime within the tube, the Nusselt number was calculated using the Petukhov correlation (Equation (9)), which is highly regarded for its accuracy.

$$Nu_{HTF} = \frac{(f/8) Re_{HTF} Pr_{HTF}}{1.07 + 12.7(f/8)^{1/2}\left(Pr_{HTF}^{2/3} - 1\right)} \tag{9}$$

The friction factor (f) required for the Petukhov correlation was calculated using the Gnielinski correlation for fully developed turbulent flow in smooth tubes, given by Equation (10) [20].

$$f = (0.790 \ln Re_{HTF} - 1.64)^{-2} \text{ for } 3000 \leq Re_{HTF} \leq 5 \times 10^6 \tag{10}$$

3. Results

3.1. Transient Thermal Dynamics of Charging and Discharging

The dynamic thermal behavior of the LHTES module was characterized through detailed time-series analysis of temperature and energy data. Figure 3 illustrates a representative experimental cycle, specifically for a discharge process with an HTF inlet temperature of 30 °C and a flow rate of 10 L/min, followed by a charging process. The discharge phase lasted 47 min, while the subsequent charging phase required 105 min. This difference in duration reveals an inherent asymmetry in the heat transfer dynamics. Charging is driven by a larger and more stable temperature difference between the 90 °C HTF and the cooler PCM, leading to a relatively consistent heat transfer rate. In contrast, during discharging, the temperature of the PCM continuously decreases, which in turn reduces the LMTD and slows the rate of heat extraction over time.

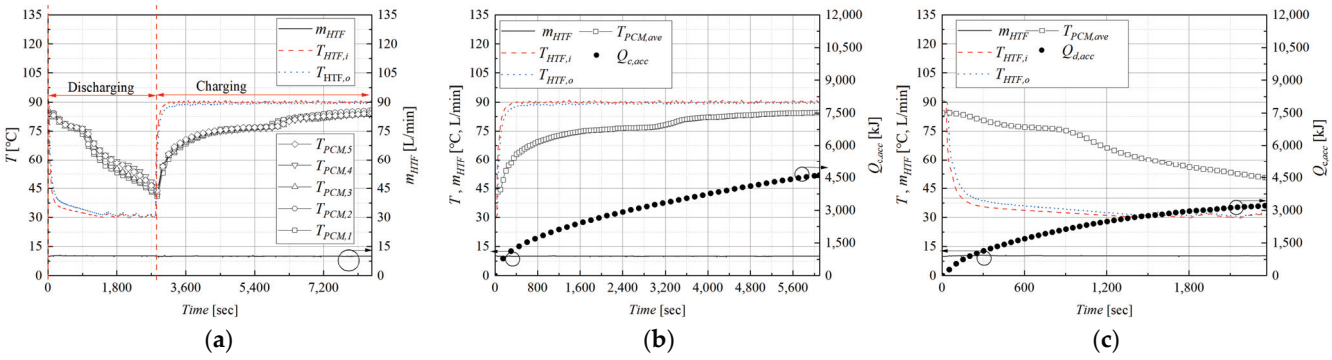


Figure 3. Heat transfer characteristics during charging and discharging of the latent heat thermal storage module: (**a**) Temperature and flow rate profiles during heat charging and discharging process (at: $\dot{m}_{HTF} = 10$ L/min, $\dot{T}_{HTF,i} = 90$ °C (Charging), $\dot{T}_{HTF,i} = 30$ °C (Discharging)). (**b**) Heat charging process (at: $\dot{m}_{HTF} = 10$ L/min, $\dot{T}_{HTF,i} = 90$ °C). (**c**) Heat discharging process (at: $\dot{m}_{HTF} = 10$ L/min, $\dot{T}_{HTF,i} = 30$ °C).

During the charging process, the average PCM temperature rises steadily. This rise is characterized by three distinct stages: a rapid increase when the PCM is in its solid state (sensible heating), followed by a much slower temperature rise or plateau near 78 °C as the PCM absorbs latent heat during melting, and finally another period of rapid temperature increase once the PCM is fully in the liquid state. Correspondingly, the accumulated stored energy increases almost linearly with time, indicating a relatively stable heat charging rate.

Conversely, during the discharging process, the average PCM temperature decreases. A similar three-stage pattern is observed: a period of sensible heat release from the liquid PCM, a prolonged period of nearly isothermal heat release at the phase-change temperature (latent heat), and a final stage of sensible heat release from the solid PCM. The temperature difference between the HTF inlet and outlet diminishes as the PCM cools, causing the rate of heat discharge to decrease over time. This results in a non-linear, decelerating curve for the accumulated discharged energy. For this specific case, the total discharged energy was 3330 kJ, compared to a stored energy of 4665 kJ, yielding a thermal utilization efficiency of 71.37%.

3.2. Heat Transfer Performance and Efficiency

As shown in Figure 4a, across all experimental conditions, excluding those with a 50 °C HTF inlet temperature, the module demonstrated consistent performance, delivering an average heat discharge of 1.027 kWh. The average thermal utilization efficiency for these conditions was calculated to be 79.25%, and under the same discharging end condition, it reached a maximum of 89.97%. This value represents a practical, system-level efficiency

that accounts not only for the thermodynamic processes but also for real-world factors such as ambient heat loss from the module's exterior and piping.

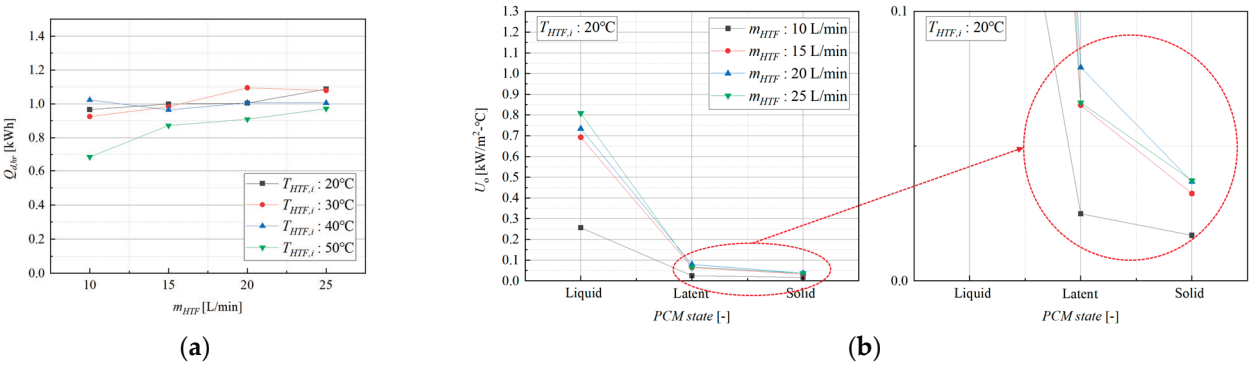


Figure 4. Heat transfer rate and overall heat transfer coefficient of a latent heat storage module: (**a**) Heat transfer rate (discharging case), and (**b**) overall heat transfer coefficient (at: $\dot{T}_{HTF,i}$ = 20 °C).

A notable deviation was observed for tests conducted with an HTF inlet temperature of 50 °C, where the average discharged energy was significantly lower at 0.859 kWh. This reduction is directly attributable to the experimental termination condition for this specific case, which was set at a PCM temperature of 55 °C instead of 45 °C. This higher cut-off temperature meant that a substantial portion of the PCM's latent heat, and some of its sensible heat in the solid phase, was not extracted before the test concluded. This finding underscores that the operational cut-off temperature is not merely a procedural detail but a critical control parameter that directly dictates the achievable energy recovery and round-trip efficiency of the system. Setting this temperature too high strands a significant portion of the stored energy within the module, while setting it too low may be impractical if the application requires a certain minimum output temperature.

A central finding of this study is the profound dependence of the overall heat transfer coefficient (U_o) on the physical state of the PCM. As shown in Figure 4b and summarized in Table 4, the heat transfer performance varies dramatically across the three phases. The highest U_o values, ranging from 0.257 to 0.863 kW/m^2·°C, were observed when the PCM was in the liquid state. In the latent phase, where both solid and liquid coexist, the U_o values were an order of magnitude lower, ranging from 0.025 to 0.072 kW/m^2·°C. The lowest performance was recorded in the solid state, with U_o values between 0.015 and 0.044 kW/m^2·°C.

This significant variation is governed by the dominant heat transfer mechanisms in each phase. In the liquid phase, natural convection currents develop within the molten PCM, creating fluid motion that significantly enhances heat transfer from the finned surface, resulting in a high U_o. During solidification, a layer of solid PCM begins to form on the cooler tube and fin surfaces. Since heat transfer through this solid layer is dominated by pure conduction, which is limited by the PCM's low thermal conductivity, it introduces a substantial thermal resistance. As this solid layer thickens, the overall heat transfer coefficient progressively decreases. Once the PCM is entirely solid, conduction becomes the sole mechanism for heat transfer on the shell side, leading to the lowest observed U_o values. This phase-dependent behavior is a critical characteristic of LHTES systems; it implies that performance is not static but changes dynamically throughout an operational cycle. Consequently, traditional heat exchanger design methods that assume a constant U-value are inadequate for LHTES modules and can lead to significant errors in performance prediction and system sizing. A dynamic or phase-averaged approach is essential for accurate engineering design.

Table 4. Heat transfer rate and overall heat transfer coefficient during discharge process.

$\dot{m}_{HTF}$	$T_{HTF,i}$	$Q_{c,hr}$	ε_{ff}	$U_{o,liquid}$	$U_{o,latent}$	$U_{o,solid}$
				Liquid	Latent	Solid
L/min	°C	kWh	%	kW/m²-°C	kW/m²-°C	kW/m²-°C
10	20	0.966	74.54	0.285	0.034	0.027
10	30	0.925	71.37	0.257	0.025	0.017
10	40	1.023	78.90	0.320	0.027	0.015
10	50	0.686	52.93	0.409	0.031	0.019
10	20	0.999	77.08	0.395	0.030	0.018
15	30	0.983	75.85	0.693	0.065	0.032
15	40	1.166	89.97	0.763	0.067	0.033
15	50	0.872	67.26	0.603	0.060	0.037
20	20	0.992	76.52	0.863	0.063	0.038
20	30	1.095	84.47	0.795	0.072	0.034
20	40	1.006	77.62	0.395	0.062	0.037
20	50	0.909	70.12	0.675	0.070	0.040
25	20	1.087	83.87	0.670	0.062	0.044
25	30	1.079	83.26	0.808	0.066	0.037
25	40	1.006	77.59	0.489	0.057	0.044
25	50	0.971	74.92	0.803	0.067	0.041

3.3. Analysis of the Outside Heat Transfer Coefficient

To isolate the performance on the PCM side, the outside heat transfer coefficient (h_o) was calculated. An analysis of the heat capacity distribution during the discharge process from 85 °C to 45 °C showed that the latent phase accounted for the majority of the heat transfer (72.94%), followed by the solid phase (22.62%), while the liquid phase contribution was minimal (4.44%). Therefore, the analysis of h_o focused on the dominant latent and solid phases.

As shown in Figure 5, h_o varied with the HTF Reynolds number (Re_{HTF}). In the latent phase, ranged from 0.033 to 0.162 kW/m^2·°C. For all discharging inlet temperatures considered (20–50 °C), a similar non-monotonic trend was observed: h_o increased with Re_{HTF} in the low-Re region, reached a local maximum in the range $Re_{HTF} \approx 1.2 \times 10^4$–$1.4 \times 10^4$, and then tended to level off or slightly decrease at higher Re_{HTF}. This behavior reveals a critical trade-off. Initially, as the HTF flow rate and Reynolds number increase, the internal convective heat transfer (h_i) improves, reducing the dominant thermal resistance on the tube side and allowing more heat to be extracted, which increases the calculated h_o. However, beyond the optimal point, the higher heat flux accelerates the formation of an insulating layer of solid PCM on the finned surface. The conductive thermal resistance of this growing solid layer eventually becomes the dominant limiting factor, causing the effective outside heat transfer performance to decline. This non-monotonic behavior indicates that simply maximizing the HTF flow rate is not an optimal strategy for enhancing the discharge rate; an optimal flow rate exists that balances internal convection with external solidification dynamics.

In the solid phase, h_o values ranged from 0.018 to 0.064 kW/m^2·°C, which is, on average, 56.4% lower than in the latent phase. This confirms that once the PCM is fully solidified, the system's performance is severely limited by the poor thermal conduction through the solid PCM layer.

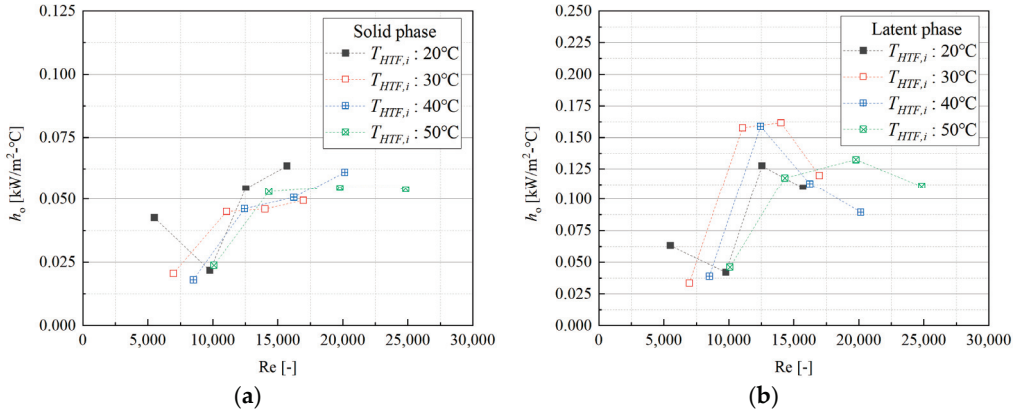


Figure 5. Outside heat transfer coefficient of a latent heat storage module: (**a**) latent phase, and (**b**) solid phase.

3.4. Statistical Analysis of Influencing Parameters

In this study, response surface methodology (RSM) was applied using Minitab (Release 14.12.0) to analyze key response variables obtained from the discharging experiments, which characterize the thermal performance of the module, with the HTF flow rate and inlet temperature treated as the main factors. In particular, the overall heat transfer coefficient U_o for each of the three PCM phases (solid, latent, and liquid) was taken as a primary response. Main effects plots and Pareto charts were generated to assess the influence of HTF flow rate and HTF inlet temperature on the overall heat transfer coefficient (U_o) of each of the three PCM phases.

As shown in Figure 6, the HTF flow rate had a large, positive, and statistically significant effect on U_o for all phases. This is visually represented by the steep upward slope in the main effects plots and the large bars for flow rate in the Pareto charts, which far exceeded the threshold for statistical significance. This is because increasing the flow rate enhances turbulence inside the tube, reducing the internal convective thermal resistance and thereby improving the overall heat transfer. In contrast, the HTF inlet temperature was found to have a minimal and statistically insignificant effect on U_o across all phases. This is evident from the nearly flat lines for temperature in the main effects plots and the very small bars in the Pareto charts. This finding is further supported by the contour plots in Figure 7, where the contour lines for constant U_o are nearly vertical, indicating strong dependence on the x-axis (flow rate) and weak dependence on the y-axis (temperature). This robust statistical confirmation has a critical implication for system design and control. It is far more effective to modulate the HTF flow rate (i.e., pumping power) to control the charge and discharge rates than it is to alter the operating temperature of the thermal source or sink. This is particularly relevant for applications such as waste heat recovery, where the source temperature may be fixed, as it demonstrates that performance can still be effectively controlled via the HTF flow.

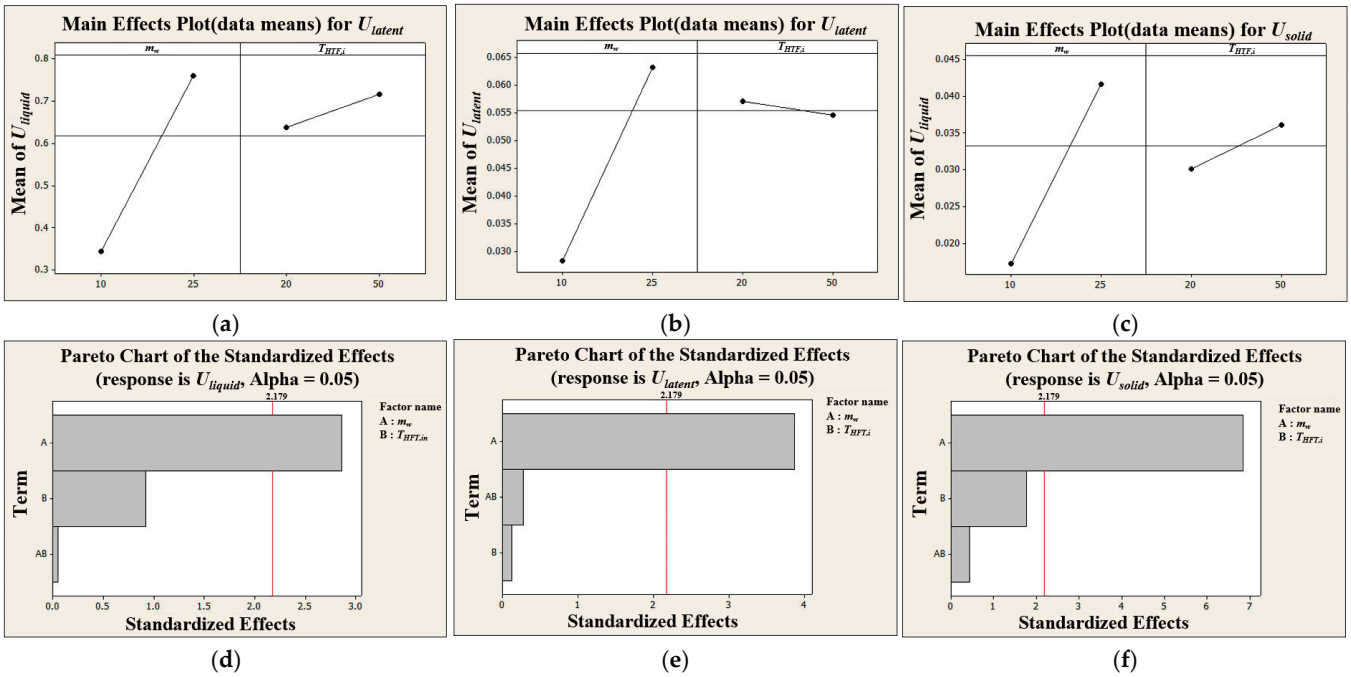


Figure 6. Main effects and pareto charts of overall heat transfer coefficient for different PCM states: (**a**) main effects of U_{liquid}, (**b**) main effects of U_{latent}, (**c**) main effects of U_{solid}, (**d**) Pareto chart of U_{liquid}, (**e**) Pareto chart of U_{latent}, and (**f**) Pareto chart of U_{soild}.

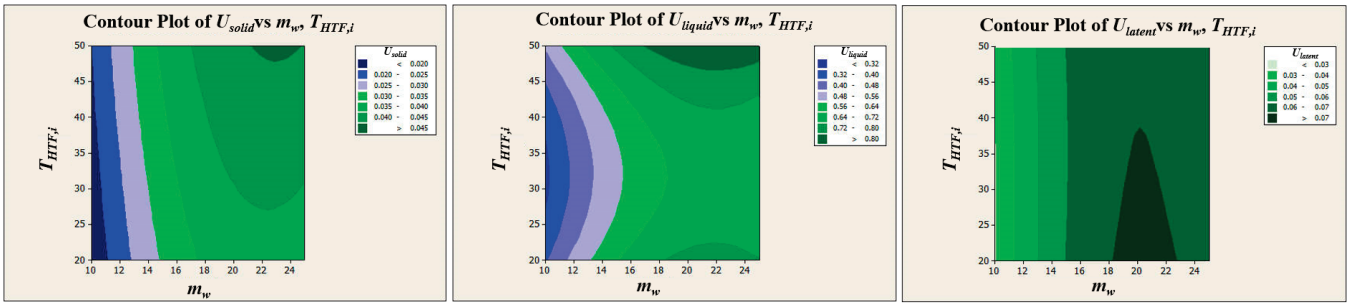


Figure 7. Contour plots of overall heat transfer coefficient according to PCM phase state: (**a**) U_{solid}, (**b**) U_{liquid}, and (**c**) U_{latent}.

4. Conclusions

In this study, an LHTES module using circular-finned tubes and an inorganic PCM (BHO) was fabricated and experimentally tested to analyze its phase-dependent heat transfer characteristics. Based on the experimental results and statistical analysis, the following conclusions were drawn:

(1) The LHTES module demonstrated a reliable average heat discharge capacity of 1.027 kWh and a thermal utilization efficiency of 79.25% under the tested conditions, confirming the viability of the design.

(2) The discharge termination temperature was identified as a critical operational parameter that directly influences the total amount of energy recovered and the overall system efficiency. Incomplete phase change due to a high cut-off temperature can lead to significant reductions in performance.

(3) Statistical analysis confirmed that the HTF flow rate is the dominant factor influencing the overall heat transfer coefficient across all PCM phases (liquid, latent, and solid). In contrast, the effect of the HTF inlet temperature was found to be statistically insignificant.

(4) The overall heat transfer coefficient is highly dependent on the PCM's phase, following the order: Liquid > Latent > Solid. The coefficient in the liquid state (up to 0.863 kW/m^2·°C) can be more than an order of magnitude greater than in the solid state (as low as 0.015 kW/m^2·°C), highlighting the necessity of using phase-aware models for system design.

Analysis of the outside heat transfer coefficient revealed that the latent and solid phases dominate the discharge process. The coefficient in the solid phase was, on average, 56.4% lower than in the latent phase, indicating that conduction through the solid PCM is the primary performance bottleneck. These two phases should be the priority for design optimization.

The experimental data and derived heat transfer coefficients obtained in this work provide a crucial foundation for the design, modeling, and operational optimization of LHTES modules. These findings are particularly valuable for integrating such storage systems into P2H applications to support the transition to renewable energy. Future studies will extend this work to investigate the heat transfer characteristics of modules connected in series and parallel, as well as the long-term cycling stability and safety of BHO under practical operating conditions.

Author Contributions: Conceptualization, S.J.O. and J.H.P.; methodology, J.-W.K.; software and validation, T.H.S., J.-H.L. and J.H.P.; formal analysis, J.-W.K.; investigation, J.-W.K.; resources, S.J.O.; data curation, T.H.S.; writing—original draft preparation, J.-W.K.; writing—review and editing, S.J.O.; visualization, J.-W.K.; supervision, J.H.P.; project administration, S.J.O.; funding acquisition, S.J.O. All authors have read and agreed to the published version of the manuscript.

Funding: This research was supported by the Korean Institute of Energy Technology Evaluation and Planning (KETEP), funded by the Ministry of Trade, Industry, and Energy (MOTIE) (grant No. 20226210100050).

Data Availability Statement: The original contributions presented in this study are included in the article. Further inquiries can be directed to the corresponding author.

Conflicts of Interest: The authors declare no conflicts of interest.

References

1. Ministry of Trade, Industry and Energy. *The 11th Basic Plan for Long-Term Electricity Supply and Demand (2024–2038)*; Public Notice No. 2025-169; MOTIE: Sejong, Republic of Korea, 2025; pp. 1–82.
2. Wang, W.; Xie, X. Flexible Heat and Power Load Control of Heating Units Based on Energy Demand-Supply Balance. *SSRN Electron. J.* **2024**, *4940421*, 1–25. [CrossRef]
3. Kauko, H.; Braekken, A.; Askeland, M. Flexibility through Power-to-Heat in Local Integrated Energy Systems with Renewable Electricity Generation and Seasonal Thermal Energy Storage. *Energy* **2024**, *313*, 134017. [CrossRef]
4. Farid, M.M.; Khudhair, A.M.; Razack, S.A.K.; Al-Hallaj, S. A Review on Phase Change Energy Storage: Materials and Applications. *Energy Convers. Manag.* **2004**, *45*, 1597–1615. [CrossRef]
5. Sharma, A.; Tyagi, V.V.; Chen, C.R.; Buddhi, D. Review on Thermal Energy Storage with Phase Change Materials and Applications. *Renew. Sustain. Energy Rev.* **2009**, *13*, 318–345. [CrossRef]
6. Jegadheeswaran, S.; Pohekar, S.D. Performance Enhancement in Latent Heat Thermal Storage System: A Review. *Renew. Sustain. Energy Rev.* **2009**, *13*, 2225–2244. [CrossRef]
7. Agyenim, F.; Hewitt, N.; Eames, P.; Smyth, M. A Review of Materials, Heat Transfer and Phase Change Problem Formulation for Latent Heat Thermal Energy Storage Systems (LHTESS). *Renew. Sustain. Energy Rev.* **2010**, *14*, 615–628. [CrossRef]
8. Chueh, C.-C.; Hung, S.-C. Numerical Investigation of Melting of a Phase-Change Material in H-type Shell Tubes. *Appl. Therm. Eng.* **2024**, *236*, 121470. [CrossRef]
9. Rolka, P.; Przybylinski, T.; Kwidzinski, R.; Lackowski, M. Investigation of low-temperature phase change material (PCM) with nano-additives improving thermal conductivity for better thermal response of thermal energy storage. *Sustain. Energy Technol. Assess.* **2024**, *66*, 103821. [CrossRef]

10. Chen, T.; Liu, S.; Khan, S.-Y.; Shen, Y.; Zhang, S.; Wang, Y.; Kumar, M.; Li, Y.; Li, X. Investigation and optimal design of partially encapsulated metal foam in a latent heat storage unit for buildings. *J. Energy Storage* **2024**, *84*, 110979. [CrossRef]
11. Mukram, T.-A.; Daniel, J. Performance evaluation of a novel cement brick filled with micro-PCM used as a thermal energy storage system in building walls. *J. Energy Storage* **2024**, *77*, 109910. [CrossRef]
12. Purohit, B.K.; Sistla, V.S. Inorganic Salt Hydrate for Thermal Energy Storage Application: A Review. *Energy Storage* **2021**, *3*, e212.
13. Kumar, N.; Ness, R.V.; Chavez, R., Jr.; Banerjee, D.; Muley, A.; Stoia, M. Experimental Analysis of Salt Hydrate Latent Heat Thermal Energy Storage System with Porous Aluminum Fabric and Salt Hydrate as Phase Change Material with Enhanced Stability and Supercooling. *J. Energy Resour. Technol.* **2021**, *143*, 041801.
14. Zhang, Z.; Duan, Z.; Chen, D.; Xie, Y.; Cao, X.; Wang, J. Sodium acetate trihydrate-based composite phase change material with enhanced thermal performance for energy storage. *J. Energy Storage* **2021**, *34*, 102186. [CrossRef]
15. Cui, W.; Yuan, Y.; Sun, L.; Cao, X.; Yang, X. Experimental studies on the supercooling and melting/freezing characteristics of nano-copper/sodium acetate trihydrate composite phase change materials. *Renew. Energy.* **2016**, *99*, 1029–1037. [CrossRef]
16. Moreno, P.; Miro, L.; Sole, A.; Barreneche, C.; Sole, C.; Martorell, I.; Cabeza, L.-F. Corrosion of metal and metal alloy containers in contact with phase change materials (PCM) for potential heating and cooling applications. *Appl. Energy.* **2014**, *125*, 238–245. [CrossRef]
17. Collar-Serradilla, V.; Silva, R.; Satchi, C.-S.; Lopez-Pedrajas, D.; Pato-Doldan, B. Multiphysics modeling and economic design of a high-temperature phase-change-material thermal energy storage, for saturated steam generation industrial applications. *Appl. Therm. Eng.* **2025**, *279*, 127678. [CrossRef]
18. Wang, Q.; Wang, J.; Chen, Y.; Zhao, C.Y. Experimental Investigation of Barium Hydroxide Octahydrate as Latent Heat Storage Materials. *Sol. Energy* **2019**, *177*, 99–107. [CrossRef]
19. Kenisarin, M.; Mahkamov, K. Salt Hydrates as Latent Heat Storage Materials: Thermophysical Properties and Costs. *Sol. Energy Mater. Sol. Cells* **2016**, *145*, 255–286. [CrossRef]
20. Incropera, F.P.; DeWitt, D.P. *Fundamentals of Heat and Mass Transfer*, 5th ed.; John Wiley & Sons: New York, NY, USA, 2003; pp. 550–553.

Disclaimer/Publisher's Note: The statements, opinions and data contained in all publications are solely those of the individual author(s) and contributor(s) and not of MDPI and/or the editor(s). MDPI and/or the editor(s) disclaim responsibility for any injury to people or property resulting from any ideas, methods, instructions or products referred to in the content.

energies

MDPI

Article

Conjugate Study on Thermal–Hydraulic Performance of Topology-Optimized Lattice-Filled Cooling Channel for Thermal Management of Solid-Oxide Fuel Cells

Kirttayoth Yeranee [1], Yuli Cheng [1] and Yu Rao [1,2,*]

[1] Institute of Turbomachinery, School of Mechanical Engineering, Shanghai Jiao Tong University, Shanghai 200240, China; nifzahunt@sjtu.edu.cn (K.Y.); chengyuli_sjtu@sjtu.edu.cn (Y.C.)
[2] Shenzhen Research Institute, Shanghai Jiao Tong University, Shenzhen 518000, China
* Correspondence: yurao@sjtu.edu.cn

Abstract: Integrated additional cooling channels offer precise thermal management for solid-oxide fuel cells (SOFCs), mitigating temperature gradients. This research studies the thermal–hydraulic performance of cooling channels integrated between SOFC interconnectors, including a Diamond-type triply periodic minimal surface (TPMS), a conventional topology-optimized structure, and a topology-optimized lattice-filled structure. A conjugate heat transfer analysis is employed to investigate the influences of flow rate within the range of Reynolds numbers from 300 to 5000, and the effects of coolant type, including air and liquid metals, as well as the impacts of structural material. The results demonstrate that the topology-optimized lattice-filled structure, generating high turbulence mixing, achieves superior temperature uniformity, especially at high flow rates, despite having higher thermal resistance and pressure loss than the conventional topology-optimized design. The coolant types show the largest influence on thermal–hydraulic performance, and the use of liquid gallium in the conventional optimized design obtains the best temperature uniformity, yielding differences between the maximum and minimum temperatures of less than 5 K. Moreover, the higher-thermal-conductivity material improves temperature uniformity, even at low flow rates. Overall, the optimized-baffle designs in the conventional topology-optimized model, utilizing high-conductivity coolant and structural materials, could be the most suitable for thermal management of the SOFC.

Keywords: solid-oxide fuel cell; temperature uniformity; thermal–hydraulic performance; topology optimization; triply periodic minimal surface

1. Introduction

Solid oxide fuel cells (SOFCs) are an advanced technology for the future of sustainable energy, capable of directly converting chemical reactions into electricity with high efficiencies exceeding 70% [1]. Their high operating temperatures, ranging from 873 K to 1273 K, enable the favorable reaction kinetics, the use of non-precious metal catalysts, and the recovery of valuable high-grade waste heat [2]. However, the heat generated from exothermic electrochemical reactions, Joule heating, and resistive losses causes substantial temperature within the cell. These non-uniform thermal gradients induce thermomechanical stresses, leading to performance degradation through mechanisms such as electrode sintering and interconnect delamination [1–3]. Aguiar et al. [4] have suggested that a maximum local temperature gradient of 10 K/cm is critical to mitigate such structural

damage, emphasizing that precise temperature control is not merely beneficial but essential for the commercial applicability and durability of SOFC systems.

Effective thermal management is therefore crucial for the SOFCs to minimize temperature gradients in the positive electrode–electrolyte–negative electrode (PEN) and interconnector structures. Enhancing thermal conduction in the PEN materials and improving convective heat transfer in gas channels are the most effective strategies to obtain high temperature uniformity. Different thermal management approaches have been investigated, including optimized air/fuel channels to increase surface area and uniform gas distribution [5,6]; flow arrangements, where adopting a co-flow arrangement generally yields a smaller temperature gradient compared to other configurations [7–9]; heat pipes [10,11], which can significantly lower gradients yet face challenges of heavy stainless-steel envelopes and long startup times; and fuel composition control [12], since endothermic reforming creates severe gradients, while adjusted air-to-fuel ratios help mitigate them.

Conventional thermal management also relies heavily on excess air circulation through cathode channels [13–16]. Experimental and numerical studies have confirmed that regulating air flow rate significantly influences thermal gradients. Wang et al. [17] demonstrated that increasing the airflow from 1.5 m/s to 7.5 m/s reduced the peak temperature gradient by around 17%. A similar increase in fuel velocity also enhances convective heat transfer and improves thermal uniformity. While increasing the air flow rate can moderate temperatures, the low volumetric heat capacity of air consumes significant pumping power for compression, accounting for up to 10% of the net output [18]. Furthermore, excessive air cooling can lower the average stack temperature, weakening electrochemical performance and reducing power density. These inherent limitations have encouraged the investigation of advanced cooling strategies [2,3].

Another innovation in thermal management for SOFCs is the use of high-performance coolants in an additional cooling channel integrated within the SOFC stack, as shown in Figure 1b–d. Promsen et al. [16] proposed a saturated water-cooled SOFC stage. They found that the water-based cooling method reduced temperature differences in planar stacks from 185 K to 26 K. This strategy also reduced the parasitic losses from the air blower, increasing the overall system efficiency. Li et al. [14] proposed a supercritical fuel-cooled SOFC scheme. They observed that this design significantly reduced the temperature gradient from 22.7 K/cm in a conventional air-cooled SOFC to 8.35 K/cm, resulting in a substantial reduction in air usage and thereby lowering parasitic power consumption, improving overall efficiency. Fan et al. [15] revealed that an additional liquid tin cooling channel achieved a highly uniform temperature of 15 K. Later, Hasbi et al. [19] demonstrated that liquid gallium flowing through additional cooling slots of SOFC interconnectors significantly improved temperature uniformity over air cooling, though its high flow rates caused a larger pumping power penalty. These methods decouple the cooling function from the oxidant supply, allowing for a drastic reduction in the excess air ratio and its associated parasitic losses.

Despite these promising results, a critical gap remains in the design and optimization of the additional cooling structures for the SOFCs. Advanced architectures, such as triply periodic minimal surface (TPMS) lattices, offer superior thermal performance and structural integrity in various thermal management systems [20]. However, their use in cooling channels often causes a high-pressure loss, which again demands excessive pumping power [21]. To address this trade-off, researchers have turned to optimization techniques [22,23]. One promising method combines density-based topology optimization with lattice infills [24]. This process first computes an optimal channel layout under defined constraints and objectives. The obtained intermediate densities are then filled with lattice structures. This hybrid approach has been shown to significantly reduce pressure loss

while maintaining excellent thermal performance, offering a potential pathway to more efficient thermal management of the SOFCs.

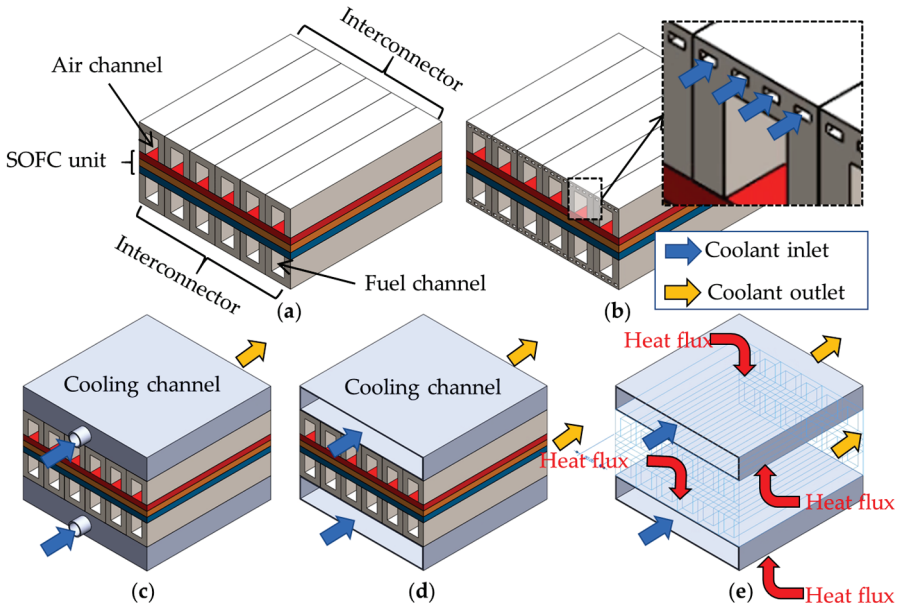


Figure 1. Different cooling strategies for SOFC stack: (**a**) excessive air; (**b**) coolant flowing through the interconnectors; (**c**,**d**) coolant passing through an additional cooling channel; and (**e**) concept of simplified boundary conditions in this study.

Hence, this study proposes high-performance cooling channel designs integrated between SOFC interconnectors [14–16], focusing on thermal–hydraulic performance and temperature uniformity of three advanced cooling structures: (1) a Diamond-type TPMS network, known for its high surface-area-to-volume ratio and efficient flow mixing [25]; (2) conventional topology-optimized structures, designed through computational methods to achieve optimal heat transfer performance under given constraints [26,27]; and (3) a hybrid topology-optimized-filled lattice structure, which combines the tailored flow paths of topology optimization with the enhanced heat transfer of an infilled lattice [24].

This investigation employs a simplified but practical approach by modeling cell heat generation as a constant heat flux boundary condition, as demonstrated in Figure 1d, allowing a comparative evaluation of these complex geometries. This methodology, successfully applied in studies on proton-exchange membrane fuel cells (PEMFCs) [28,29], enables the isolation and detailed analysis of the thermal–hydraulic performance of the cooling structures. This study further examines three critical factors that govern thermal management performance in the SOFCs. The analysis evaluates the thermal–hydraulic performance and temperature uniformity of the proposed cooling structures within the Reynolds numbers of 300 to 5000 [19], compares different coolants (air, liquid tin [15], and liquid gallium [19]), and assesses the impacts of commonly used metallic materials [30], including ferritic stainless steel [15], high-thermal conductivity metal [31], and nickel–chromium superalloy [32]. Through this comprehensive analysis, this work aims to serve as a guideline for implementing advanced cooling channels between the SOFC stacks to improve efficiency and durability.

2. Methodology

This study employs conjugate heat transfer (CHT) analysis to investigate the thermal–hydraulic performance, evaluating the impact of flow rate, coolant type, and structural material on heat transfer efficacy, pressure drop, and temperature uniformity. A compara-

tive analysis covers three cooling architectures, including the Diamond-TPMS channel, a high-performance cooling structure generated via density-based topology optimization to maximize heat transfer, and the topology-optimized lattice-filled geometry, where the optimized density fields (γ) are interpreted into a manufacturable circular pin-fin array. This lattice structure is selected for its compatibility with traditional manufacturing and integration within narrow SOFC stack interconnects.

It should be noted that this study employs 2D topology optimization for computational efficiency, justified by the narrow channel gap. While a full 3D optimization generates complex geometries requiring advanced additive manufacturing, the 2D method produces extrudable designs, which are suitable for conventional processes [33–36]. This simplification is also validated by the comparable cooling performance achieved between the 2D-derived and full 3D models [37]. The topology optimization procedure is elucidated in the Appendix A, while subsequent sections detail the numerical models, boundary conditions, mesh sensitivity, and validation.

2.1. Numerical Models

The numerical models investigated in this study are presented in Figure 2. Figure 2a shows the overall dimensions of the cooling structure, with a characteristic length (D) of 20 mm. The channel has a cross-section of 20 mm $\times$ 20 mm, attached by heated plates with a thickness of 5 mm, consistent with the previous study [16]. The length of the cooling structure (L) is 120 mm. Figure 2b shows the Diamond TPMS structure, which is generated from a mathematical equation [21]. This structure has a wall thickness of 1 mm and a unit cell size of 20 mm. The conventional topology-optimized design, shown in Figure 2c, is obtained by extracting the density field (γ) from the density-based topology optimization with an iso-contour threshold of 0.5. In Figure 2d, the optimized layout is interpreted as an array of circular pin-fins, where the pin diameter (D_p) varies consistently with the local density field ($0.1 \leq \gamma \leq 0.9$). The D_p = 1 mm corresponds to γ = 0.9, increasing consistently to D_p = 2 mm where γ = 0.1. A summary of all design parameters is provided in Table 1.

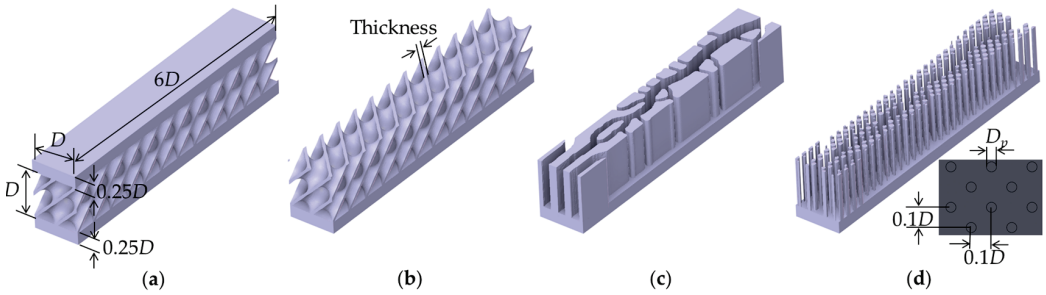


Figure 2. Numerical models in this study: (**a**) Dimension of cooling structure; (**b**) Diamond-type TPMS structure; (**c**) Conventional topology-optimized design, and (**d**) Topology-optimized lattice-filled geometry.

Table 1. Details of numerical models in this study.

Models	Details	Surface Area (mm^2)	Porosity (%)
Diamond TPMS	The unit cell size of 20 mm is arranged in the channel, and the wall thickness of TPMS is 1 mm	23,082.2	80
Conventional topology-optimized	The final optimized structure is directly extracted from the density field with a threshold value of 0.5	17,310.2	50
Topology-optimized lattice-filled	Arrays of circular pin-fin structures with a D_p of 2 mm are filled in the density field of 0.1, and the D_p decreases consistently to 0.5 mm in the density field of 0.9.	28,958.9	80

2.2. Computational Domain and Boundary Conditions

The conjugate heat transfer simulations are conducted using Ansys Fluent v. 2021R1, Ansys Inc., Canonsburg, PA, USA. Figure 3 depicts the computational domain for the cooling channel configuration. Spanwise periodic boundary conditions are applied to the Diamond TPMS model, while the symmetry conditions are used for the topology-optimized and lattice-filled models to minimize computational cost. The bottom and top walls of the solid structure are treated by a uniform heat flux of 3200 W/m^2, and this value was obtained based on an operating voltage of 0.75 V by Zhang et al. [38]. The interfaces between the solid and fluid domains are modeled using conjugate boundaries, and the rest surfaces are set as adiabatic.

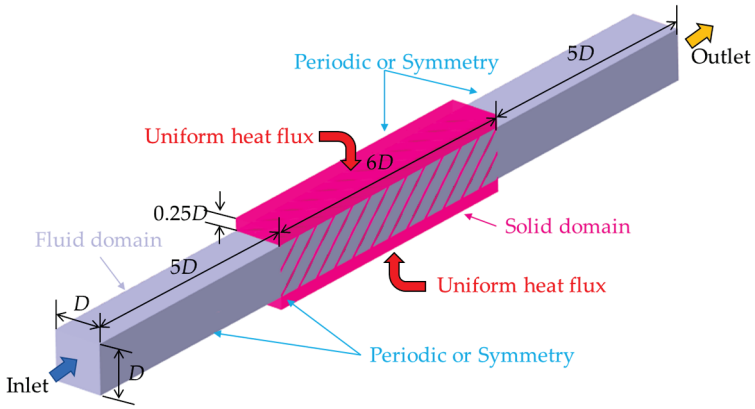


Figure 3. Computational domain and boundary conditions.

It is important to note that this study employs a uniform heat flux boundary condition to facilitate a direct cooling performance comparison of each case. In the SOFC, the current density and electrochemical reactions typically result in non-uniform heat generation within the PEN layer. While this simplification does not capture the uneven temperature distributions, it provides a consistent method for evaluating the cooling performance and temperature uniformity of each design. Future work will incorporate coupled electrochemical–thermal models to investigate the interaction between non-uniform stack generation and advanced cooling.

Three coolants, including compressible air, liquid tin, and liquid gallium, are studied. The inlet is defined with a uniform velocity profile and a constant temperature of 1073 K, while the outlet is set to a zero-gauge pressure [15,19]. The influence of the flow rate is investigated for the air-cooled channel at the Reynolds numbers of 300, 1000, and 5000 [19]. For the subsequent studies on coolant type and structural material, a Reynolds number of 300 is maintained. The solid structures are modeled with the properties of ferritic stainless steel, a high-thermal-conductivity metal, and a nickel–chromium superalloy. The corresponding thermophysical properties are detailed in Table 2, and all studied cases are summarized in Table 3.

Table 2. Material properties of the coolant and solid structure.

	Materials	Dnesity (kg/m^3)	Specific Heat Capacity (J/kg·K)	Thermal Conductivity (W/m·K)	Viscosity (Pa·s)
Fluid	Air	Compressible	Linear interpolation	Linear interpolation	Linear interpolation
	Liquid tin [15]	6330	240	33.8	0.00101
	Liquid gallium [19]	5600	374	61.67	0.00175
Solid	Ferritic stainless steel [15]	8900	444	30	-
	High-thermal-conductivity metal [19,31]	8900	450	72	-
	Nickel–chromium superalloy [32]	8330	640	22.8	-

Table 3. Studied cases in this research.

Study Case	Reynolds Number	Coolant	Structure
Coolant flow rate	300, 1000, and 5000	Air	Ferritic stainless steel
Coolant type	300	Air, liquid tin, and liquid gallium	Ferritic stainless steel
Structural material	300	Air	Ferritic stainless steel, high-thermal-conductivity metal, and nickel–chromium superalloy

2.3. Parameter Definition

The Reynolds number (Re) is calculated based on the velocity (V_{in}) at the inlet channel, as follows:

$$Re = \frac{\rho V_{in} D_h}{\mu} \tag{1}$$

where ρ and μ are the density and dynamic viscosity of the coolant, defined at the inlet.

Generally, the hydraulic diameter (D_h), applied to highly complex structures, such as porous media or two-fluid heat exchangers, is calculated as $4\psi/S_v$, where ψ is the porosity and S_v is the specific surface area [21]. However, for this study, which focuses on channel-based heat sinks, the D_h is defined using the conventional channel-flow definition [19,25]:

$$D_h = \frac{4A_{in}}{L_p} \tag{2}$$

where A_{in} indicates the cross-sectional area at the inlet of the cooling channel, and L_p is the wetted perimeter. Using this definition, all designs are created with a consistent D_h = 20 mm. Meanwhile, the D_h values calculated using the former porous media definition are provided in the Appendix A.

The Nusselt number (Nu), which is generally used to characterize the convective heat transfer in the channel, is calculated as follows:

$$Nu = \frac{hD_h}{k} \tag{3}$$

where k is the thermal conductivity of the cooling material. h is the local heat transfer coefficient, which is defined by

$$h = \frac{q}{(T_w - T_b)} \tag{4}$$

where q is the wall heat flux at the observed area. T_w and T_b are the endwall and bulk temperatures. T_b is evaluated by linearly interpolating between inlet (T_{in}) and outlet (T_{out}) temperatures.

The heat exchange capability for all cases is evaluated based on the total thermal resistance (R_{tot}), defined as follows [33]:

$$R_{tot} = \frac{T_{heat} - T_{in}}{Q} \tag{5}$$

where T_{heat} is the area-averaged temperature on the heated wall. Q is the total heat input.

For the hydraulic performance, the friction factor (f) and pumping power (P_e) of the flow along the channel are expressed as follows:

$$f = \frac{2\Delta p D_h}{\rho V L} \tag{6}$$

$$P_e = \Delta p V A_{in} \tag{7}$$

where Δp is the average pressure difference between the inlet and outlet of the cooling structure.

The performance evaluation criterion (PEC) is calculated to quantify the trade-off between heat transfer enhancement and the associated pressure loss:

$$\mathrm{PEC} = \frac{Nu_{avg}/Nu_0}{(f/f_0)^{1/3}} \tag{8}$$

where Nu_{avg} indicates the area-averaged Nusselt number. The baseline Nusselt number (Nu_0) and friction factor (f_0) are obtained from the Dittus-Boelter equation and the Blasius correlation, respectively, as follows:

$$Nu_0 = 0.023Re^{0.8}Pr^{0.4} \tag{9}$$

$$f_0 = 0.316Re^{-0.25} \tag{10}$$

where the Prandtl number (Pr) for air is assigned a value of 0.7. It should be noted that Equations (9) and (10) are valid for the turbulent regimes ($Re > 4000$).

The temperature uniformity index (TUI) is calculated to quantify the temperature uniformity on the heated surface. The TUI is defined by the following equation:

$$\mathrm{TUI} = 1 - \frac{\sum_{i=1}^{n} |T_i - T_{heat}| A_i}{2T_{heat}A} \tag{11}$$

where T_i is the local temperature, A_i is the local area, and T_{heat} is the area-averaged temperature of the heated wall.

2.4. Mesh Independence Check and Numerical Scheme

The computational domain is discretized using poly-hexcore and prism meshes generated in Fluent Meshing. Figure 4 shows the mesh system for the conventional topology-optimized design. The "Body of Influence" is activated over the cooling structure to control high-quality surface mesh. Moreover, to capture complex structures, especially the Diamond TPMS and lattice-filled models, the value of the curvature normal angle and cell per gap is set at 9 degrees and 1. The boundary layers are generated using the smooth-transition offset method with the transition ratio of 0.272. Overall, the solid and fluid domains primarily consist of hexagonal elements, while prism layers are densely generated near all no-slip walls to ensure the y^+ value below 1.0.

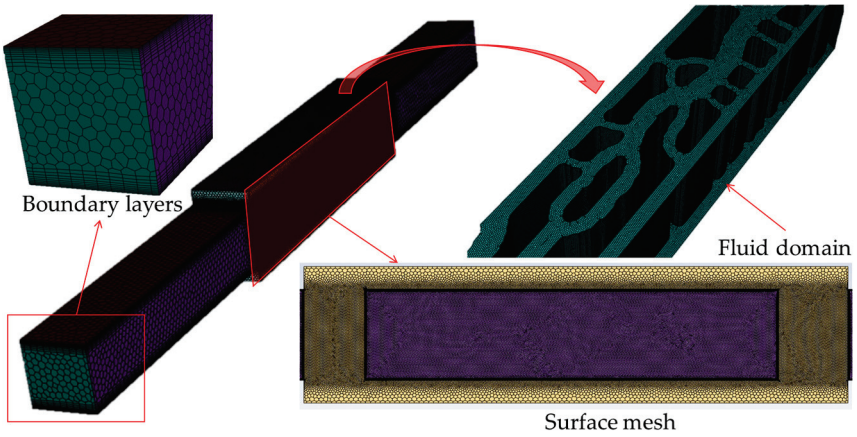


Figure 4. Overview of the mesh system in the conventional topology-optimized model.

The realizable *k*-ε turbulence model is selected for this study based on its demonstrated accuracy in predicting the thermal–hydraulic performance of complex TPMS channel geometries in previous work [25], where it showed excellent agreement with experimental transient liquid crystal thermography (TLC) data at higher Reynolds numbers (Re = 10,000–30,000). While the Reynolds number range in the present study is ranging from Re = 300 to 5000, encompassing both laminar and transitional regimes, the use of turbulence models throughout the entire range is a common approach for comparative analysis of complex geometries, as seen in various air- and liquid-cooled heat sink studies [34–37]. Since this study also focuses on a relative comparison of cooling structures under a consistent numerical setting, the use of the realizable *k*-ε turbulence model is valid due to its dampening function, which provides a reasonable approximation in transitional flows, enabling an efficient evaluation within the studied Reynolds numbers.

The mesh independence analysis is conducted by comparing the temperature distribution within three mesh systems of 4.21×10^6 (Low), 4.92×10^6 (Medium), and 7.21×10^6 (High) elements. The results in Figure 5 show that all plots are almost identical within the range of 0 mm < X < 100 mm, while small deviations can be observed near the outlet ($X \geq 100$ mm). The area-averaged Nusselt number at the endwall in the low and medium meshes is 3.3% and 0.3%, respectively, deviating from the highest mesh resolution. Therefore, the mesh with 4.92×10^6 elements is selected for the conventional topology-optimized model, due to a balance between computational cost and accuracy. Similar mesh settings are applied to all other models.

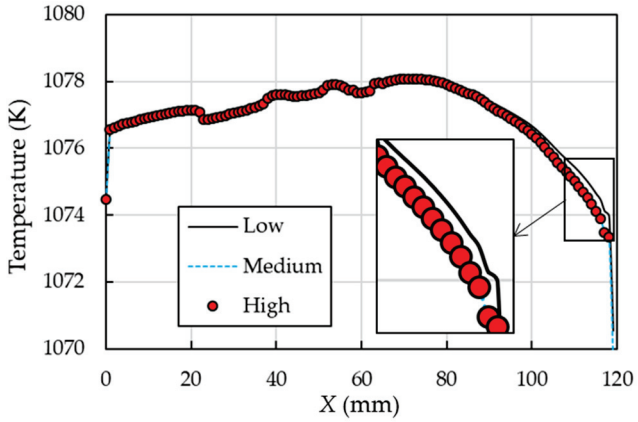


Figure 5. Plots of temperature distributions on the endwall with different meshes at Re = 5000.

2.5. Validation

To validate the present numerical models, the average Nusselt number correlation established by Xu et al. [25] from their experimental study of a Diamond TPMS structure is employed. Since their experimental data are acquired via the TLC under adiabatic conditions, a corresponding numerical model is constructed without a solid domain, as shown in Figure 6. In this model, a uniform heat flux is applied directly to the bottom endwall to emulate the TLC measurement technique. The model is validated across a range of Re = 10,000, 15,000, and 20,000, with all other boundary conditions maintained as specified in Figure 3.

Figure 7 shows the agreement between the present numerical results and the experimental correlation ($Nu_{avg}/Nu_0 = 135.1Re^{-0.34}t^{0.16}$) established by Xu et al. [25]. The data points from this numerical study closely follow the trend of the empirical correlation within Re = 10,000–20,000. The average deviation in all validated Re is 12.5%, which can be explained by the implemented periodic boundary conditions. By design, this setup excludes the side impingement flow, as found in the experiments, which is a key mechanism for

high heat transfer, leading to the observed discrepancy. Therefore, this validation ensures the ability to simulate more complex conjugate heat transfer scenarios accurately.

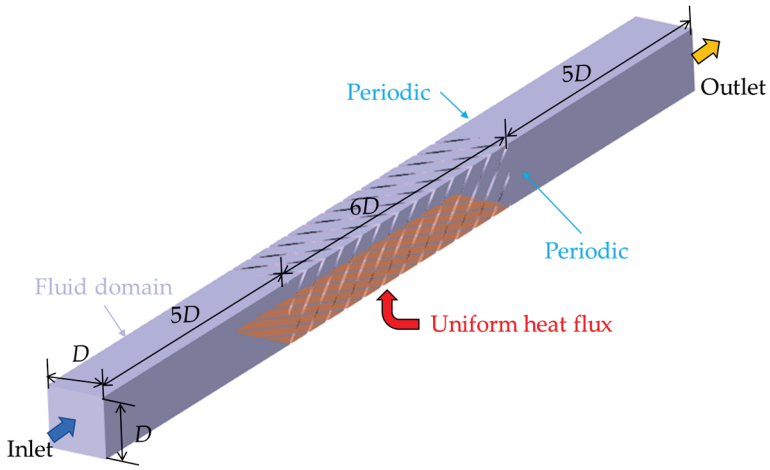


Figure 6. Numerical model of the Diamond-type TPMS structure for the validation.

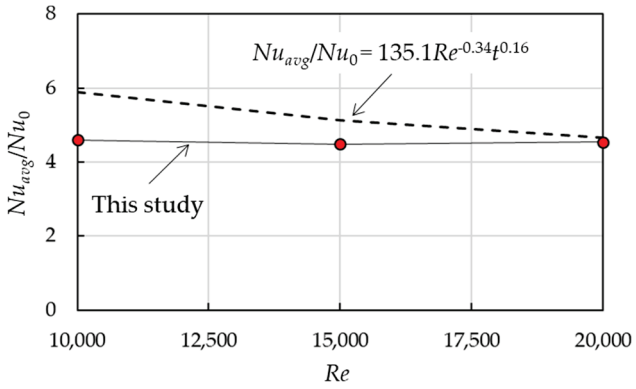


Figure 7. Plots of the average Nusselt number ratio between the present study and the correlations from experimental investigation within the Reynolds number of 10,000 to 20,000.

3. Results and Discussion

The thermal–hydraulic performance is characterized by plotting heat transfer and pressure loss to illustrate the effects of coolant flow rate, coolant type, and structural material. The flow and temperature distributions are used to explain the variations in each geometry.

3.1. Influences of Coolant Flow Rate

In this section, to effectively evaluate the influence of coolant flow rate within the range of *Re* = 300 to 5000, air and ferritic stainless steel are selected as the working fluid and structural material, respectively. Their thermal properties serve to clearly observe the thermal–hydraulic results.

3.1.1. Thermal–Hydraulic Performance

Figure 8 provides the thermo-hydraulic performance within the studied *Re* for the Diamond-type TPMS structure (DiamondTPMS), conventional topology-optimized structure (ConTopOpt), and topology-optimized lattice-filled structure (TopOptLattice). In Figure 8a, the area-averaged Nusselt number (Nu_{avg}) monotonically increases as *Re* increases due to higher flow momentum and mixing, resulting in a thinner thermal boundary layer. All models show a competitive and steadily increasing trend at *Re* = 300 and 1000.

The Diamond TPMS geometry, due to its intense flow accumulation [25], achieves the highest Nu_{avg} at higher *Re*, followed by the topology-optimized lattice-filled model. At *Re* = 5000, the Nu_{avg} value in the Diamond is 66.1, which is higher than in the conventional topology-optimized and lattice-filled models by 58.6% and 22.4%, respectively.

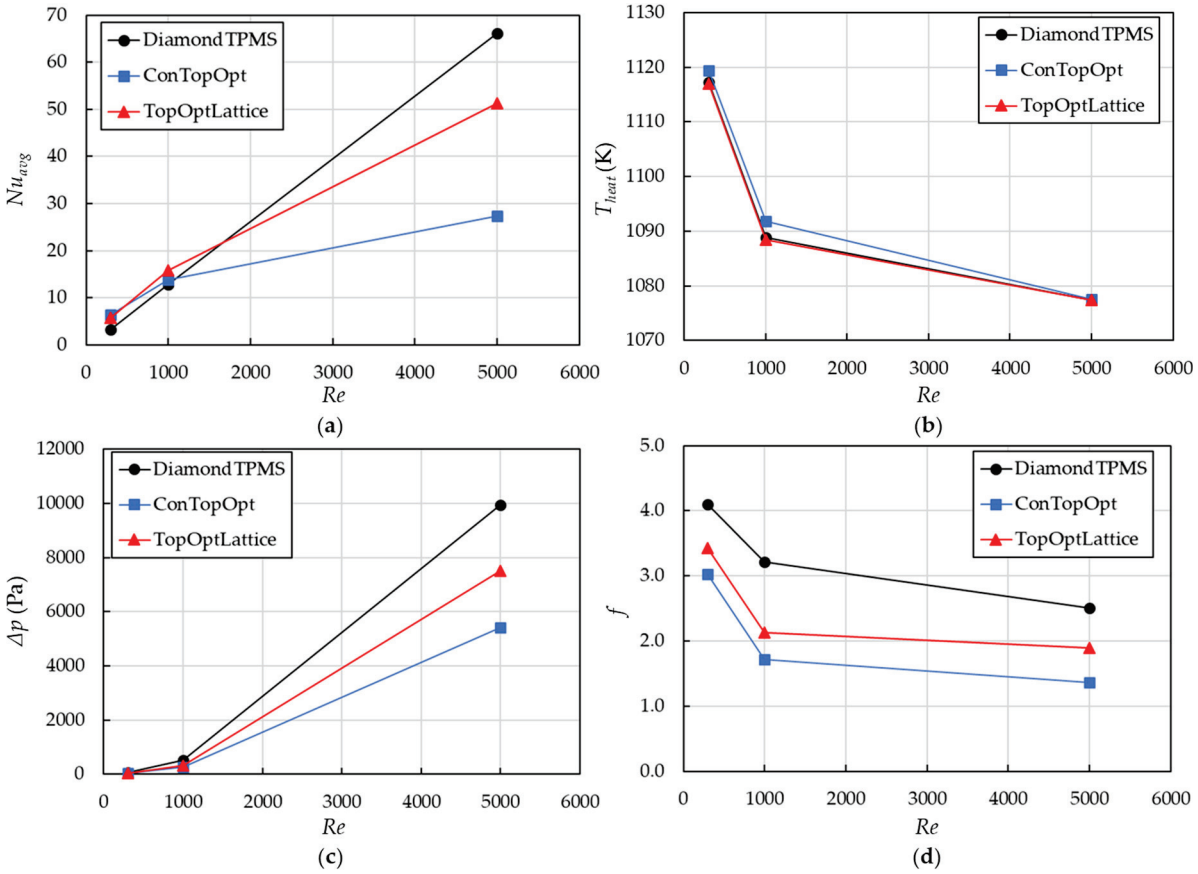


Figure 8. Thermal–hydraulic performance of all models within the range of the Reynolds numbers of 300 to 5000: (**a**) area-averaged Nusselt number on the endwall inside the cooling channel; (**b**) area-averaged temperature on the heated wall; (**c**) pressure loss; and (**d**) friction factor.

This enhanced heat removal inside the channel directly reflects the temperature removal from the heated wall in Figure 8b. All models sharply decrease wall temperatures when *Re* increases from 300 to 1000. At the highest coolant flow rate, the Diamond TPMS model shows the best cooling structure, followed by the topology-optimized lattice-filled model. However, the cooling performance in the Diamond TPMS structure causes the highest pressure loss and friction factor, as shown in Figure 8c,d. A direct consequence of the high pressure is that its topology blocks the flow passing through the cooling channel.

Meanwhile, the conventional topology-optimized and lattice-filled models demonstrate a significant advantage, as they exhibit a substantially lower pressure penalty. Compared to the Diamond TPMS model that blocks the through-flow path, the pressure loss in the conventional topology-optimized and lattice-filled models is 43.2 Pa to 5417 Pa and 48.9 Pa to 7500 Pa, which decreases by 26.2% to 45.6% and 16.4% to 24.6%, respectively, when the *Re* increases from 300 to 5000. Moreover, the friction factor, particularly in the conventional topology-optimized model, which allows for a smoother flow and reduces strong vortices, exhibits the lowest values within the studied flow rates and decreases as *Re* increases, indicating a significantly more hydraulically efficient design.

Figure 9 plots the $Nu/Nu_0, f/f_0$, and PEC of all geometries at *Re* = 5000 to evaluate the trade-off between heat transfer enhancement and flow resistance. The Diamond TPMS

geometry yields the highest Nu/Nu_0 but also incurs the largest f/f_0. For all geometries, the PEC values exceed 1.0, confirming a net performance gain. Among them, the conventional topology-optimized model achieves the highest PEC of 5.48, outperforming the Diamond TPMS and lattice-filled models by 22.5% and 11.5%, respectively. This demonstrates that while the Diamond TPMS is most effective at augmenting heat transfer, the conventional topology-optimized design offers a superior overall balance by mitigating the friction penalty.

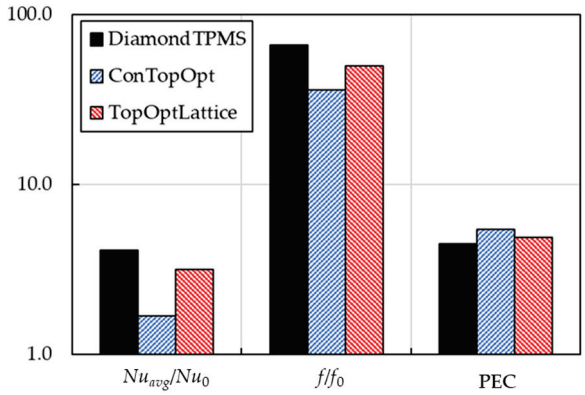


Figure 9. Plots of the heat transfer enhancement, friction factor ratio, and the performance evaluation criterion of all models at Re = 5000.

Figure 10 presents the trade-off between thermal performance and energy use by plotting thermal resistance (R_{tot}) against pumping power (P_e) for all models. The trends are similar to those in Figure 9, where the Diamond TPMS structure consistently requires the highest P_e to achieve a low R_{tot}, indicating that this cellular-lattice model is less effective at removing heat for a given pumping input. The conventional topology-optimized and lattice-filled models obtain a lower R_{tot} at a given P_e. In this comparison, the topology-optimized lattice-filled model shows the best performance at low P_e, outperforming the Diamond TPMS and conventional topology-optimized geometries. Meanwhile, the conventional topology-optimized geometry obtains a similar $R_{tot} \approx 0.55$ K/W but requires a lower P_e compared to the other models. Beyond overall heat transfer efficiency, the temperature uniformity is a critical requirement for SOFC system integrity. The following section evaluates the flow pattern, heat transfer distribution, and temperature uniformity for all designs.

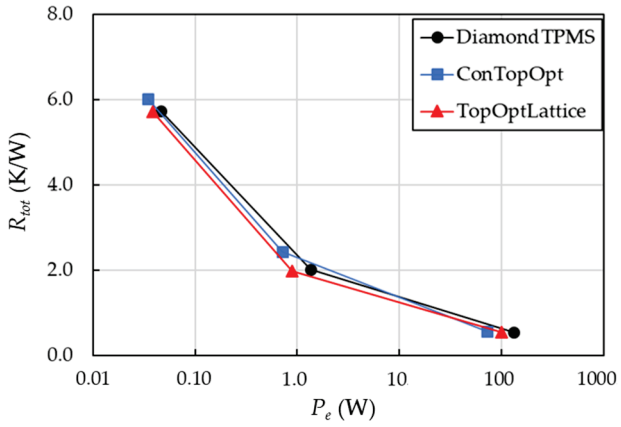


Figure 10. Plots of the thermal resistance on the heated walls against pumping power in all models.

3.1.2. Flow Characteristics

The results in the flow and heat transfer distributions at *Re* = 300 are excluded because the thermal–hydraulic performance of all geometries is insignificant, making it difficult to distinguish the flow effect. Therefore, the internal flow characteristics of all studied models are compared at *Re* = 1000 and 5000, as shown in Figure 11. The velocity contours and flow trajectories provide detailed insights into the internal flow characteristics that directly affect the cooling efficiency and temperature uniformity of the SOFC stack. As seen in Figure 11a, the Diamond TPMS lattice exhibits exceptional flow uniformity at both *Re* values [25]. Its diagonal topology provides consistent flow with minimal recirculation and promotes uniform heat transfer. These flow characteristics imply low thermal gradients across the SOFC components.

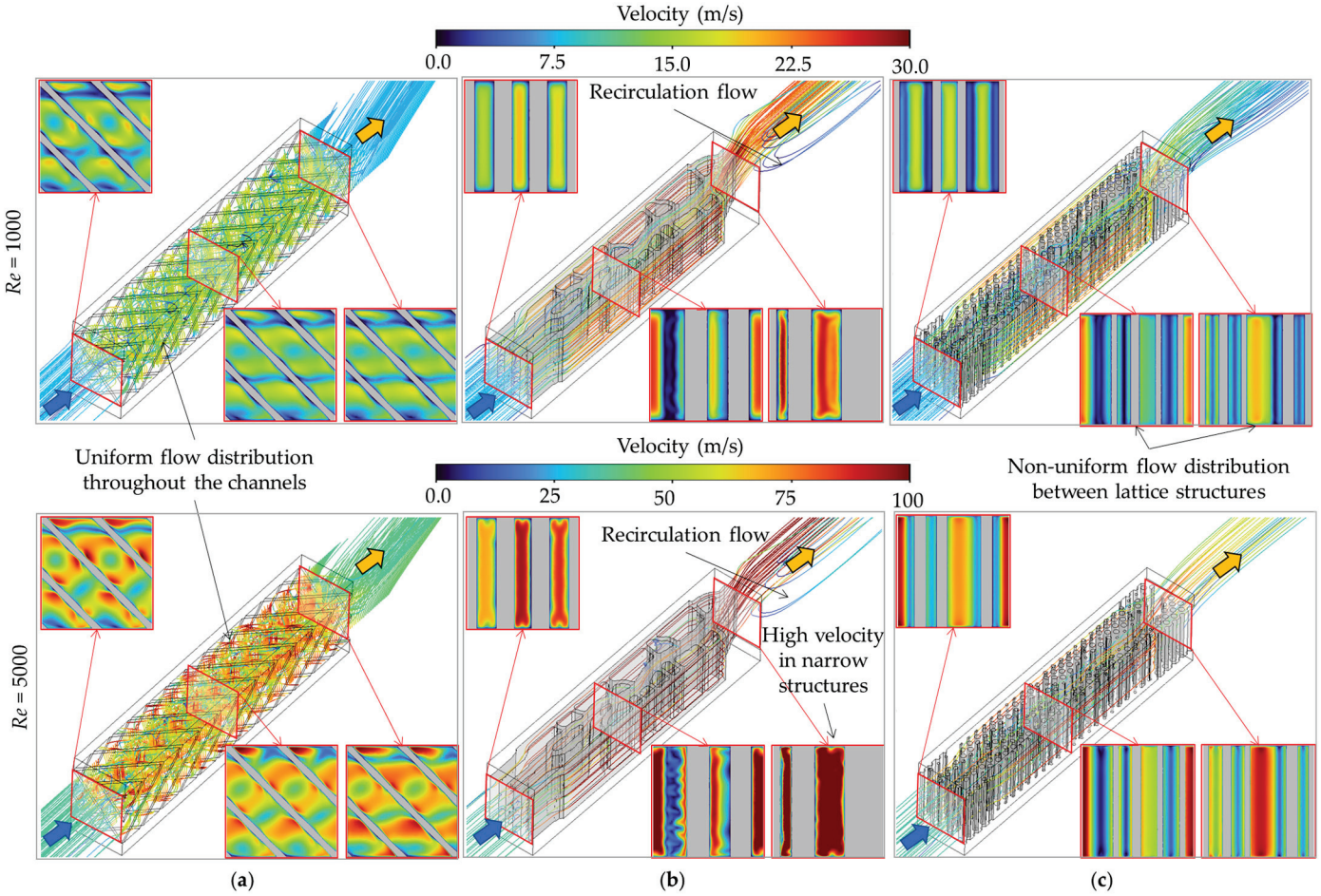


Figure 11. Flow characteristics of all models at the Reynolds numbers of 1000 and 5000: (**a**) Diamond TPMS model. (**b**) Conventional topology-optimized model. (**c**) Topology-optimized lattice-filled model.

In contrast, the conventional topology-optimized design in Figure 11b generates high-velocity jets between the baffles, leading to intense local heat transfer enhancement. However, this model generates strong recirculation zones at the outlet and a highly non-uniform flow distribution within the channel, particularly at *Re* = 5000. On the other hand, the topology-optimized lattice-filled structure in Figure 11c emerges as a hybrid solution. Although its flow distribution is not perfectly uniform as in the Diamond TPMS model, the integrated lattice structures with large surface areas induce local turbulence and mixing, enhancing overall cooling uniformity more effectively than the conventional topology-optimized model.

3.1.3. Heat Transfer Distributions

Figure 12 demonstrates the Nusselt number distributions at *Re* = 1000 and 5000 for all models. The contours indicate local heat transfer intensity, demonstrating the effectiveness and uniformity of convective heat transfer within each geometry. Based on the flow analysis, the Diamond TPMS structure demonstrates a correspondingly uniform and stable Nusselt number distribution at high *Re*, as seen in Figure 12a. The high flow uniformity translates into consistent heat transfer, confirming its capability for balanced thermal management of the SOFC system.

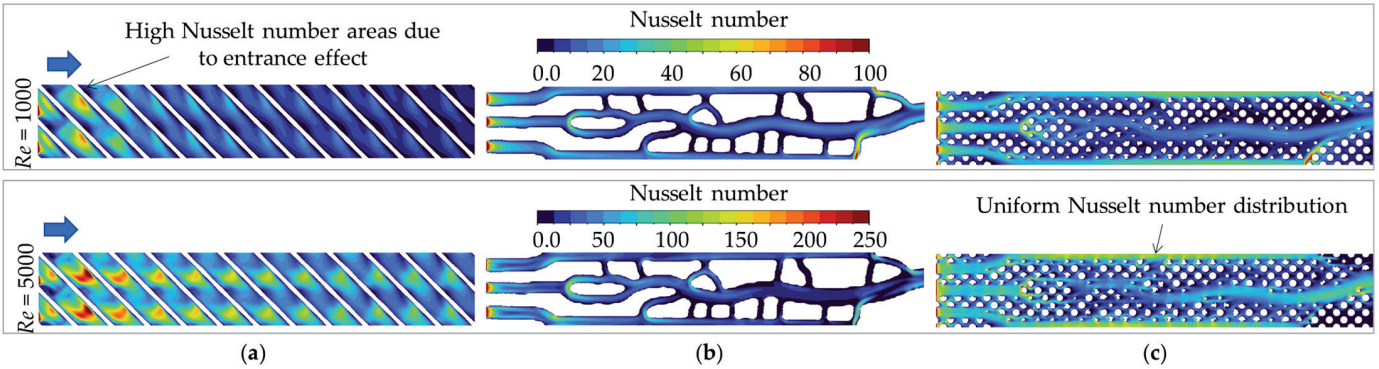


Figure 12. Nusselt number distributions on the endwall of all models at the Reynolds numbers of 1000 and 5000: (**a**) Diamond TPMS model. (**b**) Conventional topology-optimized model. (**c**) Topology-optimized lattice-filled model.

The jet impingement on the baffles and intense flow recirculation at the outlet in the conventional topology-optimized design cause non-uniform Nusselt number distribution, as observed in Figure 12b, particularly at high coolant flow rates, which can lead to high thermal stresses. Positively, the topology-optimized lattice-filled structure shows a more significant improvement with increasing flow rate. Although the non-uniform flow distribution at *Re* = 1000 results in a lower and uneven Nusselt number, the complex lattice interacts to create a uniform and enhanced heat transfer field at *Re* = 5000. This demonstrates that the lattice-filled design utilizes higher flow rates to improve heat transfer within its large surface area, thereby overcoming initial limitations.

Figure 13 shows the temperature distributions in the solid domain for all models at *Re* = 1000 and 5000. The temperature contours demonstrate the coolant flow behavior that influences heat removal and temperature uniformity in the cooling channel of the SOFC system. As shown in Figure 13a, the Diamond TPMS structure, consistent with its uniform flow, provides excellent temperature uniformity. However, at *Re* = 5000, a significant thermal gradient develops between the cooled structure and the heated walls, indicating a high thermal stress when integrating into the SOFC system. The conventional topology-optimized model in Figure 13b, which aligns with its non-uniform flow and Nusselt number distributions, exhibits uneven temperature contours and sharp gradients at both *Re* values, demonstrating a clear risk for thermal fatigue.

While the non-uniform flow characteristics in the topology-optimized lattice-filled structure at *Re* = 1000 lead to significant temperature variations, the high flow rate enhances mixing within the lattice, generating a uniform and lower overall temperature field. This structure also reduces the temperature imbalance found in the Diamond model and the high temperature in the conventional topology-optimized design. By combining a topologically guided flow path with a high-surface-area lattice, this complex structure shows a superior temperature uniformity at high coolant flow rates, ensuring effective heat dissipation and minimizing thermal variation, thereby enhancing SOFC reliability.

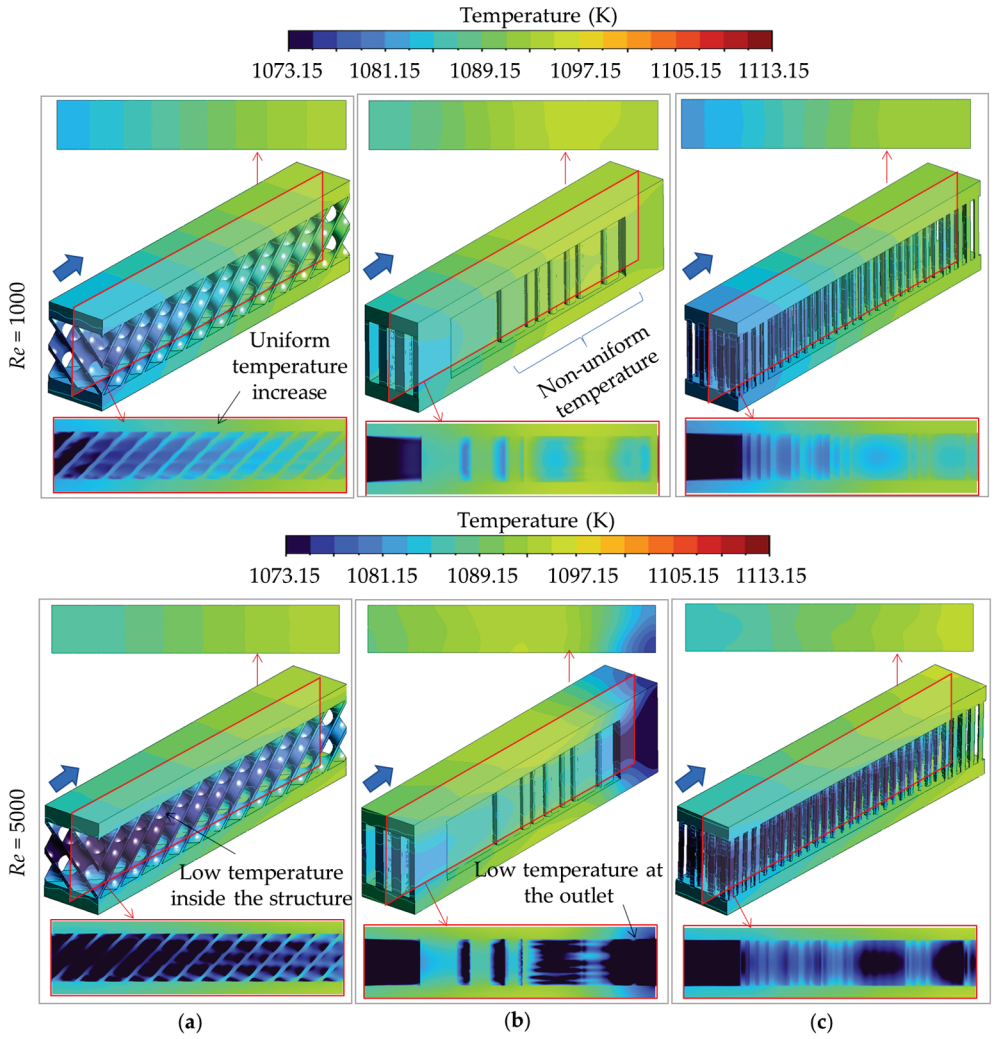


Figure 13. Temperature distributions on the solid domain of all models at the Reynolds numbers of 1000 and 5000: (**a**) Diamond TPMS model. (**b**) Conventional topology-optimized model. (**c**) Topology-optimized lattice-filled model.

3.1.4. Temperature Uniformity

Figure 14 shows the temperature uniformity (T-T_{avg}) on the heated wall for all models within the range of Re = 300–5000. The color scale, ranging from −18 K to +12 K, indicates that values closer to zero signify superior temperature uniformity. Among them, the Diamond TPMS structure in Figure 14a exhibits minimal temperature deviation from Re = 300 to Re = 5000, confirming its inherent design provides highly uniform temperature on the heated wall. Meanwhile, the conventional topology-optimized structure in Figure 14b causes a lower temperature uniformity, particularly at Re = 5000. Large and contiguous zones of positive and negative deviations are evident, revealing inherent non-uniform flow distribution, which is due to recirculation and stagnant zones. This temperature pattern fails to achieve the reliability for thermal management of the SOFC system at high coolant flow rates.

The topology-optimized lattice-filled structure in Figure 14c improves the temperature uniformity with increasing flow rate. At Re = 5000, this model achieves temperature uniformity similar to that of the Diamond TPMS model, demonstrating its advanced design effectively leverages higher flow inertia to activate uniform cooling across a complex structure. The topology-optimized lattice-fill structure could be an excellent candidate in the cooling channel between the SOFC stack, especially for high cooling air supplies.

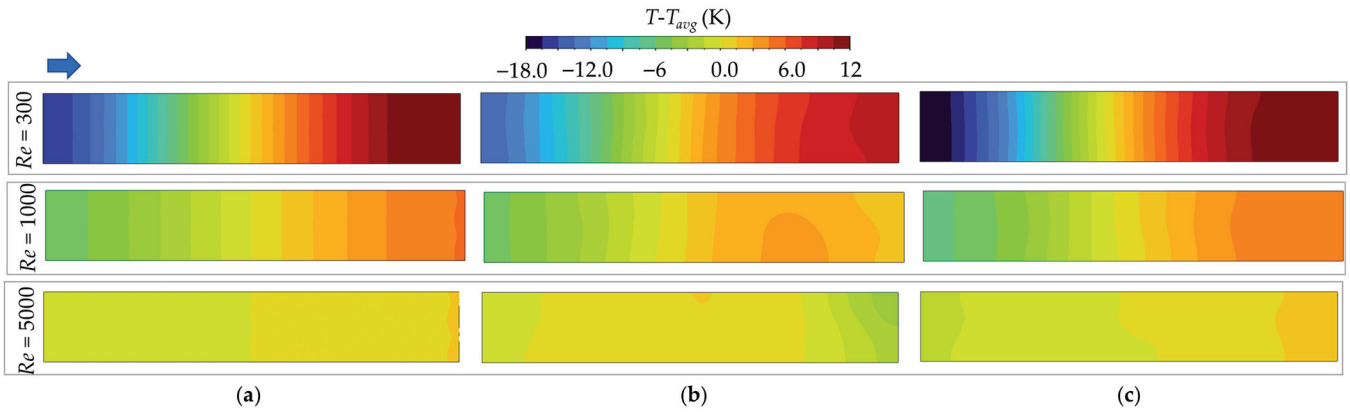


Figure 14. Contours of the temperature variation on the heated wall of all models at the Reynolds numbers of 300, 1000, and 5000: (**a**) Diamond TPMS model. (**b**) Conventional topology-optimized model. (**c**) Topology-optimized lattice-filled model.

Figure 15 provides quantitative values of the temperature range (T_{max}–T_{min}) and a temperature uniformity index (TUI) against *Re*. In Figure 15a, the conventional topology-optimized model exhibits the lowest temperature range (T_{max}–T_{min}) value of 23 K and 8.6 K when *Re* = 300 and 1000, while the Diamond TPMS and topology-optimized lattice-filled structures show a smaller temperature range of around 2 K at *Re* = 5000. Here, the smaller (T_{max}–T_{min}) value indicates a more uniform temperature field by minimizing the difference between the hottest and coldest spots, which is critical for reducing thermal stresses.

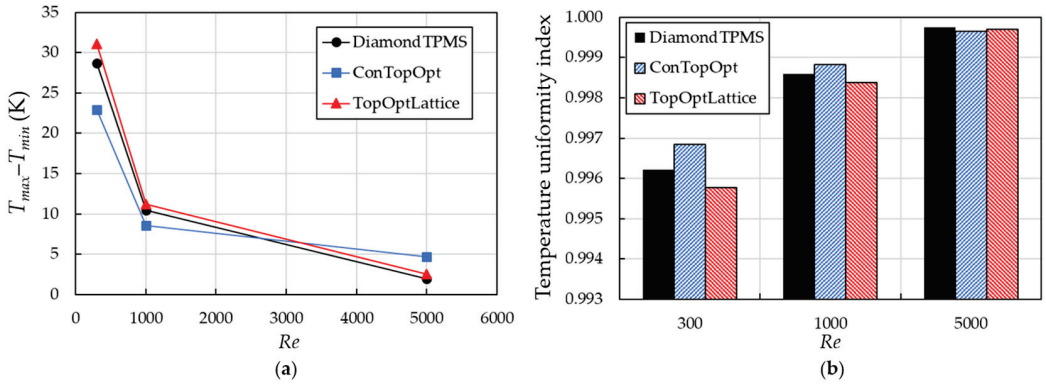


Figure 15. Evaluation of temperature uniformity on the bottom heated wall of all models at the Reynolds numbers of 300, 1000, and 5000: (**a**) T_{max}–T_{min} and (**b**) temperature uniformity index.

This superior performance is further validated in Figure 15b by the TUI, where a value closer to 1.0 represents perfect uniformity. The Diamond TPMS structure achieves the highest index values, confirming its excellent thermal distribution at *Re* = 5000. While the conventional topology-optimized models perform well at low *Re* values, the topology-optimized lattice-filled structure slightly exceeds its uniformity at higher flow rates. Overall, the analyses in this section demonstrate that the topology-optimized lattice-filled structure offers a highly uniform thermal environment on the heated wall of the air-cooled SOFC system, indicating that it is the optimal design for mitigating thermal stress and ensuring reliable operation at high cooling air flow rates in this study.

3.2. Effect of Coolant Type

To isolate the influence of coolant flow rate on thermal performance, the thermal–hydraulic performance, heat transfer distribution, and temperature uniformity are analyzed

at *Re* = 300. The following analysis utilizes a ferritic stainless steel structure to compare three coolants: air, liquid tin, and liquid gallium.

3.2.1. Thermal–Hydraulic Performance

Figure 16 compares the thermal–hydraulic performance of all models under three coolant types at *Re* = 300. The conventional topology-optimized and lattice-filled structures achieve Nu_{avg} approximately twice that of the Diamond TPMS with air cooling, as shown in Figure 16a, due to their enhanced flow redistribution and mixing. While liquid metals yield lower Nusselt number values of $Nu_{avg} < 4$ [19], the topology-optimized lattice-filled model slightly outperforms others, as its complex lattice promotes mixing even in low-flow-rate liquid metals. This translates directly to the temperature on the heated wall in Figure 16b, where liquid metals reduce wall temperatures by up to 43 K compared to air, with the gallium-cooled channel obtaining the lowest values.

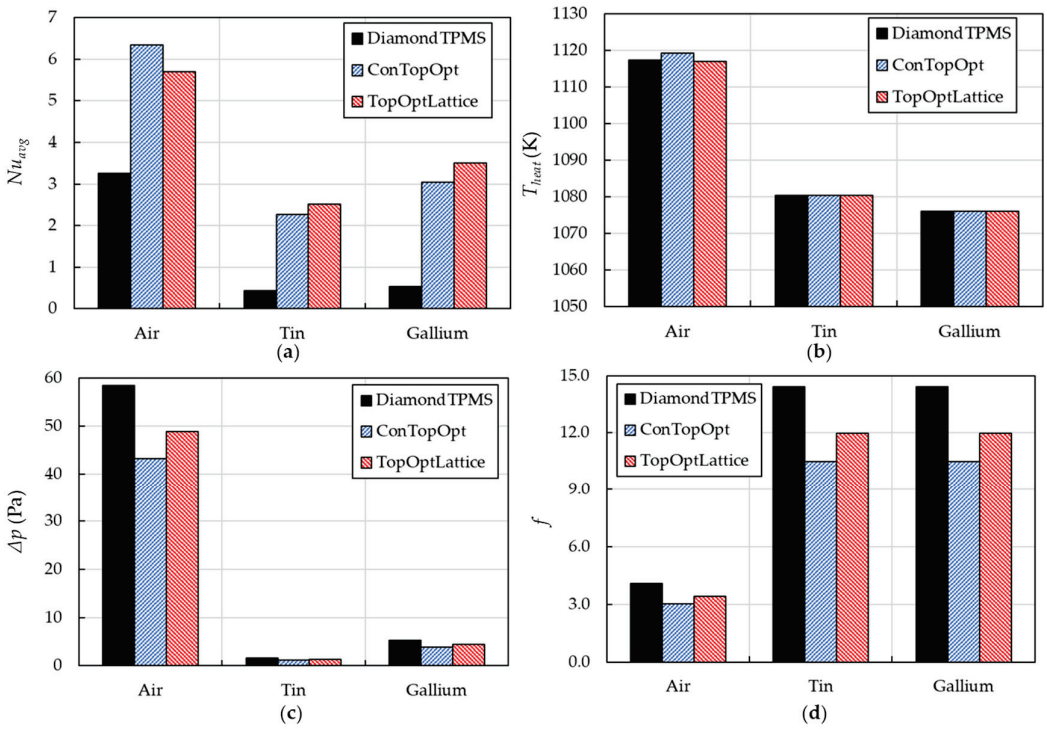


Figure 16. Thermal–hydraulic performance of all models with different coolants at Reynolds numbers of 300: (**a**) area-averaged Nusselt number on the endwall inside the cooling channel; (**b**) area-averaged temperature on the heated wall; (**c**) pressure loss; and (**d**) friction factor.

Figure 16c reveals that pressure loss is governed by both fluid properties and channel topology. For the air-cooled channel, the Diamond TPMS structure exhibits the highest pressure loss of 58.5 Pa, while the conventional topology-optimized model achieves the lowest. For liquid tin and gallium, the pressure losses are significantly lower than those of the air-cooled channel due to their higher density and lower dynamic viscosity, which drastically reduces fluid flow resistance at an equivalent *Re*. The f in Figure 16d further elucidates this hydraulic behavior, where the Diamond TPMS model exhibits the highest f value, ranging from 4.1 to 14.2, which is 26.2% to 27.2% higher than the conventional topology-optimized model, and from 16.4% to 16.9% higher than the lattice-filled design for all coolant types. The topology-optimized lattice-filled model exhibits an obviously higher f value than the conventional topology-optimized model, by 13.2% to 14.2%, because of its finer internal structures, which strongly interact with the high density of the liquid metals.

Figure 17 compares the R_{tot} and P_e for all designs with different coolants at Re = 300. As shown in Figure 17a, the R_{tot} decreases significantly when the coolant is changed from air to liquid metals. The air-cooled channel exhibits the highest R_{tot} in all geometries due to its inherently low thermal conductivity and heat capacity. Meanwhile, the liquid tin and gallium achieve higher performance, with gallium offering the lowest $R_{tot} \approx 0.25$ K/W, a reduction of 93%. A noticeable difference of approximately 60% between the liquid metals is due to variations in coolant conductivity. Notably, the geometric differences cause only minor changes in the R_{tot} with liquid metals, confirming that the coolant properties dominate heat transfer under these flow conditions. Overall, for the air-cooled channel, the topology-optimized lattice-filled structure exhibits the best performance. Meanwhile, for liquid metals, the conventional topology-optimized geometry is the most effective, indicating that its baffle structures are more efficient in removing heat at low coolant flow rates.

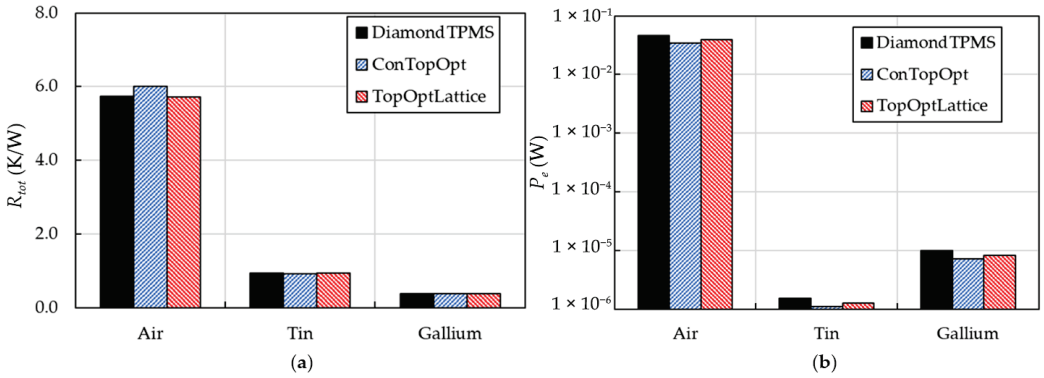


Figure 17. Influence of coolant type on: (**a**) thermal resistance and (**b**) pumping power for all models at Reynolds numbers of 300.

Figure 17b reveals that air cooling requires the highest P_e of 0.047 W, despite its low heat transfer performance, which is attributed to its low density requiring high volumetric flow rates [18]. The liquid metals significantly reduce pumping requirements, with liquid tin exhibiting the lowest P_e of up to 100% compared to the air-cooled channel, due to its viscosity–density balance. The higher viscosity and density of the gallium-cooled channel result in a 5.6% increase in its P_e compared to the tin-cooled channel. Overall, the geometric design influences on the P_e are minor for liquid metals but more pronounced for air, where the Diamond TPMS model shows higher losses.

3.2.2. Heat Transfer Distributions

Figure 18 shows the effect of coolant types on the Nusselt number distributions for all models at Re = 300. The liquid metal-cooled channels exhibit lower Nusselt numbers than the air-cooled channel despite their superior performance. It is essential to clarify that the Nusselt number is a measure of the convective relative to the conductive heat transfer. The relatively high thermal conductivity of liquid metals is the primary mechanism for their effectiveness, enabling rapid heat transfer through conduction rather than convection. This results in a lower temperature difference between the wall and the bulk fluid, which leads to a lower Nusselt number. While the air-cooled channel exhibits high Nusselt numbers, the tin- and gallium-cooled channels maintain a more uniform Nusselt number along the flow direction, even at this low flow rate. Furthermore, the Diamond TPMS structure creates a high heat transfer only at the channel entrance, whereas the conventional topology-optimized and lattice-filled models maintain a more uniform distribution.

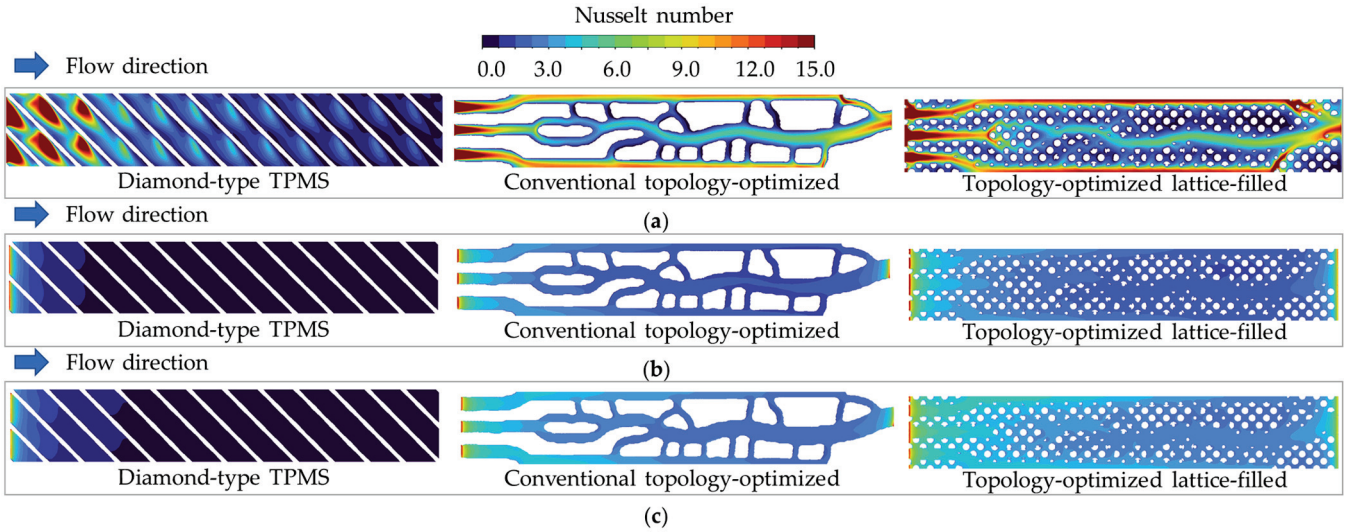


Figure 18. Nusselt number distributions on the endwall of all models at the Reynolds numbers of 300: (**a**) Air-cooled channel. (**b**) Liquid tin-cooled channel. (**c**) Liquid gallium-cooled channel.

A comparison of the liquid-metal coolants reveals that the gallium-cooled channel in Figure 18c generates a higher magnitude and a more uniform Nusselt number distribution than the tin in Figure 18b. It is noticeable that the conventional topology-optimized structures consistently demonstrate the most uniform distributions when using liquid gallium. This optimal performance arises from the combination of high thermal conductivity in the liquid gallium and the baffle topology, which provides a simple and large surface area for heat exchange while maintaining smooth flow pathways that enable efficient heat removal.

The temperature fields on the solid domain for the three coolant types at Re = 300 are compared in Figure 19. The cross-sectional views show that although the constant flow rate offers a similar temperature trend in all geometries, the liquid tin and gallium generate substantially lower and more uniform temperature distributions than the air-cooled channel. Specifically, the gallium-cooled channel in Figure 19c exhibits the most uniform temperature and the lowest peak temperature, closely followed by the tin-cooled channel in Figure 19b. Meanwhile, the air cooling in Figure 19a results in non-uniform and high peak temperatures, indicating that it is unsuitable for the cooling channel of the SOFC without substantial geometric or operational adjustments.

3.2.3. Temperature Uniformity

Figure 20 shows the impact of coolant type on the temperature uniformity for all designs at Re = 300. A dominant trend of all structures is the profound improvement in temperature uniformity when using liquid tin and gallium coolants compared to air. The air-cooled channels in Figure 20a exhibit the largest temperature change, indicating poor heat spreading and a high risk of thermal stress. On the other hand, both liquid metal coolants provide more uniform temperature fields, with significantly smaller deviations concentrated near zero. Among the liquid metals, the gallium-cooled channel in Figure 20c yields the most uniform temperature distributions, slightly outperforming the liquid tin-cooled channel in Figure 20b. This is also consistent with the higher thermal conductivity of the liquid gallium [19]. Regarding the geometries, the conventional topology-optimized structure consistently demonstrates the best uniformity with the liquid-metal coolants. Its optimized-baffle design integrates well with high-conductivity liquid metals to create a uniform temperature contour.

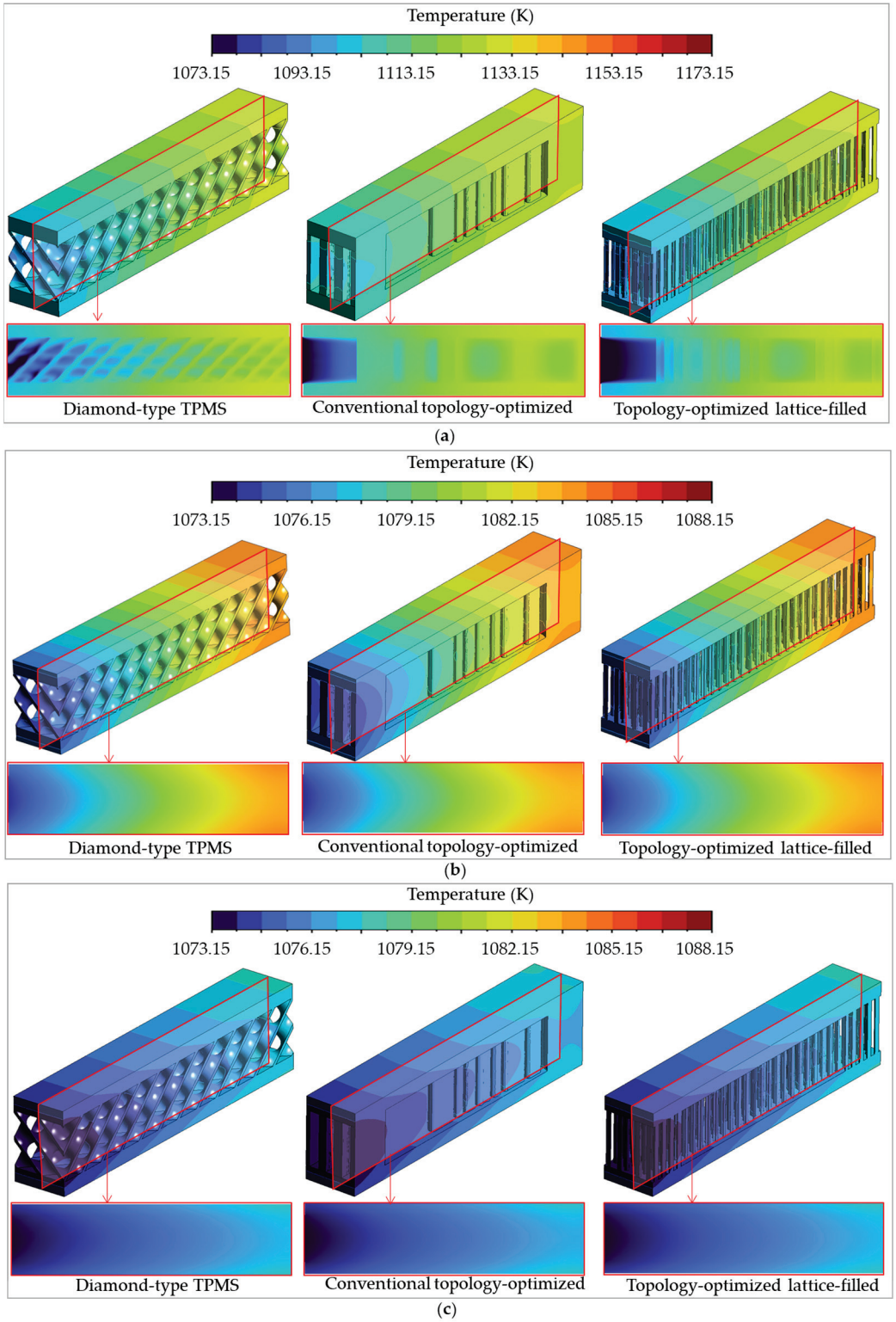


Figure 19. Temperature distributions on the solid domain of all models at the Reynolds numbers of 300: (**a**) Air-cooled channel. (**b**) Liquid tin-cooled channel. (**c**) Liquid gallium-cooled channel.

Figure 21 quantitatively evaluates the temperature uniformity on the heated wall for all models using air, liquid tin, and liquid gallium as coolants at Re = 300. With the air-cooled channel, all geometries exhibit significant temperature differences (T_{max}–T_{min}) up to 30 K and lower temperature uniformity index values, indicating limited heat spreading capability. Among the designs, the conventional topology-optimized model achieves the best air-cooled performance due to its simple baffle cooling structures, which enable smooth

flow at low *Re*. In contrast, the liquid metals drastically improve temperature uniformity, reducing the temperature difference value to below 10 K and achieving temperature uniformity index values close to 1.0. The gallium-cooled channel performs slightly better than the tin, yielding differences below 5 K due to its superior thermal conductivity. These results confirm that while the geometry influences convective heat transfer, the coolant properties dominate temperature uniformity. Consequently, these findings affirm the promise of liquid-metal coolants for thermal management in high-power-density SOFCs, though practical integration issues remain to be improved.

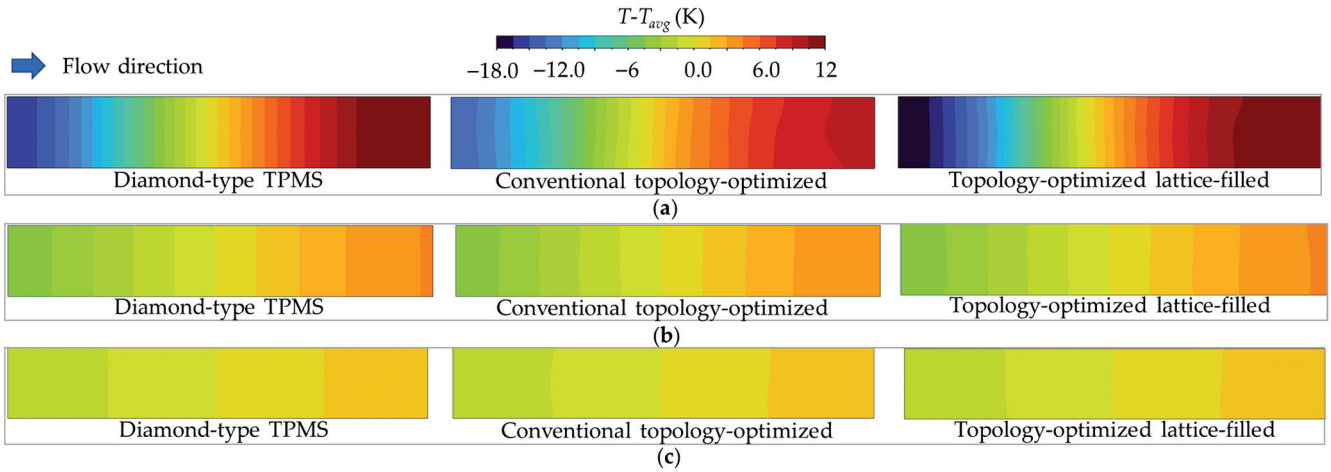


Figure 20. Contours of the temperature variation on the heated wall of all models at the Reynolds numbers of 300: (**a**) Air-cooled channel. (**b**) Liquid tin-cooled channel. (**c**) Liquid gallium-cooled channel.

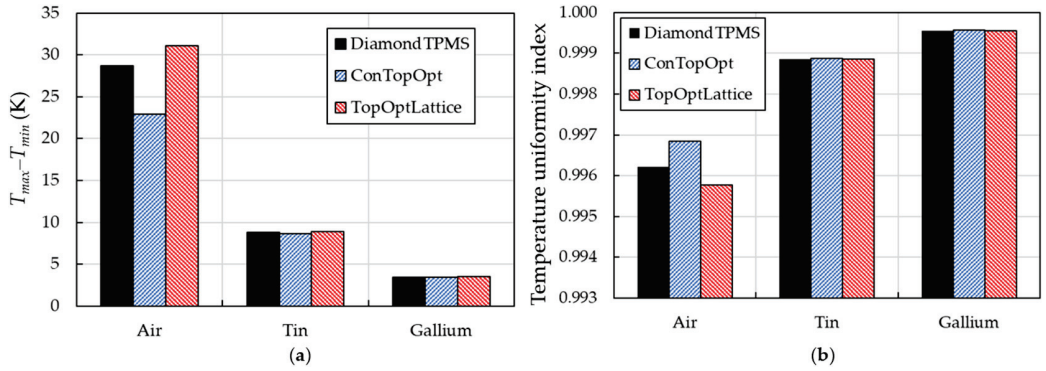


Figure 21. Evaluation of temperature uniformity on the bottom heated wall of all models with different coolants at the Reynolds numbers of 300: (**a**) T_{max}–T_{min} and (**b**) Temperature uniformity index.

Although these findings affirm the excellence of liquid-metal coolants for thermal management in high-power-density SOFCs, their practical implementation in the SOFCs requires careful consideration of material compatibility, corrosion, and cost. The liquid tin is highly corrosive to ferritic stainless steel under high operating temperatures of the SOFCs, necessitating the use of specialized nickel-based superalloys or protective ceramic coatings [15]. The liquid gallium could cause embrittlement in many structural metals and is significantly more expensive than liquid tin. Moreover, these liquid metals face wetting issues in highly complex channels. Thus, their thermal benefits must be balanced against higher costs, material problems, and potential long-term degradation.

3.3. Effect of Structural Material

This section evaluates the impact of various structural materials on the thermal performance of the air-cooled channel. A comparative analysis of pressure loss shows insignificant variation between different structural materials at Re = 300; consequently, the discussion is confined to thermal characteristics.

3.3.1. Heat Transfer Performance

Figure 22 illustrates the comparison of thermal performance parameters for all air-cooled geometries, fabricated with three different solid materials at Re = 300. The Nu_{avg} is substantially higher in the conventional topology-optimized and lattice-filled configurations than in the Diamond TPMS structure across all structural materials, as seen in Figure 22a. The improvement is significant, with the Nu_{avg} increases of 56–89% over the Diamond TPMS model. The stainless steel and nickel–chromium structures provide similar value, which is slightly higher than that of the high-thermal-conductivity metal.

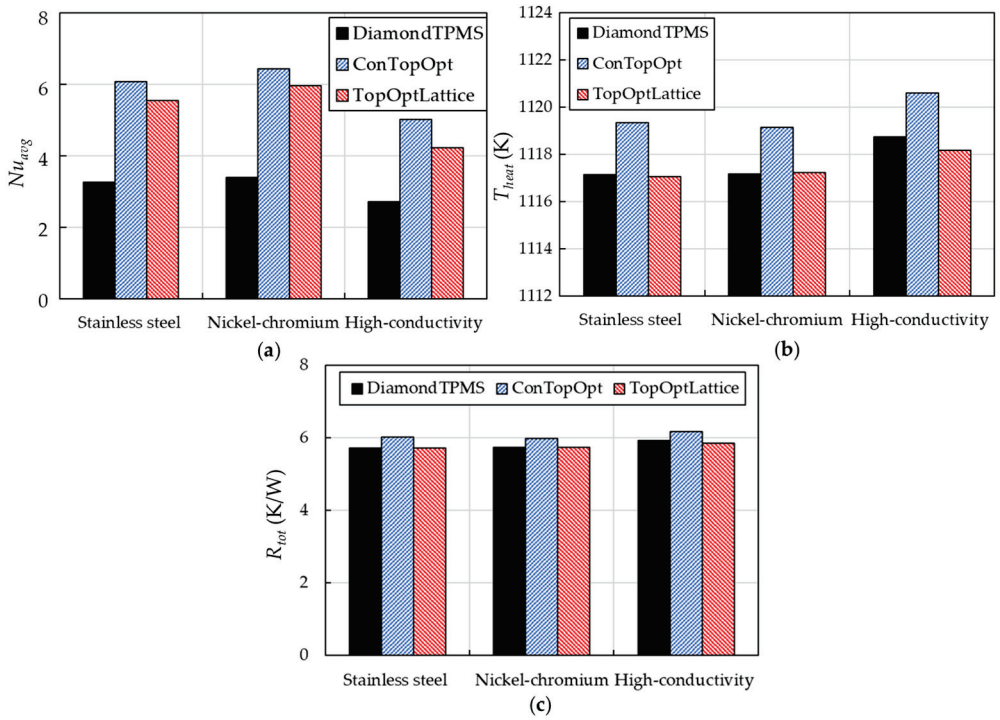


Figure 22. Thermal performance of all air-cooled geometries at the Reynolds numbers of 300: (**a**) area-averaged Nusselt number on the endwall inside the cooling channel; (**b**) area-averaged temperature on the heated wall, and (**c**) Thermal resistance.

Despite these convective heat transfer increases, the conventional topology-optimized model exhibits higher T_{heat} than the Diamond TPMS structure, as found in Figure 22b. This indicates that convective enhancement alone does not dictate the final wall temperature. The high-thermal-conduction metal causes a slightly higher T_{heat} value than the others. Lastly, the R_{tot} shows a similar value in all designs in Figure 22c, indicating that the high convective heat transfer does not translate proportionally into lower thermal resistance with different structural materials. It could also be deduced that the performance of the flow and heat transfer conditions in this study is governed by a complex balance between convection and conduction.

3.3.2. Heat Transfer Distributions

Figure 23 illustrates the Nusselt number distributions on the endwall of all designs for different structural materials at *Re* = 300. In the ferritic stainless-steel and nickel–chromium superalloy cases, as shown in Figure 23a,b, the conventional topology-optimized geometry generates high Nusselt number values along the flow direction, indicating improved convective mixing at low coolant flow rate. In contrast, the Diamond TPMS model exhibits alternating high- and low-Nusselt number values, resulting from periodic flow recirculation, which leads to more pronounced local hot spots [25]. The topology-optimized lattice-filled structure exhibits intermediate behavior, maintaining relatively continuous high-Nusselt number regions near flow passage intersections.

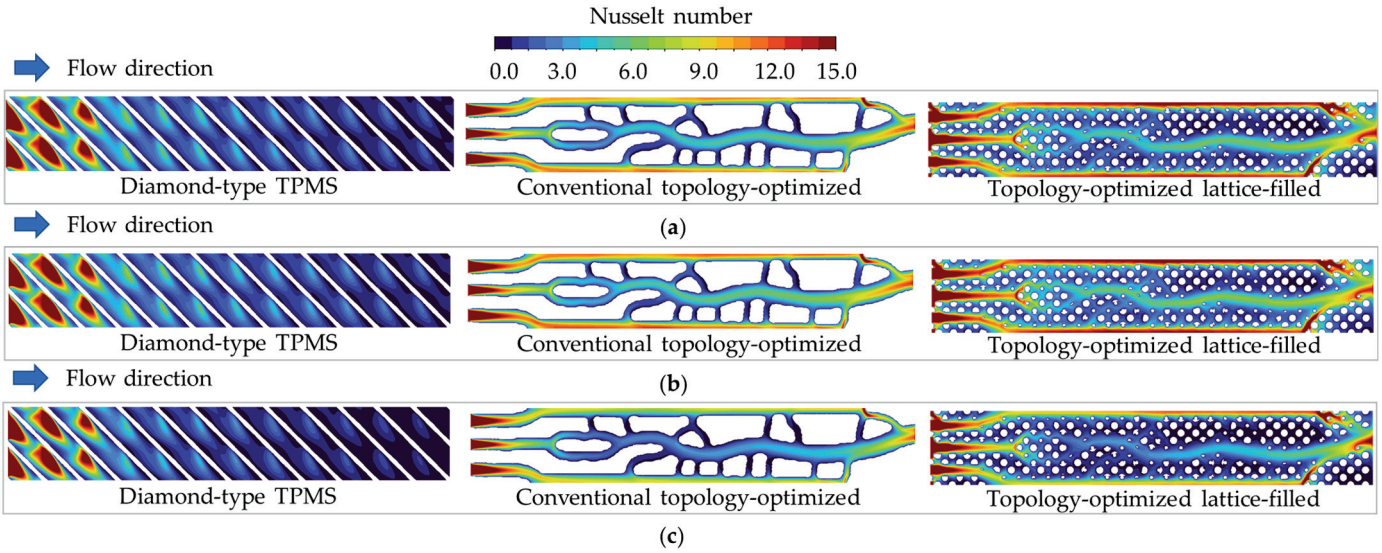


Figure 23. Nusselt number distributions on the endwall of all air-cooled geometries at the Reynolds numbers of 300: (**a**) Ferritic stainless steel. (**b**) Nickel–chromium superalloy. (**c**) High-thermal-conductivity metal.

When replacing the structural material with a high-thermal-conductivity metal in Figure 23c, the Nusselt number gradients become clearly non-uniform. Although the increased thermal conductivity promotes lateral heat spreading within the solid, a non-uniform endwall temperature distribution can be observed. Consequently, the distinction between high- and low-Nusselt number zones becomes more prominent. Among all designs, the topology-optimized lattice-filled maintains the high uniform Nusselt number regions, confirming that the topology optimization effectively tailors the internal flow paths to maximize thermal utilization of the coolant under air-cooling conditions.

Figure 24 presents the temperature distributions on the solid domain of all air-cooled geometries at *Re* = 300 for different structural materials. In the ferritic stainless-steel and nickel–chromium superalloy cases shown in Figure 24a,b, all designs exhibit noticeable temperature gradients along the flow direction, with higher temperatures near the outlet region, particularly in the topology-optimized lattice-filled structure. The conventional topology-optimized structure shows the most uniform temperature distribution, although it demonstrates slightly lower temperatures, followed by the Diamond TPMS model.

As the material changes to the high-thermal-conductivity metal in Figure 24c, the overall temperature levels increase, but the temperature variations become smaller, which can be attributed to lateral heat spreading within the solid wall, significantly reducing the thermal nonuniformity between the inlet and outlet. In this material condition, the temperature contours in all geometries become more uniform, indicating that material thermal conductivity has a significant influence on the wall temperature distribution.

Nevertheless, the conventional topology-optimized configuration consistently provides the lowest temperature variation among all designs.

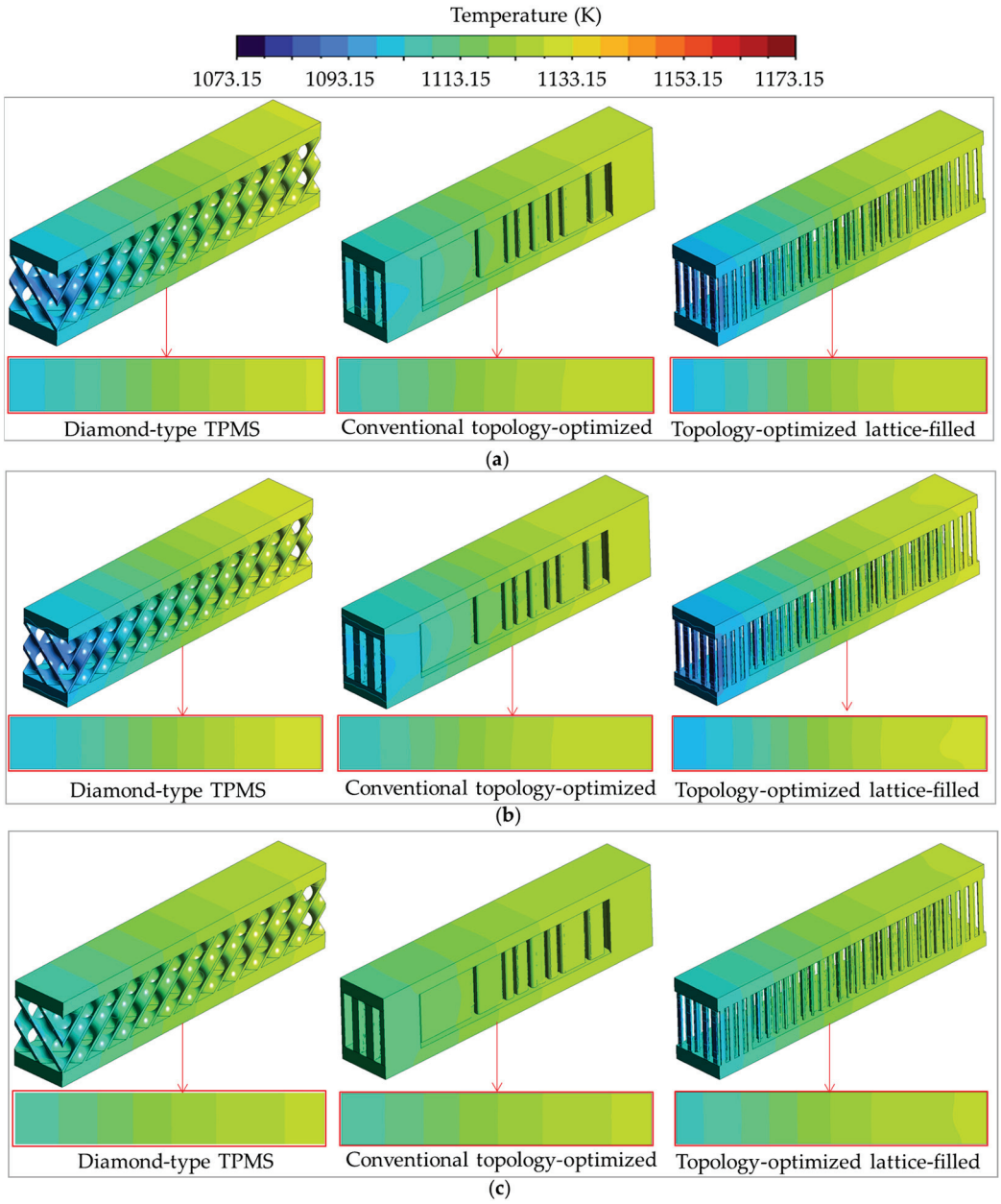


Figure 24. Temperature distributions on the solid domain of all air-cooled geometries at the Reynolds numbers of 300: (**a**) Ferritic stainless steel. (**b**) Nickel–chromium superalloy. (**c**) High-thermal-conductivity metal.

3.3.3. Temperature Uniformity

Figure 25 illustrates the contours of temperature variation (T-T_{avg}) on the heated walls of all air-cooled geometries at Re = 300 for different materials. Similar to the previous discussion, the ferritic stainless steel in Figure 25a and the nickel–chromium superalloy in Figure 25b cause significant temperature gradients. The conventional topology-optimized model exhibits the most non-uniform temperature distribution, a consequence of its less complex structure, which allows smooth flow between the baffles at low Re. The transition to the high-thermal-conductivity metal in Figure 25c shows a more uniform temperature contour. This improvement signifies that heat is being effectively conducted from hot spots, creating a more isothermal heated surface.

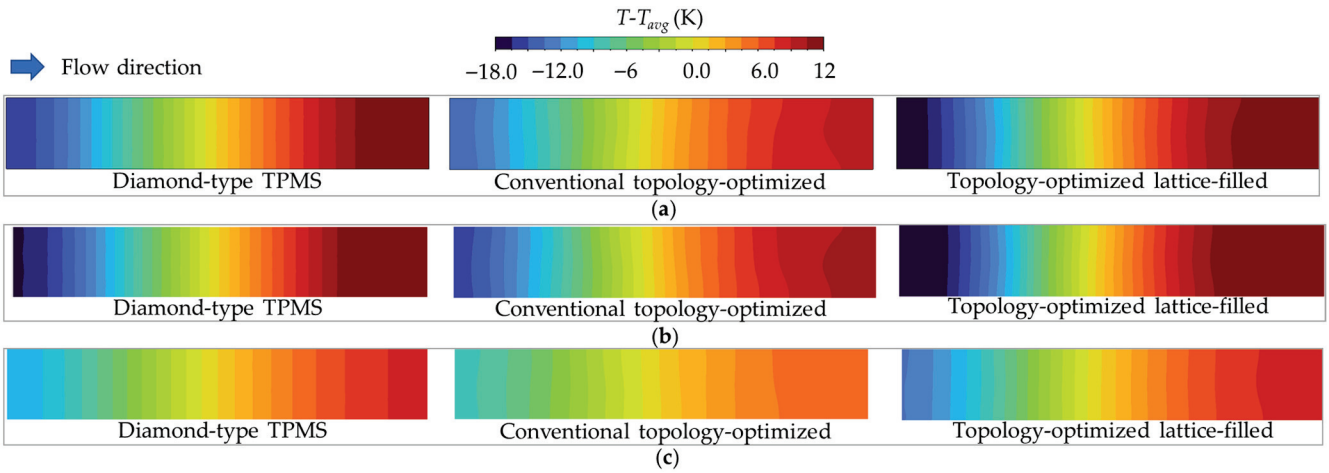


Figure 25. Contours of the temperature variation on the heated wall of all air-cooled geometries at the Reynolds numbers of 300: (**a**) Ferritic stainless steel. (**b**) Nickel–chromium superalloy. (**c**) High-thermal-conductivity metal.

Figure 26 evaluates the temperature uniformity on the heated wall of all air-cooled designs, fabricated from different materials, at Re = 300. For all materials, the conventional topology-optimized configuration exhibits the smallest temperature range (T_{max}–T_{min}) of 16 K to 30 K, as shown in Figure 26a, indicating superior temperature uniformity compared to the other geometries. Meanwhile, the topology-optimized lattice-filled structure causes the largest temperature range values, spanning 40 K to 51 K, due to complex flow recirculation behind each lattice, particularly at low Re. As the thermal conductivity of the wall material increases, from ferritic stainless steel to high-thermal-conductivity metals, the overall temperature range decreases across all designs, and the conventional topology-optimized model achieves the lowest temperature range of 16 K.

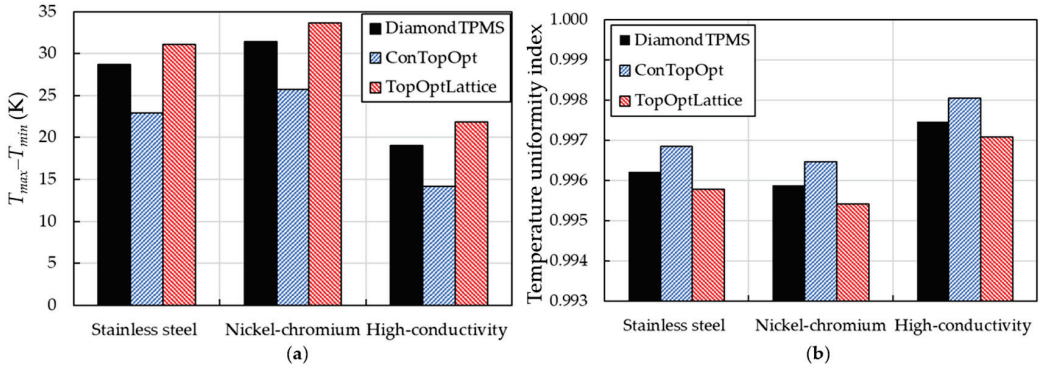


Figure 26. Evaluation of temperature uniformity on the bottom heated wall of all air-cooled geometries with different structural materials at the Reynolds numbers of 300: (**a**) T_{max}–T_{min} and (**b**) temperature uniformity index.

A similar trend is observed in the temperature uniformity index in Figure 26b, where the conventional topology-optimized model achieves the highest index for all materials. The topology-optimized lattice-filled model slightly reduces uniformity despite its enhanced surface area, implying that excessive internal complexity may hinder uniform cooling, particularly at low coolant flow rates. The Diamond TPMS model maintains moderate uniformity across studied materials, benefiting from its periodic structure but limited by reduced internal mixing.

The superior temperature uniformity observed with high-conductivity materials can also be quantitatively explained by the Biot number. For all geometries at Re = 300, the Biot

number is significantly less than 0.1. This occurs because the intricate structures have a very small characteristic length, defined by the ratio of solid volume to wetted surface area. Among the materials, the high-thermal-conductivity metal yields the lowest Biot number, confirming its minimal internal conductive resistance relative to the external convective resistance and thus the most uniform temperature field.

Overall, these findings indicate that for the air-cooled system utilizing high-conductivity materials and low coolant flow rates, the baffle-shaped designs (the conventional topology-optimized model) that enable low pressure loss and a smooth flow field are the most suitable for thermal management of the SOFC stack.

4. Conclusions

This study presents a conjugate analysis of cooling channel designs, including the Diamond TPMS, conventional topology-optimized, and topology-optimized lattice-filled structures, which integrate between the SOFCs to improve thermal management. The investigation assesses the impact of coolant flow rate, coolant type, and structural material on thermal–hydraulic performance and temperature uniformity. The conclusions can be drawn as follows:

(1) The Diamond TPMS structure provides excellent flow and heat transfer distribution, but causes a significant pressure penalty of 45.6% and 24.6% at Re = 5000, compared to the conventional topology-optimized and lattice-filled designs. The conventional optimized model minimizes pressure loss but can lead to non-uniform flow and temperature distributions at high flow rates. The topology-optimized lattice-filled structure emerges as an excellent compromise, especially at high Re. By combining the tailored flow paths from topology optimization with the high surface area of a lattice-filled array, this design in the air-cooled system achieves temperature uniformity comparable to that of the Diamond TPMS at Re = 5000, while incurring a significant reduction in pressure loss penalty.

(2) While both topology-optimized designs can improve convective heat transfer, the choice of coolant is found to be the highest dominant factor, governing the thermal–hydraulic performance. The transition coolants from air to liquid metals resulted in a significant reduction in thermal resistance, up to 93%, and a relatively high temperature uniformity index at Re = 300. The liquid gallium, with its superior thermal conductivity, outperformed liquid tin, achieving the most uniform temperature distributions on the heated wall, where the differences between the maximum and minimum temperatures (T_{max}–T_{min}) are less than 5 K in both topology-optimized designs. However, the excellent cooling performance of liquid metals might come with a higher cost and greater engineering challenges.

(3) A higher thermal conductivity material improves heat spreading within the solid structure, creating a more uniform temperature in all geometries. Under low coolant flow rates and air-cooled conditions, the baffle-like structures in the conventional topology-optimized model exhibit preferable thermal–hydraulic performance, facilitating a smooth flow field, and achieve the lowest temperature range (T_{max}–T_{min}) of 16 K at Re = 300.

(4) For maximum performance, employing a liquid metal coolant within the optimized-baffle design channel is highly recommended for the precise thermal management of the SOFC. This configuration leverages their balanced thermal–hydraulic performance and the high thermal conductivity of the liquid metals. Additionally, fabricating the channel with a high thermal conductivity material for a conventional topology-optimized design further achieves better temperature uniformity while minimizing parasitic power.

The design strategies outlined in this work offer an alternative approach to enhancing the thermal management of SOFC systems, providing significantly improved temperature uniformity. To transition these concepts from simplified simulations to real-world applications, future investigations could establish full-system computational modeling and experimental validation to quantify the realistic performance improvements.

Author Contributions: Conceptualization, K.Y. and Y.R.; methodology, K.Y. and Y.C.; software, K.Y.; validation, K.Y. and Y.C.; formal analysis, K.Y. and Y.C.; investigation, K.Y. and Y.C.; resources, K.Y. and Y.R.; data curation, K.Y. and Y.C.; writing—original draft preparation, K.Y.; writing—review and editing, K.Y., Y.R. and Y.C.; visualization, K.Y. and Y.C.; supervision, Y.R.; project administration, Y.R.; funding acquisition, K.Y. and Y.R. All authors have read and agreed to the published version of the manuscript.

Funding: This work was supported by grants from the National Natural Science Foundation of China (Nos. 11972230, 24Z033103800), the National Science and Technology Major Project of China (No. 2017-III-0009-0035), and the Science and Technology Commission of Shanghai Municipality (No. 24110712700).

Data Availability Statement: The original contributions presented in this study are included in the article. Further inquiries can be directed to the corresponding author.

Acknowledgments: Yu Rao gratefully acknowledges support from the Shandong Provincial Industrial Leading Talents Project.

Conflicts of Interest: The authors declare no conflicts of interest.

Nomenclature

A_i	Local area (m^2)
A_{in}	Inlet area of the cooling channel (m)
D	Characteristic length (m)
D_h	Hydraulic diameter of the cooling channel (m), defined in Equation (2)
D_p	Diameter of the circular pin-fin structure (m)
f	Friction factor, defined in Equation (6)
f_0	Blasius correlations, defined in Equation (10)
h	Heat transfer coefficient ($W/(m^2 \cdot K)$, defined in Equation (4)
T_b	Bulk flow temperature (K)
T_{heat}	Temperature of the heated wall (K)
T_{in}, T_{out}	Inlet and outlet coolant temperatures (K)
T_i	Local temperature (K)
T_{max}, T_{min}	Maximum and minimum temperature on the heated wall (K)
T_w	Endwall temperature(K)
L	Length of the cooling structure (m)
L_p	Wetted perimeter (m)
Nu	Nusselt number, defined in Equation (3)
Nu_{avg}	Area-averaged Nusselt number
Nu_0	Dittus-Boelter equation, defined in Equation (9)
q	Wall heat flux (W/m^2)
k	Thermal conductivity of the fluid ($W/m \cdot K$)
P_e	Pumping power (W), defined in Equation (7)
p_{in}	Coolant inlet pressure (Pa)
Re	Reynolds number, defined in Equation (1)
R_{tot}	Total thermal resistance (K/W), defined in Equation (5)
S_v	Specific area surface (m^2/m^3)
V_{in}	Velocity at the inlet (m/s)
X, Y, Z	Cartesian coordinate

Greek letter	
γ	Density field in the topology optimization
μ	Dynamic viscosity of the coolant (Pa·s)
ρ	Density of the coolant (kg/m^3)
Δp	Different pressure between the inlet and outlet boundaries (Pa)
Γ_{in}	Inlet boundary
ψ	Porosity (%)
Abbreviations	
CHT	Conjugate heat transfer
PEC	Performance evaluation criterion, defined in Equation (8)
PEMFCs	Proton-exchange membrane fuel cells
PEN	Positive electrode-electrolyte-negative electrode
TLC	Transient liquid crystal thermography
TPMS	Triply periodic minimal surface
TUI	Temperature uniformity index, defined in Equation (11)
SOFC	Solid-oxide fuel cell

Appendix A

The density-based topology optimization is used to maximize heat transfer within the internal cooling channel. This method solves a material distribution problem, defining an optimal layout of fluid and solid phases within the design domain (Ω). A continuous design variable (γ) represents the material distribution, ranging from 0 (solid) to 1 (fluid) at any cell in the design domain. A review of this approach for cooling channels is available in Refs [26,27].

To reduce the high computational cost required for convergence, a simplified 2D model is employed, as shown in Figure A1. The symmetry boundary conditions are applied to the side walls to further accelerate the optimization process. The inlet velocity (V_{in}) is typically used to determine the Reynolds number (Re). However, during topology optimization, the channel geometry changes, which alters the inlet velocity even when the input power is held constant. To maintain a consistent basis for comparison at fixed input power, the following integral equation for inlet pressure is derived [27], as follows:

$$\int_{in} p_{in} u d\Gamma_{in} = \frac{\mu Re^3}{\rho^3 D_h} \tag{A1}$$

where p_{in} is the coolant inlet pressure. u is the velocity component in the X-axis.

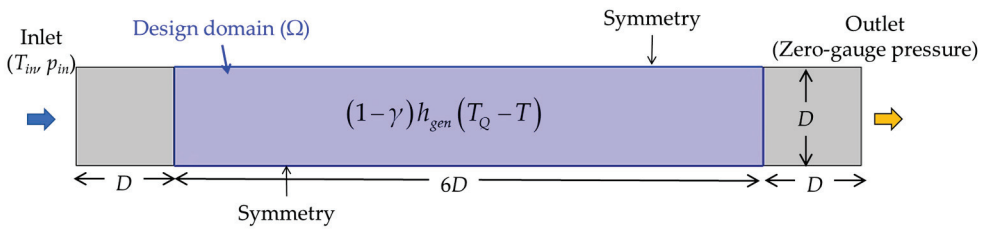


Figure A1. Design domain and boundary conditions of the optimization model.

In this topology optimization, the Reynolds number, based on the coolant hydraulic diameter, is maintained at 10,000 to facilitate the simulation. The heat generation coefficient (h_{gen}), which governs the rate of heat generation, is set to 1.3×10^6 W/(m^{3}K) to promote the formation of a complex structure. T_Q is a constant temperature applied at the heat source. A volume constraint with a volume fraction of 0.5 is also imposed. The governing equations, material interpolations, problem formulation, filtering, projection, and optimization procedures follow established methods from previous studies.

The intermediate densities ($0.1 \leq \gamma \leq 0.9$) from the topology optimization are interpreted as an array of circular pin-fins, as shown in Figure A2. This optimized 2D layout is extruded to a 20 mm height to form a 3D lattice structure. The pin diameter (D_p) varies consistently with the local density field, ranging from D_p = 1 mm for γ = 0.9 to D_p = 2 mm for γ = 0.1. The pin-fin configuration is selected for its compatibility with traditional manufacturing and its suitability for integration within the narrow interconnects of an SOFC stack.

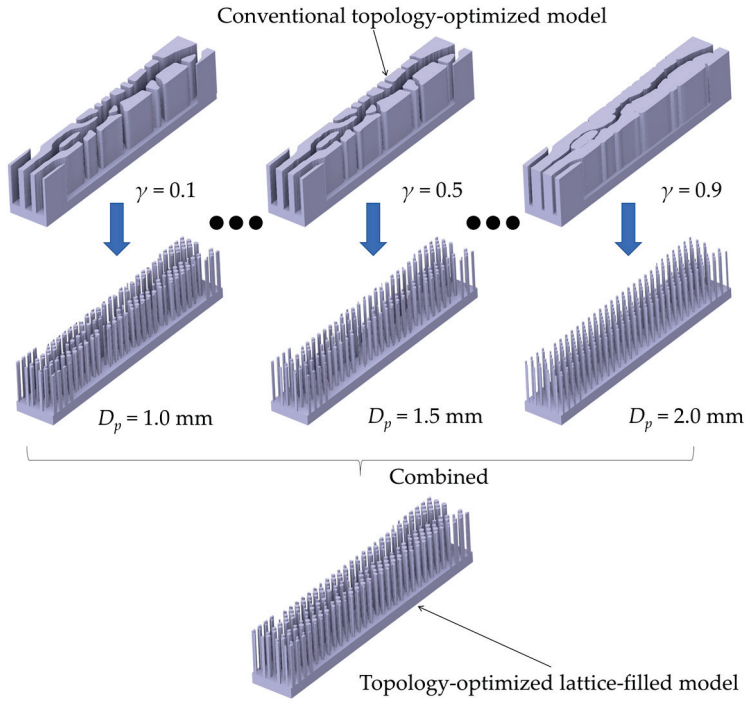


Figure A2. Procedure to obtain the cooling channel with a topology-optimized lattice-filled structure.

The hydraulic diameter of all geometries, calculated by $D_h = 4\psi/S_v$, is shown in Table A1.

Table A1. The hydraulic diameter calculated based on the porous media definition.

Geometry	Diamond TPMS Model	Conventional Topology-Optimized Model	Topology-Optimized Lattice-Filled Model
Hydraulic diameter (mm)	6.65	5.55	5.3

References

1. Lin, C.; Kerscher, F.; Spliethoff, H. Thermal Gradient Management in Solid Oxide Fuel Cells: Mechanisms, Strategies, and Future Directions. *J. Power Sources* **2025**, *656*, 238017. [CrossRef]
2. Veza, I. Fuel-Cell Thermal Management Strategies for Enhanced Performance: Review of Fuel-Cell Thermal Management in Proton-Exchange Membrane Fuel Cells (PEMFCs) and Solid-Oxide Fuel Cells (SOFCs). *Hydrogen* **2025**, *6*, 65. [CrossRef]
3. Zeng, Z.; Qian, Y.; Zhang, Y.; Hao, C.; Dan, D.; Zhuge, W. A Review of Heat Transfer and Thermal Management Methods for Temperature Gradient Reduction in Solid Oxide Fuel Cell (SOFC) Stacks. *Appl. Energy* **2020**, *280*, 115899. [CrossRef]
4. Aguiar, P.; Adjiman, C.S.; Brandon, N.P. Anode-Supported Intermediate-Temperature Direct Internal Reforming Solid Oxide Fuel Cell: II. Model-Based Dynamic Performance and Control. *J. Power Sources* **2005**, *147*, 136–147. [CrossRef]
5. Manglik, R.M.; Magar, Y.N. Heat and Mass Transfer in Planar Anode-Supported Solid Oxide Fuel Cells: Effects of Interconnect Fuel/Oxidant Channel Flow Cross Section. *J. Therm. Sci. Eng. Appl.* **2015**, *7*, 041003. [CrossRef]
6. Gonçalves, J.F.; Sá, L.F.N.; Lopes, T.; Meneghini, J.R.; Silva, E.C.N. Design of Solid Oxide Fuel Cell (SOFC) Channel Layout Using the Topology Optimization Method with a Design Variable Propagation Approach. *Struct. Multidiscip. Optim.* **2024**, *67*, 216. [CrossRef]

7. Ren, K.; Su, Y.; Zhong, Z.; Jiao, Z. Microstructure-Insight Topology Optimization for Efficient Interconnect Flow Channels in Solid Oxide Fuel Cells. *Int. J. Heat Mass Transf.* **2025**, *242*, 126823. [CrossRef]
8. Lee, W.; Lang, M.; Costa, R.; Lee, I.S.; Lee, Y.S.; Hong, J. Enhancing Uniformity and Performance in Solid Oxide Fuel Cells with Double Symmetry Interconnect Design. *Appl. Energy* **2025**, *381*, 125178. [CrossRef]
9. Gong, C.; Luo, X.; Tu, Z.; Chan, S.H. A Novel Flow Channel Design to Achieve High Temperature Homogenization in Solid Oxide Fuel Cell. *Int. J. Hydrogen Energy* **2024**, *52*, 442–453. [CrossRef]
10. Dillig, M.; Plankenbühler, T.; Karl, J. Thermal Effects of Planar High Temperature Heat Pipes in Solid Oxide Cell Stacks Operated with Internal Methane Reforming. *J. Power Sources* **2018**, *373*, 139–149. [CrossRef]
11. Dillig, M.; Meyer, T.; Karl, J. Integration of Planar Heat Pipes to Solid Oxide Cell Short Stacks. *Fuel Cells* **2015**, *15*, 742–748. [CrossRef]
12. Dokmaingam, P.; Irvine, J.T.S.; Assabumrungrat, S.; Charojrochkul, S.; Laosiripojana, N. Modeling of IT-SOFC with Indirect Internal Reforming Operation Fueled by Methane: Effect of Oxygen Adding as Autothermal Reforming. *Int. J. Hydrogen Energy* **2010**, *35*, 13271–13279. [CrossRef]
13. Dillig, M.; Leimert, J.; Karl, J. Planar High Temperature Heat Pipes for SOFC/SOEC Stack Applications. *Fuel Cells* **2014**, *14*, 479–488. [CrossRef]
14. Li, C.; Cheng, K.; Li, B.; Liu, H.; Qin, J.; Wei, L. Feasibility Study on Supercritical Fuel Cooled Solid Oxide Fuel Cell Stack with Internal Reforming. *Int. J. Hydrogen Energy* **2024**, *50*, 312–322. [CrossRef]
15. Fan, J.; Wang, Y.; Tian, R.; Shi, J.; Shi, Y.; Cao, H.; Cai, N. Thermal Management of Solid Oxide Fuel Cells with Liquid Metal. *Int. J. Hydrogen Energy* **2023**, *48*, 10659–10670. [CrossRef]
16. Promsen, M.; Komatsu, Y.; Sciazko, A.; Kaneko, S.; Shikazono, N. Feasibility Study on Saturated Water Cooled Solid Oxide Fuel Cell Stack. *Appl. Energy* **2020**, *279*, 115803. [CrossRef]
17. Wang, M.; Wang, K.; Wang, Y.; Chen, J.; An, B.; Tu, S. Effect of Operation Parameters on the Thermal Characteristics in a Planar Solid Oxide Fuel Cell. *J. Therm. Sci.* **2024**, *33*, 1974–1989. [CrossRef]
18. Peters, R.; Blum, L.; Deja, R.; Hoven, I.; Tiedemann, W.; Küpper, S.; Stolten, D. Operation Experience with a 20 KW SOFC System. *Fuel Cells* **2014**, *14*, 489–499. [CrossRef]
19. Hasbi, S.; Amber, I.; Hossain, M.; Leong, K.Y.; Saharudin, M.S. Feasibility Study of Liquid Metal-Based Thermal Management for Solid Oxide Electrolyzer Cell (SOEC). *Int. J. Green Energy* **2025**, 1–22. [CrossRef]
20. Wang, H.; Zhao, C.; Liu, W.; Liu, Z.; Bian, H.; Zhang, K. Advances in Triply Periodic Minimal Surface Structures for Thermal Management Systems: A Comprehensive Review. *Appl. Therm. Eng.* **2025**, *279*, 127481. [CrossRef]
21. Yeranee, K.; Rao, Y. A Review of Recent Investigations on Flow and Heat Transfer Enhancement in Cooling Channels Embedded with Triply Periodic Minimal Surfaces (TPMS). *Energies* **2022**, *15*, 8994. [CrossRef]
22. Cheng, L.; Liu, J.; Liang, X.; To, A.C. Coupling Lattice Structure Topology Optimization with Design-Dependent Feature Evolution for Additive Manufactured Heat Conduction Design. *Comput. Methods Appl. Mech. Eng.* **2018**, *332*, 408–439. [CrossRef]
23. Jiang, Y.; Hu, J.; Wang, S.; Lei, N.; Luo, Z.; Liu, L. Meshless Optimization of Triply Periodic Minimal Surface Based Two-Fluid Heat Exchanger. *CAD Comput. Aided Des.* **2023**, *162*, 103554. [CrossRef]
24. Yeranee, K.; Xu, C.; Rao, Y.; Zhang, Y. Experimental and Numerical Study of Improving Flow and Heat Transfer in a Serpentine Cooling Channel with Topology-Optimized TPMS Porous Structures. *Int. J. Heat Mass Transf.* **2024**, *231*, 125873. [CrossRef]
25. Xu, C.; Rao, Y.; Yeranee, K. Experiments and Numerical Analysis of Turbulent Flow Heat Transfer and Pressure Loss of a Channel with Triply Periodic Minimal Surface Structures. *Int. J. Therm. Sci.* **2026**, *220*, 110334. [CrossRef]
26. Li, H.; Ding, X.; Jing, D.; Xiong, M.; Meng, F. Experimental and Numerical Investigation of Liquid-Cooled Heat Sinks Designed by Topology Optimization. *Int. J. Therm. Sci.* **2019**, *146*, 106065. [CrossRef]
27. Matsumori, T.; Kondoh, T.; Kawamoto, A.; Nomura, T. Topology Optimization for Fluid-Thermal Interaction Problems under Constant Input Power. *Struct. Multidiscip. Optim.* **2013**, *47*, 571–581. [CrossRef]
28. Baek, S.M.; Yu, S.H.; Nam, J.H.; Kim, C.J. A Numerical Study on Uniform Cooling of Large-Scale PEMFCs with Different Coolant Flow Field Designs. *Appl. Therm. Eng.* **2011**, *31*, 1427–1434. [CrossRef]
29. Shahsavari, S.; Desouza, A.; Bahrami, M.; Kjeang, E. Thermal Analysis of Air-Cooled PEM Fuel Cells. *Int. J. Hydrogen Energy* **2012**, *37*, 18261–18271. [CrossRef]
30. Fergus, J.W. Metallic Interconnects for Solid Oxide Fuel Cells. *Mater. Sci. Eng. A* **2005**, *397*, 271–283. [CrossRef]
31. Ghorbani, B.; Vijayaraghavan, K. 3D and Simplified Pseudo-2D Modeling of Single Cell of a High Temperature Solid Oxide Fuel Cell to Be Used for Online Control Strategies. *Int. J. Hydrogen Energy* **2018**, *43*, 9733–9748. [CrossRef]
32. Liu, Y.; Tan, J.; Zhang, D.; Kuai, Z. Modeling and Performance Analysis of Solid Oxide Fuel Cell Power Generation System for Hypersonic Vehicles. *Aerospace* **2024**, *11*, 846. [CrossRef]
33. Haertel, J.; Engelbrecht, K.; Lazarov, B.; Sigmund, O. Topology Optimization of a Pseudo 3D Thermofluid Heat Sink Model. *Int. J. Heat Mass Transf.* **2018**, *121*, 1073–1088. [CrossRef]

34. Zeng, S.; Lee, P. Topology Optimization of Liquid-Cooled Microchannel Heat Sinks: An Experimental and Numerical Study. *Int. J. Heat Mass Transf.* **2019**, *142*, 118401. [CrossRef]
35. Zeng, S.; Kanargi, B.; Lee, P. Experimental and Numerical Investigation of a Mini Channel Forced Air Heat Sink Designed by Topology Optimization. *Int. J. Heat Mass Transf.* **2018**, *121*, 663–679. [CrossRef]
36. Zeng, S.; Sun, Q.; Lee, P.S. Thermohydraulic Analysis of a New Fin Pattern Derived from Topology Optimized Heat Sink Structures. *Int. J. Heat Mass Transf.* **2020**, *147*, 118909. [CrossRef]
37. Marshall, S.D.; Lee, P.S. 3D Topology Optimisation of Liquid-Cooled Microchannel Heat Sinks. *Therm. Sci. Eng. Prog.* **2022**, *33*, 101377. [CrossRef]
38. Zhang, M.; Wang, E.; Ni, M.; Zheng, K.; Ouyang, M.; Hu, H.; Wang, H.; Lu, L.; Ren, D.; Chen, Y. A Numerical Analysis of Metal-Supported Solid Oxide Fuel Cell with a Focus on Temperature Field. *Heliyon* **2024**, *10*, e37271. [CrossRef] [PubMed]

Disclaimer/Publisher's Note: The statements, opinions and data contained in all publications are solely those of the individual author(s) and contributor(s) and not of MDPI and/or the editor(s). MDPI and/or the editor(s) disclaim responsibility for any injury to people or property resulting from any ideas, methods, instructions or products referred to in the content.

energies

MDPI

Review

Pathways for Greenhouse Thermal Management's Contribution to Net-Zero Food Production

Samson Sogbaike, Celestina Ezenwajiaku, Amir Badiee, Chris Bingham and Aliyu M. Aliyu *

School of Engineering and Physical Sciences, University of Lincoln, Bayford Pool, Lincoln LN6 7TS, UK; abadiee@lincoln.ac.uk (A.B.)
* Correspondence: aaliyu@lincoln.ac.uk

Abstract

Decarbonising greenhouse food production requires improvements in thermal management, energy efficiency, and system integration. Greenhouse energy demand is shaped by coupled heat and mass transfer processes, particularly envelope performance, ventilation, and latent heat associated with humidity control. This article synthesises recent advances in greenhouse microclimate control with emphasis on heat transfer, low-carbon heating and cooling, thermal storage, renewable and waste heat integration, and advanced modelling and control approaches. The review shows that humidity control and latent load management are primary drivers of winter energy use, as moisture removal through ventilation and dehumidification directly increases the sensible heating required to maintain indoor temperature setpoints. When assessed using realistic psychrometric relationships, ventilation and dehumidification can dominate peak heating demand and seasonal consumption. The performance of heat pumps, storage systems, semi-closed greenhouse concepts, and renewable heat pathways depends on how thermal loads are defined, how system boundaries are set, and how technologies are integrated in operation. Digital twins, predictive control, and hybrid physics-data models are increasingly used to manage variability in weather, energy prices, and infrastructure constraints. Greenhouse decarbonisation cannot be treated as a simple substitution of energy sources. System performance depends on coordinated design and operation, including heat recovery, moisture removal, and integration of supply technologies. Semi-closed and heat recovery-based configurations can reduce the ventilation–heating penalty and lower primary energy demand compared with vent-to-dry approaches. Long-term market projections suggest that the commercial greenhouse sector could expand substantially by 2050 under plausible growth scenarios, reflecting increased capital investment rather than a proportional rise in global food output. Net-zero greenhouse production is achievable through combined improvements in thermal management, electrification, and renewable energy integration. However, large-scale deployment depends on consistent modelling assumptions, credible economic assessment, and alignment with heat and CO_2 supply infrastructure. The transition is therefore shaped by system integration and planning as much as by individual technologies.

Keywords: controlled-environment agriculture; greenhouse thermal management; net-zero greenhouse systems; low-carbon heating technologies; greenhouse energy systems

1. Introduction

Global food production is subject to growing pressure as a result of population growth, urbanisation, dietary change, climate change, and increasingly long and exposed supply

chains. A meta-analysis of global projections suggests a 35–56% increase in food demand between 2010 and 2050, depending on socioeconomic pathways and assumptions [1]. Climate-related extremes (e.g., heat, droughts and floods) have already affected agricultural productivity and are expected to intensify risks to food availability, prices, and livelihoods across regions (The IPCC AR6 Working Group II [2]).

Protected cultivation, including the use of greenhouses and the wider controlled-environment agriculture (CEA), has expanded as a strategy to stabilise food production, improve yield predictability, and extend growing seasons. By protecting crops from outdoor variability, greenhouse systems enable targeted management of microclimate variables such as temperature, humidity, radiation and CO_2, which improves food productivity and quality consistency. Recent reviews of greenhouse automation and CEA emphasise the roles of sensing, actuation, and integrated environmental control in this transition [3]. Benke and Tomkins [4] likewise discuss how vertical farming and other controlled-environment models are positioned as emerging food production pathways responding to land constraints, urban demand, and environmental pressures.

The benefit of protected cultivation comes with a clear trade-off, particularly the higher energy requirements for thermal regulation. As food production systems transition from open-field agriculture and conventional greenhouses towards semi-closed or fully closed structures and plant factories, the energy required for heating, cooling, dehumidification and sometimes artificial lighting will increase sharply. Mills's [5] study contrasts low-tech open greenhouses (with relatively minor energy uses) with closed/fully controlled facilities that require substantial energy for climate control and lighting, which leads to higher capital and operating costs than open-field cultivation. In temperate and colder regions, heating remains the dominant energy usage for commercial greenhouses. Vadiee and Martin [6] review energy management strategies for commercial greenhouses, with emphasis on Nordic climates, and show that fossil fuel-based heating still plays a major role, making combined conservation (energy savings) and supply strategies central to decarbonisation. In high-latitude greenhouses, energy requirements can increase further because year-round cultivation often combines heating with supplemental lighting [7].

This high level of energy use places greenhouse horticulture at the centre of the food–energy climate nexus. According to the Food and Agriculture Organization of the United Nations (FAO), agrifood systems emitted approximately 16.2 Gt CO_2-eq in 2022, essentially unchanged from 2021, corresponding to 29.7% of total anthropogenic greenhouse gas emissions. They also note that energy use along supply chains is an important and growing contributor [8]. The Sixth Assessment Report (AR6) of the Intergovernmental Panel on Climate Change (IPCC) note that climate risks to food systems grow as temperatures rise, and that mitigation and adaptation must progress together to avoid increasing food insecurity and wider socio-economic vulnerability [9,10].

From an engineering perspective, greenhouse microclimates arise from coupled heat and mass transfer processes within a semi-transparent structure that contains a crop canopy. Incoming short-wave solar radiation usually supplies most of the energy, while losses occur through long-wave radiative exchange with the sky, conduction through the cover material, and convection driven by infiltration and ventilation [11,12]. Crop evapotranspiration adds substantial latent loads, coupling temperature regulation to humidity control [13]. This coupled behaviour is well established in greenhouse climate modelling. Katzin et al. [14] developed a process-based greenhouse model and identified latent heat as a core component of the greenhouse energy balance. Other modelling studies use similar energy and mass balance formulations to capture these interactions and to evaluate energy demand and climate control performance under real operating conditions [15,16].

https://doi.org/10.3390/en19081975

Recent work on greenhouse decarbonisation focuses on cutting thermal demand, switching to low-carbon sources of heat and cooling, and improving operation through modelling and control. On the demand side, measures such as improved envelopes, thermal screens and operational strategies aim to reduce heat losses and stabilise conditions with lower energy input [6,17]. On the supply side, electrification and the integration of renewable sources are becoming more attractive as electricity systems decarbonise. The International Energy Agency (IEA) identifies heat pumps as an important option for reducing heating-related emissions, with their advantages growing as grid carbon intensity decreases [18]. Thermal energy storage, ranging from short-term buffering to seasonal storage, can capture surplus heat and improve both efficiency and flexibility in greenhouse systems [19].

Modelling, simulation, and optimisation in greenhouse research has shifted from design evaluation toward operational decision support. Alongside process-based models and computational fluid dynamics (CFD) tools, reduced-order models are now used more frequently because they allow faster optimisation and make it easier to evaluate how design decisions, ventilation strategies, and climate control actions influence energy demand [14]. At the operational level, climate control is moving beyond rule-based or simple feedback systems toward more advanced methods such as model predictive control (MPC) and AI-driven approaches [20,21]. Comparative studies that evaluate MPC against reinforcement learning (RL) methods reflect the growing interest in applying AI-based control to improve energy efficiency and overall greenhouse operation [22].

Despite these advances, research in this area is still dispersed across different climates, greenhouse designs, and technology scales. Many studies report results using metrics that are hard to compare (for example, energy savings without carbon intensity, or thermal improvements without considering cost or scalability assessment), limiting comparability and slowing translation to deployable solutions. Studies also often evaluate individual devices or strategies on their own, even though a change in one part of the system (such as lighting) can shift heat demand, electricity import or export, and CO_2 supply requirements at the system level [7]. These gaps point to the need for an integrated assessment that links heat transfer processes, technology performance, techno-economic factors, infrastructure constraints, and food security implications within a single framework.

Therefore, this review brings together recent developments in greenhouse thermal management and examines practical pathways toward net-zero food production. Rather than treating technologies, control strategies, or energy-saving measures in isolation, it considers heat transfer processes, load structure, techno-economic constraints, infrastructure requirements, and food security implications within a combined framework. It shows that greenhouse decarbonisation depends not only on the technologies adopted, but also on how thermal demand is characterised, how system boundaries are defined, and how interventions are implemented over time. Based on this, the review outlines a staged pathway linking demand reduction, electrification, renewable and waste heat integration, thermal storage, and advanced control under realistic operating conditions. It also covers heat transfer mechanisms, heating and cooling options, storage strategies, energy sources, modelling approaches, and deployment constraints (including cost, infrastructure readiness, and scalability). The aim is to clarify the state of the art, identify the main technical and deployment barriers and outline research directions most likely to accelerate low-carbon and resilient greenhouse food production.

The terms net-zero greenhouse (or net-zero energy greenhouse), low-carbon and decarbonisation are used with defined boundaries. Net-zero greenhouse may refer to balancing annual energy demand with on-site or purchased renewable energy, or to reducing operational emissions from energy use to net zero over a defined period. A broader

https://doi.org/10.3390/en19081975

interpretation includes upstream emissions from energy supply, infrastructure, inputs, and CO_2 provision. These definitions are not equivalent and can lead to different assessments of system performance. In this review, net-zero is interpreted mainly in operational terms, focusing on emissions from greenhouse energy use and related services, including heating, electricity consumption, and CO_2 supply, unless stated otherwise. Low-carbon describes approaches that reduce emissions compared with conventional fossil-based systems without eliminating them entirely. Decarbonisation refers to the reduction in emissions through demand reduction, electrification, integration of renewable or recovered heat, storage, and improved control. Where relevant, a distinction is made between operational emissions and broader life cycle impacts, as outcomes depend on factors such as grid carbon intensity, auxiliary electricity use, infrastructure configuration, and CO_2 sourcing.

1.1. Greenhouse Energy Use, Decarbonisation, and Food Security

Greenhouse horticulture is increasingly positioned to reduce food-system vulnerability under climate change, offering the ability to stabilise production, extend growing seasons, and reduce exposure to extreme weather. However, the same mechanisms that provide this stability (such as active control of temperature, humidity, radiation, and CO_2 concentration) make production highly dependent on energy availability, energy prices, and the carbon intensity of supply. As a result, greenhouse food production sits at the intersection of food security, energy security, and climate mitigation.

1.1.1. Scale and Structure of Greenhouse Energy Use

Energy use in greenhouses varies widely depending on climate, crop, structural design, and the level of environmental control. In cold and temperate regions, space heating often dominates annual demand, and in warm and humid climates, cooling and dehumidification can become the main loads. In high-latitude year-round systems, supplemental lighting adds a major electrical load and interacts with heating requirements because lighting technologies differ in their waste heat output [7].

Paris et al. [23] distinguish low-energy greenhouse systems (often relying on passive solar gains and basic ventilation) from high-energy systems where tight climate control requires substantial external energy input. Heating and cooling account for the majority of operational energy consumption, and fossil fuels remain a common heat source in many regions [23].

The Dutch greenhouse sector is a frequently cited example of intensive but highly integrated greenhouse production. Sector reports indicate that total energy consumption in Dutch greenhouse horticulture was about 106 PJ in 2019, dominated by natural gas, with extensive use of combined heat and power (CHP) systems to supply both heat and electricity [7,24]. A focused transition study shows the rapid diffusion of CHP in Dutch greenhouse horticulture, growing from about 1000 MW_{el} in 2003 to over 3000 MW_{el} in 2009, reshaping the sector's energy and CO_2 profile [25].

These arrangements also demonstrate why decarbonisation needs to be assessed at the system level. Katzin et al. [7] report that moving from high-pressure sodium (HPS) to LED lighting can lower overall energy use by about 10–25%, but often increases heating demand because LEDs release less heat. The net benefit depends on how heat is supplied (fossil or low carbon) and the carbon intensity and price of electricity [7].

1.1.2. The Food Security Lens: Why Energy and Emissions Matter

Food security is commonly described through availability, access, utilisation, and stability, as shown in Figure 1 [26]. Greenhouse production can enhance availability and stability by buffering climate variability, but dependence on external energy can introduce

https://doi.org/10.3390/en19081975

vulnerabilities that affect access and long-term stability, especially in cold-climate regions where heating can be a large share of operating cost.

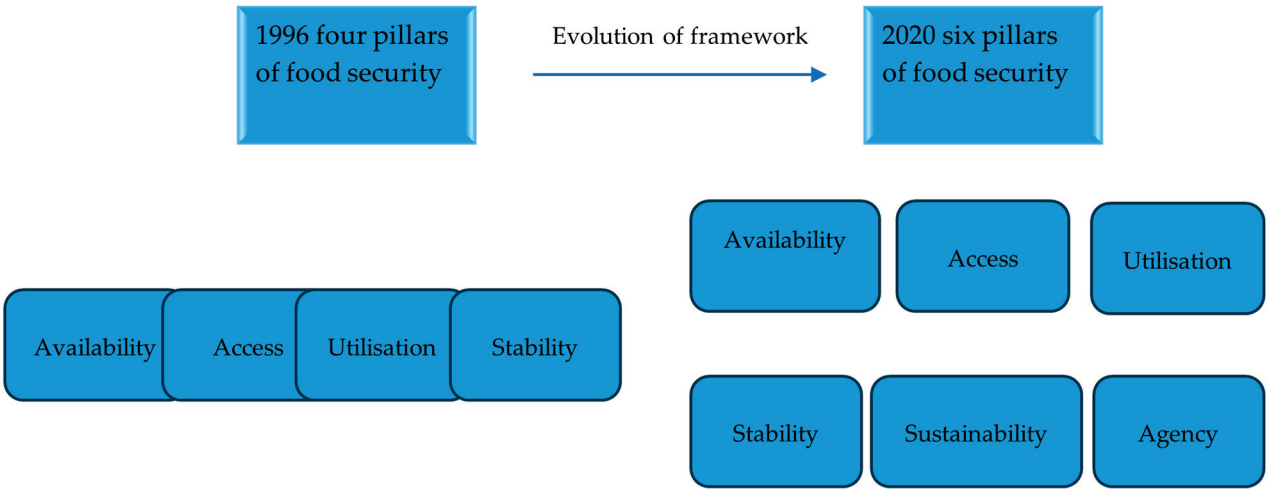


Figure 1. Evolution of food security frameworks from the four pillars (availability, access, utilisation, and stability) introduced in 1996 to the six dimensions adopted in 2020, which adds sustainability and agency [27].

Market and policy reports on Dutch horticulture during the energy crisis show how rising energy costs shaped production decisions, including scaling back winter output and reassessing crop choices [24]. From a food security perspective, such responses can reduce off-season supply and increase price volatility, particularly in regions that rely on greenhouse production during winter months. Decarbonisation options that reduce exposure to fossil fuel price swings (such as geothermal heat, waste heat, or electrification with stable tariffs or thermal storage) can therefore support both emissions reduction and greater resilience in the food system.

1.2. Summary and Contribution of Reviewed Literature

The reviewed studies show rapid progress in greenhouse heat transfer analysis, thermal technologies, energy storage, renewable and waste heat integration, and advanced control. However, the synthesis remains uneven: the results are difficult to compare across climates and greenhouse types, and practical deployment factors (such as cost, infrastructure limits, and CO_2 supply) are often treated as secondary issues. This review brings these elements together through a heat transfer-centred framework that connects technology performance and operational control with net-zero goals and practical deployment realities. This approach allows system-level trade-offs to be identified more clearly, particularly those related to humidity control, latent load management, auxiliary electricity use, supply temperature, and shared infrastructure.

A key contribution is the development of a staged decarbonisation pathway that reflects both engineering requirements and implementation constraints. The analysis shows that a credible net-zero greenhouse operation depends not only on low-carbon heat supply, but also on the sequence in which demand reduction, electrification, storage, renewable integration, and network coupling are introduced under clearly defined system boundaries. In doing so, it consolidates evidence from multiple disciplines, clarifies interactions between system components, and identifies research directions most likely to support low-carbon, resilient, and scalable greenhouse food production. Figure 2 summarises this framework, linking heat transfer processes with technologies, storage options, heat supply pathways, and the constraints that shape deployment. It also shows

how economic factors, infrastructure availability, energy price volatility, and policy support influence decarbonisation pathways.

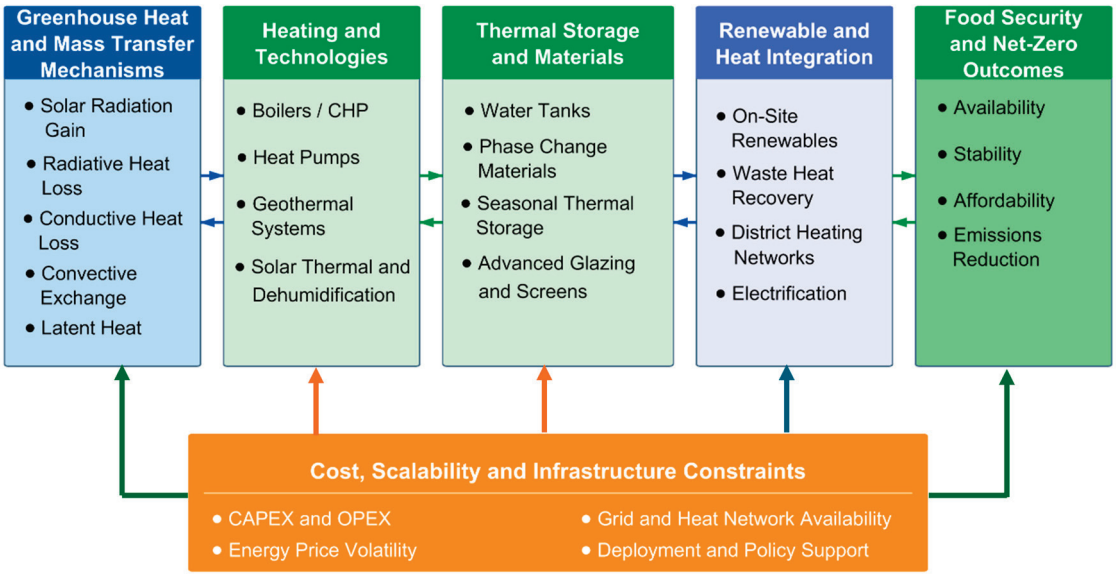


Figure 2. Greenhouse energy management framework linking heat transfer processes, heating and cooling technologies, thermal storage options, and renewable integration with system performance constrained by economic, infrastructure, and policy factors.

2. Methodology

This study was carried out as a systematic literature review using a framework-guided thematic synthesis. The evidence identification, screening, eligibility and reporting processes followed the PRISMA 2020 [28]. The review process was structured using the SALSA approach (Search, Appraisal, Synthesis, and Analysis) as described by Grant and Booth [29]. Given heterogeneity in study designs, boundary conditions and reported metrics, synthesis followed the SWiM guideline [30].

The review focused on development in greenhouse thermal management and on the feasibility of pathways toward net-zero greenhouse food production. The assessment considered operational energy-related emissions associated with heating, electricity use, and CO_2 supply, while broader life cycle impacts were included where relevant and where studies reported clearly defined boundaries. The scope was limited to protected cultivation systems in which thermal loads, heating and cooling, storage and envelope/cover measures, energy supply decarbonisation strategies, modelling and control approaches, and tech-economic constraints can be assessed using extractable quantitative or validated modelling evidence. Seven research questions guided the analysis:

- Covering dominant heat and mass transfer mechanisms (dominate greenhouse thermal loads across climates and typologies);
- Performance of thermal technologies;
- Contributions of storage and material innovations;
- Options for integrating renewable and waste heat;
- Impacts of modelling and control approaches;
- Techno-economic performance and scalability;
- Implications of net-zero feasibility and food-system resilience.

Searches were conducted in Scopus, Web of Science, and ScienceDirect, with Google Scholar used for supplementary retrieval. The primary time window was 2008–2025, with particular attention to post-2015 work reflecting rapid growth in electrified heating, thermal storage integration, and optimisation-based control. Institutional publications such

as the Food and Agriculture Organization, Intergovernmental Panel on Climate Change, and International Energy Agency were used for system boundaries (such as emissions accounting and decarbonisation context) but not used as primary sources for device-level performance. Sector guidance and market reports were used only to provide context on commercial practice, policy conditions, and market scale. They were not treated as primary evidence for technical conclusions and were considered alongside peer-reviewed studies, taking account of their scope and limitations.

Studies were considered eligible if they examined greenhouse or protected cultivation in which thermal management (heating, cooling, dehumidification, humidity control or energy modelling) formed part of the design or operation, and if they provided extractable evidence for at least one of the following:

- Quantitative thermal or energy performance;
- Validated modelling (energy balance, CFD, and reduced-order or hybrid/ML surrogate models);
- Quantified outcomes of control or optimisation strategies;
- Explicit emissions or life cycle assessment (LCA) with boundary definition;
- Techno-economic metrics (such as CAPEX, OPEX, payback, NPV, and LCOH).

Pure agronomic studies without thermal or energy relevance, papers lacking methodological detail, and duplicated publications were excluded.

The extracted data fields included system boundaries, climate context, greenhouse type, thermal load representation, technology configuration, control strategy, validation method, and reported energy, carbon and economic metrics. Studies were grouped by system layer: thermal load characterisation, heating and cooling technologies, storage and envelope measures, renewable and waste heat integration architectures, modelling and control approaches, and techno-economic and scalability constraints. Because modelling assumptions and reporting standards vary widely, cross-study averages were not used when system boundaries were not directly comparable. Instead, findings are interpreted within their climatic and operational contexts, with attention on interactions relevant to net-zero pathways, such as how envelope performance affects heat pump sizing, how LED lighting shifts the heat–electricity balance, how storage influences peak demand, and how control strategies shape ventilation-driven latent loads.

Key performance indicators such as U-value, coefficient of performance (COP), energy saving rate, and ventilation rate are interpreted in the context in which they are reported, rather than being standardised across studies. These metrics are presented using different units, boundary conditions, and evaluation methods, depending on climate, greenhouse configuration, control strategy, and modelling approach. Comparisons are therefore limited to studies with comparable assumptions. Where this is not possible, the results are discussed with reference to the conditions under which they were obtained. Table 1 summarises the main indicators, their units, and the factors that influence their interpretation.

Table 1. Key performance indicators, reported units, and factors influencing comparability across greenhouse studies.

Indicator	Typical Units	Definition/Basis	Factors Affecting Comparability	Sections
U-value (overall heat transfer coefficient)	W m^{-2} K^{-1}; in some studies, reported as W m^{-2} $°C^{-1}$	Heat transfer through the greenhouse envelope per unit area and temperature difference	Wind speed, cover condition, radiative exchange (including sky temperature), structural elements, measurement method, thermal screens	Sections 3.2.1 and 3.5.1

Table 1. *Cont.*

Indicator	Typical Units	Definition/Basis	Factors Affecting Comparability	Sections
Coefficient of performance (COP)	(dimensionless); sometimes reported as instantaneous COP or seasonal COP/COPh	Ratio of useful heating or cooling output to electrical input	Source and sink temperatures, operating mode, part-load behaviour, inclusion of auxiliary electricity, instantaneous vs. seasonal definition, system boundary (electrical vs. primary energy)	Sections 3.4.2, 3.6.1 and 3.8
Energy-saving rate	%; in some sections discussed alongside energy savings in kWh m^{-2}, and heat-cost metrics such as \$/GJ or \$/MWh_{th}	Reduction in energy use relative to a reference system	Baseline definition (critical), climate, control strategy, system boundary, inclusion of auxiliary loads and CO_2 supply	Sections 3.5, 3.8 and 3.9
Ventilation rate/air exchange	h^{-1} or s^{-1}; sometimes expressed as mass flow rate (kg s^{-1})	Rate of air exchange between greenhouse and outdoor air	Ventilation type, wind conditions, vent geometry, discharge coefficients, infiltration, control objective (temperature or humidity driven)	Sections 3.2.3 and 3.3
Latent heat/moisture removal rate	W; kg s^{-1}; L h^{-1}; sometimes discussed with energy input such as W m^{-2}	Moisture-related heat transfer from evapotranspiration or condensation	Crop transpiration, humidity definition (RH, VPD, or dew point), condensation modelling, dehumidification method	Sections 3.2.4 and 3.3.4
Heating demand/load	W, kW, W m^{-2}, kWh·m^{-2} $year^{-1}$, and in some studies MWh·$year^{-1}$	Heat required to maintain setpoint temperature	Climate, envelope performance, ventilation, latent loads, internal gains, temporal basis (peak vs. annual)	Sections 3.2 and 3.8

3. Results and Discussion

The search process outlined in Section 2 returned 1427 records in total (Scopus: 1334; Web of Science: 93). After deduplication based on DOI and title matching, 1220 unique entries remained. Screening of title and abstract against the eligibility criteria removed 103 records, mainly papers addressing greenhouse gas/climate-only studies or non-agricultural greenhouse effect. This resulted in 1117 records for full-text review.

3.1. Overview of Included Studies

All the included studies (n = 1117) were coded using the system-layer and evaluation-lens framework described in Section 2. Many publications span several analytical layers, for example, combining thermal modelling with techno-economic assessment or evaluating heat pump deployment alongside control optimisation, so theme classifications are non-mutually exclusive. Within the screened dataset (n = 1220), the most commonly represented themes were:

- Heating, cooling, and dehumidification technologies (906 records);
- Renewable and waste heat integration, including geothermal, district heat, and solar thermal systems (733 records);
- Techno-economic and life cycle/emissions assessments (466 records);

- Storage and envelope/material innovations, including phase change materials (PCM), thermal energy storage (TES), glazing systems, and thermal screens (404 records);
- Modelling, optimisation, and advanced control approaches (MPC, reinforcement learning, digital twins, surrogate modelling) (347 records);
- Heat transfer and modelling studies (181 records).

These counts reflect thematic tagging within the screened dataset and therefore exceed the total number of included publications due to multi-category classification. Publication output shows a clear shift in research focus. Early work (late 2000s to early 2010s) focused on thermal characterisation and energy balance modelling. From around 2015 onward, there has been a notable increase in research on electrification, renewable integration, storage coupling, and intelligent control. As shown in Figure 3, annual publication output increases steadily across the review period and accelerates in the most recent years, aligning with wider interest in greenhouse decarbonisation.

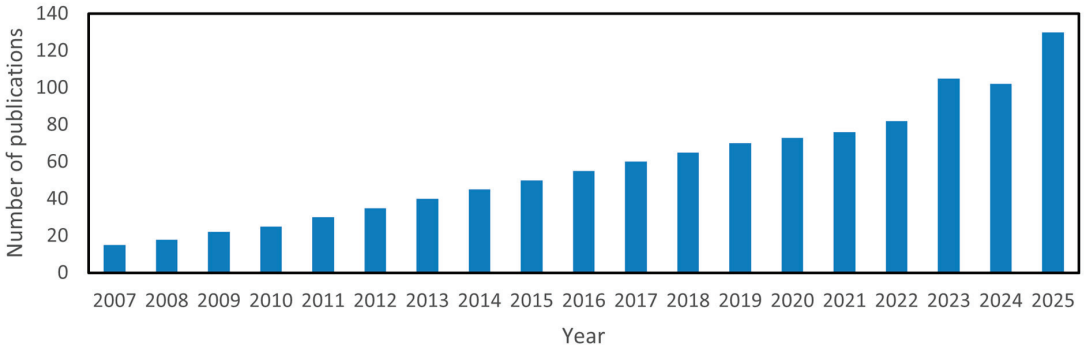


Figure 3. Annual number of publications in greenhouse agriculture from 2007 to 2025, showing a steady increase in research activity and accelerated growth in recent years.

Geographically, most publications come from countries with established greenhouse sectors or strong energy-system research infrastructures. As shown in Figure 4, China accounts for the largest number of publications, followed by the United States and several European and Asian countries. This distribution reflects differences in production scale and research investment rather than climatic similarity, so the prevalence of themes does not necessarily align with their climatic relevance, and it follows directly from the material captured in this review.

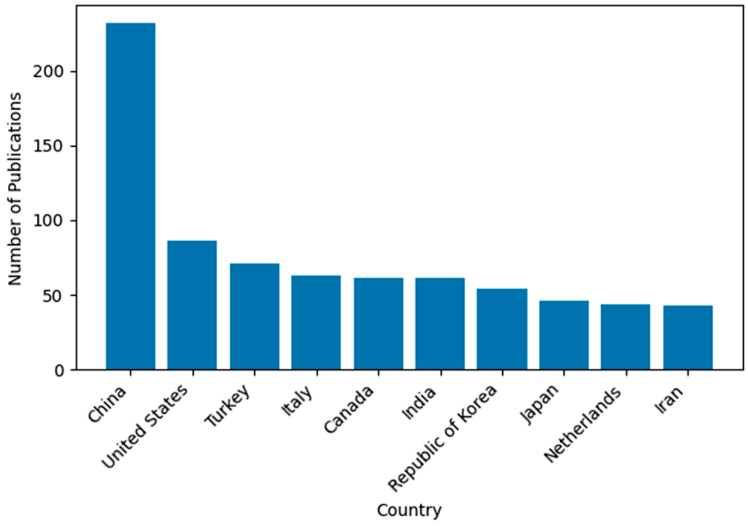


Figure 4. Distribution of publications by country within the screened dataset, with China contributing the largest share, followed by the United States, and countries across Europe and Asia.

The screened literature shows substantial coverage of technology-specific solutions and growing attention to renewable integration and economic performance. However, thematic dominance does not equate to methodological consistency/comparability. Reporting practices vary widely across studies, particularly with respect to boundary definitions, emission factors, auxiliary energy use, and economic assumptions. The following subsections, therefore, synthesise evidence within clearly defined system layers, emphasising transparency in underlying parameters and comparability across studies, consistent with the review methodology.

3.2. Heat Transfer Mechanism and Thermal Load Characterisation

A credible assessment of greenhouse decarbonisation pathways starts with a clear description/account of the thermal loads that low-carbon systems must meet/serve. The performance of heat pumps, geothermal sources, solar thermal collectors, and waste heat integration depends not only on annual energy demand, but also on how the demand is distributed over time (peaks vs. base load) and by type (sensible vs. latent). These demands arise from coupled heat and mass transfer processes across the enclosure and within the crop–air system. Process-based greenhouse climate models, ranging from compact energy balance formulations to fully dynamic simulations, share the same conservation principles and primarily differ in parameter choices, subsystem coupling, and spatial resolution [14].

A common starting point is the energy balance of the greenhouse air volume, which can be expressed as

$$C_{air}\frac{dT_{air}}{dt} = Q_{solar} + Q_{heat} - Q_{trans} - Q_{vent} - Q_{rad} - Q_{lat} \quad (1)$$

where C_{air} is the effective thermal capacitance of greenhouse air (J K^{-1}), T_{air} is the indoor air temperature (K), Q_{solar} is the absorbed short-wave radiation (W), Q_{heat} is the heating input (W), Q_{trans} is transmission losses through the envelope (W), Q_{vent} is the sensible exchange due to ventilation and infiltration (W), Q_{rad} is the net long-wave radiative exchange with the sky and surroundings (W), and Q_{lat} is the latent heat associated with evapotranspiration and condensation (W). Variants of this balance (with additional states for cover, soil, and crop) underpin most process-based greenhouse models used for design and control analysis [14]. The formulation describes the main heat transfer pathways and their interactions, rather than serving as a detailed predictive model. In practice, greenhouse thermal behaviour is analysed using coupled energy mass balance models, CFD, or hybrid approaches that resolve spatial variation, transient behaviour, and crop–climate coupling. These are discussed in Section 3.2.5. Figure 5 shows the main heat and mass transfer processes within a greenhouse, corresponding to the terms in the air energy balance.

This decomposition matters for decarbonisation because heating demand is not a fixed input; it is the residual of several interacting fluxes. Changes in cover properties, air exchange, radiative conditions, or moisture dynamics can shift peak power and seasonal energy use. These same shifts can alter the required supply temperature, which directly affects heat pump COP and the feasibility of integrating low-grade heat sources.

3.2.1. Envelope/Cover Transmission and U-Values

In cold (heating-dominated) climates, conductive heat loss through the cover and structural elements can account for a large share of seasonal heating demand. Under quasi-steady conditions, transmission loss is commonly written as

$$Q_{trans} = UA(T_{in} - T_{out}) \quad (2)$$

https://doi.org/10.3390/en19081975

where U is the overall heat transfer coefficient (W m^{-2} K^{-1}), A is the envelope/cover area (m^2), and $T_{in} - T_{out}$ is the indoor and outdoor temperature difference (K). This formulation remains the basis of most greenhouse heating load calculations [31].

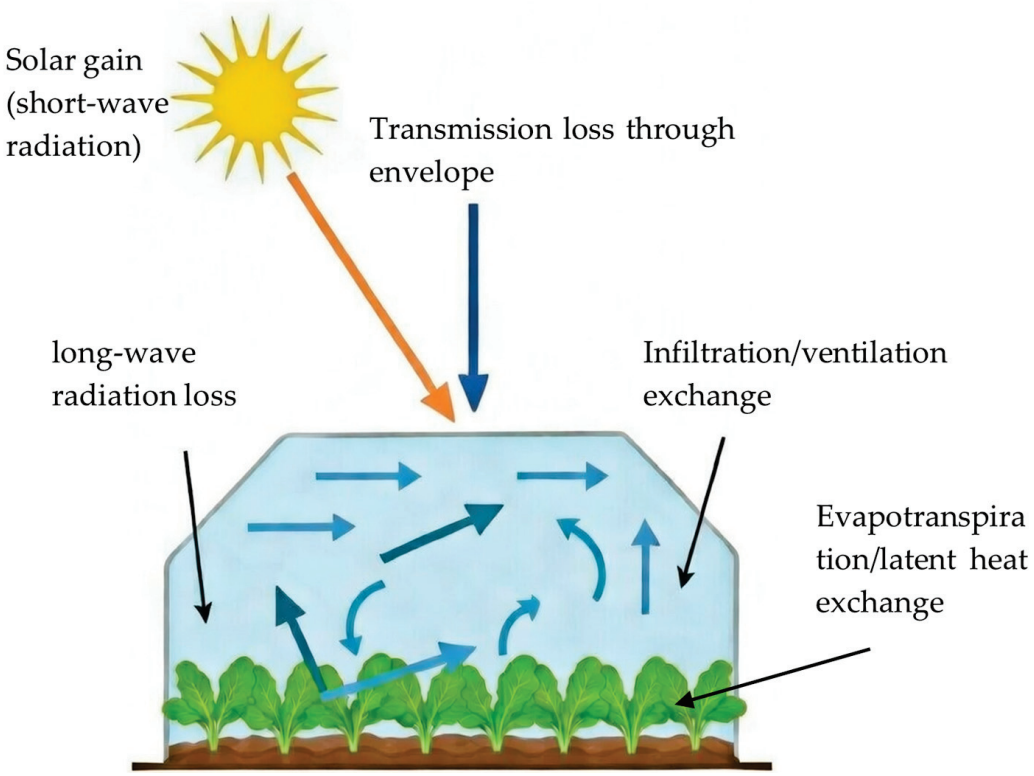


Figure 5. Heat and mass transfer processes in a greenhouse, including solar gains, transmission losses, ventilation exchange, radiative losses, and latent heat exchange associated with evapotranspiration.

The reported U-values vary widely with cladding material and external conditions (especially wind speed and whether the cover surface is dry or wet). Stanghellini et al. [32] report indicative maximum U-values at a reference wind speed of 4 m s^{-1} of approximately 8.0–8.8 W m^{-2} K^{-1} for single-glass and single-polyethylene (PE) films, around 5.2–6.0 W m^{-2} K^{-1} for double-glass or double-polyethylene film, and about 4.8 W m^{-2} K^{-1} for twin-wall polycarbonate (PC). These values show why cladding selection has a direct influence on peak heating demand. For the same indoor setpoints, a single-layer film structure loses far more heat than a multi-layer system.

The measured U-values can be lower than these maximum indicative values when specific constructions or test conditions are used. For instance, Zhang [33] reports U-values of around 2.9–3.4 W m^{-2} K^{-1} for double-polyethylene configurations. Hot-box experiments also show that thermal screens can reduce effective U-values by 50–60%, depending on screen type, sealing quality and test/boundary conditions [34]. Cross-study comparison remains difficult because U-values are often reported without consistent reporting/specification of wind conditions, radiative assumptions, wet-cover state, or which envelope components are included. These uncertainties matter because envelope assumptions feed directly into decarbonisation assessments. Lower U-values reduce peak heat demand and enable a lower supply-temperature heating system, improving heat pump performance and reducing the size requirements for storage and distribution networks. However, U-value assumptions can understate peak loads and overstate the feasibility assessment of low-grade heat integration/options [6,35,36].

https://doi.org/10.3390/en19081975

3.2.2. Longwave Radiative Exchange

During night-time and under clear-sky conditions, long-wave radiative exchange between the greenhouse cover and the sky becomes a major source of heat loss. Radiative heat exchange can be represented in simplified form as

$$Q_{rad} = \varepsilon \sigma A \left(T_{cover}^4 - T_{sky}^4 \right) \quad (3)$$

where ε is surface emissivity (-), σ is the Stefan–Boltzmann constant (W m^{-2} K^{-4}), and T_{cover} and T_{sky} are the absolute cover and effective sky temperatures (K). Although many greenhouse models linearise this term for computational efficiency, the fourth-power temperature dependence explains why radiative losses intensify during cold, clear nights when the effective sky temperature can fall below ambient air temperature.

Cover conditions further influence radiative behaviour. Condensation on the cover alters surface temperature and can increase the combined convective and radiative losses. Stanghellini et al. [32] report higher total heat loss under wet-cover conditions than under dry surfaces, illustrating the coupling between condensation processes and thermal performance. This interaction is relevant for electrified heating systems, as radiative peaks often coincide with periods of highest heating demand. These peaks shape required electrical capacity, storage sizing/requirement, and heat pump operating conditions.

3.2.3. Air Exchange (Infiltration and Ventilation)

Air exchange contributes to both sensible and latent heat transfer. Sensible ventilation and infiltration losses are commonly expressed as

$$Q_{vent} = \dot{m} c_p (T_{in} - T_{out}) \quad (4)$$

or, expressed in terms of air change rate,

$$Q_{vent} = \rho c_p V N (T_{in} - T_{out}) \quad (5)$$

where $\dot{m}$ is the mass flow rate (kg s^{-1}), c_p is the specific heat capacity of air (J kg^{-1} K^{-1}), ρ is the air density (kg m^{-3}), V is the greenhouse volume (m^3), and N is the air change rate (h^{-1} or s^{-1}) [37].

Ventilation is important for maintaining both temperature and humidity, but it also becomes a major driver of heating demand during cool periods because warm indoor air is replaced by colder outdoor air. Natural ventilation studies by Boulard and Baille [38] and Papadakis et al. [39] show that wind-driven exchange often dominates buoyancy under moderate wind speeds, and that ventilation rate formulations must account for vent geometry and discharge coefficients. Fatnassi et al. [40] further demonstrate that insect screens and vent design can reduce airflow and change greenhouse microclimate, affecting both energy use and crop conditions.

For decarbonisation analysis, the key point is the link between ventilation and humidity control. During heating seasons, ventilation-driven moisture removal introduces a sensible heating load. As a result, humidity management cannot be independent of heating load estimation. Comparison of technologies that assume a fixed ventilation rate or omit humidity-driven exchange will misrepresent both the magnitude and timing of heating demand.

https://doi.org/10.3390/en19081975

3.2.4. Latent Heat, Evapotranspiration, and Condensation

The greenhouse climate cannot be described using sensible heat transfer alone. Crop evapotranspiration requires latent heat, influences humidity and leaf temperature, and directly shapes the need for ventilation. The latent heat flux is typically expressed as

$$Q_{lat} = \lambda \dot{m}_v \quad (6)$$

where λ is the latent heat of vaporisation (J kg^{-1}) and $\dot{m}_v$ is the vapour mass flux (kg s^{-1}). This formulation underlines latent heat representation in greenhouse climate models, whether evapotranspiration is estimated through Penman–Monteith relations or semi-empirical crop functions [14,15].

Condensation on the cover releases latent heat locally, alters cover temperature and changes the balance of convective and radiative losses. Coupled CFD–energy balance studies show that omitting humidity and latent processes can lead to understated heating requirements and misrepresent spatial climate behaviour, particularly in unheated or weakly heated structures where condensation is common [41,42]. This coupling also explains interest in semi-closed greenhouse designs and heat recovery/dehumidification systems, which aim to reduce the energy penalty associated with humidity control through ventilation.

3.2.5. Modelling Approaches and Implications for Load Estimation

Three modelling approaches appear frequently in the reviewed literature. Energy balance models (EBMs) remain the standard for seasonal energy analysis and for developing control strategies because they are computationally efficient. Multi-node dynamic formulations typically resolve temperatures for the air, cover, soil, and crop, and are often calibrated against experimental measurements [15]. CFD is used when spatial variability is of primary interest (such as airflow patterns/distributions, thermal stratification, and condensation risk), but its high computational cost generally limits simulations to short time windows. To extend its use, some studies combine CFD with lower-order models. For example, Piscia et al. [42] coupled CFD with an energy balance model to examine humidity control in unheated greenhouses, while Gu and Goto [43] used CFD to investigate airflow within and around plant canopies.

Within CFD studies, turbulence modelling influences predicted airflow and heat transfer. Most applications rely on Reynolds-averaged Navier–Stokes formulations, which provide a balance between accuracy and computational cost. The k–ε model, including standard and renormalisation group (RNG) variants, is widely applied to buoyancy-driven indoor flows and greenhouse ventilation [44,45]. More advanced models, such as Reynolds Stress Models (RSMs), improve the representation of turbulence anisotropy but at a higher computational cost, which limits routine use [46]. Higher fidelity methods, including LES and scale-adaptive simulations, can resolve transient eddies and detailed flow structures, but their computational requirements remain too expensive for full-scale greenhouse studies [47]. In practice, model selection reflects a trade-off between physical detail and computational feasibility.

Reduced-order and surrogate models, including RC networks and hybrid physics-data models, are increasingly applied in optimisation and predictive control studies, reflecting the need for fast, reliable models that can support MPC and digital twin applications, as noted by Katzin et al. [14]. These differences in modelling approaches introduce a comparability issue across the literature. The reported energy savings are highly sensitive to the load-estimation method, and the results from steady-state models, fully dynamic humidity-coupled formulations, and CFD-based analyses are not directly comparable unless boundary conditions and assumptions are clearly defined. This matters for decarbonisation assessments; an intervention that appears favourable under steady-state heating

https://doi.org/10.3390/en19081975

loads may perform very differently once latent-driven ventilation, auxiliary electricity use, or radiative peaks are represented realistically.

3.2.6. Climate-Dependent Load Structure

The contribution of greenhouse heat transfer mechanisms varies with climate and operating strategy. In cold and temperate regions, winter heating demands are shaped by envelope transmission losses and long-wave radiative exchange, with ventilation for humidity control often adding a substantial sensible load. In milder climates, ventilation and moisture regulation can represent a larger share of total energy use even when temperature differences are moderate [15]. In hot climates, cooling demand is driven mainly by solar gains and latent heat processes; evaporative cooling can be effective, but its performance declines as ambient humidity increases, linking cooling performance directly to moisture control [48].

These climate-dependent load structures help explain why technology performance varies across regions. Electrified heating systems are sensitive to peak load magnitude and required supply temperatures, both of which depend on envelope performance, radiative conditions, and ventilation/humidity control strategy [49]. However, cooling and dehumidification options depend on humidity and whether latent energy can be recovered.

Across the reviewed literature, there is broad agreement that greenhouse heating and cooling demands emerge from coupled transmission, radiative, ventilation-driven and latent fluxes, and that humidity control is a primary driver of winter energy use rather than a secondary constraint. At the same time, the reported load magnitudes differ widely across climates, greenhouse typologies, and operating strategies. Direct comparison is limited by inconsistent boundary condition reporting (wind speed, sky temperature handling, infiltration characterisation), varying treatment of auxiliary electricity use, and different representations of evapotranspiration and condensation. For this reason, a single set of typical greenhouse heat-load values by climate zone cannot be defined in a meaningful way without consistent physical and operational boundaries. Heat demand depends not only on external climate, but also on greenhouse geometry, crop type, temperature and humidity setpoints, lighting, and air-exchange strategy. The reported values should therefore be interpreted within clearly stated system assumptions rather than treated as general climate-based benchmarks.

These factors show that decarbonisation evidence must be interpreted within clearly stated modelling assumptions and that technologies cannot be compared without accounting for climate-specific load structures. In heating-dominated climates, where transmission and long-wave losses define the baseline demand, effective approaches focus on envelope improvement, thermal screening, and low-temperature heat supply supported by storage. In warm and humid climates, where solar gains and latent loads dominate, system performance depends more on mitigating overheating, removing moisture, and the interaction between cooling efficiency and water use. These differences show that greenhouse energy systems cannot be ranked using a single technology hierarchy. The same measure may perform well or poorly depending on whether sensible or latent loads dominate, and on how ventilation and humidity are controlled. As a result, technology choice should therefore follow climate-specific load profiles rather than being treated as an isolated optimisation problem. The following sections build on this. Section 3.3 covers cooling and dehumidification in response to thermal loads. Section 3.4 examines heating and low-carbon heat supply options. Section 3.5 considers envelope improvements and thermal storage in shaping demand and peak loads. Section 3.6 focuses on system-level integration, including heat recovery, renewable coupling, and semi-closed greenhouse configurations.

https://doi.org/10.3390/en19081975

3.3. Cooling, Dehumidification, and Overheating Mitigation

This section examines cooling and dehumidification as responses to greenhouse thermal loads, focusing on how sensible and latent loads are managed within the indoor climate. While winter heating often receives most attention, in many regions the main challenge is summer overheating and humidity control. This is true in warm, humid, arid, and high-radiation climates, where maintaining temperature and vapour pressure deficit (VPD) within crop-safe limits becomes the factor that determines both yield and plant health. In these environments, cooling and dehumidification are not secondary services; they are central to maintaining a stable microclimate.

Cooling interventions act through three coupled pathways: they remove sensible heat (reducing dry-bulb temperature), redistribute latent fluxes (through evaporation, condensation, or moisture extraction), and change the ventilation rate required for humidity control and disease prevention. As a result, most studies treat greenhouse cooling as a coupled thermodynamic problem rather than a simple temperature control task. Most strategies combine (i) reducing solar gains and long-wave heat accumulation, (ii) enhancing convective exchange when outdoor conditions are favourable, and (iii) regulating water vapour through controlled ventilation or dedicated dehumidification systems [50,51]. In semi-closed and hybrid greenhouse configurations, available cooling capacity affects how the indoor environment can be decoupled from outdoor conditions. This shapes the viability of operating at low ventilation rates, with implications for CO_2 enrichment, water recovery potential, and overall climate stability [52].

3.3.1. Overheating as a Load Problem: Metrics Used in the Literature

Overheating is characterised solely by indoor air temperature. Most studies evaluate overheating using temperature exceedance relative to crop setpoints (ΔT), VPD, and cooling degree-hours or sensible/latent loads partitioning. This reflects the practical reality that plant stress and disease risk are governed by the combined thermal-moisture environment in the crop canopy, not dry-bulb temperature alone.

Experimental evidence from natural ventilation augmented cooling (NVAC) demonstrates this point. McCartney et al. [53] report that an NVAC configuration can produce temperature reductions of 1.9–12.6 °C under the tested conditions, while relative humidity increased by 1.4–31.2% and VPD decreased by 0.3–4.9 kPa depending on inlet conditions and misting configuration. These results show that cooling effectiveness should be evaluated as a joint temperature-humidity outcome. In several cases, VPD improved even as absolute humidity increased, indicating that plant-relevant stress can move in a favourable direction despite higher RH. This is consistent with the evaporative cooling literature by Sethi and Sharma [50], which reports 4–12 °C temperature drops under favourable psychrometric conditions.

Modelling studies reach similar conclusions. Yang et al. [54] use simplified heat-balance calculations to evaluate when natural ventilation, fan-assisted ventilation, and evaporative cooling can maintain target conditions across contrasting climates. Therefore, overheating should be framed as a load problem determined by solar gains, the outdoor air state, internally generated moisture, and achievable air exchange, rather than as a generic high temperature condition.

These metrics also have system-level implications that directly affect decarbonisation pathways. In semi-closed operation, maintaining acceptable VPD at low ventilation rates enables CO_2 retention for enrichment, supports condensate recovery, and reduces sensitivity to outdoor disturbances. Katsoulas et al. [52] show that increasing cooling capacity lowers ventilation demand and changes the coupling between indoor and outdoor conditions, with benefits for water use efficiency. This introduces a structural trade-off

https://doi.org/10.3390/en19081975

that recurs in decarbonisation studies: high-ventilation regimes dilute CO_2 and increase energy and water penalties, while low-ventilation regimes enabled by mechanical cooling and/or dehumidification improve CO_2 and water management but shift the burden toward electricity consumption. In effect, cooling demand is a system integration variable that shapes ventilation policy, CO_2 strategy, and resource efficiency rather than as a local comfort metric.

3.3.2. Overheating Mitigation

Ventilation remains the default response to overheating because it is mechanically simple and, in many regions, the lowest-cost option to deploy at scale. Its limitation is thermodynamic rather than operational: ventilation can provide cooling only when the incoming outdoor air has lower enthalpy than the indoor air it replaces. Under hot and humid conditions, increased air exchange may remove sensible heat slowly (or not at all) while introducing moisture that raises disease risk and pushes vapour pressure deficit outside crop-safe bounds. The literature, therefore, treats ventilation as a baseline strategy whose effectiveness depends on climate and greenhouse design [50,55].

Because ventilation performance is constrained by outdoor conditions, some studies focus on reducing the cooling load at the source, particularly by limiting solar gains and long-wave heat accumulation. Cover and shading strategies are often treated as first-line measures: they reduce absorbed short-wave radiation, lower air and surface temperatures, and decrease the frequency and intensity of active cooling operations. In arid and high-radiation climates, radiative and shading materials are reviewed as explicit responses to overheating, with a central design tension clearly recognised that any reduction in solar heat input must be balanced against crop light requirements [50].

3.3.3. Evaporative Cooling: Pad-Fan, Fogging/Misting, and NVAC-Type Concepts

Evaporative cooling remains a core strategy in hot and dry climates because it removes sensible heat by converting it to latent heat, often achieving substantial temperature reductions when the outdoor wet-bulb decline is high. Sethi et al. [50] group greenhouse cooling technologies into ventilation (natural and forced), shading/reflective measures, and evaporative systems (pad–fan, fogging/misting, and roof-based cooling), noting that performance depends on climate suitability.

Recent work on NVAC-type configurations demonstrates a design that combines thermal buoyancy with a targeted misting system to enhance evaporative cooling while improving airflow distribution. The naturally ventilated NVAC greenhouse delivered cooling of 1.3–3.6 °C relative to outside conditions while increasing relative humidity by 5.7–17.7% [53,56]. These paired outcomes matter for net-zero assessment because they show that modest temperature reduction can still be agronomically significant if it reduces VPD, and cooling performance cannot be assessed without its corresponding humidity trajectory.

Beyond conventional evaporative approaches, recent studies treat cooling as an integrated energy–water design problem. In subtropical scenarios, Abedrabboh et al. [57] examine renewable-driven hybrid-cooled greenhouse integrated systems and quantify the value of combining passive measures (e.g., shading and geothermal cooling concepts in their configurations) with active cooling cycles. Their results show 34–58% reductions in annual cooling load, 17–34% reductions in evapotranspiration on peak load days, and reduced life cycle cost by 5.6–28.6% (depending on configuration), alongside lower solar-panel area requirements. While specific system layouts may differ from commercial practice, the transferable insight is methodological: once cooling is treated as a coupled load (thermal + moisture + water supply), the best solution becomes context-dependent and must

https://doi.org/10.3390/en19081975

be reported with a clear system boundary definition (cooling target, water source, and electricity supply).

Across the reviewed literature, there is strong agreement that evaporative cooling performance is controlled primarily by wet-bulb depression and by how uniformly cooled air reaches the crop zone. What differs among climates is whether evaporative systems improve plant comfort without pushing RH or VPD into disease-prone ranges. The NVAC studies are informative because they report temperature, RH, and VPD responses under different inlet conditions, metrics that many cooling studies still omit.

Comparability remains limited when water consumption, control regimes, or humidity responses are not reported, or when performance is presented solely as temperature reduction. For evaporative cooling to be meaningfully evaluated across contexts, studies must document both the thermal and moisture outcomes, along with the associated water and energy requirements.

3.3.4. Dehumidification as an Energy Decision: Ventilation–Heating vs. Moisture Extraction

Humidity control is a major driver of winter energy demand because the common vent to dry, then heat to restore temperature strategy exports sensible heat. Reviews note that ventilation-based dehumidification is simple to implement but can impose large heating penalties in cold climates and performs poorly when outside air is humid [51]. Internal moisture extraction systems avoid this penalty. Heat pump-based dehumidifiers cool greenhouse air below its dew point, condense water on the evaporator surface, and then reheat the air, retaining much of the enthalpy within the enclosure [51]. Experimental studies by Migeon [58] report that such systems can achieve equivalent dehumidification with lower energy input than ventilation–heating under comparable conditions, while also reducing condensation risk on crop surfaces. In their study, the dehumidifying heat pump operated at an energy consumption of about 4 W m^{-2} and, depending on outdoor conditions, required about three to four times less energy than the ventilation–heating method to achieve comparable dehumidification. The system also condensed approximately 30 L h^{-1} of moisture, anchoring performance in a measurable moisture balance rather than qualitative claims [58].

However, the reported energy savings depend on the control strategy, the specified moisture target (RH, VPD, or dew point), and the evaluation must include auxiliary electricity use and any reheating requirements [51]. From a net-zero perspective, dehumidification is therefore not simply a humidity control choice but a thermodynamic decision between exporting enthalpy through ventilation or retaining and partially recovering it through internal condensation. Beyond its energy role, internal moisture extraction produces a measurable condensate stream. This water can be recovered and reused, linking humidity control with water management. In low-ventilation systems, particularly semi-closed configurations, recovered volumes can be significant relative to irrigation demand, depending on crop transpiration and operating conditions. This reduces heat loss and improves water use efficiency. Condensate recovery is therefore not only a result of humidity control but also part of system integration, especially in water-constrained settings or intensive greenhouse production.

3.4. Heating Technologies and Low-Carbon Heat Supply

Heating remains the dominant energy demand in commercial greenhouses across temperate and cold regions, especially where year-round production requires tight control of temperature and humidity. The heating requirement is not simply sensible heat provision; it is shaped by the load structure (envelope transmission, infiltration/ventilation, longwave exchange, and latent-heat coupling). These factors determine peak capacity, feasible

supply temperatures, and the scope for heat recovery or storage. They also influence which low-carbon heating pathways are technically viable and economically resilient.

This section reviews major heating supply routes used in greenhouse systems. Conventional boilers and CHP systems serve as the baseline, followed by electrified heat pumps, geothermal and earth-coupled systems, solar thermal and hybrid renewable technologies, and the use of waste heat or district heating networks.

3.4.1. Baseline Systems: Boilers and CHP (And Why They Persist)

Commercial heated greenhouses have traditionally relied on natural gas boilers, with CHP systems widely adopted in some regions as an integrated source of heat and electricity. Beyond their controllability and established infrastructure, CHP units offer horticulture-specific advantages: they supply on-site electricity and produce a flue-gas CO_2 stream that (once cleaned and conditioned) can be used for crop enrichment. As low-carbon heating replaces combustion-based CHP, CO_2 enrichment shifts from a by-product of heat generation to a separate supply and control requirement. This change affects system design, operation, and cost. The implications for supply routes, storage, safety, and integration with greenhouse operation are discussed in Section 3.6.5. Andrews and Pearce [59] note that biomass combustion is generally unsuitable for direct CO_2 enrichment at greenhouse scale because of pollutant risks, whereas CHP exhaust (from natural gas or biogas) can be treated to meet horticultural requirements. This capability has been a key factor in the use of CHP relative to other combustion-based alternatives.

The Netherlands remains the most prominent example of large-scale CHP deployment in greenhouse horticulture. Andrews and Pearce [59] report literature indicating approximately 2500 MW of CHP capacity associated with Dutch greenhouses, describing the sector as an established user of CHP-based heat supply. While CHP can reduce primary fuel consumption relative to separate heat and power generation, its climate benefit depends on system boundary assumptions (particularly the carbon intensity of displaced grid electricity and how exported power is accounted for).

Another reason boilers and CHP persist is that CO_2 enrichment practice has been structurally coupled to on-site fossil combustion in many greenhouse systems. Vermeulen [60] reports that CO_2 is commonly sourced from combustion gases of natural gas boilers or CHP in Dutch greenhouse horticulture. As efficiency measures expand and fossil-free heat sources (e.g., geothermal) are adopted, natural gas use declines, and with it the supply of on-site CO_2. This creates a CO_2 shortfall that must be covered through alternative sources. van Tuyll et al. [61] make the same linkage explicit in the context of electrification: historically, most supplemental CO_2 has come from natural gas combustion, and as the sector decarbonises, it must increasingly rely on non-combustion sources and/or external supply chains (pipelines or delivered food-grade CO_2).

Therefore, the implication is that greenhouse heating decarbonisation is not simply a matter of replacing the heat source. It requires a coordinated redesign of CO_2 supply strategies to avoid productivity losses and ensure safe, reliable CO_2 delivery under low-carbon energy configurations.

3.4.2. Electrification: Air-Source, Ground-Source, and Dual-Source Heat Pumps

Heat pumps are central to greenhouse heating decarbonisation because they convert electrical input into useful heat with a COP greater than unity. However, in greenhouse applications, performance depends on operating conditions, especially the temperature of the heat source and the supply temperature required for distribution.

Zhou et al. [62] evaluated a dual-source heat pump system designed to transfer surplus thermal energy from Chinese solar greenhouses (CSGs) to a multi-span greenhouse and

https://doi.org/10.3390/en19081975

reported results from a winter field test. Using CSG air as a heat source enhanced heat pump performance relative to outdoor air sourcing, increasing heating capacity by 27% and COP by 23%. Operating in dual-source mode produced a further 10.8% increase in collected heat and a 7.9% improvement in COP relative to the single air-source case. The reported COP values reached 2.8 during heat collection and 2.5 during greenhouse heating, with CSG air-sourced heat contributing between 2.1% and 28.2% of total heat over the test period. These findings are valuable because they reflect performance under realistic control and weather variability rather than idealised COP assumptions.

Ground-coupled and hybrid ground-source concepts are also being explored for greenhouse use, where the seasonal stability of the ground loop can support higher performance. Abir Ahsan et al. [63] assessed a hybrid ground-source heat pump (HGSHP) system integrated with a cooling tower for hot-humid greenhouse operation using a dynamic TRNSYS model. Their simulations show that the HGSHP configuration reduced cooling energy consumption by up to 10.8% compared with a GSHP-only system, while also improving long-term ground thermal stability by rejecting part of the cooling load through the tower. The study further includes a payback period sensitivity analysis, illustrating how boundary-condition assumptions and cost factors can influence the economic performance of electrified systems.

3.4.3. Geothermal and Earth-Coupled Heating: Deep Geothermal, Shallow Systems, and EAHE

Geothermal options for greenhouse heating range from deep geothermal wells to shallow ground-coupled systems such as GSHPs and earth-to-air heat exchangers (EAHEs) [64]. Deep geothermal resources can provide stable, high-temperature heat suitable for direct hydronic supply where geological conditions allow, substantially reducing dependence on fossil boilers. However, deployment is constrained by drilling depth, reservoir characteristics, and high upfront investment.

For shallow systems, the reported case studies show that GSHPs benefit from relatively stable ground temperatures and can reduce conventional energy consumption compared with air-source systems. Their performance depends strongly on ground-loop sizing and achieving seasonal thermal balance (continuous winter extraction without adequate summer recharge can lower ground temperature and reduce efficiency over time) [64]. EAHEs systems are primarily used as air pre-conditioning technologies that moderate inlet temperature and help reduce heating or cooling loads rather than serving as standalone heat sources.

Therefore, geothermal feasibility is shown to depend on required temperature grade, long-term ground energy balance, and site-specific infrastructure constraints [64]. These factors determine whether geothermal systems can deliver stable, low-carbon heat at scales compatible with commercial greenhouse operation.

3.4.4. Solar Thermal and Solar-Integrated Heating (Often with Storage)

Solar energy integration in greenhouse systems has been explored through solar thermal collectors, solar-air heating configurations, and photovoltaic–thermal (PVT) systems [65]. A recurring design constraint in the literature is the balance between energy capture and light transmission. Because crop growth depends on photosynthetically active radiation (PAR), any collector or shading element must be assessed against crop-specific light requirements, as excessive shading can negatively affect plant growth and yield [65].

In heating-dominated climates, the contribution of solar thermal systems is closely linked to the temporal mismatch between solar availability and heating demand. Vadiee and Martin [19] show that solar-based greenhouse concepts often rely on storing surplus summer heat for use during winter, using both short-term and seasonal thermal storage. This introduces additional operational requirements, including the need to manage excess

https://doi.org/10.3390/en19081975

heat and, in some cases, upgrade stored low-temperature heat to reach temperatures suitable for distribution [19,66].

As a result, the performance of solar-integrated heating depends not only on collector efficiency but also on how the available heat is used within the greenhouse, with further discussion provided in Section 3.6.

3.4.5. Waste Heat Recovery and District Heating: Low-Grade Heat as a Decarbonisation Lever

Waste heat and district heating provide low-carbon heat for greenhouse operation where suitable sources are available. Their use depends on the availability, temperature grade, and continuity of the external heat stream, as well as the proximity of the greenhouse to the source. Asgari et al. [67] note that colocation is a fundamental limitation for waste heat deployment in greenhouses. Even when the thermal resource is substantial (particularly in cold seasons), adoption is only possible if the greenhouse is close enough, and if the infrastructure allows heat to be transferred at an acceptable cost.

Case studies illustrate the potential scale of these sources. For a glass-furnace flue-gas system, Andrews & Pearce [59] estimate around 5.1 MW recoverable heat after imposing a non-condensing outlet temperature constraint. Under their assumptions, this output could supply approximately 3.9 acres of greenhouse area, with associated carbon offset calculations depending on how CO_2 enrichment is handled. In a low-temperature industrial discharge application, Fguiri et al. [68] report winter-period waste heat of about 145,800 MWh and estimate that it could meet the heating needs of about 45 ha of greenhouses (in southern Tunisia). They also project annual emissions reductions of roughly 746 tCO_2-eq and strong financial performance (NPV and IRR) under the assumed conditions.

These studies show that low-grade external heat can replace a substantial share of fossil-based heating where suitable sources exist. However, performance depends on source temperature, continuity, distance to the greenhouse, and the assumptions used in emissions and economic metrics.

3.4.6. Biomass and Renewable Fuel: Decarbonisation Potential with Operational Constraints

Biomass boilers and biogas-based systems are often discussed as renewable substitutes for fossil boilers in greenhouse heating, particularly in regions where electrification is limited or where agricultural residues and livestock waste are locally available. Esen and Yuksel [69] demonstrated this feasibility in a winter greenhouse, maintaining indoor temperatures near 23 °C using a biogas-integrated system that produced 2231.83 L of biogas under mesophilic digestion. Their results show that small-scale greenhouse heating can be maintained under practical operating conditions.

However, renewable combustion introduces operational requirements that extend beyond heat delivery. Fuel logistics, storage volume, moisture variability, ash handling, and emissions control (especially particulate matter and NO_x) affect both operating costs and regulatory compliance.

Life cycle analyses show that the environmental performance of pellet-based greenhouse heating depends heavily on upstream system boundaries (including feedstock sourcing and processing intensity, and supply-chain (transport)). Wu et al. [70] report cradle-to-grave emissions of 288 kg CO_2eq per tonne of Quebec wood pellets (14.89 kg CO_2eq/GJ), with notable contributions from harvesting, densification energy, and transportation. Their comparison across regions also shows considerable variability driven by drying energy sources, transport logistics, and electricity mix characteristics. These show that greenhouse gas reductions relative to natural gas depend on how the biomass supply chain is configured rather than on the combustion process itself. As a result, life cycle performance depends on clearly defined system boundaries and upstream conditions.

https://doi.org/10.3390/en19081975

3.5. Storage and Envelope/Material Innovations

Decarbonising greenhouse heating becomes considerably easier when overall thermal demand is reduced and peak loads are smoothed. The literature points consistently to two main points. The first is the use of envelope and material measures that lower transmission and long-wave radiative losses without imposing unacceptable penalties on crop light availability. The second is the use of thermal energy storage (TES) to shift heat supply in time, reduce peak heating capacity requirements, and improve compatibility with low-carbon heat sources.

3.5.1. Envelope and Material Innovations: Reducing UA and Radiative Loss Without Over-Shading the Crop

Thermal screens are among the most established envelope measures for reducing winter energy use because they act on two major night-time loss pathways (overall transmission and long-wave radiative exchange). Using hot-box measurements, Geoola et al. [34] report that deploying a thermal screen to greenhouse films can lower the effective overall heat transfer coefficient by about 50–60%, with reduction depending on thermal screen type.

However, screen performance cannot be captured by a single U-value. It depends on the radiative properties and air exchange through the screen layer. Andersson [71] shows that aluminised energy screens reduce radiative losses and that a two-layer screen can further reduce radiative exchange compared with a single layer, depending on the material combination.

Rabiu et al. [72] combined hot-box experiments with TRNSYS modelling to quantify overall heat transfer coefficients for energy-saving screens and to evaluate the effect of screen porosity and permeability. Their results show that air leakage through the screen layer has an impact on measured U-values and must be accounted for in both experimental and simulation-based evaluation [72]. Rafiq et al. [73] developed a method to determine total hemispherical long-wave radiative properties of greenhouse energy screens and reported challenges in estimating reflectance. They emphasise that incomplete radiative characterisation limits cross-study comparability. These studies show that screen performance depends on radiative properties, leakage behaviour, and test boundary conditions rather than on nominal material types alone.

Beyond internal screens, attention has moved to advanced covering materials because lower U-values make electrified heating more practical. A recent technical review by Zhang et al. [74] finds that low-emissivity coated covers can reduce total energy consumption, but realised performance is sensitive to operational factors such as condensation and climate conditions. Song et al. [75] analyse low-emissivity envelope configurations and show that larger reductions in thermal loss can coincide with lower visible light transmission. Their optimisation results underline the need to balance insulation gains with crop light requirements rather than assuming a negligible optical penalty.

In warm climates, envelope choices are used to shape cooling demand through spectral selectivity, not only through ventilation or evaporative cooling. Lin et al. [76] evaluate a low-emissivity light-blocking film (LBF) that transmits approximately 85% of photosynthetically active radiation (PAR) by roughly 27% relative to control glazing and produced cultivar and season-dependent yield responses, including significant reductions during the summer experiment. Cooling energy use increased by about 10–12% under the LBF despite its lower nominal solar heat gain coefficient. The authors attribute this to convective re-emission and airflow dynamics within the greenhouse, indicating that thermal outcomes cannot be inferred from optical specifications alone [76].

Therefore, selective spectral filtering and advanced covers must be evaluated as part of a coupled system. Material properties, climate control strategy, airflow configuration,

https://doi.org/10.3390/en19081975

and crop physiology together determine energy use and productivity. As a result, claims of energy savings or yield benefits are transferable only when optical and thermal parameters, boundary conditions, and control settings are reported with sufficient detail.

Table 2 summarises studies that report greenhouse cover materials and thermal screen or curtain configurations used to reduce night-time heat loss. The reported performance depends not only on the nominal material but also on the screen-envelope configuration, including layer arrangement, emissivity, permeability, and humidity interactions. The literature, therefore, indicates that screens and covers should be evaluated as integrated thermophysical systems, accounting for U-value reduction, radiative behaviour, air leakage, and resulting microclimate effects.

Table 2. Studies reporting greenhouse cover materials and thermal screen/curtain configurations used to reduce night-time heat loss, overall heat transfer coefficient (U-value), or seasonal heating demand. The table shows that performance depends on both material properties and operational context, including humidity management, leakage, and radiative boundary conditions.

Study	Greenhouse Cover/Cladding	Screen Type	Method	Reported Thermal or Energy Effect	Main Implication
Geoola et al. [34]	Greenhouse plastic films	Thermal screens (hotbox tested; screen types varied)	Laboratory hot-box measurements	Adding a thermal screen reduced the effective U-value by about 50–60%, with corresponding energy-saving potential of about 50–60% under the test conditions.	Thermal screens can strongly reduce conductive/convective heat loss.
Kim et al. [77]	Double-layer polyethylene greenhouse (0.1 mm PE inner and outer layers)	Internal thermal curtain	Field study in winter, Republic of Korea	U-value decreased from 3.85 to 2.76 W m^{-2} $°C^{-1}$ with the thermal curtain, and night-time use produced heating energy savings of about 28.7%.	Thermal curtains provide measurable field-scale savings, but the realised reduction is lower than the idealised hot-box results.
Akpenpuun et al. [17]	Single-layer greenhouse vs. double-layer greenhouse with polyolefin, thermal screen, and inner polyethylene layer	Thermal screen in both systems; additional inner PE in the double-layer system	Winter strawberry greenhouse comparison	The double-layer configuration improved night-time insulation and reduced operating cost relative to the single-layer system but also increased RH and reduced VPD; the single-layer system produced 14% higher yield in this case.	Better insulation can reduce heat demand, but envelope/screen combinations may create humidity and crop-performance trade-offs if ventilation and moisture control are not adjusted.
Rasheed et al. [78]	Greenhouse with alternative screen materials assessed in simulation	Polyester, Luxous, Tempa, and multi-layer night screens	Model-based optimisation under Korean winter conditions	Multi-layer night screens reduced heating requirement by 20%, 5.4%, and 13.5% relative to polyester, Luxous, and Tempa, respectively. Lower emissivity and greater thickness contributed to lower heating demand.	Screen performance depends not only on thickness but also on emissivity; multi-layer arrangements can outperform single commercial screen types.
Rafiq et al. [73]	Four representative materials: polyethylene film, Luxous-1347, white polyester, and Tempa 8672 energy-saving screen		Modified radiation-balance method using wide-band radiometers under natural conditions; values checked against spectrophotometer	The study develops and validates a method for estimating long-wave radiative properties of greenhouse screens and films, showing that radiative behaviour must be measured explicitly because simplified methods can overestimate transmission or give unstable results for some material types.	Radiative-loss control at night depends on measured emittance, reflectance, and transmittance.

Table 2. *Cont.*

Study	Greenhouse Cover/Cladding	Screen Type	Method	Reported Thermal or Energy Effect	Main Implication
Rabiu et al. [72]	Ten commercial greenhouse thermal screens, including white polyester, Luxous, PH-55, PH-super, PH-66, Clima45, New-Lux, and multilayer M1–M3 screens		TRNSYS plus experimental hotbox, combining thermophysical, radiometric, and aerodynamic characterisation	Screen thermal performance depended strongly on the combined effect of material thickness, radiative properties, and permeability. Low-porosity multilayer screens (M1 and M3) showed the lowest simulated permeable U-values (4.4 W m^{-2} K^{-1}), while more open screens showed much poorer retention.	Screen comparison should include air leakage/permeability alongside radiative and conductive properties; otherwise, U-value and energy-retention performance can be misjudged.

3.5.2. Sensible Thermal Energy Storage: Water Tanks and Rock-Bed Storage

Sensible thermal energy storage (TES) is widely used in greenhouse heating because it is technically simple, scalable, and compatible with low-temperature heat sources. In cold climates, water-based heat buffers are common. They store surplus daytime heat, often produced when gas firing is used for CO_2 enrichment, and release it at night. This separates the timing of heat generation from heat delivery and supports more stable operation [79]. Buffering storage also improves system stability by reducing part-load operation and limiting frequent start-stop cycling. Evidence from heat pump systems shows that even modest storage volumes can reduce cycling losses. Lyu et al. [80] report losses of about 12.5% without a buffer tank, falling to below 1% when a tank is added, with substantial benefits achieved at small storage volumes.

Rock-bed thermal energy storage represents an air-based alternative in which greenhouse air acts as the heat transfer medium. In the foil-tunnel application evaluated by Malinowski et al. [81] warm air accumulating near the roof is extracted by fans and forced through a packed stone bed via perforated ducts to charge the store. During discharge, airflow is routed through the bed to recover stored heat and return it to the greenhouse. Amiri et al. [82] identify pressure drop across the bed and limited heat transfer between the air and storage medium as key constraints in rock thermal storage systems. Reduced particle size improves heat transfer rates but increases flow resistance and fan power demand, while larger particles ease airflow but limit charging and discharging effectiveness. These coupled trade-offs directly influence system efficiency and must be considered explicitly in the design of packed bed systems.

3.5.3. Latent Thermal Storage Using PCMs: Promising, but Performance Hinges on Heat Transfer Design

Latent thermal energy storage (LTES) using PCMs is attractive for greenhouses because it can store and release large amounts of heat within a narrow temperature range. When the phase-transition temperature is chosen to match crop-relevant air or root-zone setpoints, PCMs can support passive night-time heating and help smooth daytime peaks. Nishad and Krupa [83] report that PCM-integrated greenhouse systems have achieved diurnal temperature reductions of up to 7 °C and nocturnal temperature increases of up to 9 °C relative to ambient conditions, contributing as much as 30% of heating demand in some configurations. They also note that performance depends strongly on PCM type, quantity, encapsulation, and how the material is incorporated into the greenhouse.

Across controlled-environment agriculture studies, PCM performance is shaped less by the base material than by heat transfer design and encapsulation strategy. Low ther-

mal conductivity, leakage during melting, and cycling stability are recurrent challenges. Zhu et al. [84] show that organic PCMs usually require conductivity enhancement (such as porous matrices or graphite additives), along with encapsulation to prevent leakage and improve heat transfer. Cui et al. [85] identify macro-encapsulated modules, shape-stabilised composites, and capsule-based systems as the main implementation pathways in greenhouse applications due to leakage and corrosion constraints.

Experimental optimisation studies further show the importance of formulation and integration. Liu et al. [86] demonstrate that additive selection and mixing ratios influence supercooling, phase-change temperature, latent heat, and discharge characteristics in a solar greenhouse PCM system. These results show that PCM performance depends on a combination of thermal properties, encapsulation quality, and system-level design rather than on the choice of PCM alone.

3.5.4. Seasonal Thermal Energy Storage (STES): Enabling High Renewable Fractions, but Highly Site-Dependent

Seasonal thermal energy storage addresses the mismatch between summer heat and winter heating demand by storing excess heat for later use. A comprehensive techno-economic review by Yang et al. [87] classifies STES technologies into sensible systems (tank, pit, borehole, aquifer), latent systems, and thermochemical systems, and compares them using metrics such as storage efficiency, energy density, and levelised cost of heat. Their analysis shows that economic viability depends heavily on configuration and site conditions, with pit storage and low-temperature aquifer systems approaching competitiveness under favourable conditions.

Borehole thermal energy storage (BTES) is widely studied at the district scale. Gao et al. [88] describe BTES systems as arrays of boreholes, typically 30 to 100 m deep, that store heat in the surrounding ground via conduction, often integrated with solar collectors and heat pumps. Performance depends on multi-year thermal stabilisation and local geological conditions, including groundwater flow and subsurface conductivity. Sadeghi et al. [89] emphasise that BTES integration depends on how well the system aligns with the heating network it serves, the operating temperature range, and subsurface conditions such as hydraulic conductivity, groundwater flow, and borehole interference. These factors make STES inherently site-dependent, with geology, land availability, drilling cost, and regulatory context determining both technical outcomes and economics.

From a net-zero planning perspective, Baeuerle et al. [90] view seasonal storage as an important infrastructure for achieving high shares of renewable heat in industrial and district-scale systems, particularly where thermal networks are constrained or where direct electrification would create a large winter peak. The literature, therefore, presents STES not as a universal solution but as a context-specific option that becomes effective when geological conditions, infrastructure needs, and scale align.

3.6. Renewable, Waste Heat, and Integration System Configurations

Decarbonising greenhouse heating is primarily a system-integration challenge rather than a matter of substituting one device for another. Closed and semi-closed greenhouse studies show that reducing ventilation losses and improving the thermal envelope performance are often prerequisites for effective heat recovery and renewable-heat integration. Most recovered heat is low temperature, which means it must be stored and, when necessary, lifted to a usable supply temperature for reuse (in the greenhouse) [66].

Comparative studies depend strongly on the modelling assumptions used. In particular, the results are sensitive to how the cover heat transfer coefficient is represented, how ventilation and humidity control are modelled, and whether radiative and latent fluxes are included explicitly in the energy balance. Clear reporting of these boundary condi-

https://doi.org/10.3390/en19081975

tions is therefore essential if the results are to be interpreted consistently and compared across studies.

3.6.1. PV-Heat Pump Coupling and Electrified Near-Zero Concepts

PV-powered heat pumps are increasingly studied as a pathway for electrifying greenhouse heating, with recent work moving beyond idealised COP assumptions. Instead, heat pump behaviour is embedded within greenhouse load models that represent air exchange, humidity control, and nonideal operating conditions. Asgari et al. [91] develop an open-source quasi-steady-state model that couples a greenhouse energy balance formulation with a non-ideal air-source heat pump (ASHP)/GSHP cycle (including vertical and horizontal ground heat exchangers) and links these to a SAM-Python PV model. A dedicated ventilation sub-model is included to represent cooling-load management.

In their Canadian case study (London, Ontario) [91], technology choice had a direct effect on PV requirements. The air-source heat pump delivered the lowest heating efficiency (COPh = 2.52 on the coldest day), while GSHP configurations performed better (vertical COPh = 3.68; horizontal GSHP COPh = 3.79). These higher efficiencies reduced the PV capacity required across greenhouse sizes. The study also identified a persistent winter mismatch between PV output and heating demand. Even with net metering-based sizing, annual self-consumption and self-sufficiency remained modest (23.5–25.1% and 23.7–26.0%, respectively).

Longer-horizon electrified concepts, therefore, rely on storage and seasonal balancing to stabilise source temperatures and protect heat pump performance. In the broader borehole thermal energy storage literature, Sadeghi et al. [89] report that coupling GSHPs with BTES/seasonal storage can raise entering water temperatures and improve system performance, while also allowing design relaxations such as reduced borehole length in the reported simulations.

3.6.2. Solar Thermal + TES and Seasonal Storage Architecture

Solar thermal integration in greenhouse systems is usually implemented with thermal energy storage to manage the mismatch between solar availability and heating demand. Two configurations dominate the literature: short-term (diurnal) storage for day-night shifting and seasonal thermal energy storage for balancing summer surplus with winter needs. STES is proposed to reduce dependence on fossil backup during winter, although its techno-economic feasibility remains strongly site dependent [87].

Greenhouse system studies increasingly evaluate combined architectures that include solar collectors, seasonal storage, and heat pumps. Kim et al. [92] examine such a configuration and report solar contribution, system COP, operating cost reductions, and emissions impacts relative to a boiler-based reference case, with the results showing strong sensitivity to investment costs and policy incentives.

Low-cost soil-based seasonal storage has also been explored. Zhang et al. [93] propose a seasonal solar soil heat storage to avoid the need for a heat pump. Under controlled indoor temperature operation, their model indicates annual savings in auxiliary electricity use, demonstrating the potential of ground-based STES where installation constraints allow. Comparative simulation studies further show that seasonal solar thermal storage can displace a measurable share of greenhouse heating demand relative to conventional HVAC systems, depending on storage scale and collector sizing [94].

Short-term storage improves nighttime heat coverage, while seasonal storage enables a much larger proportion of renewable heat to be used throughout the year. The reported performance and economic outcomes vary widely because they depend on the modelling

https://doi.org/10.3390/en19081975

assumptions and boundary conditions applied. Clear reporting of these assumptions is essential when comparing different storage configurations.

3.6.3. Waste Heat and District Heat Coupling

Industrial waste heat is widely recognised as a valuable resource for district heating networks in locations where spatial and network conditions allow integration. Many industrial processes release substantial quantities of low- to mid-temperature heat, and pinch-based screening methods have been developed to identify streams that match district heating supply temperatures [95]. However, technical compatibility does not ensure deployment. Feasibility depends on source temperature, distance to the network, operational continuity, and the complexity of integrating the heat stream [95].

Analysis of real industrial waste heat projects also shows that non-technical factors can be decisive. Project initiation, contractual clarity, risk-sharing arrangements, and business-model choices strongly influence outcomes (organisational and incentive barriers often prevent utilisation even when the technical potential is clear) [96].

For greenhouse applications, the feasibility of linking to district heating or industrial waste heat sources is shaped mainly by required supply temperature and network configuration. Effective coupling depends on temperature matching: lower greenhouse supply temperatures increase the number of industrial heat streams that can be used directly and reduce the need for temperature boosting. This reflects the same temperature-matching principles formalised in waste heat screening methods for district heating integration [95].

3.6.4. Semi-Closed/Closed Greenhouse Configurations

Semi-closed and closed greenhouse systems combine heating, cooling, dehumidification, and ventilation control within a single framework. Their performance depends not only on the heat source, but on how ventilation and humidity are managed through mechanical processes. Closed greenhouses minimise air exchange and rely on mechanical systems to regulate temperature and humidity. Semi-closed systems retain vents but limit their use by using heat exchangers for cooling and moisture control, resorting to ventilation only when mechanical capacity is insufficient [97].

van Beveren et al. [97] describe semi-closed greenhouse operation as a means of reducing energy use by minimising ventilation losses and storing surplus heat, thereby lowering natural gas demand. The system they evaluated integrates short-term thermal buffers, seasonal aquifer storage, and a heat pump that upgrades low-temperature heat for distribution within the greenhouse. This links heat supply, storage, and climate control within a single operating approach.

Work on dehumidification further illustrates this integration. In heated tomato production, Gilli et al. [98] found that heat pump-based dehumidification reduced energy use by 15% and 25% in two consecutive seasons compared with conventional ventilation and heating control, without affecting yield or fruit quality. These results show that reducing reliance on ventilation for moisture removal can lower heating demand and improve compatibility with low-temperature, electrified heat supply, as temperature and humidity are regulated through coordinated mechanical processes.

3.6.5. CO_2 Supply and Enrichment in Low-Carbon Greenhouse Systems

CO_2 enrichment in commercial greenhouses has traditionally relied on combustion-based heating. In boiler-based systems, flue gas can be treated and used for crop dosing, linking heat generation with CO_2 supply. As heating shifts toward electrification and other low-carbon sources, this link is reduced, and CO_2 provision must be addressed as a separate system requirement. The literature identifies combustion-derived CO_2, compressed or liquefied CO_2, and industrial or network-based sources as the main supply

routes. Maintaining target concentrations remains difficult, as CO_2 behaviour is closely linked to ventilation, temperature, humidity, and crop uptake [99–101].

The choice of CO_2 source shapes greenhouse design. Delivered or externally supplied CO_2 requires infrastructure for storage, pressure regulation, distribution, and controlled injection. Symbiotic or external supply depends on the availability and compatibility of nearby CO_2 sources. Studies on enrichment control highlight the need for accurate monitoring and regulation, given the interaction between CO_2 and other microclimate variables [99,102]. Work on integrated systems further shows that the feasibility of external CO_2 supply depends on how well source characteristics match greenhouse demand.

CO_2 enrichment depends on greenhouse operating mode. In ventilation-driven systems, injected CO_2 is diluted and lost through air exchange. Semi-closed systems reduce ventilation and rely on mechanical air treatment, allowing temperature, humidity, and CO_2 concentration to be regulated more independently. This improves CO_2 retention but increases dependence on air treatment, recirculation, and dehumidification systems [52,103].

External CO_2 supply introduces constraints related to gas quality and system suitability. Studies of CO_2-rich industrial streams show that impurity profiles vary with source and purification method, and that additional treatment may be required before use. In greenhouse applications, CO_2 supply cannot be assessed by quantity alone. Source quality, upgrading requirements, storage, transport, and dosing control influence system design, cost, and feasibility. Techno-economic comparisons are therefore less reliable when CO_2 provision is excluded from the system boundary, particularly in low-carbon systems that no longer obtain CO_2 as a by-product of combustion-based heating [99,101,104]. External CO_2 supply also introduces safety and handling requirements, including controlled storage, leak management, and safe dosing within greenhouse environments.

3.7. Modelling, Optimisation and Intelligent Control

As greenhouse energy systems shift from stand-alone boilers toward integrated, multi-vector architectures, operational strategy becomes as important as the technologies in use. Greenhouse climate evolves through coupled energy and mass balances that change with weather, crop stage, and choices around ventilation or dehumidification. At the same time, renewable electricity and waste heat sources introduce variability on the supply side. For these reasons, greenhouse climate management is increasingly formulated as an optimisation problem under uncertainty, typically implemented through predictive control and hybrid physics-data modelling frameworks.

Recent studies show that controller performance depends on how the underlying model is structured and on the boundary conditions applied. Assumptions about envelope heat loss, ventilation and infiltration rates, radiative boundary conditions, and latent heat coupling directly shape estimated heating and cooling loads and therefore influence the performance of different control strategies.

3.7.1. Modelling Hierarchy: From Energy Balance Models to Hybrid and Multi-Fidelity Stacks

Greenhouse climate control has traditionally been based on lumped energy and mass balance models that treat indoor air as spatially uniform and governed by conservation equations. Katzin et al. [14] review the development of these process-based models and identify recurring structural elements, including explicit long-wave radiative exchange, transpiration-driven latent heat fluxes, simplified canopy energy balances, and varying formulations for infiltration and condensation. They also show that model complexity is linked to the intended application: simplified formulations are often used for control and optimisation, while more detailed formulations are applied in design evaluation and process analysis.

https://doi.org/10.3390/en19081975

Computational fluid dynamics has been combined with energy balance modelling to capture airflow and humidity patterns that cannot be represented in spatially averaged formulations. Piscia et al. [42] coupled CFD-derived ventilation rates and convective coefficients with an energy balance model for night-time humidity analysis, showing that detailed flow simulations can inform reduced-order models while preserving the computational efficiency needed for parametric studies.

Taken together, the recent advances support a layered modelling approach in which reduced order models handle real-time optimisation and constraints, higher fidelity simulations provide structural validation and sensitivity testing, and data-driven elements deliver fast prediction and uncertainty handling.

3.7.2. PID and Rule-Based Control: Still Dominant in Practice, but Limited by Coupling and Disturbances

Proportional-Integral-Derivative (PID) and rule-based controllers remain common in commercial greenhouse climate control because they are straightforward to implement, easy to tune, and transparent in operation [105]. However, greenhouse environments are nonlinear and strongly coupled. Temperature, humidity, and CO_2 concentration interact through ventilation, heating and crop transpiration, creating behaviour that is difficult to manage with simple control loops. In these multivariable environments, PID controllers are usually applied as single-loop or in loosely coordinated arrangements, which limit their effectiveness when strong coupling or external disturbances are present [105].

Comparative evaluations illustrate these structural constraints. Mengesha et al. [106] assessed a practical PID arrangement against a feedback linearisation-LQR controller on a nonlinear multi-variable greenhouse model. The feedback linearisation-LQR design managed disturbances more effectively, with lower perturbation peaks and faster recovery, while the PID controller showed stronger setpoint tracking with minimal overshoot.

As greenhouse energy systems evolve toward hybrid configurations that include heat pumps, storage, semi-closed dehumidification, and variable energy supply, it becomes increasingly important to account for multivariable interactions, external disturbances, and operational constraints [105]. This shift has driven growing interest in predictive and optimisation-based supervisory control strategies that operate above the level of conventional feedback loops.

3.7.3. Model Predictive Control: Deterministic, Stochastic, and Economic Approaches

Model predictive control is used increasingly in greenhouse climate management because it handles multivariable interactions, actuator constraints, and forecast disturbances within a single optimisation framework. Bwambale et al. [107] identify greenhouse climate control as a suitable application for MPC because of the strong influence of weather variability and the interactions between temperature, humidity, and CO_2 [107].

Recent MPC studies fall into three broad categories. First, robust and data-driven MPC formulations address modelling uncertainty and disturbance variability. Mahmood et al. [21] propose a data-driven robust MPC framework for greenhouse temperature control and evaluate its performance under uncertain dynamics. They report more stable regulation and a clearer assessment of energy use than nominal formulations, reflecting a shift from traditional tracking MPC toward designs that explicitly account for uncertainty.

The second direction involves stochastic MPC, which represents uncertainty probabilistically. Kim and You [108] develop a stochastic MPC scheme based on Gaussian process models that combine probabilistic disturbance modelling with online learning. Their optimisation framework seeks to minimise expected operating costs while maintaining climate constraints, and their results show improved regulation and lower resource use under variable weather.

https://doi.org/10.3390/en19081975

The third direction integrates explicit electricity and CO_2 cost terms into the objective function alongside climate tracking penalties. In the formulation by Kim and You [108], the stage cost includes price-weighted energy and CO_2 consumption together with quadratic penalties for deviation from climate setpoints. Tracking remains part of the objective, but the explicit monetisation of resource use shifts the optimisation toward economically efficient operation.

Across MPC studies, the reported energy savings depend strongly on the underlying climate model assumptions, particularly ventilation-dehumidification control, latent heat coupling, and envelope heat transfer representation.

3.7.4. AI and Surrogate Models: Forecasting, Fast Optimisation, and Hybrid Physics-Data Control

In greenhouse control, AI is mostly applied in three ways. Short-horizon forecasting models are used to predict near-term disturbances and state trajectories (such as outdoor weather, solar irradiance, and indoor climate dynamics) to improve predictive control performance. Data-driven surrogate models are developed to approximate computationally intensive simulators, including CFD and detailed crop–climate models, thereby enabling rapid optimisation and real-time decision support. In addition, policy-learning approaches, notably reinforcement learning and imitation learning, are employed to derive control policies from interaction data or historical operations.

A recurring challenge is robustness outside the conditions represented in the training data. Work on machine learning for physical systems shows that out-of-distribution inputs can produce unreliable extrapolations even when in-sample fit is excellent, which remains a central barrier to reliable deployment across changing regimes [109].

In greenhouse operation, regime shifts are routine across seasons, weather patterns, and management policies. Liu et al. [110] frame this as a limitation of fixed-parameter mechanistic models under cross-seasonal nonlinear dynamics and propose a hybrid method in which deep neural networks predict time-varying calibration parameters to maintain performance across seasons.

For these reasons, hybrid strategies that keep a mechanistic backbone and use data-driven components for calibration or residual correction are increasingly reported. Zhou et al. [111] present a knowledge-based workflow in which a process-based greenhouse tomato model is first improved using particle-filter parameter estimation and then refined with a deep neural network, achieving substantial error reductions while preserving the structure of the underlying process model.

Recent work in building thermal systems shows that AI is also being used for calibration and data generation. Sun et al. [112] applied virtual samples with an autoencoder to correct sensor errors, achieving over 98.9% calibration accuracy and keeping online errors below 3%. This demonstrates that reliable measurements can be maintained without reference sensors or detailed physical models. A related approach uses knowledge-guided virtual samples to overcome limited data. Sun et al. [113] combined LLM-derived knowledge with diffusion and Monte Carlo sampling to generate synthetic fault data, reaching a diagnostic accuracy of 72.80% with improved generalisation compared to conventional small-sample training. Although developed for building systems, these methods are relevant to greenhouse operation, where sensor drift, sparse fault data, and seasonal variability remain persistent challenges.

From a net-zero perspective, surrogate models are valuable because they make large scenario ensembles computationally feasible. This supports the evaluation of alternative climate years, control strategies, tariff structures, and renewable supply profiles within optimisation and planning studies.

https://doi.org/10.3390/en19081975

3.7.5. Digital Twin: From Monitoring to Closed-Loop Optimisation

Digital twin approaches extend greenhouse modelling beyond offline simulation by linking a virtual representation to live sensor data for monitoring, state awareness, diagnosis, and decision support. The longer-term aim is to support supervisory optimisation and automated operation. A recent review of greenhouse horticulture notes that explicit digital twin implementations remain limited, although many IoT-enabled monitoring platforms and model-based decision support tools already exhibit twin-like architecture without using the term [114].

Recent application studies show how digital twin concepts are being deployed in practice. Arshad et al. [115] describe a Simulink-based digital twin integrated with greenhouse sensing and analytics, designed for remote monitoring and operational decision support, with a clear pathway toward automated environmental adjustment. Akintan et al. [116] develop a Unity-based digital twin for microclimate monitoring and adaptive sensor selection, using Thompson-sampling to identify season-specific subsets from a 56-sensor network while preserving representative temperature–humidity trends. Slimani et al. [117] present a real-time management workflow that combines IoT data acquisition, a digital twin layer, and augmented-reality visualisation to support operator-facing interpretation and decision making in an integrated cyber-physical loop.

Taken together, these studies show that the most substantive digital twin contributions are those that integrate the model, data pipeline, and decision layer into a functioning operational system, rather than presenting a static 3D visualisation or a standalone simulation with no feedback to real conditions [114].

3.7.6. Reinforcement Learning and Hybrid RL-MPC

Reinforcement learning is being explored for greenhouse climate control because it can learn nonlinear control schemes directly from measured data, which is attractive when disturbance-driven behaviour is difficult to represent with a physics-based model. Recent greenhouse studies identify two main barriers to deployment: reduced reliability when a learned policy is applied outside the operating regime present in the training data, and the difficulty of enforcing hard actuator and climate constraints during learning. Ajagekar et al. [118] show that offline value-function learning can produce out-of-distribution errors when the training data captures only a subset of operating conditions. They address constraint enforcement and disturbance uncertainty by embedding the learned value function within a robust MILP layer.

These issues have encouraged hybrid and hierarchical designs that use optimisation to structure decisions while reserving learning for adaptation and tracking. Mansour et al. [119] implement a two-level scheme in which an economic optimiser generates reference trajectories using weather and energy price forecasts, and a lower-level deep reinforcement learning controller tracks these trajectories in real time. They test the system under environmental disturbances and actuator-related uncertainties, including degraded heating capacity, and report shorter training requirements through staged training and transfer.

Comparative studies further clarify how RL and MPC differ in practice. Morcego et al. [22] contrast the two approaches in terms of prediction, objective formulation, and constraint handling. MPC embeds constraints directly within the optimisation problem, while RL typically requires additional mechanisms to maintain feasibility and operational safety. Building on this idea, Mallick et al. [120] introduce an RL-MPC design in which learning updates the parametrisation of an MPC controller online, adjusting model terms, cost weights, and constraint margins while the MPC structure ensures robust constraint management under prediction uncertainty.

https://doi.org/10.3390/en19081975

For net-zero greenhouse operation, these hybrid RL–MPC schemes are particularly relevant. Integrated systems that combine electrified heating, thermal storage, semi-closed dehumidification, and variable energy prices operate under uncertainty and multiple objectives. In these settings, fixed controller tuning is often insufficient. A design that combines optimisation-based constraint handling with adaptive learning offers a more robust pathway to maintain performance without compromising safety or energy efficiency.

3.8. Techno-Economic Performance and Scalability

3.8.1. Economic Framing of Decarbonisation Pathways

Greenhouse decarbonisation differs from building retrofits because the objective is to maintain a controlled crop microclimate, not simply to heat space. Energy demand depends on envelope performance, ventilation and humidity management, and climate control set-points. Capital and operating costs are therefore shaped by how thermal loads are defined and controlled. This section draws on reported case studies, experimental results, and simulation-based analyses to examine how these factors influence cost and performance.

In heating-dominant climates, peak winter load sets installed capacity and drives capital cost. Envelope losses and air exchange rates affect both annual energy consumption and crop requirements [6,31]. In warmer regions, the economic focus tends to shift toward cooling, ventilation and moisture control, which changes the balance between fuel and electricity use. Humidity control further shapes operating cost. Ventilation-based dehumidification during cool periods expels conditioned air and increases heating demand, while internal moisture extraction retains heat within the system [51,121]. Studies of heat pump-based dehumidification report lower primary energy use than ventilation–heating under comparable moisture targets, provided auxiliary electricity and control boundaries are included [58,121].

Feasibility also depends on financial assumptions. Payback, NPV and levelised cost metrics vary with tariffs, discount rate, project lifetime and incentives. Sector guidance reflects this by prioritising demand reduction before supply substitution, since reduced and stabilised loads improve the economic case for electrification and renewable heat integration [122,123]. For interpretation, techno-economic results are grouped by system boundaries. The first is the greenhouse-only boundary, where costs relate solely to internal heating and climate control. The second is the integrated on-site boundary, which includes components such as heat pumps, storage, solar collectors, dehumidification units, and control systems. The third is the external or networked boundary, covering district heating, waste heat, minewater, and other off-site sources, where infrastructure such as pipework, substations, and network layout forms part of the cost. CAPEX, OPEX, payback period, NPV, and LCOH are, therefore, interpreted within these boundary definitions rather than compared directly across studies.

These relationships are evident in the reported case outcomes. Thermal screens are associated with heating energy savings of around 12–35% and payback periods often below three years in commercial applications. Solar thermal systems with seasonal storage have been reported with levelised heat costs of approximately 30–36 $/GJ under favourable conditions. District and waste heat systems depend strongly on network configuration and connection density, with capital investment and pipeline routing often determining overall feasibility. As discussed in the following subsections, these findings show that techno-economic performance is shaped not only by the technology itself, but also by load characteristics, system design, and local economic conditions.

Carbon-intensity comparisons follow the same boundary constraints. The reported emissions depend on electricity emission factors, auxiliary energy use, CO_2 supply, and the infrastructure included within the system boundary. Electrified systems may reduce

https://doi.org/10.3390/en19081975

on-site emissions, but can shift impacts upstream, depending on grid carbon intensity and operating conditions. Auxiliary electricity for dehumidification, pumping, and control, along with CO_2 provision in non-combustion systems, can affect total emissions. Life cycle and carbon-intensity results are only comparable when system boundaries and energy inputs are defined consistently. For these reasons, payback figures are not transferable unless assumptions are explicit. Without clear reporting of thermal boundary (envelope, ventilation, humidity strategy), economic parameters (tariffs, discount rate, lifetime), and integration choices, reported CAPEX, OPEX and LCO values cannot be compared in a meaningful way. The techno-economic synthesis in Section 3.8, therefore, evaluates pathways within clearly stated physical and financial boundaries rather than treating individual technologies as universally cost-effective or unviable.

3.8.2. CAPEX and OPEX Structure by Pathway

The pathway-specific studies reviewed below do not share a common costing basis. Some report greenhouse-only retrofit costs, while others include storage, control upgrades, or auxiliary electricity. Networked studies extend the boundary further to external infrastructure and heat supply arrangements. The discussion, therefore, interprets the results within their stated boundary conditions and identifies the assumptions that most strongly affect CAPEX, OPEX, payback, NPV, or LCOH.

Envelope/Cover and Thermal Screens Upgrades/Retrofits

Envelope improvements and thermal screens are demand-side measures whose economic value lies in reducing annual heat use and, in many cases, reducing peak heating capacity. Because night-time transmission and radiative losses dominate heating demand in many temperate and cold-climate greenhouses (Section 3.2), reducing effective heat loss at night directly lowers fuel consumption and can also reduce peak heating requirement and associated infrastructure.

Sector guidance for covered cropping notes that thermal screens commonly deliver reductions in annual heat demand under commercial practice, although realised savings depend on screen specification and how screens are controlled alongside humidity management. In the EECA case study [123], reported energy savings range from about 12.5% to 35%, with reductions of roughly 25–35% achievable when screens are properly selected and controlled.

A commercial example from the UK HDC report (Pratt, HDC project PC 227) [124] shows this in practice. In a sweet pepper greenhouse, a moveable thermal screen delivered an additional 52 kWh·m^{-2} gas saving compared with a temporary screen. The same study shows that adjusting screen control setpoints increased savings from 29 to 52 kWh·m^{-2}, indicating that operational strategy can be as important as the hardware itself. Installed costs were reported at £4–£5 m^{-2}, and when energy savings and avoided temporary screen costs are included, simple payback can be below three years under the stated commercial assumptions [124].

From a cost-structure perspective, CAPEX is associated mainly with screen materials, installation, and integration with the control system. OPEX savings come primarily from reduced fuel use, with minimal or no added recurring energy demand unless additional sensing or control upgrades are introduced. Where such upgrades are required to achieve the reported savings, part of the investment should be attributed to improve control capability rather than to the screen hardware alone [124].

Heat Pumps and Electrification (ASHP/WSHP/GSHP)

Electrifying greenhouse heating with heat pumps changes the structure of heat supply costs. Expenditure shifts from fuel to equipment, balance-of-plant, and system integra-

https://doi.org/10.3390/en19081975

tion, while operating costs depend mainly on electricity tariffs and achieved seasonal performance. In practice, heat pump CAPEX extends beyond the unit itself and often includes compatible low-temperature distribution (e.g., larger emitters or piping), buffer storage to limit cycling, electrical upgrades, and integration with existing climate control systems such as screens, ventilation, and dehumidification. The reported capital costs, therefore, vary unless the system boundary is clearly defined. Some studies consider only the heat pump, while others include distribution upgrades, storage, electrical upgrades, and dehumidification-related equipment within the same investment boundary.

Operating cost is driven by electricity price and the seasonal coefficient of performance, which depends on source temperature and required heating water temperature. In a Polish greenhouse study, Nemś et al. [125] reported a maximum greenhouse heat demand of 17.36 kW. A 21.5 kW ground-source heat pump operated with a COP of 5.53–5.83, while a 23.00 kW air-source heat pump operated with a COP of 2.59–4.00. Annual operating costs were €385.60 and €678.64, respectively. However, the ground-source system required a significantly higher initial investment (€14,334 compared to €4952 for the air-source unit), resulting in longer payback periods (18 years vs. 5.5 years). This comparison shows the trade-off between efficiency and capital cost, and the importance of matching system capacity to actual demand.

Differences across studies also arise because electrification is often implemented as part of integrated retrofit packages rather than as a standalone intervention. Li et al. [126] evaluate a cold-region greenhouse that combines ground-source heat pumps, solar collectors, insulation upgrades, and intelligent ventilation and lighting controls. They reported an overall energy saving of 17.8%, with 17.6% attributed to heating. The ground-source heat pump system had an installation cost of 80,000 Yuan, annual savings of 16,000 Yuan, a payback period of 5 years, and a 15-year NPV of 98,450 Yuan. These results show that performance improves when heating is considered within a broader system rather than as a standalone measure.

Humidity management further affects both load and cost. Electrified heating cannot be treated solely as a sensible heat problem because the dehumidification strategy drives ventilation and electricity consumption. Sapounas et al. [103] show that semi-closed greenhouse configurations reduce reliance on window ventilation by using mechanical air handling, allowing more independent control of temperature, humidity, and CO_2. This reduces heat losses associated with ventilation but introduces additional electrical loads from fans and air-treatment equipment. The reported case evidence shows this trade-off. In a French study, gas consumption in a semi-closed greenhouse was about 10% lower than in a conventional greenhouse, while electricity use increased substantially, reaching about 510% higher during autumn under non-optimal fan operation. Other reported studies indicate energy savings of around 20% in Belgium and up to 43% improvement in energy-use efficiency in Germany when combined with thermal screens and storage. These outcomes show that air distribution design, control strategy, and humidity management directly influence operating cost.

As a result, the performance of heat pump systems in greenhouses depends on the interaction between thermal load, source conditions, control strategy, and the wider system configuration. Comparisons of CAPEX, OPEX, and payback are only meaningful when these factors are clearly defined.

Solar Thermal and Thermal Energy Storage

For solar-assisted greenhouse heating, capital cost is spread across collector area (€/m^2), seasonal storage infrastructure (borehole, tank, or pit), civil works and land preparation, pumps and heat exchangers, and integration with the existing heat distribution

system and controls. Operating costs are usually lower and are driven mainly by pumping electricity and maintenance. Economic performance is sensitive to system sizing and operating temperature, which influences both collector efficiency and storage losses [127]. The reported LCOH values are therefore not directly comparable across systems with different configurations, particularly where seasonal storage, temperature upgrading, or large collector fields are included, as these elements significantly affect both capital cost and operating requirements.

Semple et al. [127] present a large-scale tech-economic analysis for a 0.4 ha greenhouse in Southwestern Ontario, comparing low-temperature and high-temperature borehole seasonal thermal storage. Both systems are sized to supply roughly 64% of annual sensible heating demand, using 861 m^2 and 2009 m^2 of collector area, respectively. The reported levelised heat costs range from about 32.9 to 36.2 \$/GJ (115–130 \$/MWh_{th}). The high-temperature option requires greater upfront investment but reduces operating electricity demand. In their analysis, achieving a simple payback below seven years requires strong policy support, including capital subsidies and carbon pricing of around 200 \$/tonne CO_2e under the stated gas price cases [127].

Storage coupling also matters in dehumidification and heat recovery configurations. de Zwart [121] measures about 24% energy savings for an internal moisture removal system and notes that adding seasonal storage can increase savings to around 30% by extending heat pump operation and improving the use of recovered heat over the season.

Across these studies, the techno-economic results remain sensitive to modelling assumptions that affect operating temperature and seasonal availability. Semple et al. [127] show that variations in borehole spacing, soil properties, and insulation thickness alter annual heat delivery by less than about 2%. Although the thermal impact is small, such differences can still affect economic outcomes in marginal cases. More broadly, the results are more credible when load models include diurnal dynamics and humidity-driven ventilation losses, since these factors determine peak conditions and the temperature levels at which systems must operate [121,127].

Waste Heat and District Heat

Waste heat recovery and district heating options reshape the techno-economics of greenhouse heating because viability depends less on on-site conversion efficiency and more on network design, demand density, heat-pricing and contractual structure. Capital cost in these systems is driven by distribution infrastructure and connection assets, while operating costs tend to play a smaller role relative to amortisation and revenue assumptions. These systems are best interpreted within an external infrastructure boundary, where network length, substations, trenching, and long-term financing form part of the cost basis.

A district heating feasibility study for greenhouse crops in Almería illustrates the dominance of network-related costs. The optimised configuration supplies 12 greenhouses via a 1.3464 km network delivering 8621.4 MWh·$year^{-1}$, with a total initial investment of 1.7233 M€ and annual operating costs of 0.0158 M€·$year^{-1}$. Substation hardware accounts for 0.3569 M€, confirming that connection equipment forms a substantial part of upfront expenditure alongside the distribution network [128]. The study also shows that economic outcomes are highly sensitive to routing and spatial clustering. Within the optimised population, profitability is closely linked to network length, with a practical threshold in the range of 1.3–1.5 km beyond which additional distance erodes NPV under the assumed supply and demand conditions [128]. This shows that even small routing extensions can dominate project economics where greenhouse loads are dispersed.

Where waste heat comes from another primary process, the cost logic shifts from combustion efficiency to load matching and electricity pricing. Asgari et al. [67] report

that an Antminer unit dissipates roughly 3.24 kW as waste heat, consistent with near-complete conversion of electrical input to low-grade heat. This supports the point that, for co-produced heat, feasibility depends on the temporal fit between available waste heat and greenhouse heating demand, and on the tariff basis of the underlying electrical load.

UK-focused work on minewater district heating adopts a long-horizon discounted cashflow approach rather than simple payback. The Horden study models NPV, IRR, and discounted payback over 40 years and aligns with HNDU and CP1 guidance, showing that network business cases are evaluated as infrastructure investments whose viability hinges on pipework requirements and customer clustering [129].

Geothermal district heating concepts highlight the same cost structure. The Penobsquis feasibility report itemises buried HDPE pipework and trenching costs per metre, and includes well maintenance, heat exchanger servicing, and pump replacement cycles as part of ongoing O&M. In the most favourable open-loop scenario, the report estimates total capital investment of about $11.3 million and a discounted payback of approximately seven years under the stated assumptions [130].

Across the literature, waste heat and district heating shift greenhouse heating from a technology substitution problem to an infrastructure planning problem. Economic feasibility is driven primarily by network length, connection density, routing, tariff structure, and financing assumptions, rather than marginal gains in thermal efficiency. Spatial modelling and long-term financial analysis are therefore essential when evaluating district-based heating options for greenhouse systems.

Semi-Closed/Closed Greenhouse Concepts

Semi-closed configurations add capital cost through air-handling units, ducting, sensors, and advanced control systems. Operating cost is shaped by fan power and the electricity used for active dehumidification and heat recovery. Unlike ventilation-based humidity control, which expels conditioned air, semi-closed systems aim to decouple temperature and moisture regulation via mechanical air treatment. Sapounas et al. [103] show that this architectural shift alters both the greenhouse energy balance and system complexity. de Zwart [121] further demonstrates that internal moisture withdrawal with heat recovery can reduce primary energy use when realistic heat pump performance and storage are included. Therefore, these studies indicate that economic outcomes depend on how latent loads, auxiliary electricity, and operational constraints are represented in the thermal model. For this reason, the techno-economic results for semi-closed systems are only comparable where the system boundary includes fan power, dehumidification loads, auxiliary electricity, and the effect of reduced ventilation on heating demand.

3.8.3. Sensitivity Drivers: What Most Strongly Shifts Payback and NPV

Across the reviewed techno-economic studies, only a few parameters consistently drive payback and NPV outcomes. Energy prices and tariff structures are often the dominant drivers because they directly determine operating expenditure and can change the relative competitiveness of electrified heat. Tomson et al. [129] showed that moving from BEIS grid-price assumptions to lower-cost electricity supply changed viability outcomes. Under the gas boiler baseline, the 40-year NPV improved from −£5.25 million to −£1.67 million under a power purchase agreement (PPA), and to between −£0.55 million and £0.08 million when priced at onshore wind LCOE. When the baseline was changed to decentralised ASHPs, the same system became economically viable, with 40-year NPV increasing to £1.86–£7.19 million depending on the pricing scenario and configuration. These results show that tariff assumptions and baseline selection alone can move a project from unviable to viable, even when the physical system remains unchanged.

Greenhouse thermal boundary conditions exert a similar influence. Envelope heat transfer characteristics and air-exchange rates determine both annual heating demand and peak capacity requirements, shaping capital sizing and operating cost. Demand-reduction measures, therefore, shift project economics before any change in heat supply. Sector guidance for covered cropping reports that well-specified and -operated thermal screens typically reduce annual heat use by roughly 25–35% [123]. Modelling studies likewise show that modest changes in transparent-envelope properties translate into measurable differences in heating and cooling loads [75].

Latent-load representation is another key source of variation in techno-economic results. When humidity control is simplified as ventilation, the associated heat-loss penalty can be underestimated or omitted, leading to lower predicted operating costs and overstating the benefit of ventilation-based strategies. EECA [123] reports a Southern Belle case where dehumidification reduced thermal fuel use by 25%, increased production by 15%, and achieved a payback of 3–4 years in a 3000 m^2 twin-skin greenhouse with a capital cost of about $120,000. These results show that payback depends not only on the dehumidification system itself, but also on how humidity control, fan energy, and CO_2 retention are represented in the analysis. For networked heat systems, spatial layout and connection density often dominate the economic outcome. In Tomson et al. [129], the southern network required about 800.5 m of trench for the main DN80 pipeline, with pipe costs exceeding £300,000, while the northern extension involved approximately 5977 m of trench with an estimated cost of about £7.26 million and heat losses of around 75 kW. These figures show that network routing and connection density can outweigh the performance of the heat source in determining project viability, which is why feasibility assessments at the district scale focus on network design, cost structure, and heat pricing.

Financial assumptions and reporting boundaries also shape NPV. Discount rate, project lifetime, and whether crop-revenue or quality effects are included can shift economic outcomes even when underlying energy balances are similar, complicating comparison between simple payback metrics and long-horizon discounted cashflow assessments [129]. A cross-cutting issue in gas-to-electric transitions is CO_2 enrichment logistics. Dutch sector analyses indicate that a large share of greenhouse CO_2 supply has historically been sourced from CHP exhaust. Reduced CHP operation therefore increases reliance on external CO_2 supply chains, which introduces additional infrastructure and procurement costs [131]. In a decarbonised setting, CO_2 provision becomes a parallel infrastructure requirement rather than a minor operational detail [61].

In greenhouse systems without combustion-based heat sources, CO_2 provision becomes a separate cost component. Costs vary with the supply route, including delivered CO_2, industrial recovery, or network-based sources, as well as storage, transport, distribution, and injection requirements. Gas purity, compression, and dosing requirements further influence both capital and operating costs. Techno-economic comparisons are therefore incomplete if CO_2 provision is excluded from the system boundary, particularly where enrichment interacts with ventilation and humidity control. As a result, outcomes depend not only on heat and power assumptions, but also on how CO_2 supply and distribution are defined. Differences across studies reflect system boundaries, operating assumptions, and financial inputs as much as the underlying technology.

3.9. Net-Zero Pathways and Food Security Implications (System-Level Synthesis and Roadmap)

Greenhouse decarbonisation is not a simple technology substitution but a coordinated pathway that links heat and mass transfer, energy infrastructure, storage, operational control, and capital recovery under uncertainty. This system view is essential because agrifood production is a major source of global emissions. FAO estimates places agrifood

https://doi.org/10.3390/en19081975

emissions at 16.2 Gt CO_2-eq in 2022, about 29.7% of total anthropogenic emissions, with supply-chain energy use forming a substantial and growing share [8].

Within protected horticulture, life cycle assessments show that energy use is a leading contributor to environmental impact, and that outcomes depend heavily on how heat and electricity are supplied (e.g., conventional heat vs. cogeneration or geothermal sources) [132]. Resource-efficiency studies further show that the balance between heating and electricity demand varies with production typology and climate. This reinforces that decarbonisation outcomes are shaped as much by demand structure and operating conditions as by the choice of technology [133].

3.9.1. Net-Zero Greenhouse Archetypes: Four Repeatable System Architectures

Feasibility studies and greenhouse decarbonisation projects reveal a set of recurring system architectures. These archetypes are best defined not by technologies but by how they reshape thermal demand, required temperature lift, and operational flexibility. In practice, net-zero pathways emerge from different combinations of load reduction, electrification, renewable-heat integration, and infrastructure coupling rather than from a single technology acting alone.

Load-First Retrofit Pathway

A recurring net-zero pathway prioritises reducing demand and peak load before changing the heat source. Typical measures include thermal screens and night insulation, targeted envelope upgrades and sealing, infiltration reduction, and control adjustments that avoid unnecessary ventilation during heating periods. Sector guidance for covered cropping identifies this sequence as a practical starting point because it delivers immediate reductions in heat use and improves the feasibility and sizing of low-temperature supply options such as heat pumps or low-grade waste heat [123].

Net-zero implication: Reducing uncontrolled heat losses lowers direct emissions and reduces the size and cost of low-carbon heat systems. Sector guidance reports heat energy savings in the range of 12.5% to 35%, with well-selected and well-operated thermal screens typically achieving around 25% to 35% of annual heat input reduction [123].

Electrification Pathway: Heat Pumps + Low-Temperature Distribution + Buffering

Heat pump electrification works best when greenhouse heating can operate at low supply temperatures, since this limits the required temperature lift and improves seasonal performance. Outcomes depend on system boundaries, including auxiliary electricity, distribution efficiency, and the interaction between humidity control and heating demand. de Zwart [121] shows that using ventilation-based moisture removal in cool conditions increases heating requirements, whereas internal dehumidification with heat-pump-assisted condensation can reduce primary energy use by approximately 24%, with potential improvement to around 30% when seasonal storage is included.

Net-zero implication: Electrification tends to perform best when combined with reduced envelope losses, appropriate buffering, and an electricity supply with declining carbon intensity. The IEA reports that heat pumps already reduce emissions relative to fossil boilers under current power mixes and that their advantage increases as the electricity supply decarbonises [134,135].

Renewable Thermal Pathway

Solar thermal systems coupled with seasonal thermal storage can supply a significant share of greenhouse heating, but the required collector area and storage capacities are capital-intensive and sensitive to design choices such as operating temperature and field sizing. In a 0.4 ha cold-climate case study, Semple et al. [127] show that both the levelised

cost of delivered heat and the payback period shift with system configuration and policy conditions. Their results indicate that simple payback is strongly influenced by fuel prices, carbon pricing, and the level of capital support (subsidy).

Net-zero implication: This pathway is most attractive where land is available, the heating season is long, and financing or policy frameworks can support long-lived infrastructure with multi-year payback horizons.

Networked Heat Pathway: Waste Heat/District Heat/Minewater with Greenhouse as Anchor Demand

Networked heat operates as infrastructure rather than a simple technology substitution. Feasibility depends on spatial layout (including pipe routing, connection density, interface costs, and tariff structure), rather than on the intrinsic efficiency of the heat source. In the Almería greenhouse case study, a graph-theory optimisation was used to determine the network layout and demand-point selection. The results showed that investment cost and NPV were strongly shaped by routing choices and the degree of load clustering [128].

Minewater studies reach similar conclusions within discounted cashflow analyses. The Durham work evaluates NPV, IRR, and discounted payback over multi-decade horizons and finds that capital allocation to distribution infrastructure and electricity price assumptions largely determine viability [129].

Net zero implication: Greenhouses can strengthen low-carbon heat networks where demand is sufficiently concentrated to justify distribution infrastructure. Where loads are spread out, the economics are limited by network length and connection costs rather than by the thermodynamic performance of the heat source.

3.9.2. A Practical Roadmap: Staged Decarbonisation That Matches Both Physics and Finance

Across the reviewed studies, net-zero concepts underperform when the engineering sequence clashes with capital recovery logic. A common failure mode is committing early to high-capacity supply infrastructure before stabilising demand. This raises installed capacity and fixed costs and exposes modelling errors in ventilation, humidity control, and tariff exposure.

A staged roadmap that aligns heat transfer drivers with investment risk is more bankable. The early focus is on demand and controllability (thermal screens, leakage reduction, and sensor and setpoint tuning) to cut peak load and lower the required temperature lift. The next step is to electrify the base thermal load with heat pumps under explicit operating boundaries, including humidity control choices that can shift heating demand in semi-closed operation. de Zwart's [121] shows why ventilation-based moisture removal and internal condensation strategies cannot be treated as an afterthought when estimating energy use and sizing.

With a stabilised and electrified base load, renewable integration and storage can be evaluated against realistic demand profiles. Semple et al. [127] show that solar thermal with seasonal storage is technically viable but economically sensitive to configuration and policy assumptions, which argues for optimising cost-effective useful heat rather than maximum solar fraction. At longer horizons, cluster-scale integrations (district heat, minewater, or waste heat networks) become viable where spatial density supports infrastructure recovery. Feasibility studies in Almería and Durham show that routing, demand aggregation, tariff design, and discounted cashflow structure are decisive economic variables [128,129].

Advanced control and digital modelling support every stage. Predictive control, dynamic load estimation, and tariff-aware scheduling reduce uncertainty around ventilation losses, humidity management, and electricity exposure, improving sizing accuracy and the credibility of financial projections. Without realistic operational modelling, electrification and storage strategies risk misestimating both capacity and payback. The pathway follows

https://doi.org/10.3390/en19081975

thermodynamic sequencing (as shown in Figure 6), but its practical value depends on the scale of energy, emissions, cost, and load effects at each stage. Table 3 provides indicative performance ranges from the reviewed literature to support this analysis.

Table 3. Indicative performance ranges associated with staged greenhouse decarbonisation pathways.

Pathway Stage	Typical Energy Effect	Emissions Effect	Peak-Load Effect	Cost Implication	Applicability/ Scale	Literature Basis
Demand reduction and controllability	Thermal screens: about 12.5–35% heat reduction; reported payback below 3 years in some commercial cases	Reduced fuel use	Lower peak heating demand	Low to moderate CAPEX	Widely applicable, especially in heating-dominant climates	[123,124]
Electrification and humidity-aware operation	Internal moisture removal/heat pump-based dehumidification: about 24–30% energy reduction in reported cases; performance depends on tariff and COP	Depends on grid carbon intensity and auxiliary electricity use	Reduce load where ventilation losses are controlled	Moderate to high CAPEX	Greenhouse-only or integrated on-site systems	[103,121,125]
Solar thermal with storage	Around 64% annual sensible heating contribution in reported systems; LCOH about 32.9–36.2 $/GJ under stated assumptions	Depends on system configuration and policy context	Reduces seasonal fossil demand; limited by storage design	High CAPEX, long payback without support	Site-specific; more suitable for large-scale or long-term projects	[127]
Networked heat (district and waste heat)	High fossil fuel displacement where source and routing are suitable; performance sensitive to network length and demand density	Depends on source characteristics and accounting method	Supports base-load decarbonisation more than peak-load response	Infrastructure-dominated CAPEX	Cluster-scale, site-specific	[128–130]
Semi-closed/ integrated control	Energy use depends on dehumidification strategy and auxiliary electricity; some cases report lower gas use with higher electricity demand	Depends on treatment of electricity and CO_2 supply	Reduces ventilation-related heat loss	Moderate to high CAPEX	Advanced commercial systems	[103,121]

Table 3 provides indicative performance ranges for the stages shown in Figure 6. The values are drawn from the reviewed studies and represent typical orders of magnitude rather than directly comparable benchmarks, as outcomes depend on climate, system configuration, control strategy, and system boundary assumptions.

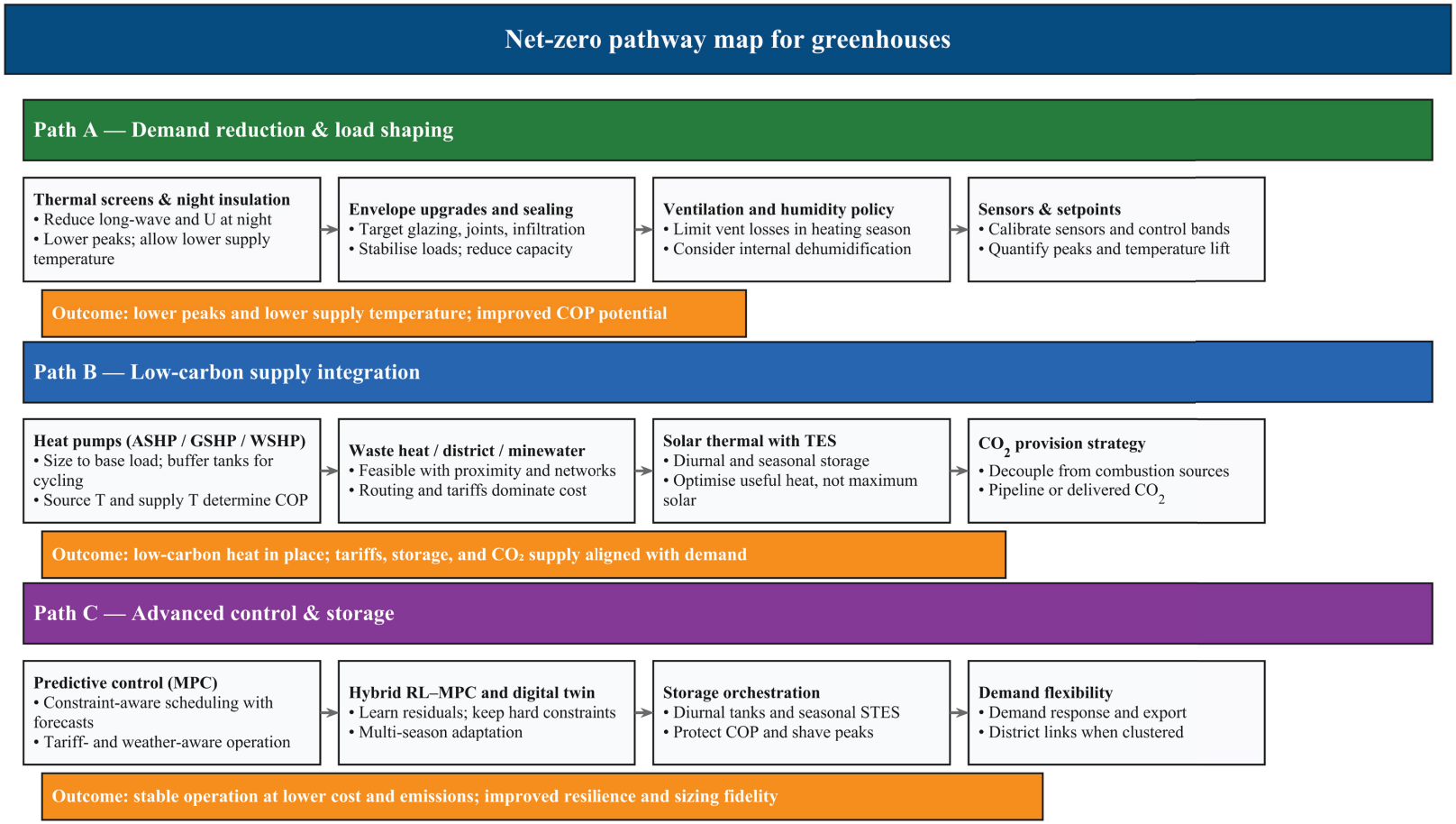


Figure 6. Net-zero pathway for greenhouse decarbonisation, showing three staged transitions: (A) reducing demand and improving controllability, (B) integrating low-carbon heat supply, and (C) improving system performance through storage and advanced control.

https://doi.org/10.3390/en19081975

3.9.3. Food Security Implications: What "Net-Zero Greenhouse" Changes and What It Risks

Net-zero transitions in protected horticulture matter for food security because they reshape both the reliability and the cost base of year-round supply. At the macro level, the case for decarbonising greenhouse energy is reinforced by the scale of agrifood emissions: FAO estimates 16.2 Gt CO_2-eq in 2022, with supply-chain energy a substantial and growing component. At the production-system level, life cycle assessments and resource-efficiency studies consistently show that energy demand is a major driver of environmental impact and that outcomes are sensitive to how heat and power are supplied, as well as to climate and production typology.

Decarbonisation can strengthen food resilience when it lowers exposure to fuel-price volatility and supply disruption. In practice, thermal reliability underpins production continuity: when heating is unaffordable or insecure, growers respond by lowering setpoints, shortening seasons, or temporarily suspending production. The staged pathway developed in this review makes the logic explicit: demand reduction and tighter controllability reduce peak vulnerability, while electrification with buffering and storage helps maintain operation through cold spells and price shocks.

The main equity risk is distributional. Capital-intensive options tend to concentrate in large, well-financed operations, leaving smaller or marginal growers exposed to volatile fossil costs or high electricity tariffs. This is not only a technology problem but also one of infrastructure and finance. Where district or minewater heat is feasible, evidence shows that spatial configuration and financing horizons dominate bankability, which implies that equitable access depends on coordinated planning, transparent connection rules, and tariff design rather than equipment performance alone.

Net-zero claims are credible only when energy sources and boundaries are stated clearly, consistent with the definitions adopted in this review. Energy consumption is among the largest environmental burdens in protected crops, and impacts can fall with a lower-carbon heat and power supply, but the results vary sharply with system definition and energy sourcing. This matters for food security narratives: high-cost green investments that do not reduce life cycle intensity (for example, electrification on a carbon-intensive grid) may raise production costs without delivering a credible climate benefit. CO_2 enrichment introduces a parallel constraint. As CHP use declines, supply increasingly depends on external sources, with added infrastructure, quality assurance, and logistics requirements. This affects reliability, as interruptions in supply can limit consistent dosing, and affordability, as CO_2 introduces an additional operating cost rather than a by-product of heat generation. It also affects production, as variations in CO_2 supply or dosing can affect yield and crop quality, particularly in systems with high ventilation rates where retention is low. CO_2 provision also depends on storage, transport, and distribution systems, linking greenhouse operation to wider supply networks. These requirements connect CO_2 enrichment to system design and planning, as detailed in Section 3.6.5.

The food security value of net-zero greenhouse pathways is highest when they deliver both operational reliability and credible life cycle emissions reduction, without shifting costs onto growers through poorly structured tariffs, fragmented infrastructure planning, or incomplete accounting of auxiliary electricity and CO_2 supply. Figure 7 shows how the sequence of net-zero measures links directly to food security outcomes and the conditions required for credible and equitable deployment.

3.10. Long-Term Projections of Commercial Greenhouse Markets and Implications for CEA in Global Food Systems

Market analyses consistently indicate rapid expansion of commercial greenhouse infrastructure, reflecting growing investment in controlled-environment agriculture. Ac-

https://doi.org/10.3390/en19081975

cording to MarketsandMarkets [136], the commercial greenhouse market is projected to grow from USD 39.6 billion in 2023 to USD 68.7 billion by 2028, equivalent to a compound annual growth rate (CAGR) of 11.6%. Comparable projections are reported by other market analyses. ResearchAndMarkets reports an increase from USD 32.0 billion in 2022 to USD 56.4 billion by 2028 (9.91% CAGR), while Grand View Research projects USD 32.84 billion in 2025, rising to USD 74.10 billion by 2033 (10.9% CAGR). Fortune Business Insights forecasts growth from USD 37.78 billion in 2025 to USD 96.13 billion by 2034 (10.95% CAGR). Despite differences in methodology and market assumptions, these studies converge on a clear finding: commercial greenhouse and associates CEA infrastructure markets are growing at roughly 10–12% per year through the 2020s and into the early 2030s [136–139]. These estimates are used as indicative commercial baselines to inform the scenario analysis, reflecting current market scale and growth trends, and do not represent independently validated forecasts of technology adoption.

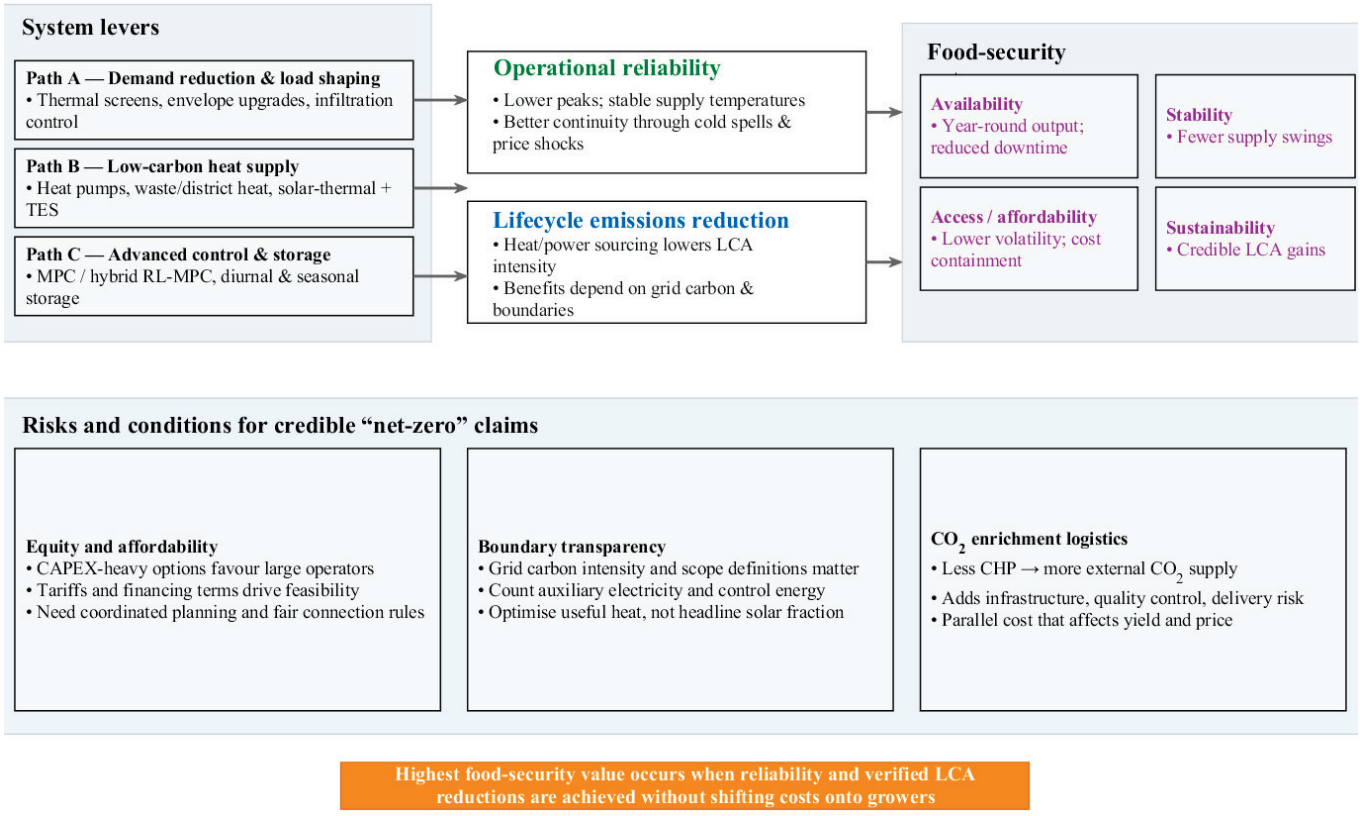


Figure 7. Net-zero greenhouse pathway showing system levers, food security benefits, and the conditions required for credible and equitable deployment.

To examine the longer-term implications of this growth for global food systems, the near-term estimates were extended to 2050 using a scenario-based compound-growth model. The analysis uses the USD 68.7 billion market value projected for 2028 as the reference point, with three annual growth rates of 6%, 8%, and 10% (representing conservative, intermediate, and upper-bound pathways within the range suggested by current market reports). These rates also recognise that the present double-digit growth is unlikely to persist indefinitely as the sector matures.

Projections (future market values) were calculated using the standard compound-growth expressions:

$$V_t = V_0(1+g)^n \quad (7)$$

where V_t is the market value in year t, V_0 is the 2028 anchor value, g is the assumed annual growth rate, and n is the number of years after the anchor year. This formulation is widely used in economic and market trend assessment and provides a transparent means of extending short- term forecasts into longer- range- scenario pathways while keeping the underlying assumptions explicit.

A limitation of this approach should be recognised. The projections are based on constant annual growth rates over the entire horizon, whereas the adoption of technology-intensive systems rarely follows such patterns. In practice, adoption develops unevenly, with slower early growth constrained by capital cost and infrastructure, followed by a period of faster expansion and eventual slowdown as markets mature. While this behaviour is often described using logistic diffusion models, the lack of long-term data for the greenhouse sector makes it difficult to define these dynamics in a consistent way. The projections should therefore not be interpreted as a model of market diffusion. Instead, they extend current growth trends under fixed-rate assumptions to illustrate possible long-term trajectories. Early-stage growth may be overstated, while later expansion may be understated. The results are best understood as scenario bounds rather than forecasts of future market behaviour. The use of multiple growth rates partly addresses this limitation by defining a range of plausible outcomes rather than a single estimate.

Applying the three growth scenarios to the 2028 anchor value of USD 68.7 billion yields a projected 2050 market size of approximately USD 247.6 billion at 6%, USD 373.5 billion at 8% and USD 559.2 billion at 10%, as shown in Figure 8. These values remain consistent with the scale and growth implied by current market assessments, while also reflecting the uncertainty associated with extending short-term trends over several decades. The trajectories in Figure 8 are based on constant growth rates and should not be interpreted as realistic diffusion pathways. Over long horizons, adoption is likely to depart from these trends as infrastructure constraints and market maturity begin to limit further expansion.

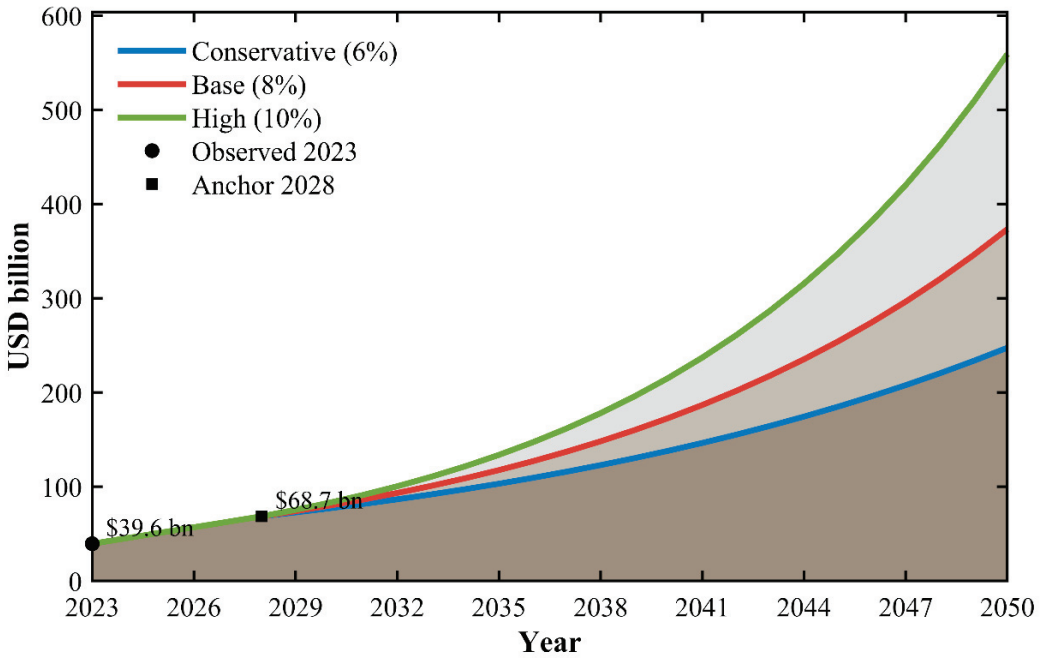


Figure 8. Commercial greenhouse market projections (2028–2050) under 6%, 8%, and 10% annual growth scenarios, anchored to the 2028 estimate of USD 68.7 billion.

To contextualise the projected growth of the commercial greenhouse sector within the wider food system, the scenario trajectories were compared against long-run projections of global agricultural production value. FAO statistics indicate that global agriculture value

added reached USD 3.8 trillion in 2022, rising to about USD 4.0 trillion in 2023 [140,141]. Extending this series to 2050 using two growth assumptions: 2.6%, reflecting the most recent year-on-year increase, and 2.9%, corresponding to the average growth observed over the past decade. Under these assumptions, global agricultural value increases to approximately USD 8.0–8.7 trillion by 2050, as shown in Figure 9.

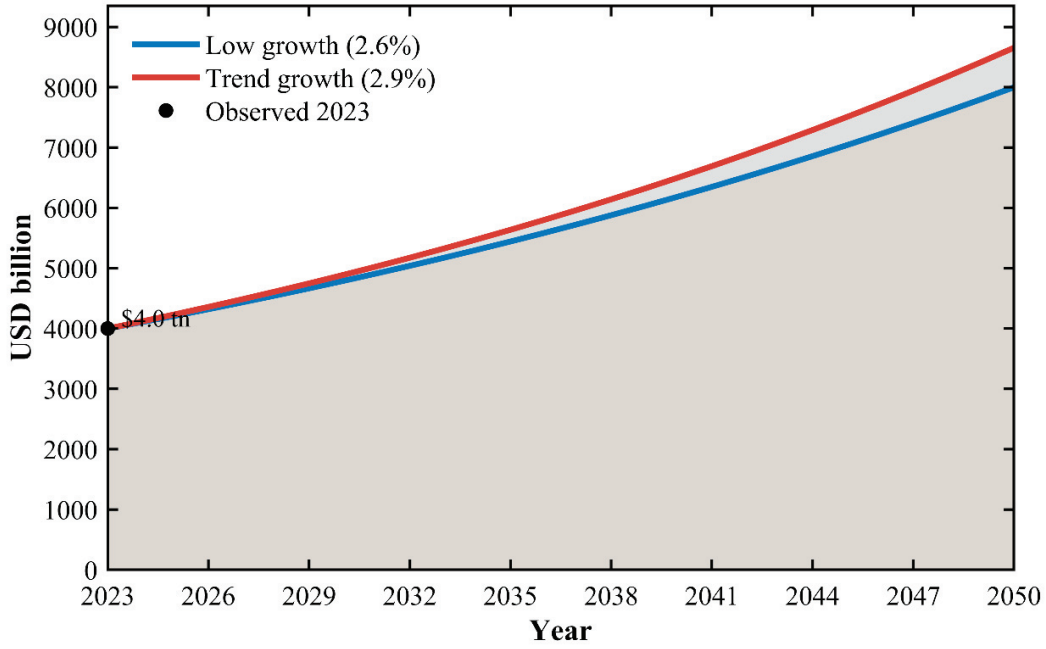


Figure 9. Global agricultural value projections for 2023–2050 under 2.6% and 2.9% annual growth scenarios.

These values are broadly aligned with the longer-term trends described in the OECD–FAO Agricultural Outlook, which anticipates a 14% increase in global agricultural production by 2034 when expressed in constant 2014–2016 prices [142]. Moreover, wider food-systems analyses suggest that global food demand will increase by roughly 35–56% between 2010 and 2050, driven by population growth, urbanisation, and dietary change [1]. These benchmarks provide a plausible reference frame for evaluating the potential scale of CEA relative to the broader agricultural economy over the coming decades.

Comparing the two projection sets provides an indication of how the scale of CEA investment may evolve relative to the wider agricultural economy. In 2023, the commercial greenhouse market accounted for approximately 1% of global agricultural value. Under the growth trajectories outlined in Figures 8 and 9, this share rises to around 3.1–6.5% by 2050 (as shown in Figure 10 and Table 4). This should not be interpreted as the proportion of global food output produced in controlled environments. The comparison places a capital-intensive infrastructure market against annual farmgate production value, and the two measure different aspects of the food system.

For this reason, the ratio is best viewed as an investment intensity indicator, signalling the relative weight of CEA infrastructure within global agricultural supply chains rather than its contribution to total food production. The upward trend nevertheless highlights the growing strategic role of controlled-environment systems, particularly in high-value horticulture and climate-sensitive regions where reliability, year-round production, and resource efficiency are increasingly important.

The analysis indicates that CEA technologies are likely to play a far more prominent role in food system resilience by mid-century, while remaining a complement rather than an alternative to open-field agriculture. Their strongest contributions are expected in

https://doi.org/10.3390/en19081975

high-value horticulture, nutrient-dense perishable crops, and regional supply systems that require greater climate tolerance, rather than in the large-scale production of staple grains. Controlled-environment systems can also enhance production stability under climate variability, water scarcity, and energy-price volatility, thereby improving the resilience of food supply chains.

Table 4. Summary of data sources, published market estimates, and long-term scenario extensions for the commercial greenhouse sector and global agricultural production value. Values for 2050 represent scenario-based extrapolations from published baselines.

Item	Source Base	Published Horizon	2050 Extension
Commercial greenhouse market [136]	USD 39.6 bn (2023)	USD 68.7 bn by 2028, 11.6% CAGR	USD 247.6 bn (6%), USD 373.5 bn (8%), USD 559.2 bn (10%)
Global agriculture value [140,141]	USD 4.0 tn (2023)	OECD-FAO: USD 3.96 tn by 2034 constant USD	USD 8.0 tn (2.6%), USD 8.66 tn (2.9%)
Greenhouse market/agriculture value	~1.0% (2023)		~3.1% to 6.5% (2050 scenarios)

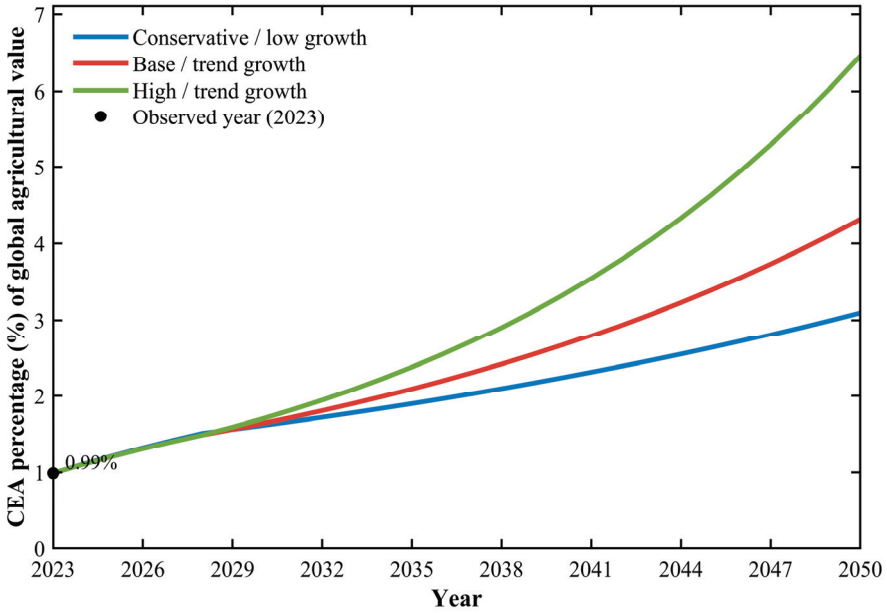


Figure 10. Commercial greenhouse industry as a share of global agricultural value, 2023–2050, based on the growth scenarios in Figures 8 and 9. Ratios reflect investment scale, not production share.

These trends have direct implications for Sustainable Development Goal 2 (Zero Hunger), which calls for secure access to safe, nutritious, and sufficient food while promoting sustainable agricultural production systems [143,144]. Greenhouse agriculture can contribute to this objective by supporting year-round production, improving yield reliability, and reducing vulnerability to climate-related disruptions, particularly in regions with extreme weather conditions or high dependence on imported produce. However, the extent to which CEA can influence food system outcomes will depend not only on market growth but also on the policy and institutional arrangements that shape technology uptake.

Several enabling conditions are therefore critical. These include concessional finance for capital-intensive infrastructure; targeted incentives/support for energy-efficient technologies such as thermal screens and heat pumps; investment in thermal storage and low-carbon heat networks; and electricity tariff structures that do not penalise electrified heating during winter peak periods. As reliance on combined heat and power (CHP) declines, CO_2 supply logistics will also require deliberate planning. Alongside this, sus-

tained public investment in research, knowledge transfer programmes, and workforce development will also be essential for large-scale deployment. Without such measures, controlled-environment agriculture is likely to remain concentrated among larger firms or high-value niche markets; with it, the sector contribution to food system resilience and progress towards SDG 2 could be considerably greater [143–145].

4. Future Directions

Advancing greenhouse decarbonisation will require improvements in how systems are analysed, specified, and deployed, rather than the addition of yet more isolated technologies. A persistent limitation across the literature is the lack of comparable system boundaries. Studies differ in how they treat latent loads and humidity control, whether auxiliary electricity is included, the choice of grid emission factors, and the financial assumptions applied (discount rate, project lifetime, and CAPEX scope). To enable comparison, future work should report: envelope performance and infiltration assumptions; the latent load modelling method; seasonal COP including auxiliaries; the scope of capital costing; lifetime and discount rate; and the emissions boundary definition used for greenhouse gas accounting.

A major priority for future work is improving the realism of performance and cost modelling. Many techno-economic assessments still rely on steady state formulations that cannot represent evapotranspiration, condensation heat recovery, or the effects of control strategy on heating and dehumidification demand. A more robust evaluation will require dynamic energy-mass balance models that include these interactions and incorporate weather and tariff variability. Digital twin approaches linking physical simulation with discounted cashflow metrics offer a credible route for exploring scenario uncertainty and testing net-zero pathways under operational constraints.

Electrification pathways also demand closer alignment with power system conditions. The feasibility of heat pump-based systems depends on tariff structure, demand charges, marginal grid carbon intensity, and interactions with on-site photovoltaics and storage. For district heat, minewater, and industrial waste heat options, research priorities lie in spatial and financial optimisation rather than component efficiency: cluster design, network cost normalisation, and shared infrastructure financing determine whether these pathways can be deployed at scale.

Finally, thermal management research must connect more directly to food system outcomes. Emissions intensity per unit of product, resilience to energy price shocks, and the relationship between capital intensity and food affordability remain insufficiently resolved, particularly in emerging-economy contexts. Without such linkage, decarbonisation pathways cannot be assessed adequately in terms of scalability, cost implications, or their contribution to wider food system resilience.

5. Conclusions

This review examined greenhouse thermal management in the context of net-zero food production, focusing on the interaction between heat transfer processes, system boundaries, operating strategy, and infrastructure constraints. The findings show that decarbonisation is not determined by individual technologies alone, but by how thermal demand, humidity control, and energy supply are represented and integrated. Envelope losses, ventilation, and latent heat exchange set the baseline demand, while tariffs, capital cost, and infrastructure access determine whether low-carbon solutions are viable in practice.

Humidity control plays a central role in greenhouse energy use. Although temperature remains the primary control variable, ventilation and latent loads often drive both seasonal energy consumption and peak heating demand, particularly in winter. This affects the performance of electrification, dehumidification, and heat recovery systems,

https://doi.org/10.3390/en19081975

whose effectiveness depends on how sensible and latent processes are managed within the control strategy. The reported results are not comparable without a clear definition of system boundaries, auxiliary electricity, and control assumptions. Greenhouse decarbonisation follows a staged pathway rather than a single-technology transition. Demand reduction through envelope improvement and thermal screening is a prerequisite for viable electrification. Electrification systems perform best when supply temperatures, humidity management, and tariff exposure are addressed together. Further reductions depend on the integration of renewable and recovered heat, storage, and, where available, networked heat systems. The sequence of implementation and system integration is therefore as important as the technologies themselves.

Long-term projections indicate substantial growth in the greenhouse sector, with market value potentially increasing from USD 68.7 billion in 2028 to USD 248–559 billion by 2050. Relative to projected global agricultural value, this reflects rising capital intensity rather than a proportional increase in food output. The review has several limitations. The reported results vary widely due to differences in boundary definitions, climate conditions, and modelling approaches, which limit direct comparison across studies. In addition, there is limited empirical evidence on integrated systems that combine heating, dehumidification, CO_2 supply, and control, and long-term operational performance is not consistently reported.

From a food security perspective, controlled-environment agriculture is likely to play a growing role in climate-resilient production, but market growth does not directly translate to increased food output. The contribution of low-carbon greenhouse systems depends on affordability, access to infrastructure, and reliable heat and CO_2 supply. While greenhouses can support stable year-round production under climate stress, wider adoption depends on coordinated energy systems, financing, and policy support. Progress will require clearer system boundaries, improved treatment of latent loads and auxiliary electricity, and closer integration of modelling, techno-economic analysis, and operational control. Under these conditions, greenhouse systems can contribute meaningfully to both decarbonisation and resilient food production.

Author Contributions: Conceptualization, S.S. and A.M.A.; methodology, S.S.; software, S.S.; formal analysis, S.S.; data curation, S.S.; writing—original draft preparation, S.S. and C.E.; writing—review and editing, S.S., C.E., A.B., C.B., and A.M.A.; supervision, A.B., C.B., and A.M.A.; project administration, S.S. and A.M.A.; funding acquisition, A.M.A. All authors have read and agreed to the published version of the manuscript.

Funding: This research was funded by the University of Lincoln's Graduate Teaching Fellow Scheme (Ref No: 1AB-2AL-539354).

Data Availability Statement: The original contributions presented in this study are included in the article. Further inquiries can be directed to the corresponding author.

Acknowledgments: The authors acknowledge the University of Lincoln for supporting Samson Sogbaike through a fully funded PhD scholarship under the Graduate Teaching Fellow Scheme (Ref No: 1AB-2AL-539354).

Conflicts of Interest: The authors declare no conflicts of interest.

Abbreviations

The following abbreviations are used in this manuscript:

AI	Artificial Intelligence
ASHP	Air-Source Heat Pump
BTES	Borehole Thermal Energy Storage

CAGR	Compound Annual Growth Rate
CAPEX	Capital Expenditure
CEA	Controlled-Environment Agriculture
CFD	Computational Fluid Dynamics
CHP	Combined Heat and Power
COP	Coefficient of Performance
CSG	Chinese Solar Greenhouse
DC	Discount Rate
DRL	Deep Reinforcement Learning
EAHE	Earth-to-Air Heat Exchanger
EECA	Energy Efficiency and Conservation Authority
FAO	Food and Agriculture Organization of the United Nations
GHG	Greenhouse Gas
GSHP	Ground-Source Heat Pump
HPS	Heat Pump System
HVAC	Heating, Ventilation, and Air Conditioning
IEA	International Energy Agency
IPCC	Intergovernmental Panel on Climate Change
IRR	Internal Rate of Return
LCA	Life Cycle Assessment
LCO	Levelised Cost of Operation
LCOH	Levelised Cost of Heat
LED	Light Emitting Diode
LTES	Latent Thermal Energy Storage
MILP	Mixed-Integer Linear Programming
ML	Machine Learning
MPC	Model Predictive Control
NPV	Net Present Value
NVAC	Natural Ventilation and Air Circulation
OECD–FAO	Organisation for Economic Co-operation and Development and Food and Agriculture Organization
OPEX	Operational Expenditure
PAR	Photosynthetically Active Radiation
PC	Polycarbonate
PCM	Phase Change Material
PE	Polyethylene
PID	Proportional Integral Derivative (controller)
PRISMA	Preferred Reporting Items for Systematic Reviews and Meta-Analyses
PV	Photovoltaics
PVT	Photovoltaic Thermal
RH	Relative Humidity
RL	Reinforcement Learning
SALSA	Search, Appraisal, Synthesis and Analysis
SDG	Sustainable Development Goal
STE	Solar Thermal Energy
STES	Seasonal Thermal Energy Storage
STH	Solar Thermal Heating/Solar Thermal Heat
TES	Thermal Energy Storage
TRNSYS	Transient System Simulation
U-value	Overall heat transfer coefficient ($W \cdot m^{-2} \cdot K^{-1}$)
UK	United Kingdom
USD	United States Dollar
VPD	Vapour Pressure Deficit
WSHP	Water-Source Heat Pump

https://doi.org/10.3390/en19081975

References

1. van Dijk, M.; Morley, T.; Rau, M.L.; Saghai, Y. A meta-analysis of projected global food demand and population at risk of hunger for the period 2010–2050. *Nat. Food* **2021**, *2*, 494–501. [CrossRef] [PubMed]
2. Intergovernmental Panel on Climate Change (IPCC). *Climate Change 2022—Impacts, Adaptation and Vulnerability*; Cambridge University Press: Singapore, 2023. [CrossRef]
3. Shamshiri, R.R.; Kalantari, F.; Ting, K.C.; Thorp, K.R.; Hameed, I.A.; Weltzien, C.; Ahmad, D.; Shad, Z.M. Advances in greenhouse automation and controlled environment agriculture: A transition to plant factories and urban agriculture. *Int. J. Agric. Biol. Eng.* **2018**, *11*, 1–22. [CrossRef]
4. Benke, K.; Tomkins, B. Future food-production systems: Vertical farming and controlled-environment agriculture. *Sustain. Sci. Pract. Policy* **2017**, *13*, 13–26. [CrossRef]
5. Mills, E. The emergence of indoor agriculture as a driver of global energy demand. *Npj Sustain. Agric.* **2025**, *3*, 52. [CrossRef]
6. Vadiee, A.; Martin, V. Energy management strategies for commercial greenhouses. *Appl. Energy* **2014**, *114*, 880–888. [CrossRef]
7. Katzin, D.; Marcelis, L.F.M.; van Mourik, S. Energy savings in greenhouses by transition from high-pressure sodium to LED lighting. *Appl. Energy* **2021**, *281*, 116019. [CrossRef]
8. Food and Agriculture Organization of the United Nations (FAO). Greenhouse Gas Emissions from Agrifood Systems: Global, Regional and Country Trends, 2000–2022. 2024. Available online: https://openknowledge.fao.org/server/api/core/bitstreams/111b7ee8-282b-42ff-ad95-cccecd90f8ea/content (accessed on 17 February 2026).
9. IPCC Sixth Assessment Report. Agriculture, Forestry and Other Land Uses (AFOLU). In *Climate Change 2022—Mitigation of Climate Change*; Cambridge University Press: Singapore, 2023; pp. 747–860. [CrossRef]
10. IPCC. Food, Fibre and Other Ecosystem Products. In *Climate Change 2022—Impacts, Adaptation and Vulnerability*; Cambridge University Press: Singapore, 2023; pp. 713–906. [CrossRef]
11. Boyacı, S.; Kocięcka, J.; Jagosz, B.; Atılgan, A. Energy Efficiency in Greenhouses and Comparison of Energy Sources Used for Heating. *Energies* **2025**, *18*, 724. [CrossRef]
12. Singh, M.C.; Singh, J.P.; Singh, K.G. Development of a microclimate model for prediction of temperatures inside a naturally ventilated greenhouse under cucumber crop in soilless media. *Comput. Electron. Agric.* **2018**, *154*, 227–238. [CrossRef]
13. Choab, N.; Allouhi, A.; El Maakoul, A.; Kousksou, T.; Saadeddine, S.; Jamil, A. Review on greenhouse microclimate and application: Design parameters, thermal modeling and simulation, climate controlling technologies. *Sol. Energy* **2019**, *191*, 109–137. [CrossRef]
14. Katzin, D.; van Henten, E.J.; van Mourik, S. Process-based greenhouse climate models: Genealogy, current status, and future directions. *Agric. Syst.* **2022**, *198*, 103388. [CrossRef]
15. Reyes-Rosas, A.; Molina-Aiz, F.D.; Valera, D.L.; López, A.; Khamkure, S. Development of a single energy balance model for prediction of temperatures inside a naturally ventilated greenhouse with polypropylene soil mulch. *Comput. Electron. Agric.* **2017**, *142*, 9–28. [CrossRef]
16. Golzar, F.; Heeren, N.; Hellweg, S.; Roshandel, R. A novel integrated framework to evaluate greenhouse energy demand and crop yield production. *Renew. Sustain. Energy Rev.* **2018**, *96*, 487–501. [CrossRef]
17. Akpenpuun, T.D.; Na, W.-H.; Ogunlowo, Q.O.; Rabiu, A.; Adesanya, M.A.; Addae, K.S.; Kim, H.-T.; Lee, H.-W. Effect of Greenhouse Cladding Materials and Thermal Screen Configuration on Heating Energy and Strawberry (*Fragaria ananassa* var. "Seolhyang") Yield in Winter. *Agronomy* **2021**, *11*, 2498. [CrossRef]
18. IEA. The Future of Heat Pumps, Paris. 2022. Available online: https://www.iea.org/reports/the-future-of-heat-pumps (accessed on 8 January 2026).
19. Vadiee, A.; Martin, V. Energy management in horticultural applications through the closed greenhouse concept, state of the art. *Renew. Sustain. Energy Rev.* **2012**, *16*, 5087–5100. [CrossRef]
20. Chen, W.-H.; Mattson, N.S.; You, F. Intelligent control and energy optimization in controlled environment agriculture via nonlinear model predictive control of semi-closed greenhouse. *Appl. Energy* **2022**, *320*, 119334. [CrossRef]
21. Mahmood, F.; Govindan, R.; Bermak, A.; Yang, D.; Al-Ansari, T. Data-driven robust model predictive control for greenhouse temperature control and energy utilisation assessment. *Appl. Energy* **2023**, *343*, 121190. [CrossRef]
22. Morcego, B.; Yin, W.; Boersma, S.; van Henten, E.; Puig, V.; Sun, C. Reinforcement Learning versus Model Predictive Control on greenhouse climate control. *Comput. Electron. Agric.* **2023**, *215*, 108372. [CrossRef]
23. Paris, B.; Vandorou, F.; Balafoutis, A.T.; Vaiopoulos, K.; Kyriakarakos, G.; Manolakos, D.; Papadakis, G. Energy Use in Greenhouses in the EU: A Review Recommending Energy Efficiency Measures and Renewable Energy Sources Adoption. *Appl. Sci.* **2022**, *12*, 5150. [CrossRef]
24. New Zealand Ministry of Foreign Affairs and Trade (MFAT). The Dutch Horticulture sector: An Innovative Sector Facing an Energy Crisis and Rising Costs. 2022. Available online: https://www.mfat.govt.nz/en/trade/mfat-market-reports/the-dutch-horticulture-sector-an-innovative-sector-facing-an-energy-crisis-and-rising-costs-september-2022 (accessed on 8 January 2026).

25. van der Veen, R.A.C.; Kasmire, J. Combined heat and power in Dutch greenhouses: A case study of technology diffusion. *Energy Policy* **2015**, *87*, 8–16. [CrossRef]
26. FAO; IFAD; UNICEF; WFP; WHO. *The State of Food Security and Nutrition in the World 2023*; FAO: Rome, Italy, 2023. [CrossRef]
27. Termine, P. Ensuring Food Security: Why Agency and Sustainability Matter, FAO (2024). Available online: https://www.fao.org/cfs/cfs-hlpe/insights/news-insights/news-detail/ensuring-food-security--why-agency-and-sustainability-matter/en (accessed on 17 February 2026).
28. Page, M.J.; McKenzie, J.E.; Bossuyt, P.M.; Boutron, I.; Hoffmann, T.C.; Mulrow, C.D.; Shamseer, L.; Tetzlaff, J.M.; Akl, E.A.; Brennan, S.E.; et al. The PRISMA 2020 statement: An updated guideline for reporting systematic reviews. *BMJ* **2021**, *372*, n71. [CrossRef]
29. Grant, M.J.; Booth, A. A typology of reviews: An analysis of 14 review types and associated methodologies. *Health Inf. Libr. J.* **2009**, *26*, 91–108. [CrossRef]
30. Campbell, M.; McKenzie, J.E.; Sowden, A.; Katikireddi, S.V.; Brennan, S.E.; Ellis, S.; Hartmann-Boyce, J.; Ryan, R.; Shepperd, S.; Thomas, J.; et al. Synthesis without meta-analysis (SWiM) in systematic reviews: Reporting guideline. *BMJ* **2020**, *368*, l6890. [CrossRef]
31. D'Arpa, S.; Colangelo, G.; Starace, G.; Petrosillo, I.; Bruno, D.E.; Uricchio, V.; Zurlini, G. Heating requirements in greenhouse farming in southern Italy: Evaluation of ground-source heat pump utilization compared to traditional heating systems. *Energy Effic.* **2016**, *9*, 1065–1085. [CrossRef]
32. Stanghellini, C.; Ooster, B.V.; Heuvelink, E. Heating in climate-controlled greenhouses. In *Greenhouse Horticulture*; Brill | Wageningen Academic: Gelderland, The Netherlands, 2024; pp. 164–192. [CrossRef]
33. Zhang, Y. Effect of covering materials on energy consumption and greenhouse microclimate. *Agric. For. Meteorol.* **1996**, *82*, 227–244. [CrossRef]
34. Geoola, F.; Kashti, Y.; Teitel, M.; Levi, A.; Brickman, R.; Esquira, I. A study of u value of greenhouse films with thermal screens using the hot box method. *Acta Hortic.* **2011**, *893*, 367–372. [CrossRef]
35. Rasheed, A.; Lee, J.W.; Lee, H.W. A Review of Greenhouse Energy Management by Using Building Energy Simulation. *Prot. Hortic. Plant Fact.* **2015**, *24*, 317–325. [CrossRef]
36. Song, A.; Kim, Y.; Hwang, S.; Shin, M.; Lee, S. A Comprehensive Review of Thermal Transmittance Assessments of Building Envelopes. *Buildings* **2024**, *14*, 3304. [CrossRef]
37. Ahamed, M.S.; Guo, H.; Tanino, K. A quasi-steady state model for predicting the heating requirements of conventional greenhouses in cold regions. *Inf. Process. Agric.* **2018**, *5*, 33–46. [CrossRef]
38. Boulard, T.; Baille, A. Modelling of Air Exchange Rate in a Greenhouse Equipped with Continuous Roof Vents. *J. Agric. Eng. Res.* **1995**, *61*, 37–47. [CrossRef]
39. Papadakis, G.; Mermier, M.; Meneses, J.F.; Boulard, T. Measurement and Analysis of Air Exchange Rates in a Greenhouse with Continuous Roof and Side Openings. *J. Agric. Eng. Res.* **1996**, *63*, 219–227. [CrossRef]
40. Fatnassi, H.; Boulard, T.; Demrati, H.; Bouirden, L.; Sappe, G. SE—Structures and Environment. *Biosyst. Eng.* **2002**, *82*, 97–105. [CrossRef]
41. Piscia, D. Analysis of Night-Time Climate in Plastic-Covered Greenhouses. Ph.D. Thesis, Universitat Politècnica de Catalunya, Barcelona, Spain, 2012.
42. Piscia, D.; Muñoz, P.; Panadès, C.; Montero, J.I. A method of coupling CFD and energy balance simulations to study humidity control in unheated greenhouses. *Comput. Electron. Agric.* **2015**, *115*, 129–141. [CrossRef]
43. Gu, X.; Goto, E. Computational Fluid Dynamics Model with Realistic Plant Structures to Study Airflow in and around a Plant Canopy on a Cultivation Shelf in a Plant Factory with Artificial Light. *Agriculture* **2024**, *14*, 1199. [CrossRef]
44. Bazgaou, A.; Fatnassi, H.; Bouharroud, R.; Tiskatine, R.; Wifaya, A.; Demrati, H.; Bammou, L.; Aharoune, A.; Bouirden, L. CFD Modeling of the Microclimate in a Greenhouse Using a Rock Bed Thermal Storage Heating System. *Horticulturae* **2023**, *9*, 183. [CrossRef]
45. Kibwika, A.K.; Seo, H.-J.; Seo, I.-H. CFD Model Verification and Aerodynamic Analysis in Large-Scaled Venlo Greenhouse for Tomato Cultivation. *Agriengineering* **2023**, *5*, 1395–1414. [CrossRef]
46. Norton, T.; Sun, D.W.; Grant, J.; Fallon, R.; Dodd, V. Applications of computational fluid dynamics (CFD) in the modelling and design of ventilation systems in the agricultural industry: A review. *Bioresour. Technol.* **2007**, *98*, 2386–2414. [CrossRef]
47. Sudirman, M.; van Hooff, T.; Gillmeier, S.; Blocken, B. Validation study of cross-ventilation in a realistic building geometry: RANS, SAS and LES. *Build. Environ.* **2024**, *269*, 112354. [CrossRef]
48. Allali, F.E.; Fatnassi, H.; Demrati, H.; Errais, R.; Wifaya, A.; Aharoune, A. Greenhouse cooling systems: A systematic review of research trends, challenges, and recommendations for improving sustainability. *Clean. Eng. Technol.* **2025**, *26*, 100973. [CrossRef]
49. Tantau, H.-J.; Akyazi, G. The low energy greenhouse—Heat transfer by long wave radiation. *Acta Hortic.* **2017**, *1170*, 847–854. [CrossRef]

50. Sethi, V.P.; Sharma, S.K. Survey of cooling technologies for worldwide agricultural greenhouse applications. *Sol. Energy* **2007**, *81*, 1447–1459. [CrossRef]
51. Amani, M.; Foroushani, S.; Sultan, M.; Bahrami, M. Comprehensive review on dehumidification strategies for agricultural greenhouse applications. *Appl. Therm. Eng.* **2020**, *181*, 115979. [CrossRef]
52. Katsoulas, N.; Sapounas, A.; De Zwart, F.; Dieleman, J.A.; Stanghellini, C. Reducing ventilation requirements in semi-closed greenhouses increases water use efficiency. *Agric. Water Manag.* **2015**, *156*, 90–99. [CrossRef]
53. McCartney, L.; Orsat, V.; Lefsrud, M.G. An experimental study of the cooling performance and airflow patterns in a model Natural Ventilation Augmented Cooling (NVAC) greenhouse. *Biosyst. Eng.* **2018**, *174*, 173–189. [CrossRef]
54. Yang, Y.; Guo, S.; Chen, Y. Estimated viability of greenhouse cooling technologies for growing a tomato crop under various climates. *Int. J. Agric. Biol. Eng.* **2021**, *14*, 90–95. [CrossRef]
55. Abdel-Ghany, A.M.; Al-Helal, I.M.; Alzahrani, S.M.; Alsadon, A.A.; Ali, I.M.; Elleithy, R.M. Covering Materials Incorporating Radiation-Preventing Techniques to Meet Greenhouse Cooling Challenges in Arid Regions: A Review. *Sci. World J.* **2012**, *2012*, 906360. [CrossRef]
56. McCartney, L.; Lefsrud, M.G. Field trials of the Natural Ventilation Augmented Cooling (NVAC) greenhouse. *Biosyst. Eng.* **2018**, *174*, 159–172. [CrossRef]
57. Abedrabboh, O.; Koç, M.; Biçer, Y. Comparative thermoeconomic assessment of renewable-driven hybrid-cooled sustainable greenhouses for subtropical regions. *Energy Convers. Manag.* **2024**, *300*, 117990. [CrossRef]
58. Migeon, C.; Pierart, A.; Lemesle, D.; Travers, A.; Chassériaux, G. A dehumidifying heat pump for greenhouses. *Acta Hortic.* **2012**, *952*, 485–492. [CrossRef]
59. Andrews, R.; Pearce, J.M. Environmental and economic assessment of a greenhouse waste heat exchange. *J. Clean. Prod.* **2011**, *19*, 1446–1454. [CrossRef]
60. Vermeulen, P. Alternative Sources of CO_2 for the Greenhouse Horticulture. 2014. Available online: https://www.researchgate.net/publication/282006970 (accessed on 17 February 2026).
61. van Tuyll, A.; Graamans, L.; Boedijn, A. *Carbon Dioxide Enrichment in a Decarbonised Future*; Wageningen University & Research: Wageningen, The Netherlands, 2022. [CrossRef]
62. Zhou, B.; Sun, W.; Guo, W.; Zheng, W.; Qu, M. Performance of a greenhouse heating system utilizing energy transfer between greenhouses based on the dual source heat pump. *Appl. Therm. Eng.* **2025**, *261*, 125088. [CrossRef]
63. Ahsan, T.M.A.; Ahamed, M.S.; Hassan, A.A. Hybrid ground source heat pump for sustainable greenhouse climate control in hot and humid region. *Sustain. Energy Technol. Assess.* **2025**, *83*, 104615. [CrossRef]
64. Ahsan, T.M.A.; Rahman, M.S.; Ahamed, M.S. Geothermal energy application for greenhouse microclimate management: A review. *Geothermics* **2025**, *127*, 103209. [CrossRef]
65. Gorjian, S.; Calise, F.; Kant, K.; Ahamed, M.S.; Copertaro, B.; Najafi, G.; Zhang, X.; Aghaei, M.; Shamshiri, R.R. A review on opportunities for implementation of solar energy technologies in agricultural greenhouses. *J. Clean. Prod.* **2021**, *285*, 124807. [CrossRef]
66. Vadiee, A.; Martin, V. Thermal energy storage strategies for effective closed greenhouse design. *Appl. Energy* **2013**, *109*, 337–343. [CrossRef]
67. Asgari, N.; McDonald, M.T.; Pearce, J.M. Energy Modeling and Techno-Economic Feasibility Analysis of Greenhouses for Tomato Cultivation Utilizing the Waste Heat of Cryptocurrency Miners. *Energies* **2023**, *16*, 1331. [CrossRef]
68. Fguiri, A.; Fatnassi, H.; Jeday, M.R.; Marvillet, C. Study of the energetic and the economic feasibility of a heating agricultural greenhouse using industrial waste-heat at low temperatures. *Int. J. Energy Environ. Econ.* **2017**, *25*, 269–282.
69. Esen, M.; Yuksel, T. Experimental evaluation of using various renewable energy sources for heating a greenhouse. *Energy Build.* **2013**, *65*, 340–351. [CrossRef]
70. Wu, T.; Mukhopadhyay, K.; Thomassin, P.J. A life cycle inventory analysis of wood pellets for greenhouse heating: A case study at Macdonald campus of McGill University. *AIMS Energy* **2016**, *4*, 697–722. [CrossRef]
71. Andersson, N.-E. *Properties of Thermal Screens Used for Energy Saving in Greenhouses*; Aarhus University: Aarhus, Denmark, 2010. Available online: https://pure.au.dk/ws/files/4247455/ref403.pdf (accessed on 18 February 2026).
72. Rabiu, A.; Na, W.-H.; Akpenpuun, T.D.; Rasheed, A.; Adesanya, M.A.; Ogunlowo, Q.O.; Kim, H.T.; Lee, H.-W. Determination of overall heat transfer coefficient for greenhouse energy-saving screen using Trnsys and hotbox. *Biosyst. Eng.* **2022**, *217*, 83–101. [CrossRef]
73. Rafiq, A.; Na, W.H.; Rasheed, A.; Lee, J.W.; Kim, H.T.; Lee, H.W. Measurement of longwave radiative properties of energy-saving greenhouse screens. *J. Agric. Eng.* **2021**, *52*, 1209. [CrossRef]
74. Zhang, E.; Elmi, M.; Jahid, A.; Duan, Q.; Wang, J. Assessing greenhouse covering systems for energy efficiency and solar irradiance modulation: A technical review. *Green Technol. Sustain.* **2026**, *4*, 100281. [CrossRef]
75. Song, S.; Jeon, J.; Yoon, S. Optimizing Energy Efficiency and Light Transmission in Greenhouses Using Rotating Low-Emissivity-Coated Envelopes. *Energies* **2025**, *18*, 1613. [CrossRef]

76. Lin, T.; Maier, C.R.; Liang, W.; Klause, N.; He, J.; Tissue, D.T.; Lan, Y.-C.; Sethuvenkatraman, S.; Goldsworthy, M.; Chen, Z.-H. A light-blocking greenhouse film differentially impacts climate control energy use and capsicum production. *Front. Energy Res.* **2024**, *12*, 1360536. [CrossRef]
77. Kim, H.-K.; Kang, G.-C.; Moon, J.-P.; Lee, T.-S.; Oh, S.-S. Estimation of Thermal Performance and Heat Loss in Plastic Greenhouses with and without Thermal Curtains. *Energies* **2018**, *11*, 578. [CrossRef]
78. Rasheed, A.; Na, W.H.; Lee, J.W.; Kim, H.T.; Lee, H.W. Optimization of Greenhouse Thermal Screens for Maximized Energy Conservation. *Energies* **2019**, *12*, 3592. [CrossRef]
79. Seginer, I.; van Straten, G.; van Beveren, P.J.M. Day-to-night heat storage in greenhouses: 1 Optimisation for periodic weather. *Biosyst. Eng.* **2017**, *161*, 174–187. [CrossRef]
80. Lyu, W.; Wang, Z.; Li, X.; Deng, G.; Xu, Z.; Li, H.; Yang, Y.; Zhan, B.; Zhao, M. Influence of the water tank size and air source heat pump size on the energy saving potential of the energy storage heating system. *J. Energy Storage* **2022**, *55*, 105542. [CrossRef]
81. Malinowski, M.; Bodziacki, S.; Famielec, S.; Huptyś, D.; Kurpaska, S.; Latała, H.; Basak, Z. Environmental Impact Assessment of Heat Storage System in Rock-Bed Accumulator. *Energies* **2025**, *18*, 3360. [CrossRef]
82. Amiri, L.; Ermagan, H.; Kurnia, J.C.; Hassani, F.; Sasmito, A.P. Progress on rock thermal energy storage (RTES): A state of the art review. *Energy Sci. Eng.* **2024**, *12*, 410–437. [CrossRef]
83. Nishad, S.; Krupa, I. Phase change materials for thermal energy storage applications in greenhouses: A review. *Sustain. Energy Technol. Assess.* **2022**, *52*, 102241. [CrossRef]
84. Zhu, J.; Zhang, X.; Hua, W.; Ji, J.; Lv, X. Current status and development of research on phase change materials in agricultural greenhouses: A review. *J. Energy Storage* **2023**, *66*, 107104. [CrossRef]
85. Cui, Y.; Gulfam, R.; Ishrat, Y.; Iqbal, S.; Yao, F. Recent Progress of Phase Change Materials and Their Applications in Facility Agriculture and Related-Buildings—A Review. *Buildings* **2024**, *14*, 2999. [CrossRef]
86. Liu, W.; Liu, G.; Shi, W.; Tang, X.; Wu, X.; Wu, J.; Xu, Z.; Zhang, F.; Yang, M. Experimental Investigation on Thermal Performance Optimization of Na2HPO4·12H2O-Based Gel Phase Change Materials for Solar Greenhouse. *Gels* **2025**, *11*, 434. [CrossRef] [PubMed]
87. Yang, T.; Liu, W.; Kramer, G.J.; Sun, Q. Seasonal thermal energy storage: A techno-economic literature review. *Renew. Sustain. Energy Rev.* **2021**, *139*, 110732. [CrossRef]
88. Gao, W.; Qadrdan, M.; Chaudry, M.; Wu, J.; Cardiff University. *Seasonal Storage of Heat in Boreholes*; UK Energy Research Centre: London, UK, 2023.
89. Sadeghi, H.; Jalali, R.; Singh, R.M. A review of borehole thermal energy storage and its integration into district heating systems. *Renew. Sustain. Energy Rev.* **2024**, *192*, 114236. [CrossRef]
90. Baeuerle, Y.I.; Arpagaus, C.; Haller, M.Y. A Review of Seasonal Energy Storage for Net-Zero Industrial Heat: Thermal and Power-to-X Storage Including the Novel Concept of Renewable Metal Energy Carriers. *Energies* **2025**, *18*, 2204. [CrossRef]
91. Asgari, N.; Hayibo, K.S.; Groza, J.; Rana, S.; Pearce, J.M. Greenhouse applications of solar photovoltaic driven heat pumps in northern environments. *Renew. Sustain. Energy Rev.* **2025**, *207*, 114920. [CrossRef]
92. Kim, D.-W.; Kim, M.-H.; Lee, D.-W. Economic and Environmental Analysis of Solar Thermal and Seasonal Thermal Energy Storage Based on a Renewable Energy Conversion System for Greenhouses. *Energies* **2022**, *15*, 6592. [CrossRef]
93. Zhang, L.; Xu, P.; Mao, J.; Tang, X.; Li, Z.; Shi, J. A low cost seasonal solar soil heat storage system for greenhouse heating: Design and pilot study. *Appl. Energy* **2015**, *156*, 213–222. [CrossRef]
94. Byon, Y.-S.; Jeong, J.-W. Energy Efficiency of Seasonal Solar Thermal Energy Storage System for Greenhouse Heating. In *5th International High Performance Buildings Conference*; Purdue University: West Lafayette, Indiana, 2018. Available online: https://docs.lib.purdue.edu/ihpbc/299 (accessed on 5 February 2026).
95. Boldyryev, S.; Krajačić, G.; Garafulić, E. Identification of industrial waste heat potential for district heating systems by pinch-based systematic graphical approach. *Energy Convers. Manag.* **2025**, *333*, 119804. [CrossRef]
96. Moser, S.; Jauschnik, G. Using Industrial Waste Heat in District Heating: Insights on Effective Project Initiation and Business Models. *Sustainability* **2023**, *15*, 10559. [CrossRef]
97. van Beveren, P.J.M.; Bontsema, J.; van 't Ooster, A.; van Straten, G.; van Henten, E.J. Optimal utilization of energy equipment in a semi-closed greenhouse. *Comput. Electron. Agric.* **2020**, *179*, 105800. [CrossRef]
98. Gilli, C.; Kempkes, F.; Munoz, P.; Montero, J.I.; Giuffrida, F.; Baptista, F.J.; Stepowska, A.; Stanghellini, C. Potential of different energy saving strategies in heated greenhouse. *Acta Hortic.* **2017**, *1164*, 467–474. [CrossRef]
99. Li, Y.; Ding, Y.; Li, D.; Miao, Z. Automatic carbon dioxide enrichment strategies in the greenhouse: A review. *Biosyst. Eng.* **2018**, *171*, 101–119. [CrossRef]
100. Marchi, B.; Zanoni, S.; Pasetti, M. Industrial Symbiosis for Greener Horticulture Practices: The CO_2 Enrichment from Energy Intensive Industrial Processes. *Procedia CIRP* **2018**, *69*, 562–567. [CrossRef]
101. Wang, A.; Lv, J.; Wang, J.; Shi, K. CO_2 enrichment in greenhouse production: Towards a sustainable approach. *Front. Plant Sci.* **2022**, *13*, 1029901. [CrossRef] [PubMed]

102. Ghiat, I.; Mahmood, F.; Govindan, R.; Al-Ansari, T. CO_2 utilisation in agricultural greenhouses: A novel 'plant to plant' approach driven by bioenergy with carbon capture systems within the energy, water and food Nexus. *Energy Convers. Manag.* **2021**, *228*, 113668. [CrossRef]
103. Sapounas, A.; Katsoulas, N.; Slager, B.; Bezemer, R.; Lelieveld, C. Design, Control, and Performance Aspects of Semi-Closed Greenhouses. *Agronomy* **2020**, *10*, 1739. [CrossRef]
104. Kajolinna, T.; Balshakou, S.; Mustonen, J. Assessment of carbon dioxide quality from industrial point sources for carbon utilization. *Int. J. Greenh. Gas Control.* **2025**, *148*, 104527. [CrossRef]
105. Chen, S.; Liu, A.; Tang, F.; Hou, P.; Lu, Y.; Yuan, P. A Review of Environmental Control Strategies and Models for Modern Agricultural Greenhouses. *Sensors* **2025**, *25*, 1388. [CrossRef]
106. Mengesha, K.A.; Jin, G.-G.; Son, Y.-D. Comparison of the feedback linearization plus LQR controller and the PID controller for greenhouse indoor climate. *Int. J. Agric. Biol. Eng.* **2025**, *18*, 74–82. [CrossRef]
107. Bwambale, E.; Wanyama, J.; Adongo, T.A.; Umukiza, E.; Ntole, R.; Chikavumbwa, S.R.; Sibale, D.; Jeremaih, Z. A review of model predictive control in precision agriculture. *Smart Agric. Technol.* **2025**, *10*, 100716. [CrossRef]
108. Kim, J.; You, F. Energy-efficient greenhouse climate control using Gaussian process-based stochastic model predictive control. *Appl. Energy* **2025**, *391*, 125841. [CrossRef]
109. Beucler, T.; Gentine, P.; Yuval, J.; Gupta, A.; Peng, L.; Lin, J.; Yu, S.; Rasp, S.; Ahmed, F.; O'Gorman, P.A.; et al. Climate-invariant machine learning. *Sci. Adv.* **2024**, *10*, eadj7250. [CrossRef]
110. Liu, K.; Ji, T.; Li, M.; Yang, X.; Sun, J.; Liu, H.; Liu, R. Prediction of greenhouse temperature and humidity across growing seasons: Hybridization of process-based model and deep neural networks. *Inf. Process. Agric.* 2025, *in press*. [CrossRef]
111. Zhou, X.; Liu, Q.; Katzin, D.; Qian, T.; Heuvelink, E.; Marcelis, L.F.M. Boosting the prediction accuracy of a process-based greenhouse climate-tomato production model by particle filtering and deep learning. *Comput. Electron. Agric.* **2023**, *211*, 107980. [CrossRef]
112. Sun, Z.; Yao, Q.; Jin, H.; Xu, Y.; Hang, W.; Chen, H.; Li, K.; Shi, L.; Gu, J.; Zhang, Q.; et al. A novel in-situ sensor calibration method for building thermal systems based on virtual samples and autoencoder. *Energy* **2024**, *297*, 131314. [CrossRef]
113. Sun, Z.; Yao, Q.; Shi, L.; Jin, H.; Xu, Y.; Yang, P.; Xiao, H.; Chen, D.; Zhao, P.; Shen, X. Virtual sample diffusion generation method guided by large language model-generated knowledge for enhancing information completeness and zero-shot fault diagnosis in building thermal systems. *J. Zhejiang Univ. A* **2025**, *26*, 895–916. [CrossRef]
114. Ariesen-Verschuur, N.; Verdouw, C.; Tekinerdogan, B. Digital Twins in greenhouse horticulture: A review. *Comput. Electron. Agric.* **2022**, *199*, 107183. [CrossRef]
115. Arshad, J.; Sheheryar, C.A.A.; Rahmani, M.K.I.; Qayyum, A.; Nasir, R.; Chauhdary, S.T.; Almalki, K.J. Simulink-Driven Digital Twin Implementation for Smart Greenhouse Environmental Control. *Egypt. Inform. J.* **2025**, *30*, 100679. [CrossRef]
116. Akintan, O.; Babawale, S.; Olomo, A.; Adeyemo, R.; Opadotun, O.; Ajayi, J.T.; Mba, P.C.; Njoku, J.N.; Chesang, A.; Zahid, A.; et al. A Digital Twin Framework for Sensor Selection and Microclimate Monitoring in Greenhouses. *AgriEngineering* **2025**, *7*, 315. [CrossRef]
117. Slimani, H.; El Mhamdi, J.; Jilbab, A. Real-time greenhouse management using IoT, digital twin, and augmented reality for optimal control and decision-making. *Acta IMEKO* **2025**, *14*, 1–15. [CrossRef]
118. Ajagekar, A.; Mattson, N.S.; You, F. Energy-efficient AI-based Control of Semi-closed Greenhouses Leveraging Robust Optimization in Deep Reinforcement Learning. *Adv. Appl. Energy* **2023**, *9*, 100119. [CrossRef]
119. Mansour, M.; Sathyanarayanan, K.K.; Sauerteig, P.; Streif, S. Adaptive robust greenhouse climate control: Combining deep reinforcement learning and economic optimization. *Smart Agric. Technol.* **2025**, *12*, 101327. [CrossRef]
120. Mallick, S.; Airaldi, F.; Dabiri, A.; Sun, C.; De Schutter, B. Reinforcement learning-based model predictive control for greenhouse climate control. *Smart Agric. Technol.* **2025**, *10*, 100751. [CrossRef]
121. de Zwart, H.F. Energy conserving dehumidification of greenhouses. *Acta Hortic.* **2014**, *1037*, 203–210. [CrossRef]
122. Energy Efficiency and Conservation Authority (EECA). Covered Cropping Pathway. Available online: https://www.eeca.govt.nz/co-funding-and-support/products/covered-cropping-decarbonisation-pathway/ (accessed on 14 February 2026).
123. EECA. What's Right for Your Greenhouse? 2024. Available online: https://www.eeca.govt.nz/assets/EECA-Resources/Co-funding/Sector-Decarb-Files/Reducing-Energy-Emissions-Decision-Trees-for-Covered-Cropping.pdf (accessed on 14 February 2026).
124. Pratt, C.T. Optimising Greenhouse Environment and Energy Inputs for Sweet Pepper Production in the UK—A Commercial Demonstration of the Use of Thermal Screens and Advanced Climate Control. 2006. Available online: https://projectbluearchive.blob.core.windows.net/media/Default/Research%20Papers/Horticulture/PC%20227%20Final%20report%202007.pdf (accessed on 14 February 2026).
125. Nemś, A.; Nemś, M.; Świder, K. Analysis of the Possibilities of Using a Heat Pump for Greenhouse Heating in Polish Climatic Conditions—A Case Study. *Sustainability* **2018**, *10*, 3483. [CrossRef]

126. Li, N.; Xu, W.; Zhang, Y.; Ma, W.; Ren, Y. Energy Saving Technologies and Practices in Facility Agriculture in Cold Regions. *Agronomy* **2025**, *15*, 204. [CrossRef]
127. Semple, L.; Carriveau, R.; Ting, D.S.-K. A techno-economic analysis of seasonal thermal energy storage for greenhouse applications. *Energy Build.* **2017**, *154*, 175–187. [CrossRef]
128. Ramos-Teodoro, J.; Álvarez, J.D.; Torres, J.L. A methodology for feasibility analyses of district heating networks: A case study applied to greenhouse crops. *Energy* **2024**, *301*, 131695. [CrossRef]
129. Tomson, F.; Lovegrove, T.; Allen, O.; Honid, D. Feasibility Study Minewater District Heat Network Horden, Durham County Council. 2023. Available online: https://communityenergypathways.org.uk/wp-content/uploads/2023/11/Durham-Feasibility-Study-FINAL.pdf (accessed on 14 February 2026).
130. Banks, V.; Krebs, M. Final Report: Technical Feasibility Study of the Geothermal Capability of the Penobsquis Mine Site, Penobsquis, NB, Fredericton, New Brunswick, Canada. 2018. Available online: https://sussex.ca/media/Phase-1-Final-Report-Geothermal-Feasibility-Study-1.pdf (accessed on 14 February 2026).
131. Mikunda, T.; Neele, F.; Wilschut, F.; Hanegraaf, M. *A Secure and Affordable CO_2 Supply for the Dutch Greenhouse Sector*; TNO: The Hague, The Netherlands, 2015.
132. Torrellas, M.; Antón, A.; Ruijs, M.; Victoria, N.G.; Stanghellini, C.; Montero, J.I. Environmental and economic assessment of protected crops in four European scenarios. *J. Clean. Prod.* **2012**, *28*, 45–55. [CrossRef]
133. Graamans, L.; Baeza, E.; van den Dobbelsteen, A.; Tsafaras, I.; Stanghellini, C. Plant factories versus greenhouses: Comparison of resource use efficiency. *Agric. Syst.* **2018**, *160*, 31–43. [CrossRef]
134. IEA. Energy Efficiency 2025, Paris. 2025. Available online: https://www.iea.org/reports/energy-efficiency-2025 (accessed on 15 February 2026).
135. IEA. Heat Pumps. 2024. Available online: https://www.iea.org/energy-system/buildings/heat-pumps (accessed on 15 February 2026).
136. MarketsandMarkets. Commercial Greenhouse Market Trends, Growth, and Forecast. 2023. Available online: https://www.marketsandmarkets.com/Market-Reports/commercial-greenhouse-market-221045451.html (accessed on 17 February 2026).
137. ResearchAndMarkets. Global Commercial Greenhouse Market to 2028: Ability to Provide High Yield Production Drives Growth. 2023. Available online: https://www.businesswire.com/news/home/20230425005608/en/Global-Commercial-Greenhouse-Market-to-2028-Ability-to-Provide-High-Yield-Production-Drives-Growth---ResearchAndMarkets.com (accessed on 17 February 2026).
138. Grand View Research. Greenhouse Market (2026–2033). 2024. Available online: https://www.grandviewresearch.com/industry-analysis/greenhouse-market-report (accessed on 17 February 2026).
139. Insights, F.B. Commercial Greenhouse Market Size. 2026. Available online: https://www.fortunebusinessinsights.com/commercial-greenhouse-market-114996 (accessed on 17 February 2026).
140. FAO. *World Food and Agriculture—Statistical Yearbook 2024*; FAO: Rome, Italy, 2024. [CrossRef]
141. FAO. *Gross Domestic Product and Agriculture Value Added 2014–2023*; FAO: Rome, Italy, 2025. [CrossRef]
142. OECD-FAO. *OECD-FAO Agricultural Outlook 2025–2034*; OECD Publishing: Paris, France, 2025. [CrossRef]
143. United Nations. Goal 2: Zero Hunger, United Nations. Available online: https://www.un.org/sustainabledevelopment/hunger/ (accessed on 17 February 2026).
144. Nations, U. Food Security and Nutrition and Sustainable Agriculture, United Nations. Available online: https://sdgs.un.org/topics/food-security-and-nutrition-and-sustainable-agriculture (accessed on 17 February 2026).
145. FAO. Achieving SDG 2 Without Breaching the 1.5 °C Threshold: A Global Roadmap Part 1. Available online: https://www.fao.org/interactive/sdg2-roadmap/en/ (accessed on 17 February 2026).

Disclaimer/Publisher's Note: The statements, opinions and data contained in all publications are solely those of the individual author(s) and contributor(s) and not of MDPI and/or the editor(s). MDPI and/or the editor(s) disclaim responsibility for any injury to people or property resulting from any ideas, methods, instructions or products referred to in the content.

energies

MDPI

Review

Applications of Methods of Solving Inverse Heat Conduction Problems for Energy-Intensive Industrial Processes and Energy Conversion—Current State of the Art and Recent Challenges

Magda Joachimiak * and Damian Joachimiak

Faculty of Environmental Engineering and Energy, Institute of Thermal Energy, Poznan University of Technology, 60-965 Poznań, Poland; damian.joachimiak@put.poznan.pl
* Correspondence: magda.joachimiak@put.poznan.pl

Abstract

This paper presents methods and applications of inverse heat conduction problems (IHCPs) that are ill-posed in the Hadamard sense. The IHCP solution allows for the determination of boundary conditions in the form of heat flux or temperature in places where measurement is impossible or difficult to perform. The applications of IHCP solutions to energy-intensive industrial processes, such as heat treatment and thermochemical treatment, are described. Examples are given of determining boundary conditions on the inner surface of the wall of a power boiler and piston machine, as well as on the surface of a gas turbine blade. It is noted that the application of IHCP solutions to the above-mentioned issues often requires simplification of the computational model, in particular, the method of stabilising the inverse problem (IP). For this purpose, quasi-regularisation of IP and machine learning are currently used. Methods with stabilising properties and neural networks were identified as a challenging and interesting direction for the development of IHCP solutions.

Keywords: heat transfer; inverse heat conduction problem (IHCP); quasi-regularisation; regularisation; neural networks; boilers; gas turbines; heat treatment; thermochemical treatment

1. Introduction

The concept of a well-posed problem was introduced by Jacques Hadamard [1]. According to him, a problem is well-posed when its solution exists, is unique and stable. In such a case, we say that a so-called direct problem (DP) is being solved. This type of analysis involves determining the differential or integral equations that describe the problem, the shape, type, and size of the area, the initial and boundary conditions, the properties of the substances contained in the area, as well as the internal energy sources and external forces acting on the system. If all information regarding the mathematical model is known, then the problem is well-posed [2]. The state of knowledge necessary to pose and solve a direct problem is often impossible to obtain in real-world engineering problems. If any of the above information from the mathematical model is unknown, for example, about the boundary conditions or the shape of the area, then the inverse problem is considered. Inverse problems are ill-posed in the Hadamard sense [1]. The solution to the inverse heat conduction problem (IHCP) involves determining the initial conditions, the boundary conditions, or the properties of the material, such as the thermal conductivity coefficient or the specific heat, based on the observed temperature values within the area [3,4]. The most

common inverse problem during the exploitation of industrial machinery and equipment is to determine the boundary condition in the form of temperature or heat flux for a part of the area based on the temperature measurement inside it. This problem is termed the boundary inverse problem [3–6]. The second type of inverse problem used in solving engineering problems is the Cauchy problem. In this case, the boundary condition for part of the area is unknown, while for another part of the area, two boundary conditions are known, most often temperature and heat flux [3–6].

The solution of the IHCP comes down to solving a differential equation of heat conduction of the form [7]

$$\frac{\partial}{\partial x}\left(\lambda\frac{\partial T}{\partial x}\right)+\frac{\partial}{\partial y}\left(\lambda\frac{\partial T}{\partial y}\right)+\frac{\partial}{\partial z}\left(\lambda\frac{\partial T}{\partial z}\right)+q_V=c\rho\frac{\partial T}{\partial t} \tag{1}$$

where x, y, z—coordinates in the Cartesian system [m], T—temperature [K], t—time [s], λ—thermal conductivity [W/mK], c—specific heat [J/kgK], ρ—density [kg/m^3], and q_V—power of internal heat sources related to the unit volume [W/m^3]. The differential Equation (1) is solved with the known boundary condition on the part of the boundary Γ_1 and the sought boundary condition on the part of the boundary Γ_2, taking into account the measurement of the temperature on the curve Γ*, as shown in Figure 1. Depending on the problem under consideration, Equation (1) can be simplified in practice. The absence of heat sources will mean $q_V = 0$. When solving IHCPs, it is important to determine the direction of heat transfer in the case under consideration. Knowledge of physical phenomena is the basis for determining whether calculations can be performed for a one-dimensional $\left(\frac{\partial T}{\partial x}\neq 0, \frac{\partial T}{\partial y}=0, \frac{\partial T}{\partial z}=0\right)$ or two-dimensional $\left(\frac{\partial T}{\partial x}\neq 0, \frac{\partial T}{\partial y}\neq 0, \frac{\partial T}{\partial z}=0\right)$ problem. For a boiler wall or gas turbine blade, the problem often comes down to a two-dimensional equation. The question must be asked whether a non-stationary $\left(\frac{\partial T}{\partial t}\neq 0\right)$ or stationary $\left(\frac{\partial T}{\partial t}=0\right)$ problem should be considered. When temperature changes over time can be omitted, the steady-state problem is analysed. Many studies consider the optimal cooling of gas turbine blades as a steady-state problem. On the other hand, heat treatment and thermochemical treatment problems analysed using the IHCP solution are non-stationary problems. Significant changes in the thermal conductivity coefficient λ, specific heat c, and density ρ also affect the differential equation considered when solving IHCPs. In heat treatment (e.g., hardening) and thermochemical (e.g., nitriding) processes, taking into account the temperature ranges of these processes and the properties of the steels being treated, the dependence of the thermal conductivity coefficient λ and specific heat c on temperature must be taken into account when solving IHCPs.

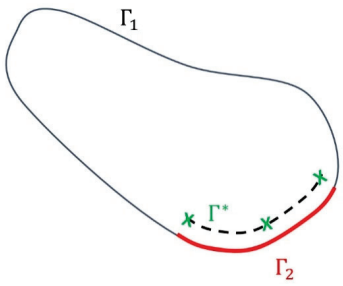


Figure 1. Boundaries Γ_1, Γ_2 and measurement points on the curve Γ*.

To calculate the temperature or heat flux at the boundary Γ_2, the minimum of the functional of the form should be determined.

$$I_1=\sum_{i=1}^{M}\left(T_i^c-T_i^*\right)^2 \tag{2}$$

https://doi.org/10.3390/en19051291

Functional (2) describes the sum of squares of distances between the calculated temperature T_i^c and the measured temperature T_i^* at the i-th measurement point for $i = 1, 2, \ldots, M$. Using various numerical techniques, the differential Equation (1) is algebraised. Taking into account the information contained in the boundary condition at the boundary Γ_1 and the temperature measured at the measurement points on the curve Γ^*, together with the functional (2), the IHCP can be reduced to solving a system of equations

$$\boldsymbol{A}\{x\} = \{b\} \tag{3}$$

where the elements of the vector $\{x\}$ are the requested boundary condition or parameters that allow the aforementioned boundary condition to be determined at the boundary Γ_2. The elements of matrix $\boldsymbol{A}$ and vector $\{b\}$ usually result from the form of the direct problem.

During the operation of machines and equipment, it is sometimes impossible to measure the temperature of walls with high thermal loads, or the measurement is subject to a very large error [7,8]. Examples of surfaces where measurement is difficult or impossible include: the inner wall of a power boiler, the surface of a gas turbine blade, the body of a gas or steam turbine, the surface of a charge being processed in a furnace for thermochemical treatment, and many others. Determining the temperature or heat flux on such surfaces is based on solving the inverse heat conduction problem. Inverse problems have very widespread technical applications in the analysis of heat flow in machines and devices [6,9].

Inverse problems are often numerically unstable. This is because inverse problems are numerically ill-posed in the Hadamard sense. This means that a small disturbance in the input data can cause a very large disturbance in the result. In such cases, the IHCP solution may be ineffective. In industrial applications, the input data are measurement data. The measured variables are temperature and heat flux. Measurement errors result from the type and accuracy of measuring instruments such as thermocouples and heat flux sensors. When measuring temperature and heat flux, contact resistance occurs at the point of contact between the measured surface and the measuring sensor. This is particularly important for highly dynamic heat transfer processes. In addition, there are thermocouple positioning errors of ± 0.2 mm, which also affect the accuracy of the result. In most cases, the result is a boundary condition in the form of temperature or heat flux on a surface where measurement is impossible or very difficult to perform. In addition, the possibility of placing a limited number of thermocouples and the inability to place thermocouples at points that are advantageous for calculations must be taken into account.

Currently, multiple numerical studies are being conducted on computational methods that allow stable solutions to be obtained for IHCPs [3–6,10]. Computational techniques that stabilise the solution to an inverse problem (IP) are referred to as regularisation.

One of the IHCP regularisation techniques is Tikhonov regularisation [10], which boils down to correcting the functional (2)

$$J = I_1 + \gamma I_2 \tag{4}$$

where the functional I_1 is described in Formula (2), γ is the regularisation parameter, and I_2 is the regularisation functional. The application of regularisation also modifies matrix A in matrix Equation (3). The difficulty lies in selecting the regularisation parameter γ in such a way that it stabilises the IP. The Morozov criterion [11–19], the L-curve method [14,20–22], and the energy integral [14] are used for this purpose. In [23], a method for automatic selection of the regularisation parameter is presented. Modifications of the classical Tikhonov regularisation method [24,25] and the iterative Tikhonov regularisation method [26] were investigated. Regularisation of the IHCP was also performed using the

https://doi.org/10.3390/en19051291

SVD algorithm [27,28], discrete Fourier transform [29], and optimal selection of the integral parameter [30].

This paper presents numerous applications of IHCP solutions for energy-intensive industrial processes and energy conversion. It indicates areas of possible application of quasi-regularisation and machine learning for solving IHCPs in terms of the aforementioned industrial applications.

2. Methods of Solving IHCPs and Their Quasi-Regularisation for Industrial Applications

To date, many methods have been developed to solve IHCPs. These methods vary greatly depending on the geometry of the area and whether a steady-state or unsteady problem is being considered. For simple geometries such as a rectangle, circle, or ring, numerical studies were conducted to develop analytical–numerical solutions [3–6,31–38]. The solution to the unsteady inverse problem for a circle and a ring is presented in [31,34], respectively. An analytical–numerical calculation method for the stationary inverse problem of heat conduction using Chebyshev polynomials for rectangular geometry was also analysed [36]. In turn, in [37,38], the method of fundamental solutions was also applied to a rectangle. The heat conduction equation was also solved using the Treffetz function [32,33,39]. Numerous research works on methods for solving inverse problems for simple geometries and analysing their stability formed the basis for the development of numerical methods for complex geometries and industrial applications.

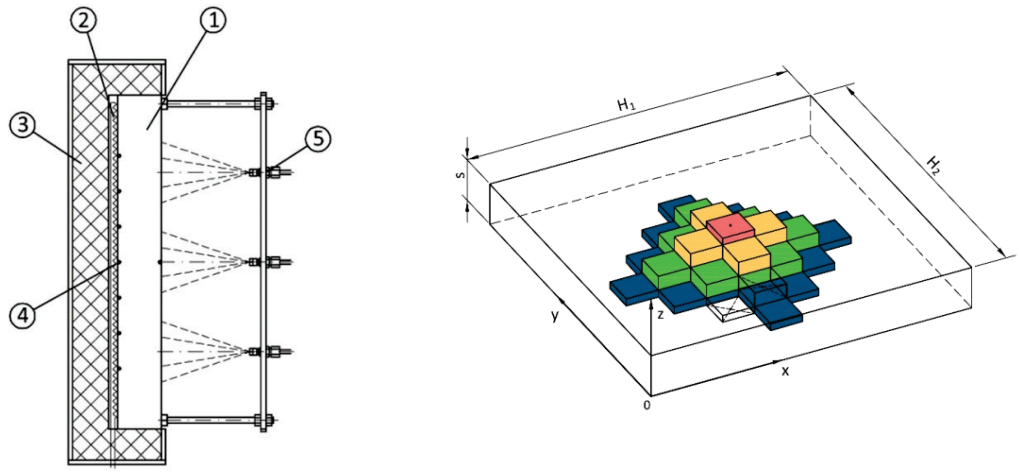
In order to be used in industry, the IHCP solution must be numerically stable. The solution is stabilised by IHCP regularisation. Currently, a quasi-regularisation approach is also used to solve IHCPs. In this case, the Tikhonov regularisation with the selection of the regularisation parameter according to Formula (4) is not used. The solution is stabilised by selecting, for example, the time step or the integration method in such a way as to average the input data or values in the calculation process. A properly selected quasi-regularisation method allows for the stabilisation of the IHCP solution while preserving information about the heat transfer process, enabling its analysis. The quasi-regularisation method should be selected individually for each calculation model and industrial application. Quasi-regularisation approaches are often characterised by a simpler mathematical model than models using classical regularisation, which creates great potential for the application of these solutions in industrial applications. Despite its many advantages, quasi-regularisation is a compromise between accuracy and stability of the solution.

2.1. Boilers and Heating Devices

The studies in [40,41] present a solution to the geometric IP in determining the thickness of the stone in a steam boiler pipe. Inverse methods were also used to determine the thermal boundary conditions of the boiler membrane water-wall [42]. Simulations of changing thermal loads on the wall of a heating device using Chebyshev polynomials to solve IHCPs are presented in [43]. The inverse heat transfer method was used to identify the sediment profile in a heat exchanger pipe with two-phase and turbulent flow [44]. Sediments that exist in industrial heat exchangers reduce the thermal efficiency of the exchanger and consequently cause energy losses. To solve the problem, the conjugate gradient method and the volume of fluid method in Open FOAM were used. The inverse problem solution method used is stable and inexpensive, making it suitable for real-world industrial problems. In turn, the estimation of the heat flux and convective heat transfer coefficient in the water membrane of a steam boiler by solving the IHCP using an iterative algorithm is described in [45].

https://doi.org/10.3390/en19051291

It is possible to determine thermal stresses in the boiler pressure components if the fluid temperature and heat transfer coefficient on the inner surface are known. Determining these values under industrial conditions is difficult. However, it is possible to calculate the boundary conditions by solving the IHCP, as described in [46]. The inverse space marching method (ISMM) is presented to determine the heat transfer coefficient on the surface of a thick-walled plate that is sprayed with water (Figure 2a). The experimental stand consists of a steel plate (Figure 2a-1) heated by electric heaters (Figure 2a-2) and insulated on the heater side (Figure 2a-3). The thermocouples are placed on the plate on the side of the heaters (Figure 2a-4). The other surface of the plate is sprayed with water (Figure 2a-5). The plate was divided into control volumes (Figure 2b). Each of the control volume layers is marked with a different colour in Figure 2b. The temperature values measured in the blue layer are used to determine the temperatures in the control volumes of the green layer. In the next step, the temperatures in the yellow layer are calculated, and finally, at the edge of the plate in the red layer.



(**a**) (**b**)

Figure 2. (**a**) Cross-section of the spray cooling stand for thick-walled plate; (**b**) dividing the plate into control volumes [46].

For each control volume, the finite volume method was used to write the energy balance equation. Through step-by-step calculations in the control volumes, the boundary condition is determined. The ISMM method is easy to use and demonstrates numerical stability. The short calculation time for this computational method allows it to be used for online monitoring of thermal stresses in power plant components. The appropriate selection of the number of control volumes allows a stable solution to be obtained without a significant loss of information on the temperature distribution in the wall [46], which gives the regularisation properties of the method. The ISMM method includes a quasi-regularisation approach and has been applied to analyse heat transfer in power boilers.

In the next step, ISMM was used to develop a new technique to measure the temperature of superheated steam in conventional power plants [47] and to calculate the transient thermal stresses on the internal surface of a thick-walled pipe weakened by a hole [48]. The subject of controlling the temperature and thermal stress in the components of the power boiler during start-up, shutdown, and load change to reduce the unit's connection time to the power grid using ISMM, which is a method that uses quasi-regularisation, is presented in [49].

https://doi.org/10.3390/en19051291

2.2. Heat Treatment and Thermochemical Treatment

Another area of research worth mentioning where IHCP solutions are applied is heat treatment [50–58] and thermochemical treatment [24,59–62]. In [51], a solution to the one-dimensional IHCP was proposed for heat-treated surfaces. Analyses were performed to determine the temperature of the laser-heated surface and the spray-cooled surface. A mathematical model of the solution was developed using the shifting function method, the least-squares method, and measured temperatures. Quenching of moving metal plates using water jets was analysed using a two-dimensional inverse heat conduction solution [52]. Analyses of the quenching process using IHCPs are also described in [53–56,58].

Machine components such as crankshafts and gears are gas-nitrided. Controlling the surface temperature of thermochemically treated components is difficult to achieve in a closed furnace, where the gas surrounding the load is in constant motion, forced by a fan, and the gas temperature rises to 550 °C. Heat transfer in the furnace occurs through forced convection and, to a large extent, through radiation from the furnace and gas [59,62]. Knowledge of the edge temperature of treated components allows the process to be carried out in such a way that surfaces with the required properties are produced [63]. Controlling this temperature also allows the process time to be reduced without exceeding the thermal stresses [61]. The boundary conditions on elements subjected to thermochemical treatment can be determined by solving the IHCP. This issue has been considered in [24,59–62,64]. The study in [62] presents an analytical and numerical model to solve the IHCP for a cylinder. In industrial applications, it is very important that the method used to solve the IP is stable and does not require regularisation, or that the regularisation method is reliable and automatic. The study presented in [62] describes a quasi-regularisation method consisting of selecting the time step Δt in such a way as to eliminate oscillations in the solution. The time step Δt was introduced by writing the partial derivative on the right-hand side of the heat conduction differential Equation (1).

$$\frac{\partial T}{\partial t} = \frac{T(x, y, t_k) - T(x, y, t_{k-1})}{\Delta t} \tag{5}$$

The stabilisation method obtained by selecting Δt was used to determine the boundary conditions (T—temperature, q—heat flux, and h—heat transfer coefficient) for a cylinder subjected to thermochemical treatment at different heating rates and fan speeds [62]. In numerical tests, the relative error of the boundary condition δBC was calculated according to the formula

$$\delta BC = \frac{\left| BC_{as} - BC_{ip} \right|}{BC_{as}} \tag{6}$$

where BC is the boundary condition (T, q, or h), as is the analytical solution, and ip is the inverse problem. The ratio of the average relative error for the time step $\Delta t = i$ to the average relative error for the time step $\Delta t = 1$ is described by the formula

$$f(\Delta t) = \frac{av[\delta BC(\Delta t = i)]}{av[\delta BC(\Delta t = 1)]} \tag{7}$$

The ratio of the maximum relative error for the time step $\Delta t = i$ to the maximum relative error for the time step $\Delta t = 1$ is described by the formula

$$g(\Delta t) = \frac{max[\delta BC(\Delta t = i)]}{max[\delta BC(\Delta t = 1)]} \tag{8}$$

Based on the research presented in [62], it can be concluded that changing the time step from $\Delta t = 1$ to $\Delta t = 10$ resulted in a decrease in the ratio of the average relative errors f (Formula (7)) from 1 to 0.5145 for temperature, 0.1441 for heat flux, and 0.1503

https://doi.org/10.3390/en19051291

for the heat transfer coefficient (Table 1). In turn, for the ratio of maximum relative errors g (Formula (8)), the change in the time step resulted in a decrease in the value of the g function to 0.3486 for temperature, 0.0947 for heat flux, and 0.0945 for heat transfer coefficient (Table 1). The data in Table 1 clearly indicate the significant impact of the time step Δt on the stability of the solution to the IHCP.

Table 1. Values of functions $f(\Delta t)$ and $g(\Delta t)$ for different types of boundary conditions *BC* (temperature T, heat flux q, and heat transfer coefficient h) for time steps $\Delta t = 1$, $\Delta t = 2$, $\Delta t = 5$, $\Delta t = 10$ s.

	Type of *BC*	***i* = 1 [s]**	***i* = 2 [s]**	***i* = 5 [s]**	***i* = 10 [s]**
$f(\Delta t)$	T	1	0.7526	0.5921	0.5145
	q	1	0.5508	0.2298	0.1441
	h	1	0.5532	0.2362	0.1503
$g(\Delta t)$	T	1	0.6732	0.4431	0.3486
	q	1	0.6603	0.2256	0.0947
	h	1	0.6300	0.2209	0.0945

The time step was also a method of stabilising the IHCP solution, where the obtained temperature distribution was used to determine thermal stresses in cylindrical pressure components [65].

In [24], the analysis of heat transfer during the gas nitriding process was extended to include a detailed analysis of the cooling stage. The computational model was supplemented with a modified Tikhonov regularisation method. In turn, in [59], an analysis of experimental studies obtained under industrial conditions was presented and a method using the Broyden–Fletcher–Goldfarb–Shanno algorithm (BFGS) was applied to solve the IHCP. The studies presented in [60,62] were used to analyse heat transfer in an aluminium extrusion die subjected to gas nitriding [64].

A new method for solving the inverse heat conduction problem for the Helmholtz equation using the Trefftz function is presented in [61]. The heat flux sought at the edge Γ_2 of the thermochemically treated roller is approximated using a step function (Figure 3) and is written using a linear combination

$$q(x) = \sum_{i=0}^{N} q_i(x) = \sum_{i=0}^{N} \varphi_i(x) c_i \tag{9}$$

of the sought coefficients c_i and the functions φ_i for $i = 0, 1, 2, \ldots, N$. The function φ_i was defined by the formula

$$\varphi_i(x) = \begin{cases} 1 \text{ for x} \in \Gamma_{2,i} \\ 0 \text{ for } \notin \Gamma_{2,i} \end{cases} \tag{10}$$

and shown in Figure 4. For the method under consideration, the functions $\varphi_i(x)$ can be interpreted as an impulse with a value of 1 on the i-th fragment of the boundary Γ_2, which is marked $\Gamma_{2,i}$ (Figure 4). The heat flux $q(x)$ on the boundary Γ_2 is sought, which is a composite of heat fluxes with a constant value $q_i(x)$ for successive fragments of the boundary. The coefficients c_i are obtained from the IHCP solution. As a result, the flux $q(x)$ is a step function (Figure 3) that is the average of the heat flux on the boundary. The temperature in the analysed area can be written as a combination of the Trefftz functions $\psi_i(x, y)$ added to the value of the function $T_1(x, y)$ obtained from the solution of the direct problem of the form.

$$T(x, y) = T_1(x, y) + \sum_{i=0}^{N} \psi_i(x, y) c_i \tag{11}$$

https://doi.org/10.3390/en19051291

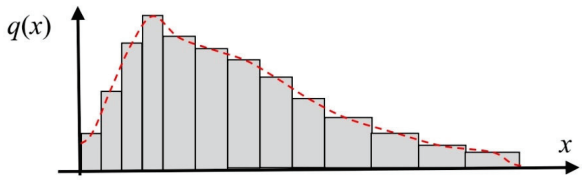


Figure 3. Approximation of the heat flux using a step function.

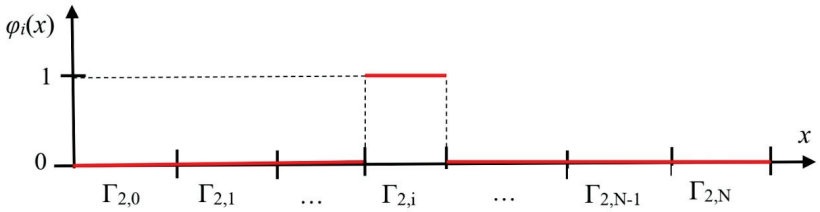


Figure 4. Distribution of the step function $\varphi_i(x)$ (red line) at the boundary Γ_2.

Examples of distributions of the functions $\psi_i(x, y)$ for $i = 0, 1, 2, \ldots, 5$ are shown in Figure 5.

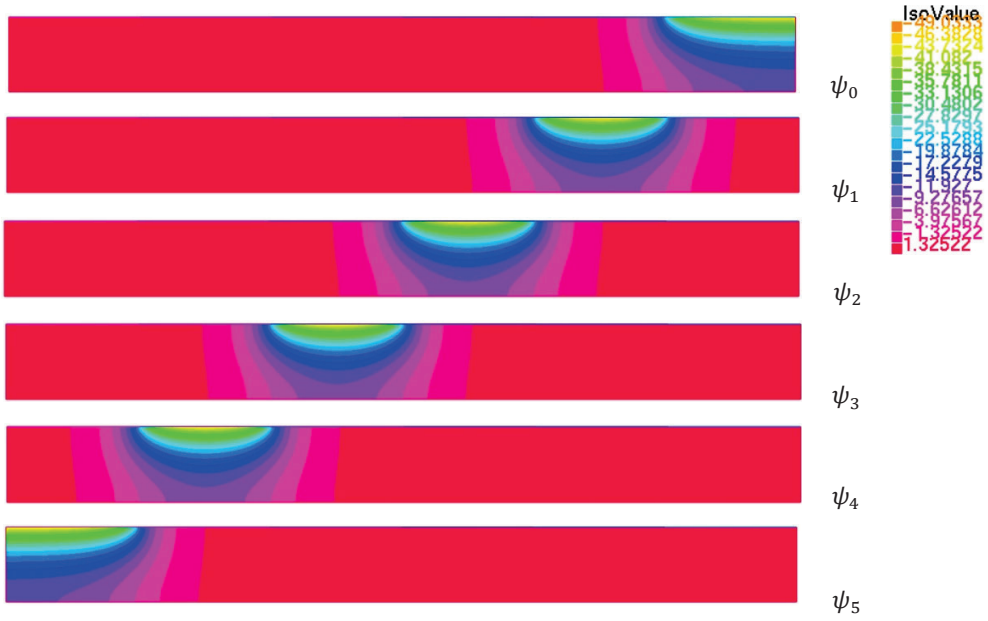


Figure 5. Trefftz functions $\psi_0, \psi_1, \psi_2, \psi_3, \psi_4$ and ψ_5.

This method is described in more detail for steady-state IHCPs in [66,67], and for the unsteady-state problem in [61].

It has been shown that the appropriate selection of the number of functions φ_i and the division of the boundary Γ_2 into segments $\Gamma_{2,0}, \Gamma_{2,1}, \ldots, \Gamma_{2,N-1}, \Gamma_{2,N}$ has a significant impact on the stability of the IP solution. The appropriate selection of step functions allowed for the stabilisation of the inverse problem solution without the need to apply classical Tikhonov regularisation. The appropriate selection of the number of segments and their length on the boundary Γ_2 constitutes a quasi-regularisation of the IHCP solution method described in [61,66,67]. A dense division of the boundary Γ_2 allows for a more accurate approximation of the boundary condition. On the other hand, a smaller number of segments on the boundary Γ_2 results in greater averaging properties and thus stabilises the method. Increasing the density of the division for a fragment of the boundary with greater temperature and heat flux variability allows us to approach a division that is a compromise

https://doi.org/10.3390/en19051291

between the accuracy and stability of the IHCP solution through quasi-regularisation. The method can be successfully applied to the analysis of heat transfer in elements with complex geometry. The calculations are based on variational calculus and are performed in the freeFEM solver [68]. In the initial part of the algorithm, a complex geometry is assumed, which is described parametrically. The known boundary conditions, the division of the boundary where the boundary condition is sought, the coordinates of the temperature measurement points, and the measured values should also be adjusted to the problem under consideration. For geometries such as a gas turbine blade or a cross-section of a real heating device wall, the calculation scheme is analogous. In this case, the functions $\varphi_i(x)$ should be replaced with functions dependent on, for example, two variables $\varphi_i(x, y)$ (Formula (10)).

The presented method was also used to determine the heat flux on the surface of the T-shaped stator cavities of steam turbines [66] and the cross-section of a piston machine body with a cooling channel [69]. The calculation time indicates the possibility of using this method for online temperature control during thermochemical treatment processes. For gas nitriding, the calculation time was approximately 2 s for the assumed time step Δt = 30 s.

2.3. Gas Turbines

A very important challenge in the energy sector is to increase the efficiency of gas turbines. Efficiency increases with the temperature of the gas flowing around the blades. The gas temperature is limited by the properties of the material from which the blades are made. Too high a gas temperature can cause the blades to lose their strength properties and, as a result, damage the turbine. In order for the turbine to operate at a higher gas temperature without risking damage to the blades, cooling systems and protective coatings are used. Optimisation of the gas turbine blade cooling process based on IHCP solutions is discussed in [70–74]. The research area where IHCP solutions were applied to the analysis of thermal loads on gas turbine blades with a protective layer is described in [75–78]. The study in [72] presents an iterative algorithm that allows solving the IHCP for Laplace's equation in a multiply-connected domain. A Cauchy-type problem was solved, where two boundary conditions were known on the outer boundary, while the sought condition was on the inner boundary of an elliptical ring with a shifted inner boundary. The IP solution is based on the DP, where the heat flux on the inner boundary of the domain was assumed and iteratively changed in such a way as to minimise the functional. The aforementioned functional determines the distance between the calculated and specified temperature at the outer boundary and includes a regularisation term. This method, which also uses variational calculus, was developed by the authors and applied to the analysis of the cooling of gas turbine blades [70]. In [70], two iterative algorithms were compared to determine the temperature at the inner limit of the blade. The first one is based on variational calculus, while the second one boils down to solving the least squares approximation problem. The temperature on the outer surface of the blade was assumed to be T_0 = 600 K. The IP solution was stabilised using a discrete Fourier transform. The calculation results showed that there was a local loss of stability of the IHCP solution near the leading and trailing boundaries. In these areas, the temperature exceeded the assumed value of T_0. This means that the cooling channel is not able to absorb the amount of heat that is transferred from the gas surrounding the blade. In the next step of the investigation, the authors developed an iterative algorithm that allowed the analysis of the cooling of the gas turbine blades using the IHCP solution, where porous material was present in the cooling channels [73]. The temperature of the blade boundary and the porosity distributions in the cooling channel were determined.

https://doi.org/10.3390/en19051291

Another way to increase the temperature of the working medium in a gas turbine is to use ceramic coatings on the surface of the blades. This creates thermal resistance on the surface of the blade. The studies presented in [75–78] describe calculations for an area of metal covered with a layer of ceramic with low thermal conductivity. The issue under consideration is a Cauchy problem. In [77], the influence of thermal conductivity and the thickness of the ceramic layer on the temperature at the metal–ceramic interface was investigated, as exceeding this temperature may cause the blade to lose its mechanical properties. This issue was continued in [75,76], where the stability of the IHCP solution was investigated. This IP was stabilised by means of an energy balance equation for the ceramic layer, which constitutes its quasi-regularisation.

3. Applications of Neural Networks for Solving IHCPs

In recent years, a new approach to solving IHCPs has also been proposed. Genetic algorithms [79–81] and machine learning [82–92] are used. Research on the application of machine learning to solve IHCPs is carried out using Artificial Neural Networks (ANNs) [82–92]. ANNs are algorithms whose structure resembles that of the brain [93]. They consist of an input layer N_{inp}, hidden layers N_h, and an output layer N_{out} (Figure 6). The transition between neurons causes the output value of the previous layer to be multiplied by the weight and the assigned bias to be added, and the activation function [82]. The optimisation problem consists of determining the appropriate weights at the network learning stage so that in the next step, the network can be used for data where the expected result is unknown. A special example of a neural network (NN) used to solve IHCPs is Physics-Informed Neural Networks (PINNs) [82,86,87,89,91,92,94–100]. A PINN is a NN that uses fundamental laws of physics, making it a good tool to solve heat transfer problems.

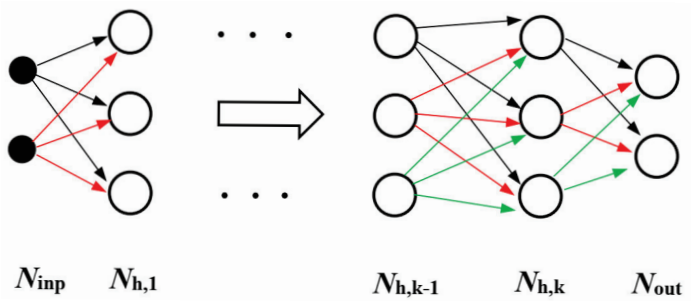


Figure 6. Neural network.

In the analysis of boiler and other heating device operation based on the measurement of the temperature inside the wall, the boundary condition in the form of temperature or heat flux on an unavailable surface is calculated. In [91], a PINN model was proposed, which simultaneously identifies the boundary heat flux and thermal conductivity based on temperature values. The mathematical description of the method was prepared for a non-stationary, one-dimensional IHCP. However, it allows the analysis to be extended to two- and three-dimensional problems. The one-dimensional case concerns heat conduction through a flat wall with a thickness of 20 mm, in which the measurement points are located 10 mm and 20 mm from the wall surface where the heat flux is sought. The NN used to predict the solution consists of three blocks: a fully connected NN, a PINN, and a feedback mechanism. The loss function is the sum of functions representing penalty terms for the residuals of the governing equations, boundary conditions, and initial conditions. In the one-dimensional model, transient heat flux $q_{in}(t)$ was assumed at the left end, while the right end exchanges heat through natural convection. Radiation was taken into account at both ends. The normalised mean squared error (NMSE) was used to evaluate the accuracy

https://doi.org/10.3390/en19051291

of the heat flux sought. In the hidden layers, the activation function was the hyperbolic tangent. The output layer uses a linear activation function. The thermal conductivity of the material was assumed to be k = 5 W/mK. Numerical tests were performed for five different NN architectures (Net-i for i = 1, 2, . . ., 5). The analysed networks have 2, 3, 3, 3, and 4 hidden layers, respectively. The Net-1 has 80 and 60 neurons in its hidden layers, respectively. Accordingly, the Net-2 consists of 80, 60, and 40 neurons; the Net-3 consists of 130, 100, and 70 neurons; the Net-4 consists of 200, 150, and 100 neurons; and the Net-5 consists of 200, 150, 100, and 50 neurons.

For the Net-3 neural network, the NMSE value of heat flux was 0.028, the relative thermal conductivity error was 0.13%, and the training time was approximately 840 s. The authors considered the Net-3 NN to be the best compromise between accuracy of results and training time. The values for the other networks were referenced to Net-3 and are shown in Table 2. During training, the loss function reaches a value below 10^{-3} after 20,000 epochs. Training was conducted for up to 50,000 epochs. Numerical tests for Net-3 and Net-4 were also performed for temperature-dependent thermal conductivity described by a linear function using two coefficients. The determination of the heat flux reaches a relatively stable and accurate level after approximately 25,000 epochs (loss function for Net-3 of the order of 10^{-4}, and for Net-4 of the order of 10^{-5}). Meanwhile, the identification of two thermal conductivity coefficients converges much more slowly and requires a significantly higher number of iterations.

Table 2. NMSE values of heat flux (q_{NMSE}), relative error of thermal conductivity (δk), and training time (t) for Net-i referred to Net-3.

i	q_{NMSE}(Net-i)/q_{NMSE}(Net-3)	δk(Net-i)/δk(Net-3)	t(Net-i)/t(Net-3)
1	3.1429	25.0769	0.6212
2	1.1786	2.5385	0.7657
3	1	1	1
4	0.9286	0.6923	1.3457
5	0.6429	0.6154	1.5295

Numerical tests in [91] were performed for measurement data disturbances of 1%, 2%, 4%, and 8%. For the Net-3 test, Table 3 shows the NMSE values for heat flux and the relative error for thermal conductivity, taking into account disturbances in the input data for calculations in relation to values without disturbances. The method described in [91] allows for satisfactory accuracy in heat flux reconstruction despite noise, which is even greater than that encountered in industry. Slightly worse results were obtained for the thermal conductivity coefficient k. However, in many applications, the values of k are known. A two-dimensional heat conduction model was also considered for a rectangular area with dimensions L = 0.05 m and W = 0.02 m at a constant thermal conductivity k = 3 W/mK. The aim of the analysis was to investigate the effect of sensor placement on the result. The number of neurons in the hidden layers was 180, 100, and 150. Simply increasing the number of temperature sensors or improving the sampling resolution in the time–space domain did not lead to a significant improvement in identification results. In the case of the two-dimensional test, taking into account a specific parametric form of heat flow significantly improved accuracy. The PINN method achieved an NMSE value of 0.003 for heat flux and a relative error of 0.3% in identifying thermal conductivity. For this two-dimensional problem, it was found that using four or more sensors yielded satisfactory identification results for both parameters. It is worth noting that the numerical tests were performed for low thermal conductivity values and small areas with simple geometry. In such cases, the wall experiences significantly higher temperature gradients than for thermal

conductivity values of 30–50 W/mK, which are typical for steel. In such cases, obtaining an IHCP solution may prove more difficult.

Table 3. The q_{NMSE} and δk values with noise level (NL) of input temperature relative to corresponding values without disturbance.

NL [%]	$q_{NMSE}(NL)/q_{NMSE}(0)$	δk(NL)/δk(0)
0	1	1
1	1.1429	10.46
2	1.3929	26.62
4	2.1071	55.86
8	3.5714	110.46

The boundary condition in the form of heat flux for a one-dimensional problem was also determined using a PINN [89]. The NN was trained taking into account physical constraints such as the equation, boundary conditions, initial conditions, and temperature values. The results indicate that the PINN has satisfactory effectiveness, is efficient, and represents a promising direction for the development of methods to solve IP. The studies in [89,91] present the application of PINNs to model the problem of heat transfer through a flat wall. This issue can be developed for future application to the analysis of heat transfer in the walls of thermal devices. However, the cases analysed are theoretical examples at this stage, far from industrial applications.

A comparison of two machine learning-based approaches to solving a nonlinear IHCP in a one-dimensional domain with constant and moving boundary conditions (Case 3 with constant material properties and Case 4 with temperature-dependent material properties) is described in [82]. The issue under consideration corresponds to the analysis of heat transfer through spacecraft panels without and with consideration of the thermal expansion of the plate material. The surface heat flux was determined using ANNs and temperature measurements inside the area. The length of the area was L = 2 cm, and the temperature measurement was taken on one of the surfaces (x = 0) and in the middle of the area, 1 cm from the edge, where the heat flux was determined (x = 1 cm). An Autoregressive-Exogenous Recurrent Neural Network (NARX) and a Feed-Forward Neural Network (FFNN) were used to analyse the four calculation examples. The network consisted of four hidden layers composed of 3, 5, 11, and 21 neurons for the FFNN and one hidden layer composed of 10 neurons for the NARX. Numerical tests were performed for three training cases and three validation cases (parabolic, triangular, and step functions). The training examples were simpler, while the validation examples were more complex.

The training algorithm used was the Levenberg–Marquardt algorithm. Temperature-dependent material (carbon phenolic) properties were taken into account. Thermal conductivity ranged from 0.62 W/mK to 2.77 W/mK. Specific heat ranged from 795.5 J/kgK to 2386.48 J/kgK. In order to compare the FFNN and NARX networks, r^2 values (coefficient of determination) and training time were used. The r^2 values for Case 3 are higher for the FFNN (from 0.9279 to 0.9891), while for Case 4, they are higher for the NARX (from 0.9458 to 0.9939). For cases with a moving boundary, the FFNN is trained faster. Training times for the FFNN range from 1.8 to 6.75 s, while for the NARX they range from 0.66 to 2.18 s. The analysed networks were shown to show promising properties in solving IHCPs.

Despite favourable r^2 values and short learning times, the graphs show significant discrepancies in the heat flow for the stepwise validation function. The paper uses Tikhonov regularisation in the digital filter method. The authors of [82] did not specify the value of the regularisation parameter or the method of its selection.

https://doi.org/10.3390/en19051291

Research on IHCPs through multilayer materials with an insulating layer using neural networks is described in [86,101]. A PINN was used to analyse the heat flow in a multilayer material used as thermal protection for reusable launch vehicles [101]. An improved PINN framework was developed to solve transient nonlinear and inhomogeneous heat conduction problems [86]. These networks were used to optimise the design of thermal protection structures for hypersonic vehicles. Existing numerical methods required the use of a large number of meshes. The use of a NN is a non-mesh method, which has a positive impact on the efficiency of calculations.

In [97], a nonlinear IHCP solution using PINNs was presented to determine the temperature fields, heat flux, and effective thermal conductivity in porous material. The average relative error was 4.5%, 14.4%, and 2.73%, respectively. Compared to numerical calculations using the finite volume method (FVM), a five-order-of-magnitude acceleration of calculations was achieved. The study presented in [102] analysed heat conduction processes in porous materials using machine learning and Fourier transforms. The results presented in [97,102] indicate that PINNs are promising tools for researching heat conduction issues in porous materials.

In [101], the heating of a sample made of carbon fibre–epoxy composite with thermal conductivity k = 0.47 W/mK, density ρ = 1573 kg/m^3, and specific heat c = 967 J/kg K was analysed in an oven under convective conditions. The calculations were performed for heat transfer coefficients ranging from 10 W/m^{2}K to 100 W/m^{2}K. The calculations were performed using finite element methods (FEMs) and NNs, including a PINN. Numerical tests for NNs were performed for various activation functions that are exponential functions (ELU, adaptive-ELU) and for the hyperbolic tangent (adaptive-tanh). The activation function for the PINN was selected based on governing heat transfer equations. The network was trained during the first 15 min of heating, which lasted 45 min. The temperature consistency in the central part of the sample was taken into account in the network training process. In the second part of the heating process, the temperature curve was predicted using a NN, and the results were compared with the FEM solution. The curves for ELU, adaptive-ELU, and adaptive-tanh deviated significantly from the assumed function. For adaptive-ELU and adaptive-tanh, the temperature in subsequent heating time units decreased, even reaching zero for adaptive-ELU, which is contrary to the physical phenomena occurring in the oven. The temperature curve obtained for the PINN was almost identical to the curve obtained from the FEM and the assumed function. Calculations using the PINN network were faster than the FEM. The example presented in [101] clearly indicates the usefulness of using PINNs for the analysis of heat transfer processes.

4. Conclusions

The difficulties with industrial applications of solutions for IHCPs stem from the fact that these problems are ill-posed in the Hadamard sense. Solving them requires extensive mathematical knowledge, in particular numerical methods, knowledge of computational tools, measurement techniques, and an understanding of the physical phenomena occurring during the operation of machines and equipment. Practical knowledge of the realities of operating these machines and devices in industrial conditions is also important. Therefore, the application of IHCPs in industry is an interdisciplinary issue that is very difficult to implement. There are many scientific papers presenting computational models for stationary and non-stationary one-dimensional simple geometries. They often describe complex IHCP regularisation methods, the application of which in industry could be impractical. Many works also present IHCP solutions for stationary two-dimensional problems for simple and complex geometries, such as gas turbine blades. The difficulty remains in solving unsteady, two-dimensional, and three-dimensional IHCPs for complex

https://doi.org/10.3390/en19051291

geometries. New computational tools such as the freeFEM solver, Python, and COMSOL are creating ever greater opportunities in this field. When controlling the operation of machines and devices using IHCP solutions, we want the calculations to be performed correctly and quickly, and the solution to be numerically stable so that we can obtain results without the need for intervention by a person highly specialised in solving IP. Currently, efforts are being made to automate and simplify methods for solving IHCPs that may have industrial applications. In connection with the above, methods are being sought that allow for online control during the heating or cooling process of walls that are inaccessible for measurement and are most heavily loaded thermally. In order for online control to be possible without human intervention in industrial conditions, the IHCP solution must first undergo a series of numerical tests. These tests cover the impact of temperature and heat flux measurement errors, location, and measurement sensor installation errors on the result, taking into account the heat flow intensity in a given device. It is also very important that the calculation time allows information to be obtained on, for example, the surface temperature, where measurement cannot be performed in real time. Elements with significant thermal loads include the inner wall of a boiler, the casing of a steam and gas turbine, the blades of the gas turbine, and the surfaces of elements subjected to heat or thermochemical treatment. Numerous studies were conducted on IHCP solutions dedicated to these issues and their regularisation for the above-mentioned components, machines, and devices. According to the authors, automation of the control of thermally stressed surfaces may occur when methods for solving inverse heat conduction problems that do not require classical Tikhonov regularisation with the selection of a regularisation parameter are developed and tested. In this case, the IHCP solution can be stabilised using a quasi-regularisation approach, e.g., by selecting the time step, control volume size, or additional energy balance equations. When selecting a large time step, some data may be lost due to high averaging, e.g., of temperature curves, but on the other hand, this is very beneficial in terms of stability. On the other hand, a small time step may mean that the solution obtained will oscillate significantly. The possibility of large oscillations mainly concerns the heat flux and heat transfer coefficient. The quasi-regularisation approach involves finding a compromise between the stability and accuracy of the IHCP solution. Quasi-regularisation methods should be selected individually depending on the technical problem, heat transfer dynamics, and IHCP solution method. A well-chosen quasi-regularisation method does not require human intervention in the IHCP solution during the industrial process. Quasi-regularisation has been applied to control and analyse heat transfer for boilers, gas turbines, and thermochemical treatment. It is also worth mentioning that online control of heat transfer processes using IHCPs and quasi-regularisation was applied to power boiler components and components subjected to gas nitriding. Recently, many papers have been published that describe new approaches to solving IHCPs using neural networks. The use of machine learning makes it possible to simplify the mathematical model and omit the regularisation of the IHCP. Often, the model is trained on the basis of the solution of the DP, which is numerically stable. The trained model then solves the IP, which is no longer an ill-posed problem. Despite many potential benefits, based on the literature presented, there are doubts regarding the effectiveness and applicability of NNs. Calculations using NNs were most often performed for one-dimensional cases. The two-dimensional examples given in the literature concern simple geometries with small dimensions. Numerical tests for heat flow using NNs were performed for materials with a relatively low thermal conductivity coefficient. The maximum value in the analysed papers was 4.4 W/mK. A low thermal conductivity coefficient causes large temperature gradients and facilitates the analysis of the issue. Materials commonly used in industry (e.g., steels) generally have thermal conductivity and specific heat that vary significantly within their

applicable temperature range. The analysed studies noted significant difficulties in training networks due to the variability in k with temperature. This is not a major problem for solving IHCPs using classical numerical methods.

In heat treatment and thermochemical treatment, to be able to use neural networks, it would be necessary to perform a large number of experiments to determine the boundary conditions and combine the results with furnace operating parameters such as gas temperature, load weight, load surface properties, etc. Then, surface control could be performed online during the process, without having to solve the ill-posed problem. The possibility of online control springs from shorter computation times for NNs than for classical numerical methods. Therefore, it is very important to train models effectively, acquire training data, and calculate learning time and costs. However, the use of neural networks at their current stage of development for the analysis of very expensive equipment, such as processing furnaces, gas turbines, or power boilers, in industry raises doubts. Currently, there are no methods for certifying these machine learning devices that guarantee their effectiveness. However, quasi-regularisation methods can be successfully applied to them. The application of neural networks to solve IHCPs makes it possible to simplify computational models used to control energy-intensive industrial processes and energy conversion. In numerical tests, the best results were obtained for the PINN. Obtaining a stable solution to the IP allows its industrial application. Nevertheless, in the authors' opinion, at the current stage of research into IHCP solutions using NNs, their effective application to real industrial problems seems unlikely. Currently, the use of neural networks to solve IHCPs is an interesting research direction. Research on solving IHCPs using NNs would need to include larger elements with more complex geometries made from materials commonly used in manufacturing processes.

Author Contributions: Conceptualisation, M.J.; methodology, M.J. and D.J.; software, M.J. and D.J.; investigation, M.J. and D.J.; writing—original draft preparation, M.J.; writing—review and editing, M.J. and D.J.; visualisation, M.J. and D.J. All authors have read and agreed to the published version of the manuscript.

Funding: This research received no external funding.

Data Availability Statement: No new data were created.

Conflicts of Interest: The authors declare no conflicts of interest.

Abbreviations

The following abbreviations are used in this manuscript:

ANNs	Artificial neural networks
BFGS	Broyden–Fletcher–Goldfarb–Shanno algorithm
DP	Direct problem
IHCP	Inverse heat conduction problem
IP	Inverse problem
ISMM	Inverse space marching method
NNs	Neural networks
PINNs	Physics-informed neural networks

References

1. Hadamard, J. Sur les problèmes aux dérivées partielles et leur signification physique. *Princet. Univ. Bull.* **1902**, *13*, 49–52.
2. Grysa, K. *Trefftz Functions and Their Applications in Solving Inverse Problems*; Publishing House of the Kielce University of Technology: Kielce, Polish, 2010; ISSN 1897-2691. (In Polish)
3. Ciałkowski, M. *Selected Methods and Algorithms for Solving Inverse Problems of Heat Conduction Equation*; Poznań University of Technology Publishing House: Poznań, Polish, 1996; ISBN 8371431619. (In Polish)

4. Taler, J.; Duda, P. *Solving Direct and Inverse Heat Conduction Problems*, 1st ed.; Springer: Berlin/Heidelberg, Germany, 2006; ISBN 978-3-540-33470-X.
5. Alifanov, O.M. *Inverse Heat Transfer Problems*; Springer: Berlin/Heidelberg, Germany, 1994; ISBN 13:978-3-642-76438-7.
6. Woodbury, K.A.; Najafi, H.; de Monte, F.; Beck, J.V. *Inverse Heat Conduction: Ill-Posed Problems*; John Wiley & Sons: Hoboken, NJ, USA, 2023; ISBN 9781119840190.
7. Taler, J. *Theory and Practice of Identifying Heat Transfer Processes*; Zakład Narodowy imienia Ossolińskich: Wrocław Warszawa Kraków, Polish, 1995; ISBN 83-04-04276-2. (In Polish)
8. Incropera, F.P.; de Witt, D.P. *Fundamentals of Heat and Mass Transfer*; Wiley: New York, NY, USA, 1996.
9. Orlande, H.R.B. *Inverse Heat Transfer: Fundamentals and Applications*, 2nd ed.; CRC Press: Boca Raton, FL, USA, 2021. [CrossRef]
10. Tikhonov, A.N.; Arsenin, V.Y. *Solution of Ill-Posed Problems*; Wiley: New York, NY, USA, 1977.
11. Bedin, L.; Bazán, F.S.V.; Quiroz, J.R. Method for recovering boundary data in a two-dimensional Poisson equation on annular domain. *J. Comput. Appl. Math.* **2018**, *342*, 83–95. [CrossRef]
12. Chen, B.; Sun, Y.; Zhuang, Z. Method of fundamental solutions for a Cauchy problem of the Laplace equation in a half-plane. *Bound. Value Probl.* **2019**, *2019*, 34. [CrossRef]
13. Han, H.; Ling, L.; Takeuchi, T. An energy regularization for Cauchy problems of Laplace equation in annulus domain. *Commun. Comput. Phys.* **2011**, *9*, 878–896. [CrossRef]
14. Joachimiak, M. Choice of the regularization parameter for the Cauchy problem for the Laplace equation. *Int. J. Numer. Methods Heat Fluid Flow* **2020**, *30*, 4475–4492. [CrossRef]
15. Marin, L. An invariant method of fundamental solutions for two-dimensional steady-state anisotropic heat conduction problems. *Int. J. Heat Mass Transf.* **2016**, *94*, 449–464. [CrossRef]
16. Morozov, V.A. *Methods for Solving Incorrectly Posed Problems*; Springer: New York, NY, USA, 1984.
17. Sun, Y. A meshless method based on the method of fundamental solution for solving the steady-state heat conduction problems. *Int. J. Heat Mass Transf.* **2016**, *97*, 891–907. [CrossRef]
18. Sun, Y.; He, S. A meshless method based on the method of fundamental solution for three-dimensional inverse heat conduction problems. *Int. J. Heat Mass Transf.* **2017**, *108*, 945–960. [CrossRef]
19. Wei, T.; Wang, J. A modified quasi-boundary value method for an inverse source problem of the time-fractional diffusion equation. *Appl. Numer. Math.* **2014**, *78*, 95–111. [CrossRef]
20. Jin, B.; Zheng, Y. A meshless method for some inverse problems associated with the Helmholtz equation. *Comput. Methods Appl. Mech. Eng.* **2006**, *195*, 2270–2288. [CrossRef]
21. Marin, L. Numerical solution of the Cauchy problem for steady-state heat transfer in two-dimensional functionally graded materials. *Int. J. Solids Struct.* **2005**, *42*, 4338–4351. [CrossRef]
22. Marin, L.; Munteanu, L. Boundary reconstruction in two-dimensional steady state anisotropic heat conduction using a regularized meshless method. *Int. J. Heat Mass Transf.* **2010**, *53*, 5815–5826. [CrossRef]
23. Pacheco, C.C.; Lacerda, C.R.; Colaço, M.J. Automatic selection of regularization parameter in inverse heat conduction problems. *Int. Commun. Heat Mass Transf.* **2022**, *139*, 106403. [CrossRef]
24. Joachimiak, M.; Joachimiak, D. Stabilization of boundary conditions obtained from the solution of the inverse problem during the cooling process in a furnace for thermochemical treatment. *Int. J. Heat Mass Transf.* **2024**, *224*, 125274. [CrossRef]
25. Yang, F.; Fu, C.; Li, X. A modified Tikhonov regularization method for the Cauchy problem of Laplace equation. *Acta Math. Sci.* **2015**, *35*, 1339–1348. [CrossRef]
26. Ngendahayo, J.P.; Minani, F.; Thim, J.; Berntsson, F. Convergence Analysis of Iterative Tikhonov Regularization Applied to an Inverse Heat Conduction Problem. *Int. J. Appl. Comput. Math.* **2025**, *11*, 149. [CrossRef]
27. Hasanov, A.; Mukanova, B. Relationship between representation formulas for unique regularized solutions of inverse source problems with final overdetermination and singular value decomposition of input-output operators. *J. Appl. Math.* **2015**, *80*, 676–696. [CrossRef]
28. Marin, L.; Karageorghis, A.; Lesnic, D. Regularized MFS solution of inverse boundary value problems in three-dimensional steady-state linear thermoelasticity. *Int. J. Solids Struct.* **2016**, *91*, 127–142. [CrossRef]
29. Frąckowiak, A.; Ciałkowski, M. Application of discrete Fourier transform to inverse heat conduction problem regularization. *Int. J. Numer. Methods Heat Fluid Flow* **2018**, *28*, 239–253. [CrossRef]
30. Joachimiak, M.; Ciałkowski, M. Optimal choice of integral parameter in a process of solving the inverse problem for heat equation. *Arch. Thermodyn.* **2014**, *35*, 265–280.
31. Ciałkowski, M.; Grysa, K. A sequential and global method of solving an inverse problem of heat conduction equation. *J. Theor. Appl. Mech.* **2010**, *48*, 111–134.
32. Grysa, K.; Maciąg, A. Trefftz Method in Solving Inverse Heat Conduction Problems. In *Encyclopedia of Thermal Stresses*; Hetnarski, R.B., Ed.; Springer: Dordrecht, The Netherlands, 2014. [CrossRef]
33. Grysa, K.; Maciag, A.; Pawinska, A. Solving nonlinear direct and inverse problems of stationary heat transfer by using Trefftz functions. *Int. J. Heat Mass Transf.* **2012**, *55*, 7336–7340. [CrossRef]

34. Joachimiak, M.; Ciałkowski, M. Non-linear unsteady inverse boundary problem for heat conduction equation. *Arch. Thermodyn.* **2017**, *38*, 81–100. [CrossRef]
35. Joachimiak, M.; Ciałkowski, M. Stable solution to non-stationary inverse heat conduction equation. *Arch. Thermodyn.* **2018**, *39*, 25–37.
36. Joachimiak, M.; Ciałkowski, M.; Frąckowiak, A. Stable method for solving the Cauchy problem with the use of Chebyshev polynomials. *Int. J. Numer. Methods Heat Fluid Flow* **2020**, *30*, 1441–1456. [CrossRef]
37. Mierzwiczak, M.; Kołodziej, J.A. The determination of heat sources in two dimensional inverse steady heat problems by means of the method of fundamental solutions. *Inverse Probl. Sci. Eng.* **2011**, *19*, 777–792. [CrossRef]
38. Mierzwiczak, M.; Kołodziej, J.A. The determination temperature-dependent thermal conductivity as inverse steady heat conduction problem. *Int. J. Heat Mass Transf.* **2011**, *54*, 790–796. [CrossRef]
39. Hożejowska, S.; Piasecka, M. Numerical Solution of Axisymmetric Inverse Heat Conduction Problem by the Trefftz Method. *Energies* **2020**, *13*, 705. [CrossRef]
40. Joachimiak, M.; Ciałkowski, M.; Bartoszewicz, J. Analysis of temperature distribution in a pipe with inner mineral deposit. *Arch. Thermodyn.* **2014**, *35*, 37–49. [CrossRef]
41. Soloviev, A.N.; Shevchenko, M.A.; Germanchuk, M.S. The Inverse Geometric Problem of Thermal Conductivity for Determining the Thickness of Scale in Steam Boiler Pipes. *J. Math. Sci.* **2025**, *287*, 664–672. [CrossRef]
42. Lv, C.; Wang, G.; Chen, H. Estimation of time-dependent thermal boundary conditions and online reconstruction of transient temperature field for boiler membrane water wall. *Int. J. Heat Mass Transf.* **2020**, *147*, 118955. [CrossRef]
43. Joachimiak, M.; Joachimiak, D.; Ciałkowski, M. Investigation on thermal loads in steady-state conditions with the use of the solution to the inverse problem. *Heat Transf. Eng.* **2023**, *44*, 963–969. [CrossRef]
44. Jamail Arand, H.; Sefid, M.; Goudarzi, K. Identification of Fouling Profiles in a Heat Exchanger Pipe with Presence of Two-Phase Flow Using Inverse Heat Transfer Method, a Numerical Study. *Int. J. Eng. Trans. B Appl.* **2026**, *39*, 694–704. [CrossRef]
45. Duda, P.; Konieczny, M. An Iterative Algorithm for the Estimation of Thermal Boundary Conditions Varying in Both Time and Space. *Energies* **2022**, *15*, 2686. [CrossRef]
46. Jaremkiewicz, M.; Taler, J. Online Determining Heat Transfer Coefficient for Monitoring Transient Thermal Stresses. *Energies* **2020**, *13*, 704. [CrossRef]
47. Jaremkiewicz, M.; Taler, D.; Dzierwa, P.; Taler, J. Determination of Transient Fluid Temperature and Thermal Stresses in Pressure Thick-Walled Elements Using a New Design Thermometer. *Energies* **2019**, *12*, 222. [CrossRef]
48. Jaremkiewicz, M. Analysis of the Accuracy of the Inverse Marching Method Used to Determine Thermal Stresses in Cylindrical Pressure Components with Holes. *Energies* **2025**, *18*, 4546. [CrossRef]
49. Taler, D.; Taler, J.; Kaczmarski, K.; Jaremkiewicz, M.; Dzierwa, P.; Trojan, M. Monitoring of thick-walled pressure elements to determine transient temperature and stress distributions using the measured fluid's pressure and wall's temperature. *Energy* **2024**, *309*, 133121. [CrossRef]
50. Duarte Benther, J.; Chalhub, D.J.N.M.; Franklin, E.; Lappas, P.; Rosengarten, G. Semi-analytical solution of transient heat conduction for spray cooling. *Int. J. Therm. Sci.* **2025**, *218*, 110148. [CrossRef]
51. Lee, S.-Y.; Yan, Q.-Z. Inverse analysis of heat conduction problems with relatively long heat treatment. *Int. J. Heat Mass Transf.* **2017**, *105*, 401–410. [CrossRef]
52. Gopalkrishna, S.B.; Kulkarni, G.A.; Ryll, S.; Specht, E. Heat transfer analysis during quenching of moving metal plates using water jets from a mold. *Therm. Sci. Eng. Prog.* **2025**, *64*, 103792. [CrossRef]
53. Barrena-Rodríguez, M.d.J.; Acosta-González, F.A.; Téllez-Rosas, M.M. A Review of the Boiling Curve with Reference to Steel Quenching. *Metals* **2021**, *11*, 974. [CrossRef]
54. Gomez, C.F.; Nieuwenhuizen, R.; van der Geld, C.W.M.; Kuerten, H.G.M.; Bsibsi, M.; van Esch, B.P.M. Inaccuracies in the inverse heat conduction problem solution and their effect on the estimation of heat fluxes during quenching. *Int. J. Heat Mass Transf.* **2022**, *194*, 122953. [CrossRef]
55. Jahedi, M.; Berntsson, F.; Wren, J.; Moshfegh, B. Transient inverse heat conduction problem of quenching a hollow cylinder by one row of water jets. *Int. J. Heat Mass Transf.* **2018**, *117*, 748–756. [CrossRef]
56. Nieuwenhuizen, R. The Inverse Heat Conduction Problem in Quenching of a Hot Steel Plate. MSc. Thesis, Eindhoven University of Technology, Eindhoven, The Netherlands, 2019.
57. Sun, Y.; Jian, H.; Xiong, P.; Zhou, L. An Experimental Study of Boiling Heat Transfer and Quench Front Propagation Velocity During Quenching of a Cylinder Rod in Subcooled Water. *Energies* **2024**, *17*, 5236. [CrossRef]
58. Szénási, S.; Felde, I. Database for Research Projects to Solve the Inverse Heat Conduction Problem. *Data* **2019**, *4*, 90. [CrossRef]
59. Joachimiak, D.; Joachimiak, M.; Frąckowiak, A. Determination of boundary conditions from the solution of the inverse heat conduction problem in the gas nitriding process. *Energy* **2024**, *300*, 131497. [CrossRef]
60. Joachimiak, M. Analysis of Thermodynamic Parameter Variability in a Chamber of a Furnace for Thermo-Chemical Treatment. *Energies* **2021**, *14*, 2903. [CrossRef]

61. Joachimiak, M.; Frąckowiak, A. Analysis of heat transfer in a cylinder being treated in a gas nitriding furnace using a new inverse problem solving method. *Energy* **2025**, *333*, 137318. [CrossRef]
62. Joachimiak, M.; Joachimiak, D.; Ciałkowski, M.; Małdziński, L.; Okoniewicz, P.; Ostrowska, K. Analysis of the heat transfer for processes of the cylinder heating in the heat-treating furnace on the basis of solving the inverse problem. *Int. J. Therm. Sci.* **2019**, *145*, 105985. [CrossRef]
63. Małdziński, L. *Thermodynamic, Kinetic and Technological Aspects of Nitrided Layer Production on Iron and Steel in Gas Nitriding Processes*; Poznań University of Technology Publishing House: Poznań, Polish, 2002. (In Polish)
64. Joachimiak, D.; Judt, W.; Joachimiak, M. Numerical analysis of the heating of a die for the extrusion of aluminium alloy profiles in terms of thermochemical treatment. *Arch. Thermodyn.* **2023**, *44*, 159–175. [CrossRef]
65. Jaremkiewicz, M. Analysis of the accuracy of the inverse marching method used to determine thermal stresses in cylindrical pressure components. *Arch. Thermodyn.* **2024**, *45*, 95–105. [CrossRef]
66. Frąckowiak, A.; Spura, D.; Gampe, U.; Ciałkowski, M. Determination of heat transfer coefficient in a T-shaped cavity by means of solving the inverse heat conduction problem. *Int. J. Numer. Methods Heat Fluid Flow* **2020**, *30*, 1725–1742. [CrossRef]
67. Frąckowiak, A.; Wróblewska, A.; Ciałkowski, M. Trefftz numerical functions for solving inverse heat conduction problems. *Int. J. Therm. Sci.* **2022**, *177*, 107566. [CrossRef]
68. Hecht, F. FreeFEM Documentation Release 4.13, 2026. Available online: https://doc.freefem.org/introduction/index.html (accessed on 24 February 2026).
69. Joachimiak, M.; Frąckowiak, A.; Joachimiak, D. Determination of the Temperature on the Inner Wall of the Piston Machine Body by Solving the Inverse Problem. *Heat Transf. Eng.* **2025**, *46*, 1982–1991. [CrossRef]
70. Frąckowiak, A.; Ciałkowski, M.; Wróblewska, A. Application of iterative algorithms for gas-turbine blades cooling optimization. *Int. J. Therm. Sci.* **2017**, *118*, 198–206. [CrossRef]
71. Frąckowiak, A.; Ciałkowski, M.; Wróblewska, A. Iterative algorithms for solving inverse problems of heat conduction in multiply connected domains. *Int. J. Heat Mass Transf.* **2012**, *55*, 744–751. [CrossRef]
72. Frąckowiak, A.; von Wolfersdorf, J.; Ciałkowski, M. An iterative algorithm for the stable solution of inverse heat conduction problems in multiply-connected domains. *Int. J. Therm. Sci.* **2015**, *96*, 268–276. [CrossRef]
73. Frąckowiak, A.; von Wolfersdorf, J.; Ciałkowski, M. Optimization of cooling of gas turbine blades with channels filled with porous material. *Int. J. Therm. Sci.* **2019**, *136*, 370–378. [CrossRef]
74. Frąckowiak, A.; von Wolfersdorf, J.; Ciałkowski, M. Solution of the inverse heat conduction problem described by the Poisson equation for a cooled gas turbine blade. *Int. J. Heat Mass Transf.* **2011**, *54*, 1236–1243. [CrossRef]
75. Ciałkowski, M.; Joachimiak, M.; Mierzwiczak, M.; Frąckowiak, A.; Olejnik, A.; Kozakiewicz, A. Cauchy Type Nonlinear Inverse Problem in a Two-Layer Cylindrical Area. *Heat Transf. Eng.* **2025**, *46*, 2005–2017. [CrossRef]
76. Ciałkowski, M.; Joachimiak, M.; Mierzwiczak, M.; Frąckowiak, A.; Olejnik, A.; Kozakiewicz, A. The analysis of the stability of the Cauchy problem in the cylindrical double-layer area. *Arch. Thermodyn.* **2023**, *44*, 563–579. [CrossRef]
77. Ciałkowski, M.; Olejnik, A.; Frąckowiak, A.; Lewandowska, N.; Mosiężny, J. Cauchy type inverse problem in a two-layer area in the blades of gas turbine. *Energy* **2020**, *212*, 118751. [CrossRef]
78. Ciałkowski, M.; Olejnik, A.; Joachimiak, M.; Grysa, K.; Frąckowiak, A. Cauchy type nonlinear inverse problem in a two-layer area. *Int. J. Numer. Methods Heat Fluid Flow* **2022**, *32*, 313–331. [CrossRef]
79. Allard, D.; Najafi, H. Genetic Algorithm as the Solution of Non-Linear Inverse Heat Conduction Problems: A Novel Sequential Approach. *J. Heat Mass Transf.* **2024**, *146*, 091404. [CrossRef]
80. Liu, W.; Guo, S.; Zhang, S. Temperature field modeling of the plate during hot rolling based on inverse heat conduction problem. *J. Phys. Conf. Ser.* **2019**, *1300*, 1. [CrossRef]
81. Xie, J.; Zhang, H.; Zhu, Z. Analysis of temperature field for rotary friction welding based on genetic-conjugate gradient hybrid inverse algorithm. *Appl. Therm. Eng.* **2025**, *279*, 127508. [CrossRef]
82. Allard, D.; Najafi, H. A systematic study of two machine learning-based approaches for solving non-linear inverse heat conduction problems in one-dimensional domains. *Int. Commun. Heat Mass Transf.* **2024**, *155*, 107494. [CrossRef]
83. Deng, S.; Hwang, Y. Applying neural networks to the solution of forward and inverse heat conduction problems. *Int. J. Heat Mass Transf.* **2006**, *49*, 4732–4750. [CrossRef]
84. Kowsary, F.; Mohammadzaheri, M.; Irano, S. Training based, moving digital filter method for real time heat flux function estimation. *Int. Commun. Heat Mass Transf.* **2006**, *33*, 1291–1298. [CrossRef]
85. Krejsa, J.; Woodbury, K.A.; Ratliff, J.D.; Raudensky, M. Assessment of strategies and potential for neural networks in the inverse heat conduction problem. *Inverse Probl. Eng.* **1999**, *7*, 197–213. [CrossRef]
86. Li, Y.; Liu, W.; Ren, J.; Cui, M.; Zhang, Z.; Nikolaitchik, M.A. An improved physics-informed neural network framework for solving transient nonlinear and inhomogeneous heat conduction problems. *Int. J. Heat Mass Transf.* **2025**, *252*, 127515. [CrossRef]

87. Ma, X.; Qiu, L.; Zhang, B.; Wu, G.; Wang, F. Adaptive fractional physics-informed neural networks for solving forward and inverse problems of anomalous heat conduction in functionally graded materials. *Int. J. Heat Mass Transf.* **2025**, *236*, 126393. [CrossRef]
88. Madir, B.-E.; Luddens, F.; Lothodé, C.; Danaila, I. Physics Informed Neural Networks for heat conduction with phase change. *Int. J. Heat Mass Transf.* **2025**, *252*, 127430. [CrossRef]
89. Qian, W.; Hui, X.; Wang, B.; Zhang, Z.; Lin, Y.; Yang, S. Physics-informed neural network for inverse heat conduction problem. *Heat Transf. Res.* **2023**, *54*, 65–76. [CrossRef]
90. Sablani, S.S.; Kacimov, A.; Perret, J.; Mujumdar, A.S.; Campo, A. Non-iterative estimation of heat transfer coefficients using artificial neural network models. *Int. J. Heat Mass Transf.* **2005**, *48*, 665–679. [CrossRef]
91. Shang, Y.; Ban, H.; Liu, D. Simultaneous identification of boundary heat flux and thermal conductivity in inverse heat conduction problems using physics-informed neural networks. *Therm. Sci. Eng. Prog.* **2025**, *65*, 103905. [CrossRef]
92. Sivalingam, S.M.; Govindaraj, V.; Dubey, S. An improved physics informed neural network with theory of functional connections for fractional differential equations. *Eng. Anal. Bound. Elem.* **2025**, *178*, 106281. [CrossRef]
93. Aggarwal, C.C. *Neural Networks and Deep Learning*; Springer Nature Switzerland: Cham, Switzerland, 2023.
94. Ding, S.; Tian, Y.; Qin, L.; Ma, H.; Yang, R. Physics-informed hierarchical neural operator for solving inverse problem of unsteady heat conduction. *Int. J. Heat Mass Transf.* **2026**, *258*, 128335. [CrossRef]
95. Islam, M.S.; Dutta, P. Machine learning assisted inverse heat transfer problem to find heat flux in ablative materials. *Mater. Today Commun.* **2025**, *45*, 112337. [CrossRef]
96. Molchanov, A.M.; Yanyshev, D.S.; Ezhov, A.D.; Bykov, L.V. Solution of the inverse problem of heat conduction using neural networks. *Heat Transf. Res.* **2025**, *56*, 1–12. [CrossRef]
97. Puttock-Brown, M.R.; Mahesh Bindhu, G.K.; Ashby, C.E. A Physics Informed Neural Network for Solving the Inverse Heat Transfer Problem in Gas Turbine Rotating Cavities. *J. Turbomach.* **2025**, *147*, 071010. [CrossRef]
98. Shang, Y.; Tan, C.; Tan, C.; Yu, X.; Hu, X.; Jiang, H.; Ma, W.; Liu, D. Using neural networks: A guidance with application in inverse heat conduction problem. *Eur. J. Phys.* **2025**, *46*, 2. [CrossRef]
99. Xu, J.; Wei, H.; Bao, H. Physics-informed neural networks for studying heat transfer in porous media. *Int. J. Heat Mass Transf.* **2023**, *217*, 124671. [CrossRef]
100. Zobeiry, N.; Humfeld, K.D. A physics-informed machine learning approach for solving heat transfer equation in advanced manufacturing and engineering applications. *Eng. Appl. Artif. Intell.* **2021**, *101*, 104232. [CrossRef]
101. Chen, Y.; Chen, Q.; Ma, H.; Chen, S.; Fei, Q. Transfer machine learning framework for efficient full-field temperature response reconstruction of thermal protection structures with limited measurement data. *Int. J. Heat Mass Transf.* **2025**, *242*, 126785. [CrossRef]
102. Yahya, M.; Saghir, M.Z. Machine Learning and Physics-Informed Neural Networks for Thermal Behavior Prediction in Porous TPMS Metals. *Fluids* **2026**, *11*, 29. [CrossRef]

Disclaimer/Publisher's Note: The statements, opinions and data contained in all publications are solely those of the individual author(s) and contributor(s) and not of MDPI and/or the editor(s). MDPI and/or the editor(s) disclaim responsibility for any injury to people or property resulting from any ideas, methods, instructions or products referred to in the content.

energies

MDPI

Perspective

The Port-Hamiltonian Formulation of Thermodynamics—A New Perspective

Janusz Badur * and Piotr Józef Ziółkowski

Energy Conversion Department, Institute of Fluid Flow Machinery, Polish Academy of Sciences, 80-231 Gdańsk, Poland; pjziolkowski@imp.gda.pl
* Correspondence: jb@imp.gda.pl

Abstract

This paper proposes a change in the traditional epistemological paradigm and a look at classical thermodynamics from the point of view of control theory, with the aim of discovering energy state variables. The paper proposes a transition from "causality" to "purposefulness" in nature, which is called port-Hamiltonian thermodynamics. It is unclear whether classical thermodynamics can be incorporated into the formalism of port-Hamiltonian field theory, and it is likely that thermodynamics will need to be expanded or even completely reformulated. The main goal is to satisfy the First and Second Laws of Thermodynamics a priori.

Keywords: continuum thermodynamics; Hamiltonian field theory; port-Hamiltonian thermodynamics; theory of control; Poisson brackets; energy dissipation; Rayleighian

1. Port-Hamiltonian Formalism and Its Significance in Engineering

Based on Hellenistic science, Western civilization has achieved its goals and exhausted its potential for development. The tasks of humanity related to building, designing, and simply imitating natural phenomena have already been completed. We are now entering a period called the "civilization of sustainable development", so the new tasks are optimization, maintenance, control, and artificial intelligence. The exhaustion of Hellenistic civilization was accompanied by the exhaustion of its main driving force—what we call "Aristotle's thermodynamics". Thermodynamics, as a thoroughly practical science, covered all levels: from quantum thermodynamics, field theory thermodynamics, statistical thermodynamics, phenomenological non-equilibrium thermodynamics, through classical thermodynamics of technical devices, to the thermodynamics of the atmosphere, the sun, the solar system, and the cosmos.

Due to its fundamental motivations, thermodynamics has thus far been a technical art of describing phenomena in which, as Sadi Carnot put it, we are able to obtain mechanical power from a thermal source of power. Thermodynamics thus had anthropological goals, namely, to replace expensive workers and soldiers with cheap mechanical power generated from thermal energy sources. Today, human labor has been completely eliminated, and thermodynamics has new goals, such as maintenance, optimization, control, and AI thermodynamics. These new goals have been taken up by a science called "port-Hamiltonian thermodynamics" [1–3]. Its pioneers are B. Maschke and A.J. van der Schaft [4,5], and the following disciples from their school: R. Ortega, G. Escobar [6], K. Krhac [7], and D. Jeltsema [8]. Among the veterans are also Duindam, Macchelli, Stramigioli nad Bruyncks [9], R. Rashiad [10,11], F. Califano [12], Brugnoli [13], Jäschke [14], Cardoso-Ribeiro [15], R.

Altmann and P. Schulze [16], H. Ramirez and Y. Le Gorrec [17,18], L. Mora [19], and others [1,17] (see reviews).

The importance of the port-Hamiltonian formalism (pH) and its powerful advantages over the Lagrange formalism are evidenced by the extraordinary number of works that have appeared over the last three years (see: van der Schaft [2]). We will mention them in the text, keeping in mind the historical outline of the lecture.

Jean-Francois Pommaret, an eminent theorist and specialist in control theory, elevates the role of control theory above the contemporary foundations of gauge theory and gravitational theory, arguing that when the formalism (pH) is applied to the description of nature, "nothing remains of the mathematical foundations of both general relativity and gauge theory" [20]. He is right in this, because Hamilton's formalism is, by its very nature, a deeper and more comprehensive way of studying the laws of conservation and the equations of evolution of natural phenomena. Pioneers point to the need to rebuild the foundations of the theory of electromagnetism and gravity (Pommaret [21]), rebuild quantum physics (Alicki and Koslof [22]), and rebuild thermodynamics (Beris and Edwards [23], Grmela [3,24]; Sípka et al. [25]; M. Sýkora et al. [26]; Grmela and Pavelka [3], Pavelka, Klika and Grmela [27]). Therefore, if pH thermodynamics is to be based on solid foundations, a reconstruction and modernization of the foundations of both general relativity and gauge theory is needed (Pommaret [21,28], Badur and Dudda [29], Yahalom [30,31]).

Why are both practitioners and theorists involved in the control of natural and technical systems so eager to base their reasoning, tools, and methods of implementation on port-Hamiltonian formalism? This is because this formalism uses the concept of "energy" as a *lingua franca*. This allows two subsystems defined in different physical domains to be coupled by a connection that conserves energy flows. In this sense, within pH, two types of energy-preserving connections are commonly used: a port connection preserving stored energy flows through the Hamiltonian and an energy connection preserving dissipated energy flows through the Rayleighian [23].

The reconstruction of thermodynamics in the new formalism does not have to follow the guidelines set out by the practical principles of thermodynamics. This review investigates the manifestations of thermodynamic laws in the context of thermodynamic pH.

- The Zeroth Law of Thermodynamics establishes empirical methods for determining state parameters and their identities.
- The First Law of Thermodynamics prohibits the creation of energy from nothing (ex nihilo) and mandates the conversion of field energy in the presence of matter.
- The Second Law is a requirement for the perpetual conversion of energy and a prohibition on the reversibility of dynamics: the breaking of time reversal symmetry.
- The Third Law is a requirement for the existence of absolute values of extensive state parameters and a prohibition on the existence of vacuum energy (matter without fields).

The aim of this publication is to show that conventional thermodynamics cannot be directly applied to pH thermodynamics, but must undergo expansion, modernization, and paradigm shifts. It must be based on new experiments and laboratory research.

2. Building a Set of Evolutionary Equations Using the Poisson Bracket Apparatus

The motivation for research based on the Poisson brackets came not only from Hamiltonian mechanics, but more generally, from the needs of engineering. Western civilization is based on the undisputed role of mathematical models in recognizing and harnessing natural phenomena. Only harnessed phenomena we can use in technology. This means that only those devices and human products that correctly utilize natural phenomena, which

we can control and make the correct predictions. Therefore, most researchers agree that the objects of our civilization possess "harnessed" natural phenomena, described by a set of equations called "governing equations", which are controlled by appropriate boundary and initial conditions. Now is the time for engineers to begin to control all of this.

Researchers who study the construction of the Poisson brackets, understood as a general research tool, are approaching the aforementioned describing equations as a "poor junkyard", viewing the system of equations describing them as a jumble of equations of motion (evolution), conservation laws, and laws of thermodynamics. In other words, the governing equations are not valid for the control equations. Sometimes, it is obvious that the governing equations do not satisfy the conservation laws or one of the laws of thermodynamics. We then say that the system of conservation equations violates the laws, and the simulation of reality performed with this model deviates from the experimental data. These equations cannot be used to achieve control or achieve true goals [32].

Given this state of affairs, researchers in engineering and applied physics as well as chemistry have developed a need to build a research tool that provides more efficient and comprehensive procedures than those derived from the traditional Lagrangean formalism. Reasoning based on the classical Lagrangean apparatus leads to poorer understanding than the more extensive procedures such as GRIMEC, Poisson brackets, or M-Matrix (Grmela and Öttinger [33], Zafferi et al. [34], Grmela [35–37]).

The aim of the Hamiltonian approach, based on the Poisson brackets, is to seek the complete physics of natural phenomena—which practically means that the number of primary variables is many times greater, perhaps even complete, compared to the Lagrangean approach. Furthermore, the structure of the model resulting from the Hamiltonian approach is more flexible, more physical, and more effective in simulations. One of the goals of the Hamiltonian approach is to reinterpret known and worn-out field-theoretic models, for example, extending the fluid model previously known as the "Navier–Stokes–Fourier equation". It is therefore important to understand that the Hamiltonian approach is not simply an approach that re-writes the Navier–Stokes–Fourier equations, but rather an approach that constructs a new physical description for this type of fluid, with new constants, new measurement methods, and new numerical methods. Referring to the well-known and understood name CFD (Computational Fluid Dynamics), which is the research paradigm of the 21st century, it must be said that we are looking for a new science that can be called Hamiltonian-CDF.

The main task of pH thermodynamics can be summarized as follows. The basic structure of equations describing the real world in the Hamiltonian approach using Poisson brackets has the general form, proposed by Grmela [35,36], Morrison [38]:

$$\dot{x} = \{x, H\} + [x, H]. \tag{1}$$

The most important object here is the object named by the letter x. This is a state variable that is the fundamental unknown of the control system. It consists of n components with different physical dimensions: $x = (x_1, x_2, x_3, \ldots, x_n)$. Finding and defining these variables for a given physical phenomenon, such as the flow of a Navier–Stokes fluid or a Cosserat fluid, is the most difficult part of control theory—we cannot rely on the simplified knowledge provided by a Lagrangean-type approach. The notation x is not accidental and refers to control theory. Equation (1) contains two brackets, $\{,\}$ and $[,]$, and a Hamiltonian H defining the stored energy of the system.

The equations Equation (1) are evolution equations and fortunately, they can be used in this form appropriate to the control systems. Control practice and theory recognize various variables, but energy variables have been denoted by the letter x for years. Control

https://doi.org/10.3390/en19020324

is most often used in the linear version as (Pommaret [28], Gawroński [32], Ogata [39], Mieloszyk [40]):

$$\dot{x} = Ax + Bu,\ y = Cx + Du, \tag{2}$$

or in the case of field variables

$$\dot{x} = A_{zz}\frac{\partial^2 x}{\partial^2 z} + A_z\frac{\partial x}{\partial z} + Ax + Bu;\ y = Cx + Du, \tag{3}$$

where $A,\ A_z,\ A_{zz}$ are state matrices, z is a spatial variable, B is a control matrix, u and y are the control and the effect—a control output, $C,\ D$ are the output and transmissibility matrices, respectively. Above we have an example of control with a proportional term $y(t) = Cx(t)$ where the output signal is defined in proportion to the state signal. More complex controls are based on a derivative term: $y(t) = k\dot{x}(t)$ or on an integral term: $y(t) = k\int_0^t x(\tau)d\tau$ [40].

Fundamental to the theory of energy control is the system graph (Ogata [39]). Learning how to construct a system graph should become a fundamental element of pH thermodynamics. For example, for the system of Equation (2) consisting of state evolution equations and output equations, the graph is shown in Figure 1, this method of presentation is known from classical monographs [32,39,40].

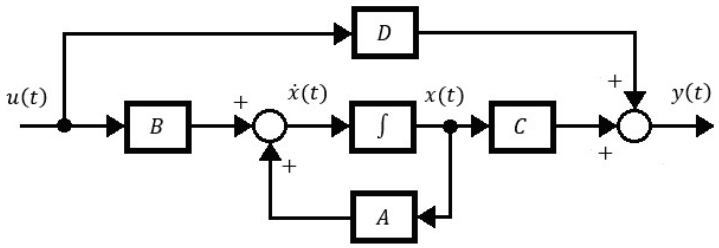


Figure 1. Graphical representation of the control system given by Equation (2).

Unfortunately, in control theory, the state variable x is arbitrary defined—frequently uncorrelated with the energy state of the system. However, in the special case where we want to correlate the evolution of the system $\dot{x} = \frac{\partial}{\partial t}x$ with the energy carried by the Hamiltonian, we will call such variables energy variables. This allows us to derive part of the control Equation (2) from the evolution equations placed on Poisson brackets (Equation (1)).

However, let us emphasize that searching for the Hamiltonian is usually a hopeless task and even for a linear system $\dot{x} = Ax + Bu$ is difficult to find. However, if we introduce a function w that is a co-state, then $H(w, x, u) = w^T(Ax + Bu)$ can be a Hamiltonian if we add some adjoint equations to the system of equations [4]. For a system of linear control equations, the most important is the transfer function, which requires the resolvent, i.e., the inverse matrix: $\mathrm{R} = (sI - A)^{-1}$. For a system not exceeding 3×3, it can be found analytically. Modern control theory has also adopted a number of artificial intelligence methods (neural networks, fuzzy logic, genetic algorithms, expert systems). Numerical methods, computational environments such as Matlab (including its Simulink toolkit) or Mathcad, and programming environments such as LabVIEW are also used.

3. The Idea of the Hamilton Formalism

In 1834, William Rowan Hamilton showed that Newton's equations: $m_i\dot{q}_i = f_i$ for a set of particles in a conservative force field $f_i = \mathrm{grad}\ V_i$ with "potential energy"

https://doi.org/10.3390/en19020324

V_i $(i = 1,\ 2,\ 3, \ldots, n)$ can be derived from a single function, which he called the "characteristic function",

$$H(p, q, t) = \sum_i \left[\frac{p_i^2}{2m_i} + V_i(q_1, q_2, \ldots., q_i, \ \ldots q_n) \right]. \tag{4}$$

Here q_i is the position of the i-th particle, whose mass is m_i and p_i is its canonical momentum $p_i = m_i q_i$. The positions and momenta form the state vector of unknowns $x = (q, p)$. The equations of motion (evolution) are obtained from the formula: $\dot{x} = \mathcal{J}\delta_x H = \mathcal{J}\frac{\delta H}{\delta x}$, which in turn can be transformed to the Newtonian form. The solutions $\dot{x} = \mathcal{J}\delta_x H$ with respect to time form trajectories [28].

At first glance, Hamilton's formula seems to provide only a convenient formulation of Newton's system—a convenience perhaps most obvious, since the scalar function $H(p, q, t)$ encodes all information not in n second-order equations but in 2n first-order equations. Only after the work of Grmela [35], Grmela and Öttinger [33], and Mielke [41] did it become clear that the Hamiltonian formalism offers much more than just this simplification of calculations—it is, in fact, a proper tool for the theory of evolution, control, and optimization. Nature is not inherently optimal and constantly wanders; only humans can teach it how to achieve its goals. The challenges of pH thermodynamics are countless. Never before in the history of the world has man faced such a difficult problem.

Indeed, if we allow for more general functions $H(p, q, t)$ and a more general relation between canonical momenta and position velocities, then practically all previously known models of classical physics fall under the Hamiltonian formalism. Moreover, quantum field theory is formally obtained from Hamiltonian fields by replacing the canonical momentum in the Hamiltonian with a differential operator (Pommaret [42]).

The Hamiltonian formalism, however, imposes strong constraints on the physics of the modeled phenomena. Simply put, when $H(p, q, t)$ is independent of time (it is autonomous), its value is constant along the trajectories: the energy $E = H(q, p)$ is constant. This also implies the fulfillment of the First Law of Thermodynamics, which states that the energy of a system cannot arise from nothing (*ex nihilo*). Similarly, if the Hamiltonian is independent of one of the position variables, e.g., q_a (this variable is negligible), this means that the corresponding canonical momentum p_a is constant—it is an invariant of the evolutionary process. This provides a simple explanation of the relationship between symmetries (e.g., rotational symmetry) and invariants (e.g., angular momentum) and leads to Noether's theorems [43].

One of the stronger constraints imposed by the Hamiltonian structure concerns stability: any trajectory cannot be asymptotically stable in the Hamiltonian system. There is also an even deeper feature: for each equilibrium eigenvalue, there is a corresponding opposite (negative) eigenvalue [28,40].

Another important implication for physics is that knowledge of the invariants of motion (evolution $\dot{x} = \mathcal{J}\delta_x H$) is sufficient to fully characterize the solution of $2n$ equations for a system with n degrees of freedom when the Hamiltonian is integrable. This follows from Liouville's integrability theorem [28]. This strong structural stability of Hamiltonian dynamics was unexpected even in the mid-20th century, when physicists began the first computer simulations of control systems (see: [20,28,31]).

4. The Essence of the Poisson Brackets

The Poisson's brackets apparatus gained importance and became "fashionable" only after Dirac used it in quantum mechanics in 1930. Previously, it was used in Hamiltonian mechanics [26]. The starting point is the mechanics of a swarm of points carrying mass m_i, $i = 1, 2, 3, \ldots, n$ with position $q_i = q_i(t)$, in which spatial relations play no role and only the changes in positions over time are important: $\partial_t q_i \equiv \dot{q}_i$.

https://doi.org/10.3390/en19020324

It involves reformulating (but with equivalent physics) the Lagrangean approach by introducing new n variables $p_i = \frac{\partial L}{\partial \dot{q}_i}$ called generalized momenta, and transforming the Lagrangean of the action into the Hamiltonian: $H(q,p,t) = \sum p_i \dot{q}_i - L(q,\dot{q},t)$—this is called the Legendre transformation and allows for the elimination of time derivatives of the fundamental variables and their replacement with generalized momenta. By this operation, we reduce the order of differentiation at the expense of increasing the number of unknowns. In this case, it is a doubling. Instead of the Lagrange-Euler equations of motion, we now have Hamiltonian equations of motion (evolution):

$$\dot{p}_i = -\frac{\partial H}{\partial q_i} + Q \text{ and } \dot{q}_i = \frac{\partial H}{\partial p_i}. \tag{5}$$

The dynamics equations become the evolution equations of a system based on energy variables. They have an interesting structure, called the Dirac structure, and can be expressed by formal operations contained within the Poisson bracket. For example, if we have two functions $f(p,q)$ and $g(p,q)$ in the state space, the Poisson bracket is defined as a commutator [27,35]:

$$\{f,g\} = \frac{\partial f}{\partial q_i}\frac{\partial g}{\partial p_i} - \frac{\partial f}{\partial p_i}\frac{\partial g}{\partial q_i}, \tag{6}$$

in which the indices $i = 1,2,3,\ldots,n$ should be traversed. This pattern was used by Dirac to build a quantum commutator on matrices A, B as $[A,B] = AB - BA$. Now, taking as one of the functions the state vector: $x = (q,p)$ and with the other the Hamiltonian H, we have the fundamental component of the evolution equation:

$$\dot{x} = \frac{\partial}{\partial t}\begin{pmatrix} q \\ p \end{pmatrix} = \{x,H\} = \frac{\partial x}{\partial q}\frac{\partial H}{\partial p} - \frac{\partial x}{\partial p}\frac{\partial H}{\partial q} = \begin{pmatrix} \frac{\partial H}{\partial p} \\ -\frac{\partial H}{\partial q} \end{pmatrix} = \begin{pmatrix} 0 & 1 \\ -1 & 0 \end{pmatrix}\begin{pmatrix} \partial_q H \\ \partial_p H \end{pmatrix} \equiv \mathcal{J}\partial_x H. \tag{7}$$

We introduced above a dimensionless, skew-symmetric Dirac structure matrix $\mathcal{J} = -\mathcal{J}^T$ and a shortened notation for the generalized derivative of the Hamiltonian $\delta_x H \equiv \partial_x H - \mathrm{div}(\partial_{\nabla x} H) + \cdots$. It is also called "variational derivative" or "functional derivative" in the literature. Due to the physical (thermodynamic) interpretation in the literature over the last 20 years (see review [2,17]), the state variables x are also called energy variables. Now, if the Hamiltonian has a special quadratic form $H = \frac{1}{2}x^T K x$ (for instance, in a case of linear spring, $K = K^T$), then the above evolution system takes the form:

$$\frac{\partial x}{\partial t} = \{x,H\} = \mathcal{J}\frac{\delta H}{\delta x} = \mathcal{J}\delta_x\left(\frac{1}{2}x^T K x\right) = \mathcal{J}Kx \equiv Ax. \tag{8}$$

This control matrix $A = \mathcal{J}K$, known from linear control theory, appears as an object in the fundamental control equation (Equation (2)). This means that only a portion of the control theory tasks—which, as we know, applies to all natural phenomena and phenomena used in technology—is subject to a Hamiltonian approach. We will call such phenomena "Hamiltonian systems". This approach to natural variability has much in common with the Aristotelian thermodynamics, based on the Hamiltonian understanding of the concept of "energy". Therefore, when constructing thermodynamics "a la Hamilton", we call the set of variables x energy variables, which have nothing in common with the state variables defined by the traditional thermodynamics of Clausius, Thomson, and Boltzmann.

Let us recall that when constructing Poisson brackets for field phenomena—that is, when constructing the still very poorly understood Hamiltonian field theory—we must remember that the tool provided by the Poisson bracket is a very blunt one, which often serves to limit rather than expand our knowledge of reality (Sieniutycz and Berris [44]). Therefore, when taking Poisson brackets as a tool for understanding the world, we

https://doi.org/10.3390/en19020324

must remember that they satisfy, for example, the following constraints: asymmetry: $\{f,g\} = -\{g,f\}$; the linearity necessary for the proper evaluation of the phenomenon: $\{\alpha f + \beta g, h\} = \alpha\{f,h\} + \beta\{g,h\}$ for arbitrary real numbers α, β; and the key identity imposed on nature by Jacobi: $\{f,\{g,h\}\} + \{g,\{h,f\}\} + \{h,\{f,g\}\} = 0$. In practice, to prove that our devised Poisson bracket satisfies this theorem, we need a large piece of paper and a "hot cup of coffee". Then we expand out all 24 terms and watch them cancel one by one [31].

5. Origin of the Control Port

This means that the Poisson bracket can be used to write the control system, as follows:

$$\dot{x} = \mathcal{J}\delta_x H(x) + G(x)u(t), \tag{9}$$

when, physically speaking, it represents a skew-symmetric matrix structure allowing energy flows between different regions of the system. If $\mathcal{J}$ is constant, usually $\mathcal{J}(x)$ is a differential operator consisting of skew-symmetric matrices, as follows: $\mathcal{J}(x) = J_0 + a_1 J_1 \partial/\partial\overleftrightarrow{x} + a_2 J_2 \partial/\partial\vec{x}(\partial/\partial\vec{x}) + a_3 J_3 \partial^3_{\vec{x}\,\vec{x}\,\vec{x}} + \cdots$; then, it satisfies the Jacobi identity, because for two functions, f, g, it is expressed in the form $\{f,g\} = \frac{\partial f}{\partial x}^T \mathcal{J}(x) \frac{\partial g}{\partial x}$, which leads to the following control equations: $\dot{x} = \{x, H\} + G(x)u(t)$.

A further interpretation of the Hamiltonian formalism in the language of control theory is obtained when we exclude from the total degrees of freedom some of the already known degrees q_a with a given momentum Q, and we give them a different meaning. When we ask what the change in energy system is, we obtain the following, using Equation (7):

$$\dot{H} = \frac{\partial H}{\partial q}^T \cdot \dot{q} + \frac{\partial H}{\partial p}^T \cdot \dot{p} = -\left(\dot{p} - Q\right)^T \cdot \dot{q} + \left(\dot{q}\right)^T \cdot \dot{p} = Q^T \cdot \dot{q}. \tag{10}$$

Now, by cutting out the degrees of freedom pertaining to the given momentum Q and introducing the notation $u \equiv Q$ and $y = \dot{q}$ for these special degrees of freedom, we have a rearranged system of equations:

$$\dot{q} = \frac{\partial H}{\partial p},\ \dot{p} = -\frac{\partial H}{\partial q} + Gu, \quad y = G^T \frac{\partial H}{\partial p}, \tag{11}$$

where the output equation appears, which is part of the initial equation $\dot{q}_a = \frac{\partial H}{\partial p_a}$, and the matrix G is generated by the "potential" part of the Hamiltonian. Now calling the "extended" degrees of freedom in the language of control theory, respectively, the control u and the output y, we can write the change in the Hamiltonian (Equation (10)) as $\dot{H} = Q^T \cdot \dot{q} = u^T \cdot y$ and express it as follows: the change in the system's energy occurs as a result of the supplied (from the outside) energy $u^T \cdot y$. This reasoning, transforming the control system (Equation (2)) into a problem of the evolution of Hamiltonian field theory, assumes that if the dimensions of the control and output are the same, then the matrix $C = B^T$ in Equation (2) also holds.

6. Transition to the Continuum

The above brackets are constructed for "swarm material points" and therefore do not have a field-like character dependent on spatial variables. However, Poisson brackets for the theory of elasticity, Navier–Stokes fluids, and other field models have a differential structure and behave analogously to the "Lie derivative" first used in differential geometry by Wł. Ślebodziński [43]. It is obvious that for any field, relations of the type $\{q_i, q_i\} = 0$; $\{p_i, p_j\} = 0$; $\{q_i, p_j\} = \delta_{ij}$j will hold. For a free function—this is most often an invariant

https://doi.org/10.3390/en19020324

of Hamiltonian motion—$f(q,p,t)$, the complete time change, denoted by the letter dt, is equal to [27]:

$$\frac{df}{dt} = \frac{\partial f}{\partial p}\dot{p} + \frac{\partial f}{\partial q}\dot{q} + \frac{\partial f}{\partial t} = -\frac{\partial f}{\partial p}\frac{\partial H}{\partial q} + \frac{\partial f}{\partial q}\frac{\partial H}{\partial p} + \frac{\partial f}{\partial t} = \{f,H\} + \frac{\partial f}{\partial t}. \tag{12}$$

When the function f does not depend directly on time t, we have $\frac{df}{dt} = \{f,H\}$. We emphasize this notation of the derivative here, as numerous other notations appear in the literature, leading to unnecessary doubts. Let us emphasize the convention of the "energy control theory" notation, in which $\dot{x} = \frac{\partial}{\partial t}x$. In Hamiltonian thermodynamics, therefore, there are numerous energy invariants of motion. If $\dot{I} = 0$ (invariant), then the condition is that $\{I,H\} = 0$. Conversely, some quantity I is called an energy invariant of motion when the condition $\{I,H\} = 0$ is satisfied [27].

The invariant of motion does not have to be a scalar; it can be any quantity used in Hamiltonian thermodynamics—e.g., if several positions q_j do not appear in the Hamiltonian, then the corresponding object called linear momentum p_j is an invariant of motion $\{p_j,H\} = 0$. This is the case of cyclic variables introduced into Helmholtzian thermodynamics [43]. The most famous invariant in classical Hamiltonian thermodynamics is the "adiabatic invariant": $I = \frac{1}{2\pi}\oint pdq$ and the transition from classical to quantum Poisson brackets $\{,\}_{classical} \rightarrow -\frac{i}{\hbar}[,]_{quantum}$ allows us to find all fundamental laws of Hamiltonian quantum thermodynamics "for free" [20]:

$$\dot{f} = \{f,H\} \qquad \rightarrow \qquad i\hbar\,\dot{f} = [f,H]. \tag{13}$$

We mentioned above the "problems" associated with the enormous number of transformations when transforming classical control theory into energy-based Hamiltonian control theory, because in practice, the transition from the classical linear control theory formulae $\dot{x} = Ax$ to the energy (thermodynamic) Hamiltonian approach $\frac{\partial x}{\partial t} = \mathcal{J}\frac{\delta H}{\delta x}$ is extremely difficult and usually requires various omissions and "cuts" in the control system. This is because not every control system has a Dirac structure. An even greater limitation of the structure is the Stokes–Dirac structure, which allows the introduction of special ports into the system. Then, the control matrix B in Equation (2) takes on a special (energy) form.

7. The Nambu Brackets

Another tool for studying the evolution of natural and technical phenomena is the Nambu bracket [45,46], introduced in 1973. Knowing that natural and technical control systems, $\dot{x} = Ax + Bu,\ y = Cx + Du$, contain larger structures than the Dirac and Stokes–Dirac structures, Nambu proposes formulating the laws of evolution of field and matter physics in the form of brackets based not on one but on two Hamiltonians. Instead of the canonical pair of variables representing positions and momenta (q_i, p_i), Nambu proposes triplets $x = (q_i, p_i, r_i)$ where $i = 1,2,3\ldots,n$. The system has dimension $3n$. It is impossible to determine what these additional state variables are before determining the state of the control system. The Nambu bracket takes the form of a commutator consisting of six terms [47]:

$$\{f,g,h\} = \frac{\partial f}{\partial q}\frac{\partial g}{\partial p}\frac{\partial h}{\partial r} - \frac{\partial f}{\partial q}\frac{\partial g}{\partial r}\frac{\partial h}{\partial p} + \frac{\partial f}{\partial r}\frac{\partial g}{\partial q}\frac{\partial h}{\partial p} - \frac{\partial f}{\partial r}\frac{\partial g}{\partial p}\frac{\partial h}{\partial q} + \frac{\partial f}{\partial p}\frac{\partial g}{\partial r}\frac{\partial h}{\partial q} - \frac{\partial f}{\partial p}\frac{\partial g}{\partial q}\frac{\partial h}{\partial r}. \tag{14}$$

https://doi.org/10.3390/en19020324

This satisfies the asymmetry condition $\{f,g,h\} = -\{g,f,h\} = \{g,h,f\}$, and the Leibniz–Jacobi condition. If we define two energy functional H, G (e.g., energy and entropy), then any state function evolves according to the following law:

$$\dot{x} = \{x, H, G\}. \tag{15}$$

Without a doubt, a broader class of control systems can be described using Nambu brackets, and new quantum mechanics can be easily derived. Hence, the Nambu brackets formalism with two Hamiltonians is not a historical curiosity, as evidenced by the works of Nevir and Blender [45], Blender and Badin [46], and Sato [47].

8. The Rayleighian Formalism

If the Hamiltonian includes the energetic effects of the dynamics of inertial (completely reversible) phenomena, then the energetic effects of the dynamics of non-inertial (coercive, dissipation-dominated, and completely irreversible) phenomena are included in the Rayleighian, denoted by the letter $\mathcal{R}$. Typically, in natural phenomena, coercion is mixed with inertia, and reversibility with irreversibility; hence, the two functional $\mathcal{H}$ and $\mathcal{R}$ appear together in a single balanced formalism. The undoubted advantage of this formalism is the development of more physically grounded, structure-preserving numerical methods that are less sensitive to energy dissipation phenomena [48]. A possible connection of the Rayleigh functional to pH thermodynamics is presented in Section 15.

9. The GENERIC Formalism

Other Hamiltonian formulations of the thermodynamics of irreversible processes require both the conservation of energy and the irreversible entropy creation. Grmela and Öttinger [33] proposed reformulating a conventional thermodynamic system along the lines of a mechanical system in Hamiltonian representation. In this line, the "General Equation for the Non-Equilibrium Reversible Irreversible Coupling", or simply GENERIC, proposes to "complete" the Hamiltonian (reversible) part of a system with a purely dissipative (irreversible) part.

The GENERIC system is expressed with respect to two generating functions, total energy and total entropy, and with respect to two geometric structures, a Poisson bracket and a pseudo-Riemannian metric. This representation is capable to express simultaneously the conservation of energy and the irreversible creation of entropy as a geometric property of the system [34,49].

The reversible part of the evolution is described in terms of the Poisson bracket and the Hamiltonian, which is a function of the total energy of the system. The dissipative part is defined as pseudo-energy and generated by the total entropy as a potential function. The GENERIC formalism proposes the time evolution of the state variables x in the following form [49]:

$$\frac{\partial}{\partial t}x = J(x)\frac{\partial H(x)}{\partial x} + M(x)\frac{\partial S(x)}{\partial x}, \tag{16}$$

where H, S are the total energies and entropy of the control system and the matrices J, M are defined by the Poisson bracket and the "pseudo-Riemannian metric". The matrix $J(x)$ is skew-symmetric and the matrix M is symmetric [27]. They satisfy the following conditions of invariability:

$$J(x)\frac{\partial S(x)}{\partial x} = 0 \text{ and } M(x)\frac{\partial H}{\partial x} = 0. \tag{17}$$

https://doi.org/10.3390/en19020324

If, in analogy to the Poisson bracket, we define the Grmela bracket as $[f,g]_M = \frac{\partial f(x)}{\partial x}^T M(x) \frac{\partial g(x)}{\partial x}$, then using two generators, H, S, we can represent the GENERIC formalism using two brackets [27,34,37,41,49]:

$$\frac{\partial}{\partial t} x = \{x, H\}_J + [x, S]_M. \tag{18}$$

This means that the two rules of evolution of functionals are also satisfied:

$$\dot{H} = \{H, H\}_J + [H, S]_M = 0;\ \dot{S} = \{S, H\}_J + [S, S]_M = \sigma_{int} \geq 0, \tag{19}$$

where σ_{int} is the irreversible entropy production [35]). This means that the GENERIC formalism satisfies the first and second laws of thermodynamics with an excess.

Remark 1. *It must be admitted that the form (Equation (18)) is very attractive for control theory in the Hamilton energy approach. It should be used, but only as a model. Therefore, for practical reasons, it is completely impossible to use the dissipative bracket* $[x, S]_M$ *based on the entropy functional, because the Port-Hamiltonian approach is based on energy and its modes of dissipation and destruction. Moreover, the introduction of the bracket* $[x, S]_M$ *limits the class of real systems to a narrow group of problems. Here, one must acknowledge the validity of the control theory approach, which views the problem of energy dissipation and the description of irreversible phenomena in a more general way, devoid of unnecessary assumptions of non-equilibrium thermodynamics acting as a priori imposed simplifications of phenomena. Control theory, arising from the paradigm of the nature purposefulness, has an epistemological advantage over non-equilibrium phenomenological thermodynamics arising from the paradigm of the nature causality.*

10. Port-Hamiltonian–Energy Variables

In this article, after introducing port-Hamiltonian systems, the focus is on "connection control" to stabilize the set point of nonlinear physical systems. Most of this theory is well established, see, e.g., [1,7], but new solutions using "energy ports" instead of "power ports" are also considered.

Port-Hamiltonian systems theory emphasizes open systems and their control using additional feedback loops and connections to control systems. This leads to modeling a complex system as an energy-efficient combination of elements responsible for energy storage, dissipation, and "control". Using energy and power as a lingua franca between different physical domains (gravity, electrodynamics, optics, mechanics, electricity, chemistry, and thermodynamics), port-Hamiltonian theory provides a systematic framework for modeling multiphysical systems; see, e.g., [8,9,17]. Moreover, it is not limited to systems with concentrated parameters, but also extends to systems with distributed parameters (with boundary control); see, e.g., [4,10]. In other words, control theory based on port-Hamiltonian thermodynamics allows the achievement of set goals in accordance with the laws of thermodynamics describing "evolutionism" rather than "creationism".

11. The Concept of Energy Ports

The essence of port-based modeling and port-Hamiltonian (pH) systems theory is presented in Figure 2. The fundamental element of Hamilton's thermodynamics is that the way the control system is reorganized allows for the modeling of both reversible (energy-storing) and irreversible (energy-dissipating) phenomena. Now let us look at the control system in a new energy-based graphic version. These phenomena can be imagined using ideal energy storage elements $\mathcal{S}$ (capacitors, coils, masses, springs, etc.) and energy-dissipating control elements $\mathcal{R}$ (resistors, dampers, friction elements, etc.),

https://doi.org/10.3390/en19020324

connected to each other by a central energy-converting structure denoted by the letters $\mathcal{S}$-$\mathcal{D}$ (Stokes–Dirac). In some cases, the $\mathcal{S}$-$\mathcal{D}$ structure has physical representations (Krhac, Maschke, and Schaft [7]).

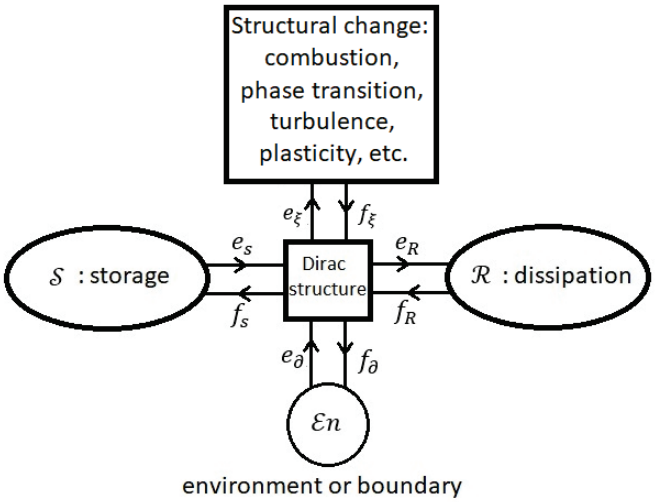


Figure 2. Van der Schaft's connection graph for an energy port system containing storage, dissipation, structural change, and environment.

Since control systems are often open systems that interact with their environment, there is an exchange port with the environment $\mathcal{E}n$ from which the control u and the output vector y often originate. The latter, in order to satisfy the conditions of the pH formalism, must be dimensionally correlated and form the so-called supply rate function. Such a function is possible with the interpretation presented in (Equation (9)). It has the form $s(u,y) = u^T \cdot y$ and denotes the power supply to the control system. If we treat the Hamiltonian $H(x)$ as an energy storage function, the ideal situation would be one in which the rate of energy storage would be equal to the rate of its supply through the exchange port: $\dot{H}(x) = s(u,y)$. Practical experience shows that this condition is impossible to achieve. Therefore, if we have a control system measured at two moments t_0, t_1 where $t_1 > t_0$, the Hamilton function (stored energy) should satisfy the dissipation inequality [1,2]:

$$H(x(t_1)) \leq H(x(t_0)) + \int_{t_0}^{t_1} s(u(\tau), y(\tau)) d\tau. \tag{20}$$

This equation does not say where the dissipated part of the energy that has not been stored "flows away", because in technology it is usually not recovered or controlled. However, adding irreversible ports allows us to find the physical cause of the shortcomings of energy storage and the amount of dissipated energy that is uselessly released into the environment.

12. Fluxes and Efforts—The Dual Pairs

The formalism of pH thermodynamics radically changes the foundations of control theory, as it seeks energy pairs in all phenomena. Hence, the connection in the energy control graph is made through a pair of objects with identical dimensions. Let us write them generally as abbreviations of the words *flux* and *effort*—this is the pair (f,e), the first of which is called flux and the second effort. Since these are energy state variables, their product, properly defined, is expressed in units of J/s, i.e., it is energy power. Any pair of vectors (f,e) defines an energy port, and the entire set of variables f,e is also called the set of energy variables of this port [7,9,12].

https://doi.org/10.3390/en19020324

A control system containing three such ports: port (f_s, e_s), which connects to an ideal energy storage device $\mathcal{S}$, port $(f_R,\ e_R)$, corresponding to the dissipation of available energy $\mathcal{R}$, and external port (f_∂, e_∂), through which the system interacts with the environment $\mathcal{E}n$ (including the operation called "control"). The scalar quantities of pH theory form the products $f_s^T \cdot e_s$, $f_R^T \cdot e_R$, $f_\partial^T \cdot e_\partial$, which are instantaneous energy powers transferred by links or "bonds", using the terminology of bond graphs (Ortega et al. [6]).

In particular, the boundary (external) port (f_∂, e_∂), (f_ξ, e_ξ) appears in two variants: once as a controllable port (controllable external energy sources) and once as an uncontrollable port (uncontrollable external energy sources). Then the variables are decomposed: $(f_\partial, e_\partial) \rightarrow (f_C, e_C) \bigoplus (f_I,\ e_I)$.

Remark 2. *This division of boundary ports results from practice and is best explained using a specific, well-known example of forced vibrations of a solid body Ω in the shape of a slender rod, one end of which $\partial\Omega_a$ is fixed and at the other end $\partial\Omega_b$. There is an exciting force $\vec{\sigma}_{ext} = \vec{F}_{ext}(t)/A$, which we can consider as control $\vec{u}$ and the corresponding velocity of the rod end as output $\vec{y}$. The remaining sides of the rod $\partial\Omega_c$ are located in atmospheric air, which we can consider to be a constant, zero-force, uncontrollable forcing. The fixed end belongs to the uncontrollable boundary variables in which the value of the state variable (zero velocity and momentum) is set, while the fixing force, called the "reaction", is unknown. No energy flows into the system through this port.*

Considering that practical division of the boundary into three parts $\partial\Omega = \partial\Omega_a \cup \partial\Omega_b \cup \partial\Omega_c$, the Hamiltonian takes the form:

$$\mathcal{H}(x) = \iiint H\, d\Omega + \iint_{\partial\Omega} H_{ext}\, dA, \tag{21}$$

where $H = \frac{1}{2}\rho \dot{\vec{u}}^2 + \rho u(\overleftrightarrow{\varepsilon})$ is a function of kinetic and internal energy $u(\overleftrightarrow{\varepsilon})$ dependent on deformation $\overleftrightarrow{\varepsilon}$ caused by displacement $\vec{u}$. On the other hand, $H_{ext} = \vec{u} \cdot \vec{\sigma}_{ext}(t)$ acts only at the boundary $\partial\Omega_b$. In Lagrange mechanics, vibrations are described by a single variable, which is the displacement $\vec{u}$:

$$\rho \partial_{tt} \vec{u} = \operatorname{div} \overleftrightarrow{\Sigma} + \rho \vec{b}, \tag{22}$$

where the stress tensor $\overleftrightarrow{\Sigma} = \frac{\partial u}{\partial \overleftrightarrow{E}} = \mathcal{L}\overleftrightarrow{E}$ and the strain tensor is a symmetric object, $2\overleftrightarrow{E} = \operatorname{grad} \vec{u} + \operatorname{grad}^{\mathrm{T}} \vec{u}$, while $\mathcal{L}$ is a matrix of elastic constants. If we choose the energy state vector as

$$x = \begin{pmatrix} \vec{x}_u = \rho \dot{\vec{u}} \\ \overleftrightarrow{x}_E = \overleftrightarrow{E} \end{pmatrix} \text{ and } H(x) = \frac{1}{2}\rho^{-1}(\vec{x}_u)^2 + \frac{1}{2}(\mathcal{L}\overleftrightarrow{x}_E) \cdot \overleftrightarrow{x}_E, \tag{23}$$

it will obtain the following storage ports:

$$f_s = -\frac{\partial}{\partial t} x = \begin{pmatrix} -\partial_t \vec{x}_u \\ -\partial_t \overleftrightarrow{x}_E \end{pmatrix};\ e_s = \delta_x H = \begin{pmatrix} \vec{e}_u \\ \overleftrightarrow{e}_E \end{pmatrix} = \begin{pmatrix} \delta_{\vec{x}_u} H \\ \delta_{\overleftrightarrow{e}_E} H \end{pmatrix} = \begin{pmatrix} \dot{\vec{u}} \\ \overleftrightarrow{\Sigma} = \mathcal{L}\overleftrightarrow{E} \end{pmatrix}, \tag{24}$$

allowing the momentum evolution to be written as $\dot{x} = \mathcal{J}\delta_x H + Gu$:

$$\frac{\partial}{\partial t} \begin{pmatrix} \vec{x}_u \\ \overleftrightarrow{x}_E \end{pmatrix} = \begin{pmatrix} 0 & \operatorname{div} \\ \operatorname{grad}_{\mathrm{s}} & 0 \end{pmatrix} \begin{pmatrix} \vec{e}_u \\ \overleftrightarrow{e}_E \end{pmatrix} + \begin{pmatrix} 1 \\ 0 \end{pmatrix} \rho \vec{b}, \tag{25}$$

https://doi.org/10.3390/en19020324

where the control matrix G and mass force control appear: $u_{\underset{b}{\rightarrow}} = \rho \vec{b}$. The control Equation system (25) consists of 3 + 6 = 9 evolution equations and contains only the first derivatives with respect to time and space. Such low derivatives allow for a completely different discretization than the discretization of the Lagrange approach system (Equation (22)). However, it is important to remember not to spoil the Stokes–Dirac structure with unfortunate discretization; hence, the term "structure preserving discretization" has become common in the literature [5,17,18].

The variation in the Hamiltonian in the region is equal to

$$\begin{array}{c} \dot{\mathcal{H}} = \iiint (\vec{e}_u \cdot \partial_t \vec{x}_u + \overleftrightarrow{e}_E \cdot \partial_t \overleftrightarrow{x}_E) d\Omega = \iiint (\vec{e}_u \cdot \mathrm{div} \overleftrightarrow{e}_E + \overleftrightarrow{e}_E \cdot \mathrm{grad_s} \vec{e}_u) d\Omega = \\ \iiint \mathrm{div}(\overleftrightarrow{e}_E \vec{e}_u) d\Omega = \iint_{\partial\Omega} \vec{e}_u \cdot (\overleftrightarrow{e}_E \vec{n}) \, dA. \end{array} \tag{26}$$

By remembering that the boundary $\partial\Omega = \partial\Omega_a \cup \partial\Omega_b \cup \partial\Omega_c$, the following is obtained:

$$\dot{\mathcal{H}} = \vec{e}_u(\partial\Omega_a) \cdot (\overleftrightarrow{e}_E \vec{n}) + \vec{e}_u(\partial\Omega_b) \cdot (\overleftrightarrow{e}_E \vec{n}) + \vec{u}(\partial\Omega_b) \cdot \vec{\sigma}_{ext}(t).$$

By defining boundary ports $f_\partial = u_\partial = \begin{pmatrix} \vec{e}_u(\partial\Omega_a) \\ \overleftrightarrow{e}_E(\partial\Omega_b)\vec{n}_b \end{pmatrix}$ and $e_\partial = y_\partial = \begin{pmatrix} \overleftrightarrow{e}_E(\partial\Omega_a)\vec{n}_a \\ \vec{e}_u(\partial\Omega_b) \end{pmatrix}$, the following can be written:

$$\begin{pmatrix} f_\partial \\ e_\partial \end{pmatrix} = \begin{bmatrix} \mathcal{B}_u\begin{pmatrix}\vec{n}\end{pmatrix} \\ \mathcal{B}_y\begin{pmatrix}\vec{n}\end{pmatrix} \end{bmatrix} (\delta_x H), \tag{27}$$

The boundary ports use storage-type effort: e_s, and $\dot{\mathcal{H}} = (u_\partial)^T y_\partial$.

13. Energy-Storing Elements

In the connection graph (Figure 2), the Stokes–Dirac connection structure plays a central role. It is a structure that conserves Hamiltonian energy, i.e., $\dot{H} = \{H, H\} = 0$. This means that the energy flux (power) passing through all ports is conserved. It is said that the Stokes–Dirac structure has the property of power conservation, or the conservation of power built up by flows and forces. It combines three flows $f = (f_s, f_R, f_\partial)$ with efforts $e = (e_s, e_R, e_\partial)$ in such a way that the total power connecting the ports is equal to zero: $f^T \cdot e = 0$. From a mathematical point of view, there is a flow space—let us say $\mathcal{F}$—and an effort space that is energetically dual to it $\mathcal{E} = \mathcal{F}^*$. Holding on to mathematical precision, which, incidentally, is often unnecessary, it is said that the energy port variables f, e form a dual product (duality product) $< f \dagger e >$. It is said that the structure $\mathcal{S}$-$\mathcal{D} \subset \mathrm{F} \times \mathrm{E}$ has a Stokes–Dirac structure if $< f \dagger e > = 0$. The simplest example of a structure $\mathcal{S}$-$\mathcal{D}$ is a skew-symmetric connection matrix $\mathcal{J} = -\mathcal{J}^T$ (Equation (7)).

Now, let us note that the port (f_s, e_s) connecting to the reversible energy storage $\mathcal{S}$ can be treated as "energy-storing elements". It turns out that the flow variables f_s satisfy the condition of state variable evolution, $\dot{x} = -f_s$, and energy can be stored in the Hamiltonian $H(x)$, defining the dual variable $e_s = \delta_x H$. Hence, the evolution equation (Equation (15)) can be written algebraically as follows:

$$\frac{\partial x}{\partial t} = \{x, H\} = \mathcal{J}\frac{\delta H}{\delta x} \quad \rightarrow \; -f_s = \mathcal{J} e_s, \tag{28}$$

as the relationship between the flux and the effort of the storage port. The change in Hamiltonian (power) is then equal to the following:

$$\frac{\partial}{\partial t} H(x) = \left(\frac{\partial H}{\partial x}\right)^T \cdot \dot{x} = -e_s \cdot f_s = e_s^T \mathcal{J} e_s = 0. \tag{29}$$

https://doi.org/10.3390/en19020324

However, $\dot{H} = 0$ only when the power of the other ports is equal to zero.

14. Damping in Control Theory

It must be admitted that in control theory, the issue of separating reversible and irreversible phenomena can be resolved by supplementing the initial linear control system (Equation (2)) with additional dissipation matrices (Ogata [39], Gawroński [32]):

$$\dot{x} = (A - R)x + (B + P)u, \tag{30}$$

$$y = (C + P)x + (D + M)u. \tag{31}$$

The condition of the dissipativity of the control system requires that not only the resistance matrix be positive definite, but that the entire "resistance" system is

$$\begin{pmatrix} R & P \\ P & M \end{pmatrix} \geq 0. \tag{32}$$

15. The Control System Based on the Irreversible Port-Hamilton System

An open question is the port $(f_R,\ e_R)$ connecting the $\mathcal{S}$-$\mathcal{D}$ system with the lost energy reservoir $\mathcal{R}$. There is no known way to determine dissipative energy variables, but a one-way flow of dissipated power can be assumed:

$$f_R^T \cdot e_R \leq 0, \qquad \text{for all} \qquad (f_R,\ e_R) \in \mathcal{R}. \tag{33}$$

From the above arrangement of irreversible phenomena, it follows that Hamilton's thermodynamics elevates energy balances in the form of their power and explicitly defines the power dissipated by the port $(f_R,\ e_R)$. This distinguishes it from Lagrange's formalism, which adopts the First Law of Thermodynamics as an energy balance that is conserved and in which there are no energy sources (internal or boundary).

A specific class of port-Hamiltonian systems, often used for control, is obtained in such a way as to preserve the skew-symmetric graph called the Stokes–Dirac structure. Only part of this definition is based on Poisson brackets—the rest requires one to impose a model structure in the form of a skew-symmetric matrix (Equation (8)):

$$\begin{pmatrix} f_s \\ f_R \\ f_\partial \end{pmatrix} = \begin{bmatrix} \mathcal{J} & G_R & -G_\partial \\ -G_R^T & 0 & 0 \\ -G_\partial^T & 0 & 0 \end{bmatrix} \begin{pmatrix} e_s \\ e_R \\ e_\partial \end{pmatrix}. \tag{34}$$

The relationship for the dissipated power port can be analogous to Onsager's constitutive equations known in linear irreversible thermodynamics, $e_R = Sf_R$, where similar to the fourth law of thermodynamics, it is assumed that the matrix of coefficients between the effort and the flux is symmetrical and positive definite: $S = S^T$. Furthermore, in Equation (34), by substituting $G_R e_R = -G_R S f_R = -G_R S G^T e_s$ and $e_s = \delta_x H$, it can be reduced (Equations (30) and (31)) to the desired port Hamiltonian of a control system with a specific control and output port:

$$\dot{x} = [\mathcal{J} - R]\delta_x H(x) + Gu; \quad y = G^T \delta_x H(x), \tag{35}$$

where the resistance matrix $R = G_R S G_R^T$ is substituted for the control $u \equiv e_\partial$ and the output $y \equiv f_\partial$. This means that there is a formal possibility of maintaining the Stokes–Dirac structure for a system with dissipation and boundary ports.

https://doi.org/10.3390/en19020324

In general, the definition of $e_R = Sf_R$ irreversible fluxes and efforts can be replaced by Rayleigh's dissipation functional $\mathcal{R}(f_R)$ [9,10,23], which allows for nonlinear relations:

$$e_R = -\frac{\partial^2 \mathcal{R}(f_R)}{\partial f_R (\partial f_R)^T} f_R \cong S f_R. \tag{36}$$

This allows us to write down the evolution of the state (Equation (35)) in a more developed form:

$$\dot{x} = [\mathcal{J} - G_R \frac{\partial^2 \mathcal{R}(f_R)}{\partial f_R (\partial f_R)^T} (G_R)^T] \delta_x H(x) + Gu; \quad y = G^T \delta_x H(x). \tag{37}$$

Note that the introduction of Rayleigh's dissipation functional does not necessarily mean that a model is consistent with any of the extreme variational principles. It should be remembered that most thermodynamicists avoid variational principles and mathematical models based on them [44].

Maintaining the Stokes–Dirac structure guaranteed by Equation (34) is not obvious and should be verified in each case. For solids, this structure is ensured by Betti's theorem [50], while for fluids, this structure is guaranteed only for the Navier–Stokes fluids [8,18]. In a more general case, such as that described in [51], the maintained SD structures of boundary ports must be proven for specific geometries and a specific control.

16. Energy-Dissipating Boundary Ports

Another open issue concerns the external (boundary port variables) ports (f_∂, e_∂) connecting the system with the environment $\mathcal{E}n$. It is unclear how to approach them. However, it will be desirable to limit their description to algebraic equations that are analogous to $y = Cx + Du$ causal control rather than, for example, differential control: $y = C\dot{x}$. In general, as was pointed out in Equation (34), boundary port variables are not only functions of storage efforts e_s but also of dissipation efforts e_R. If the boundary is oriented by the normal vector $\vec{n}$, then according to Cauchy's lemma, boundary variables are defined as follows:

$$\begin{pmatrix} f_\partial \\ e_\partial \end{pmatrix} = \mathcal{B}_{\vec{n}} \begin{pmatrix} e_{s\|\partial\Omega} \\ e_{R\|\partial\Omega} \end{pmatrix}, \tag{38}$$

where the boundary operator $\mathcal{B}_{\vec{n}}$ has a Stokes–Dirac structure and is skew-symmetric. It provides normal and tangential projections onto the boundary surface $\partial\Omega$. Now, taking into account dissipative and boundary ports, the Hamiltonian increment is expressed as follows:

$$\dot{\mathcal{H}} = \iint_{\partial\Omega} f_\partial \cdot e_\partial \, dA + \iiint_\Omega f_R \cdot e_R d\Omega \leq \iint_{\partial\Omega} f_\partial \cdot e_\partial \, dA. \tag{39}$$

where $\iint_{\partial\Omega} f_\partial \cdot e_\partial \, dA$ denotes the power supplied by the boundary ports and $\iiint_\Omega f_R \cdot e_R d\Omega$ denotes the power dissipated in the form of an internal source. In words, the power flow law can be expressed as follows: the change in energy storage is the result of the power supplied by the boundary ports minus the internal energy dissipation through the dissipative ports. This is, admittedly, a groundbreaking and creative interpretation of the First Law of Thermodynamics. Colloquially speaking, it turns the First Law of Thermodynamics "upside down".

Remark 3. *In this paper, there is no focus on known methods of controlling pH systems; however, from a thermodynamic point of view, there is potential interest in this group of methods, which is suitable for controlling Hamiltonian thermodynamics, i.e., power-producing systems. The best-known energy control method is the IDA-PBC method developed by Ortega et al. [6]. A discussion*

https://doi.org/10.3390/en19020324

of pH system control methods can be found in the mathematical works of Pommaret [42], Mehrmann and Unger [52], and Gawroński [32].

17. Maschke–Kirchhoff Formalism

Maschke and Kirchhoff [50] consider supplementing the equations of evolution with irreversible effects of a mechanical, electrical, or chemical nature. Entropy does not appear in the state vector x they have proposed; hence, this mathematical model has limited value. They do not refer to Rayleigh's dissipative potential, but to an enigmatic function $\mathcal{S}$ with unknown entropy dimensions, almost impossible to define, which they call the "entropy function" satisfying the Poisson bracket conditions, $\{\mathcal{S}, H\} = \delta_x \mathcal{S} J(x)\ \delta_x H$, calculated for the skew-symmetric matrix J and calculable $\delta_x S$. The equations of evolution of the dissipative Dirac system now have the form proposed by Maschke and Kirchhoff:

$$\partial_t x = \gamma(x, \delta_x H)\{\mathcal{S}, H\}\ J\ \delta_x H + \gamma_{port}(x, \delta_x H, u)\{\mathcal{S}, H\}_{port} G u, \tag{40}$$

$$y = \gamma_{port}(x, \delta_x H, u)\{\mathcal{S}, H\}_{port} G^T \delta_x H, \tag{41}$$

where an empirical function $\gamma(x, \delta_x H)$ appears, the content of which is unknown, and its reflecting boundary function $\gamma_{port}(x, \delta_x H, u)$. The proposal by Maschke and Kirchhoff [50] strictly adheres to the research paradigms of control theory, but treats the thermodynamics of phenomena somewhat "neglectfully". The authors' thesis that the product of the bracket $\{\mathcal{S}, H\}$ and the skew-symmetric Dirac structure matrix J "ensures that the second law of thermodynamics is satisfied" is also unconvincing. This may be true, but only in a case simplified to mechanical friction. The formalism presented in Equations (40) and (41) is developed by Ramirez et al. [17,18].

Remark 4. *An example of the separation of dissipation port can be found in the Hamiltonian formulation of Fourier heat transport in solids described by the equation (Brugnoli et al. [13], Jäschke et al. [14]):*

$$c_p\, \partial_t T(\vec{x}, t) = \mathrm{div}(\overleftrightarrow{\lambda}\, \mathrm{grad} T) + u_T, \tag{42}$$

where c_p is heat capacity, T_0 is reference temperature, $\overleftrightarrow{\lambda}$ is thermal conductivity, and u_T is internal radiation source. This is represented by the storage variable $x_T = c_p T$, and the following Hamiltonian:

$$\mathcal{H}(x_T) = \int_\Omega H\, d\Omega = \int_\Omega c_p T_0 \left(\frac{T}{T_0}\right)^2 d\Omega = \int_\Omega x_T \frac{T}{T_0} d\Omega. \tag{43}$$

This allows us to define thermal effort as $e_T = \partial_{x_T} H = T/T_0$ and the flux as $f_T = \dot{x}_T$. In addition to the port pair (f_T, e_T) of the storage type, there is also a dissipation pair $(f_R,\ e_R) \equiv (f_{\vec{q}}, e_{\vec{q}})$ defined as $e_{\vec{q}} = \vec{q}$, $f_{\vec{q}} = -\vec{q}$. Now, both the Fourier conductivity and the constitutive equation of the type $e_R = S f_R = (T_0\ \overleftrightarrow{\lambda})^{-1} f_R$ can be jointly represented as follows:

$$\begin{pmatrix} 1 & 0 \\ 0 & 0 \end{pmatrix} \begin{pmatrix} f_T \\ f_{\vec{q}} \end{pmatrix} = \begin{pmatrix} 0 & \mathrm{div}(\cdot) \\ -\mathrm{grad}(\cdot) & (T_0\ \overleftrightarrow{\lambda})^{-1} \end{pmatrix} \begin{pmatrix} e_T \\ e_{\vec{q}} \end{pmatrix} + \begin{pmatrix} 1 \\ 0 \end{pmatrix} u_T. \tag{44}$$

By taking the fluxes and efforts together, $f = (f_T, f_{\vec{q}})^T$ and $e = (e_T, e_{\vec{q}})^T$, and defining the matrices as follows:

$$P = \begin{pmatrix} 1 & 0 \\ 0 & 0 \end{pmatrix};\quad J = \begin{pmatrix} 0 & \mathrm{div}(\cdot) \\ -\mathrm{grad}(\cdot) & 0 \end{pmatrix};\ R = \begin{pmatrix} 0 & 0 \\ 0 & (T_0\ \overleftrightarrow{\lambda})^{-1} \end{pmatrix};\ G = \begin{pmatrix} 1 \\ 0 \end{pmatrix}, \tag{45}$$

https://doi.org/10.3390/en19020324

the following control system consistent with Equation (30) is obtained:

$$P\,f = (J + R)e + Gu_T. \tag{46}$$

18. Hamilton's Formalism in Physics

Hamiltonian formalism stems from the analytical mechanics of discrete systems and is not suitable for use in classical field theory covering such continua as gravitational fields, electromagnetic fields, and continuous matter fields. There are few attempts in the literature to apply Hamilton's approach to the theory of gravity [28–30], and there are also few Hamiltonian representations of Maxwell's electrodynamics, Infeld–Born, Kauffman, etc. (see: Pavelka [53]; Pavelka et al. [27]). Unsuccessful attempts to find a Hamiltonian may stem from a misunderstanding of Hamilton's concept, from "groping" with blunt mathematical tools such as "contact transformation" or co-tangential bundles. Meanwhile, without the Hamiltonian, there is no correct quantum physics, and the one that exists limits natural phenomena to a reduced minimum.

A completely chaotic situation occurs in the field of fluid or solid material continuum physics. Here, there is no single Hamiltonian approach, and each case has its own mathematical model that is incompatible with others in terms of Hamiltonian and Rayleighian structure. This conceptual chaos stems from the fact that Hamiltonian field theory has virtually no physical foundations and has too many mathematical assumptions and limitations. That is why there are many attempts in the literature to address this topic, which may, after years of struggle, lead to realistic foundations [24,27,54].

The objective epistemological cause of chaos is a certain objective property of continuum physics that discrete systems do not possess. The point is that continuum theories are formulated in different descriptions, i.e., settings of the observer and his measuring instruments. Four descriptions are known: material (Lagrangean), spatial (Eulerian), referential (ALE), and waveform [55]. There are no known general methods in the literature for transitioning between these four descriptions, which is why individual models, such as the model of fluid flow with cavitation, are somewhat trapped within a single description and difficult to transform into another. Meanwhile, as the examples show, a Lagrangean field theory model originally presented in a material description often has its representation as a Hamiltonian field theory in a spatial description. The works [54,56] illustrate this unsatisfactory state of affairs well.

Remark 5. *We propose here that a significant reason for the stagnation of pH formalism is the narrow, impoverished mathematical formalism developed in the works of van der Schaft, Maschke, Gilbert, Vanneste, Rashad, Califano, Stramigioli, etc. It is based on differential forms that prefer a notation which, although mathematically correct, deviates in its physical content from the existing classical field theory (Truesdell and Toupin, [55]). For example, bearing in mind the practical computational aspect, we see that the physical content of the three equations of momentum conservation for a viscoelastic fluid (expressed without indices) has its tensor representation and, in differential forms, respectively (Equation (47)-Reynolds (1886) [55], Equation (48)-Califano et al. [20]).*

$$\partial_t(\rho\overrightarrow{v}) + \operatorname{div}(\rho\overrightarrow{v} \bigotimes \overrightarrow{v}) = \operatorname{div}[-p\overleftrightarrow{I} + \overleftrightarrow{\tau}] + \rho\overrightarrow{b}. \tag{47}$$

$$\dot{v} + \mathrm{d}\left(\frac{1}{2} * (v \wedge *v)\right) + \iota_v \mathrm{d}v = -\frac{1}{*\mu}\,\mathrm{d}p + \frac{1}{*\mu}(*_2 \mathrm{d}_\nabla \mathcal{T}) + *b \tag{48}$$

This means that instead of the classic operators div, grad, $\bigotimes$ and tensors $\overleftrightarrow{I} = \delta_{ij}\overrightarrow{e}_i \otimes \overrightarrow{e}_j$, $\overleftrightarrow{\tau} = \tau_{ij}\overrightarrow{e}_i \otimes \overrightarrow{e}_j$ are replaced by the following: the Hodge star-dual $*_2$,

https://doi.org/10.3390/en19020324

two forms of covector-valued $\mathcal{T}$, the $\wedge$ operator, and the exterior derivative operator d, where the fluid velocity vector $\vec{v}$ is uniquely identified with a vector valued zero-form v. It is not just about the notation (old wine in a new bottle), but about something more; this apparatus of thinking requires the creation of a new continuum of thermomechanics from scratch.

The geometric formalism of pH thermodynamics forces us to abandon classical notation and classical definitions. But, not only that, it also forces us to conduct new experimental research and broaden our perception of the fundamental concepts of continuum thermodynamics. For example, Cauchy's lemma, well-known in thermodynamics, which defines the way in which the tensor field "comes out" at the edge of the area, $\overleftrightarrow{t}\,\vec{n} \equiv \vec{f}_{ext}$, is challenged by authors such as Califano et al. [20].

19. Hamiltonian Formulation of Fluid Mechanics

In this paper, we limit ourselves to the thermodynamics of viscous and conducting gases, which are the mainstay of classical thermodynamics and fluid mechanics. If we ask about a Hamiltonian formulation of classical thermodynamics, focused on the study of changes in a stationary gas that conducts neither heat nor work, the literature is so limited (see Grmela et al. [24,36]) that it can be concluded that Hamiltonian classical thermodynamics does not exist. We will return to the urgent need for Hamiltonian thermodynamics in the conclusion (Section 23)—however, we must begin with a revision of the foundations of quantum thermodynamics [22].

One of the first works on the Hamiltonian formalism of ideal fluid mechanics with energy conversion is the work of Morrison [38]. Here, the problem is the proper formulation of the so-called family of "generalized momenta" and "generalized positions" from which we build the state vector $x = (q, p)$. Unfortunately, the aim of Morrison's work was not to supplement Euler's ideal fluid mechanics with new Hamiltonian variables, but rather to reformulate the classical system of ideal fluid equations consisting of five equations (mass balance, momentum balance, and internal energy) into a Hamiltonian system consisting of five equations (mass balance, momentum balance, and specific entropy), having the state vector $x = (\rho, \vec{v}, s)$, respectively:

$$\begin{array}{c} \partial_t \rho = -\mathrm{div}\,(\rho \vec{v}\,) \\ \partial_t\,(\rho \vec{v}\,) = -\,\mathrm{div}\,(\rho \vec{v} \otimes \vec{v}\,) + \mathrm{grad}\; p + \rho \vec{b}. \\ \partial_t\,(\rho s\,) = -\,\mathrm{grad}\,(\rho s\,)\vec{v} \end{array} \tag{49}$$

Following the pioneers, Morrison [38] uses a different representation of the d'Alembert–Euler acceleration, $\vec{a} = \partial_t \vec{v} + (\mathrm{grad}\ \vec{v}\,)\vec{v} \equiv \partial_t \vec{v} + \mathrm{grad}\ (\frac{1}{2}\vec{v}^{\,2}) + \vec{v} \times (\mathrm{rot}\ \vec{v})$, sometimes neglects the mass force $\vec{b} = 0$, and transforms the conservative system of equations (Equation (49)) into a system of the (non)conservative form:

$$\begin{array}{c} \partial_t \rho = -\mathrm{div}\,(\rho \vec{v}\,) \\ \partial_t \vec{v} = -\mathrm{grad}\ (\frac{1}{2}\vec{v}^{\,2}) - \vec{v} \times (\mathrm{rot}\ \vec{v}\,) - \frac{1}{\rho}\mathrm{grad} p + \vec{b}. \\ \partial_t s = -\,\mathrm{grad}\,(s\,)\vec{v} \end{array} \tag{50}$$

where ρ is the density of the gas, p is the pressure, $\vec{v}$ is its velocity, and s is its specific entropy. Morrison, not knowing the solution to the general problem, puts forward a truncated thesis that Hamiltonian Eulerian fluid mechanics has a mathematical model for which a degenerate Poisson bracket exists. Knowing that this is an invalid bracket, he calls

https://doi.org/10.3390/en19020324

it a "non-canonical Poisson bracket" and no longer attempts to find a canonical (correct) Poisson brace.

It defines an object which, *ex catedra*, is called the Hamiltonian:

$$\mathcal{H}(x) = \iiint_{\Omega} H \, d\Omega = \iiint_{\Omega} \left(\frac{1}{2}\rho \overrightarrow{v}^2 + \rho u(\rho, s)\right) d\Omega. \tag{51}$$

This definition has guided blind research for many years. It contains an unusual object: the mass density of internal energy $u = u(\rho, s)$ from which we obtain the definitions of temperature and pressure in classical thermodynamics: $T = \partial_s u$; $p = \rho^2 \partial_\rho u$. This means that Hamiltonian thermodynamics agrees with this unjustified definition.

Morrison [38] proposes the following three-term non-canonical Poisson bracket:

$$\{f, g\} = \iiint_{\Omega} \left\{ \begin{array}{c} \left[\frac{\delta f}{\delta \rho} \operatorname{div}\left(\frac{\delta g}{\delta \overrightarrow{v}}\right) + \operatorname{div}\left(\frac{\delta f}{\delta \overrightarrow{v}}\right) \frac{\delta g}{\delta \rho}\right] \\ + \left[\rho^{-1} (\operatorname{rot} \overrightarrow{v}) \cdot \left(\frac{\delta g}{\delta \overrightarrow{v}} \times \frac{\delta g}{\delta \overrightarrow{v}}\right)\right] + \left[+\rho^{-1} \operatorname{grad} s \cdot \left(\frac{\delta f}{\delta s} \frac{\delta g}{\delta \overrightarrow{v}} - \frac{\delta g}{\delta s} \frac{\delta f}{\delta \overrightarrow{v}}\right)\right] \end{array} \right\} d\Omega. \tag{52}$$

Let us now show that by taking the state vector x as the function f and the Hamiltonian H as the function g and performing the derivative of the Hamiltonian, we can reduce the system of equations (Equation (50)) to the form $\dot{x} = \{x, H\}$, with the following specific form:

$$\frac{\partial}{\partial t} \begin{pmatrix} \rho \\ \overrightarrow{v} \\ s \end{pmatrix} = \begin{pmatrix} \{\rho, H\} \\ \{\overrightarrow{v}, H\} \\ \{s, H\} \end{pmatrix} = \begin{pmatrix} -\operatorname{div} H_{\overrightarrow{v}} \\ -\operatorname{grad} H_\rho + \rho^{-1} (\operatorname{rot} \overrightarrow{v} \times \overleftrightarrow{I}) \, H_{\overrightarrow{v}} + \rho^{-1} \operatorname{grad} s H_s + 2\operatorname{grad}(\mathrm{gz}) \\ \rho^{-1} \operatorname{grad} s \, H_{\overrightarrow{v}} \end{pmatrix}. \tag{53}$$

where definitions and notations consistent with control theory were introduced as follows:

$$\begin{array}{c} \frac{\partial}{\partial \rho} H = \partial_\rho H \equiv H_\rho = \left(\frac{1}{2} \overrightarrow{v}^2 + \mathrm{gz} + u(\rho, s)\right) + \rho^{-1} p \\ \frac{\partial}{\partial \overrightarrow{v}} H = \partial_{\overrightarrow{v}} H \equiv H_{\overrightarrow{v}} = \rho \overrightarrow{v} \\ \frac{\partial}{\partial s} H = \partial_s H \equiv H_s = \rho \partial_s u = \rho T \end{array} . \tag{54}$$

The extensive parameters of the state p, T are the thermodynamic pressure and temperature. In the momentum evolution Equation $(53)_2$, a mass force $\overrightarrow{b} = \operatorname{grad}(\mathrm{gz}) = \mathrm{g} \overrightarrow{e}_z$ appears, acting vertically (perpendicular to the Earth's surface), where g is the Galilean gravitational constant. In the momentum equation, a non-canonical term also appears: grad$s$, which comes at the cost of introducing H_ρ into the description and the need to calculate the gradient gradH_ρ.

$$\operatorname{grad} H_\rho = \operatorname{grad}\left(\left(\frac{1}{2} \overrightarrow{v}^2 + \mathrm{gz} + u(\rho, s)\right) + \rho^{-1} p\right), \tag{55}$$

where the internal energy gradient is expressed by gradients ρ, s, respectively.

$$\operatorname{grad} u(\rho, s) = \partial_\rho u \operatorname{grad} \rho + \partial_s u \operatorname{grad} s. \tag{56}$$

By separating the mass force—treated as an external control in any direction, not only in the z direction—the system of evolution equations (Equation (53)) can be written as a control system:

$$\frac{\partial}{\partial t} \begin{pmatrix} \rho \\ \overrightarrow{v} \\ s \end{pmatrix} = \begin{pmatrix} 0 & -\operatorname{div}(\cdot) & 0 \\ -\operatorname{grad}(\cdot) & \overleftrightarrow{m} & \rho^{-1} \operatorname{grad} s \\ 0 & \rho^{-1} \operatorname{grad} s & 0 \end{pmatrix} \begin{pmatrix} H_\rho \\ H_{\overrightarrow{v}} \\ H_s \end{pmatrix} + \begin{pmatrix} 0 \\ 2 \\ 0 \end{pmatrix} u_{\overrightarrow{b}} = \mathcal{J}_{5\times 5} \begin{pmatrix} H_\rho \\ H_{\overrightarrow{v}} \\ H_s \end{pmatrix} + G_{1\times 3} u_{\overrightarrow{b}}. \tag{57}$$

https://doi.org/10.3390/en19020324

where $\overleftrightarrow{m} = \rho^{-1}(\text{rot}\,\vec{v} \times \overleftrightarrow{I})$. Taking full components of the structural matrix $\mathcal{J}$ we are going into the $\mathcal{J}_{5\times5}$ matrix. This matrix is skew-symmetric, so it is consistent with the pH formulation of control theory: $\dot{x} = [\mathcal{J} - R]\delta_x H(x) + Gu.$, $R \equiv 0$.

Going on to the energetic formulation of pH we have the definition of fluxes and efforts (f_s, e_s), given as follows:

$$f_s = \dot{x} = \frac{\partial}{\partial t}\begin{pmatrix}\rho\\ \vec{v}\\ s\end{pmatrix}; \quad e_s = \partial_x H = \begin{pmatrix}H_\rho\\ H_{\vec{v}}\\ H_s\end{pmatrix}, \tag{58}$$

with the help of which the correctness of the energy flux conservation formulation can be demonstrated: $\dot{H} = \{H, H\}_J = 0$.

Remark 6. *Let us also note that in the continuum approach, spatial derivative operators appear:* $\text{grad}(\cdot)$, $\text{div}(\cdot)$ *or laplacian:* $\text{lap}(\cdot) = \text{grad}(\text{div}(\cdot))$. *In general, the matrix* $\mathcal{J}(x)$ *becomes an operator with respect to spatial variables, traditionally denoted in fluid mechanics by* $\vec{x}$. *Then, the matrix* $\mathcal{J}(x)$ *can be represented as a composition of dimensionless skew-symmetric matrices* J_m, $m = 0, 1, 2, 3\ldots$ *where the first matrix* J_0, *traditionally, is denoted without an index. In the case of a compressible Eulerian fluid, we have only the first derivatives* $\mathcal{J}(x) = J_0 + a_1 J_1 \partial_{\vec{x}}$, *where the coefficient* a_1 *equalizes the dimensions. Here,* $(\text{div}(\cdot))^T = -\text{grad}(\cdot)$ *also holds, which preserves skew symmetry.*

Remark 7. *The convective derivative* $\frac{d}{dt}(\cdot)$, *appearing in the definition of the d'Alembert–Euler acceleration* $\vec{a} = \frac{d}{dt}\vec{v} = \partial_t \vec{v} + (\text{grad}\,\vec{v})\vec{v}$, *appears in all other balances, not only in the momentum balance; hence, the main problem of Hamiltonian fluid mechanics is to find the "fluid displacement field" in the form of scalar, vector, or even tensor gauge potentials [43]. Morrison [38] reviewed and classified these solutions concerning different representations of the velocity field* $\vec{v}$ *in Hamiltonian fluid mechanics. He synthesized the scalar potentials of Euler [57], Helmholtz [58], Clebsch [59], Bateman [60], and Eckart [61] into one general representation:*

$$\vec{v} = A\,\text{grad}\,a + B\,\text{grad}\,b + C\,\text{grad}\,c + \cdots = A_m \text{grad}\,a_m. \tag{59}$$

As an example we have $\vec{v} = \xi_v\,\text{grad}\,v + \xi_s\,\text{grad}\,s + \text{grad}\,\phi$, which is an example of defining the velocity field using three potentials ξ_v, ξ_s, ϕ and gradients of specific volume grad v and specific entropy grad s. We must agree here that inventing potentials opens the way to gauge field theory (for instance, Helmholtz: $\vec{v} = \text{grad}\,\phi + \dot{\vec{A}}$ leads toward U(1)-Maxwell continuum). Sieniutycz and Berry [44] believe that these are ad hoc solutions that do not develop the foundations of Hamiltonian field theory. Pommaret even requires the search for new potentials that open up unknown internal symmetries [42].

20. Hamiltonian Formulation of Boundary Conditions

Another difficulty is deriving the fluxes f_s and efforts e_s at the boundary of the region $\partial\Omega$ occupied by the fluid, as they do not coincide with the physical conditions for fluids at the boundary known from the literature. The boundary also contains irreversible ports (f_R, e_R) and boundary ports (f_∂, e_∂).

Recall that in fluid thermomechanics, there are two types of boundary conditions. They are related to boundary types. The first are conceptual cross-sections through channels (computational regions, most often inlets and outlets), where we impose conditions on the

https://doi.org/10.3390/en19020324

state parameters x_{inlet} and x_{outlet}. The second type of conditions are conditions imposed on the constant boundary on the flows:

$$\mathcal{F}\vec{n} = \not{p}^{data}, \tag{60}$$

where $\mathcal{F}$ are, respectively, the fluxes of mass, momentum, angular momentum, entropy, volume, current, etc. On this boundary, control can occur by a known quantity $\not{p}^{data}$.

When setting boundary conditions for an Eulerian fluid, we must remember that they must have a general structure that easily overlaps with the boundary conditions of a Navier–Stokes fluid and other fluids, such as two-phase fluids and fluids undergoing phase changes, combustion, and turbulence. Therefore, we are dealing with a skew-symmetric Dirac structure that maintains the boundary conditions proposed by du Buite, Navier, Duhem, Stokes, Poisson, Reynolds, Maxwell, Helmholtz and Piotrowski, von Rybczyński, von Smoluchowski, and others (Badur et al. [51]). Also, approaching the interface with the fluid from the solid side creates a complicated physical situation, the existence of which is unknown. This skew-symmetric structure of boundary conditions is called the Stokes–Dirac structure in the literature (Maschke and van der Schaft [4]).

21. Energy Picture

In 1866, J.W. Gibbs proposed two equivalent thermodynamic pictures, which, in the case of an Eulerian fluid, lead to two equivalent definitions of energy state variables (Sieniutycz and Berry [44]):

$$\text{Energy picture } x = (\rho, \vec{p}, e), \tag{61}$$

$$\text{Entropy picture } x = (\rho, \vec{p}, s) \tag{62}$$

It should be emphasized that the Eulerian energy picture of fluid mechanics is the oldest, most reliable, and undoubtedly the most important from the point of view of everyday computational practice. It also served as a starting point for other models, for example, solid mechanics and complex fluid mechanics (viscosity and rheology).

This picture is usually used for research on connections with mechanics, kinetic theory, and equilibrium thermodynamics. Almost all branches of classical field theory [55] arose from these studies. Moreover, this picture is considered to have an epistemological connection with Newtonian mechanics, and the ideal Eulerian fluid is treated as a continuation of Newtonian point particle mechanics. During the evolution of $\dot{x} = \{x, H\}$, the constant quantities are mass [kg], momentum [Ns], and energy [J]:

$$M = \int_\Omega \rho d\Omega, \ \vec{P} = \int_\Omega (\rho \vec{v}) d\Omega = \int_\Omega \vec{p}\ d\Omega; \ E = \int_\Omega (\rho\epsilon) d\Omega = \int_\Omega e\ d\Omega. \tag{63}$$

And entropy can change [J/K]:

$$S = \int_\Omega (\rho\eta) d\Omega = \int_\Omega s\ d\Omega. \tag{64}$$

Here we use the volumetric densities of mass, momentum, energy and entropy—$\rho, \vec{p}, e, s$ referred to the unit volume, while ν, $\vec{v}$, ϵ, η are the proper densities which referred to the unit mass. The system of evolution equations in the energy picture has the implicit (incomplete) form (Grmela [36,37]):

$$\frac{\partial}{\partial t}\rho = \{\rho, H\} = \operatorname{div}(\rho H_{\vec{p}}) = -\operatorname{div}(\vec{J}^{\rho}) + s_\rho, \tag{65}$$

https://doi.org/10.3390/en19020324

$$\frac{\partial}{\partial t}\vec{p} = \{p, H\} = \mathrm{div}\,(\vec{p} \bigotimes H_{\vec{p}} + ???) = -\mathrm{div}\,(\overleftrightarrow{J}^{v}) + \vec{s}_p, \tag{66}$$

$$\frac{\partial}{\partial t}e = \{e, H\} = \mathrm{div}\,(eH_{\vec{p}}) = -\mathrm{div}\,(\vec{J}^{e}) + s_e. \tag{67}$$

where $\vec{J}^{\rho}$, $\overleftrightarrow{J}^{v}$, $\vec{J}^{e}$ are called mass, momentum, and energy fluxes, respectively. Specification of the fluid type requires constitutive equations for the fluxes. The internal sources of mass and energy are equal to zero according to the First Law of Thermodynamics $s_\rho = s_e = 0$, while the internal source of momentum $\vec{s}_p = \rho\vec{b}$ comes from the gravitational field permeating matter. The momentum evolution equation is traditionally treated as a continuum version of Newton's second law ($m_i\dot{\vec{v}}_i = \vec{f}_i + \sum_k \overleftrightarrow{f}_{ik}$), for the case when there are no dissipative collisions in the swarm of particles $i = 1, 2, 3 \ldots, n$). Unfortunately, the Poisson bracket expressing the kinematics of the evolution of $x = (\rho, \vec{p}, e)$ is unknown in the literature, even in the pioneering works of Miroslav Grmela. This creates an obstacle to a formal reconstruction of non-equilibrium thermodynamics that favors and exalts the energy balance; this situation is completely inconsistent with the energetic picture of the Port-Hamiltonian formalism.

The Port-Hamiltonian formalism favors the entropy picture. It tacitly assumes that the two energy and entropy pictures are equivalent. However, such equivalence does not occur in practice.

Thus, by necessity rather than choice, we are left with an entropy picture defining the energy state variables as $x = (\rho, \vec{v}, \eta)$ or, more correctly, as $x = (\rho, \vec{p}, s)$. The Poisson bracket expressing the convective part of the evolution $x = (\rho, \vec{p}, s)$ is as follows (Grmela [24]):

$$\begin{array}{c} \{f, g\}_C = \iiint \rho\,(\,\mathrm{grad}\,(f_\rho)\cdot g_{\vec{p}} - \mathrm{grad}\,(g_\rho)\cdot f_{\vec{p}}\,)\,d\Omega \\ + \iiint \vec{p}\cdot(\mathrm{grad} f_{\vec{p}} \otimes g_{\vec{p}} - \mathrm{grad} g_{\vec{p}} \otimes f_{\vec{p}}\,)\,d\Omega \\ + \iiint s\,(\mathrm{grad}(f_s)\cdot g_{\vec{p}} - \mathrm{grad}(g_s)\cdot f_{\vec{p}}\,)\,d\Omega. \end{array} \tag{68}$$

This bracket allows the formal derivation of the evolution equations without requiring an explicit definition of the Hamiltonian. The following shorthand notations were introduced above:

$$H_\rho = \delta_\rho H = \frac{\partial H}{\partial \rho},\ H_{\vec{p}} = \delta_{\vec{p}} H = \frac{\partial H}{\partial \vec{p}};\ H_s = \delta_s H = \frac{\partial H}{\partial s}. \tag{69}$$

This allows both sides of the equation $\partial_t f = \{f, \mathcal{H}\}$ to be written as follows:

$$\begin{array}{c} \iiint_\Omega (f_\rho \partial_t \rho + f_{\vec{p}}\cdot\partial_t\vec{p} + f_s\partial_t s)d\Omega \\ = \iiint \{f_\rho\,[-\mathrm{div}\,(\rho H_{\vec{p}}\,)\,] + \ f_{\vec{p}}\cdot[-\mathrm{div}\,(\vec{p}\otimes H_{\vec{p}}\,) - \vec{p}\,\mathrm{div}\,(H_{\vec{p}}\,) - \rho\mathrm{grad}(H_\rho) - s\mathrm{grad}(\,H_s)\,] + \\ f_s\,[-\mathrm{div}\,(sH_{\vec{p}}\,)\,]\}\,d\Omega. \end{array} \tag{70}$$

In Equation (70), we used integration by parts. Since the evolution equations hold for every functional, with $\partial_t f = \{f, \mathcal{H}\}$ we have a family of five evolution equations:

$$\partial_t \rho = -\mathrm{div}\,(\rho H_{\vec{p}}\,) = -\mathrm{div}\,(\vec{J}_\rho). \tag{71}$$

$$\partial_t\vec{p} = -\mathrm{div}\,(\vec{p}\bigotimes H_{\vec{p}}\,) - \vec{p}\,\mathrm{div}\,(H_{\vec{p}}\,) - \rho\mathrm{grad}\,(H_\rho) - \ s\mathrm{grad}\,(\,H_s\,)\,] = -\mathrm{div}\,(\overleftrightarrow{J}^{p}). \tag{72}$$

$$\partial_t s = -\mathrm{div}\,(sH_{\vec{p}}\,) = -\mathrm{div}\,(\vec{J}_s). \tag{73}$$

https://doi.org/10.3390/en19020324

The terms in the momentum evolution equation can be written as the divergence of a scalar p called the Hamiltonian pressure:

$$p = -H + \rho H_\rho + sH_s + \vec{p}\cdot H_{\vec{p}}. \tag{74}$$

Since the identity holds, grad $H = H_\rho \text{grad}\rho + H_{\vec{p}}\text{grad}\vec{p} + H_s\text{grad}s$, Equation (36) can be replaced by the following:

$$-\vec{p}\,\text{div}\,(H_{\vec{p}}) - \rho\text{grad}\big(H_\rho\big) - s\text{grad}(H_s)] \equiv \text{div}\,[-p\overleftrightarrow{I}\,] = -\text{grad}p. \tag{75}$$

The uniform derivation of the evolution equations based on Poisson brackets (Equation (68)) has the advantage of opening a potential path to generalizations of continuum models. If evolution (motion) is a group of Lie-type continuum transformations, then there is always a Poisson bracket that is canonically associated with the Lie group. This opens the possibility of describing the continuum within the framework of a gauge field theory based on symmetries and their Lie algebras (Pommaret [20], Grmela [24]).

The advantage of this approach is the strict definition of the mass, momentum, and entropy fluxes ($\vec{J}_\rho$, $\overleftrightarrow{J}^{\,p}$, $\vec{J}_s$) in terms of the pH effort, $e_s = \delta_x H$, which allows us to write the system of Equations (71)–(73) in terms of the storage ports of the pH system:

$$\partial_t \begin{pmatrix} \rho \\ \vec{p} \\ s \end{pmatrix} = \begin{pmatrix} 0 & -\text{div}(\rho\ldots) & 0 \\ -\rho\text{grad}\ldots & -\text{div}\,(\vec{p}\otimes\ldots) - \vec{p}\text{grad}(\ldots) & s\text{grad}\ldots \\ 0 & -\text{div}(s\ldots) & 0 \end{pmatrix} \begin{pmatrix} H_\rho \\ H_{\vec{p}} \\ H_s \end{pmatrix} = \mathcal{J}(x) \begin{pmatrix} H_\rho \\ H_{\vec{p}} \\ H_s \end{pmatrix}. \tag{76}$$

which maintains the Dirac structure, $f_s = \mathcal{J}e_s$. Comparing the previous result (57) with (76), we note that using the specific entropy η (per kilogram) and the volume entropy density s leads to slightly different formulations of pH.

Remark 8. *Now calculating the change in the Hamiltonian* $\dot{\mathcal{H}} = \{\mathcal{H}, \mathcal{H}\}_C = 0$, *we can determine the form of the boundary ports* (f_∂, e_∂). *Remembering the definitions,* $e_s = \delta_x H = \begin{pmatrix} H_\rho & H_{\vec{p}} & H_s \end{pmatrix}^T$ *and* $f_s = -\partial_t x = \begin{pmatrix} -\partial_t\rho & -\partial_t\vec{p} & -\partial_t s \end{pmatrix}$, *we calculate the change in the Hamiltonian using (Equations (71)–(73)) as follows:*

$$\begin{array}{l} \dot{\mathcal{H}} = \iiint_\Omega e_s^T f_s\, d\Omega = -\iiint_\Omega\, (H_\rho\dot{\rho} + H_{\vec{p}}\dot{\vec{p}} + H_s\dot{s}\,)\, d\Omega = \iiint_\Omega (H_\rho \text{div}\,(\rho H_{\vec{p}}) + H_{\vec{p}}\cdot \\ [-\text{div}\,(\vec{p}\otimes H_{\vec{p}}) - \vec{p}\,\text{div}\,(H_{\vec{p}}) - \rho\text{grad}\big(H_\rho\big) - s\text{grad}(H_s)\,] + H_s\text{div}\,(sH_{\vec{p}}))\, d\Omega \\ \dot{\mathcal{H}} = \iiint_\Omega [-\text{div}\,(\rho H_\rho H_{\vec{p}}) + \text{grad}\big(H_\rho\big)\cdot(\rho H_{\vec{p}}) - \text{div}\,((\vec{p}\cdot H_{\vec{p}})H_{\vec{p}}) + \text{grad}\,(H_{\vec{p}})\cdot \\ (\vec{p}\otimes H_{\vec{p}}) - H_{\vec{p}}\cdot\text{grad}p - \text{div}\,(sH_sH_{\vec{p}}) + \text{grad}\,(H_s)\cdot(sH_{\vec{p}})]d\Omega = \iiint_\Omega \{-\text{div}[(\rho H_\rho + \\ \vec{p}\cdot H_{\vec{p}} + sH_s)H_{\vec{p}}]\,\}d\Omega = -\iiint_\Omega \{-\text{div}\,[(p+H\,)H_{\vec{p}}\,]\,\}d\Omega. \end{array} \tag{77}$$

According to Stokes' theorem on the conversion of a volume integral into a surface integral, we obtain the following:

$$\dot{\mathcal{H}} = \iint_{\partial\Omega} \{\ (\rho H_\rho + \vec{p}\cdot H_{\vec{p}} + sH_s\,)H_{\vec{p}}\cdot\vec{n}_{\partial\Omega}\ \}dA. \tag{78}$$

This formula means that the boundary ports (f_∂, e_∂) can be determined by the efforts $e_s = \delta_x H$ going to the boundary $\partial\Omega$. Unfortunately, if we do not allow any simplifications, the boundary ports should also be a function of the energy state variables $x = (\rho, \vec{p}, s\,)$. This important fact is not reflected in the literature; see [1,2,62].

https://doi.org/10.3390/en19020324

Remark 9. *Including a state variable such as entropy is not an easy matter and has its unsuccessful attempts in the literature [2,8,10,16,18,62].*

Remark 10. *The control system of an ideal Eulerian fluid maintains its Dirac structure if we introduce internal friction of the Navier–Stokes type. To obtain this, we must follow the procedure shown in Section 13 above, where we first define the energetic variables* $(f_R,\ e_R)$*, which will be "added" to the port structure of the Eulerian fluid. In this case, there are no problems with the identification of the variables—they are the viscous fluid stresses and the deformation velocity,* $(f_R,\ e_R) = (\overleftrightarrow{\tau},\ \overleftrightarrow{d})$*, which are related to each other by the dissipative constitutive equation,* $\overleftrightarrow{\tau} = 2\mu\overleftrightarrow{d} + \lambda(\mathrm{tr}\overleftrightarrow{d})\overleftrightarrow{I}$*, where* μ, λ *are the Navier–Lamé viscosity coefficients. This equation can be written in matrix form as follows:*

$$e_{R(6\times1)} = S^{NS}_{(6\times6)} f_{R(6\times1)}. \tag{79}$$

We supplement the evolution equations with fluid viscosity effects as follows:

$$\partial_t x = Euler + \begin{bmatrix} 0 \\ \mathrm{div} \\ 0 \end{bmatrix}_{(5\times6)} e_{R(6\times1)} = \{x, H\}_C + Ge_R, \tag{80}$$

where (Equation (35)) is used and the operator introducing the structure is the matrix $G = G_{5\times6}$. As the structure (Equation (34)) shows, dissipative port variables can be kept in play, but then the Dirac structure must be extended:

$$\begin{pmatrix} \partial_t x \\ f_R \end{pmatrix} = \begin{pmatrix} \mathcal{J} & G \\ G^* & 0 \end{pmatrix} \begin{pmatrix} \delta_x H \\ e_R \end{pmatrix} \quad \text{with} \quad e_R = S^{NS} f_R. \tag{81}$$

Then, however, the dissipative ports extend to the boundary of the region and make the definition of the boundary variables $(f_\partial,\ e_\partial)$ difficult. The geometric relations $f_{r(6\times1)}$ with the effort $e_s = \partial_x H_{(5\times1)}$ is as follows:

$$f_{R(6\times1)} = \begin{bmatrix} 0 & \mathrm{grad_s} & 0 \end{bmatrix}_{6\times5} \begin{pmatrix} \delta_\rho H \\ \delta_{\overrightarrow{p}} H \\ \delta_s H \end{pmatrix} = G^* \delta_x H. \tag{82}$$

This allows the evolution of the Navier–Stokes fluid (Equation (80)) to be written as follows:

$$\partial_t x = \{x, H\}_C + Ge_R = [\mathcal{J} - G(S^{NS})G^*]\delta_x H. \tag{83}$$

Let us emphasize that the constitutive relation (Equation (81)) can be replaced by a more general, nonlinear formula using the Rayleigh dissipative functional. In the case of the Navier–Stokes fluid, remembering that $f_R \equiv \overleftrightarrow{d} = \frac{1}{2}\left(\mathrm{grad}\overrightarrow{v} + \mathrm{grad}^T\overrightarrow{v}\right) \equiv \mathrm{grad_s}\overrightarrow{v}$, we obtain the following (Badur et al. [63]):

$$\mathcal{R}(f_R) = \iiint_\Omega \left(\frac{1}{2}\mu\overleftrightarrow{d}\cdot\overleftrightarrow{d} + \frac{1}{2}\lambda(\mathrm{tr}\overleftrightarrow{d})^2\right)d\Omega. \tag{84}$$

Remark 11. *From the above, it follows that the use of the Rayleigh functional is possible directly if the flux variables* f_R *are easily expressible in terms of the storage efforts* $e_s = \delta_x H$ *(see Equation (82)). When this is not possible (it is not possible to write the Rayleighian), we must*

https://doi.org/10.3390/en19020324

extend the control system to the form given by (Equation (40)). The question is, how will the second law of thermodynamics be satisfied in this case? Note that the dissipative part is expressed here entirely in terms of $\delta_{\vec{p}}H$*, which does not mean that extra definitions of the dissipative ports* f_R *are necessary. However, Cardoso-Ribeiro et al. [15] decompose the definition (Equation (82)) into a divergent part* $\mathrm{div}\ H_{\vec{p}}$ *and a rotational part* $\mathrm{rot}\ H_{\vec{p}}$ *to explicitly maintain the Dirac structure.*

Remark 12. *In 1830, Fourier presented a system of simultaneous flow equations in a viscous and conducting fluid, consisting of a mass balance, a momentum balance, and a temperature field evolution. This system of equations is today the basis of the computer science known as Computational Fluid Dynamics (CFD). In the literature, it is also referred to as the Navier–Stokes–Fourier fluid. It imposes a choice of state energy variables as* $x = (\rho, \vec{p}, T)$*, or, worse, as* $x = (\rho, \vec{v}, T)$*. From the point of view of the Hamiltonian approach, the Fourier temperature field evolution equation is the specific entropy evolution equation, while from the point of view of the Lagrangean approach, in contrast, it is a total energy balance in which the internal energy contained in the Hamiltonian has the simplified form:* $u = u(\rho, s) = c_v T$*.*

$$\partial_t(\rho c_v T) + \mathrm{div}\,(\rho c_v T \vec{v}\,) = \mathrm{div}(\,\kappa\,\mathrm{grad}\,T) + \mathrm{div}\,(-p\vec{v} + \overleftrightarrow{\tau}\vec{v}\,) + \rho s_e, \tag{85}$$

where the contribution to the energy flux comes from both the temperature field and the mechanical field. This setting of energy variables was described in Remark 5 as an example for dissipative conduction in a solid. It means that it is possible to find the dissipative port variables corresponding to the heat conduction as $(f_R, e_R) = (\vec{g}, \vec{q}\,)$ where $\vec{q}$ is the Carnot heat flux and $\vec{g} = \mathrm{grad}T$ the temperature gradient. The variables $x = (\rho, \vec{v}, T)$ are the basis of the following works: [12,13,18,56].

Remark 13. *In thermodynamics, the thermal energy flux* $\vec{q}$ *is related to the entropy flux by the relation:* $\vec{q} = T\vec{h}_s$ *and the mechanical energy flux to the momentum flux. What is the meaning of the mechanical entropy flux* $\vec{h}_m = T^{-1}\vec{q}_m$*? In the work of Mora et al. [19], a vector of state variables was proposed:* $x = (v, \vec{v}, s)$ *consisting of specific volume, velocity, and specific entropy. This state vector is defined under the assumption that the fluid density is a passive quantity and equal to* $\rho = 1$*. The evolution on* $\partial_t s$ *proposed by these authors does not have a reversible term (recoverable)* $\partial_t s = \{s, H\} \equiv 0$ *and has only a dissipative term in the form of the following equation:*

$$\partial_t(\rho c_v T) + \mathrm{div}\,(\rho c_v T \vec{v}\,) = \mathrm{div}(\,\kappa\,\mathrm{grad}\,T) + \mathrm{div}\,(-p\vec{v} + \overleftrightarrow{\tau}\vec{v}\,) + \rho s_e, \tag{86}$$

where the dissipation matrix $R = (\partial_s H)^{-1} S^{NS} G^T \delta_{\vec{v}} H$ *has a mechanical origin. This is represented by the equation* $\partial_t s = -div(\vec{h}_m)$*, where the mechanical term of the entropy flux is defined by* $\vec{h}_m = T^{-1}\vec{q}_m = T^{-1}(\overleftrightarrow{\tau}\vec{v}\,)$*. In the pH notation of the control theory,* $\partial_{\vec{v}} H = \vec{v}$*,* $\overleftrightarrow{\tau} = e_R$ *and* $\partial_s H = T$*. The thermodynamics proposed here cannot be accepted because the potential* H *is not used in the evolution equation for* $\partial_t s$*. Nevertheless, there is a proposal here for a thermodynamic temperature rather than an empirical one. There is also a mechanical entropy flux* $\vec{h}_m$*, which has no deeper justification and is formally incorrect. There is also no reference in (Equation (86)) to the Fourier coefficient of diffusive heat transport.*

Remark 14. *Recall that it is more reasonable to choose the variables* $x = (\rho, \vec{p}, s)$*. This is performed by several authors, including Grmela, Klika, and Pavelka [28,46,64].*

Seeking the correct form of the evolution equation for entropy s, Grmela, Klika, and Pavelka [44] propose a "reduction path" from the fine scale, which makes some physical sense by referring to the fundamental phenomena of coercive motion. In ideal gases, these

https://doi.org/10.3390/en19020324

phenomena were studied by Boltzmann, Grad, Chapman, Enskog, Fokker, and Planck. By separating the phenomena into those with different time scales, one can finally obtain the level equations of gas dynamics of turbulent flows, in which the evolution of entropy takes the following form (Grmela, Klika and Pavelka [64]):

$$\partial_t s = -\mathrm{div}\,(sH_{\vec{p}}) - \mathrm{div}\left(\int \eta \frac{\partial H_f}{\partial H_{\vec{p}}}\, dv\right) + \frac{1}{H_s}\int f \frac{\partial H_f}{\partial H_{\vec{p}}}\frac{\partial H_f}{\partial H_{\vec{p}}}\, dv. \tag{87}$$

In this equation, it is easy to isolate the convective term, the diffusion flux of entropy, and its production. The proposal by Grmela, Klika, and Pavelka is extremely attractive—it opens the door to Hamiltonian thermodynamics. Unfortunately, in nature, there are no easy discoveries. Here, although we achieve an extremely suggestive and physically justified entropy evolution equation, we must close the four-state parameter system $x = (\rho, \vec{p}, s, f)$ with an additional evolution equation for the scattering function f, e.g., in the form of the Fokker–Planck equations [28].

The great advantage of these evolutionary equations $\partial_t x$, proposed by the aforementioned authors, is the first thermodynamically consistent (coherent) system of turbulent fluid evolution in the literature. By "coherent", we mean consistent with a uniform time scale in which, after exceeding a critical turbulent energy threshold, turbulent fluxes of specific volume, specific momentum, and specific entropy naturally emerge. The most valuable term is the entropy production term, about which thermodynamics is usually silent or told fairy tales. This term, recalled by Clausius in 1854 as "uncompensated heat transformation" (unkompensierte Verwandlung), is the most rotten root in the foundations of thermodynamics.

22. Water Flow Undergoing a "Flashing" Phase Transition

Flashing is the rapid evaporation of hot water ($t \geq 100$ °C) and, like cold water cavitation, is induced by a local decrease in pressure below the saturation pressure. Under equilibrium conditions, knowing the pressure and temperature, one can determine the equilibrium degree of filling ξ_{eq} from the internal energy, while the non-equilibrium of the phenomenon and its depth of entry into a metastable state is determined by the non-equilibrium degree of filling with steam $\xi \in (0, 1)$. It is a function of spatial variables (position in the channel) and time. The moment of the beginning of the evolution $\partial_t \xi \to 0$ is determined by a special closure resulting from the critical overheating of water, determined empirically (Bilicki and Kestin [65]). The Hamiltonian of the system has the following form:

$$\begin{gathered}\mathcal{H} = \iiint_\Omega H(\rho, \xi_{eq}, s, \vec{p},\ \xi, \nabla\xi)\, d\Omega = \\ \iiint_\Omega \left(H(\rho, s, \vec{p}) + \alpha(\xi - \xi_{eq})^2 + \beta(\xi - \xi_{eq})^4 + \kappa(\nabla\xi)^2\right)\, d\Omega,\end{gathered} \tag{88}$$

where, alongside the classical Hamiltonian, there is a contribution to the stored energy, which is controlled by three constants: $\alpha, \beta,$ and κ. This means that the energy parameter of the state is the vector $x = (\rho, \vec{p}, s, \xi)$. The evolution of the parameter ξ (from water to steam) is described by three elements: convection, diffusion, and relaxation to equilibrium, as follows:

$$\partial_t \xi = -\mathrm{div}\,(\xi H_{\vec{p}}) - \mathrm{div}\,(\vec{e}_\xi) - \Gamma H_\xi, \tag{89}$$

which should be corresponding to the composition of three Poisson brackets:

$$\partial_t \xi = \{\xi, H\}_C + \{\xi, H\}_D + \{\xi, H\}_{Relax}. \tag{90}$$

https://doi.org/10.3390/en19020324

The following definitions occur:

$$H_\xi = \delta_\xi H = \frac{\delta H}{\delta \xi} = \frac{\partial H}{\partial \xi} - \mathrm{div}\left(\frac{\partial H}{\partial(\nabla \xi)}\right) \tag{91}$$

where, due to the presence of the gradient ξ, defined as $\mathrm{grad}\xi \equiv \nabla\xi$ in the Hamiltonian, the derivative with respect to ξ takes the form of a Volterra variational derivative. In the literature, the quantity H_ξ is called affinity $H_\xi \equiv \mathcal{A}$. The quantity $\vec{e}_\xi$ in Equation (89) is called the diffusion effort of the pair (e_R, f_R) (see Equation (79)) and corresponds to its diffusion flux $\vec{f}_\xi = \mathrm{grad}(\mathcal{A}) = \mathrm{grad}H_\xi$:

$$\vec{e}_\xi = \frac{\partial \mathcal{R}(\vec{f}_\xi)}{\partial \vec{f}_\xi} \equiv \frac{\partial^2 \mathcal{R}(\vec{f}_\xi)}{\partial \vec{f}_\xi \otimes \partial \vec{f}_\xi} \vec{f}_\xi = \overleftrightarrow{S}^\xi \vec{f}_\xi. \tag{92}$$

It is based on diffusive Rayleighian $\mathcal{R}(\vec{f}_\xi) = \frac{1}{2}\overleftrightarrow{S}^\xi \cdot (\vec{f}_\xi \otimes \vec{f}_\xi)$. The corresponding dissipative bracket (Equation (89)) has the following form:

$$\{f, g\}_D = \iiint_\Omega \left(-\overleftrightarrow{S}^\xi \cdot \mathrm{grad}\,(f_\xi) \bigotimes \mathrm{grad}\,(g_\xi)\right) d\Omega, \tag{93}$$

which leads to dissipative evolution of the following type:

$$\partial_t \xi = \{\xi, H\}_D = -\mathrm{div}\,(\vec{e}_\xi) = -\mathrm{div}\left(\overleftrightarrow{S}^\xi\, \mathrm{grad}(H_\xi)\right). \tag{94}$$

This structure is known in the literature as the Cahn–Hilliard evolution. The phenological constants $\overleftrightarrow{S}^\xi$ are analogous to the diffusion constants of the Onsager diffusion model, which means a symmetric and positive definite matrix.

As for the relaxation bracket, it has a simple structure, as follows:

$$\{f, g\}_{Relax} = \iiint_\Omega (-\Gamma f_\xi g_\xi) d\Omega. \tag{95}$$

which allows us to calculate the relaxation evolution as follows:

$$\partial_t \xi = \{\xi, H\}_{Relax} = -\Gamma H_\xi = -\Gamma\left(\frac{\partial H}{\partial \xi} - \mathrm{div}\left(\frac{\partial H}{\partial(\nabla \xi)}\right)\right). \tag{96}$$

The parameter $\Gamma > 0$ is the inverse of the relaxation time of the phenomenon (Bilicki and Kestin [65]) and is determined based on the relaxation Rayleighian, $\mathcal{R}(H_\xi) = \frac{1}{2}\Gamma(H_\xi)^2$, through derivatives $\Gamma = \frac{\partial^2 \mathcal{R}}{\partial H_\xi \partial H_\xi}$.

The convective bracket, in the part corresponding to the parameter ξ, has the following form:

$$\{f, g\}_C = \iiint_\Omega (\xi \mathrm{grad}\,(f_\xi) \cdot (g_{\vec{p}})) d\Omega. \tag{97}$$

which allows to calculate convective evolution as follows:

$$\partial_t \xi = \{\xi, H\}_C = -\mathrm{div}\,(\xi H_{\vec{p}}). \tag{98}$$

The evolution of the entire state vector $x = (\rho, \vec{p}, s, \xi)$ is described by a family of variational derivatives $e_s = (H_\rho \quad H_{\vec{p}} \quad H_s \quad H_\xi)$. The contribution to the structure matrix

https://doi.org/10.3390/en19020324

and resistance matrix derived from the evolutionary Equations (94), (96) and (98) and from the appearance of the variational force H_ξ (Equation (91)) has the following form:

$$\partial_t \begin{pmatrix} \rho \\ \overrightarrow{p} \\ s \\ \xi \end{pmatrix} = \begin{bmatrix} 0 & 0 & 0 & 0 \\ 0 & 0 & 0 & J^*_{\xi \overrightarrow{p}} \\ 0 & 0 & 0 & J^*_{\xi s} \\ 0 & J_{\xi \overrightarrow{p}} & J_{\xi s} & 0 \end{bmatrix}_{6\times 6} \begin{pmatrix} H_\rho \\ H_{\overrightarrow{p}} \\ H_s \\ H_\xi \end{pmatrix} - \begin{bmatrix} 0 & 0 & 0 & 0 \\ 0 & 0 & 0 & R_{\xi \overrightarrow{p}} \\ 0 & 0 & 0 & R_{\xi s} \\ 0 & R_{\xi \overrightarrow{p}} & R_{\xi s} & R_{\xi\xi} \end{bmatrix}_{6\times 6} \begin{pmatrix} H_\rho \\ H_{\overrightarrow{p}} \\ H_s \\ H_\xi \end{pmatrix}. \tag{99}$$

This corresponds to the structure (Equation (35)) $\dot{x} = [\mathcal{J} - R]\delta_x H(x)$ in which the structure matrix $\mathcal{J}$ and the resistance matrix R have the dimensions 6×6. Additionally, as follows from Equations (93) and (95), the resistance matrix has the traditional form $R = G_R S G_R^T$. Obviously, the complete set of evolutionary equations, taking into account convection, resistance, and relaxation, is a full combination of Equations (76), (83), (87) and (99). It is important that the introduction of the variational effort H_ξ, despite spatial derivatives reaching the fourth order, allows for discretization that will not destroy the structure of the problem and will preserve the identity of the matrices $\mathcal{J}$ and R.

Remark 15. *A few remarks are necessary here. The structure of Equation (99) shows the power of pH thermodynamics formalism. In order to preserve the essence of pH thermodynamics, i.e., the skew symmetry of the Stokes–Dirac matrix $\mathcal{J}$ and the symmetry of the resistance matrix R, it was necessary to introduce couplings $J^*_{\xi \overrightarrow{p}}$ in the momentum evolution equation. Classical non-equilibrium thermodynamics knows nothing about this fact. It can be explained as follows: affinity H_ξ, determined by the variational derivative (91), contributes to the energy storage H (Equation (88)) through the constant κ interpreted as the surface tension of a vapor bubble. The continuous contribution of millions of bubbles per unit volume can be expressed as elastic shear stress in a fluid medium:*

$$\overleftrightarrow{\pi} = (\text{grad}\, \xi) \bigotimes \frac{\partial H}{\partial(\nabla \xi)}, \tag{100}$$

which leads, by supplementing the thermodynamic pressure in Equation (72), to the divergence of pressure being the divergence of the pressure dyad, as follows: $div(-p \overleftrightarrow{I}) \rightarrow div(-p \overleftrightarrow{I} + \overleftrightarrow{\pi})$. The induced stress $\overleftrightarrow{\pi}$ has a certain analogy here with the capillary stress introduced by Korteweg in 1901, but on completely different assumptions. In the present work, we rely on gradients $\nabla\xi$, while Korteweg relied on $\nabla\rho$.

Similarly, a dissipative term $R_{\xi \overrightarrow{p}}$, about which little is known in non-equilibrium thermodynamics, can be introduced into the system. It can be interpreted as turbulent momentum transport induced by phase transition—that is, it would be an additional Reynolds turbulent stress tensor.

However, not much is known about the contribution of convective heat transport $J_{\xi s}$ induced by phase transition H_ξ and turbulent heat transport $R_{\xi s}$ induced by the transition. Both of these quantities have physical meaning, although they have not yet been discovered by phenomenological nonequilibrium thermodynamics. The pH thermodynamics formalism immediately addresses this issue, demanding new experimental research.

The contribution $R_{\xi\xi}$, as stated in Equations (94) and (96) consists of dissipative elements whose magnitude is determined by the matrix $\overleftrightarrow{S}^{\xi}$ and the relaxation coefficient Γ.

To summarize point 22, the formalism of pH thermodynamics, applied to a specific example of a well-known phase transition flow, opens up a "thermodynamic treasure trove" of new issues to be solved. First, we need to completely rebuild the entropy evolution equation, and the Grmela Equation (87) provides a certain clue.

https://doi.org/10.3390/en19020324

23. Applications of pH Thermodynamics Formalism in Power Systems

The question remains whether pH control is used in engineering and technology. It is well-known that technical thermodynamics is the basis for the design, monitoring, and regulation of various types of power plants (Szewalski [66]). However, a new challenge for control and regulation theory has recently emerged in connection with the dominance of renewable and decentralized energy sources on the market. New necessities have also emerged, such as electric vehicles and AI electronics. In formulating the principles of control theory, a new situation is arising in which, due to the use of energy storage in renewable power plants, it is necessary to rebuild the foundations of control theory and control methods. Port-Hamiltonian systems are most widely used in power plants, where they are the best tool for optimizing operations and maximizing financial profits.

An overview of the applications of pH systems for systems including wind turbines, fuel cells, photovoltaic modules, as well as electrical, thermal, chemical, and other energy storage systems is presented in the work of Tönso, Kapain and Belikov [67], which demonstrates the practical potential of the pH formalism and its advantages in terms of approaches to control theory. This is not surprising, as the pH energy formalism is dedicated to this part of the economy.

However, studies of these individual applications lead to an unpleasant conclusion. The state of development of pH models in specific applications raises concerns and fears, as each of these models has an apparatus created for its own limited needs. This means that the physical foundations of pH formalism are insufficient, inconsistent, limited, opaque, non-universal, non-interdisciplinary, and perhaps also non-thermodynamic. However, works dedicated to specific situations (for instance, [48,68–72]) allow for the development of practical tools and contribute to the development of theoretical foundations.

24. Prospects and Open Issues

This paper is summarized in Table 1 and Figure 2. Table 1 lists the efforts, fluxes, energy variables, and control equations for the three fluid models discussed in the paper: Euler fluid, Navier fluid, and flashing flow.

Table 1. List of the efforts, fluxes, energy variables, and control equations for the three fluid models discussed in the paper.

	Effort	**Flux**	**Energetic Variable**	**Control Equation**
Euler fluid	$e_s = \begin{pmatrix} H_\rho \\ H_{\vec{v}} \\ H_s \end{pmatrix}$	$f_s = \partial_t \begin{pmatrix} \rho \\ \vec{v} \\ s \end{pmatrix}$	$x = \left(\rho,\ \vec{p}\right)$	Equation (57)
Navier fluid	$e_s = \begin{pmatrix} H_\rho \\ H_{\vec{v}} \\ H_s \end{pmatrix}$	$f_s = \partial_t \begin{pmatrix} \rho \\ \vec{v} \\ s \end{pmatrix}$	$x = \left(\rho,\ \vec{p}, s\right)$	Equation (80)
Flashing flow	$e_s = \begin{pmatrix} H_\rho \\ H_{\vec{v}} \\ H_s \\ H_\xi \end{pmatrix}$	$f_s = \partial_t \begin{pmatrix} \rho \\ \vec{v} \\ s \\ \xi \end{pmatrix}$	$x = \left(\rho,\ \vec{p}, s, \xi\right)$	Equation (99)

Figure 2 shows control system containing four ports: port (f_s, e_s), which connects to an ideal energy storage device $\mathcal{S}$, port $(f_R,\ e_R)$, corresponding to the dissipation of available energy $\mathcal{R}$, port $\left(f_\xi, e_\xi\right)$, corresponding structural changes such as combustion, phase transition, turbulence, plasticity, etc., and external port (f_∂, e_∂), through which the system interacts with the environment $\mathcal{E}n$ (including the operation called "control").

https://doi.org/10.3390/en19020324

This paper provides an answer to the following question: is it possible to formulate thermodynamics in a way that follows from Hamilton and Rayleigh's formalism based on two new concepts: "available energy storage" and "energy lost" during flow between energy ports. From technical practice and the observation of nature, it is known that ideal energy stores are not possible, nor are systems that only destroy available energy. Technical reality is an unrecognized composition of reversible and irreversible phenomena governed jointly by inertia and coercion. The thermodynamics of port-Hamiltonian formalism attempts to combine these two phenomena, but gives priority to reversible phenomena in mathematical formalism. The most popular model is the additive combination of phenomena through the difference between the $\mathcal{J} - R$ matrices. This model is accepted by control theory, but is not necessarily correct from the point of view of pH thermodynamics.

In other words, the additive combination of "reversibility" and "irreversibility" is a temporary solution that completely misses the needs of pH thermodynamics. It is important to remember that we live in an age dominated by additively manufactured materials, which are purpose-built materials. Their design is controlled to meet the new goals facing technology. When designing these materials, there is a constant need to refine models, including thermodynamic ones. This opens up opportunities for the pH thermodynamics approach, which shows promise in this field. We need to look for new, general Poisson brackets that will not only repeat rusty patterns, but will also reach for qualitatively new elements (e.g., see Edwards and Beris [73]). The latest literature review contained in Cardoso-Ribeiro et al. [74] confirms the dynamic development towards new applications and completely new "structure-preserving" numerical methods. However, this review is not conducted from the point of view of thermodynamics, which is why our article is a modest attempt to supplement this state of affairs and point out existing gaps and inconsistencies.

The recent revision of thermodynamics by Arjan van der Schaft [2] exposes the fundamental concepts of classical thermodynamics (technical and non-equilibrium), thereby enabling a new framework for integrating thermodynamics with system modeling and control. This thermodynamics integrated with control theory is called pH thermodynamics. Van der Schaft also shows that systems and control theory is a natural requirement for a radically new formulation and understanding of classical thermodynamics. In particular, pH thermodynamics places the theory of dissipativity, as it were, at the level of the First and Second Laws of Thermodynamics from the outset. It is pH thermodynamics that allows, for the first time in the literature, a field-theoretical approach to the properties of the state and dynamics of control systems.

On the other hand, thanks to pH thermodynamics, it turns out that not everything in the current control theory is consistent. It turns out that pH thermodynamics provides premises and arguments for radical paradigm shifts in systems and control; in particular, for the use of non-minimal state space formulations and a geometric view of them. Moreover, while systems and control theory was based primarily on linear systems with quadratic cost criteria, in accordance with basic models of systems in electrical and mechanical engineering (RLC circuits, mass-spring-damper systems, etc.) [28,32,39,40], pH thermodynamics requires research tools that go beyond this linear–quadratic paradigm.

Author Contributions: Conceptualization, J.B.; methodology, J.B.; formal analysis, J.B.; investigation, J.B. and P.J.Z.; writing—original draft preparation, J.B.; writing—review and editing, J.B. and P.J.Z.; supervision, J.B.; project administration, J.B.; funding acquisition, J.B. All authors have read and agreed to the published version of the manuscript.

Funding: This research received no external funding.

Data Availability Statement: The original contributions presented in the study are included in the article, further inquiries can be directed to the corresponding author.

Conflicts of Interest: The authors declare no conflicts of interest.

References

1. Rashad, R.; Califano, F.; van der Schaft, A.J.; Stramigioli, S. Twenty years of distributed port-Hamiltonian systems: A literature review. *IMA J. Math. Control Inform.* **2020**, *37*, 1400–1422.
2. van der Schaft, A.J. Classical thermodynamics revisited: A systems and control perspective. In *IEEE Control Systems Magazine*; IEEE: New York, NY, USA, 2021; Volume 41, pp. 32–60.
3. Grmela, M.; Pavelka, M. Classical and Multiscale Non-equilibrium Thermodynamics. *arXiv* **2025**, arXiv:2510.00610v1. [CrossRef]
4. Maschke, B.; van der Schaft, A.J. Port-controlled Hamiltonian systems: Modelling origins and system theoretic properties. In *Nonlinear Control Systems (NOLCOS 2004), Proceedings of the 2nd IFAC Symposium, Bordeaux, France, 4–26 June 1992*; Fliess, M., Ed.; Elsevier: Amsterdam, The Netherlands, 1993; pp. 359–365.
5. van der Schaft, A.J.; Maschke, B.M. Hamiltonian formulation of distributed-parameter systems with boundary energy flow. *J. Geom. Phys.* **2002**, *42*, 166–194. [CrossRef]
6. Ortega, R.; van der Schaft, A.J.; Maschke, B.; Escobar, G. Interconnection and damping assignment passivity-based control of port-controlled Hamiltonian systems. *Automatica* **2002**, *38*, 585–596. [CrossRef]
7. Krhac, K.; Maschke, B.; van der Schaft, A.J. Port-Hamiltonian systems with energy and power ports. In Proceedings of the 8th IFAC Symposium on Lagrangian and Hamiltonian Methods in Nonlinear Control (LHMNC 2024), Besancon, France, 10–12 June 2024.
8. van der Schaft, A.J.; Jeltsema, D. On energy conversion in port-Hamiltonian systems. In Proceedings of the 60th IEEE Conference on Decision and Control (CDC), Austin, TX, USA, 13–17 December 2021; pp. 2421–2427.
9. Duindam, V.; Macchelli, A.; Stramigioli, S.; Bruyninckx, H. *Modeling and Control of Complex Physical Systems: The Port-Hamiltonian Approach*; Springer: Berlin/Heidelberg, Germany, 2009; pp. 1–423.
10. Rashad, R.; Califano, F.; Schuller, F.P.; Stramigioli, S. Port-hamiltonian modeling of ideal fluid flow: Part I. foundations and kinetic energy. *J. Geom. Phys.* **2021**, *164*, 104201. [CrossRef]
11. Rashad, R.; Califano, F.; Schuller, F.P.; Stramigioli, S. Port-hamiltonian modeling of ideal fluid flow: Part II. compressible and incompressible flow. *J. Geom. Phys.* **2021**, *164*, 104199. [CrossRef]
12. Califano, F.; Rashad, R.; Schuller, F.P.; Stramigioli, S. Geometric and energy-aware decomposition of the Navier–Stokes equations: A port-Hamiltonian approach. *Phys. Fluids* **2021**, *33*, 047114.
13. Brugnoli, A.; Alazard, D.; Pommier-Budinger, V.; Matignon, D. A Port-Hamiltonian formulation of linear thermoelasticity and its mixed finite element discretization. *J. Therm. Stress.* **2021**, *44*, 643–661. [CrossRef]
14. Jäschke, J.; Ehrhardt, M.; Günther, M.; Jacob, B. A Two-Dimensional port-Hamiltonian Model for Coupled Heat Transfer. *Mathematics* **2022**, *10*, 4635.
15. Cardoso-Ribeiro, F.L.; Matignon, D.; Pommier-Budinger, V. Port-Hamiltonian model of two-dimensional shallow water equations in moving containers. *IMA J. Math. Control Inform.* **2020**, *37*, 1348–1366.
16. Altmann, R.; Schulze, P. A port-Hamiltonian formulation of the Navier–Stokes equations for reactive flows. *Syst. Control Lett.* **2017**, *100*, 51–55.
17. Ramirez, H.; Le Gorrec, Y. An overview on irreversible port-Hamiltonian systems. *Entropy* **2022**, *24*, 1478. [CrossRef] [PubMed]
18. Ramirez, H.; Le Gorrec, Y.; Maschke, B. Boundary controlled irreversible port-Hamiltonian systems. *Chem. Eng. Sci.* **2022**, *248*, 117107. [CrossRef]
19. Mora, L.A.; Le Gorrec, Y.; Matignon, D.; Ramirez, H. Irreversible port-Hamiltonian modelling of 3D compressible fluids. *IFAC Papers OnLine* **2023**, *56*, 6394–6399. [CrossRef]
20. Pommaret, J.-F. From Kalman to Einstein and Maxwell: The Structural Controllability Revisited. *Adv. Pure Math.* **2025**, *15*, 570–628. [CrossRef]
21. Pommaret, J.-F. Nonlinear Conformal Gravitation. *J. Mod. Phys.* **2023**, *14*, 1464–1496. [CrossRef]
22. Alicki, R.; Koslof, R. Introduction to Quantum Thermodynamics: History and Prospects. *arXiv* **2019**, arXiv:1801.08314.
23. Beris, A.N.; Edwards, B.J. Dissipation in nonequilibrium thermodynamics and its connection to the Rayleighian functional. *Phys. Fluids* **2024**, *36*, 013102. [CrossRef]
24. Grmela, M. Roles of energy and entropy in multiscale dynamics and thermodynamics. *J. Phys. Commun.* **2024**, *8*, 072001. [CrossRef]
25. Sípka, M.; Pavelka, M.; Esen, O.; Grmela, M. Direct Poisson neural networks: Learning nonsymplectic mechanical systems. *J. Phys. A Math. Theor.* **2023**, *56*, 495201.

26. Sýkora, M.; Pavelka, M.; Peshkov, I.; Minakowski, P.; Klika, V.; Romenski, E. Comparison of the symmetric hyperbolic thermodynamically compatible framework with Hamiltonian mechanics of binary mixtures. *Contin. Mech. Thermodyn.* **2024**, *36*, 539–559. [CrossRef]
27. Pavelka, M.; Klika, V.; Grmela, M. *Multiscale Thermo-Dynamics*; de Gruyter: Berlin, Germany, 2018.
28. Pommaret, J.-F. *Partial Differential Control Theory*; Kluwer: Dordrecht, The Netherlands, 2001; Volume VIII, p. 957.
29. Badur, J.; Dudda, W. From the Cosserat continuum backgrounds to modern field theory. *Tech. Sci.* **2024**, *27*, 211–264.
30. Yahalom, A. Gravitational Hamiltonian Systems and the Retarded Gravity Inequality. *Entropy* **2024**, *26*, 986. [CrossRef]
31. Tong, D. Classical Dynamics, University of Cmbridge Part II Mathematical Tripos. 2004. Available online: http://www.damtp.cam.ac.uk/user/tong/dynamics.html (accessed on 28 October 2025).
32. Gawroński, W. *Advances Structural Dynamics and Active Control of Structures*; Springer: Berlin/Heidelberg, Germany, 2004; p. 396.
33. Grmela, M.; Öttinger, H.C. Dynamics and thermodynamics of complex fluids. I. Development of a general formalism. *Phys. Rev. E* **1997**, *56*, 6620–6632. [CrossRef]
34. Zafferi, A.; Peschka, D.; Thomas, M. GENERIC framework for reactive fluid flows. *Z. Angew. Math. Mech.* **2023**, *103*, e202100254.
35. Grmela, M. Bracket formulation of diffusion-convection equations. *Phys. D* **1986**, *21*, 179–212.
36. Grmela, M. Thermodynamics and Rate Thermodynamics. *J. Stat. Phys.* **2024**, *191*, 75. [CrossRef]
37. Grmela, M. Rheological modeling with GENERIC and with the Onsager principle. *arXiv* **2025**, arXiv:2507.22144. [CrossRef]
38. Morrison, P.J. Hamiltonian Description of the Ideal Fluid. *Rev. Mod. Phys.* **1998**, *70*, 467–521. [CrossRef]
39. Ogata, K. *Modern Control Engineering*; Prentice Hall: Hoboken, NJ, USA, 1997.
40. Mieloszyk, E. *Rachunek Operatorów w Zagadnieniach Uogólnionych Układów Dynamicznych*; Wyd. Politechniki Gdańskiej: Gdańsk, Poland, 1999.
41. Mielke, A. Formulation of thermoelastic dissipative material behavior using GENERIC. *Contin. Mech. Thermodyn.* **2011**, *23*, 233–256. [CrossRef]
42. Pommaret, J.-F. Minimum Parametrization of the Cauchy Stress Operator. *arXiv* **2023**, arXiv:2101.03959. [CrossRef]
43. Badur, J. *Eternal Noether's Symmetries*; IMP Press: Gdańsk, Poland, 2021; pp. 1–514.
44. Sieniutycz, S.; Berry, R.S. Conservation laws from Hamilton's principle for nonlocal thermodynamic equilibrium fluids with heat flow. *Phys. Rev. A* **1989**, *40*, 348–361. [CrossRef] [PubMed]
45. Nevir, P.; Blender, R. A Nambu representation of incompressible hydrodynamics using helicity and enstrophy. *J. Phys. A Math. Gen.* **1993**, *26*, 1189–1193. [CrossRef]
46. Blender, R.; Badin, G. Hydrodynamic Nambu Brackets derived by Geometric Constraints. *J. Phys. A* **2015**, *48*, 105501.
47. Sato, N. Generalization of Hamiltonian mechanics to a three-dimensional phase space. *Prog. Theor. Exp. Phys.* **2021**, *2021*, 063A01. [CrossRef]
48. Brugnoli, A. A Port-Hamiltonian Formulation of Flexible Structures. Ph.D. Thesis, Universite de Toulouse, Toulouse, France, 2020.
49. Mielke, A.; Peletier, M.A.; Zimmer, J. Deriving a GENERIC system from a Hamiltonian system. *arXiv* **2024**, arXiv:2404.09284. [CrossRef]
50. Maschke, B.M.; Kirchhhoff, J. Port maps of irreversible port-Hamiltonian systems. *IFAC-Papers OnLine* **2023**, *56*, 6796–6800.
51. Badur, J.; Ziółkowski, P.; Ziółkowski, P.J. On angular velocity slip in nanoflows. *Microfluid. Nanofluid.* **2015**, *19*, 191–199.
52. Mehrmann, V.; Unger, B. Control of port-Hamiltonian differential-algebraic systems and applications. *Acta Numer.* **2023**, *32*, 395–515.
53. Pavelka, M. Multiscale Geometric Approach to Continuum Mechanics and Thermodynamics. Habilitation Thesis, Faculty of Mathematics and Physics, Charles University, Prage, Czech Republic, November 2021.
54. Szücs, M.; Pavelka, M.; Kovács, R.; Fülöp, T.; Ván, P.; Grmela, M. A case study of non-Fourier heat conduction using internal variables and GENERIC. *J. Non-Equilib. Thermodyn.* **2021**, *47*, 31–60. [CrossRef]
55. Truesdell, C.; Toupin, R. The classical field theories. In *Handbuch der Physik*; Flügge, S., Ed.; Springer: Berlin/Heidelberg, Germany, 1960; Volume III/1, pp. 226–793.
56. Bendimerad-Hohl, A.; Haine, G.; Matignon, D.; Maschke, B. Structure-preserving discretization of a coupled Allen-Cahn and heat equation system. *IFAC Papers OnLine* **2022**, *55*, 99–104.
57. Euler, L. Principia motus fluidorum, Opera Omnia Series 2. *Novi Comment. Acad. Sci. Petropolitanae* **1752**, *12*, 133–168.
58. von Helmholtz, H. Over integrals of the hydrodynamic equations, which correspond to eddy movements. *J. Reine Angew. Math.* **1858**, *55*, 22–55.
59. Clebsch, A. Ueber die Integration der hydrodynamischen Gleichunge. *J. Reine Angew. Math.* **1859**, *56*, 1–10.
60. Bateman, H. Notes on a Differential Equation Which Occurs in the Two-Dimensional Motion of a Compressible Fluid and the Associated Variational Problems. *Proc. R. Soc. London* **1929**, *125*, 598–618.
61. Eckart, C.H. The electrodynamics of material media. *Phys. Rev.* **1938**, *54*, 920–923.

62. Sanders, J.W.; DeVoria, A.C.; Washuta, N.J.; Elamin, G.A.; Skenes, K.L.; Berlinghieri, J.C. A canonical Hamiltonian formulation of the Navier–Stokes problem. *J. Fluid Mech.* **2024**, *984*, A27. [CrossRef]
63. Badur, J.; Ochrymiuk, T.; Kowalczyk, T.; Dudda, W.; Ziółkowski, P. From fluid mechanics backgrounds to modern field theory. *Acta Mech.* **2022**, *223*, 3453–3465. [CrossRef]
64. Grmela, M.; Klika, V.; Pavelka, M. Gradient and GENERIC time evolution towards reduced dynamics. *Phil. Trans. R. Soc. A* **2020**, *378*, 20190472.
65. Bilicki, Z.; Kestin, J. Physical aspects of the relaxation model in two-phase flow. *Proc. R. Soc. London Ser. A.* **1990**, *428*, 379–397.
66. Szewalski, R. Zjawisko Drobnych Drgań Regulatora i Jego Znaczenie dla Dynamiki Sprawności Regulacji. Ph.D. Thesis, Wydział Mechaniczny, Politechnika Lwowska, Lwów, Ukraine, 1935.
67. Tönso, M.; Kapain, V.; Belikov, J. Port-Hamiltonian framework in power systems domain: A survey. *Energy Rep.* **2023**, *10*, 2918–2930. [CrossRef]
68. Wang, Y.; Sun, Z.; Li, P.; Ai, J.; Wu, C.; Shen, Z.; Deng, F. A Port-Hamiltonian Perspective on Dual Active Bridge Converters: Modeling, Analysis, and Experimental Validation. *Energies* **2025**, *18*, 5197. [CrossRef]
69. Rettberg, J.; Wittwar, D.; Buchfink, P.; Brauchler, A.; Ziegler, P.; Fehr, J. Port-Hamiltonian fluid–structure interaction modelling and structure-preserving model order reduction of a classical guitar. *Math. Comput. Model. Dyn. Syst.* **2023**, *29*, 116–148. [CrossRef]
70. Lasarzik, R. Analysis of a thermodynamically consistent Navier-Stokes-Cahn-Hilliard model. *Nonl. Anal.* **2021**, *213*, 112526. [CrossRef]
71. Pavelka, M.; Peshkov, I.; Klika, V. On Hamiltonian continuum mechanics. *J. Phys. D Nonlinear Phenom.* **2020**, *408*, 132510.
72. Kekana, M.; Badur, J. An analysis of a piezo-elastic restrictors using a capacitive shunt. *TASK Quaterly* **2004**, *8*, 377–384.
73. Edwards, J.; Beris, A.N. Unified view of transport phenomena based on the generalized bracket formulation. *Ind. Eng. Chem. Res.* **1991**, *30*, 873–881. [CrossRef]
74. Cardoso-Ribeiro, F.L.; Haine, G.; Le Gorrec, Y.; Matignon, D.; Ramirez, H. Port-Hamiltonian formulations for the modelling, simulations and control of fluids. *Comput. Fluids* **2024**, *283*, 106407. [CrossRef]

Disclaimer/Publisher's Note: The statements, opinions and data contained in all publications are solely those of the individual author(s) and contributor(s) and not of MDPI and/or the editor(s). MDPI and/or the editor(s) disclaim responsibility for any injury to people or property resulting from any ideas, methods, instructions or products referred to in the content.

MDPI AG
Grosspeteranlage 5
4052 Basel
Switzerland
Tel.: +41 61 683 77 34

Energies Editorial Office
E-mail: energies@mdpi.com
www.mdpi.com/journal/energies



Disclaimer/Publisher's Note: The title and front matter of this reprint are at the discretion of the Guest Editors. The publisher is not responsible for their content or any associated concerns. The statements, opinions and data contained in all individual articles are solely those of the individual Editors and contributors and not of MDPI. MDPI disclaims responsibility for any injury to people or property resulting from any ideas, methods, instructions or products referred to in the content.





Academic Open
Access Publishing

mdpi.com

ISBN 978-3-7258-8404-9